Mechanics-based approaches for the flexural and shear behaviour of ultra-high performance fibre reinforced concrete beams

by

Alexander Bonaparte Sturm

Thesis submitted for the degree of Doctor of
Philosophy at The University of Adelaide
(The School of Civil, Environmental and
Mining Engineering)
Australia

-July 2020-

TABLE OF CONTENTS

ABSTRACT

This thesis presents a series of journal articles outlining a mechanics-based analysis approach for the flexural and shear behaviour of ultra-high performance fibre reinforced concrete beams. These solutions apply the mechanical principles of partial interaction, shear friction and segmental analysis to the design of fibre reinforced concrete (FRC) and ultra-high performance fibre reinforced concrete (UHPFRC) beams. The analysis techniques are developed for both normal strength FRC and UHPFRC, which is important as these materials have in the past often treated separately, but should be treated together the mechanical principles do not change, rather only the material properties. Further, because of their mechanics foundation, these approaches can also be applied to conventional reinforced concrete without modification by simply ignoring all terms relating to fibre properties.

In the first part of this thesis the bond, tension and shear friction properties of UHPFRC are obtained through material testing. A significant part of this research is the development of a new apparatus for determining the shear friction properties. The development of this apparatus is important as it allows for the precise control of the confining force applied to the shear plane and because tests can be conducted using standard cylinders, it allows for rapid, low-cost testing of the large number of samples required to understand the impact of different fibre types and volumes.

In the second part of the thesis closed form mechanics solutions are developed for the tension stiffening properties including crack spacing and the crack opening stiffness. These are then used to develop closed form solutions for the deflections and crack widths at the serviceability limit state.

Next, experimental work is conducted to investigate the impact of hybridising fibres by testing UHPFRC beams with varying cross sections and fibre types. This is followed by tests to investigate the impact of prestressing with either steel or fibre reinforced polymer (FRP) tendons. Having experimentally investigated this behaviour, a segmental analysis technique, is developed to predict deflections at all load levels and crack widths. Finally, closed-form solutions are developed for predicting moment redistribution behaviour of continuous reinforced concrete beams including those constructed of UHPFRC at all limit states.

Having investigated flexural performance at both the serviceability and ultimate limit state, a numerical and analytical approach which is mechanically consistent with the proposed flexural analysis is developed to predict member shear capacity. The solutions are validated against 31 tests, including two conducted by the author on UHPFRC I-sections in order to demonstrate accuracy compared to codified solutions and those available from the literature. Simplified solutions are then developed in a form which can be implemented in routine design.

In the final section of this thesis further applications of partial interaction theory are developed. In this section closed-form solutions are derived for FRP to substrate joints with and without anchors. In this section it is shown that the same theory used to analyse conventional, FRC and UHPFRC reinforcement can also be applied, without fundamental modification to predict the behaviour of FRP retrofitted sections.

STATEMENT OF ORIGINALITY

I certify that this work contains no material which has been accepted for the award of any other degree or diploma in my name, in any university or other tertiary institution and, to the best of my knowledge and belief, contains no material previously published or written by another person, except where due reference has been made in the text. In addition, I certify that no part of this work will, in the future, be used in a submission in my name, for any other degree or diploma in any university or other tertiary institution without the prior approval of the University of Adelaide and where applicable, any partner institution responsible for the joint-award of this degree.

I acknowledge that copyright of published works contained within this thesis resides with the copyright holder(s) of those works.

I also give permission for the digital version of my thesis to be made available on the web, via the University's digital research repository, the Library Search and also through web search engines, unless permission has been granted by the University to restrict access for a period of time.

I acknowledge the support I have received for my research through the provision of an Australian Government Research Training Program Scholarship.

9/07/2020

Alexander Sturm Date

LIST OF PUBLICATIONS

Journal Papers

Visintin, P., Sturm, A. B., Mohamed Ali, M. S. and Oehlers, D. J. (2018) "Blending macro and micro fibres to enhance the serviceability behaviour of UHPFRC." *Australian Journal of Civil Engineering*, 16(2), 106-121.

Sturm, A. B. and Visintin, P. (2019) "Local bond slip behaviour of steel reinforcing bars embedded in UHPFRC." *Structural Concrete*, 20(1), 108-122.

Sturm, A. B., Visintin, P., Farries, K. and Oehlers, D. J. (2018) "A new testing approach for extracting the shear friction material properties of ultra-high performance fibre reinforced concrete." *Journal of Materials in Civil Engineering*, 30(10), 04018235.

Sturm, A. B., Visintin, P., Oehlers, D. J. and Seracino, R. (2018) "Time dependent tension stiffening mechanics of fibre reinforced and ultra-high performance fibre reinforced concrete." *Journal of Structural Engineering*, 144(8), 04018122.

Sturm, A. B., Visintin, P., and Oehlers, D. J. (2019) "A rational design approach for the instantaneous and time dependent serviceability deflections and crack widths of FRC and UHPFRC continuous and simply supported beams." *Journal of Structural Engineering*, 145(11), 04019138.

Sturm, A. B., Visintin, P. and Oehlers. D. J. (2020) "Blending fibres to enhance the flexural properties of UHPFRC beams." *Construction and Building Materials*, 244, 118328.

Sturm, A. B., Visintin, P., Seracino, R., Lucier, G. W. and Oehlers, D. J. (2020) "Flexural performance of pretensioned ultra-high performance fibre reinforced concrete beams with CFRP tendons." *Composite Structures*, 243, 112223.

Sturm, A. B., Visintin, P. and Oehlers. D. J. (2020) "Closed form expressions for predicting moment redistribution in reinforced concrete beams with application to conventional concrete and UHPFRC." *Structural Concrete*, in press.

Sturm, A. B., Visintin, P., and Oehlers, D. J. (2020) "Mechanics of shear failure in fibre reinforced concrete beams." Submitted to *Journal of Structural Engineering*.

Sturm, A. B., Visintin, P., and Oehlers, D. J. (2020) "Design oriented solutions for the shear capacity of reinforced concrete beams with and without fibres." Submitted to *Journal of Structural Engineering*.

Vaculik, J., Sturm, A. B., Visintin, P. and Griffith, M. C. (2018) "Modelling FRP-to- substrate joints using the bilinear τ-δ rule with allowance for friction—Full-range analytical solutions for long and short bonded lengths." *International Journal of Solids & Structures*, 135, 245-260.

Sturm, A. B., Visintin, P., Vaculik, J., Oehlers, D. J., Seracino, R., and Smith, S. T. (2019) "Analytical approach for global load-slip behaviour of FRP plates externally bonded to brittle substrates with anchors." *Composites Part B: Engineering*, 160(2019), 177-194.

ACKNOWLEDGEMENTS

I wish to extend my sincere gratitude to Assoc. Prof. Phillip Visintin and Emeritus Prof. Deric Oehlers for their excellent supervision over the duration of my doctoral studies. I also wish to thank Prof. Rudolf Seracino for his hospitality when I visited North Carolina State University.

I also acknowledge my fellow co-authors Dr. Mohamed Ali, Dr. Jaroslav Vaculik, Prof. Scott Smith and Prof. Michael Griffith.

I acknowledge all those who assisted with the experimental portions of my research at the University of Adelaide including Mr. Kevin Farries, Mr. Jon Ayoub, Mr. Ian Ogier, Mr. Simon Holding, Dr. Fereydoon Pooya, Mr. Nicholas Burton, Mr. Dale Hodson and Mr. Adam Ryntjes.

I also acknowledge those who assisted with the experimental portions of my research at North Carolina State University including Dr. Gregory Lucier, Mr. Johnathan McEntire, Mr. Jerry Atkinson, Dr. Brad McCoy, Dr. Jordan Firth, Mr. Zakariya Bourara, Mr. Ye Zhang, Mr. Sheng-Hsuan Lin, Mr. Francisco Jativa, Mr. Oscar Santoyo, Mr. Luis Aguilar, Mr. Guillermo Gonzalez and Mr. Hussam Nimeh. I also wish to acknowledge the assistance of ST Wooten Corporation who provided the concrete truck and Tokyo Rope Corporation who provided the coupling system for the carbon fibre reinforced polymer reinforcement.

I also wish to acknowledge the Australian Government Research Training Program for my providing for my living expenses for the duration of my PhD. I also acknowledge the Air Force Office of Scientific Research as well as the Australian Research Council Discovery Project DP190102650 which funded the experimental work presented in this thesis.

Finally, I wish to express my gratitude to my parents Leila and Jeffrey. This thesis is dedicated to them.

INTRODUCTION & GENERAL OVERVIEW

This thesis outlines a mechanics-based approach for the flexural and shear behaviour of beams suitable for all types of fibre reinforced concrete (FRC) including ultra-high performance fibre reinforced concrete (UHPFRC). The approach is based on application of the mechanical principles of partial interaction, shear friction and segmental analysis. The direct application of these mechanics principles is significant as it allows for the development of solutions that can be adapted to any type of FRC with any type of reinforcement provided the basic material properties are known. These material properties are available from the following six basic tests: compression; tension; bond; shear friction; shrinkage and direct tension of the reinforcement removing the need for member level testing to calibrate empirical factors.

This thesis is a collection of manuscripts that are submitted, accepted or published in internationally recognised journals, where the titles of Chapters reflect the overall research outcomes. Each chapter takes the following format: an introduction explaining the key theory and results of the chapter, a list of all the manuscripts presented in the chapter, and finally the presentation of each manuscript.

The goal of the first chapter is to develop test methods to obtain the fundamental material properties of UHPFRC and demonstrate how to extract the material properties that are required for the member level research presented in the subsequent chapters. This is important due to the large number of potential combinations that arise from the different types of fibres available in various volumes. In the first paper 69 pullout tests are performed on reinforcement embedded in UHPFRC. These results are then combined with results from the literature to regress a material model for the bond stress-slip relationship. The second paper presents 18 direct tension and 18 tension stiffening tests which were performed to allow the validation of the models for the tension stiffening and the flexural behaviour. The third paper presents a novel testing apparatus for obtaining the direct shear properties of UHPFRC which uses standard concrete cylinders while allowing precise control of the confining stress across the shear plane. A series of 16 tests were then performed to obtain the frictional and cohesive components of the shear friction capacity for UHPFRC. These parameters are used later in the thesis to obtain the angle of the softening wedge which is an important parameter for simulating the flexural behaviour as well as to simulate the capacity of the critical shear crack to resist sliding under shear load.

The second chapter explores the flexural behaviour of UHPFRC at serviceability. The first paper investigates the tension stiffening behaviour of UHPFRC using partial interaction theory which involved developing closed form solutions for the crack spacing and crack opening stiffness. These were then validated on 39 tension stiffening tests. The solutions where then implemented within a segmental model to produce closed form solutions for the deflections and crack width at serviceability presented in the second paper. These solutions were then validated on 26 FRC and UHPFRC beam tests.

The third chapter explores the flexural behaviour of UHPFRC at the ultimate limit state. The first paper explores the effect of different types of fibres on UHPFRC beams. In this experimental study a beam and a slab cross-section are considered. Three mix designs were the fibres are varied. The first considers the case when hooked steel fibres are used, the second considers straight steel fibres and the third considers a 50:50 mix of the two fibres. A segmental analysis was then applied where partial interaction was applied to simulate the internal

reinforcement and shear friction was applied to simulate the concrete softening. The second paper explores the behaviour of UHPFRC beams pretensioned with carbon fibre reinforced polymer (CFRP) or steel tendons. Four beams are tested: two with CFRP tendons and two with steel tendons. A digital image correlation system is used to monitor the cracking. The deflections and crack widths are then predicted using the same segmental model utilised for the non-prestressed beams. The third paper in this section presents closed-form solutions for the moment redistribution of beams with varying flexural rigidities between the hogging and sagging regions. The ultimate moment redistribution is validated against 17 beams from the literature including 4 constructed from UHPFRC.

The fourth chapter presents two papers on predicting the shear capacity of FRC and UHPFRC beams. In the first numerical and analytical solutions are developed where the segmental method is applied to determine the sliding force along the critical shear crack and shear friction theory is applied to predict the capacity of the critical shear crack to resist this sliding force. This is validated against 31 shear beam tests where the accuracy of the proposed approach is proven against codified approaches as well as approaches from the literature. The second paper then simplifies these solutions into a form that could be applied in routine design.

The fifth chapter presents further applications of partial interaction theory that arose from exploring the mechanics of tension stiffening presented in the second chapter. The first paper presents a closed form solution that were developed for fibre reinforced polymer (FRP) to brittle substrate joints. These solutions are then used to calibrate the local bond-stress slip relationship based on the global load-slip response. The second paper in this chapter presents closed form solutions for the load-slip response of fibre reinforced polymer (FRP) to brittle substrate joints secured with anchors. This solution allows for both the contribution of the bond between the plate and the substrate as well as the anchors to the transfer of the interfacial shear stress. To avoid having to define many different solution cases this approach applies an innovative transfer matrix approach to solve this problem.

The final chapter then presents concluding remarks as well as possible avenues for future research. The possible extensions that are explored include the post-yield bond behaviour of steel reinforcement embedded in UHPFRC as well as the seismic behaviour of UHPFRC columns.

CHAPTER 1

Background

In this chapter the material behaviour of UHPFRC is explored to provide the inputs used in the subsequent chapters. The phenomena explored include bond between UHPFRC and reinforcement, tensile stress crack width behaviour of UHPFRC and shear friction cross cracked UHPFRC interfaces.

The first publication "Blending macro and micro fibres to enhance the serviceability behaviour of UHPFRC" presents an experimental study into the tension and tension stiffening behaviour of UHPFRC. The main parameter that is explored is the effect of using short straight or long hooked fibres on the material behaviour and whether improvements can be obtained by using a mixture of the two types of fibres.

The second publication "Local bond slip behaviour of steel reinforcing bars embedded in UHPFRC" presents an experimental study into the pullout behaviour of reinforcement embedded in UHPFRC. These results combined with other results available from the literature to regress a material model describing the bond stress-slip relationship. The effect of using short straight or long hooked fibres on the bond behaviour is also explored.

The third publication "A new testing approach for extracting the shear friction material properties of ultra-high performance fibre reinforced concrete" presents a novel testing apparatus for obtaining the shear friction properties of UHPFRC. The advantage of the new apparatus is that it utilises standard concrete cylinders and allows precise control of the confining stress across the shear plane. This test allows the frictional and cohesive components of the shear friction behaviour to be determined.

List of Manuscripts

Visintin, P., Sturm, A. B., Mohamed Ali, M. S. and Oehlers, D. J. (2018) "Blending macro and micro fibres to enhance the serviceability behaviour of UHPFRC." *Australian Journal of Civil Engineering*, 16(2), 106-121.

Sturm, A. B. and Visintin, P. (2019) "Local bond slip behaviour of steel reinforcing bars embedded in UHPFRC." *Structural Concrete*, 20(1), 108-122.

Sturm, A. B., Visintin, P., Farries, K. and Oehlers, D. J. (2018) "A new testing approach for extracting the shear friction material properties of ultra-high performance fibre reinforced concrete." *Journal of Materials in Civil Engineering*, 30(10), 04018235.

STATEMENT OF AUTHORSHIP

Blending macro and micro fibres to enhance the serviceability behaviour of UHPFRC
Australian Journal of Civil Engineering, 16(2), 106-121.

Visintin, P.

Supervised and contributed to research, and acted as corresponding author (35%)

I certify that the candidate's stated contribution to the publication is accurate (as detailed above); permission is granted for the candidate in include the publication in the thesis; and the sum of all co-author contributions is equal to 100% less the candidate's stated contribution.

Signed … …….. Date 07/07/2020

Sturm, A. B. (Candidate)

Prepared manuscript, performed all analyses, and developed model and theory (50%)

This paper reports on original research I conducted during the period of my Higher Degree by Research candidature and is not subject to any obligations or contractual agreements with a third party that would constrain its inclusion in this thesis. I am the primary author of this paper.

Signed Date 9/07/2020

Mohamed Ali, M. S.

Contributed to research (5%)

I certify that the candidate's stated contribution to the publication is accurate (as detailed above); permission is granted for the candidate in include the publication in the thesis; and the sum of all co-author contributions is equal to 100% less the candidate's stated contribution.

Signed Date …7th July 2020…….

Oehlers, D. J.

Supervised and contributed to research (10%)

I certify that the candidate's stated contribution to the publication is accurate (as detailed above); permission is granted for the candidate in include the publication in the thesis; and the sum of all co-author contributions is equal to 100% less the candidate's stated contribution.

Signed Date ….7/7/20….

BLENDING MACRO AND MICRO FIBRES TO ENHANCE THE SERVICEABILITY BEHAVIOUR OF UHPFRC

Visintin, P., Sturm, A. B., Mohamed Ali, M. S., Oehlers, D. J.

ABSTRACT

The incorporation of steel fibres into ultra-high performance fibre reinforced concrete (UHPFRC) leads to an overall improvement in the tensile and compressive ductility of the material. At the serviceability limit, fibres bridging cracks in the tension region, increase member stiffness and improve crack control. At the ultimate limit, fibres crossing concrete-to-concrete sliding panes increase compressive ductility and ultimate material strains. In this paper, a method is developed for assessing the effect of different fibre types on serviceability behaviour (tension stiffening and crack width), without the necessity of performing large-scale beam tests. As an example of this approach, a series of direct tension and tension stiffening tests are performed on UHPFRC with blended fibres to determine the optimal mix design. The direct tension and tension stiffening results are then used to predict the moment curvature behaviour of a beam allowing the direct comparison of each mix without the necessity of expensive beam tests.

INTRODUCTION

Previous experimental and analytical research has shown that the introduction of fibres into a mortar or concrete matrix can reduce deflections and crack widths at serviceability limit (Stang & Aare 1992) and improve the strength and ductility at ultimate limit (Schumacher 2006). This improvement arises due to the transfer of stresses across tensile cracks and concrete-to-concrete sliding planes.

The significant improvement in behaviour resulting from the addition of fibres, has seen much research devoted to the development of fibre reinforced concrete (FRC), a subset of FRC is Ultra-high performance fibre reinforced concrete (UHPFRC), which is characterised by very high compressive (AFGC 2013), tensile (Wille et al. 2014) and bond (Yoo et al. 2014) strengths, as well as high ductility (Wille et al. 2014). As a result of these material properties it has been suggested that UHPFRC is ideal for structures subjected to blast loading (Wu et al. 2009) and for bridge design applications (Russell & Graybeal 2013).

The design of FRC is complicated by the vast array of possible fibre shapes (such as straight, hooked end and crimped), sizes (6-60 mm) and materials (such as steel, PVA and polyolefin) and is further complicated as the blending of fibres can have synergistic effects (Banthia et al. 2014). That is, the behaviour of an FRC utilising a blend of fibres can be superior to that of an FRC with a single fibre type. Hence in this paper a methodology is presented for evaluating the potential serviceability behaviour of UHPFRC structural members using a variety of FRC mix designs to select the optimal combination of fibres. Importantly this can be done without having to perform full-scale beam tests as the range of possible mix designs to be investigated will be large. Specifically, the paper will focus on the influence of fibres in the tension region as it has previously been shown at this presence of fibres substantially improves behaviour at the serviceability limit (Schumacher 2006). That is, this paper will empirically investigate the influence of blending fibres on tension stiffening and crack formation and widening via a series of direct tension and tension stiffening tests on UHPFRC with blended fibres. It will then be shown how the results of these simple tests can be incorporated into a beam moment curvature model to investigate the material performance at a member level. It is envisaged that this will

reduce the cost of developing FRC with blended fibres as it is not required that large scale member tests be performed.

The remainder of the paper is structured as follows. A literature review is presented focusing on (i) potential test methodologies to determine the tensile properties of FRC (ii) previous research into the tensile properties of UHPFRC utilising blended fibres and (iii) previous experimental research investigation the tension stiffening behaviour of FRC. This literature review is presented to justify both the testing procedure chosen as well as the materials investigated. Following the literature review, the UHPFRC mix designs with blended fibres under investigation are presented, along with the methodologies for both the direct tension and tension stiffening tests. The results of the experiments are then presented and the influence of blending fibres discussed in terms of changes in tension stiffening and crack opening behaviour. Finally, the results are incorporated into a beam analysis procedure to simulate the moment-curvature behaviour of a UHPFRC at serviceability limit. By comparing the results of the tests, as well as the member simulation, the optimal mix design can then be chosen.

LITERATURE REVIEW

Tensile strength test approaches

As the primary influence of the fibres is on the tensile behaviour, existing test setups for determining the tensile behaviour of UHPFRC are reviewed here. Three main types of tests are used to obtain the tensile strength of concrete; these include: direct tension, splitting and flexural tests. Graybeal (2006) has previously compared the results of these three different types of tests on the measured tensile strength of UHPFRC. It was noted that the tensile strength predicted by the splitting test was a third larger than the value obtained under direct tension, while the results from the prism tests were slightly higher. However the result obtained from the prism test required the application of an empirical correction factor without which the tensile strength estimated from the flexural test was double that obtained under direct tension.

Further results from Wille and Parra-Montesinos (2012) suggest that significant scatter in the results arise from variations in size, support condition and method of casting when using the flexural test. Another disadvantage of the use of the splitting tensile test is that it does not produce a pure tensile failure, with some researchers reporting the occurrence of compressive crushing (Hassan et al. 2012). For FRC and UHPFRC, direct tension and flexural tests are preferred as they can measure the ductile post-cracking behaviour of these types of concrete. The advantage of using the direct tension test is that results are unambiguous for properly designed specimens and the advantage of the flexural test is that it is an easier test to perform, however a correction is required to yield the actual tensile strength or otherwise an inverse analysis is required (fib 2012; AFGC 2013). As the interpretation of the results of the direct tension test does not required the use of empirical correction factors the direct tension test methodology will be applied in this study.

Direct tension tests have been performed previously on dogbone, unnotched or notched prismatic specimens (Wille et al. 2014), with each approach presenting a distinct shortcoming. For example, the use of a notch predefines the position of the crack and introduces stress concentrations into the prism. As a result there is a tendency to underestimate the tensile strength (Wille et al. 2014). Unnotched prismatic specimens are generally bonded or glued into the testing apparatus. Not only does this increases the time of setup, the lack of a notch means the specimen is more likely to undergo a bond failure through attachment to the machine. Thus a dogbone type specimen is used in this paper since it can be mechanically anchored into the

apparatus. Considerations with choosing the geometry of a dogbone specimen include the length of the constant area region as well as the width and depth at that section. These considerations are required such that the length of the constant area region is sufficiently long so as not to predefine the position of the crack, as well as allowing for the positioning of instrumentation. Secondly, the end of the specimen should be designed so that any stress concentrations that occur where the specimen is gripped do not prematurely fail the specimen. This is achieved by increasing the cross-section at the end of the specimen, as well as tapering the cross-section from the end into the body of the specimen thus avoiding abrupt changes in cross-section. Wille et al. (2014) provides a summary of previously used end geometries for dogbone specimens. Thirdly, the cross-sectional area should be chosen so that the distribution of fibres is not disturbed; that is edge effects are reduced by using a sufficiently large specimen. This last aspect is particularly important as it suggests that if the cross-section is of insufficient size the tensile stress will be overestimated.

Existing studies investigating blended fibres

Having identified that the direct tension test is most appropriate for further study now consider previous research into the direct tensile behaviour of UHPFRC with blended fibres. This research is reviewed with a particular focus on identifying any synergistic effects arising from blending, as well as identifying any influences which may arise due to test procedure.

Early work on fibre blending was conducted by Rossi (1997) who performed direct tension tests on notched cylinders with a blend of 5 mm and 25 mm long straight fibres. In these tests no control mixes with a single fibre type were considered, and hence any synergistic effects arising from fibre blending could not be identified.

Benson and Karihaloo (2005) performed direct tension tests on UHPFRC with a mix of 6 mm and 13 mm long short straight steel fibres on dogbone shape specimens with a width of 100 mm and a thickness of 35 mm. As with the work of Rossi (1997) no control mixes were performed, such that any synergistic effects could not be identified. It is also worth noting that the aspect ratio of the specimen relative to the fibre size may have resulted in edge effects, that is, a preferential distribution of fibres.

Markovic (2004) considered the direct tensile behaviour of concrete with a strength of 120 MPa including both short straight and long hooked steel fibres. Blends of 50:50, 67:33 and 33:67 were considered. It was found that the first cracking stress was lower for mixes with blended fibres compared to those with only short straight fibres, however similar tensile strengths were obtained despite the fibre volume for the blended fibre mix being 0.5% lower. Importantly, Markovic (2004) identified a significant improvement in the ductility of mixes with hybrid fibres. The dogbone specimens tested had a continuously varying cross-section with the smallest dimension being 70 mm by 70 mm and as with the tests of Benson and Karihaloo (2005) this may have influenced the fibre orientation and hence the results of the test.

Park et al. (2012) considered the direct tension behaviour of UHPFRC for four different types of macro fibre that is long straight fibres, two types of hooked fibres as well as twisted fibres. It was found that twisted fibres provided the best performance prior to blending and that a further improvement in performance could be obtained with the addition of micro fibres. However in the tests with blended fibres the total fibre volume was not kept constant, hence it is unknown what quantity of the improvement is associated with the blending of fibres and what is due to the overall increase in fibre volume. Furthermore, Park et al. (2012) considered

dogbone specimens which had a cross-sections of 50 by 50 mm and the largest fibre used was 62 mm in length. Hence again the results obtained may have been influenced by edge effects associated with specimen size.

Fantilli et al. (2018) investigated whether synergy can be obtained by blending long hooked and short straight steel fibres in UHPFRC. In this study, a model was also derived which related the synergy to the measured spacing of cracks in the direct tension specimen. Fantilli et al. (2018) predicted that the quantity of this synergy would vary as a function of the volume of macrofibres such that for low fibre volumes there would be a negative synergy while for intermediate volumes there is significant positive synergy and finally for higher volumes there would be a small positive synergy. Each of these regimes are defined by the critical volume fraction required to initiate strain hardening in the single fibre and blended mixes. As a constant fibre volume was not maintained; it is unknown what proportion of the overall improvement can be attributed to fibre blending and what proportion is due to the increase in fibre volume. Note that the direct tension specimens used in this study had a cross-section of 30 mm by 30 mm which is the same size as the largest fibre used.

From the studies by Park et al. (2012) and Fantilli et al. (2018), the benefits of the hybrid mix could not be determined as the fibre volume was not constant. However the study by Markovic (2004) indicated that the hybrid mix could offer improvements over mixes with a single type of fibre. All three of these studies were also performed with specimens which had a maximum fibre length that was of similar magnitude to the dimension of the specimen.

Tension stiffening

Let us consider previous studies focusing on the structural level in to form of tension stiffening prisms. A focus on tension stiffening prisms is considered important here as the result of this relatively simple test provides substantial information on the expected performance of flexural members at the serviceability limit state.

Previous studies investigating the effect of blending of fibres on the tension stiffening behaviour include those by Noghabai (2000), Tiberti et al. (2015) and Moreno et al. (2014). Noghabai (2000) considered a 50:50 blend of short straight and long hooked steel fibres in a concrete with a strength of 127 MPa, however only one specimen was tested. A small improvement in behaviour was noted for the series with a blend of fibres. Tiberti et al. (2015) also considered a 50:50 blend of hooked and straight fibres in a concrete with a compressive strength of 43.3 MPa. Again an improvement in tension stiffening was observed. Moreno et al. (2014) considered mixing different lengths of hooked steel fibres with PVA fibres in a concrete with strengths between 31 and 40 MPa. Similar responses were observed between specimens with 30 mm long hooked fibres as well as PVA fibres and specimens with a mix of 30 and 60 mm long hooked fibres as well as PVA fibres.

It should be noted that the influence of fibre blending has been investigated at a member level by Voo and Foster (2006) who tested prestressed UHPFRC I girders failing in shear that contained a blend of short straight and hooked end fibres. They observed that the shear strength of the specimens decreased as the volume of hooked end fibres increased.

Reviewing previous studies under direct tension, there appears to be benefits due to the blending of fibres. However, this was shown by just one study that used specimens with a smaller than optimal cross-section, as the other studies did not allow the effect of blending and fibre volume to be separated. Blending of fibres appears to have a small positive effect on the

tension stiffening, however there is a paucity of testing on FRCs with strength in excess of 100 MPa. Conversely, Voo and Foster (2006) suggested that the introduction of hooked fibres negatively affected the shear capacity of prestressed UHPFRC I girders, which suggests that the blending of fibres may not be uniformly positive. This motivated the present study into the effect of blending fibres on the direct tension and tension stiffening behaviour of UHPFRC.

DESIGN OF BLENDED FIBRE UHPFRC

To design an FRC with two types of fibres, it is suggested that a control mix is tested for each type of fibre, as well as a series of other mixes where the proportion of the two fibre types are varied while the fibre volume is maintained at a constant value. In the example presented in this paper, the fibre types considered include a short straight steel fibre with a length of 13 mm and a diameter of 0.2 mm (microfibre in Fig. 1) and a long hooked steel fibre with a length of 35 mm and a diameter of 0.55 mm (macrofibre). The fibres are manufactured from cold drawn steel wire with the macro fibres having a yield strength of 1100 MPa and the micro fibres having a yield strength of 2850 MPa. Three control mixes are considered: one without fibres (no fibres); one with only macro fibres (1 Macro: 0 Micro); and one with only micro fibres (0 Macro: 1 Micro). Three blended mixes are considered, consisting of a mix with: 60% Macro and 40% Micro (0.6 Macro: 0.4 Micro); 50% Macro and 50% Micro (0.5 Macro:0.5 Micro); and 40% Macro and 60% Micro (0.4 Macro: 0.6 Micro). These mixes are based on a preliminary study on fibre blending by Tian et al. (2016).

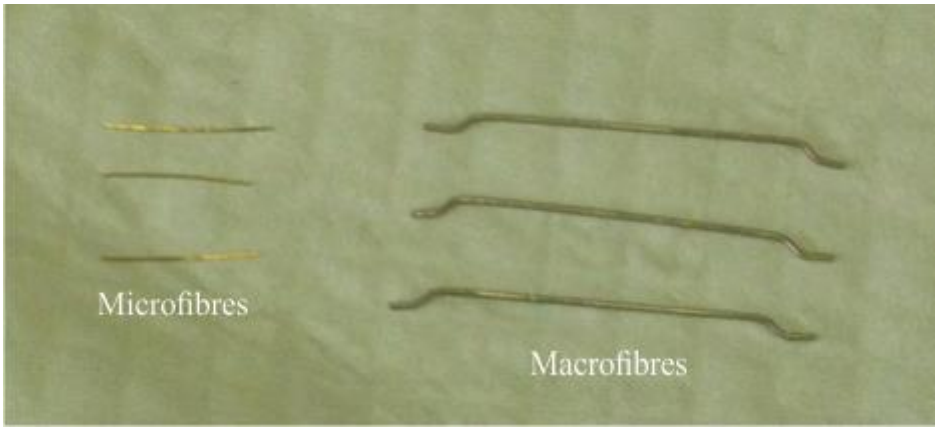

Fig. 1 Macro and micro fibres

The basis of the proposed mix design is that proposed by Sobuz et al. (2016) in which the fineness modulus of the sand, water cement ratio (w:c) and superplasticiser cement ratio (sp:c) were varied to determine the optimum values. Sobuz et al. (2016) used 2% by volume of long hooked steel fibres of the same type as the macro fibres in this study, and suggested basic proportions for the mix as 1:1:0.266:0.233 ratio by weight of sulphate resisting cement, fine aggregate (washed river sand), silica fume and steel fibres. The suggested values for the water to cement ratio was 0.1775 and the superplasticiser to cement ratio was 0.045. This resulted in the mix designs summarised in Table 1.

Table 1. Proposed mix designs

Mix designation	Cement (kg/m^3)	Sand (kg/m^3)	Silica fume (kg/m^3)	Water (kg/m^3)	Superplasticiser (kg/m^3)	Macro fibres (kg/m^3)	Micro fibres (kg/m^3)
No fibres	978	973	260	171	44	0	0
1 Macro: 0 Micro	950	951	253	161	43	222	0
0.6 Macro: 0.4 Micro	950	945	253	166	43	88	133
0.5 Macro: 0.5 Micro	950	944	253	167	43	111	111
0.4 Macro: 0.6 Micro	950	944	253	167	43	133	88
0 Macro: 1 Micro	950	943	253	168	43	0	222

The sulphate resisting cement had: a fineness modulus of $365m^2/kg$; a 28 day compressive strength as determined in accordance with AS 2350.11-2006 (Standards Australia 2006a) of 60MPa; and a 28 day mortar shrinkage strain determined in accordance with AS 2350.13-2006 (Standards Australia 2006b) of $650x10^{-6}$/mm. The sand was a washed river sand and had a fineness modulus of 2.34. A third generation high range water reducer with an added retarder was used to improve the workability.

The mixing procedure consisted of first mixing all the dry components for 1 minute in a pan mixer until well combined. The water and superplasticiser were then added and the concrete mixed until visibly flowable. After the concrete started to flow, the fibres were added and mixed for a further 5 minutes.

TEST DESIGN

For each mix design, three direct tension and three tension stiffening (two for the no fibres mix) specimens were tested. Additionally the compressive strength of the concrete was determined at the beginning and end of each series of tests on a given fibre type. The direct tension tests were performed to determine the stress that can be transferred by fibres across cracks. The tension stiffening tests were performed to investigate the effect of the fibres on the stiffness of the tension chord.

Direct Tension

The direct tension tests were performed on the dogbone specimens in Fig. 2. Specimens of this shape had previously been employed by Singh et al. (2017). Note that the deformation of the specimen was measured over the central 300 mm of the specimen using four LVDTs (2 mounted on each side). The specimens were tested under displacement control at a rate of 0.05 mm/min until a displacement of 1.5 mm was achieved. After this, the rate was increased to 0.2 mm/min until a displacement of 4 mm was achieved. Finally a rate of 1 mm/min was employed until a displacement of 10 mm was achieved.

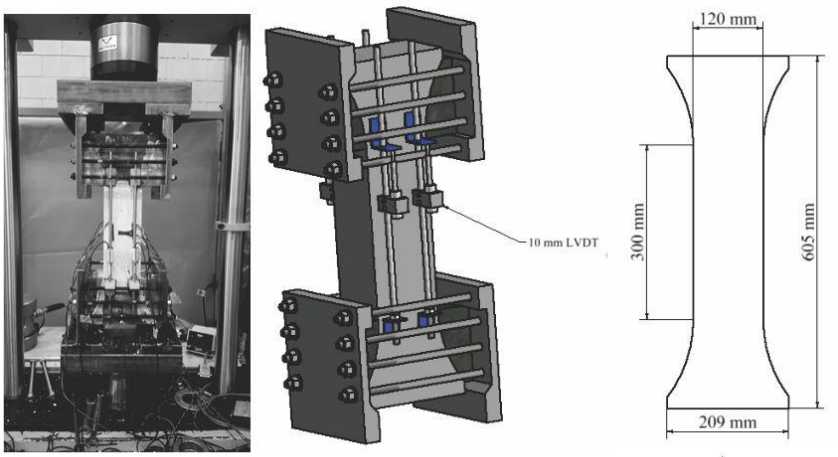

Fig. 2 Direct tension test set-up; a) photograph; b) 3D-model; c) elevation

Tension Stiffening

The tension stiffening tests were performed on rectangular concrete prisms with a single reinforcing bar as in Fig. 3. All specimens: had a cross-section of 75 by 75 mm; were reinforced with a 16 mm reinforcing bar; and had a length of 660 mm. Two LVDTs were provided on each side to measure the overall elongation of the specimen. These LVDTs were anchored to stainless steel rods which were in turn anchored to a mounting plate located on the top concrete surface as in Fig. 3(b). The specimens were tested at a rate of 0.6 mm/min through the machine crosshead until just prior to the yield of the reinforcing bar at a load of 100 kN. The width and location of cracks were measured at 20 kN increments using a handheld digital microscope with a magnification of 220 times.

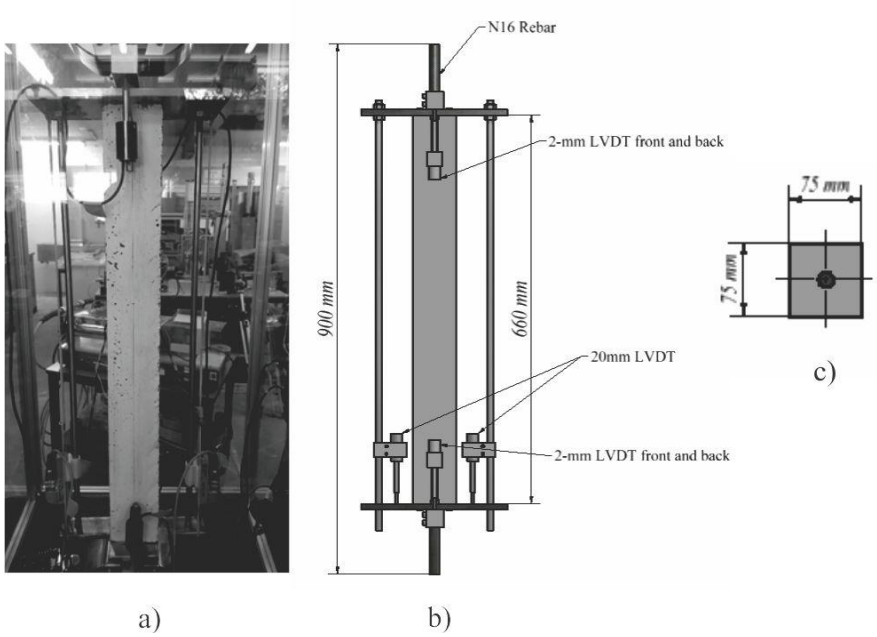

Fig. 3 Tension stiffening test set-up; a) Photograph of setup; b) elevation; c) cross-section

Material Properties

At the beginning and end of the specimen testing, the compressive strength and elastic modulus of each mix was determined in accordance with AS1012.9-2000 (Standards Australia 2000) and AS1012.17-1997 (Standards Australia 1997). These properties were determined on

cylinders with a height of 200 mm and a diameter of 100 mm. For the uniaxial compression test, the cylinder was loaded at a rate of 20 MPa/mm until the cylinder failed. For the determination of the elastic modulus, the specimen was loaded to 40% of the ultimate strength at a rate of 15 MPa/mm and then unloaded for five cycles; the last two cycles were recorded to determine the elastic modulus. The axial strains were recorded using two strain gauges on each side of the specimen. The results are given in Table 2.

Table 2. Compressive strength and elastic modulus for each mix

	Before Testing			After Testing		
Mix	Age at Testing (days)	f_c (MPa)	E_c (MPa)	Age at Testing (days)	f_c (MPa)	E_c (MPa)
No Fibres	29	150	48158	54	169	47864
1 Macro: 0 Micro	27	160	51061	40	171	48453
0.6 Macro: 0.4 Micro	27	157	49073	48	157	52013
0.5 Macro: 0.5 Micro	63	151	49314	84	157	58202
0.4 Macro: 0.6 Micro	44	156	50060	65	157	51521
0 Macro: 1 Micro	24	154	50402	48	156	49538

RESULTS

Direct Tension

The experimental load elongation curve, as shown in Fig. 4(a), obtained from the specimens illustrated in Fig. 2, is comprised of a hardening linear elastic branch, an inelastic strain hardening portion and a softening portion. The hardening portion is associated with microcracking while softening is induced when a macrocrack forms and the fibres pullout. For analysis, the first two portions are represented by a stress-strain relationship as illustrated in Fig. 4(b). This approach is taken as the microcracks are assumed be uniformly distributed through the volume. As the softening portion is associated with localisation of the deformations at the macrocrack, it is instead represented by a stress-crack width relationship as illustrated in Fig. 4(c).

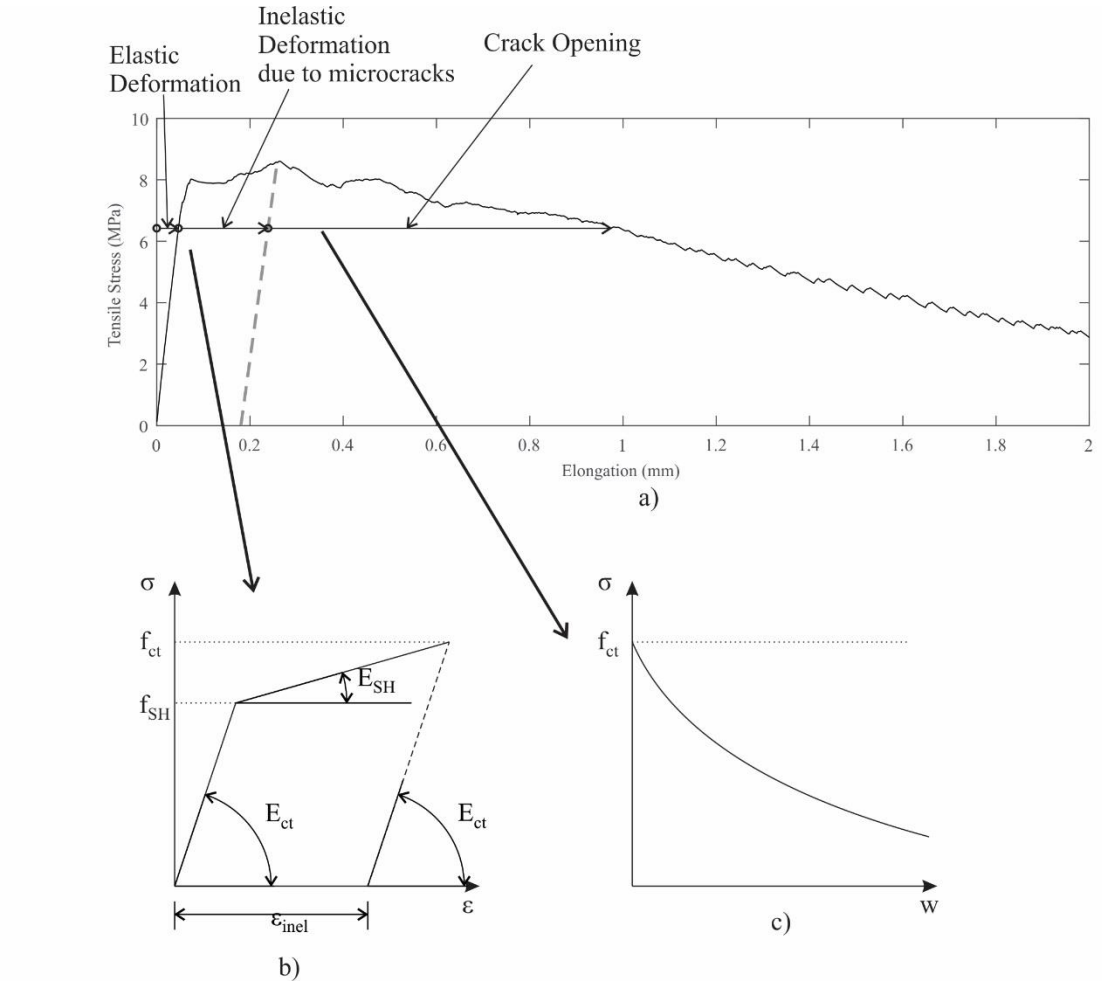

Fig. 4 a) Experimental Load-Elongation; b) Idealised stress-strain relationship; c) idealised stress crack width relationship

The results of each individual test presented in Appendix A in the form of a stress-strain and stress-crack width relationship. From the pre-peak stress-strain relationship, the key points (illustrated in Fig. 4b) can be extracted. These include is the stress to cause microcracks (f_{SH}), the stress to cause macrocracks (f_{ct}), the modulus of the linear elastic portion (E_{ct}), the modulus of the inelastic hardening portion (E_{SH}) and the permanent strain due to microcracking ε_{inel}. Where, ε_{inel} is the residual strain that would be obtained if the specimen was loaded up to the point of macrocracking and is then unloaded.

Table 3. Comparison of key points on stress-strain curve

Mix	f_{SH} (MPa)	f_{ct} (MPa)	E_{ct} (MPa)	E_{SH} (MPa)	ε_{inel}
No Fibres		5.40	39500		
		5.58	39580		
		5.18	39610		
1 Macro: 0 Micro		7.08	41470		
	5.43	6.18	42120	1252	0.000581
	6.01	6.83	43000	3484	0.000216
0.6 Macro: 0.4 Micro	7.21	8.26	39890	2113	0.000471
	6.42	6.66	43600	4601	0.000467
	6.68	6.68	39370	0	0.000083
0.5 Macro: 0.5 Micro	7.79	8.17	42190	3797	0.000091
	8.22	8.54	42730	1056	0.000296
	7.97	8.38	41870	11608	0.000026
0.4 Macro: 0.6 Micro		8.08	40500		
	6.57	7.36	42860	1091	0.000706
		7.38	38120		
0 Macro: 1 Micro		7.89	40380		
	7.45	8.31	40450	3941	0.000197
	8.02	8.61	35930	929	0.000619

The key points from Table 3 are plotted as a function of the percentage of microfibres as a proportion of the total volume of fibres in the mix in Fig. 5. From the line of best fit, it can be seen: that the stress to cause both macro cracking f_{ct} in Fig. 5(b) and micro cracks f_{SH} in Fig. 5(a) increases as a function of the proportion of microfibers; while the elastic modulus of the concrete E_{ct} in Fig. 5(c) slightly decreases with the increase in the proportion of microfibres. That is, replacing the macrofibres with microfibres results in an increase in microcracking strength f_{SH} of up to 35%, macrocracking strength f_{ct} up to 23% and a decrease in elastic modulus, E_{ct} of up to 8%.

It is suggested that the increase in tensile strength of mixes with a greater proportion of microfibres is a result of the larger number of individual fibres crossing each crack which compensates for the reduced bond strength of the straight versus hooked end fibres. Neither the strain hardening modulus E_{sh} in Fig. 5(d) nor the permanent strain due to microcracking in Fig. 5(e) show any correlation with the proportion of the microfibres in the mix. In this regard, Naaman (2007) has previously demonstrated the critical fibre volume to achieve strain hardening behaviour in FRC is a function of aspect ratio of the fibres, the tensile strength of

the concrete matrix and the bond stress developed along the fibres. As the first two parameters are held constant in these tests, this implies that, at the microcracking stage, for the fibres tested, the bond stress development must be similar between the straight and hooked fibres. This result is similar to that found by Wille and Naaman (2012) in single fibre pullout tests, where it was concluded that while the peak bond stresses differ greatly between the hooked end and straight fibres, the initial stiffness of the bond-slip relationship is the same; hence for the very fine crack widths observed during the strain hardening stage the overall bond stress in the hooked end and straight fibres is the same. It is suggested that the high variability in the strain hardening behaviour is due to random variations in the orientation of fibres across cracks.

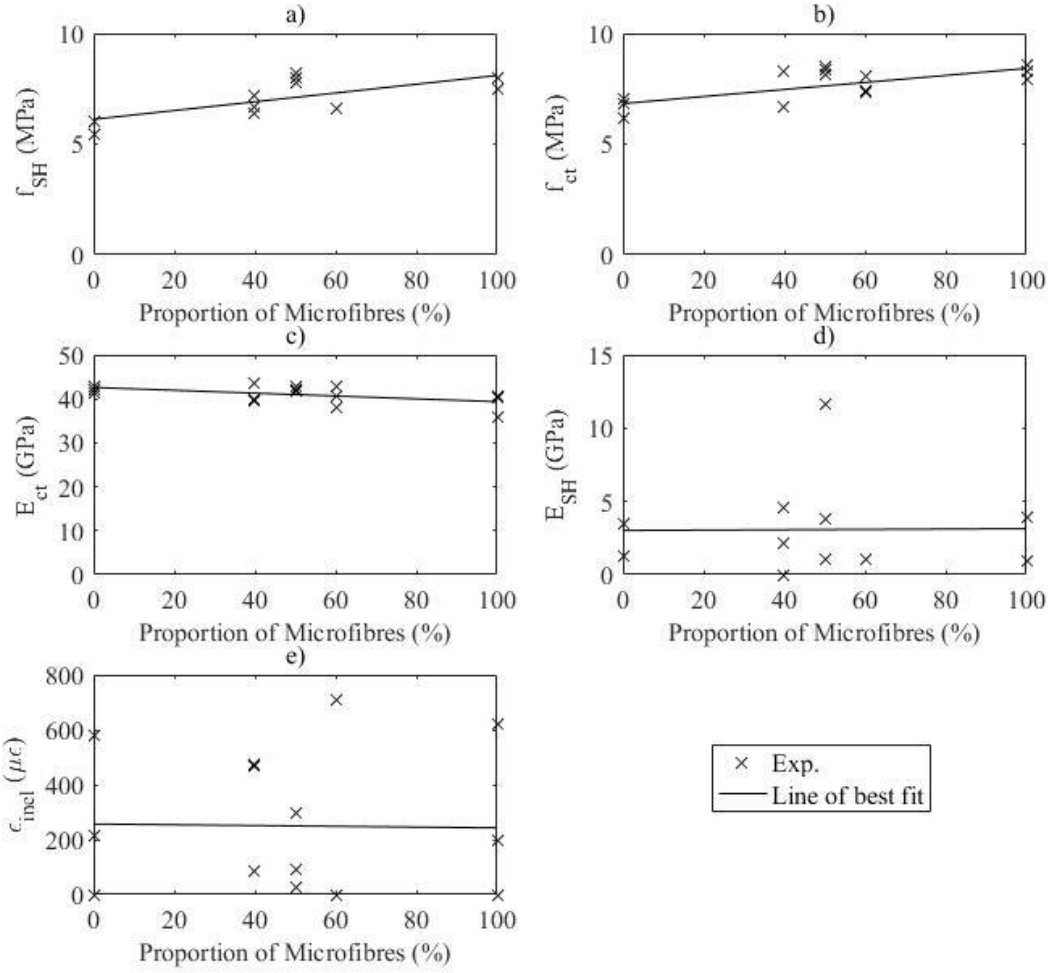

Fig. 5 Variation of key points as a function of the proportion of microfibres

The post-peak stress crack width relationships are compared in Fig. 6. In Fig. 6(a) for small crack widths it can be seen that the mix without any micro fibres (1 Macro: 0 Micro) has the worst performance. Further it can also be seen that all the blended fibre mixes had better performance than 0 Macro: 1 Micro after a crack width of 0.4 mm. In Fig. 6(b) for large crack widths it can be seen that the blended mixes offer the best performance across the full range. At a crack width of 3 mm the stress in 0 Macro: 1 Micro becomes less than that in 1 Macro: 0 Micro. This demonstrates the efficacy of the long fibres at bridging the larger cracks. This demonstrates the improvement to the strength and ductility of the concrete introduced by blending the fibres at all stages of crack opening.

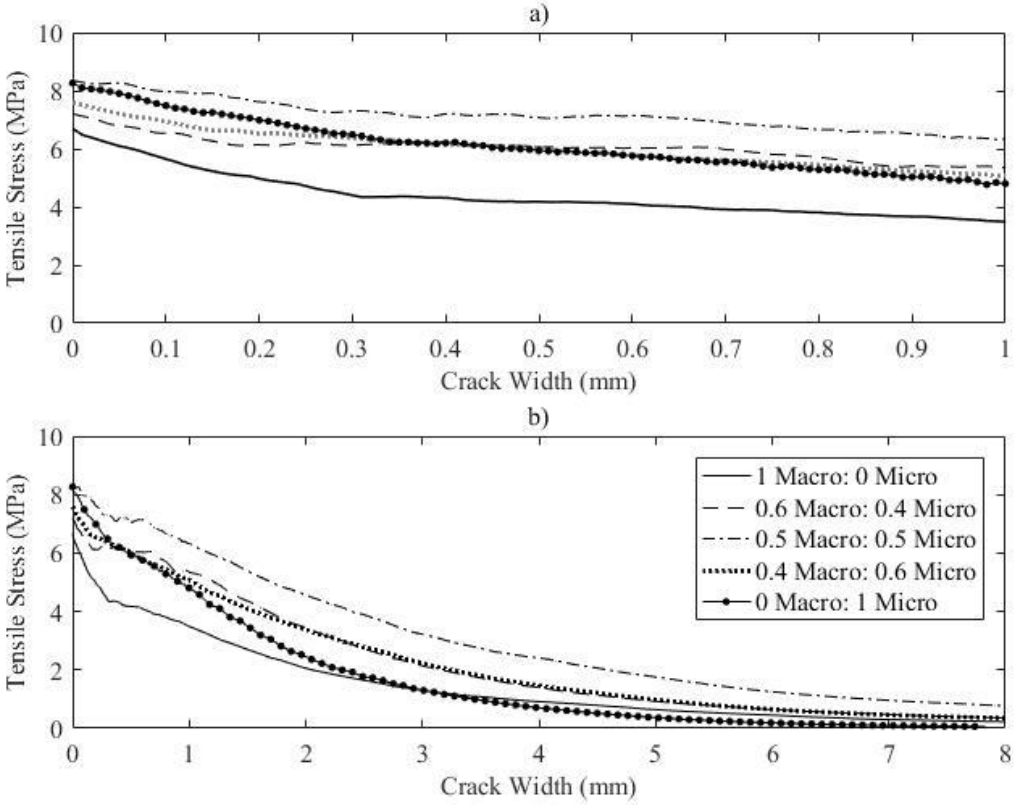

Fig. 6 Comparison of average tensile stress-crack width for each mix

Tension Stiffening

From previous research (Bischoff 2001), it has been recognised that shrinkage is a significant confounding variable affecting the empirically determined tension stiffening behaviour. To explore this behaviour, consider a reinforcing bar embedded in a concrete prism; a longitudinal section of which is illustrated in Fig. 7(a). At casting, the end of the tension stiffening prism is at profile A-A. As shrinkage strains develop and if it is assumed that there was no bond between the reinforcement and the concrete, the end of the prism would contract to the profile B-B. The distance between profile A-A and B-B is equal to the shrinkage strain (ε_{sh}) multiplied by the length of the prism L_{def}. However in reality there is bond between the reinforcement and the surrounding concrete. Hence at the time of testing, the end of the concrete specimen is at profile C-C. Profile C-C is displaced from profile A-A by a distance equal to the shrinkage offset o_{sh} multiplied by L_{def}. Due to the displacement from profile A-A, a compressive force results in the reinforcing bar equal to the shrinkage offset multiplied by the axial rigidity of the bar. Similarly, a tensile force develops in the surrounding concrete equal to the difference between the shrinkage strain and the shrinkage offset multiplied by the axial rigidity of the concrete. This offset displaces the load-strain relationship leftwards as illustrated in Fig. 7(b). If before the test, no load is applied to the section than these two forces are equal and opposite. From this analysis the result obtained by Bischoff (2001) for the initial offset in strains due to shrinkage can be obtained as

$$\mathrm{o_{sh}} = \frac{\varepsilon_{sh}}{1 + \frac{E_r A_r}{E_c A_c}} \tag{1}$$

where E_rA_r is the axial rigidity of the reinforcement and E_cA_c is the axial rigidity of the concrete in the tension stiffening prism. Eq. (1) can then be applied to remove the effect of shrinkage from the experimental results by translating the results leftwards by the offset so that only the

quantum of tension stiffening is compared. This is only exact if the concrete is uncracked under shrinkage before loads are applied. If this correction is not performed then the level of tension stiffening is underestimated and the tension stiffening between specimens with different levels of shrinkage cannot be compared.

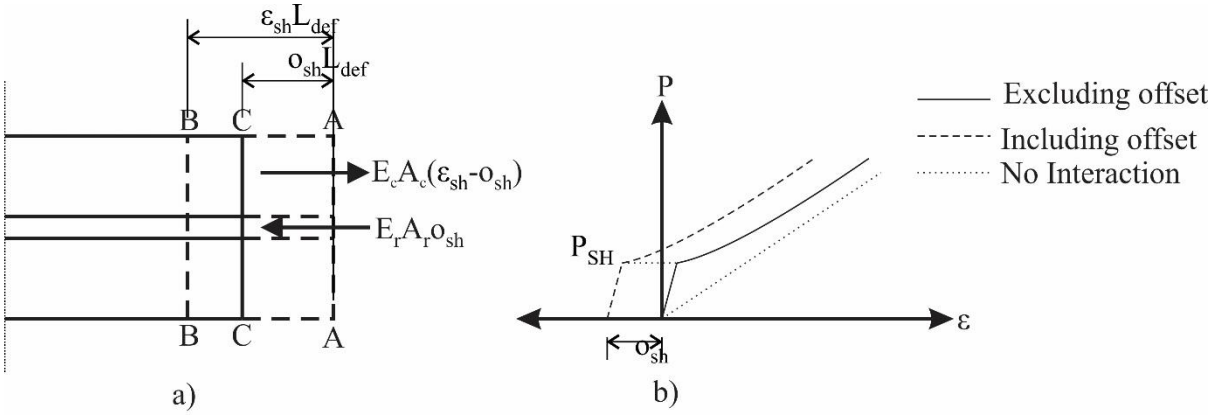

Fig. 7 The effect of shrinkage on the: a) tension stiffening prism; b) load-strain relationship

An appropriate value of the shrinkage strain is required to apply Eq. (1). Most previous researchers have approached this by assuming that the shrinkage can be estimated from an associated shrinkage specimen, with two main exceptions. Bischoff (2003) estimated shrinkage strains by testing a specimen with unbonded reinforcement while Leutbecher and Fehling (2012) estimated the shrinkage in their tension stiffening specimens from the measured change in length between casting and testing. As an alternative approach in this study, the shrinkage will be estimated directly from the test specimen by considering the point of first non-linearity in the axial load-strain profile, that is the point of microcracking as shown in Fig. 7(b). Up to these points, the behaviour of the specimen is assumed to be linear elastic with full interaction between the concrete and the reinforcement. Hence the following equation for estimating the load for first cracking suggested by Sturm et al. (2017) for ordinary reinforced concrete can be applied.

$$P_{SH} = f_{SH}A_c + E_rA_r\left(\frac{f_{SH}}{E_c} - \varepsilon_{sh}\right) \quad (2)$$

where in Eq. (2), $_{SH}$ is the stress to cause microcracking (note if strain hardening does not occur f_{SH} is replaced by the cracking strength f_{ct}), E_r and E_c are the elastic moduli of the reinforcement and concrete while A_r and A_c are the cross-sectional areas of the reinforcement and the concrete, respectively. Eq. (2) is justified because if no cracks have formed the fibres are not yet activated. This load is derived by assuming that the strain in the concrete is equal to the strain to initiate microcracks f_{SH}/E_c and then assuming that the strain in the reinforcement is offset from the strain in the concrete by the shrinkage strain.

Rearranging Eq. (2) gives the shrinkage strain as

$$\varepsilon_{sh} = f_{SH}A_c\left(\frac{1}{E_rA_r} + \frac{1}{E_cA_c}\right) - \frac{P_{SH}}{E_rA_r} \quad (3)$$

In Eq. (3), f_{SH} is estimated from the direct tension tests and P_{SH} is estimated from the tension stiffening tests. The results of applying Eq. (3) are listed in Table 4 as well as the results of conventional shrinkage specimens monitored according to AS1012.8.4:2015 (Standards Australia 2015).

Table 4. Shrinkage strain estimated from tension stiffening test and conventional shrinkage prism

Mix	ε_{sh} (με)		% Difference
	Eq. (3)	Shrinkage prism	
No Fibres	167	476	-64.9
1 Macro: 0 Micro	500	-	-
0.6 Macro: 0.4 Micro	295	216	36.6
0.5 Macro: 0.5 Micro	467	460	1.5
0.4 Macro: 0.6 Micro	207	329	-37.1
0 Macro: 1 Micro	218	425	-48.7

Note that the high strain difference for the no fibres mix of 64.9%, in column 4 of Table 4, can be attributed to the direct tension test underestimating the stress to cause microcracking f_{sh}, hence requiring a corresponding reduction in shrinkage to match the result from the tension stiffening test. This is due to stress concentrations within the grips of the direct tension specimen, as it was observed that for the specimens without fibres that the tensile crack formed in the jaws rather than the body of the specimen. This did not occur in the specimen with fibres, as the fibres assisted in distributing stresses away from the jaws. To explain the difference in results for the other cases it is to be considered that the measured shrinkage can have a variation of up to ±30% (Standards Australia 2009), also while the shrinkage and tension stiffening specimens had the same cross-section, the tension stiffening specimen was longer which would have inhibited the drying of the most central part of the specimen.

With the shrinkage determined, the offset in strains can be evaluated using Eq. (3). The average-load/strain curve for each mix design is plotted in Fig. 8; the individual tests are given in Appendix A. Note that in Fig. 8 the axial strain is set to be zero when the specimen is at the initial length of the specimen at casting before a shrinkage strain has been applied. The stress-strain relationship assuming no interaction between the reinforcement and concrete is also plotted, that is the bare bar response. The difference between the experimental load-strain and the bare bar response curve represents the increase in stiffness due to tension stiffening.

From Fig. 8, it can be seen that the introduction of fibres produces a significant improvement in tension stiffening over the non-fibre case and that the blended mix 0.5 Macro: 0.5 Micro gives the best results.

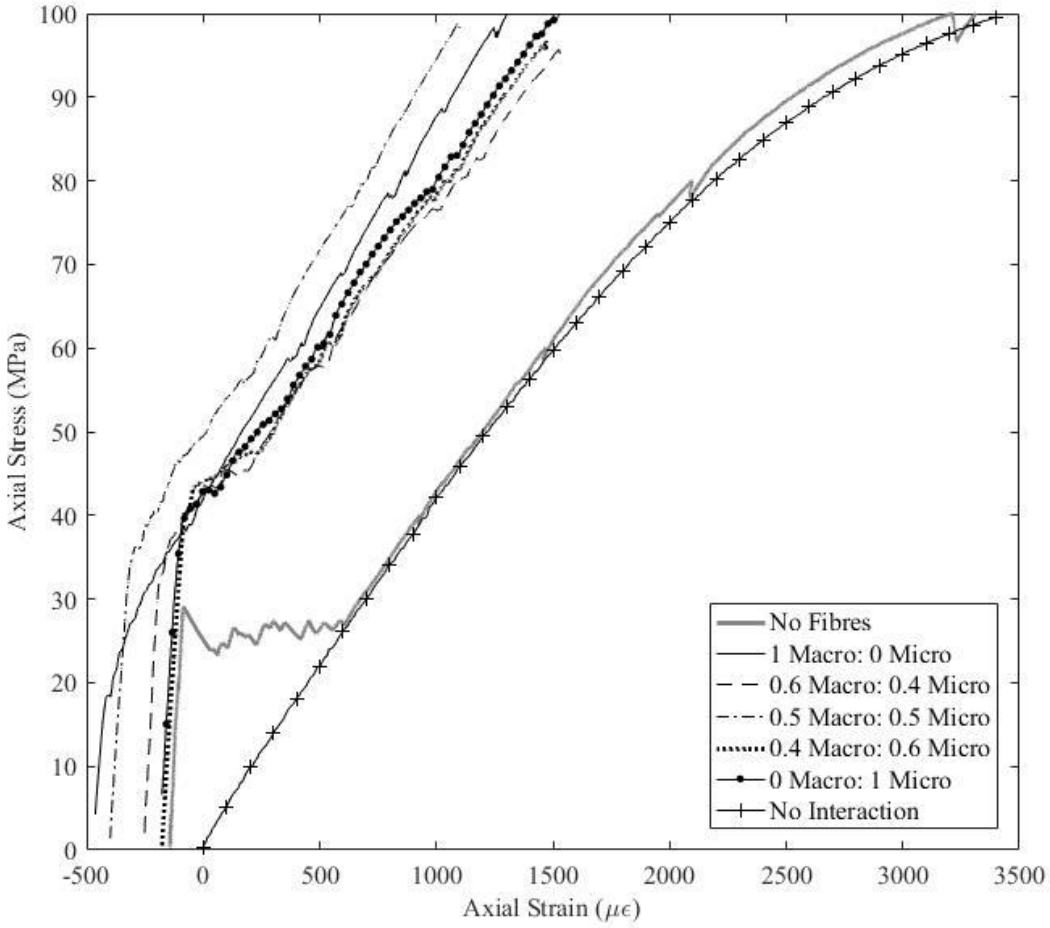

Fig. 8 Comparison of average axial load-strain for each mix

Fig. 9 compares the axial load crack width behaviour of the tension stiffening specimens, from which it can be seen that the introduction of fibres significantly reduces the average and maximum crack width. It can also be seen that the average crack widths are similar. There are differences in terms of the maximum crack width, however this likely to be due to the random variation rather than any real difference in behaviour as the average crack width were similar between the specimens. This greater scatter is due to the maximum value being based on single data point which is the maximum observed from three specimens whereas the average value is calculated from all the cracks within the three specimens. It is worth noting that in all cases the maximum crack widths are significantly smaller than the minimums required for durability (Jong & Papworth 2017).

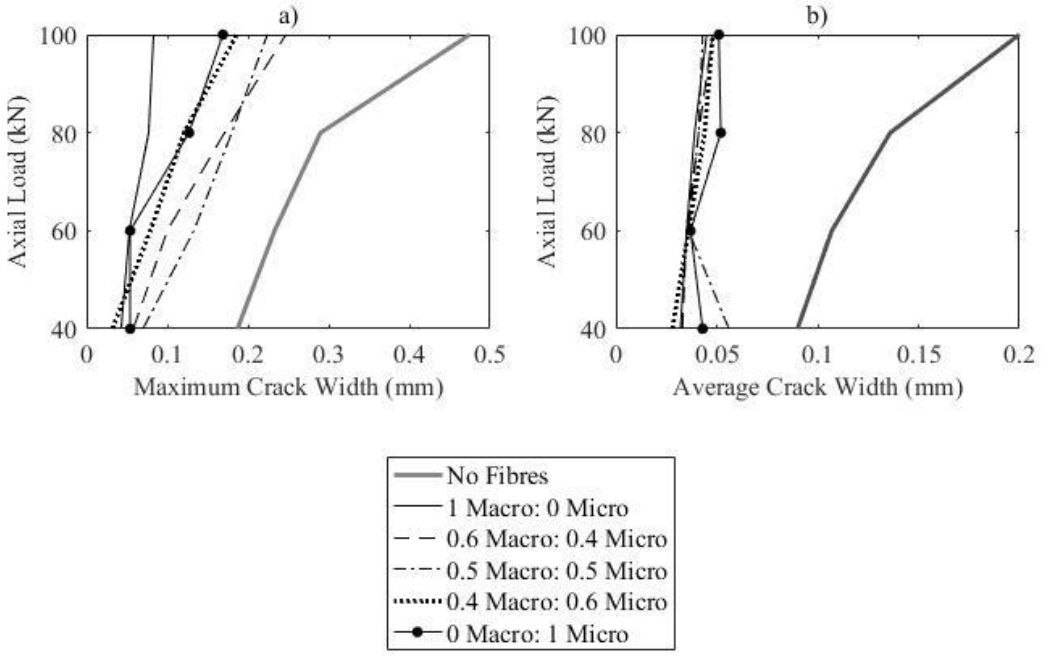

Fig. 9 Comparison of: a) Average crack width versus load; b) maximum crack width versus load

ANALYSIS OF RESULTS

A moment-curvature analysis was performed using the obtained experimental results to investigate the change in serviceability behaviour produced by blending the fibres. To apply this analysis the section was divided into three zones as indicated in Fig. 10. The first zone is the compression zone where the concrete is assumed to be linear elastic, as the load case considered is at serviceability, hence the stress is given by the elastic modulus, E_c. In the tension zone the stress in the concrete is assumed to be given by the experimental results obtained from the direct tension test. The load carried by the effective tension stiffening prism is given by the load-strain behaviour derived from the tension stiffening test. The dimensions of the effective tension stiffening prism are illustrated in Fig. 10(a) where *b* is the width, *D* is the depth and *d* is the effective depth of the section. For the tension zone up to cracking the pre-peak stress-strain curve can be used. However, after cracking it is considered that the average strain at a given depth is given by

$$\varepsilon_c = \frac{w}{l_c} + \varepsilon_{inel} + \frac{\sigma_c}{E_{ct}} \tag{4}$$

where w is the crack width, l_c is a characteristic length, ε_{inel} is the permanent strain due to strain hardening, σ_c is stress and E_{ct} is the elastic tensile modulus. Note that for this virtual analysis that l_c is assumed to be 2/3 the depth of the section as given by the French UHPFRC recommendations (AFGC 2013).

For the analysis a linear strain profile is assumed as illustrated in Fig. 10(b). The strain profile is defined by the curvature χ and the neutral axis depth d_{NA} of the section. Considering the different behaviours of each of the three zones the stress profile in Fig. 10(c) is determined. This stress profile can then be integrated to give the forces in Fig. 10(d) and then the moment applied to the section. Note that the curvature is imposed and then the neutral axis depth is varied until the force equilibrium is reached. In Fig. 10, A_{rt} is the area of tensile reinforcement,

P_{ts} is the load carried by the effective tension stiffening prism, P_{ct} is the load in the tensile concrete and P_{cc} is the load in the compressive concrete.

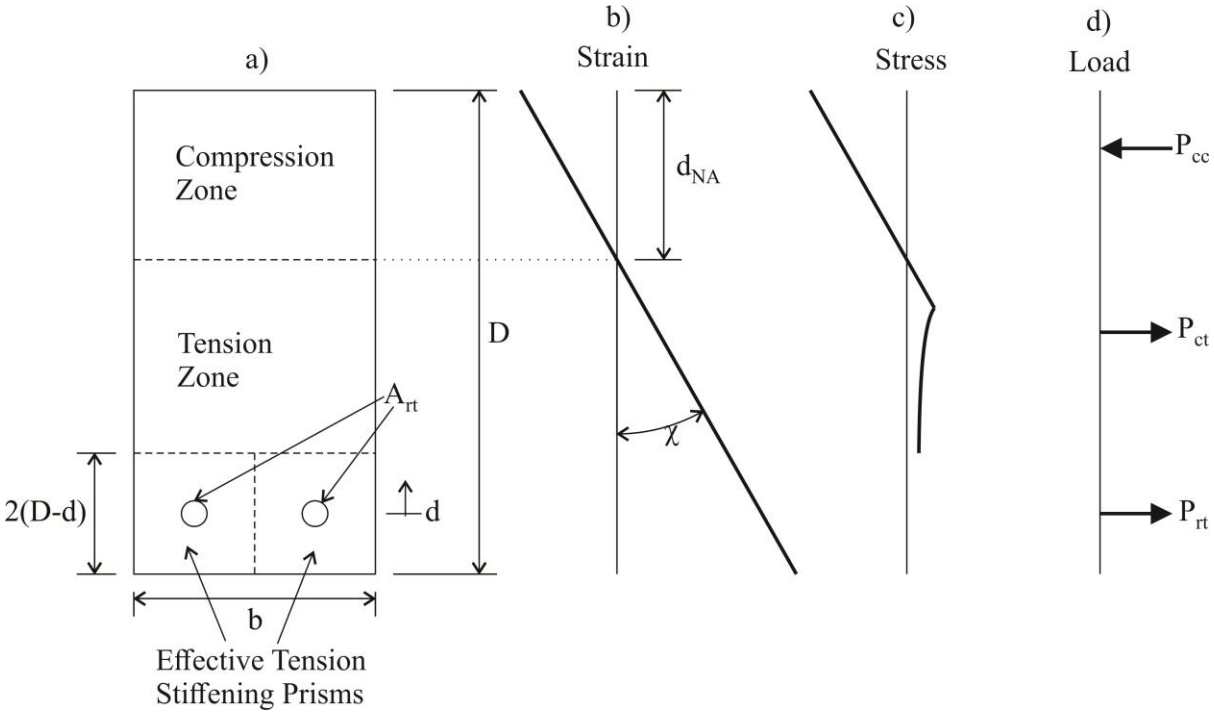

Fig. 10 Section for moment-curvature analysis

Using this approach a virtual beam with a total depth of 300 mm, a width of 150 mm and a depth to the tensile reinforcement of 262.5 mm was simulated for each of the different mixes. The results are shown in Fig. 11(a). Note that the area of the tensile reinforcement was 402 mm^2. The area of the tensile reinforcement and the geometry of the virtual section were chosen so that the size of the effective tension stiffening prism was same dimensions as the specimens used in the tension stiffening test. To demonstrate that the results are independent of the chosen reinforcement ratio and the dimensions of the beam a second virtual beam was simulated as shown in Fig. 11(b). This virtual beam had a total depth of 150 mm, a width of 300 mm and a depth to the tensile reinforcement of 112.5 mm. The area of the tensile reinforcement was 804 mm^2. From this it can be seen that the particular choice of the specimen does not affect the conclusions from the analysis.

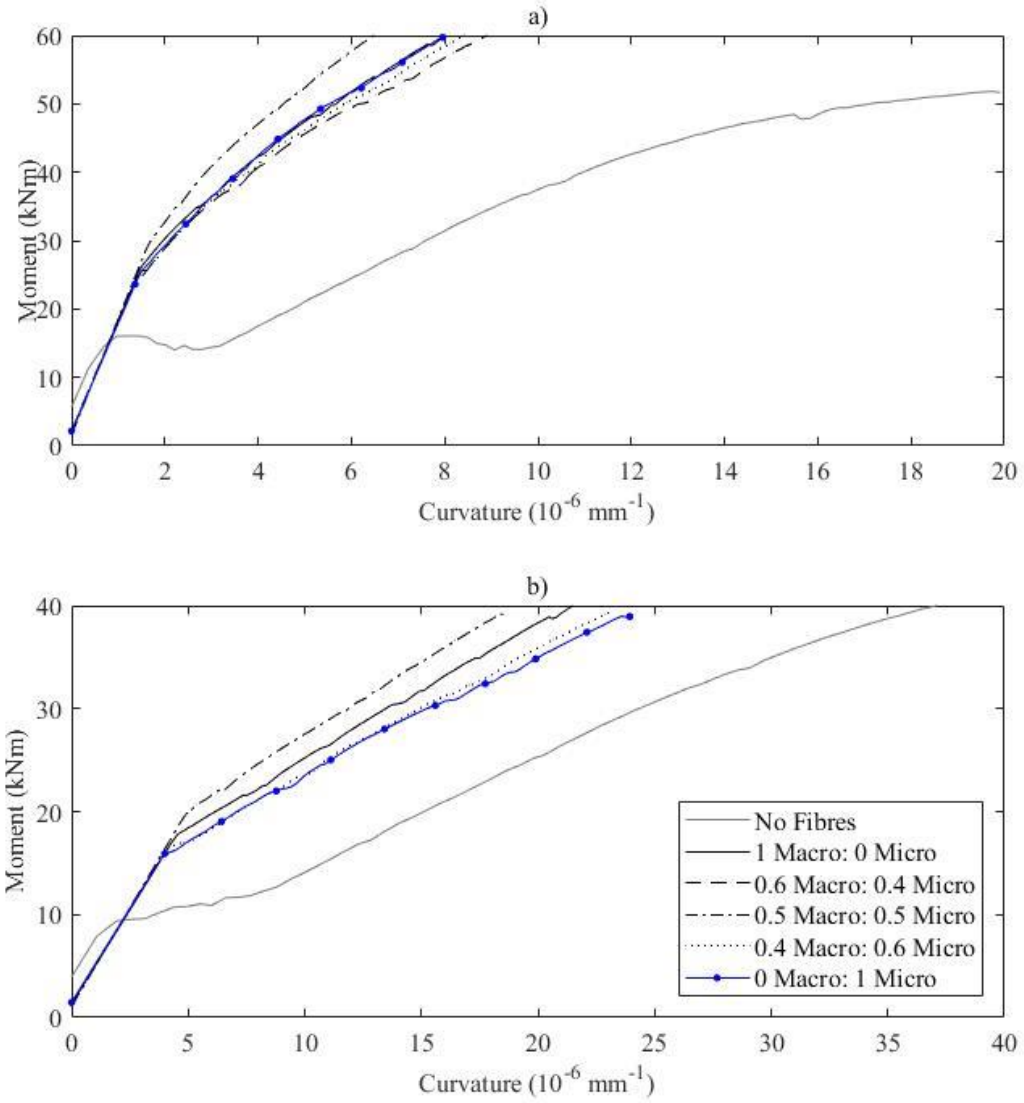

Fig. 11 Comparison of moment curvature before yield

From Fig. 11(a) it can be seen that the introduction of fibres significantly improves the stiffness of the section. It also noted that for specimen without fibres there is a step change in curvature at the cracking moment, whereas only a change in slope of the moment-curvature relationship is observed with fibres. This is due to the fibres allowing additional tensile stresses to be transferred by the tensile concrete as well as increasing the load that can be carried by the effective tension stiffening prism. It can be seen, from Fig. 11(a), that 0.5 Macro: 0.5 Micro had the best performance from the 5 mixes. Note that the range of performance was similar to that seen from the tension stiffening tests, suggesting that beam tests are not required.

VALIDATION

To validate this analysis the results of this analysis are compared to a test result from Sturm et al. (2020) in Fig. 12. This beam was 260 mm deep and 200 mm wide with a span of 4200 mm. This beam contained 2 12 mm reinforcing bars top and 2 20 mm reinforcing bars bottom. This

specimen contained 2% by volume 35 mm long hooked end steel fibres. From this comparison the analysis is close enough to the real beam behaviour.

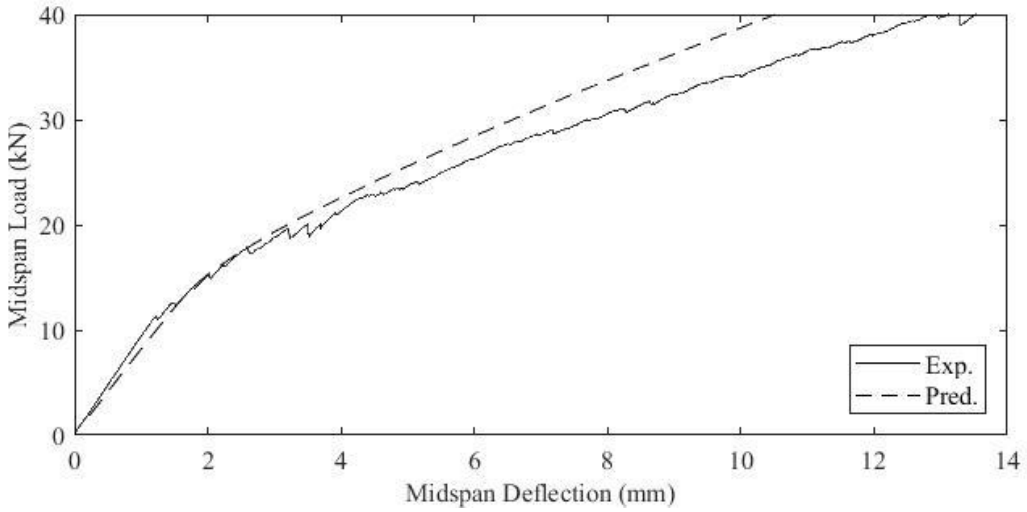

Fig. 12 Validation

CONCLUSION

In this paper a methodology is developed for determining the effect of blending different fibre types on the serviceability behaviour of FRC without performing large scale beam tests. As an example of the method, the effect of blending short straight (micro) and long hooked (macro) fibres on the behaviour of an UHPFRC mix was investigated. From this investigation it was seen that mixes where a higher proportion of the included fibres were microfibres had higher tensile strengths as well as higher stresses to initiate microcracking. It was found that the blended mixes had more ductility under tension than any of the singly reinforced mixes. 0.5 Macro: 0.5 Micro was found to have the highest quantity of tension stiffening and the average crack widths were similar between the different mix designs. These results were then used to simulate the moment-curvature behaviour of a virtual beam. From this it was found that 0.5 Macro: 0.5 Micro had the best overall performance under serviceability loads. Hence, the methodology has been shown to assess the benefits available on the serviceability behaviour of UHPFRC beams due to the blending of fibres, without large scale beam tests.

APPENDIX A STRESS-STRAIN AND STRESS-CRACK WIDTH RELATIONSHIP

In Fig. A1 the results from the individual direct tension tests are illustrated.

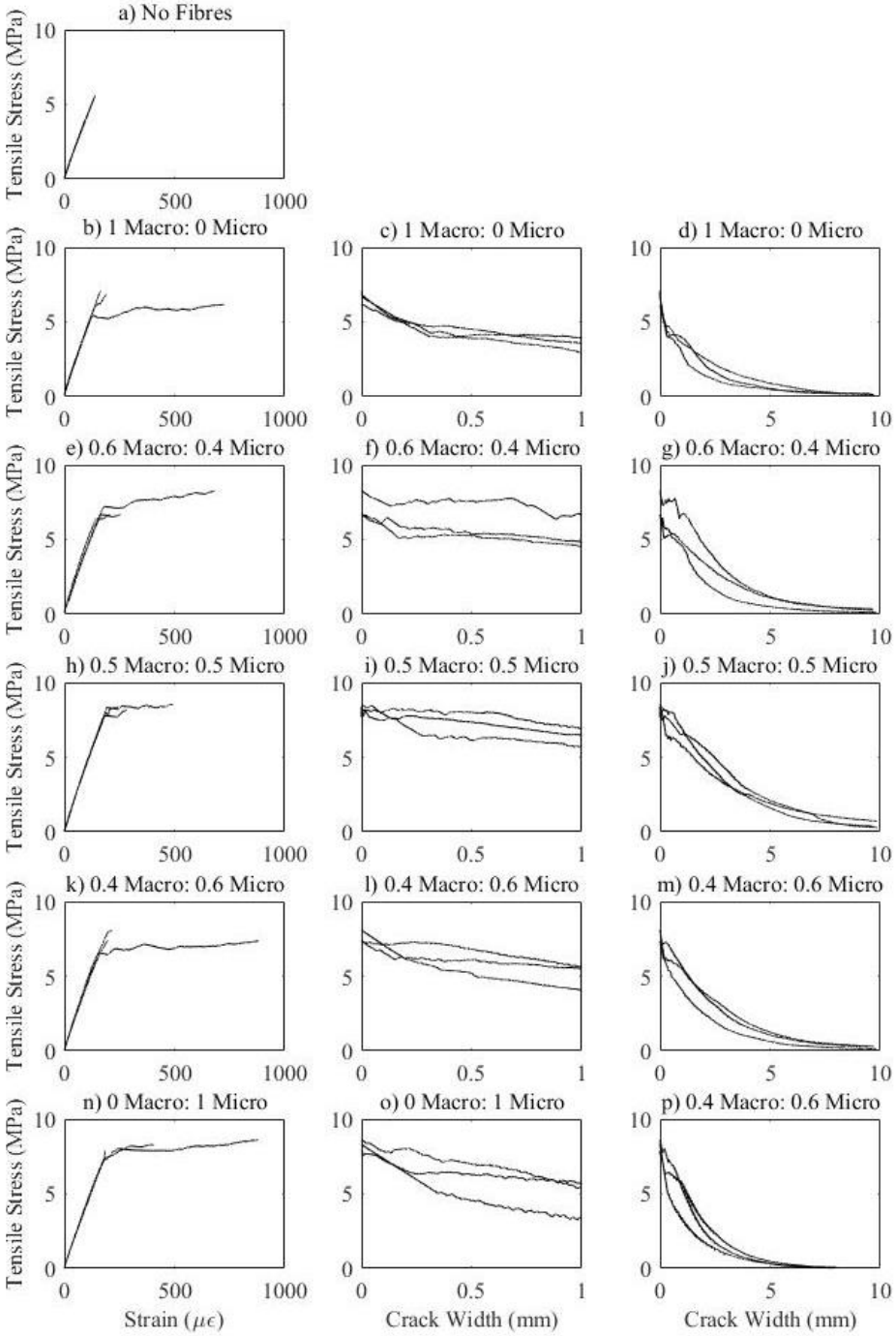

Fig. A1 Stress-strain and stress-crack width results for each test

APPENDIX B TEST DATA FOR TENSION STIFFENING

Fig. B1 contains the results for each individual tension stiffening tests.

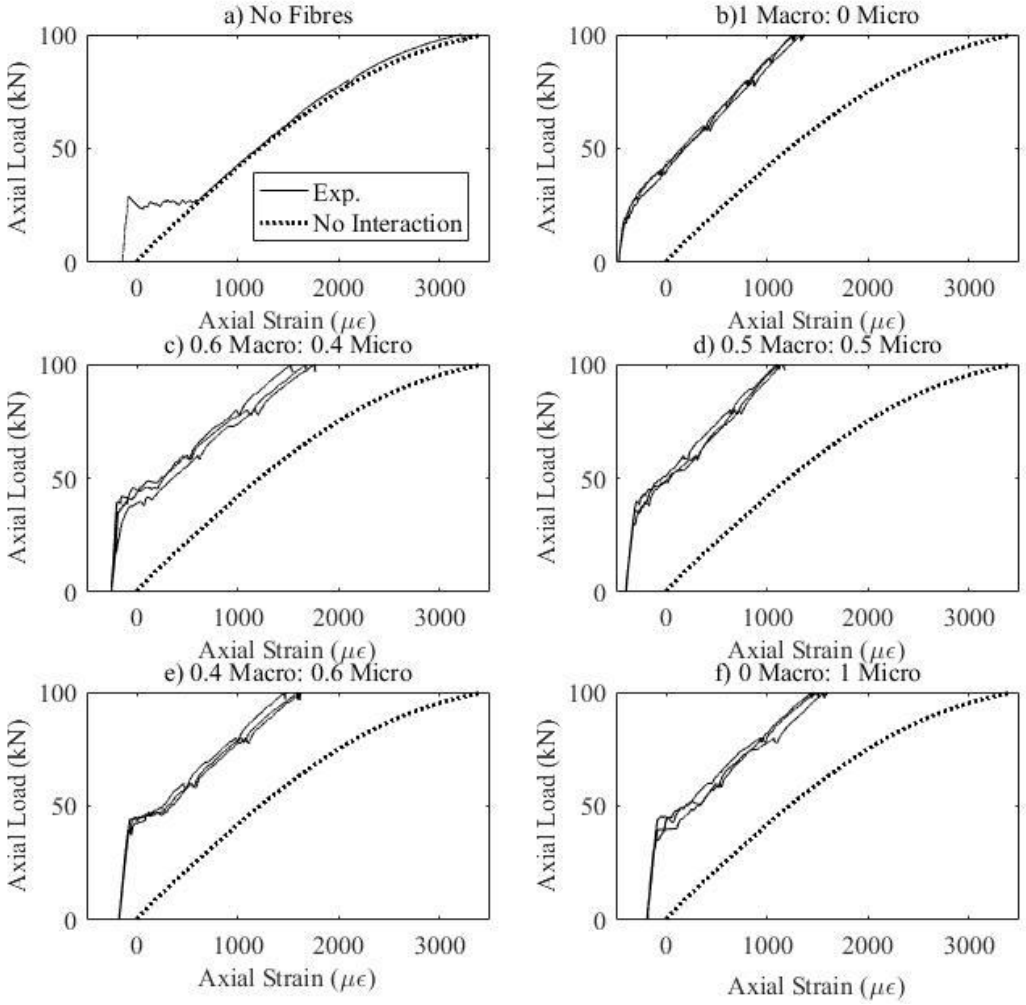

Fig. B1 Load versus strain results for each test

ACKNOWLEDGEMENTS

This material is based upon work supported by the Air Force Office of Scientific Research under award number FA2386-16-1-4098.

REFERENCES

AFGC (French Association of Civil Engineering). (2013). “Betons fibres a ultra-hautes performances: Recommandations [Ultra high performance fibre reinforced-concretes: Recommendations].” Paris.

Banthia, N., Majdzadeh, F., Wu, J., and Bindiganavile, V. (2014). "Fiber synergy in Hybrid Fiber Reinforced Concrete (HyFRC) in flexure and direct shear." *Cement and Concrete Composites*, 48, 91-97.

Benson, S., and Karihaloo, B. L. (2005). "CARDIFRC®–Development and mechanical properties. Part III: Uniaxial tensile response and other mechanical properties." *Magazine of Concrete Research*, 57(8), 433-443.

Bischoff, P. H. (2001). "Effects of shrinkage on tension stiffening and cracking in reinforced concrete." *Canadian Journal of Civil Engineering*, 28(3), 363-374.

Bischoff, P. H. (2003). "Tension stiffening and cracking of steel fiber-reinforced concrete." *Journal of Materials in Civil Engineering*, 15(2), 174-182.

Fantilli, A. P., Kwon, S., Mihashi, H., and Nishiwaki, T. (2018). "Synergy assessment in hybrid ultra-high performance fiber-reinforced concrete (UHP-FRC)." *Cement and Concrete Composites*, 86, 19-29.

fib (International Federation for Structural Concrete). (2013). "fib model code for concrete structures 2010." Lausanne.

Graybeal, B. A. (2006). "Material property characterization of ultra-high performance concrete." *FHWA-HRT-06-103*, Federal Highways Administration, McLean.

Hassan, A., Jones, S., and Mahmud, G. (2012). "Experimental test methods to determine the uniaxial tensile and compressive behaviour of ultra high performance fibre reinforced concrete (UHPFRC)." *Construction and building materials*, 37, 874-882.

Jong, H., and Papworth, F. (2017). "Allowable crack widths and design crack widths versus Australian code minimum reinforcement quantities." *Proc., Concrete 2017*, Adelaide.

Leutbecher, T., and Fehling, E. (2012). "Tensile Behavior of Ultra-High-Performance Concrete Reinforced with Reinforcing Bars and Fibers: Minimizing Fiber Content." *ACI Structural Journal*, 109(2), 253-364.

Markovic, I. (2004). "High-performance hybrid-fibre concrete development and utilisation." Ph.D. Thesis, Delft University of Technology.

Moreno, D. M., Trono, W., Jen, G., Ostertag, C., and Billington, S. L. (2014). "Tension stiffening in reinforced high performance fiber reinforced cement-based composites." *Cement and Concrete Composites*, 50, 36-46.

Naaman, A. E. (2007). "Tensile strain-hardening FRC composites: Historical evolution since the 1960." *Advances in Construction Materials*, 2007, 181-202.

Noghabai, K. (2000). "Behavior of tie elements of plain and fibrous concrete and varying cross sections." *ACI Structural Journal*, 97(2), 277-284.

Park, S. H., Kim, D. J., Ryu, G. S., and Koh, K. T. (2012). "Tensile behavior of ultra high performance hybrid fiber reinforced concrete." *Cement and Concrete Composites*, 34(2), 172-184.

Rossi, P. (1997). "High performance multimodal fiber reinforced cement composites (HPMFRCC): The LCPC experience." *ACI Materials Journal*, 94(6), 478-483.

Russell, H. G. and Graybeal, B. A. (2013). "Ultra-high performance concrete: A state-of-the-art report for the bridge community." *FHWA-HRT-13-060*, Federal Highways Administration, McLean.

Schumacher, P. (2006). "Rotation Capacity of Self-Compacting Steel Fibre Reinforced Concrete." Ph.D. Thesis, Delft University of Technology.

Singh, M., Sheikh, A., Mohamed Ali, M. S., Visintin, P., and Griffith, M. C. (2017). "Experimental and numerical study of the flexural behaviour of ultra-high performance fibre reinforced concrete beams." *Construction and Building Materials*, 138, 12-25.

Sobuz, H., Visintin, P., Mohamed Ali, M. S., Singh, M., Griffith, M., and Sheikh, A. (2016). "Manufacturing ultra-high performance concrete utilising conventional materials and production methods." *Construction and Building Materials*, 111, 251-261.

Standards Australia. (1997). "Determination of the static chord modulus of elasticity and Poisson's ratio of concrete specimens." *AS 1012.17*. Sydney.

Standards Australia. (2000). "Methods of testing concrete- Compressive strength tests - Concrete, mortar and grout specimens. *AS 1012.9*. Sydney.

Standards Australia. (2006a). "Methods of testing portland, blended and masonry cements Determination of drying shrinkage of cement mortars." *AS 2350.11*. Sydney.

Standards Australia. (2006b). "Determination of drying shrinkage of cement mortars." *AS 2350.13*. Sydney.

Standards Australia. (2009). "Concrete structures." *AS 3600*. Sydney.

Standards Australia. (2015). "Method for making and curing concrete-Drying shrinkage specimens prepared in the field or in the laboratory." *AS 1012.8.4*. Sydney.

Stang, H., and Aarre, T. (1992). "Evaluation of crack width in FRC with conventional reinforcement." *Cement and Concrete Composites*, 14(2), 143-154.

Sturm, A. B., Visintin, P., and Oehlers, D. J. (2018). "Time-dependent serviceability behavior of reinforced concrete beams: Partial interaction tension stiffening mechanics." *Structural Concrete*, 19(2), 508-523.

Sturm, A. B., Visintin, P., and Oehlers, D. J. (2020). "Blending fibres to enhance the flexural properties of UHPFRC beams." *Construction and Building Materials*, 244, 118328.

Tian, Z., Liu, Y., and Yuan, C. (2016). "Influences of macro and micro steel fiber ratios on the Mechanical Properties of Ultra-High Performance Concrete." Master's Thesis, University of Adelaide.

Tiberti, G., Minelli, F., and Plizzari, G. (2015). "Cracking behavior in reinforced concrete members with steel fibers: A comprehensive experimental study." *Cement and Concrete Research*, 68, 24-34.

Voo, Y. L., Foster, S. J., and Gilbert, R. I. (2006). "Shear strength of fiber reinforced reactive powder concrete prestressed girders without stirrups." *Journal of Advanced Concrete Technology*, 4(1), 123-132.

Wille, K., El-Tawil, S., and Naaman, A. E. (2014). "Properties of strain hardening ultra high performance fiber reinforced concrete (UHP-FRC) under direct tensile loading." *Cement and Concrete Composites*, 48, 53-66.

Wille, K., and Naaman, A. E. (2012). "Pullout Behavior of High-Strength Steel Fibers Embedded in Ultra-High-Performance Concrete." *ACI Materials Journal*, 109(4), 479-487.

Wille, K., and Parra-Montesinos, G. J. (2012). "Effect of Beam Size, Casting Method, and Support Conditions on Flexural Behavior of Ultra High-Performance Fiber-Reinforced Concrete." *ACI Materials Journal*, 109(3), 379-388.

Wu, C., Oehlers, D., Rebentrost, M., Leach, J., and Whittaker, A. (2009). "Blast testing of ultra-high performance fibre and FRP-retrofitted concrete slabs." *Engineering Structures*, 31(9), 2060-2069.

Yoo, D.-Y., Shin, H.-O., Yang, J.-M., and Yoon, Y.-S. (2014). "Material and bond properties of ultra high performance fiber reinforced concrete with micro steel fibers." *Composites Part B: Engineering*, 58, 122-133.

STATEMENT OF AUTHORSHIP

Local bond slip behaviour of steel reinforcing bars embedded in UHPFRC
Structural Concrete, 20(1), 108-122.

Sturm, A.B. (Candidate)

Prepared manuscript, performed all analyses, and developed model and theory (80%)

This paper reports on original research I conducted during the period of my Higher Degree by Research candidature and is not subject to any obligations or contractual agreements with a third party that would constrain its inclusion in this thesis. I am the primary author of this paper.

Signed ..... Date 9/07/2020

Visintin, P.

Supervised and contributed to research, and acted as corresponding author (20%)

I certify that the candidate's stated contribution to the publication is accurate (as detailed above); permission is granted for the candidate in include the publication in the thesis; and the sum of all co-author contributions is equal to 100% less the candidate's stated contribution.

Signed ..... Date 02/07/2020

LOCAL BOND SLIP BEHAVIOUR OF STEEL REINFORCING BARS EMBEDDED IN UHPFRC

Sturm, A.B., Visintin, P.

ABSTRACT

The local bond stress slip behaviour is a fundamental property required for the analysis and design of concrete structures at both serviceability and at ultimate limit. The addition of fibres has been shown to significantly improve the bond between normal strength concrete and steel reinforcement but little work has investigated the bond between reinforcing and Ultra High Performance Fibre Reinforced Concrete (UHPFRC). In this paper a series of 69 pull tests are carried out on UHPFRC with either short straight or long hooked steel fibres including mixes where the two fibre types have been blended. The results of this study were combined with the results from existing literature to regress a material model for the bond slip behaviour between UHPFRC and ribbed steel reinforcing bars. Importantly, it is shown that models for normal strength fibre reinforced concrete cannot be extrapolated to UHPFRC.

INTRODUCTION

The local bond stress slip (τ-δ) behaviour of a reinforcing bar embedded in concrete (Fig 1a and b) is a fundamental property required for the analysis and design of concrete structures. Bond controls: tension stiffening, cracking and deflection at the serviceability limit (Balazs 1993; Muhamad et al. 2012); and is essential for the adequate anchorage of reinforcement at the ultimate limit (Eligehausen et al. 1983; Cosenza et al. 2002).

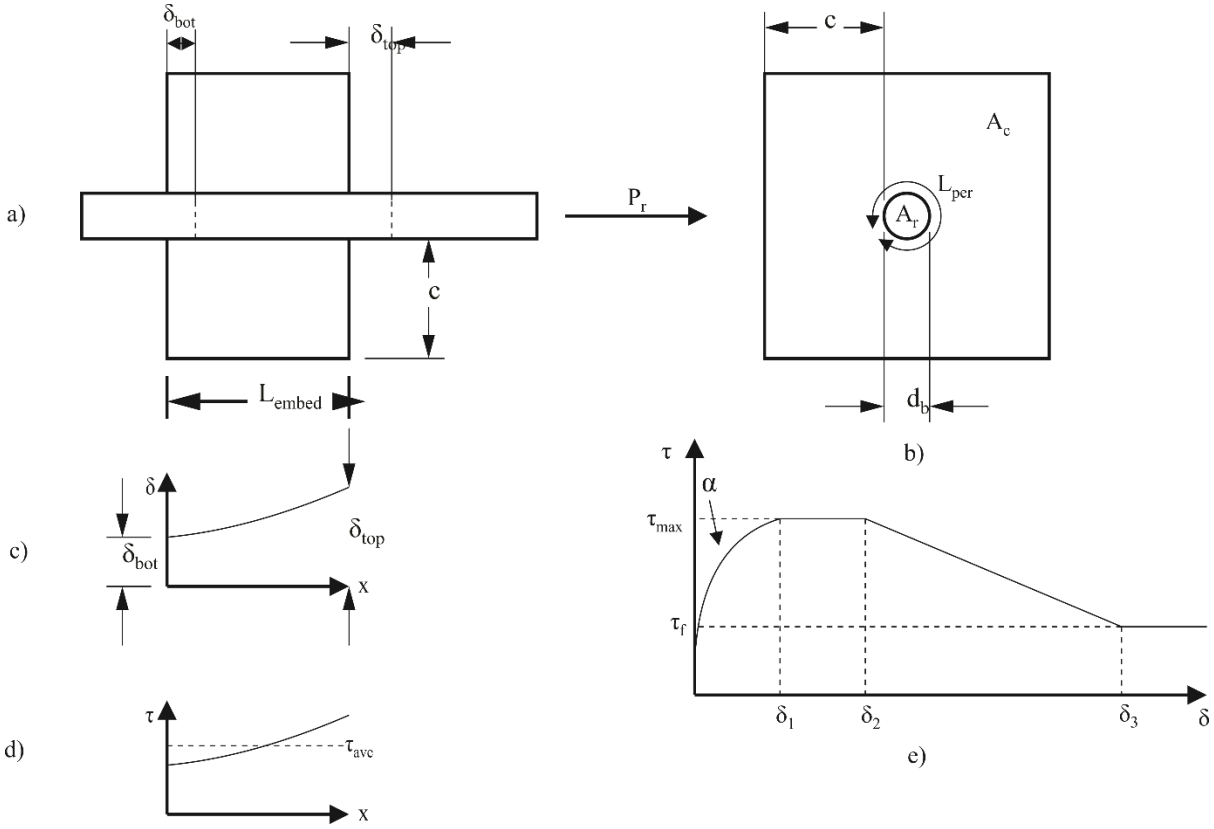

Fig. 1 Pullout test; a) longitudinal section; b) variation in slip; c) variation in slip stress; d) cross-section; e) local bond slip property

Bond refers to the magnitude of shear stress (τ) that can be transferred between the reinforcing bar and surrounding concrete due to their interaction and is a function of the local slip of the reinforcing bar (δ), where the slip is the difference in the axial deformation between the concrete and reinforcement, as indicated in Fig. 1(a-d). This behaviour is represented by the local bond slip relationship shown in Fig. 1(e) which is commonly derived from pull tests performed on short bonded lengths such that the reinforcement remains elastic (Eligehausen 1983; fib 2000). It should be noted that the change in bond properties after yielding of the reinforcement is an area of active research (Ruiz et al. 2007; Lee et al. 2011; Ashtiani et al. 2013) but is outside of the scope of this paper.

From the vast quantity of bond testing conducted on normal strength concrete it is known that the local bond slip characteristic is a function of the following factors (fib 2000):

- Material properties of the concrete including: strength of the concrete, consistency of the concrete and the change in properties due to shrinkage and creep.
- Material properties of the bar including: surface treatment e.g. smooth or ribbed bars and corrosion.
- Geometry of the reinforcement including: position of bar i.e. bar cover and spacing, and the presence of transverse reinforcement which induces confinement.
- Type of loading such as: sustained loading, reversed loading, cyclic loading.

The addition of short random fibres of any type, and in at any volume fraction to create fibre reinforced concrete (FRC) adds additional complexity to the factors listed above. For example:

- Fibres act to change the material properties of the concrete (strength, consistency and long term shrinkage and creep).
- They may increase the durability of structural elements due to reduced crack widths and there by reduce the risk corrosion.
- The improved strength and durability of FRC may lead to reduced cover and increased bar spacing,
- The addition of fibres provides confinement by bridging cracked planes and may reduce the need for transverse reinforcement and the propensity for splitting failure.
- Finally, all of the above characteristics may be influenced by sustained or cyclic loading which may act to reduce the effectiveness of fibres.

For normal strength FRC the effect of fibre volume and type has been widely investigated and has been shown to strongly influence bond performance (Harajli et al. 2002; Chao et al. 2009). This paper seeks to further extend experimental investigations to cover ultra-high performance fibre reinforced concrete (UHPFRC), which is a type of FRC where the compressive strength exceeds 150 MPa (AFGC 2013).

In this paper the available test data is collected and combined with new test results to develop an empirical model for the local τ-δ behaviour of deformed steel reinforcing bars in UHPFRC. To fill the gaps in the available data set, the results of 69 new pull tests are added to existing test data to determine the effect of variations in cover and fibre type (including hybrid fibres) on the local bond-slip behaviour.

LITERATURE REVIEW

Experimental studies

Initial work to quantify the bond between reinforcement and UHPFRC was conducted in small scale studies by Reineck & Greiner (2004) and Jungwirth & Muttoni (2004). Reineck & Greiner

(2004) performed pull-out tests on specimens with 4 mm reinforcing bars, while Jungwirth & Muttoni (2004) performed pull-out tests on bars with a diameter of either 12 mm or 20 mm and a variety of embedment lengths. Importantly, the latter study showed that for embedment lengths longer than 2 bar diameters which typically result in pull-out failure in normal strength concrete may lead to yielding or rupture of the reinforcement in UHPFRC. That is the tests highlighted the need for very short bonded lengths to investigate the local τ-δ bond properties.

A more detailed study of bond was later conducted by Oesterlee (2010) who performed a series of pull tests investigating the influence of specimen age (yielding a variation in compressive strength), fibre volume and bar surface (either deformed or plain). Similarly, Yoo et al.(2014) performed 16 pull tests on a UHPFRC containing short straight fibres where the fibre volume was varied between 1 and 4 % and the embedment length was varied between 16 and 32 mm (1 and 2 times the bar diameter). For each combination of embedment length and fibre volume 2 tests were performed. For each test both the slip at the loaded and free ends was measured. Slips up to 20 mm were reported giving insight into the bond behaviour at large deformations.

Marchand et al. (2016) performed a series of both monotonic and cyclic pull tests where the bar diameter, concrete cover and embedment length were varied. Interestingly the average slip was measured by determining the slip at the free end of the specimen and using an optical fibre embedded in the reinforcing bar to give continuous strain measurements along the length of the bar. This instrumentation methodology avoids the need to allow for the elastic extension of the reinforcing bar when determining the slip at the loaded end, but requires care to ensure the placement of the optical fibre does not interfere with the bond of the reinforcing bar.

Finally, Yuan & Graybeal (2014) performed a very large series of pull tests on a relatively long bonded lengths in order to identify the development length of a range of reinforcement in UHPFRC. The parameters investigated include casting orientation, embedment length, cover, compressive strength, bar diameter and bar type. The bars investigated included both Grade 60 (413 MPa) and Grade 120 (827 MPa) reinforcing bars, some of which had epoxy coatings. The higher strength reinforcing bars were important as this prevented the yielding of a significant number of bars for the longer bonded lengths.

A summary of the range of test parameters for each study is contained in Table 1. Note that the number of included tests refers to those which meet the criteria for the later development of a bond model rather than the total number of tests performed.

Table 1. Summary of test parameters

Reference	No. of Tests	No. of Included Tests	f_c (MPa)	c (mm)	d_b (mm)	c/d_b	V_f (%)	Fibre Type
Jungwirth & Muttoni (2004)	6	2	199	70-74	12-20	3.5-6.2	2.5	Straight 20/0.3
Reineck & Greiner (2004)	1	1	160	40	4	10	2	Straight 13/0.2
Oesterlee (2010)	20	5	155-219	21	8	2.6	0-3	Straight 13/0.16
Yoo et al. (2014)	16	6	185-207	67.1	15.9	4.2	1-4	Straight 13/0.2
Yuan & Graybeal (2014)	252	157	82-137	12.7-48.3	12.7-22.2	0.16-3.52	2	Straight 12.7/0.2
Marchand et al. (2016)	51	0	205	20-194	8-16	1.67-16.2	2.5	Straight 20/0.3

Note: Straight 20/0.3 means a straight steel fibre with length 20 mm and diameter of 0.3 mm

Analytical models

Modifications to the CEB-FIP bond slip model for extension to UHPFRC have been suggested by Yoo et al. (2014) and Marchand et al. (2016). Yoo et al. (2014) based his analytical model on 16 pull-out tests where the concrete strength varied between 184.9 and 207.2 MPa. Only a single cover (67.1 mm) and reinforcing bar diameter of (15.9 mm) was considered while the fibre volume was varied between 1 and 4%.

The analytical model suggested by Marchand et al. (2016) is based on 51 tests performed in their own study, as well as 26 tests taken from existing literature. The concrete strength was varied from 155 to 207 MPa, the cover was varied from 13 to 194 mm, the bar diameter was varied from 8 to 22 mm and the fibre volume was varied from 1 to 4%. Unfortunately, Marchand et al. (2016) did not present the data in such that it could be included in the regression in this paper as either the reinforcement yielded or the tests were performed under cyclic loading, hence these 51 tests are excluded from Table 1.

EXPERIMENTAL PROGRAM

From the literature summarised in Table 1 the primary research gaps were found to be: the influence of fibre type and the variation in behaviour with cover. To address this a series of 69

pull-out tests were performed across six different mixes to investigate the influence of these parameters in more detail.

Materials

Concrete

A UHPFRC developed at the University of Adelaide by Sobuz et al. (2016) which can be manufactured using materials and equipment utilised in the manufacture of normal strength concrete has been investigated. The basic mix design is provided in Table 2 where it can be seen that six variations in fibre type were considered. These include: (i) a control with no fibres, (ii) only macrofibres, (iii) only microfibres, (iv) a 50:50 mix of macro and micro, (v) a 60:40 mix of macro and micro as well as (vi) a 40:60 mix of macro and micro. Note that the macrofibres have hooked ends and are 35 mm long with a diameter of 0.55 mm and the microfibers are straight with a length of 13 mm and a diameter of 0.2 mm.

Table 2. UHPFRC mix design

Mix designation	Cement (kg/m^3)	Sand (kg/m^3)	Silica fume (kg/m^3)	Water (kg/m^3)	Superplasticiser (kg/m^3)	Macro fibres (kg/m^3)	Micro fibres (kg/m^3)
No fibres	978	973	260	171	44	0	0
1 Macro: 0 Micro	950	951	253	161	43	222	0
0 Macro: 1 Micro	950	943	253	168	43	0	222
0.5 Macro: 0.5 Micro	950	944	253	167	43	111	111
0.6 Macro: 0.4 Micro	950	945	253	166	43	88	133
0.4 Macro: 0.6 Micro	950	944	253	167	43	133	88

The compressive strength of each mix was obtained by testing of 100 mm x 200 mm cylinders at a load rate of 20 MPa/min before and after each series of pull tests. The results of these tests are summarised in Table 3. The tensile behaviour is also available in Visintin et al. (2018) and a summary of the obtained stress-crack width relationships is given in Fig. 2. These results were obtained under uniaxial direct tension, using the methodology and specimens developed by Singh et al.(2017)

Table 3. Concrete compressive strength

	Before Testing		After Testing	
Mix	Age at Testing (days)	f_c (MPa)	Age at Testing (days)	f_c (MPa)
No Fibres	29	150	54	169
1 Macro: 0 Micro	27	160	40	171
0 Macro: 1 Micro	24	154	48	156
0.5 Macro: 0.5 Micro	63	151	84	157
0.6 Macro: 0.4 Micro	27	157	48	157
0.4 Macro: 0.6 Micro	44	156	65	157

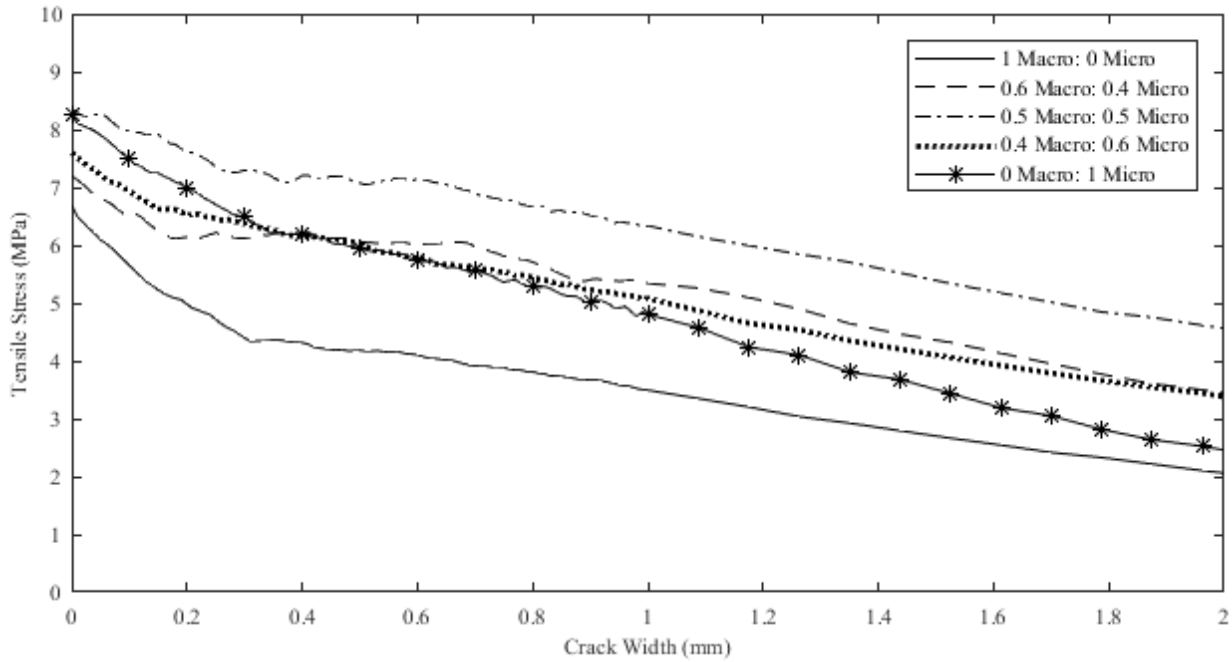

Fig. 2 Average stress-crack width relationship for each mix

Reinforcement

The reinforcement used in this study was a cold worked 16 mm deformed reinforcing bar complying with AS/NZS4671:2001 (Standards Australia 2001) as shown in Fig. 3. Based on direct tension tests, the elastic modulus of this bar was 200 GPa, the yield stress was 530 MPa (0.2% proof stress) and the ultimate stress is 690 MPa. The rib spacing was 8.65 mm and the rib height was 0.75 mm. The relative rib area was 0.0632.

Fig. 3 16 mm reinforcing bar

Specimen design

For each concrete type a single UHPC block of 891 mm length, 300mm depth and 150 mm thickness (Fig. 4) was cast. Each prism was embedded with 12 16 mm diameter ribbed steel bars complying to AS/NZS4671:2001(Standards Australia 2001) and with an experimentally measured elastic modulus of 200 GPa. Concrete cover was varied from 20 mm to 75 mm and the bonded length was taken as twice the bar diameter. To measure the slips of the reinforcing bar a single 15 mm LVDT was provided at the loaded end and two 15 mm LVDTs at the free end. Note that the the choice of embedment length and instrumentation was based on the analytical modelling summarised in the following section.

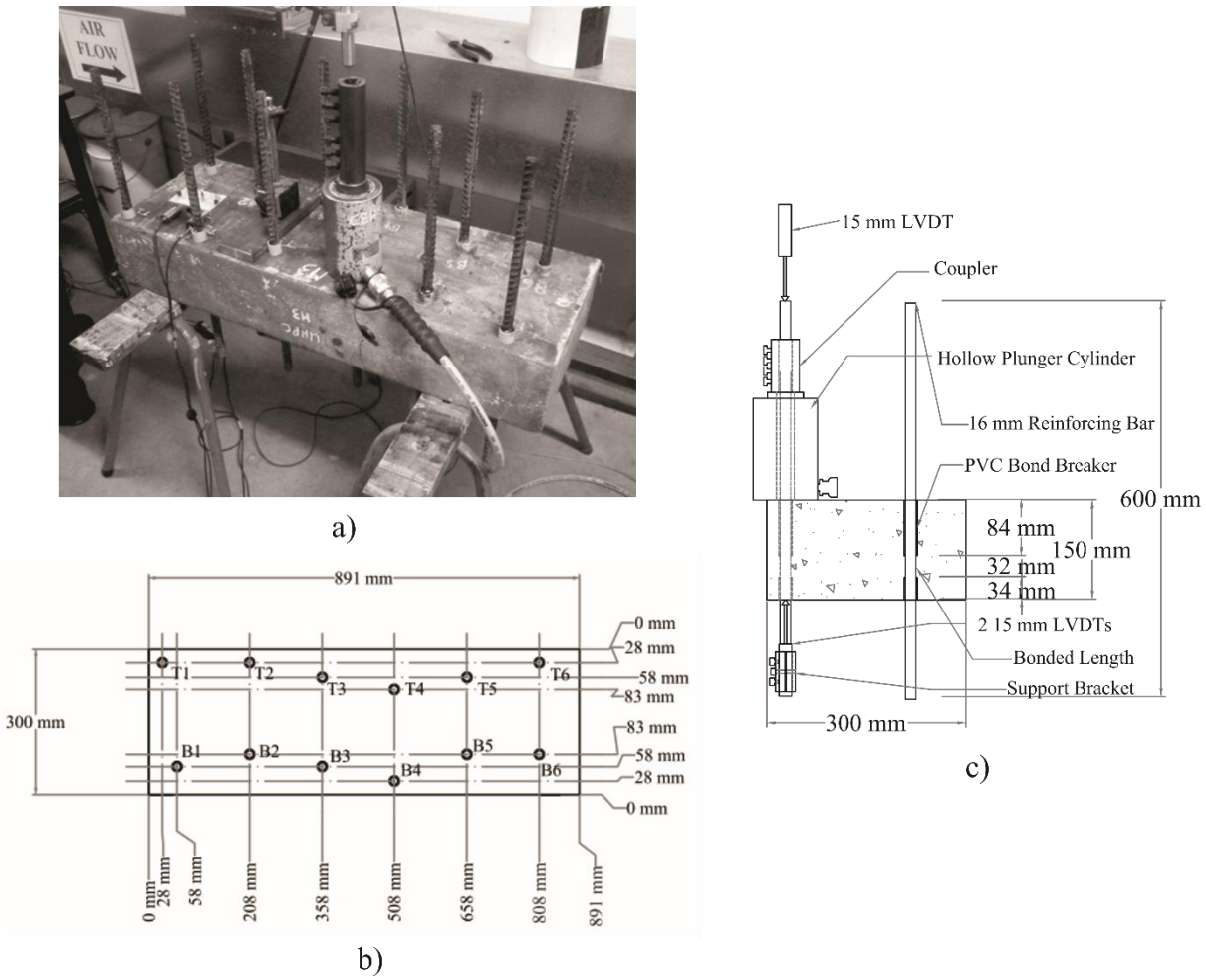

Fig. 4 a) Photograph of Test Setup; b) Plan view of specimen; c) elevation through specimen

Determination of bonded length

An important consideration in determining the local bond slip relationship from experimental data is the effect of the bonded length. If the bonded length is too long the commonly applied assumption that the slip and therefore stress is constant no longer holds. In this case, it is not possible to determine the local τ-δ relationship in Fig. 1(e) by simply determining the average bond stress, rather more advanced inverse analysis techniques such as those suggested by Haskett et al. (2008) and Visintin et al. (2012) are required. Moreover, for very high concrete strengths, where the bond can be expected to be very high it has been shown that traditionally applied rules of thumb such as bonded lengths of five times the bar diameter (RILEM 1994) may cause the reinforcement to yield or rupture (Jungwirth & Muttoni 2004).

The problem of defining a suitable bond length for ultra-high performance materials cannot be solved by an arbitrary reduction in bonded length. For example, take the extreme case of an infinitesimal bonded length. At this extreme level the problem of treating bond as a material property rather than a pseudo material property arises due to the mechanism of bond stress development. For example, Yoo et al. (2014) tested bonded lengths of one and two bar diameters and found that significant scatter was introduced for the shorter bonded length. This variation can be simply explained by considering the uncertainty in the number of bar ribs within the bonded length, since it is the local damage caused by the bearing of the local ribs which causes the typical variation in local bond properties in Fig. 1(b-c) (Tepfers 1973). Hence the solution is to choose a compromise bonded length that is sufficiently short that the assumption of a constant bond stress and slip across the bonded length is still valid but long enough so that the variation from local effects is minimised.

To determine the bonded length for the experimental design a numerical parametric study was performed by assuming a typical local bond slip relationship and using partial interaction mechanics (Haskett et al. 2008) to explore the variation in bond stress and slip for different bonded lengths. From this the actual bond stress-slip relationship can be compared to that obtained by averaging the observed shear stresses and slips or only measuring the slips at the loaded or unloaded end of the specimen as illustrated in Fig. 1(a).

From previous research (Balazs 1993; Muhamad et al. 2012) the bond stress and slip at an interface can be related by the following second order ordinary differential equation.

$$\frac{d^2\delta}{dx^2} = \tau L_{per}\left(\frac{1}{E_r A_r} + \frac{1}{E_c A_c}\right) \quad (1)$$

where τ is the bond stress, δ is the slip, x is position along the bonded length, L_{per} is the bonded perimeter of the reinforcing bar, E_r and E_c are the elastic moduli and A_r and A_c are the cross-sectional area of the reinforcement and concrete as indicated by the subscripts, these parameters are illustrated in Fig. 1(b).

To solve Eq. (1) boundary conditions need to be established. For a reinforcing bar with an embedded length that is sufficiently short such that there is slip at the free end the boundary conditions are

$$\left.\frac{d\delta}{dx}\right|_{x=L_{embed}} = \frac{P_r}{E_r A_r} \quad (2)$$

and

$$\sigma_r(x = 0) = 0 \quad (3)$$

where P_r is the load applied at the end of the reinforcing bar and σ_r is the stress in the reinforcing bar as a function of position. That is at the loaded end the slip strain ($d\delta/dx$) is simply equal to the strain in the reinforcing bar at that point and at the free end the bar must be unloaded.

To perform the parametric study a local bond slip relationship was assumed based on the functional form in the CEB-FIP Model Code 2010 (fib 2012) as illustrated in Fig. 1(e) with τ_{max} = 50 MPa, δ_1 = 0.2 mm, α = 0.4, δ_2 = 1 mm and τ_f = 10 MPa.

Since for a non-linear local bond slip relationship the governing differential equation (Eq. 1) is not solvable analytically for the boundary conditions in Eq. (2) and (3) here a numerical solution is instead considered. The numerical approach is illustrated in the flow chart in Fig. 5 and it should be noted that this procedure has been widely validated and applied for the analysis of reinforced concrete members (Knight et al. 2013; Visintin et al. 2013).

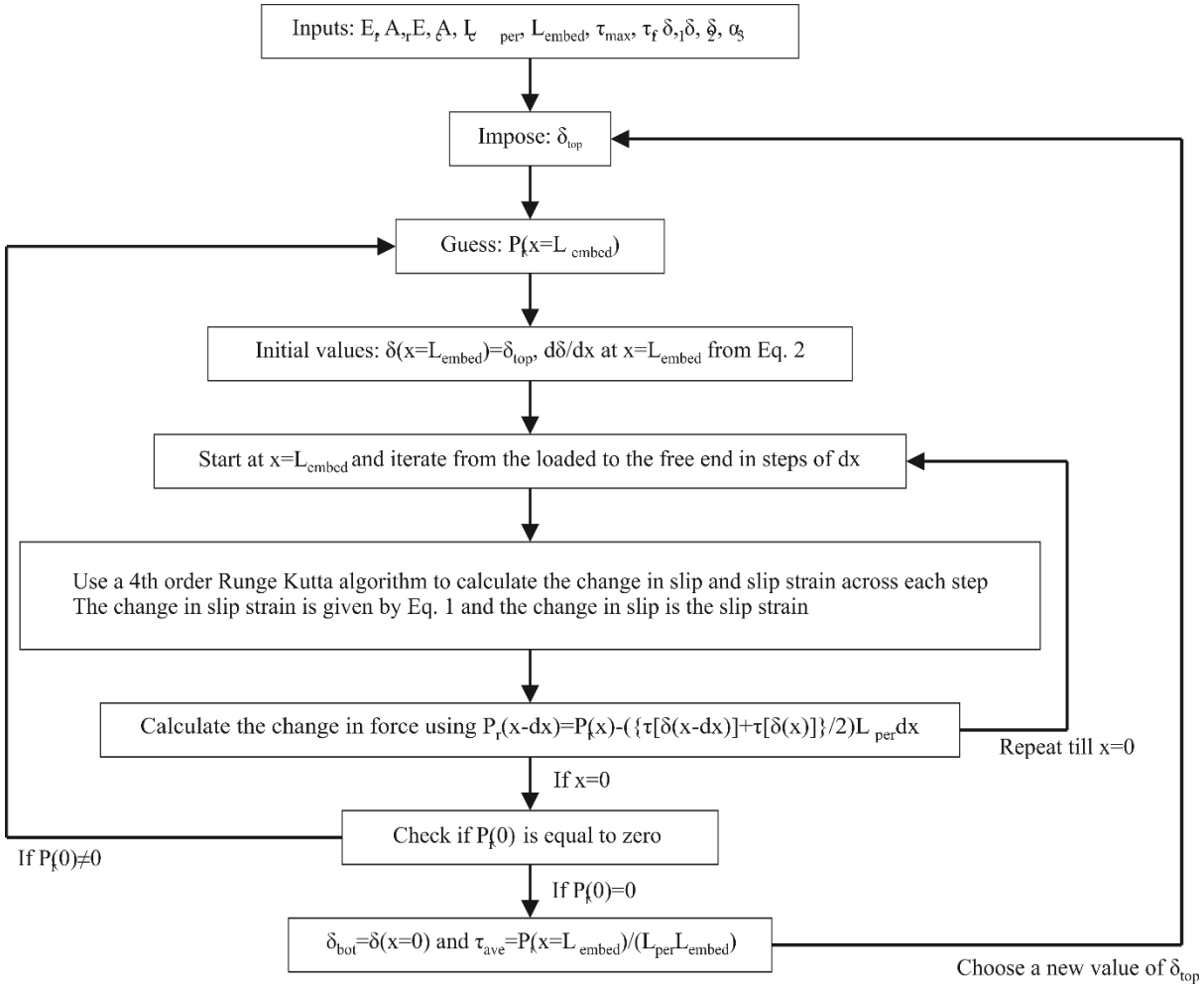

Fig. 5 Flow chart for the numerical solution of Eq. (1)

The results of the parametric study are shown in Figs. 6 and 7, where the difference between the local bond stress slip relationship, (which should be identical to the average bond stress slip relationship if the bond length is sufficiently short), and the observed local bond slip relationship is investigated for four different bonded lengths.

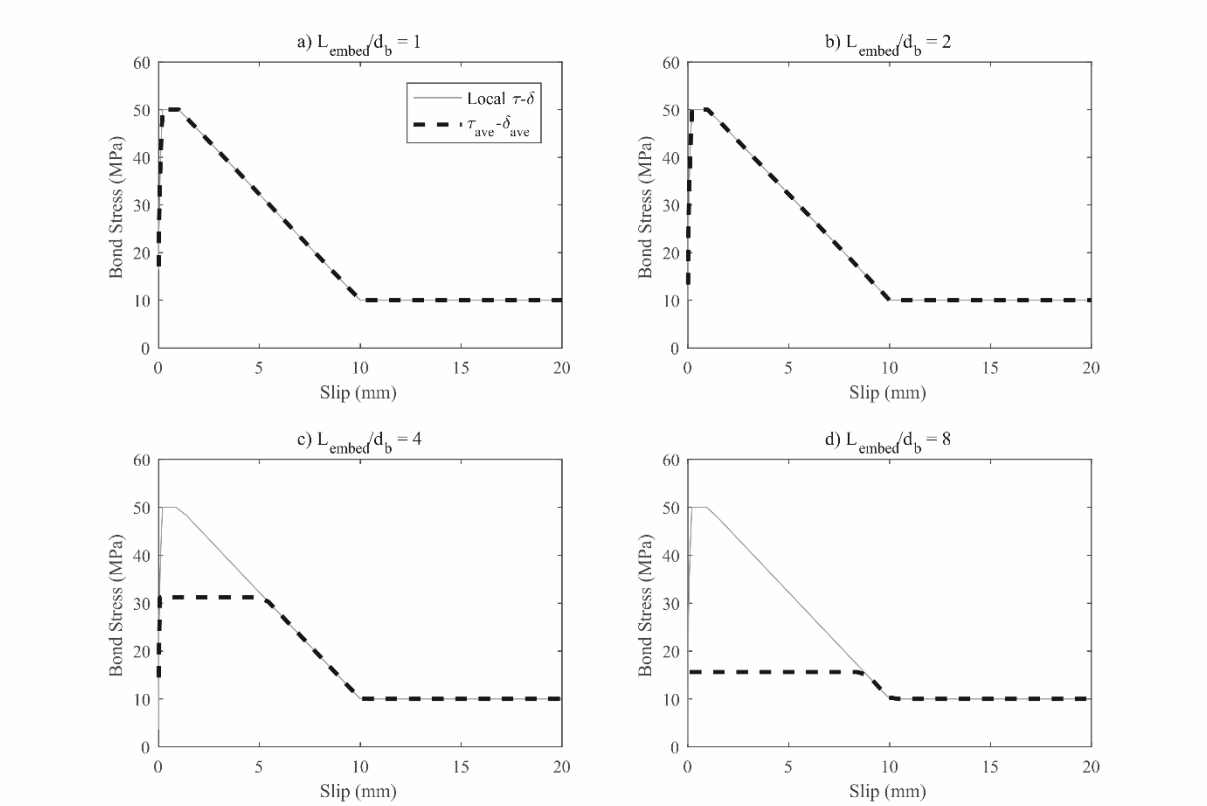

Fig. 6 Comparison of actual and estimated bond slip relationships for different bonded lengths (Slips up to 20 mm)

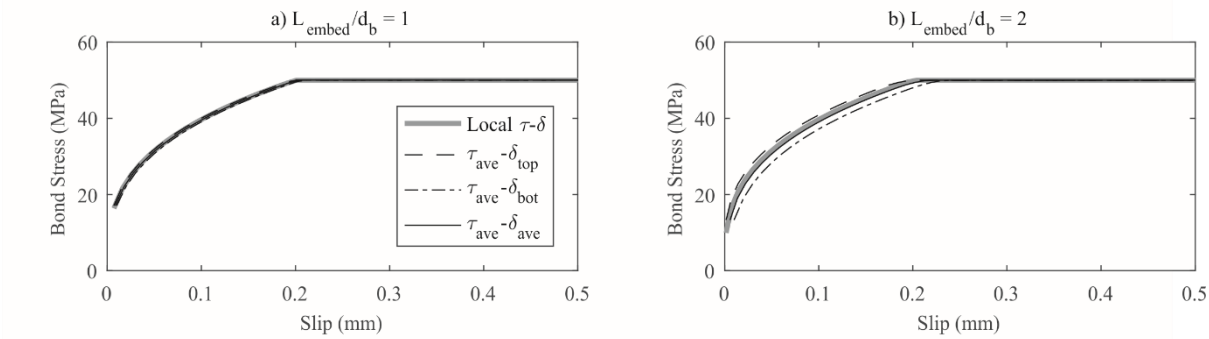

Fig. 7 Comparison of actual and estimated local bond slip relationships for different bonded lengths (Slips up to 0.5 mm)

As can be seen from Fig. 6 the post peak behaviour of the bond slip relationship is well characterised for any bonded length as long as the bar is prevented from yielding, noting that the plateau in Fig. 6(c-d) corresponds to yield of the reinforcement.

As a further comparison for the pre-peak behaviour the first two bonded lengths are now compared in Fig. 7.

From this comparison it is seen that for a bonded length of one bar diameter there is no discernible difference between the actual and observed bond slip behaviour irrespective of whether the slip was measured at the loaded or free ends or whether the average of those two values is taken. On the other hand for a bonded length of two diameters, the location of the slip measurement effects the observed behaviour as it is seen that the top slip represents a lower bound on the bond stress and the bottom slip represents an upper bound. If the slip is averaged

from both the top and bottom measurements a close estimate of the actual local bond property is obtained.

Hence for the experimental program a bonded length of two bar diameters is provided to avoid the inconsistent results observed experimentally for a bonded length of one bar diameter (Yoo et al. 2014) and the slip will be estimated by measuring the slip at both the loaded and free ends and then taking the average of this value.

TEST RESULTS

The results of all pull tests are shown in Fig. 8 for slips up to 2 mm and for a selected number of fibre types the bond slip relationship is shown for slips up to 20 mm in Fig. 9.

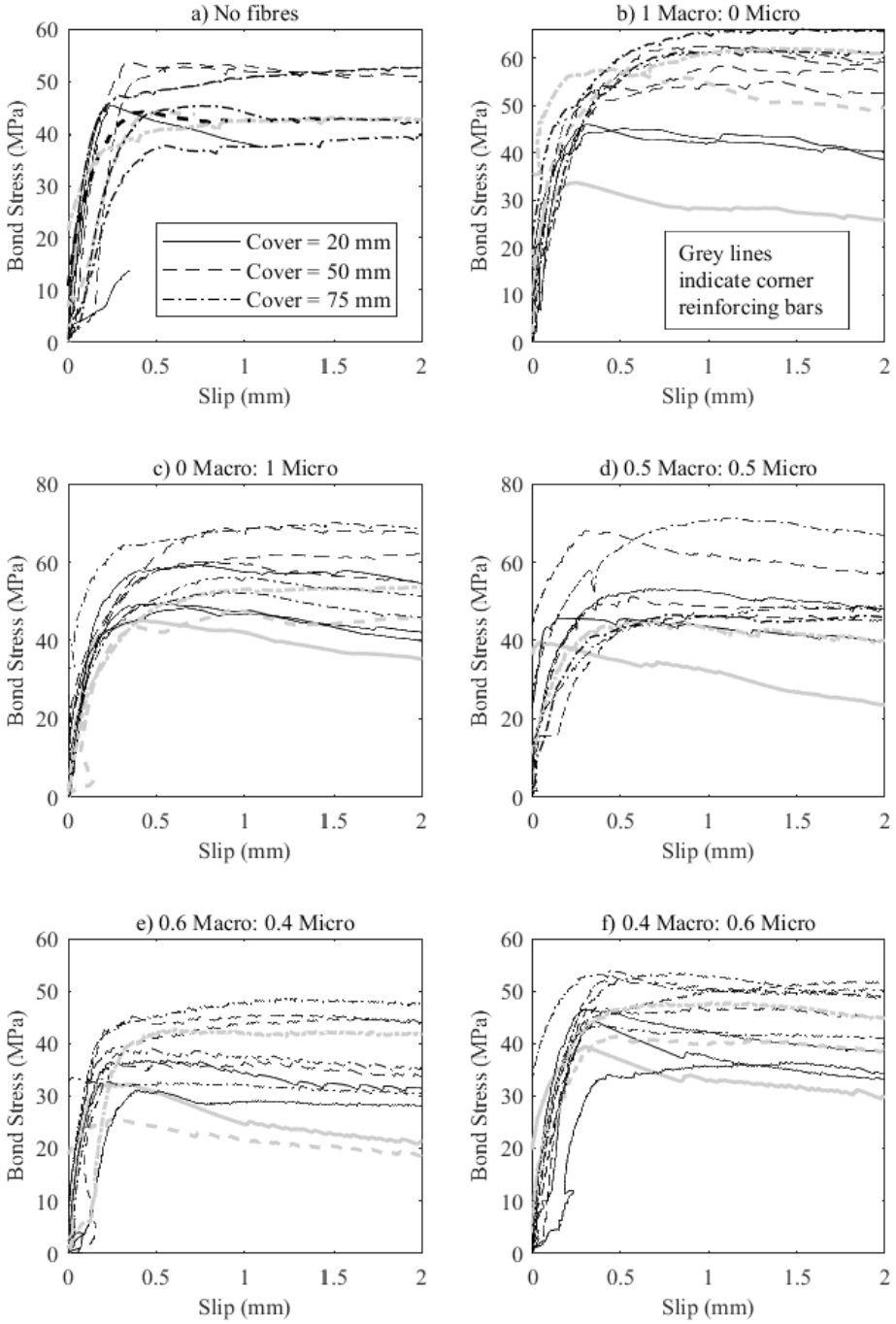

Fig. 8 Bond Slip Relationship up to 2 mm

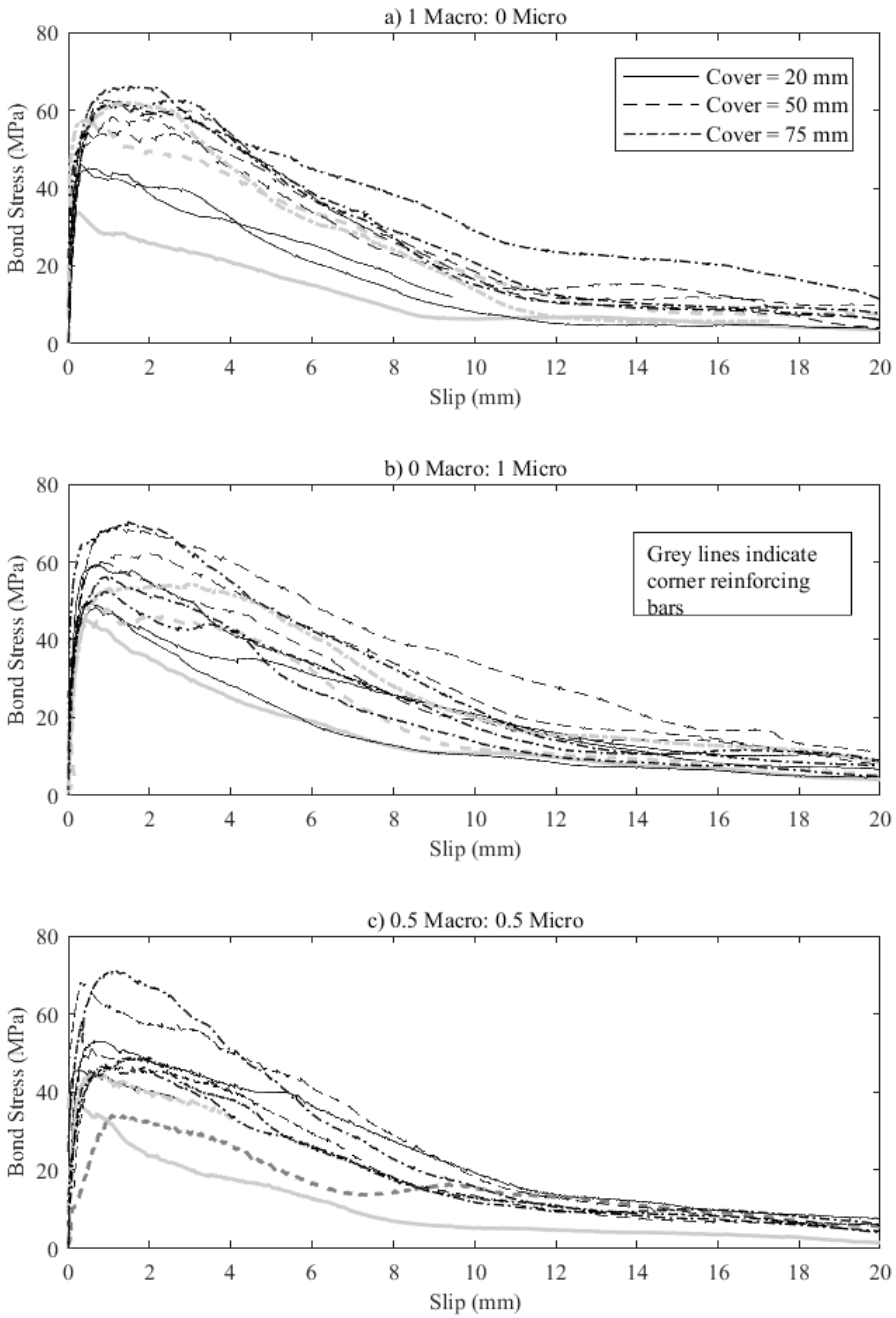

Fig. 9 Bond Slip Relationship up to 20 mm

Test Database

In order to identify trends in behaviour the new test results are added to those already available in the literature to form a database. For the purpose of discussion and model development from each test the following key points illustrated in Fig. 10 were determined and are summarised in Table A1.

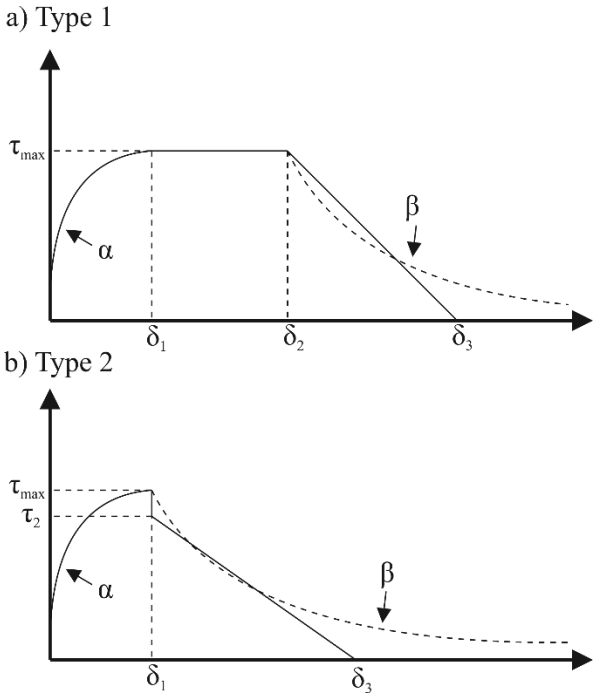

Fig. 10 Key points for test database

In Fig. 10 it has been identified that two distinct forms of τ-δ relationship may occur. Type 1 is similar to that obtained for well confined concrete of normal strength and is characterised by a plateau at the maximum bond stress between δ_1 and δ_2 (fib 2000). Type 2 curves are similar to those observed for splitting failure in normal strength concrete and is characterised by a step reduction at the formation of a splitting crack at a slip δ_1 which results in an instantaneous reduction in stress from τ_{max} to τ_2, followed by a more gradual reduction in bond stress. It should be noted that for both Type 1 and Type 2 curves, linear and non-linear descending branches have been considered as shown in Fig 10.

The ascending portion of the τ-δ relationship for both types of curves in Fig. 10 is

$$\tau = \tau_{max}\left(\frac{\delta}{\delta_1}\right)^{\alpha}; \delta < \delta_1 \quad (4)$$

For a type 1 relationship in the constant bond region

$$\tau = \tau_{max}; \delta_1 < \delta < \delta_2 \quad (5)$$

For the descending portion a type 1 relationship is given by

$$\tau = \tau_{max}\left(1 - \frac{\delta - \delta_2}{\delta_3 - \delta_2}\right); \delta_2 < \delta < \delta_3 \quad (6)$$

for a linear descending branch or

$$\tau = \tau_{max} e^{-\beta(\delta - \delta_2)}; \delta > \delta_2 \quad (7)$$

For a non-linear descending branch. For a type 2 relationship the descending curve is given by

$$\tau = \tau_2\left(1 - \frac{\delta - \delta_1}{\delta_3 - \delta_1}\right); \delta_1 < \delta < \delta_3 \quad (8)$$

for a linear descending branch or

$$\tau = \tau_{max} e^{-\beta(\delta - \delta_1)}; \delta > \delta_1 \quad (9)$$

for a non-linear descending branch.

To determine the key points in Table A1 the type of plot was determined visually by considering if a plateau was present. The maximum bond stress, τ_{max} was identified as either

the average bond stress within the plateau (Type 1) or the peak of the relationship (Type 2). δ_1 and δ_2 could then be determined by considering where a horizontal line with bond stress τ_{max} intersected the bond stress slip relationship for the first and last times. The α parameter was then fit by plotting the ascending portion of each test result. For the descending portion δ_3 was determined by fitting a linear curve for the descending portion between 100 and 50 percent of the maximum bond stress. Finally β was determined by considering the descending curve up to a slip of 20 millimetres.

Inclusion of the key point within the database was subject to the following caveats:

- The full load slip relationship was provided or the key points such as τ_{max} were tabulated.
- δ_1 and α parameters were only included if the test was conducted on a bonded length of two bar diameters or less and low variability was observed between repeated measurements.
- Slip was to be monitored at both the free and loaded ends so that an average could be taken
- The reinforcing bar did not yield or rupture.
- The test was performed under monotonic loading

Effect of adding fibres

The effect of adding fibres on the bond slip relationship is demonstrated in Fig. 11(a-c) for all three covers considered (20, 50 and 75 mm). It can be seen that for covers of 20 and 50 mm, that without fibres splitting failure occurs as indicated by the end of the test in Fig. 11(a-b). When splitting occurs in specimens without fibres, catastrophic failure with an immediate reduction in load was observed. It can further be seen that the addition of fibres, regardless of type, serves to prevent this catastrophic failure. Where splitting cracks were observed (only for corner bars with 20 mm cover) the confinement provided by the fibres ensured no sudden loss of bond strength.

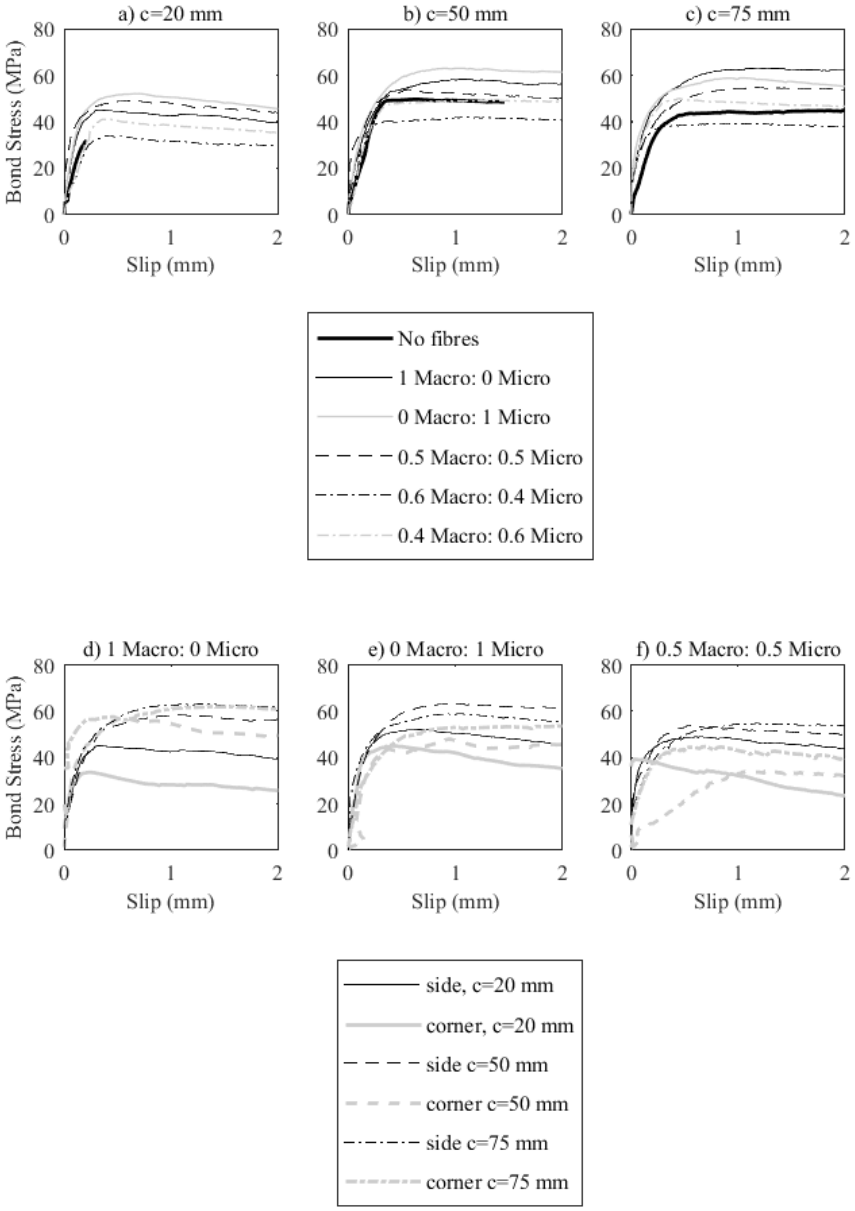

Fig. 11 Comparison of bond slip relationships to experimental results for slips up to 2 mm

Table 4 summarises and compares the key points between the fibre and no fibre case. It can be seen that for four of the five mixes the addition of fibres results in an increase in the maximum bond stress, three of the five mixes also experienced an increase in the slip to reach the maximum bond stress as well as the length of the stress plateau. The shape of the initial portion of the curve was also effected with all mixes having fibres displaying a steeper rising branch. Oesterlee (2010) also observed an increase in maximum bond stress and slip with increased fibre volumes. The α parameter was also observed to be higher for specimens without fibres.

Table 4. Comparison of average values of key points between the fibre and no fibre case

	1 Macro: 0 Micro	0 Macro: 1 Micro	0.5 Macro: 0.5 Micro	0.6 Macro: 0.4 Micro	0.4 Macro: 0.6 Micro
$\tau_{max}/\tau_{max\text{-}nf}$	1.289	1.327	1.202	0.889	1.098
$\delta_1/\delta_{1\text{-}nf}$	1.106	1.244	1.161	0.971	0.935
$\delta_2/\delta_{2\text{-}nf}$	1.444	1.413	1.109	0.983	0.938
α/α_{nf}	0.530	0.531	0.610	0.820	0.766

Dependence on ratio of macro to microfibres

The effect of fibre type is indicated in Fig. 11(a-c) where it can be seen that for covers of 20 and 50 mm specimens that 0 Macro: 1 Micro had the best performance and for a cover of 75 mm it was observed that 1 Macro: 0 Micro had the best performance. 0.4 Macro: 0.6 Micro had the weakest performance. 0.5 Macro: 0.5 Micro and 0.6 Macro: 0.4 Micro had performances intermediate between these two extremes.

To investigate quantitatively whether there is a dependence on fibre type a linear regression was performed in terms of the proportion of microfibres. The 95% confidence interval of the fitted slope was investigated and if zero was included in the interval the dependence was considered to be insignificant (Cox & Hinckley 1979). In Table 5 the fitted slopes are presented for each bond parameter as well as the 95% confidence interval on the value of this slope. As zero was included in the interval for every case, the bond parameter can not be conclusively identified as either increasing or decreasing as a function of the proportion of fibres. Hence it is suggested that based on these tests, the bond parameters are not functions of the ratio of macro to micro fibres. That is the blending of fibres does not have a significant effect on the bond parameters as the variation in behaviour seen in the 0.6 Macro:0.4 Micro results in Table 4 can be considered an outlier as they do not follow the general trend that occurs with increasing microfiber content. This can be contrasted with the tensile behaviour of the material where it was found that the relative proportion of fibre types had a significant effect on the observed stress-crack width behaviour under tension (Visintin et al. 2018). The difference in behaviour between the direct tensile and bond behaviour is likely due to a non-uniform distribution of fibres around the reinforcement.

Table 5. Dependence of parameter on fibre type

Parameter	Slope (lower bound, upper bound)
τ_{max}	3.54 (-5.15, 12.2)
τ_2	9.18 (-9.72, 28.1)
δ_1	0.0677 (-0.238, 0.374)
δ_2	-0.221 (-1.03, 0.592)
δ_3	1.27 (-1.13, 3.67)
α	-0.0123 (-0.138, 0.113)
β	-0.0212 (-0.0476, 0.00516)

Note: Slope refers to the slope of the curve obtained from a linear regression with proportion of microfibres as the explanatory variable and the bond parameter as the predicted variable.

Shape of bond slip relationship – influence of cover

In Fig. 11(d-f) for three mixes the effect of cover is investigated. It can be seen that a cover of 20 mm resulted in a lower bond strength while for increased cover there is no clear trend in the result. The lack of strong dependency on cover is likely the result of the confinement provided by the fibres.

The effect of bar position was also investigated and it can be seen that a bar placed in the corner has a lower strength and the bond strength reduces more quickly after reaching the peak than for a bar placed at the side. One manner in which this is represented is by the shape of the bond slip relationship. In Table 6 the percentage of either type 1 or 2 bond slip relationships (see Fig. 10) as a function of cover and bar position is recorded. Note that the relationship between the shape and the type of failure could not be confidently determined because in the vast majority of cases, even when a type 2 failure occurred the splitting cracks could not be observed.

Table 6. Shape of curve as a function of cover and position of reinforcing bar

Cover (mm)	Proportion of type 2 relations (%)	
	Side	Corner
20	50	100
50	33.3	60
75	36.4	20

As can be seen decreasing the cover or placing the bar in the corner increases the chance of producing a type 2 relationship. Hence for applying the following material model a type 2 relationship should be used if the cover is less than 50 mm or for corner bars if the cover is less than 75 mm otherwise a type 1 relationship can be used. Note that as the largest cover considered was 75 mm, more testing would be required to make conclusive statements for covers larger than this value.

REGRESSION OF LOCAL BOND-SLIP RELATIONSHIP

The data from the test database was integrated together with that from the current experimental investigation so that a material model could be developed. For the gathered data the predictive parameters were considered to be the concrete strength, cover, fibre volume and the bar diameter. It should be noted that the proportion of fibre type had been dismissed as a predictive variable based on the statistical analysis in the previous section.

The following procedure was used to identify the regression with the lowest error. First the most important variable was identified and the functional form varied to minimise the error. When this functional form is found, the residuals were investigated to determine the dependence on the other variables. If a dependence was found, the other variable was introduced and then functional forms involving both variables investigated. The residuals are then investigated again and this procedure is continued until no more dependences are found.

Based on this multivariable regression the following model is obtained

$$\tau_{max} = (0.0018c + 0.186)f_c \quad (10)$$

$$\tau_2 = (0.0008c + 0.941)\tau_{max} \leq \tau_{max} \quad (11)$$

$$\delta_1 = (-0.0002c + 0.001)f_c + 0.0386c + 0.0715 \quad (12)$$

$$\delta_2 = 2.42 \quad (13)$$

$$\delta_3 = 0.179\tau_{max} + 0.74 \quad (14)$$

$$\alpha = 0.0183d_b - 0.0055\tau_{max} + 0.304 \quad (15)$$

$$\beta = -0.0015\tau_{max} + 0.217 \quad (16)$$

where each parameter is defined in Fig. 10 and all units are in Millimetres and Megapascals. Note that as Eqs. (10-16) represents a purely empirical material model, it should not be used outside of the bounds of the testing parameters from which it was derived.

The goodness of fit for each of the key parameter predicted using Eqs. (10-12) and (14-16) is determined by comparing the ratio of the experimental to predicted results. The statistics describing the goodness of fit, including the mean, standard deviation, confidence limits and extreme values are summarised in Table 7. The ratio of the predicted to experimental values are also shown in Fig. 12.

Table 7. Summary statistics for regression

	Exp./Pred.					
	τ_{max}	τ_2	δ_1	δ_3	α	β
Mean	1.004	0.994	0.977	1.001	1.012	0.996
SD	0.206	0.035	0.566	0.230	0.419	0.223
COV	0.206	0.035	0.579	0.230	0.414	0.224
5% CL	0.664	0.937	0.046	0.622	0.323	0.629
95% CL	1.343	1.051	1.908	1.379	1.701	1.363
Min.	0.595	0.922	0.091	0.229	0.352	0.645
Max.	1.801	1.045	3.093	1.519	2.497	1.491

Notes:
SD is standard deviation
COV is coefficient of variation
5% CL is the 5% confidence limit and it is equal to Mean – 1.695SD
95% CL is the 5% confidence limit and it is equal to Mean +1.695SD

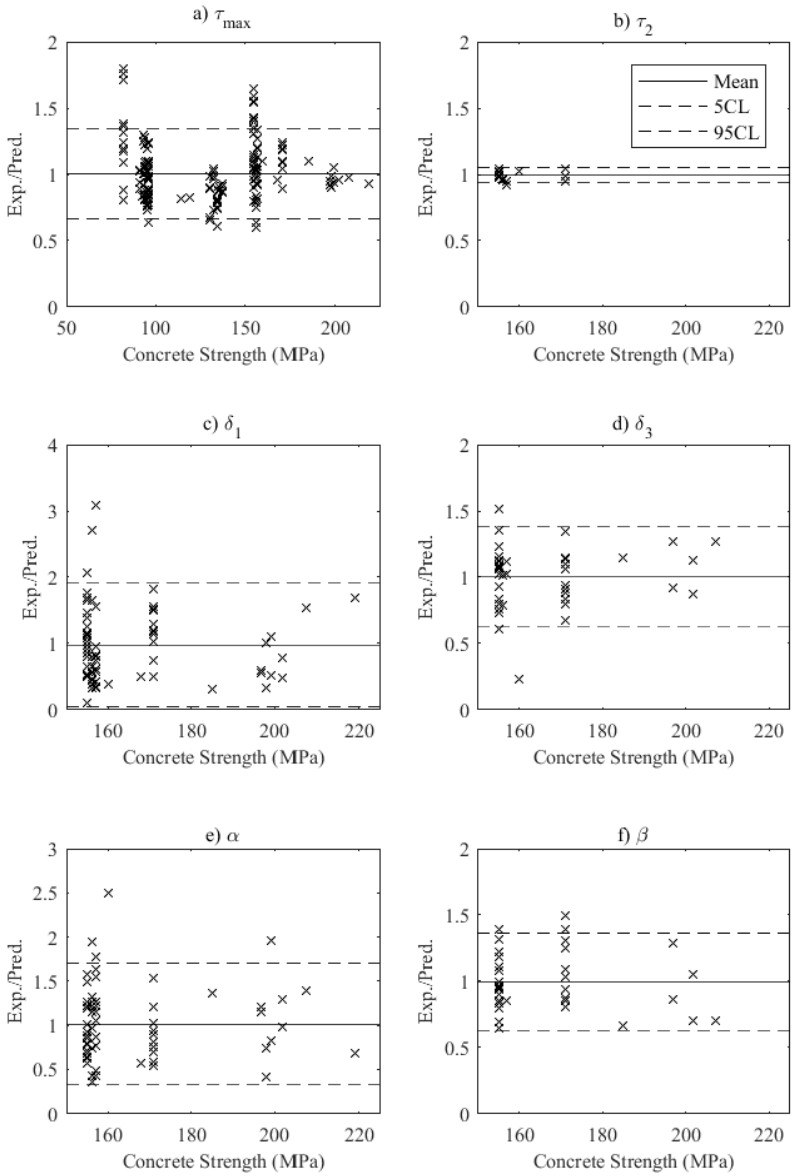

Fig. 12 Residual plot for each parameter

Note that no expression was fitted for δ_2 since this parameter did not appear to have a clear dependence on any of the predictive variables, hence a constant value equal to the mean of 2.42 mm was assumed. The standard deviation of δ_2 is 0.719. The 95% confidence limits are 1.24 and 3.6 mm. The minimum value is 0.793 mm and the maximum value is 4.14 mm.

From this it can be seen that good fits were obtained for τ_{max}, τ_2, δ_3 and β. More scatter was present for the fitted α expression and very high scatter was observed in the slip to first reach the peak stress, δ_1. It was seen that the primary predictive variables were concrete strength, cover and the maximum bond stress, though the maximum bond stress is seen as a composite of the previous two variables. None of the bond parameters had a dependence on fibre volume and only the shape parameter α had a dependence on the bar diameter. This though could be a result of the limited range of values explored for these two variables with a maximum bar diameter of 22.2 mm and the majority of tests using approximately 16 mm diameter bars. Further only Oesterlee (2010) and Yoo et al. (2014) varied the fibre volume, with all other tests using either 2 or 2.5% by volume. Hence it is expected that the material model is valid for bar

diameters less than 20 mm and fibre volumes between 2 and 3 percent but beyond this range more caution should be utilised.

CROSS-VALIDATION AND COMPARISON

Other bond stress slip relationship suggested for UHPFRC include those of Yoo et al.(2014) and Marchand et al.(2016) and the functional forms are illustrated in Table 8. In this section these relationships are compared to the model suggested in this paper. As a point of reference, the relationships suggested by fib (2013) for ordinary reinforced concrete without fibres and Harajli et al. (2002) for normal strength fibre reinforced concrete are also compared. In Fig. 13 the relationships are compared up to 2 mm illustrate the prepeak behaviour and in Fig. 14 the relationships are compared for the full bond slip relationship to demonstrate the post peak behaviour. In Fig. 15 the expressions for the peak bond stress are also compared.

Table 8. Summary of other bond slip relationships for UHPFRC

Reference	Expressions
Yoo et al. (2014)	$\tau = \tau_{max}\left(e^{-\frac{\delta}{s_r}}\right)$ $\tau_{max} = 5\sqrt{f_c}$ $s_r = 0.07$ $\beta = 0.8$
Marchand et al. (2016)	Rising branch given as $\tau = \tau_{max}\left(1 - \left(1 - \frac{\delta}{\delta_1}\right)^3\right); \delta < \delta_1$ For $\tau_{max} = 3.9\sqrt{f_c}\,; \frac{c}{d_b} > 4$ $\tau_{max} = 3.9\sqrt{f_c}\,\frac{\left(\frac{c}{d_b}\right)}{4}; \frac{c}{d_b} < 4$ $\delta_1 = 0.1$ After peak follows fib Model Code 2010[26] with δ_2=0.6 mm

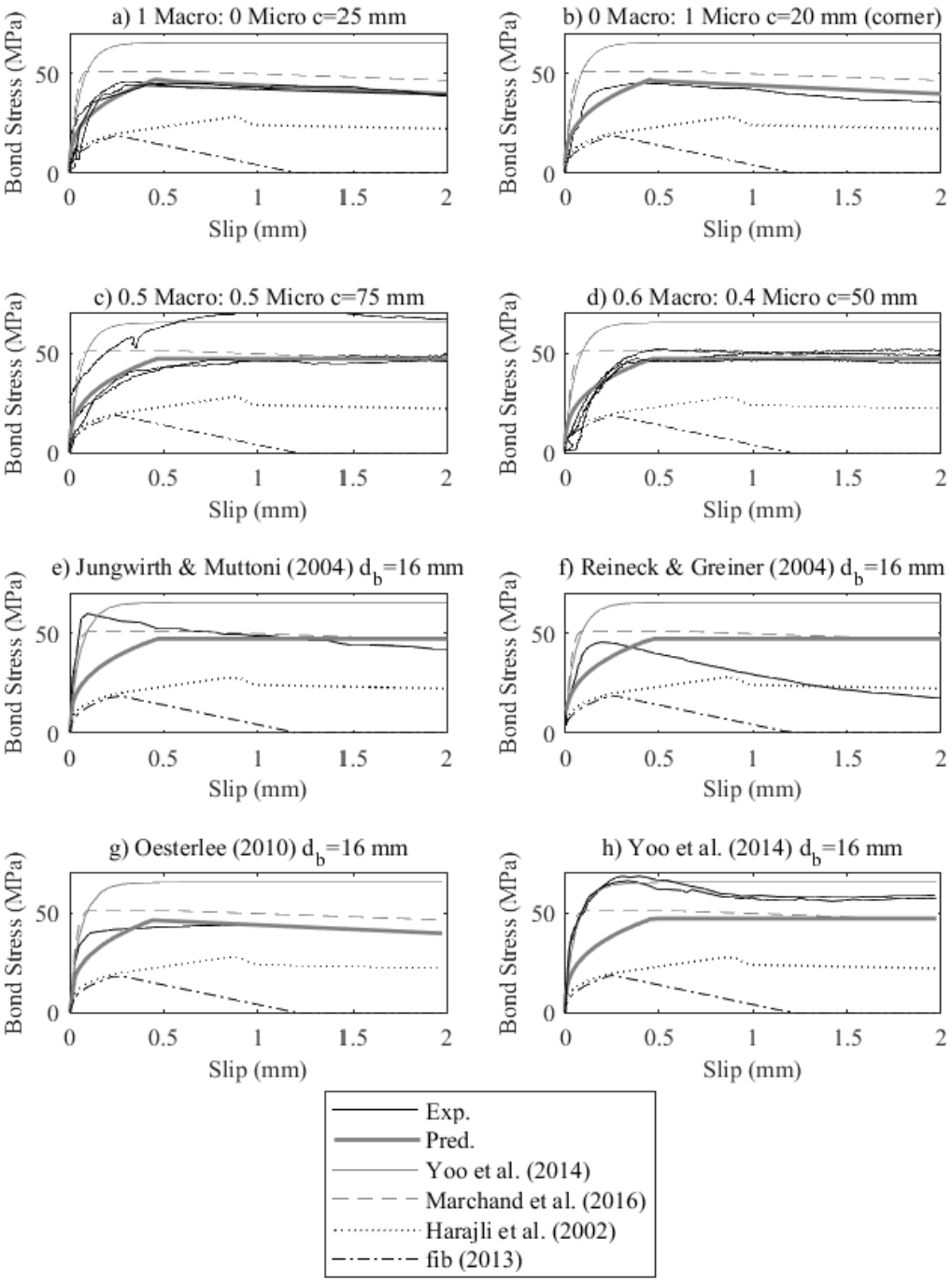

Fig. 13 Comparison of bond slip relationships to experimental results for slips up to 2 mm

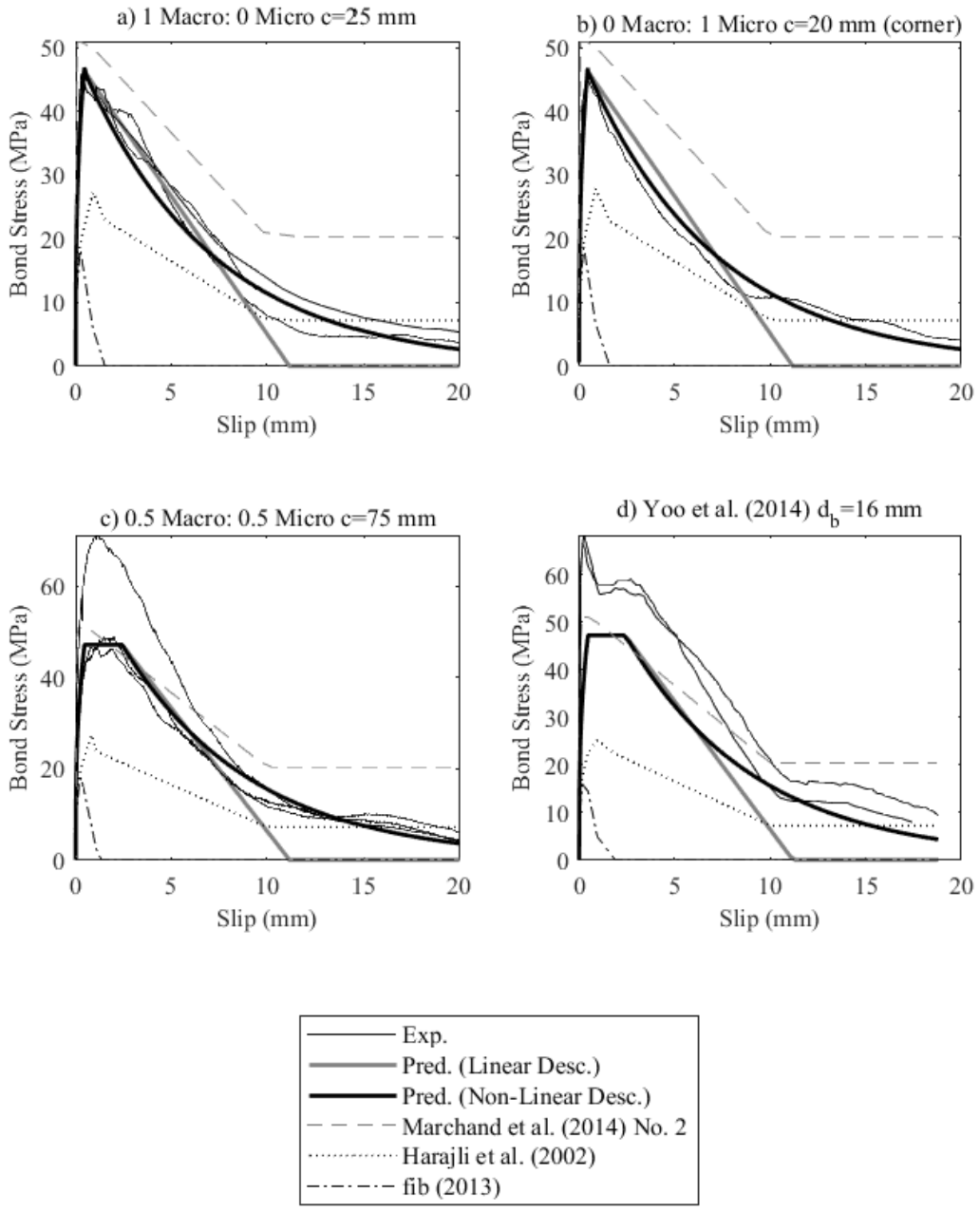

Fig. 14 Comparison of bond slip relationships to experimental results for slips up to 20 mm

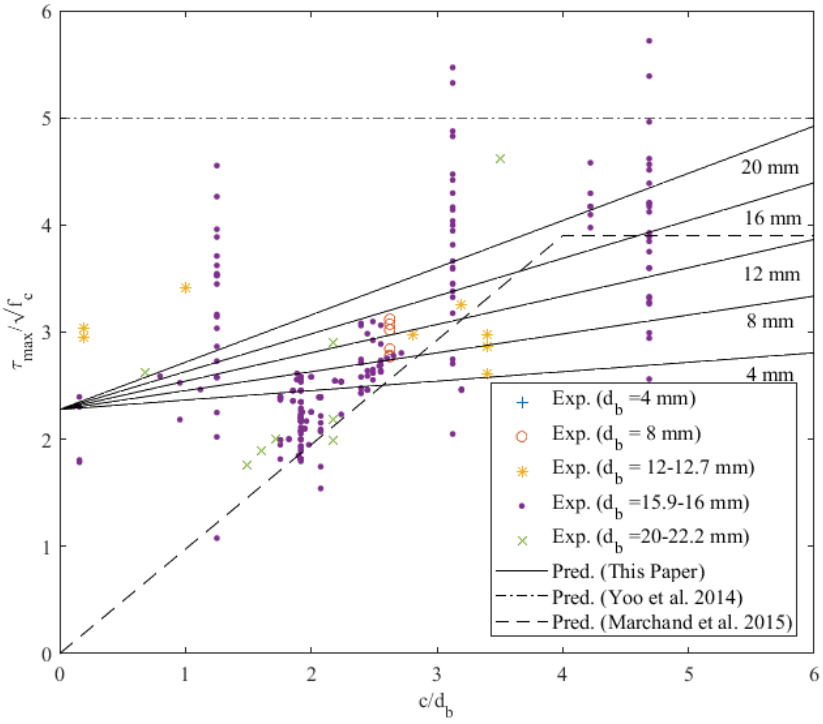

Fig. 15 Comparison of expressions for peak bond stress

From Fig. 13(a-d) it is shown that the regressed model has good agreement with the presented test results. The expressions suggested by Yoo et al. (2014) and Marchand et al.(2016) are in general too stiff in the rising branch and the maximum bond stress is over estimated. For Fig. 13(e) the suggested relationship is not stiff enough though better agreement is seen post peak. Yoo et al. (2014) and Marchand et al. (2016) have the correct stiffness though Yoo et al. (2014) overestimates the maximum bond stress. None of the models accurately predict the behaviour of Fig. 13(f) though the rising branch of Marchand et al. (2016) has the correct stiffness and the peak value is close. The regressed model most closely estimates the experimental curve for Fig. 13(g) followed by Marchand et al. (2016). For Fig. 13(h) Yoo et al. (2014) has the best agreement for the rising branch though the plateau is too high. Both Marchand et al. (2016) and the regressed model underestimate the bond stress for Fig. 13(h).

It was observed that the models for both ordinary reinforced concrete and normal strength fibre concrete greatly underestimate the bond stress for UHPFRC demonstrating the necessity of a bond slip model specific to this material.

From Fig. 14(a-c) the regressed model shows the best agreement with Marchand et al. (2016) overestimating the bond strength. For Fig. 14(d) both Marchand et al.(2016)and the regressed model underestimate the bond strength except for the frictional component where Marchand et al. (2016) is an overestimate. In general, Yoo et al. (2014) is seen to be an overestimate in all cases, Marchand et al. (2016) is generally a slight overestimate and the presented model is either close to the experimental or slightly conservative.

In Table 9 the peak bond stress expressions are compared it is shown that the proposed model has improved accuracy and reduced scatter, likely due to the larger range of test results from which it was derived. The results are also compared in Fig. 15. Note that to compare the proposed relationship on the axes given a curve is given for each bar diameter (as Eq. 10 is a

function of cover and not cover to diameter ratio) and the concrete strength is assumed to be 150 MPa (as Eq. 10 is a linear function of the concrete strength and is not a function of the square root). Note that one issue with the proposed expression in this paper is that the peak bond stress increases without bound with the increase in cover which is unphysical. However, for the range of covers considered it was not possible to determine when the peak bond stress would cease increasing with an increase in cover. This due to the empirical nature of the model hence it is unwise to extrapolate beyond the bounds of the testing regime. However, if an estimate of the bond stress is required for a cover greater than 75 mm, then the bond stress should be assumed to be equal to the cover at 75 mm.

Table 9. Comparison of expressions for peak bond stress

	Exp./Pred.		
	Eq. (13)	Yoo et al. (2014)	Marchand et al. (2016)
Mean	1.004	0.564	0.722
SD	0.206	0.168	0.216
COV	0.206	0.298	0.298
5% CL	0.664	0.287	0.368
95% CL	1.342	0.839	1.076
Min.	0.595	0.308	0.395
Max.	1.801	1.144	1.466

CONCLUSION

Bond is a fundamental property for both serviceability and ultimate behaviour of reinforced concrete structures. In this paper the available literature on the bond behaviour of UHPFRC is investigated and the gaps identified, namely the effect of mixing different fibre types. An experimental program of 69 pull tests was then conducted to further investigate the significance of these parameters. Importantly, the results of these tests show that fibre type does not have a significant effect on the bond behaviour in contrast to the behaviour under direct tension.

Importantly, it has been shown how fundamental partial interaction mechanics can be applied to the design of test specimens. In doing so it it has been identified that pull-tests to extract bond properties for UHPFRC should be limited to 2 times the bar diameter and slips should be recorded at both the loaded and unloaded end.

The existing and new test results were then used to regress a new material model for the bond slip behaviour of steel reinforcing bars in UHPFRC and are shown to have a better fit and less scatter then existing models. It should however be noted that significant scatter still exists due to the very small range of parameters investigated. It is suggested that further testing is required, particularly for reinforcing bars larger than 20 mm and for fibre volumes significantly higher or lower than 2%.

ACKNOWLEDGEMENT

This material is based upon work supported by the Air Force Office of Scientific Research under award number FA2386-16-1-4098."

NOTATION

A_c, A_r = cross-sectional areas of concrete and reinforcement, respectively;
c = cover;
d_b = bar diameter;
E_c, E_r = elastic modulus of concrete and reinforcement, respectively;
L_{embed} = embedment length;
L_{FI} = minimum length to reach the full interaction boundary condition;
L_{per} = bonded perimeter;
P_r = force applied to reinforcing bar;
x = distance from free end of reinforcing bar;
V_f = proportion of fibres by volume;
α = non-linearity of ascending portion of bond slip relationship;
β = shape parameter for non-linear descending portion of bond slip relationship;
δ = interface slip;
δ_{bot} = slip at free end;
δ_{top} = slip at loaded end;
δ_1 = slip to reach peak bond stress;
δ_2 = slip at transition from constant to reducing bond stress;
δ_3 = slip when τ=0 for linear descending portion of bond slip relationship;
δ'= slip strain;
λ = bond parameter;
σ_r = axial stress in reinforcement;
τ = bond stress; interface shear stress;
τ_{max} = peak bond stress;
τ_2 = post peak bond stress for type 2 bond slip relationships;

REFERENCES

AFGC (Association Francaise de Genie Civil). (2013). *Betons fibres a ultra-hautes performances- Recommandations* [Ultra high performance fibre reinforced-concretes – Recommendations], Paris.

Ashtiani, M. S., Dhakal, R. P., and Scott, A. N. (2013). "Post-yield bond behaviour of deformed bars in high-strength self-compacting concrete." *Construction and Building Materials*, 44, 236-248.

Balazs, G. L. (1993). "Cracking analysis based on slip and bond stresses." *ACI Materials Journal*, 90(4), 340-348.

Chao, S. H., Naaman, A. E., and Parra-Montesinos, G. J. (2009). "Bond behavior of reinforcing bars in tensile strain-hardening fiber-reinforced cement composites." *ACI Structural Journal*, 106(6), 897-906.

Cosenza, E., Manfredi, G., and Realfonzo, R. (2002). "Development length of FRP straight rebars." *Composites Part B: Engineering*, 33(7), 493-504.

Cox, D. R., and Hinkley, D. V. (1979). *Theoretical statistics*. CRC Press, Boca Raton.

Eligehausen, R., Popov, E. P. and Bertero, V. V. (1983). “Local Bond Stress-Slip Relationship of Deformed Bars Under Generalized Excitations.” University of California, Berkeley.

fib (International Federation for Structural Concrete). (2000). “Bond of reinforcement in concrete.” *Bulletin 10*, Lausanne.

fib (International Federation for Structural Concrete). (2013). “CEB-FIP Model Code 2010”, Lausanne.

Harajli, M., Hamad, B., and Karam, K. (2002). “Bond-slip response of reinforcing bars embedded in plain and fiber concrete.” *Journal of Materials in Civil Engineering*, 14(6), 503-511.

Haskett, M., Oehlers, D. J., and Mohamed Ali, M. S. (2008). “Local and global bond characteristics of steel reinforcing bars.” *Engineering Structures*, 30(2), 376-383.

Jungwirth, J., and Muttoni, A. (2004). Structural behavior of tension members in Ultra High Performance Concrete. *Proc., International Symposium on Ultra High Performance Concrete*, Kassell, 533-544.

Knight, D., Visintin, P., Oehlers, D. J., and Mohamed Ali, M. S. (2013). “Short-term partial-interaction behavior of RC beams with prestressed FRP and steel.” *Journal of Composites for Construction*, 18(1), 04013029.

Lee, S. C., Cho, J. Y., and Vecchio, F. J. (2011). “Model for post-yield tension stiffening and rebar rupture in concrete members.” *Engineering Structures*, 33(5), 1723-1733.

Marchand, P., Baby, F., Khadour, A., Battesti, T., Rivillon, P., Quiertant, M, Nguyen, H-H.,Genereux, G., Deveaud, J-P., Simon, A. and Toutlemonde, F. (2016). “Bond behaviour of reinforcing bars in UHPFRC.” *Materials and Structures*, 49(5), 1979-1995.

Muhamad, R., Mohamed Ali, M. S., Oehlers, D. J., and Griffith, M. (2012). “The tension stiffening mechanism in reinforced concrete prisms.” *Advances in Structural Engineering*, 15(12), 2053-2069.

Oesterlee, C. (2010). “Structural response of reinforced UHPFRC and RC composite members.” Ph.D. Thesis, Ecole Polytechnique Federale de Lausanne.

Reineck., K. H. and Greiner, S. (2004). “Tests on ultra-high performance fibre reinforced concrete designing hot-water tanks and UHPFRC-shells.” *Proc., International Symposium on Ultra High Performance Concrete*, Kassell, 361-374.

RILEM (International Union of Laboratories and Experts in Construction Materials, Systems and Structures) (1994). “RC 6 Bond test for reinforcement steel. 2. Pull-out test, 1983.” *RILEM recommendations for the testing and use of constructions materials*, RILEM, London, 218-220.

Ruiz, M. F., Muttoni, A., and Gambarova, P. G. (2007). “Analytical modeling of the pre-and postyield behavior of bond in reinforced concrete.” *Journal of Structural Engineering*, 133(10), 1364-1372.

Singh, M., Sheikh, A. H., Mohamed Ali, M. S., Visintin, P., and Griffith, M. C. (2017). "Experimental and numerical study of the flexural behaviour of ultra-high performance fibre reinforced concrete beams." *Construction and Building Materials*, 138, 12-25.

Sobuz, H. R., Visintin, P., Mohamed Ali, M. S., Singh, M., Griffith, M. C., and Sheikh, A. H. (2016). "Manufacturing ultra-high performance concrete utilising conventional materials and production methods." *Construction and Building Materials*, 111, 251-261.

Standards Australia (2001) "Steel Reinforcing Materials." *AS/NZS 4671:2001*, Sydney.

Tepfers, R. (1973). "A theory of bond applied to overlapped tensile reinforcement splices for deformed bars." Ph.D. Thesis, Chalmers University of Technology.

Visintin, P., Oehlers, D. J., Wu, C., and Griffith, M. C. (2012). "The reinforcement contribution to the cyclic behaviour of reinforced concrete beam hinges." *Earthquake Engineering & Structural Dynamics*, 41(12), 1591-1608.

Visintin, P., Oehlers, D. J., Muhamad, R., and Wu, C. (2013). "Partial-interaction short term serviceability deflection of RC beams." *Engineering Structures*, 56, 993-1006.

Visintin, P., Sturm, A. B., Mohamed Ali, M. S. and Oehlers, D. J. (2018) "Blending macro and micro fibres to enhance the serviceability behaviour of UHPFRC." *Australian Journal of Civil Engineering*, 16(2), 106-121.

Yoo, D.-Y., Shin, H.-O., Yang, J.-M., and Yoon, Y.-S. (2014). "Material and bond properties of ultra high performance fiber reinforced concrete with micro steel fibers." *Composites Part B: Engineering*, 58, 122-133.

Yuan, J., and Graybeal, B. A. (2014)."Bond behavior of reinforcing steel in ultra-high performance concrete." *FHWA-HRT-14-090*, Federal Highway Administration, McLean.

STATEMENT OF AUTHORSHIP

Sturm, A.B., Visintin, P., Farries, K. and Oehlers, D.J. (2018)
A new testing approach for extracting the shear friction material properties of ultra-high performance fibre reinforced concrete.
Journal of Materials in Civil Engineering, 30(10), 04018235.

Sturm, A. B. (Candidate)

Prepared manuscript, performed all analyses, and developed model and theory (50%)

This paper reports on original research I conducted during the period of my Higher Degree by Research candidature and is not subject to any obligations or contractual agreements with a third party that would constrain its inclusion in this thesis. I am the primary author of this paper.

Signed … Date 9/07/2020

Visintin, P.

Supervised and contributed to research, and acted as corresponding author (10%)

I certify that the candidate's stated contribution to the publication is accurate (as detailed above); permission is granted for the candidate in include the publication in the thesis; and the sum of all co-author contributions is equal to 100% less the candidate's stated contribution.

Signed Date 07/07/2020

Farries, K.

Contributed to research and designed experimental apparatus (30%)

I certify that the candidate's stated contribution to the publication is accurate (as detailed above); permission is granted for the candidate in include the publication in the thesis; and the sum of all co-author contributions is equal to 100% less the candidate's stated contribution.

Signed Date 7/7/20

Oehlers, D. J.

Supervised and contributed to research (10%)

I certify that the candidate's stated contribution to the publication is accurate (as detailed above); permission is granted for the candidate in include the publication in the thesis; and the sum of all co-author contributions is equal to 100% less the candidate's stated contribution.

Signed Date 7/7/20

A NEW TESTING APPROACH FOR EXTRACTING THE SHEAR FRICTION MATERIAL PROPERTIES OF ULTRA-HIGH PERFORMANCE FIBRE REINFORCED CONCRETE

Sturm, A. B., Visintin, P., Farries, K., Oehlers, D. J.

ABSTRACT

Shear friction (SF) theory governs the relationship between the stresses and displacements that occur due to sliding along a concrete to concrete interface subjected to varying degrees of lateral confinement. This theory is commonly applied to predict: the transverse shear strength of reinforced concrete beams and slabs; the longitudinal shear capacity and behaviour of precast connections; the size effect and confinement in compression members; and flexural failure in the compression region flexural members. The SF material properties required for this theory are commonly determined from tests where the confining force across the sliding plane is passively induced through transverse reinforcement and, therefore, difficult to quantify and to isolate from the reinforcement dowel action. In this paper, a new test apparatus is presented to determine the SF properties of ultra-high performance fibre reinforced concrete (UHPFRC). The proposed setup has the following benefits: it removes the need for passive reinforcement by applying a normal stress hydraulically, thereby allowing confinement to be directly measured and controlled; it removes the effect of dowel action; and it allows the use of specimens manufactured from 200x100 mm cylinders which is beneficial as they can be cored from larger specimens to investigate the influence of fibre orientation. To verify this new apparatus, a series of 16 tests are conducted on UHPFRC with a range of short straight and long hooked steel fibres as well as a range of normal confining stresses.

INTRODUCTION

The shear friction or aggregate interlock mechanism defines the rigid body sliding, Δ, and associated crack opening, h, which occurs along a concrete to concrete interface when a specimen is subjected to a shear τ_{cr} and normal stress σ_{cr} in Fig. 1(a) (Oehlers et al. 2012). The shear friction properties, that is the interaction between Δ, h, σ_{cr} and τ_{cr}, are often presented in the form of Fig. 1(b) (Haskett et al. 2010) and are known to be strongly related to: the strength of the mortar and aggregate which make up the concrete; the grading of the aggregate which controls the roughness of the sliding plane; and the normal stress across the sliding plane σ_{cr}.

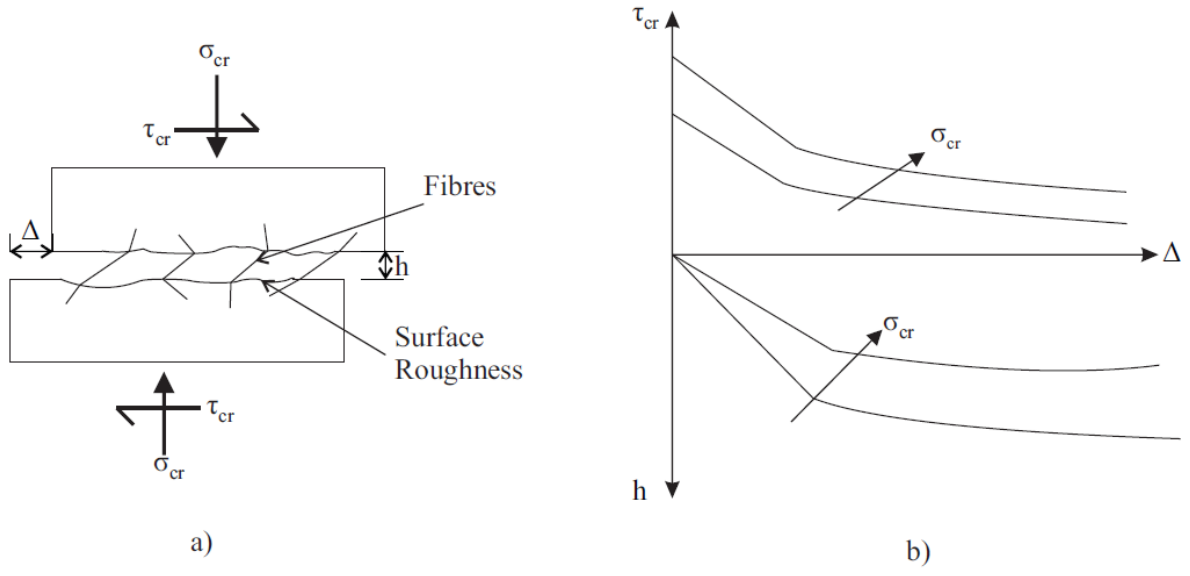

Fig. 1 a) the shear sliding mechanism and b) shear friction properties

Shear sliding is a common mechanism in reinforced concrete behaviour, particularly at the ultimate limit state. As such, it has been widely applied in analysis and design. For example to:

- Quantify the shear strength of connections between pre-cast elements and concrete cast at different times (Birkeland & Birkeland 1966; Mast 1968; fib 2013).
- Quantify the shear strength of corbels (Mast 1968).
- Quantify the shear strength of RC beams (Vecchio & Collins 1986; Zhang 1997; Loov 1998; Lucas et al. 2011; 2012; fib 2013; Zhang et al. 2014a,b;2015;2016;2017; Chen et al. 2015).
- Quantify the punching shear strength of RC slabs (Muttoni 2008; Muttoni & Fernandez Ruiz 2008; fib 2013).
- Describe and quantify the mechanism of flexural failure in the compressive region of reinforced concrete beams and columns (Haskett et al. 2009; Visintin et al. 2012).
- Describe the mechanism and quantify the magnitude of confinement in compression members (Mohamed Ali et al. 2010; Haskett et al. 2011; Visintin et al. 2015a).
- Describe the mechanism of size effect in compression members (Chen et al. 2013; Visintin et al. 2015b).

The broad applications of the shear sliding mechanism highlights the importance of quantifying the shear friction properties. For conventional concrete, significant empirical research has yielded a number of different shear friction material models (Hofbeck et al. 1969; Mattock & Hawkins 1972; Paulay & Loeber 1974; Walraven & Reinhardt 1981; Millard & Johnson 1984; 1985; Tassios & Vintzeleou 1987; Kahn & Mitchell 2002; Sonnenberg et al. 2003; Wong et al. 2007; Mansur et al. 2008; Harries et al. 2012) but being empirically derived these are not necessarily applicable for new types of concrete such as ultra-high performance fibre reinforced concrete (UHPFRC).

UHPFRC is an advanced concrete technology initially developed in Denmark in 1986 (Buitelaar 2004) and characterised by outstanding mechanical behaviour and durability (Russell & Graybeal 2013). Fibres are added to control the brittleness of the material and to create a ductile tensile behaviour. The shear friction behaviour of this material is expected to be significantly different to that of ordinary reinforced concrete due to: the lack of coarse aggregates which will result in a reduced surface roughness; and the presence of fibres which provides both passive confinement along a sliding plane and dowel action as the fibres bend and kink Furthermore, the increase strength of the concrete matrix with respect to compression and tension is expected to improve the resistance to sliding.

Previous research has considered the shear friction behaviour of fibre reinforced concrete with compressive strengths of up to 80 MPa containing both course aggregate and volumes of fibres of up to 2% (Tan & Mansur 1990; Valle & Buyukozturk 1992; Balaguru & Dipsia 1993; Khaloo & Kim 1997; Mirsayah & Banthia 2002; Barragan et al. 2006; Rao & Rao 2009; Boulekbache et al. 2012; Khanlou et al. 2012; Soetens & Mathys 2017). This research has shown that improvements in shear strength of 60 % are possible for high strength concrete and 36 % for normal strength concrete reinforced with 1% by volume steel fibres. It is worth noting here that none of the studies to date on fibre reinforced concrete have suggested a design equation relating the shear capacity to the applied normal stress, as is widely available for concrete without fibres. This is due to the focus of the studies being on the improvement in behaviour with the addition of fibres rather than on the influence of normal stress. Tan & Mansur (1990) and Valle & Buyukozturk (1992) however have developed numerical models

that can allow for the effect of the normal stress. Soetens & Mathys (2017) have also suggested expressions that allow for the normal stress but the manner in which the fibre contribution is assessed is complex as it as a function of the pullout behaviour of a single fibre.

Very few studies have sought to quantify the shear friction properties of UHPFRC. The only study identified to date is that of Crane (2010) who tested 12 monolithic specimens and 26 composite specimens. The composite specimens consists of a cold joint of UHPFRC and high strength concrete, while the monolithic specimens consist only of UHPFRC. In this study, push-off specimens of the type first developed by Anderson (1960) in Fig. 2(b) were used and the influence of pre-cracking the sliding plane and the quantity of transverse reinforcement crossing the shear plane was investigated. It should be noted that the passive normal stress developed was very small with a maximum normal stress of 1% of the compressive strength, assuming all the transverse reinforcement had yielded.

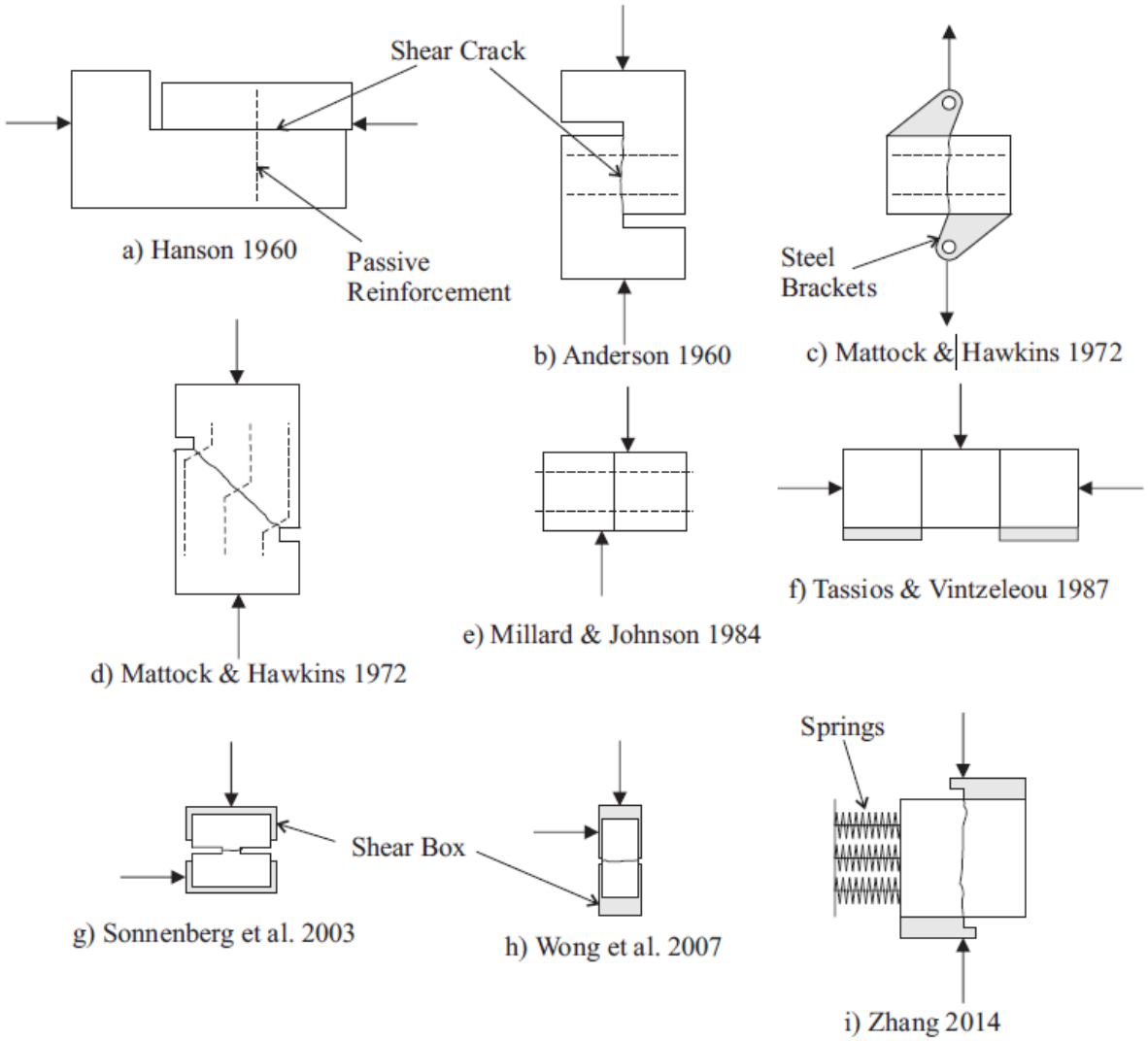

Fig. 2 Previous shear friction tests setups

The wide application of the shear sliding mechanism to describe the behaviour of reinforced concrete and the paucity of shear friction properties for UHPFRC highlights the need for further experimental work to quantify these properties. However, the very high strength of UHPFRC means that testing for the shear friction properties of the material is challenging. In this paper,

existing test arrangements for lower strength concretes with and without fibres is explored. Based on these previous test setups, a new arrangement suitable for UHPFRC is suggested. To verify the operation of this setup, a series of 16 shear friction tests are performed where the applied normal stress and fibre type are varied. Provisional relationships are then suggested for the shear friction properties.

PREVIOUS EXPERIMENTAL APPROACHES TO OBTAINING THE SHEAR FRICTION PROPERTIES

The first shear friction tests were performed by Hanson (1960) and Anderson (1960), on specimens illustrated in Fig. 2(a) and 2(b), respectively. These tests were performed to investigate the transfer of shear in composite specimens. A normal stress is induced across the cracked plane via the extension of the internal reinforcement. The test specimen used by Anderson (1960) is the basis of the vast majority of future tests (Hofbeck et al. 1969; Mattock & Hawkins 1972; Paulay & Loeber 1974; Walraven & Reinhardt 1981; Tan & Mansur 1990; Valle & Buyukozturk 1992; Balaguru & Dipsia 1993; Khaloo & Kim 1997; Kahn & Mitchell 2002; Barragan et al. 2006; Mansur et al. 2008; Crane 2010; Harries et al. 2012) with the shape of the specimen being retained but with the dimensions and reinforcing details varying markedly. These specimens can be used to determine both uncracked and cracked properties. Specimens with this shape will be henceforth referred to as the Anderson push-off specimen in the remainder of the paper.

Mattock & Hawkins (1972) developed two variations on the Anderson push off specimens as illustrated in Fig. 2(c-d) to investigate the effect of either having a direct tensile stress parallel to the shear plane [Fig. 2(c)], or, an inclined shear plane such that the applied load caused a transverse compressive stress as well as shear [Fig. 2(d)]. It was found that the parallel tensile stress caused a reduction in shear strength while the normal stress due to the applied load was additive to the normal stress developed by the internal reinforcement.

Walraven & Reinhardt (1981) performed two sets of tests; one set on Anderson push-off specimens with internal reinforcement and another with external reinforcement. This approach was taken as the presence of internal reinforcement contributes to the resistance of shear sliding across the cracked plane through dowel action, making it difficult to isolate the contribution of the concrete alone. The interaction between the shear sliding mechanism and dowel action was further investigated by Millard & Johnson (1984) who considered two types of specimens to isolate the effects of aggregate interlock and dowel action and hence obtain the concrete shear friction properties. The specimens had the same shape and were tested in the manner illustrated in Fig. 2(e). For the aggregate interlock test the reinforcement was fully unbonded by being placed in 25 mm ducts. For the dowel action test the block was cast in two parts with a polyethene sheet along the crack plane to produce an extremely smooth crack. An alternate approach was taken by Zhang (2014) who used springs to provide the normal stress, as illustrated in Fig 2(i).

As an alternative to the ‘Anderson style’ tests, a double plane shear test design has been utilised by Tassios & Vintzeleou (1987) on precracked unreinforced specimens, as shown in Fig. 2(f). A similar set up has been proposed by the Japanese Society of Civil Engineering (JSCE) for uncracked fibre reinforced concrete specimens (JSCE 1990). The advantage of this style of specimen is that since no internal reinforcement is provided, these tests directly provide the shear friction properties. Further, these tests have been designed such that they could be performed on small scale beam specimens of the type used for modulus of rupture

testsInstrumentation is also simplified as the two outer portions of the specimen are stationary throughout the test. This also assists in the application of the external normal stress.

Tests utilising a shear box with a single sliding plane have also been performed by Sonnenberg et al. (2003) and Wong et al. (2008) as illustrated in Figs. 2(g-h). Again no internal reinforcement is required and the normal stress can be applied hydraulically. A further advantage is that by having only one shear plane and no internal reinforcement, small scale specimens can be utilised thereby simplifying the test procedure and reducing the cost of testing. The risk of an asymmetric failure is also reduced relative to a double shear plane design. The disadvantage of this kind of test relative to the double shear plane test is that the specimen is not visible, hence the geometry of the shear crack can only be observed once the test is completed.

An important factor to consider when choosing a test setup is the means by which the normal stress is provided across the shear sliding plane. It can be seen that for many of the test designs [Figs. 2(a-e)], the normal stress is provided by stirrups crossing the shear plane. The primary issue with this approach is that the normal stress across the plane in Fig. 1(a) varies with the crack opening h until yielding of the reinforcement occurs. As a result, many of the previous design expressions have been derived based on the assumption that the reinforcement has yielded at the point that the peak shear stress is reached. The validity of this assumption was investigated by Chen et al. (2015a) who reanalysed 53 existing test results and showed that in the majority of cases (42 out of 53 tests) the reinforcement was elastic when the peak shear stress was reached. Hence for extracting the shear friction properties for constant normal stresses as is shown in Fig. 1(b) a setup where the normal stress is applied hydraulically is best suited.

For application to UHPFRC, a double shear plane setup based on the design of the JSCE (1990) and illustrated in Fig. 3 was first investigated. Note that slots were cut as shown to reduce the load to shear the specimen as well as to control the position of the shear cracks. The slots were sawn to avoid disturbing the distribution of fibres. In preliminary testing, it was found that for initially uncracked specimens there was a tendency for the shear crack to form at one plane resulting in significant rotation of the specimen thereby making the results unreliable. The tendency of the specimen to rotate is worsened by the high post-cracking strength of the material meaning that the second potential sliding plane is less likely to crack. Moreover, when using the apparatus in Fig. 3 it was found that, due to the double shear plane, the peak shear load was approaching the compressive strength of the test specimen. As a result, to obtain reasonable range of parameters, the specimen had to be small in size thereby introducing the potential for edge effects and limiting the extent of instrumentation which could be attached to the specimen to record deformations.

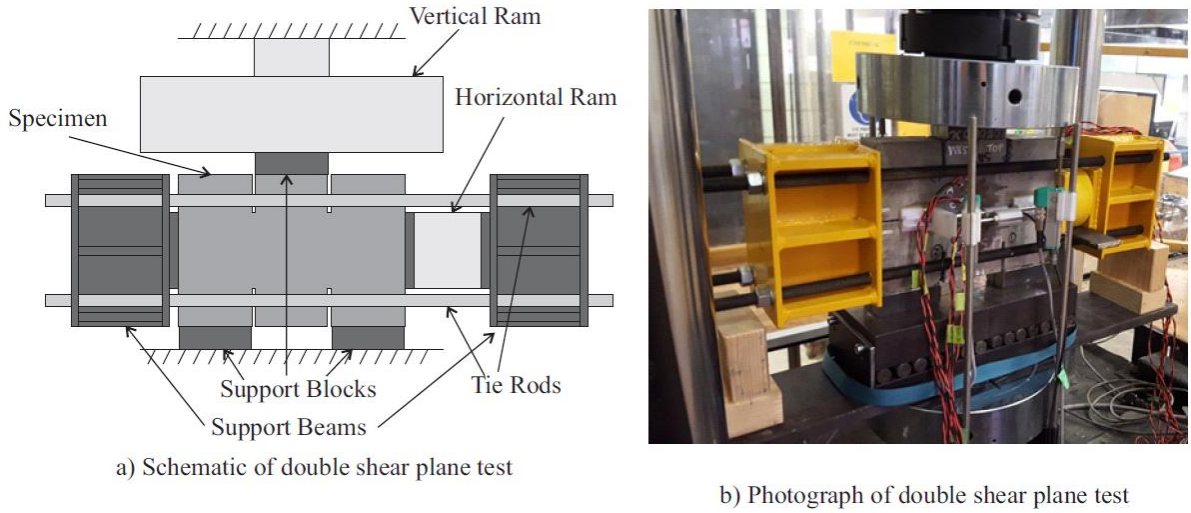

a) Schematic of double shear plane test

b) Photograph of double shear plane test

Fig. 3 Double Shear Plane Setup

As the initially uncracked properties such as the shear load to initiate a shear crack are required for analyses such as predicting the shear capacity of a beam (Zhang et al. 2014a,b;2015;2016;2017) or the post peak softening behaviour of a flexural member (Haskett et al. 2009; Visintin et al. 2012), a new test apparatus is proposed in this paper to extract the initially uncracked shear friction properties for all types of concrete including UHPFRC. This new apparatus based on the shear box design of Sonnenberg et al. (2003) but redesigned for a much higher strength concrete as outlined below.

DIRECT SHEAR TEST SETUP

A diagram of the proposed direct shear test is given in Fig. 4(a) and a photograph is provided in Fig. 4(b). The primary component of the apparatus is the shear box, which is made up of two halves. A horizontal ram applies a shearing load to the lower half of the shear box which can translate freely on the rollers while the upper half is restrained by a rocker assembly. The rocker prevents horizontal movement and rotation of the upper half of the assembly, while preventing any restraint being applied normal to the shear crack. The normal stress was applied to the upper half of the shear box by a vertical ram. A spherical seat is provided to ensure a vertical load in spite of any inclination to the shear plane. Rollers are used to allow the lower half of the shear box to displace and to prevent the transfer of horizontal loads into the ram through the upper half. Due to the very high load, and to minimise friction, hardened steel bearing blocks and rollers are used. The frictional resistance to longitudinal movement of the rollers was tested and was found to be less than 0.0125 under the highest vertical load applied during the test regime. The entire assembly is contained within a rigid steel frame. The dashed grey outline represents the position of the specimen within the apparatus.

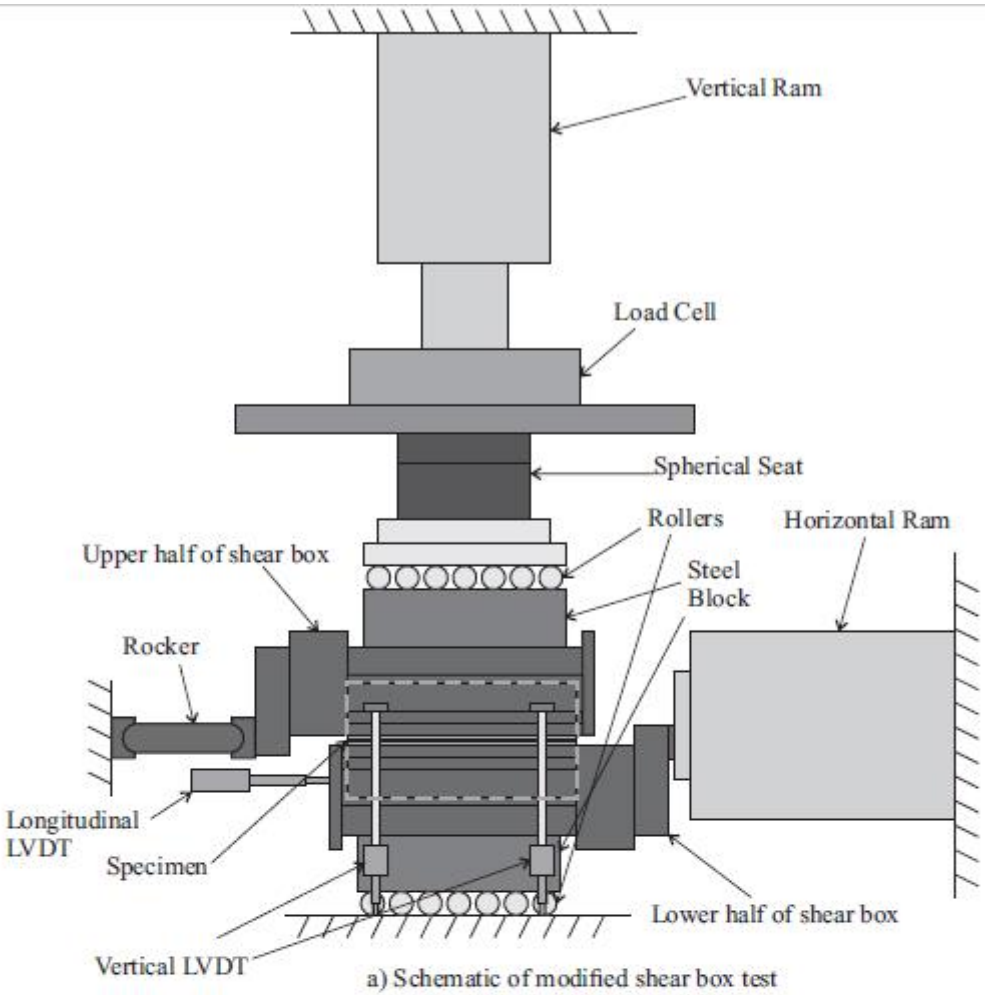

a) Schematic of modified shear box test

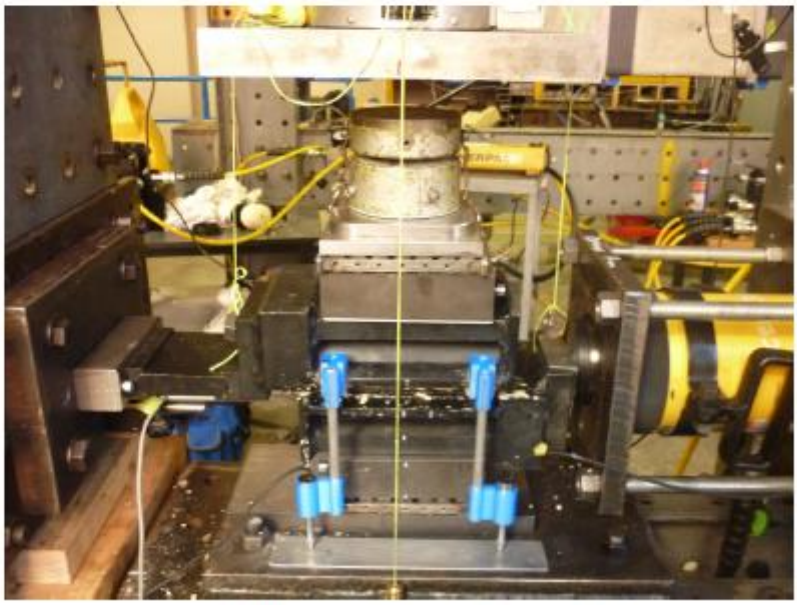

b) Photograph of modified shear box test

Fig. 4 Setup of direct shear test

Shear box design

The shear box is made up of two identical halves, with one half illustrated in Fig. 5. The box is manufactured from Grade 300 steel components that are machined and then welded together. These components include a pipe section which contains the specimen as well as a series of plate elements to maintain stiffness and to distribute the high loads required for testing UHPFRC. The back plate and end plate restrain each end of the specimen. In the lower assembly, the load plate transfers the shearing load from the horizontal ram into the specimen and in the upper assembly, the rocker seat is attached to the load plate by screws. The side stiffener stiffens the shear box against the horizontal load. The top plate transfers the vertical load into the specimen and stiffens the shear box against the horizontal load.

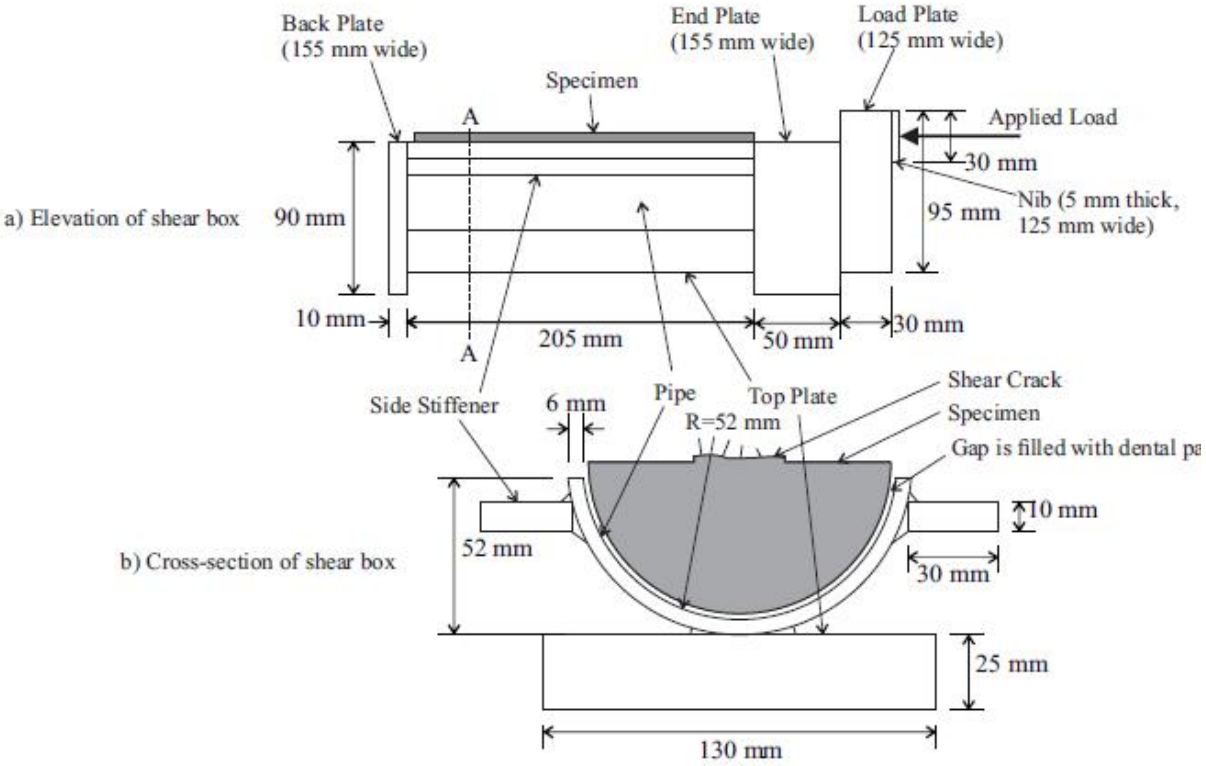

c) Photograph of shear box

Fig. 5 Shear box design

The specimens are manufactured from standard 200x100 mm cylinders by cutting slots along each side of the specimen, as shown in Fig. 6(a). These slots control the position of the shear crack as well as reducing the load required to shear the specimen. This is important since if no slot was provided the load to shear the specimen would approach the compressive strength of

the concrete. A cylindrical specimen was chosen to improve the practicality of the test since the specimens can be manufactured using standard formwork. This innovation was made possible by the removal of the internal reinforcement as well as having only one shear plane.

There are however some limitations. Under low vertical loads there is a tendency for the back of the shear box to rise. Thus to allow operation under low loads the back of the shear box would need to be fixed by the insertion of a concrete anchor into the specimen to prevent the inclination of the shear plane, but this component of the apparatus was not tested in this programme. Rockers provided on both ends of the upper assembly of the shear box may also be a solution.

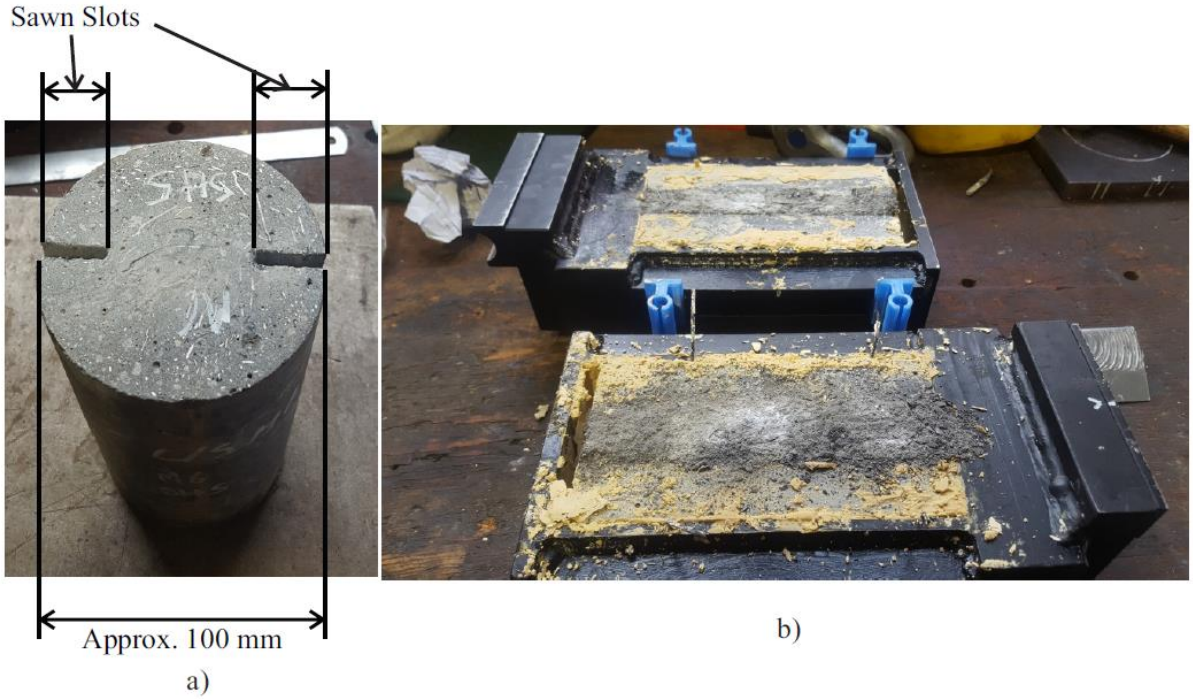

Fig. 6 Test specimen before and after testing

Test procedure and instrumentation

Before the test, slots are sawn along the length of each cylinder as shown in Fig. 6(a). Rubber bands are placed around the cylinder which is then placed into the lower half of the shear box and dental paste (high strength gypsum "Kaffir D") used to bond the specimen to the inside of the steel pipe and to seat the specimen on the bearing end plate. The rubber bands controls the seating depth, allowing proper alignment of the specimen. Allowing the dental paste to set, the lower half of the assembly is then be placed on top of the rollers and the steel block. Dental paste is then applied to seat the specimen into the upper half of the shear box. Care is taken at this time to ensure that the top half of the specimen is level. After the second application of dental paste is set, the rest of the apparatus is assembled as indicated in Fig. 4(a). Care is taken to ensure that the entire apparatus is centred with respect to the vertical and horizontal rams.

During the test, the vertical load, which was measured using a 240 kN load cell, was first applied using a hydraulic ram and the load was maintained throughout the test through the use of a pressure relief valve which acts to hold the pressure and vertical load constant. After applying the normal stress, a shearing load is applied via a 350 kN capacity hydraulic ram which had been calibrated and controlled by a hand jack.

During testing, each specimen was loaded at a rate of 50 kN/min until the peak shear stress was reached and after a constant shear displacement of 2 mm/min was applied. Note that the hand jack only provides an approximate load and displacement rate.

The position of the LVDTs is illustrated in Fig. 4(a). The shear displacement is determined by measuring the horizontal displacement of the lower part of the shear box with a 25 mm LVDT. The crack opening is determined by four 5 mm LVDTs that are attached to the top of the side stiffener attached to the upper half of the shear box and contacted to a polished steel plate on the base of the setup. Note that the flexibility of the rig was not considered an issue, as the primary interest was in the relative displacements of the shear crack once it had formed at the peak stress. That is any bedding in of the apparatus occurs prior to the formation of the shear crack.

EXPERIMENTAL PROGRAMME

A series of 16 tests were performed to verify the operation of the new shear apparatus. The effect of the normal stress and fibre type were investigated. These parameters were chosen since, from the previous research, for a given type of concrete, the normal stress was identified as the most significant variable effecting the shear friction behaviour (Mattock & Hawkins 1972). The vast array of possible fibre shapes and sizes is a significant complicating factor in the design of experimental programmes for FRC. Previous researchers have explored the effect of aspect ratio (Balaguru & Dipsia 1993; Boulekbache et al. 2012), the effect of fibre material (Buyukozturk & Valle 1992; Banthia et al. 2014) as well as the influence of using flat end, crimped or hooked end fibres (Mirsayah & Banthia 2002; Banthia et al. 2014). These previous researchers have identified that there is in an increase in shear strength with higher aspect ratio fibres and that hooked end fibres are more effective than flat end fibres, which are in turn more effective than crimped fibres. However none of the previous researchers have investigated the influence short straight versus longer hooked end fibres (note the two fibres chosen have the same aspect ratio), which are the most common types used with UHPFRC. Banthia et al. (2014) has also considered the impact of mixing of cellulose, hooked end and deformed end steel fibres though the results were inconclusive. As it has been shown that the blending of fibres has a positive impact on the tensile behaviour of UHPFRC (Visintin et al. 2018) this aspect will be investigated further here. Based on these considerations the following five mix designs were considered shown in Table 1. Note that the mix designation refers to the ratio of macro to micro fibres used in the mix. For each mix the compressive strength was determined from tests on 100 mm diameter, 200 mm high cylinders. Note that the total fibre volume in each mix (except No Fibres) was 2%.

Table 1. Mix Design for experimental programme

Mix designation	Cement (kg/m^3)	Sand (kg/m^3)	Silica fume (kg/m^3)	Water (kg/m^3)	Superplasticiser (kg/m^3)	Macro fibres (kg/m^3)	Micro fibres (kg/m^3)	f_c (MPa)
No fibres	978	973	260	171	44	0	0	172
1 Macro: 0 Micro	950	951	253	161	43	222	0	167
0 Macro: 1 Micro	950	943	253	168	43	0	222	164
0.5 Macro: 0.5 Micro	950	944	253	167	43	111	111	150
0.6 Macro: 0.4 Micro	950	945	253	166	43	88	133	162

The macrofibres were hooked-end steel fibres with a length of 35 mm and a diameter of 0.55 mm and the microfibres were straight steel fibres with a length of 13 mm and a diameter of 0.2 mm. The mix design is based on that developed by Sobuz et al. (2016) and has been used in previous experimental studies into the tensile (Visintin et al. 2018) and bond (Sturm & Visintin 2019) behaviour of UHPFRC. Note that at the time of mixing the water content was adjusted to allow for the moisture content of the sand.

For all mixes in Table 1 the mix proportion is 1:1:0.266:0.233 ratio by weight of sulphate resisting cement, fine aggregate (washed river sand), silica fume and steel fibres, as only the type of fibre used was varied. The sulphate resisting cement has a fineness modulus of 562 m^2/kg, a 28 day compressive strength of 60 MPa and a 28 day shrinkage strain of 650 $\mu\varepsilon$. The silica fume had a bulk density of 625 kg/m^3 and the sand had a fineness modulus of 2.34. The superplasticiser was a third generation high range water reducer with added retarder. The macrofibres had a yield strength of 1100 MPa while the microfibres had a yield strength of 2850 MPa.

For the first four mixes, 3 tests were performed with a vertical load of 40, 60 and 80 kN with approximately 35 mm deep slots cut into each side. For the 0.6 Macro: 0.4 Micro mix, 4 tests were performed as part of a pilot study during the development of the test setup. However, the results were of sufficient quality to be included within the main series of data. These confining loads correspond to normal stresses ranging from 4% to 9.1% of the unconfined concrete strength f_c. For 0.6 Macro: 0.4 Micro the same tests were performed as well as one with a vertical load of 40 kN and 30 mm slots. Note that for the actual calculations the dimensions of the shear plane were measured with callipers and the vertical load recorded continuously with a load cell.

RESULTS

Examples of typical horizontal load vs horizontal displacement and horizontal load vs vertical displacement curves are shown in Fig. 7 for a given vertical force P_v.

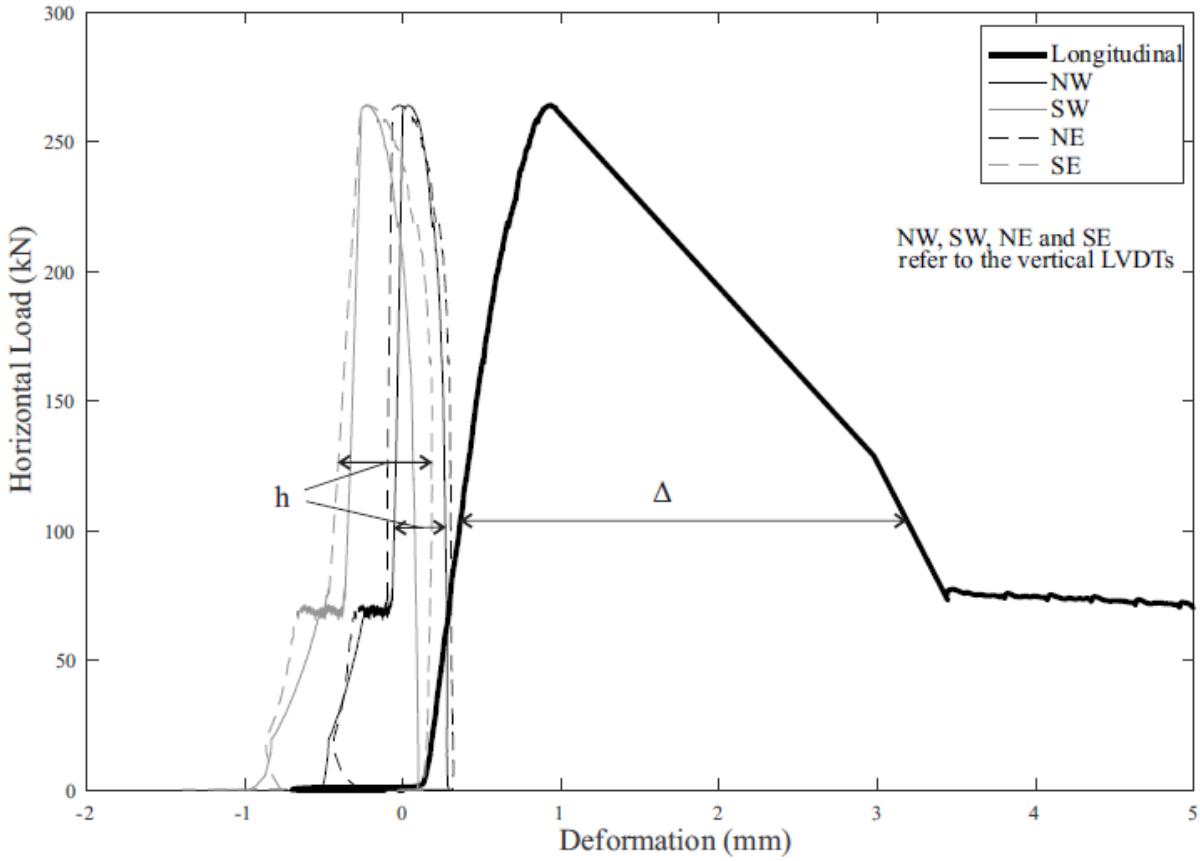

Fig. 7 Determination of the slip and crack opening from the experimental load-deformation curves

To obtain the shear friction properties in the form of Fig. 1(b) the average normal stress across the sliding plane is calculated as

$$\sigma_{cr} = \frac{P_v}{A_{cr}} \tag{1}$$

where P_v is the applied vertical load and A_{cr} is the area of the shear plane. The average shear stress across the plane is given by

$$\tau_{cr} = \frac{P_h}{A_{cr}} \tag{2}$$

where P_h is the horizontal load applied to the specimen.

The slip along the sliding plane, Δ and the crack opening. h can be determined by defining the sliding deformation and crack opening as the total measured deformation minus the elastic deformation determined for a given value of P_h from the rising and falling branches shown in Fig. 7. The slip along the sliding plane is determined from the longitudinal LVDT and the crack opening is measured by the vertical LVDTs (NW, SW, NE and SE).

The resulting experimental shear stress-slip τ_{cr}-Δ and crack width-slip h-Δ relationships are recorded in Fig. 8 grouped by fibre type and in Fig. 9 grouped by normal stress. The peak shear stress, v_u and normal stresses, σ_{cr} are summarised in Table 2 and plotted in Fig. 10. In the supplementary material the raw load deformation data is presented.

Table 2. Summary of peak shear and average normal stress

Mix	P_v (kN)	v_u (MPa)	σ_{cr} (MPa)	f_c (MPa)
No Fibres	40	22.3	6.90	172
	60	27.6	10.39	
	80	33.1	14.23	
1 Macro: 0 Micro	40	40.6	6.82	167
	60	44.3	11.07	
	80	48.5	13.97	
0 Macro: 1 Micro	40	36.2	6.82	164
	60	43.5	10.41	
	80	49.3	13.74	
0.5 Macro:0.5 Micro	40	41.9	7.17	150
	60	42.7	10.62	
	80	46.5	13.64	
0.6 Macro: 0.4 Micro	40[a]	31.1	5.41	162
	40	35.6	7.30	
	60	43.9	10.87	
	80	46.2	14.21	

[a] This specimen had 30 mm slots while the others had 35 mm

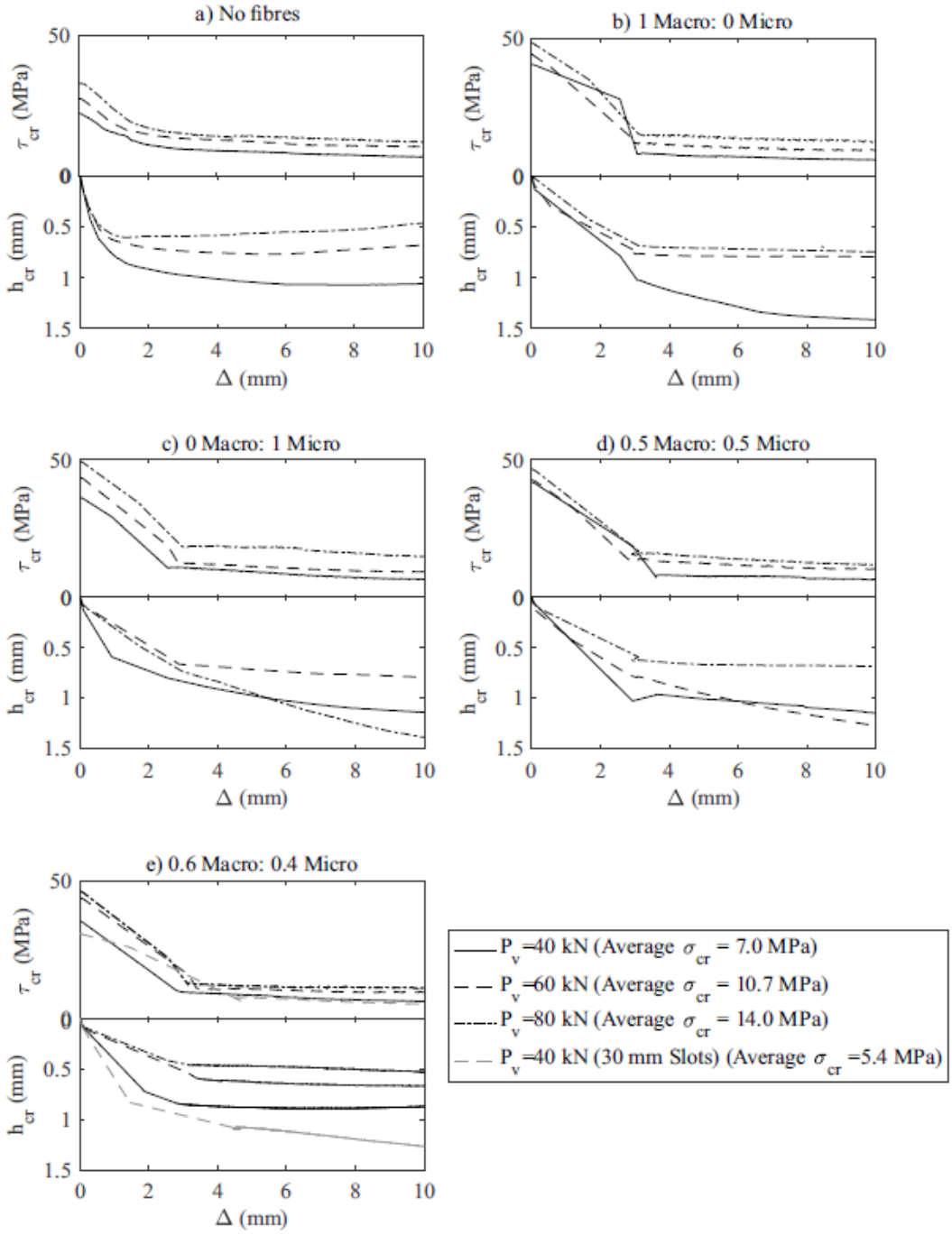

Fig. 8 Shear stress-slip and crack width-slip curves (sorted by fibre type)

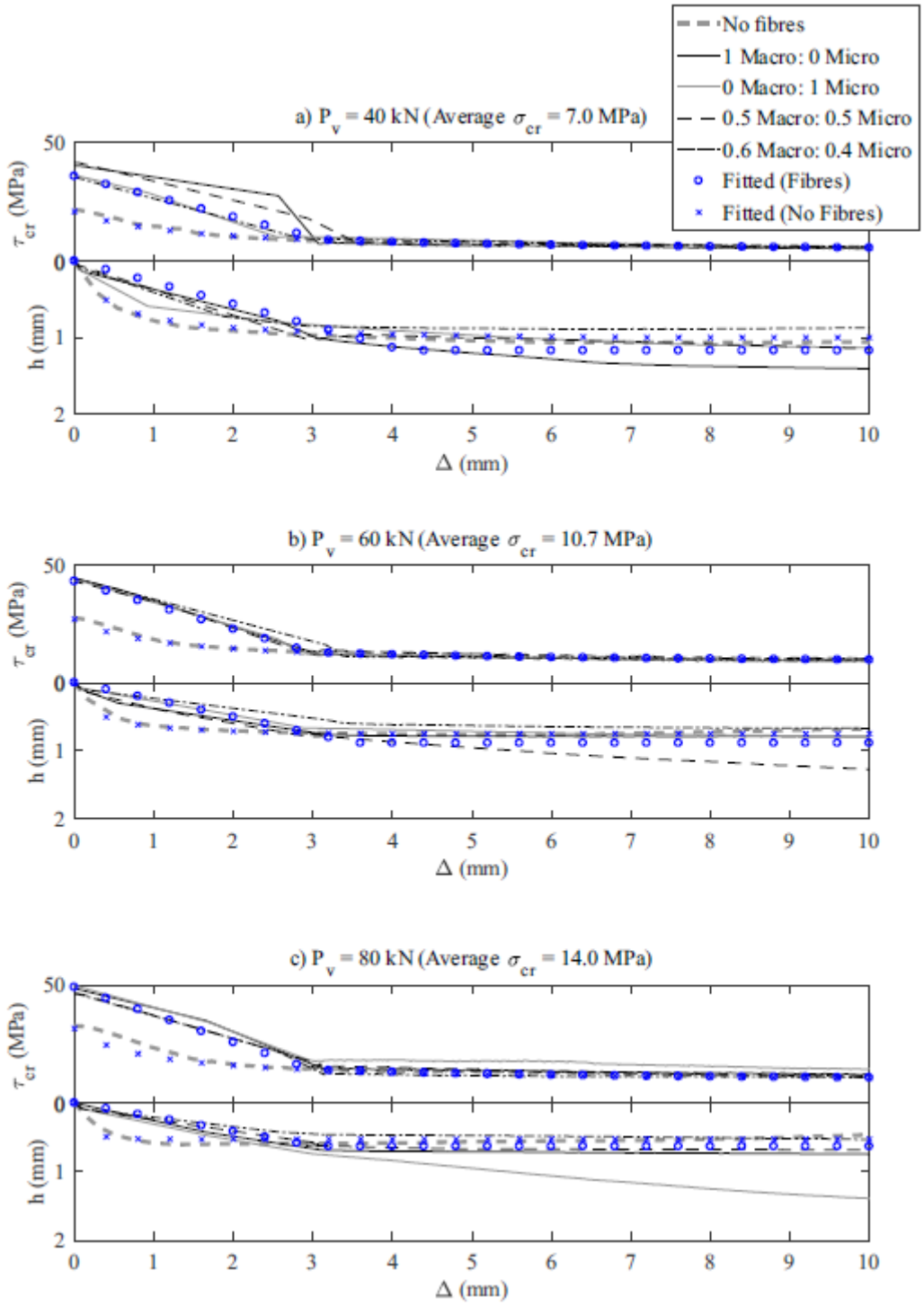

Fig. 9 Shear stress-slip and crack width-slip curves (sorted by normal stress)

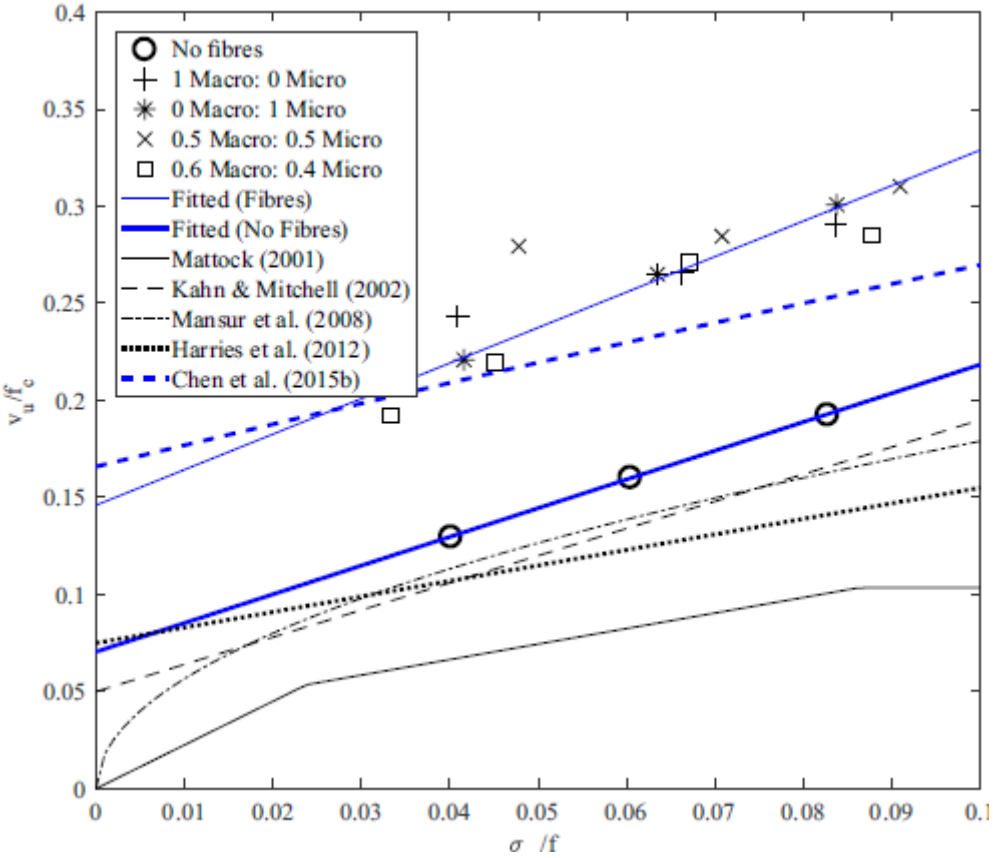

Fig. 10 Shear Capacity vs Normal Stress.

Shear Capacity

From Fig. 8 the maximum shear stress, v_u that can be transferred across the shear plane can be seen as the peak points of shear stress-slip curve, that is the shear capacity, which occurs at Δ_{wdg}= 0. The variation of this shear capacity with normal stress is given in Fig. 10. From this, it can be seen that the shear capacity substantially improves with increasing normal stress as well as the introduction of fibres. It should be noted that there is no significant influence from fibre type nor from the blending of fibres is observed in Fig. 10 which is likely due to the very small crack width at the point of maximum shear stress. To explore this effect quantitatively, a linear relationship is fitted for the variation of shear capacity with normal stress for specimens with and without fibres respectively.

For specimens with 2% by volume fibres the results of the statistical analysis yielded:

$$\frac{v_u}{f_c} = 1.83\frac{\sigma_{cr}}{f_c} + 0.146 \tag{3}$$

and for specimens without fibres:

$$\frac{v_{u-nf}}{f_c} = 1.48\frac{\sigma_{cr}}{f_c} + 0.0705 \tag{4}$$

In this fit all mixes with fibres are treated as one data set. This approach has been taken as a statistical analysis in which each fibre type was treated separately showed no correlation between the ratio of micro fibre addition and shear capacity. This finding may be due to the small number of tests conducted and hence further validation testing is required in the future. Significantly, in Fig 10 it can be seen that the introduction of fibres increases the frictional component of the shear capacity by 24% and the cohesive component of the shear capacity by 107%. It is proposed that this increase in capacity is due to the crack opening associated with sliding stressing: the fibres thus increasing the normal stress at the crack face; there is also dowel action associated with the introduction of fibres that can be treated as a component of

the shear capacity for UHPFRC. Note that Eqs. (3) and (4) are purely empirical and caution should be used if these expressions are extrapolated beyond the bounds of the testing regime.

In Fig. 10, the test results are compared to existing expressions for the shear friction behaviour of normal and high strength concrete. The capacity for specimens without fibres are close to the predictions made by Kahn & Mitchell (2002) and Mansur et al. (2008) using their expressions for high strength concrete (that is a concrete with a strength of up to 124 MPa and a maximum aggregate size of 20 mm). This indicates that the reduced roughness of the interface due to the removal of coarse aggregates is counteracted by the increased strength of the material. The prediction by Chen et al. (2015b) is close to the values for the specimens with fibres, this is interesting as the formula suggested by Chen et al. (2015b) is based on the inverse analysis of compression tests on ordinary reinforced concrete cylinders and the other formulas are fitted to results from shear friction tests. From this, it can be seen that for specimens without fibres the values are within the range expected for high strength concrete. This is likely due to the failure plane of high strength concrete forming through the aggregate rather than around the aggregate resulting in a smooth crack face similar to that observed for ultra-high performance concrete without fibres.

The addition of fibres is also shown to provide a substantial increase in shear capacity in Fig. 10 over that of the specimens with no fibres. This improvement can be attributed to the increase in normal stress provided by the fibres across microcracks prior to the peak shear stress being reached.

Note that to perform the comparison with existing material models for non-fibre reinforced concrete in Fig. 10, a number of assumptions were made including that ρf_y is equivalent to the normal stress, where ρ is the reinforcement ratio for stirrups crossing the shear plane and f_y is the yield stress of the reinforcement. Additionally to compare the expression given by Harries et al. (2012), a strain in the reinforcement of 0.0025 was assumed to convert the expression into a coefficient of friction multiplied by a normalised normal stress; this may have contributed to the inaccuracy in this expression.

From Fig. 10, it is also seen that the shape of fibres did not affect the shear capacity which is contrary to that observed in lower strength fibre concretes (Mirsayah & Banthia 2002; Banthia et al. 2014). This finding may be because the steel fibres used in previous studies were of similar size to each other, while in this research, the straight fibres are substantially smaller than the hooked fibres. Hence even though the bond strength of the hooked end fibres are substantially higher than that of the straight fibres (Wille & Naaman 2012), for a given volume of fibres within the mix a larger number of the smaller straight fibres are present thereby compensating for the reduction in bond strength of a single fibre without hooked ends. Also note here that it is not possible to compare the shear capacities obtained in this study with those from previous studies on fibre reinforced concrete as existing studies have not developed design equations that relates the shear capacity to the applied normal stress across the interface in a straightforward manner.

Shear-stress/slip behaviour

Considering the full shear-stress/slip relationship in Fig. 9. Initially, the effect of the fibres is to cause a substantial increase in the shear stress that can be transferred. However, as the slip along the sliding plane increases the behaviour converges to that of a specimen without fibres, as shown in Fig. 9. The initial increase is due to the shear crack opening stressing the fibres. The fibres act as additional passive reinforcement similar to the effect of stirrups in

conventional push-off specimens. However as the shear crack continues to slide there is a reduction in normal stress due to the fibres as they are bent, kinked and pulled out by the transverse displacement. This bending and kinking of fibres can be seen in Fig. 11. It can be seen that bending is the predominant mode for the thicker hooked fibres while bending and kinking is seen for the thinner straight fibres. A clear example of this kind of behaviour can also be seen in the radiographic images taken by Foster et al. (2007) of a pushoff test on a normal strength FRC, where it was observed that the bending of the fibres can significantly reduce the stresses that can be developed. This reduction in capacity due to this bending and kinking is complete at a slip of approximately 3 millimetres. The shape of the fibres and their relative proportions have negligible effect on the observed behaviour as shown in Fig. 9. Note that for the lowest confining load, the stress-slip relationship shows some instability during the falling branch. This is due to the brittle behaviour of the concrete with fibres upon reaching the shear capacity.

Fig. 11 Fibres at shear crack

Based on these test results, a shear-stress/slip relationship can be fitted. For specimens without fibres, an expression is proposed that is the function of the ratio of two linear functions. This curve can be seen to be similar in shape to the serpentine curve proposed by Chen et al. (2015b) for ordinary reinforced concrete without fibres. That is

$$\frac{\tau_{cr}}{v_{u-nf}} = \frac{A\Delta + B}{\Delta + B} \tag{5}$$

where

$$A = \min(\, 6.11\frac{\sigma_{cr}}{f_c} - 0.065, 0.304) \tag{6}$$

and

$$B = 0.183\left(\frac{\sigma_{cr}}{f_c}\right)^{-0.654} \tag{7}$$

where A and B control shape of the curve and are functions of the applied normal stress, $v_{u\text{-}nf}$ is the shear capacity without fibres and Δ is the slip along the shear crack.

For specimens with 2% by volume of fibres an initial linear proportion is proposed following which the behaviour follows that of Eq. (5). The initial linear proportion is given by

$$\frac{\tau_{cr}}{v_u} = 1 - 0.233\Delta \tag{8}$$

And the intersection of Eqs. (5) and (8) is given by the following quadratic equation

$$0 = 0.233\Delta_1^2 + \left(\frac{v_{u-nf}}{v_u}A + 0.233B - 1\right)\Delta_1 - B\left(v_u - v_{u-nf}\right) \tag{9}$$

Eq. (5) and (8) are superposed on the results shown in Fig. 10.

Crack width-slip behaviour

From Fig. 8, it was shown that the observed crack widths decrease with increasing normal stress. Comparing tests results both with and without fibres in Fig. 9, it can be seen that fibres initially restrain the opening of the crack but do not significantly influence the maximum crack widths. This is in accordance with the hypothesis that crack opening initially induces large

additional normal stresses in the crack face due to the passive resistance of the fibres which then decrease due to bending and kinking. For specimens without fibres, it was also observed that after the maximum crack width was reached the crack width reduces. This is due to the erosion of the sliding plane and this effect is not generally observed for specimens with fibres, as the fibres resist this erosion by holding the loose material on the sliding plane together. Note in accordance with the shear capacity and the shear stress-slip behaviour, fibre type was found to have negligible effect of the crack width-slip relationship. For each confining stress it can also be seen that there is one series with a significantly larger crack width. This due to the sensitivity of the crack width to the profile of the shear crack.

Having explored the observed trends qualitatively, these are then explored quantitatively by fitting a slip-crack width relationship. For specimens without fibres, an expression that is a function of the ratio of two linear expressions is proposed followed by a constant portion once the maximum crack width has been reached. From this, the initial portion of the stress-crack width relationship is given by

$$\frac{h}{h_{max}} = \frac{1.15\frac{\Delta}{\Delta_2}}{\frac{\Delta}{\Delta_2}+0.15} \tag{10}$$

where the maximum attained crack width is a reducing function of the normal stress

$$h_{max-nf} = 1.48 - 10.9\frac{\sigma_{cr}}{f_c} \tag{11}$$

and which occurs when the slip is equal to

$$\Delta_2 = 13.7 - 146\frac{\sigma_{cr}}{f_c} \tag{12}$$

For specimens with 2% by volume fibres, a bilinear relationship is fitted with the linear portion given as

$$h = h_1\left(\frac{\Delta}{\Delta_1}\right) \tag{13}$$

where

$$h_1 = 1.16 - 6.15\left(\frac{\sigma_{cr}}{f_c}\right) \tag{14}$$

And after the maximum crack width is attained, the crack width remains at a value of

$$h_{max} = 1.72 - 12.4\left(\frac{\sigma_{cr}}{f_c}\right) \tag{15}$$

Comparing Eqs. (11) and (15), the fibres increase the maximum crack width under zero normal stress by 16%, and increase the maximum crack width by 23% for a normal stress equal to 10% of the peak compressive strength of the material. Eq. (10) and (13) are compared to the experimental results in Fig. 10, demonstrating the fit.

CONCLUSION

In this paper, a new testing apparatus has been presented for determining the shear friction properties of UHPFRC. There are four main advantages of this setup over previous test setups as the new set up: (1) can cope with the very large stresses required for testing UHPFRC; (2) provides active confinement hydraulically rather than relying on passive confinement due to internal reinforcement which depends on crack width and, therefore, not directly quantifiable; (3) furthermore eliminating internal reinforcement eliminates the associated dowel action so that the shear friction properties are measured directly; and (4) the test setup makes use of standard cylindrical specimens, hence, removing the need for the construction of any special formwork to use the apparatus.

To verify the operation of the new apparatus, 16 shear friction tests were performed for various mix designs where the type and proportion of fibres were varied as well as the normal stress. From these tests, the relationships between the shear capacity, shear stress, normal stress, slip and crack opening were regressed. From this, it was seen that the normal stress is the primary explanatory variable with the effect of fibre type found to negligible, though specimens with fibres had significantly higher shear capacity than those without. However, the stresses were similar between the fibrous and non-fibrous specimens for large slips. This is a result of the crack opening stressing the fibres increasing the normal stress at the shear crack, however this effect is reduced as the slip increases due to the kinking and bending of the fibres. It was also demonstrated that the shear capacity of ultra high performance concrete without fibres can be described adequately by existing expressions for the shear capacity of high strength concrete.

Having now developed a test set-up specifically for UHPFRC it is recommended that continued experimental work be conducted to more broadly investigate the impact of fibre volume and fibre type. This work should also include sufficient replicates of individual test specimens to enable a statistical investigation of the scatter of material properties.

ACKNOWLEDGEMENTS

This material is based upon work supported by the Air Force Office of Scientific Research under award number FA2386-16-1-4098."

NOTATION

A,B = shape parameters for τ_{cr}-Δ_{wdg} relationship;
A_{cr} = area of shear plane;
A_g = cross-sectional area of prism;
E_c = elastic modulus of concrete;
f_c = compressive strength of concrete;
h = crack opening of the sliding plane;
h_1 = crack opening at Δ_1;
L = height of prism;
m = slope of τ_{cr}-Δ_{wdg} relationship;
P_h = load applied by horizontal ram;
P_v = load applied by vertical ram;
v_u = peak shear stress applied to shear plane;
Δ = slip of the sliding plane;
Δ_1 = slip at the intersection of the fibre and non-fibre shear stress-slip relationships;
Δ_2 = slip at the maximum crack width for mixes without fibres;
σ_{ax} = axial stress;
σ_{cr} = normal stress across shear plane;
τ_{cr} = shear stress across shear plane;

REFERENCES

Anderson, A. R. (1960). "Composite designs in precast and cast-in-place concrete." *Progressive Architecture*, 41(9): 172-179.

Balaguru, P., and Dipsia, M. G. (1993). “Properties of fiber reinforced high-strength semi-lightweight concrete.” *ACI Materials Journal*, 90(5), 399-405.

Banthia, N., Majdzadeh, F., Wu, J., and Bindiganavile, V. (2014). “Fiber synergy in Hybrid Fiber Reinforced Concrete (HyFRC) in flexure and direct shear.” *Cement and Concrete Composites*, 48, 91-97.

Barragan, B., Gettu, R., Agullo, L., and Zerbino, R. (2006). “Shear failure of steel fiber-reinforced concrete based on push-off tests.” *ACI Materials Journal*, 103(4), 251-257.

Birkeland, P. W., and Birkeland, H. W. (1966). “Connections in precast concrete construction.” *ACI Journal*, 63(3), 345-368.

Boulekbache, B., Hamrat, M., Chemrouk, M., and Amziane, S. (2012). “Influence of yield stress and compressive strength on direct shear behaviour of steel fibre-reinforced concrete.” *Construction and Building Materials*, 27(1), 6-14.

Buitelaar, P. (2004). “Heavy reinforced ultra high performance concrete.” *Proc., International Symposium on Ultra High Performance Concrete*, Kassell, 25-36.

Chen, Y., Visintin, P., Oehlers, D. J., and Alengaram, U. J. (2013). “Size-dependent stress-strain model for unconfined concrete.” *Journal of Structural Engineering*, 140(5), 04013088.

Chen, Y., Zhang, T., Visintin, P., and Oehlers, D. J. (2015a). “Concrete shear-friction material properties: Application to shear capacity of RC beams of all sizes.” *Advances in Structural Engineering*, 18(8), 1187-1198.

Chen, Y., Visintin, P., and Oehlers, D. J. (2015b). “Concrete shear-friction material properties: Derivation from actively confined compression cylinder tests.” *Advances in Structural Engineering*, 18(8), 1173-1185.

Crane, C. K. (2010). “Shear and shear friction of ultra-high performance concrete bridge girders.” Ph.D. Thesis, Georgia Institute of Technology.

fib (International Federation for Structural Concrete). (2013). *CEB-FIP Model Code 2010*, Lausanne.

Foster, S. J., Lee, G. G., and Htut, T. N. S. (2007). “Radiographic imaging for the observation of Modes I and II fracture in fibre reinforced concrete.” *Proc., 6th International Conference on Fracture Mechanics of Concrete and Concrete Structures*. Catania.

Hanson, N. W. (1960). "Precast-Prestressed Concrete Bridges: 2. Horizontal Shear Connections." *Journal of the PCA Research and Development Laboratories*, 2(2): 38-58.

Harries, K. A., Zeno, G., and Shahrooz, B. (2012). “Toward an improved understanding of shear-friction behavior.” *ACI Structural Journal*, 109(6), 835-844.

Haskett, M., Oehlers, D. J., Mohamed Ali, M. S.., and Wu, C. (2009). “Rigid body moment–rotation mechanism for reinforced concrete beam hinges.” *Engineering Structures*, 31(5), 1032-1041.

Haskett, M., Oehlers, D. J., Mohamed Ali, M. S., and Sharma, S. K. (2010). "The shear friction aggregate interlock resistance across sliding planes in concrete." *Magazine of Concrete Research,* 62(12), 907-924.

Haskett, M., Oehlers, D. J., Mohamed Ali, M. S., and Sharma, S. K. (2011). "Evaluating the shear-friction resistance across sliding planes in concrete." *Engineering Structures,* 33(4), 1357-1364.

Hofbeck, J. A., Ibrahim, I. O., and Mattock, A. H. (1969). "Shear transfer in reinforced concrete." *ACI Journal*, 66(2), 119-128.

JSCE (1990) "Method of Test for Shear Strength of Steel Fiber Reinforced Concrete (SFRC)." *JSCE SF-6,* Japan Society of Civil Engineers, Tokyo.

Kahn, L. F., and Mitchell, A. D. (2002). "Shear friction tests with high-strength concrete." *ACI Structural Journal*, 99(1), 98-103.

Khaloo, A. R., and Kim, N. (1997). "Influence of concrete and fiber characteristics on behavior of steel fiber reinforced concrete under direct shear." *ACI Materials Journal*, 94(6), 592-601.

Khanlou, A., MacRae, G. A., Scott, A. N., Hicks, S. J., and Clifton, G. C. (2012) "Shear performance of steel fibre-reinforced concrete." *Proc., Australasian Structural Engineering Conference*, Perth.

Loov, R. E. (1998). "Review of A23. 3-94 simplified method of shear design and comparison with results using shear friction." *Canadian Journal of Civil Engineering*, 25(3), 437-450.

Lucas, W., Oehlers, D. J., and Mohamed Ali, M. S. (2011). "Formulation of a shear resistance mechanism for inclined cracks in RC beams." *Journal of Structural Engineering*, 137(12), 1480-1488.

Lucas, W., Oehlers, D. J., Mohamed Ali, M. S. and Griffith, M. C. (2012). "The FRP reinforced shear-friction mechanism." *Advances in Structural Engineering*, 15(4), 615-623.

Mansur, M. A., Vinayagam, T., and Tan, K. H. (2008). "Shear transfer across a crack in reinforced high-strength concrete." *Journal of Materials in Civil Engineering*, 20(4), 294-302.

Mast, R. F. (1968) "Auxiliary Reinforcement in Concrete Connections." *Journal of Structural Division.* 94(6), 1485-1504.

Mattock, A. H., and Hawkins, N. M. (1972). "Shear transfer in reinforced concrete—Recent research." *PCI Journal*, 17(2), 55-75.

Mattock, A. H. (2001). "Shear friction and high-strength concrete." *ACI Structural Journal*, 98(1), 50-59.

Millard, S. G., and Johnson, R. P. (1984). "Shear transfer across cracks in reinforced concrete due to aggregate interlock and to dowel action." *Magazine of Concrete Research*, 36(126), 9-21.

Millard, S. G., and Johnson, R. P. (1985). “Shear transfer in cracked reinforced concrete.” *Magazine of Concrete Research*, 37(130), 3-15.

Mirsayah, A. A., and Banthia, N. (2002). “Shear strength of steel fiber-reinforced concrete.” *ACI Materials Journal*, 99(5), 473-479.

Mohamed Ali, M. S., Oehlers, D. J., and Griffith, M. C. (2010). “The residual strength of confined concrete.” *Advances in Structural Engineering*, 13(4), 603-618.

Muttoni, A. (2008). “Punching shear strength of reinforced concrete slabs without transverse reinforcement.” *ACI Structural Journal*, 105(4), 440-450.

Muttoni, A., Ruiz, M. F. (2008). “Shear strength of members without transverse reinforcement as a function of critical shear crack width.” *ACI Structural Journal*, 105(2), 163-172.

Oehlers, D. J., Mohamed Ali, M. S., Griffith, M. C., Haskett, M., and Lucas, W. (2012). “A generic unified reinforced concrete model.” *Proceedings of the Institution of Civil Engineers-Structures and Buildings*, 165(1), 27-49.

Paulay, T., and Loeber, P. J. (1974). “Shear transfer by aggregate interlock.” *ACI Special Publication*, 42, 1-16.

Rao, G. A., and Rao, A. S. (2009). “Toughness indices of steel fiber reinforced concrete under mode II loading.” *Materials and Structures*, 42(9), 1173-1184.

Russell, H. G. and Graybeal, B. A. (2013). "Ultra-high performance concrete: A state-of-the-art report for the bridge community." *FHWA-HRT-13-060*, Federal Highways Administration, McLean.

Sobuz, H. R., Visintin, P., Mohamed Ali, M. S., Singh, M., Griffith, M. C., and Sheikh, A. H. (2016). “Manufacturing ultra-high performance concrete utilising conventional materials and production methods.” *Construction and Building Materials*, 111, 251-261.

Soetens, T., and Matthys, S. (2017). “Shear-stress transfer across a crack in steel fibre-reinforced concrete.” *Cement and Concrete Composites*, 82, 1-13.

Sonnenberg, A. M. C., Al-Mahaidi, R., and Taplin, G. (2003). “Behaviour of concrete under shear and normal stresses.” *Magazine of Concrete Research*, 55(4), 367-372.

Sturm, A.B. and Visintin, P. (2019) “Local bond slip behaviour of steel reinforcing bars embedded in UHPFRC.” *Structural Concrete*, 20(1), 108-122.

Tan, K. H., and Mansur, M. A. (1990). “Shear transfer in reinforced fiber concrete.” *Journal of Materials in Civil Engineering*, 2(4), 202-214.

Tassios, T. P., and Vintzēleou, E. N. (1987). “Concrete-to-concrete friction.” *Journal of Structural Engineering*, 113(4), 832-849.

Valle, M., and Buyukozturk, O. (1993). “Behavior of fiber reinforced high-strength concrete under direct shear.” *ACI Materials Journal*, 90(2), 122-133.

Vecchio, F. J., and Collins, M. P. (1986). "The Modified Compression-Field Theory for Reinforced Concrete Elements Subjected to Shear." *ACI Structures Journal*, 83(2), 219-231.

Visintin, P., Oehlers, D. J., Haskett, M., and Wu, C. (2012). "Mechanics-based hinge analysis for reinforced concrete columns." *Journal of Structural Engineering*, 139(11), 1973-1980.

Visintin, P., Chen, Y., and Oehlers, D. J. (2015a). "Simulating the behavior of FRP-confined cylinders using the shear-friction mechanism." *Journal of Composites for Construction*, 19(6), 04015014.

Visintin, P., Chen, Y., and Oehlers, D. J. (2015b). "Size dependent axial and lateral stress strain relationships for actively confined concrete." *Advances in Structural Engineering*, 18(1), 1-20.

Visintin, P., Sturm, A. B., Mohamed Ali, M. S. and Oehlers, D. J. (2018) "Blending macro and micro fibres to enhance the serviceability behaviour of UHPFRC." *Australian Journal of Civil Engineering*, 16(2), 106-121.

Walraven, J. C., and Reinhardt, H. W. (1981). Theory and experiments on the mechanical behaviour of cracks in plain and reinforced concrete subjected to shear loading." *Heron*, 26(1A), 1-68;

Wille, K., and Naaman, A. E. (2012). "Pullout Behavior of High-Strength Steel Fibers Embedded in Ultra-High-Performance Concrete." *ACI Materials Journal*, 109(4).

Wong, R. C. K., Ma, S. K. Y., Wong, R. H. C., and Chau, K. T. (2007). "Shear strength components of concrete under direct shearing." *Cement and Concrete Research*, 37(8), 1248-1256.

Zhang, J. P. (1997). "Diagonal cracking and shear strength of reinforced concrete beams." *Magazine of Concrete Research*, 49(178), 55-65.

Zhang, T. (2014) "A generic mechanics approach for predicting shear strength of reinforced concrete beams", Ph.D. Thesis, University of Adelaide.

Zhang, T., Visintin, P., Oehlers, D. J., and Griffith, M. C. (2014a). "Presliding shear failure in prestressed RC beams. I: Partial-Interaction mechanism." *Journal of Structural Engineering*, 140(10), 04014069.

Zhang, T., Oehlers, D. J., and Visintin, P. (2014b). "Shear strength of FRP RC beams and one-way slabs without stirrups." *Journal of Composites for Construction*, 18(5), 04014007.

Zhang, T., Visintin, P., and Oehlers, D. J. (2015). "Shear strength of RC beams with steel stirrups." *Journal of Structural Engineering*, 142(2), 04015135.

Zhang, T., Visintin, P., and Oehlers, D. J. (2016). "Shear strength of RC beams without web reinforcement." *Australian Journal of Structural Engineering*, 17(1), 87-96.

Zhang, T., Visintin, P., and Oehlers, D. J. (2017). "Shear strength of RC beams subjected to axial load." *Australian Journal of Civil Engineering*, 15(1), 1-17.

CHAPTER 2

Background

In this chapter the flexural behaviour of UHPFRC at the serviceability limit state is explored. Closed-forms solutions are derived for the tension stiffening behaviour, serviceability deflections and crack widths of UHFPRC beams.

The first publication "Time dependent tension stiffening mechanics of fibre reinforced and ultra-high performance fibre reinforced concrete" develops a model for the tension stiffening behaviour of FRC and UHPFRC by application of partial interaction theory. The model is then used to develop closed-form solutions for the crack spacing and the load-slip relationships of FRC and UHPFRC. This allows the tension stiffening behaviour to be determined from the bond and tension properties in Chapter 1.

The second publication "A rational design approach for the instantaneous and time dependent serviceability deflections and crack widths of FRC and UHPFRC continuous and simply supported beams" presents closed-form solutions for the serviceability deflections and crack widths of FRC and UHPFRC. The solutions are developed by applying a segmental analysis where the closed-form solutions from the previous publication are used to simulate the response of the tensile reinforcement.

List of Manuscripts

Sturm, A. B., Visintin, P., Oehlers, D. J. and Seracino, R. (2018) "Time dependent tension stiffening mechanics of fibre reinforced and ultra-high performance fibre reinforced concrete." *Journal of Structural Engineering*, 144(8), 04018122.

Sturm, A. B., Visintin, P., and Oehlers, D. J. (2019) "A rational design approach for the instantaneous and time dependent serviceability deflections and crack widths of FRC and UHPFRC continuous and simply supported beams." *Journal of Structural Engineering*, 145(11), 04019138.

STATEMENT OF AUTHORSHIP

Time dependent tension stiffening mechanics of fibre reinforced and ultra-high performance fibre reinforced concrete
Journal of Structural Engineering, 144(8), 04018122.

Sturm, A.B. (Candidate)

Prepared manuscript, performed all analyses, and developed model and theory (75%)

This paper reports on original research I conducted during the period of my Higher Degree by Research candidature and is not subject to any obligations or contractual agreements with a third party that would constrain its inclusion in this thesis. I am the primary author of this paper.

Signed Date 9/07/2020

Visintin, P.

Supervised and contributed to research, and acted as corresponding author (10%)

I certify that the candidate's stated contribution to the publication is accurate (as detailed above); permission is granted for the candidate in include the publication in the thesis; and the sum of all co-author contributions is equal to 100% less the candidate's stated contribution.

Signed Date 07/07/2020

Oehlers, D.J.

Supervised and contributed to research (10%)

I certify that the candidate's stated contribution to the publication is accurate (as detailed above); permission is granted for the candidate in include the publication in the thesis; and the sum of all co-author contributions is equal to 100% less the candidate's stated contribution.

Signed Date 7/7/20

Seracino, R.

Contributed to research (5%)

I certify that the candidate's stated contribution to the publication is accurate (as detailed above); permission is granted for the candidate in include the publication in the thesis; and the sum of all co-author contributions is equal to 100% less the candidate's stated contribution.

Signed Date … July 7, 2020….

TIME DEPENDENT TENSION STIFFENING MECHANICS OF FIBRE REINFORCED AND ULTRA-HIGH PERFORMANCE FIBRE REINFORCED CONCRETE

Sturm, A. B., Visintin, P., Oehlers, D. J., and Seracino, R

ABSTRACT

The tension stiffening behaviour of fibre reinforced concrete is of fundamental importance for the characterisation of crack widths and spacings, and the determination of the tensile response of fibre reinforced concrete members with internal reinforcement. In this paper a model is presented for the tension stiffening behaviour of strain softening and strain hardening fibre reinforced and ultra-high performance fibre reinforced concrete with an allowance for the long term creep and shrinkage effects of the concrete. Closed form analytical solutions are derived to describe the crack spacings and the load slip behaviour assuming either a simplified linear ascending bond stress-slip relationship or the more realistic CEB-FIP bond stress-slip relationship. Further, it is shown for design, how the stiffness of the reinforcement can be characterised using an effective modular ratio which can easily be incorporated into member analysis techniques to characterise the serviceability behaviour of flexural members. Finally, the results are validated against a broad range of fibre reinforced concretes of normal, high and ultra-high strength, thus demonstrating validity for a wide range of different FRCs.

INTRODUCTION

Fibre reinforced concrete (FRC) is of great interest due to its ability to increase the ductility by restraining sliding wedges in compression (Schumacher 2006) and to restrain flexural cracking in tension (Stang & Aare 1992). The restraint of flexural cracks suggests that the addition of fibres can improve the serviceability behaviour of reinforced concrete members by increasing the cracked stiffness. This increase in stiffness leads to a reduction in deflections and crack widths relative to a beam without fibre reinforcement. To benefit from this improved capacity, designers require analysis techniques which can accurately characterise the effect of fibres.

An important phenomenon that effects the performance of reinforced concrete at the serviceability limit is tension stiffening. This behaviour controls the spacing and width of cracks, and the effective tensile response of the reinforcement (Balazs 1993; Visintin et al. 2013). In the tension region of a reinforced concrete member the interaction between the reinforcing bar and the concrete produces the tension stiffening effect, where due to partial interaction (PI) along the concrete-reinforcing bar interface the bar is effectively stiffened by the surrounding concrete. The effect of interaction can be visualised in terms of the stiffness of the bond stress slip relationship, as indicated in Fig. 1(a), where full interaction (FI) is infinitely stiff, no interaction (NI) has zero stiffness and PI is intermediate between the two. The increased stiffness of the tensile response due to partial interaction is illustrated in Fig. 1(b).

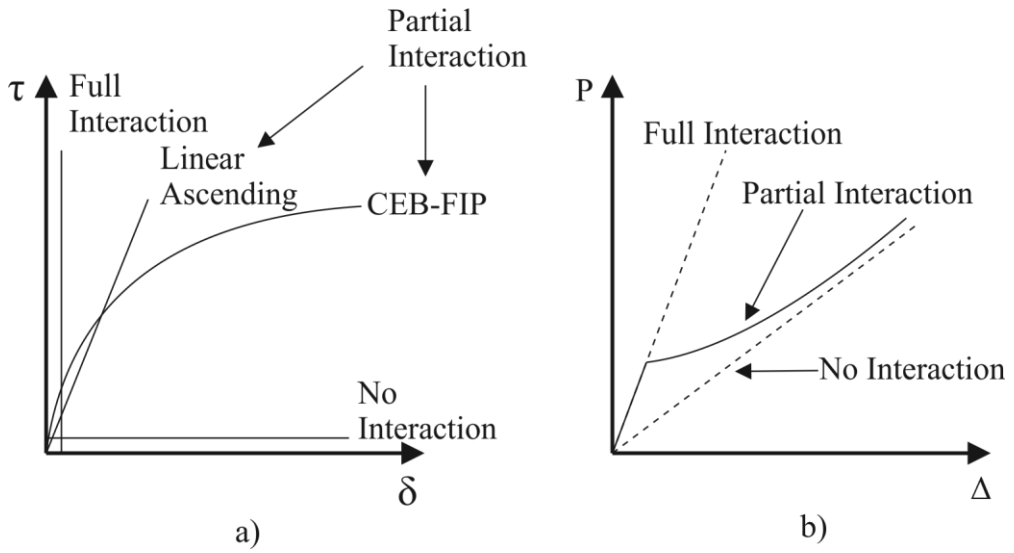

Fig. 1a) Bond stress slip relationship; b) Load slip relationship

To allow for tension stiffening in ordinary reinforced concrete, it is common practice to use an empirically derived bond factor (Bischoff 2001). The bond factor is defined as the ratio of the mean stress in the concrete to the peak tensile strength of the concrete and through the definition of an offset the effect of shrinkage can be quantified (Bischoff 2001).

To allow for fibres, Bischoff (2003) extended this approach by including an additional term proportional to the ratio of the stress in the fibres at the crack to the cracking stress of the concrete. The limitation of this approach is that from the direct tensile testing of FRC it is known that the stress at the crack face reduces as the crack widens, (Deluce 2011; Wille et al. 2014). Hence the term to allow for fibres is necessarily an averaged value, and for each new type of fibre developed a series of calibration tests are required. A similar approach is explored by Leutbecher & Fehling (2012) for estimating crack widths, in which a bond factor is taken to calculate the difference in average strains between the concrete and the reinforcement and a constant bond stress is assumed between the reinforcement and the concrete to estimate the crack spacing. This model allows for both shrinkage strains and the bridging force in the fibres.

An alternative to the bond factor approaches, is to use partial interaction mechanics to simulate the slip along the reinforcement-concrete interface. For ordinary reinforced concrete this approach has been extensively explored by: Gupta & Maestrini (1990); Wu et al (1991); Balazs (1993); Choi & Cheung (1996); Muhammad et al. (2012); Zhang et al. (2016); Sturm et al. (2017).

Based on partial interaction mechanics, Yuguang et al. (2009) and Amin et al. (2016) have modelled the reinforcing bar-concrete interface and estimated the bridging force in the fibres. In this analysis a constant bond and constant tensile stress were assumed. While these assumptions result in simple analytical solutions this approach has the disadvantage or requiring calibration to obtain the most appropriate constant material properties.

To avoid the need for calibration Lee et al. (2013) developed a numerical tension stiffening model for FRC based on the realistic CEB-FIP bond slip relationship. While allowing for the complexities of non-linear behaviour, this model is not suitable for obtaining closed form solutions due to the complex modelling associated with ascertaining the fibre contribution (Lee et al. 2011a; Lee et al. 2011b). The fibre contribution is derived by considering the pull-out

behaviour of a single fibre as a function of the length of embedment and angle of inclination with respect to the crack. An average fibre contribution at a given cross-section is then obtained by assuming some statistical distribution of the embedment length and angle of inclination and then taking a weighted mean. There are two issues with this approach from the perspective of this current paper, first the mathematical complexity prevents the reduction of this model to closed form and secondly the experimental complexity of determining the cohesive behaviour of a single fibre. Determining the pull-out behaviour of a single fibre is problematic as it is known to vary as a function of inclination angle (Ouyang et al. 1995; Lee & Foster 2007), thus requiring multiple tests as this parameter is varied. Further, this test is more specialised then conventional direct tension test performed on a dogbone specimens and thus increases the difficulty and cost of developing new materials. Hence, considering that the aim of this paper is to develop a closed form solution that could be incorporated into routine limit state design, the decision was made to allow for the fibre contribution empirically from direct tension tests, rather than analytically from the consideration of a single fibre.

In this paper, the non-linear tension stiffening approach developed by Muhammad et al. (2012) for the short term tension stiffening behaviour of concrete members, which was then extended to the long term case by Sturm et al. (2017), will be further extended to FRC. For this extension, the previous assumption, that the force in the concrete is zero at the crack face is no longer applicable and thus a stress-crack width relationship is assumed such that the model can be applied to a range of fibre types simply by changing the input stress crack width relationship. The CEB-FIP bond slip relationship will be used to determine crack spacings since it has been successfully used for ordinary reinforced concrete (Balazs 1993) and is widely applicable. Since closed form solutions cannot be obtained for this relationship beyond the initiation of primary cracking, a simplified linear ascending bond slip relationship will be used to characterise the load slip behaviour of the reinforcement. This approach has successfully been applied to ordinary reinforced concrete (Mohamed et al. 2012; Sturm et al. 2017) and can be justified as the slip of the reinforcement at the crack is generally an order of magnitude smaller than the slip at the peak bond stress illustrated in Fig. 1(b), that is only the ascending portion of the bond-slip relationship needs to be considered.

In the remainder of the paper, the tensile behaviour of FRC members will be explored starting from the behaviour of unreinforced FRC to the full interaction behaviour of uncracked reinforced FRC and finally partial interaction mechanics are used to explain the behaviour of cracked reinforced FRC. It should be noted here that the term FRC is used generically to describe any concrete with fibre reinforcement and includes UHPFRC which is differentiated by the presence of a strain hardening stress strain relationship prior to macro cracking. With the mechanics established, analytical closed form solutions are presented for the crack spacing using the CEB-FIP bond slip relationship and for the load slip behaviour using the simplified linear ascending relationship. A parametric study is performed to investigate the effect of strain hardening (such as that which occurs in UHPFRC) versus strain softening on the tension stiffening behaviour. Finally, the solutions developed are compared to experimental results covering normal, high and ultra-high strength FRC with a range of fibre types, hence showing the broad applicability of the approach. In the solutions that follow, the effect of fibre volume and orientation are allowed for implicitly by the choice of material properties, that is, in the definition of the stress-crack width relationship obtained from direct tension tests.

TENSILE BEHAVIOUR OF UNREINFORCED FRC

Consider a direct tension test as illustrated in Fig. 2(a-b). As the specimen is initially loaded it experiences an elastic material deformation. For fibre volumes below a critical fraction the deformation will localise at a single crack when the cracking load is reached (Naaman 2007). As the crack opens, load is transmitted across the crack by the fibres and softening occurs (Fig. 2d). This is contrasted with the case for ordinary reinforced concrete where the load reduces quickly after cracking as the interaction of the aggregate is lost (Li et al. 1993). For fibre contents above the critical fraction, there exists an intermediate stage where microcracking occurs (Fig. 2b), this causes strain hardening as shown in Fig. 2(c). (Tjiptobroto & Hansen 1993). At the peak load the deformations will localise at a macrocrack inducing softening.

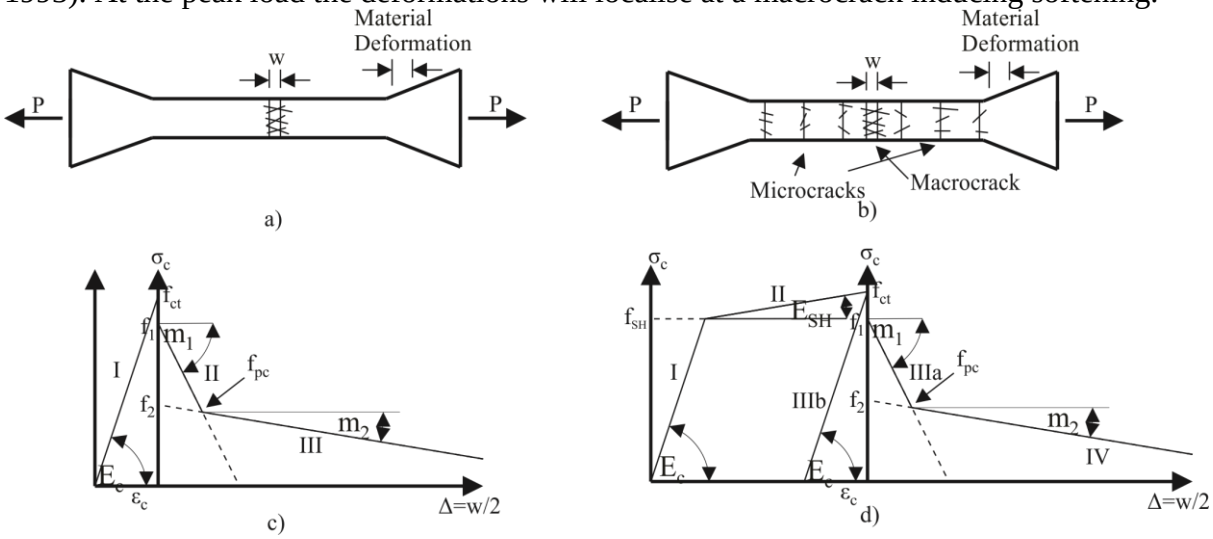

Fig. 2 Tensile response of FRC

To establish a basis of future partial interaction modelling, let us consider each stage of cracking in more detail.

Uncracked phase

When uncracked (stage I in Fig. 2c) the stress-strain relationship is given by Eq. (1) for both the non- strain hardening and strain hardening case.

$$\sigma_c(\varepsilon_c) = E_c\varepsilon_c;\ \varepsilon_c < \frac{f_{ct}}{E_c} \quad (non-strain\ hardening) \tag{1a}$$

$$\sigma_c(\varepsilon_c) = E_c\varepsilon_c;\ \varepsilon_c < \frac{f_{SH}}{E_c} \quad (strain\ hardening) \tag{1b}$$

Microcracking phase

Strain hardening concrete undergoes microcracking when the stress reaches the microcracking stress, f_{SH} in Fig 2c). At this stage the stress-strain relationship can be expressed as

$$\sigma_c(\varepsilon_c) = E_{SH}\left[\varepsilon_c + f_{SH}\left(\frac{1}{E_{SH}} - \frac{1}{E_c}\right)\right];\ \frac{f_{SH}}{E_c} < \varepsilon_c < \frac{f_{SH}}{E_c} + \frac{f_{ct} - f_{SH}}{E_{SH}} \tag{2}$$

Macrocracking phase

For either strain hardening or non-strain hardening concrete, when the macrocracking stress f_{ct} is reached the deformation is localised at a single crack. The behaviour after macrocracking is determined by the stress-strain relationship of the uncracked concrete between the cracks and the stress-crack width relationship of the fibres bridging the crack.

A number of different expressions have been used to characterise the tensile stress-crack width relationship including linear descending (Kooiman 2000; Barragan 2002; Sorelli 2003; Meda et al. 2004; Grünewald 2004; Löfgren et al. 2004; Pereira et al. 2004; Schumacher 2006), non-linear descending relationships (Stang & Aare 1992) as well as those derived from considering the pullout of a single fibre (Li et al. 1993; Leutbecher & Feuling 2012). In this paper a linear descending stress-crack width relationship is assumed as it is the simplest case. This is justified as it has been shown experimentally that relatively small cracks are observed in FRC members subjected to service loads, therefore significant non-linearity in the stress-crack width relationship has not occurred (Visintin et al. 2018b).

Any linear descending relationship can be described in the form given by Eq. (3)

$$\sigma_f(w) = f_i - \frac{m_i}{2}w = f_i - m_i\Delta;\ i = 1,2,3,\ldots \tag{3}$$

Where i is an index indicating the piecewise component of the slope being considered. m_i is the slope of this i^{th} component of the stress-crack width relationship and f_i is the intercept with the stress axis. Note that f_1 is typically equal to f_{ct}. This definition of an index i allows the consideration of linear piecewise stress-crack width relationships.

Upon the initiation of macrocracking in UHPFRC the uncracked concrete between the cracks unloads as the stress at the crack face decreases. For non-strain hardening FRC the concrete unloads along curve I in Fig. 2(c) therefore the stress-strain relationship can still be described using Eq. (1a). For strain hardening FRC, due to the inelastic strains developed due to microcracking, the concrete between the macrocracks will instead unload along the curve III illustrated in Fig. 2(c). The stress-strain relationship for this unloading curve is

$$\sigma_c(\varepsilon_c) = E_c\left[\varepsilon_c - (f_{ct} - f_{SH})\left(\frac{1}{E_{SH}} - \frac{1}{E_c}\right)\right] = E_c(\varepsilon_c - \varepsilon_{inel}) \tag{4}$$

where ε_{inel} is the permanent inelastic strain due to strain hardening. It should be noted that the only difference between Eq. (1a) and Eq. (4) is the inelastic strain term, which is equal to zero for non-strain hardening concrete.

FULL INTERACTION (FI) TENSION STIFFENING

Let us first consider the behaviour of a reinforced prism (referred to as a tension chord) which has yet to form macrocracks. In the most general case (Fig. 2c), the first phase is a strain based linear elastic phase where the concrete is uncracked, and this may be followed depending on the volume and type of fibres by a strain based strain hardening phase associated with microcracking (Wille et al. 2014). The initiation of macrocracking causes the transition into a displacement based softening phase (Fig. 2d). For the first two phases compatibility is assumed between the concrete and the reinforcement, under this full interaction assumption the load and the deformation of the tension chord will be derived.

Uncracked Phase

For analysis, consider the concrete prism in Fig. 3(a-b) with cross-sectional area A_c with an embedded reinforcing bar of area, A_r and the bonded perimeter of the interface between the reinforcing bar and the prism is given by L_{per}. The prism is subjected to both an axial load and a shrinkage strain ε_{sh}. Note that the shrinkage strain, ε_{sh} results in the offset of strains in the reinforcement and concrete, as illustrated in Fig. 3(d). That is, in the subsequent analysis we have defined the strains in the reinforcement and concrete relative to the positions at which the load in each component is zero. Hence, the concrete strain includes elastic and creep components with the effect of shrinkage being allowed for by this offset. This was the approach to modelling shrinkage used by Visintin et al. (2013).

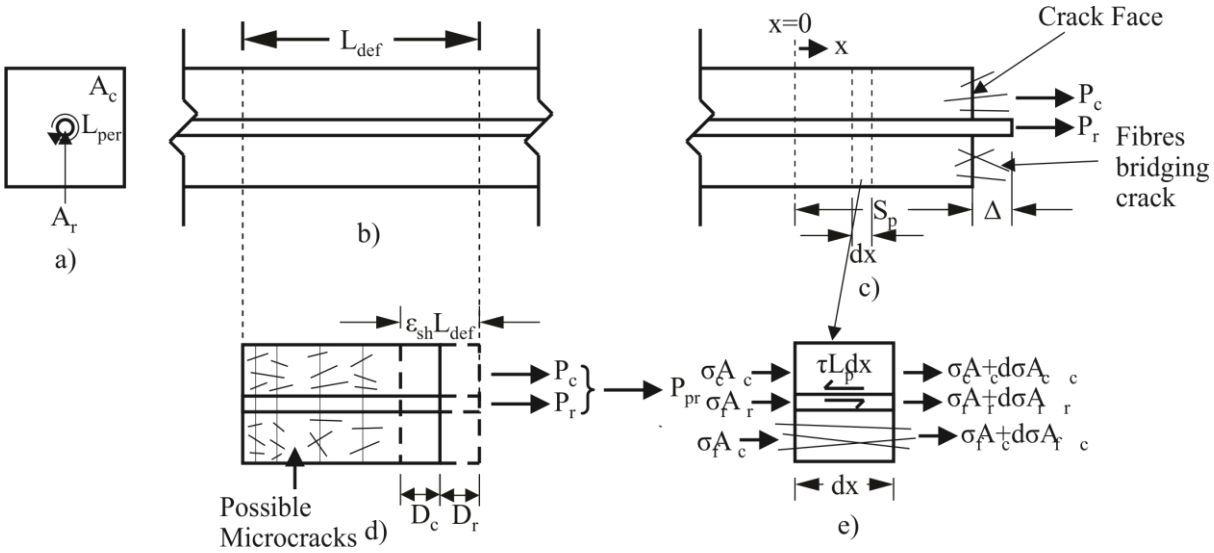

Fig. 3 Tension chord; a) cross-section; b) longitudinal section (FI); c) longitudinal section (PI); d) segment (FI); e) infinitesimal segment (PI)

Prior to cracking the forces illustrated in Fig. 3(d) are given by,

$$P_r = \frac{D_r}{L_{def}} E_r A_r \tag{5}$$

$$P_c = \frac{D_c}{L_{def}} E_c A_c \tag{6}$$

In which the elastic modulus of the concrete may be reduced using any appropriate method to allow for creep (Dilger & Neville 1971; Bazant 1972; Neville et al. 1983), and the total load in the tension chord is $P_{pr}=P_r+P_c$.

To maintain compatibility, the deformations in the concrete and the reinforcement are related by

$$\varepsilon_{sh} L_{def} = -D_r + D_c \tag{7}$$

Note that D_r and D_c are defined as positive for deformation that cause tension and negative for deformations that cause tension (that is deformations to the right are positive and those to the left are negative in Fig. 3.

For non-strain hardening concrete, cracking will commence when the strain in the concrete, D_c/L_{def} is equal to f_{ct}/E_c, hence and hence from Eq. (7), the strain in the reinforcement is D_r/L_{def} is equal to f_{ct}/E_c-ε_{sh}. The total load in the tension chord at cracking is, therefore

$$P_{pr-cr} = f_{ct} A_c + E_r A_r \left(\frac{f_{ct}}{E_c} - \varepsilon_{sh} \right) \tag{8}$$

Setting $P_{pr\text{-}cr}$ to zero gives the minimum shrinkage strain to cause cracking without the application of an external load in Eq. (9).

$$\varepsilon_{sh-cr} = \frac{f_{ct}}{E_c} \left(1 + \frac{E_c A_c}{E_r A_r} \right) \tag{9}$$

Similarly, by substituting the microcracking strain, f_{SH}/E_c for the macrocracking strain, f_{ct}/E_c in Eq. (8) the load to commence microcracking is

$$P_{SH} = f_{SH} A_c + E_r A_r \left(\frac{f_{SH}}{E_c} - \varepsilon_{sh} \right) \tag{10}$$

Microcracking Phase

In the presence of microcracks, which occur predominately in UHPFRC, the force in the reinforcement may still be expressed as Eq. (5) and the force in the concrete is

$$P_c = f_{SH}A_c + E_{SH}A_c\left(\frac{D_c}{L_{def}} - \frac{f_{SH}}{E_c}\right) \tag{11}$$

To determine the load to induce macrocracking, consider that the concrete strain at the initiation of macrocracking is given by

$$\frac{D_c}{L_{def}} = \frac{f_{ct}}{E_c} + \varepsilon_{inel} \tag{12}$$

Applying the conditions of compatibility, that is, using Eq. (7), the strain in the reinforcing bar is

$$\frac{D_r}{L_{def}} = \frac{f_{ct}}{E_c} + \varepsilon_{inel} - \varepsilon_{sh} \tag{13}$$

and for strain hardening concrete, the total load in the tension chord to cause macrocracking is

$$P_{pr-cr} = f_{ct}A_c + E_rA_r\left(\frac{f_{ct}}{E_c} + \varepsilon_{inel} - \varepsilon_{sh}\right) \tag{14}$$

Importantly, comparing Eqs. 8 and 14 reveals that the inelastic strains associated with microcracking delay the formation of macrocracks. That is the macrocracking force is increased by $\varepsilon_{inel}E_rA_r$ due to microcracking.

Finally, setting $P_{pr\text{-}cr}$ to zero in Eq. (14), the shrinkage strain to crack the tension chord with no additional loads in the presence of microcracking is

$$\varepsilon_{sh-cr} = \frac{f_{ct}}{E_c}\left(1 + \frac{E_cA_c}{E_rA_r}\right) + \varepsilon_{inel} \tag{15}$$

This expression is the same as Eq. (9), except the shrinkage strain to cause a macrocrack is increased by the inelastic strain associated with microcracking.

PARTIAL INTERACTION (PI) TENSION STIFFENING

Again, consider the tension stiffening prism in Fig. 3(a) which is now subjected to partial interaction conditions (Fig. 3c). The behaviour of the prism as a function of position is quantified by the following scalar fields; (i) strain and axial deformation in the concrete, $u_c(x)$ and $\varepsilon_c(x)$ and the reinforcement, $u_r(x)$ and $\varepsilon_r(x)$; (ii) the stresses induced by these strains, $\sigma_c(x)$ and $\sigma_r(x)$; (iii) the interface shear stress between the concrete and the reinforcement, $\tau(x)$; and (iv) the slip, $\delta(x)$ induced between the concrete and the reinforcement.

PI governing mechanics

In Fig. 3(e), the change in stress in the concrete and reinforcement as a function of the interface shear stress along an infinitesimal segment of the tension chord is

$$\frac{d\sigma_r}{dx} = \frac{\tau(x)L_{per}}{A_r} \tag{16}$$

$$\frac{d\sigma_c}{dx} = -\frac{\tau(x)L_{per}}{A_c} - \frac{d\sigma_f}{dx} \tag{17}$$

where σ_f is the portion of the stress at the cross-section carried by the fibres.

The presence of differential axial stresses in the reinforcement and concrete as well as the shrinkage strain induces a slip of the bar relative to the surrounding concrete, as follows

$$\delta(x) = u_r(x) - u_c(x) + \int \varepsilon_{sh}dx \tag{18}$$

Differentiating the slip $\delta(x)$ in Eq. (18) gives the interface slip strain

$$\frac{d\delta}{dx} = \varepsilon_r - \varepsilon_c + \varepsilon_{sh} \tag{19}$$

Assuming that the reinforcement strain is elastic and the concrete strain can be determined from Eq. (4), the slip strain as a function of the reinforcement and concrete stress is

$$\frac{d\delta}{dx} = \frac{\sigma_r(x)}{E_r} - \frac{\sigma_c(x)}{E_c} + \varepsilon_{sh} - \varepsilon_{inel} \tag{20}$$

Further differentiating the slip strain yields

$$\frac{d^2\delta}{dx^2} = \frac{1}{E_r}\left(\frac{d\sigma_r}{dx}\right) - \frac{1}{E_c}\left(\frac{d\sigma_c}{dx}\right) \tag{21}$$

Finally substituting Eqs. (16) and (17) into Eq. (21) gives the governing equation

$$\frac{d^2\delta}{dx^2} = \beta\tau(x) + \frac{1}{E_c}\frac{d\sigma_f}{dx} \tag{22}$$

where

$$\beta = L_{per}\left(\frac{1}{E_r A_r} + \frac{1}{E_c A_c}\right) \tag{23}$$

Note that to solve Eq. (22) it is assumed that the load from the fibres at the crack face is instantaneously transferred into the concrete matrix, that is, $d\sigma_f/dx$ is equal to 0. This simplifies finding closed form solutions. If the transfer of stress into the concrete matrix over the length of the fibre is to be considered, numerical modelling in a similar form to Lee et al. (2013) can be undertaken. The simplification that $d\sigma_f/dx$ is equal to 0 is made as the ultimate goal of this work is to derive a closed form solution simple enough for use in design practice, it will also be shown later that the predicted performance of a tension stiffening prism is not sensitive to this approximation.

PI boundary conditions

From Eq. (20), the slip strain at the loaded end is given by Eq. (24). In the derivation of Eq. (24) the strain in the reinforcement is taken as P_r/E_rA_r,. From Eq. (4) the strain in the concrete can be rearranged as $\sigma_c/E_c+\varepsilon_{inel}$ and then taking the stress in the concrete as equal to the stress in the fibres from Eq. (3) yields

$$\left.\frac{d\delta}{dx}\right|_{x=L_{def}} = \frac{P_r}{E_r A_r} + \varepsilon_{sh} - \frac{f_i}{E_c} + \frac{m_i}{E_c}\Delta - \varepsilon_{inel} \tag{24}$$

When applying Eq. (24), the deformation length L_{def} is equal to the crack spacing S_p for a prism with initial crack and $S_p/2$ for a prism with primary cracks as indicated in Fig. 4.

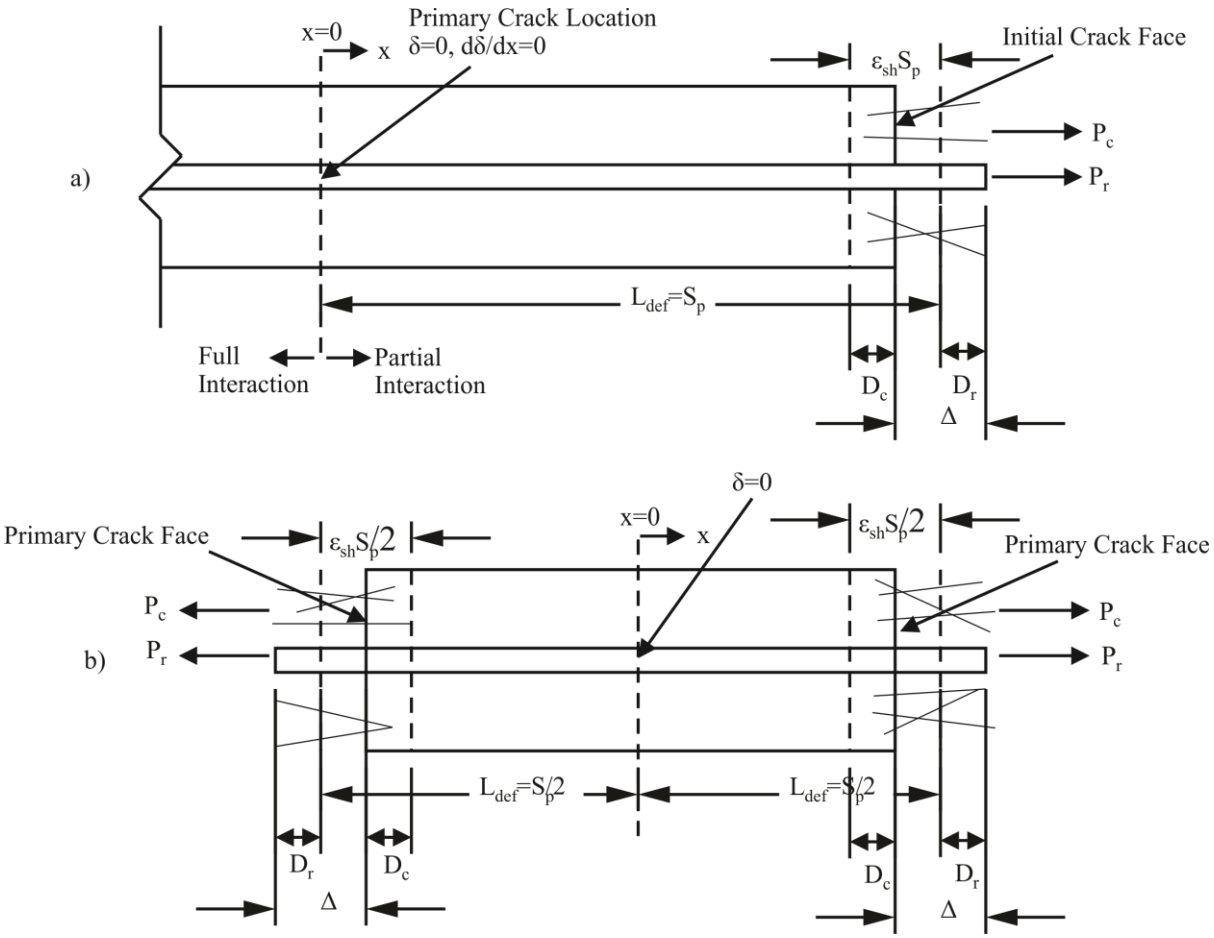

Fig. 4 PI prism deformations and boundary conditions; a) initial crack; b) primary crack

To determine the boundary condition for a prism with an initial crack (Fig. 4a), consider that at a distance S_p from the initial crack behaviour will tend to that of full interaction. That is both the slip and the slip strain are equal to zero:

$$\frac{d\delta}{dx} = 0 \text{ and } \delta = 0 \text{ at } x = 0 \tag{25}$$

A primary crack will form at a distance of S_p or more from the initial crack in Fig. 4(a), when the applied load reaches the cracking load. Note that primary cracks, are the cracks that are present when the crack pattern stabilises after the macrocracking load is reached.

After the formation of a primary crack the boundary condition changes to that of the symmetrically loaded prism in Fig. 4(b), where by symmetry, at the midpoint of the prism the slip is zero, i.e.

$$\frac{d\delta}{dx} \neq 0 \text{ and } \delta = 0 \text{ at } x = 0 \tag{26}$$

If the load and the bond strength is sufficiently high such that the cracking stress is reached at the centre of the prism, this will cause a secondary crack to form. Note that a secondary crack, is a crack that forms midway between two primary cracks after a stable crack pattern has formed. The boundary conditions for secondary cracking are again given by Eq. (26).

SOLUTIONS FOR CRACK SPACING USING THE CEB-FIP BOND SLIP RELATIONSHIP

Using the boundary conditions above, the governing equation Eq. (17) can now be solved for a specific combination of bond slip and stress crack width relationship. As these analyses are

for the serviceability limit state, and for reinforcing bars with strong bonds (such as steel reinforcing bars) only the ascending portion of the bond slip relationship is considered.

Note that the non-linear CEB-FIP bond slip relationship is used for determining the crack spacings as this has been successfully used for ordinary reinforced concrete by Balazs (1993) and the linear ascending relationship requires the definition of a tolerance of which the value is not obvious, this is also the case for ordinary reinforced concrete (Sturm et al. 2017). In Supplementary Material A the crack spacing is determined for the linear ascending bond characteristic to demonstrate this issue.

Applying the CEB-FIP bond slip relationship

The CEB-FIP bond slip relationship is given as (CEB 1993; fib 2013)

$$\tau = \tau_{max}\left(\frac{\delta}{\delta_1}\right)^{\alpha} \tag{27}$$

Substituting Eq. (27) into Eq. (22) the governing equation can now be expressed as

$$\frac{d^2\delta}{dx^2} = \lambda_2 \delta^{\alpha} \tag{28}$$

where

$$\lambda_2 = \frac{\tau_{max}}{\delta_1^{\alpha}}\beta \tag{29}$$

Using the identity

$$\frac{d\delta^2}{dx^2} = \delta' \frac{d\delta'}{d\delta} \tag{30}$$

and taking δ' to be $d\delta/dx$, Eq. (28) can be solved by applying the boundary condition in Eq. (25) to gives the variation in slip strain

$$\frac{d\delta}{dx} = \sqrt{\frac{2\lambda_2 \delta^{1+\alpha}}{1+\alpha}} \tag{31}$$

Eq. (31) can then be solved to yield the variation is slip by separating variables and integrating to give

$$\delta(x) = \left[\frac{(1-\alpha)^2\lambda_2}{(1+\alpha)2}\right]^{\frac{1}{1-\alpha}} x^{\frac{2}{1-\alpha}} \tag{32}$$

Determination of the crack spacing

Note that a primary crack can form at any location where the stress in the concrete is equal to the tensile strength of the concrete, f_{ct}. However the concrete stress is reduced in the vicinity of an initial crack. Hence, a minimum distance, S_p exists within which a new crack cannot form, as insufficient stress has been transferred from the reinforcing bar into the surrounding concrete, hence in this section this minimum distance will be quantified.

To determine the crack spacing there are a two possible approaches, the first approach is to model the rate of stress transfer from the fibres into the concrete matrix. This approach allows for the PI behaviour of each fibre, but this approach does not yield closed form solutions. This approach has been explored numerically by Lee et al. (2011a; 2011b; 2013).

The second option is to consider a drop in stress (f_{ct}-f_{pc}). To apply this approach f_{pc} is defined as the value of stress after the initial linear descending portion, where the stress-crack width relationship changes slope as illustrated in Fig. 2(d). This is a lower bound estimate on the stress in the fibres at the crack face when the new crack forms. Alternatively, (f_{ct}-f_{pc}) could be

calibrated as an effective material property using a numerical model that directly simulates the fibre stresses such as Lee et al. (2013).

To determine the crack spacing consider that the stress at the location of the new primary crack is f_{ct} and the stress at the initial crack face due to fibres is given as f_{pc}. Hence the change in stress between the initial and primary crack, considering that the rate of change in stress is given by Eq. (17) and assuming that the $d\sigma_f/dx$ is zero is

$$f_{ct} - f_{pc} = \int_{x=S_p}^{x=0} \frac{d\sigma_c}{dx} dx = \int_{x=0}^{x=S_p} \frac{\tau(x) L_{per}}{A_c} dx \tag{33}$$

Substituting Eq. (27) into Eq. (33) gives the following, where $\delta(x)$ is taken from Eq. (32)

$$f_{ct} - f_{pc} = \frac{\tau_{max} L_{per}}{\delta_1^{\alpha} A_c} \int_{x=0}^{x=S_p} \delta(x)^{\alpha} dx = \frac{\tau_{max} L_{per}}{\delta_1^{\alpha} A_c} \left[\frac{(1-\alpha)^2 \lambda_2}{(1+\alpha)2}\right]^{\frac{\alpha}{1-\alpha}} \left(\frac{1-\alpha}{1+\alpha}\right) S_p^{\frac{1+\alpha}{1-\alpha}} \tag{34}$$

Which can be rearranged to give the primary crack spacing

$$S_p = \left[\frac{2^{\alpha}(1+\alpha)}{\lambda_2 (1-\alpha)^{1+\alpha}}\right]^{\frac{1}{1+\alpha}} \left[\frac{f_{ct} - f_{pc}}{E_c} \left(\frac{E_c A_c}{E_r A_r} + 1\right)\right]^{\frac{1-\alpha}{1+\alpha}} \tag{35}$$

This is similar to the expression for ordinary reinforced concrete derived by Balazs (1993), except that the cracking stress has been reduced by the stress in the concrete at the initial crack face. It should be further noted that the presence of microcracks or shrinkage in the specimen does not affect the crack spacing.

Determination of the load slip behaviour using the CEB-FIP bond slip relationship

In Supplementary Material B solutions for the load slip relationship are given for the CEB-FIP bond slip relationship. Since the solutions developed are not explicit in terms of the half crack width in the next section the load slip behaviour is instead investigated using the simplified linear ascending bond slip relationship.

SOLUTIONS FOR LOAD SLIP RELATIONSHIP USING LINEAR ASCENDING BOND SLIP RELATIONSHIP

Since the CEB-FIP bond slip relationship is too complex to result in simple closed form solutions for initial cracking, and closed form solutions do not result for primary cracking, in this part the load-slip relationship will be derived using a simplified linear ascending bond slip relationship illustrated in Fig. 1(a). This simplification is appropriate since the linear ascending bond slip relationship shows a good correlation with the non-linear ascending relationship for slips significantly smaller than the slip at the peak stress. This corresponds to small crack widths that are expected to occur at serviceability and has been shown to be suitable for predicting the tension stiffening and crack width behaviour of ordinary concrete with steel reinforcement (Visintin et al. 2016; Visintin et al. 2018a).

Applying the linear ascending bond-slip relationship

The linear ascending bond slip relationship is given as

$$\tau(x) = k\delta(x) \tag{36}$$

where k is the stiffness of the local bond slip relationship

Substituting Eq. (36) into the governing equation Eq. (22), gives the second order differential equation

$$\frac{d^2\delta}{dx^2} = \beta k \delta(x) \tag{37}$$

Solving Eq. (37) the variation in slip along the prism length is

$$\delta(x) = c_1 \cosh(\lambda_1 x) + c_2 \sinh(\lambda_1 x) \tag{38}$$

where

$$\lambda_1 = \sqrt{\beta k} \tag{39}$$

Note that from Eqs. (25) and (26), in all cases $\delta = 0$ at x = 0, hence Eq. (38) simplifies to

$$\delta(x) = c_2 \sinh(\lambda_1 x) \tag{40}$$

Differentiating the distribution of slip given by Eq. 40 yields the slip strain

$$\frac{d\delta}{dx} = \lambda_1 c_2 \cosh(\lambda_1 x) \tag{41}$$

In Eqs. (40) and (41) the constant c_2 will now be solved through the application of the boundary conditions to give specific solutions.

Determination of the load slip relationship

Since the slip at the centre of the prism and the slip strain at the loaded end of the prism are the same for any stage of cracking, with the only difference being the length of the prism being considered, L_{def}, the equations below are applicable for any loading stage if the appropriate deformation length L_{def} considered. That is L_{def} should be taken as S_p for initial cracking and $S_p/2$ for primary cracking.

Constant of integration c_2

Applying the slip strain boundary condition (Eq. 24) at the loaded end to Eq. (41), yields the constant of integration

$$c_2 = \frac{1}{\lambda_1}\left(\frac{P_r}{E_r A_r} + \varepsilon_{sh} - \frac{f_i}{E_c} + \frac{m_i}{E_c}\Delta - \varepsilon_{inel}\right)\frac{1}{\cosh(\lambda_1 L_{def})} \tag{42}$$

Half width of crack Δ (w/2)

Substituting Eq. (42) into Eq. (40) and taking $\Delta = \delta$ at $x = L_{def}$, the half crack width can be expressed as a function of the force in the reinforcement

$$\Delta = \frac{\left(\frac{P_r}{E_r A_r} + \varepsilon_{sh} - \frac{f_i}{E_c} - \varepsilon_{inel}\right)}{\left(\frac{\lambda_1}{\tanh \lambda_1 L_{def}} - \frac{m_i}{E_c}\right)} \tag{43}$$

Prism elongation adjacent to crack (D_c)

To derive the concrete strain and therefore the concrete prism elongation, consider that the rate of change in the concrete strain is given by dividing Eq. (17) by the elastic modulus of concrete to yield

$$\frac{d\varepsilon_c}{dx} = -\frac{\tau(x) L_p}{E_c A_c} = -\frac{k L_{per}}{E_c A_c}\delta(x) \tag{44}$$

Integrating both sides with respect to x and considering that the strain in the concrete at the crack face is given by $\sigma_c(w)/E_c + \varepsilon_{inel}$ and $\sigma_c(w)$ is given by Eq. (3), the concrete strain is

$$\varepsilon_c(x) = \int \frac{d\varepsilon_c}{dx} dx = \frac{f_i - m_i \Delta}{E_c} + \frac{\left(\frac{\lambda_1}{\tanh \lambda_1 L_{def}}\Delta\right)}{\left(\frac{E_c A_c}{E_r A_r} + 1\right)}\left(1 - \frac{\cosh \lambda_1 x}{\cosh \lambda_1 L_{def}}\right) + \varepsilon_{inel} \tag{45}$$

Further integrating the concrete strain gives the concrete prism extension in Fig. 4

$$D_c = \int_0^{L_{def}} \varepsilon_{sh} dx = \frac{f_i - m_i \Delta}{E_c} L_{def} + \frac{\Delta}{\left(\frac{E_c A_c}{E_r A_r} + 1\right)}\left(\frac{\lambda_1 L_{def}}{\tanh \lambda_1 L_{def}} - 1\right) + \varepsilon_{inel} L_{def} \tag{46}$$

Note that since the force in the fibres is assumed to immediately transfer into the concrete prism this represents a conservative upper bound on the prism deformation. From Eq. (46) it can be seen that strain hardening concretes have considerably larger concrete deformations as a result of the final term ($\varepsilon_{inel} L_{def}$).

Crack opening stiffness (K_{PI}) and offset due to shrinkage and fibres (Δ_0)
Rearranging Eq. (43) as a function of the load in the reinforcing bar gives

$$P_r = K_{pi}(\Delta - \Delta_0) \tag{47}$$

Where the crack opening stiffness is

$$K_{PI} = E_r A_r \left(\frac{\lambda_1}{\tanh \lambda_1 L_{def}} - \frac{m_i}{E_c} \right) \tag{48}$$

And the offset due to shrinkage is given by

$$\Delta_0 = \frac{\left(\varepsilon_{sh} - \frac{f_i}{E_c} - \varepsilon_{inel} \right)}{\left(\frac{\lambda_1}{\tanh \lambda_1 L_{def}} - \frac{m_i}{E_c} \right)} \tag{49}$$

The load slip relationship with the indicating the stiffness and offset is illustrated in Fig. 5.

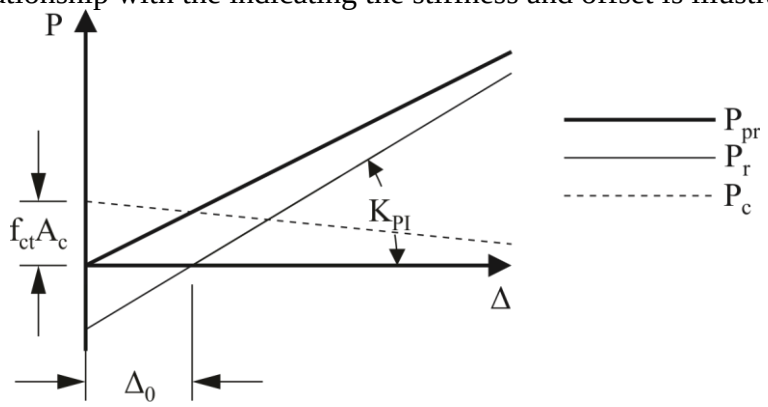

Fig. 5 Crack opening stiffness and slip due to shrinkage

Further, by considering that the average axial strain in the tension chord is given by Δ/L_{def}, then from Eq. (48) the effective flexural rigidity is $K_{pi}L_{def}$. From this definition of the effective flexural rigidity the effective modular ratio can then be defined as

$$n_{PI} = \frac{K_{PI} L_{def}}{E_c A_r} = \left(\frac{\lambda_1 L_{def}}{\tanh \lambda_1 L_{def}} - \frac{m_i}{E_c} L_{def} \right) n_{FI} \tag{50}$$

in which $n_{FI}=E_r/E_c$ is the conventional full interaction modular ratio. This is important for serviceability analysis since the increased stiffness due to tension stiffening can be allowed for simply by increasing the modular ratio.

Finally, the total load in the tension chord at the primary crack face considering the load carried by the reinforcement and the fibres is given by Eq. (51), this demonstrates the large increase in force carried in the tension chord due to the addition of fibres particularly for small deformations as indicated in Fig. 5.

$$P_{pr} = K_{PI}(\Delta - \Delta_0) + f_i A_c - m_i A_c \Delta \tag{51}$$

By expressing the reinforcement load slip behaviour in terms of an effective stiffness, K_{PI}, it can be seen from Eq. (48) that the crack opening stiffness is independent of the shrinkage strain, but it is dependent on the slope of the stress-crack width relationship of the fibres m_i. Eq. (48) demonstrates that fibres reduce the crack opening stiffness due to the reduced influence of the uncracked concrete between the cracks on the stiffness of the reinforcing bar.

The initial deformation due to shrinkage Δ_0 given by Eq. (49) is also reduced by the presence of fibres, this effect is even more pronounced for strain hardening concretes due to the inelastic strain term in the numerator. To further demonstrate the influence of fibres, in Fig. 6 a brief parametric study is presented with the parameters given in Table 1, to show the influence of the stress crack width parameter m. In this example it is shown that the influence of the slope

of the stress crack width behaviour of the concrete *m* is of minor importance when considering the offset due to shrinkage (Fig 6b), but of major importance when considering the crack opening stiffness (Fig 6a).

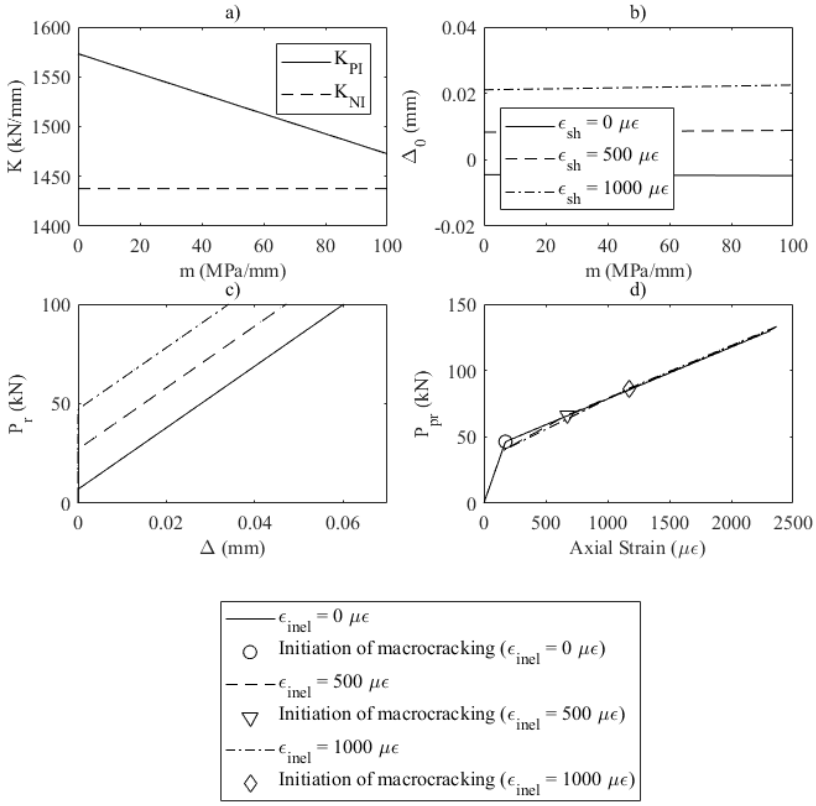

Fig. 6 Variation in: a) K_{PI} with *m*; b) Δ_0 with *m*; c) load-slip with strain hardening; d) load-elongation with strain hardening

Next consider the same prism with strain hardening and in which the shrinkage strain is zero. The influence of strain hardening can be considered by adjusting ε_{inel} since decreasing f_{SH} or E_{SH} increases the inelastic strain. In Eq. (35) it was shown that strain hardening does not affect the crack spacing, hence let us only consider the load slip behaviour.

In Fig. 6(c) the relationship is shown between the load in the reinforcement and the half crack width demonstrates that strain hardening concretes have smaller crack widths and that strain hardening delays the formation of macrocracks. Significantly, Fig. 6(d) also demonstrates that if the prism deformation is also taken into account there is minimal difference in overall elongation. This indicates that the strain hardening behaviour is desirable for controlling crack widths but otherwise does not have much effect on the tensile response.

Note that from Deluce (2011) and Visintin et al. (2018b), unreinforced FRC shows considerable variability in its tensile response, particularly in terms of the presence or absence of strain hardening and the length of the strain hardening plateau. Thus it has been shown that this variability has minimal effect on the load elongation behaviour, while causing extra variability in crack widths. This suggests that a simplification for FRC with variable strain hardening behaviour, is to analyse it as non-strain hardening, as this results in the correct crack spacing and load-elongation behaviour, while giving the maximum possible crack width.

This could help explain the observation of Deluce et al. (2013) that the variability in crack widths increases as the volume of fibres increases. That is, since increased fibre volumes are associated with strain hardening (Deluce 2011) and from Fig. 6(d) if portions of the section did have microcracks and other portions did not the local load slip relationship would vary. The ratio of maximum to average crack widths would increase, as the maximum crack width would occur in the non-strain hardening portion, while the crack widths would be reduced in the strain hardening portion, reducing the overall average crack width.

VALIDATION

In this section the expressions developed are compared to experimental tension stiffening results produced by Noghabai (2000), Jungwirth & Muttoni (2004), Oesterlee (2010), Deluce (2011) and Visintin et al. (2018b). The comparison of the elongation curves are in Fig. 7 and the details of each test are summarised in Table 2. Note that the application of the expressions derived in this paper to beam tests is beyond the scope of this work, but identical mechanics solved numerically have been successfully applied to beam tests in Visintin and Oehlers (2017).

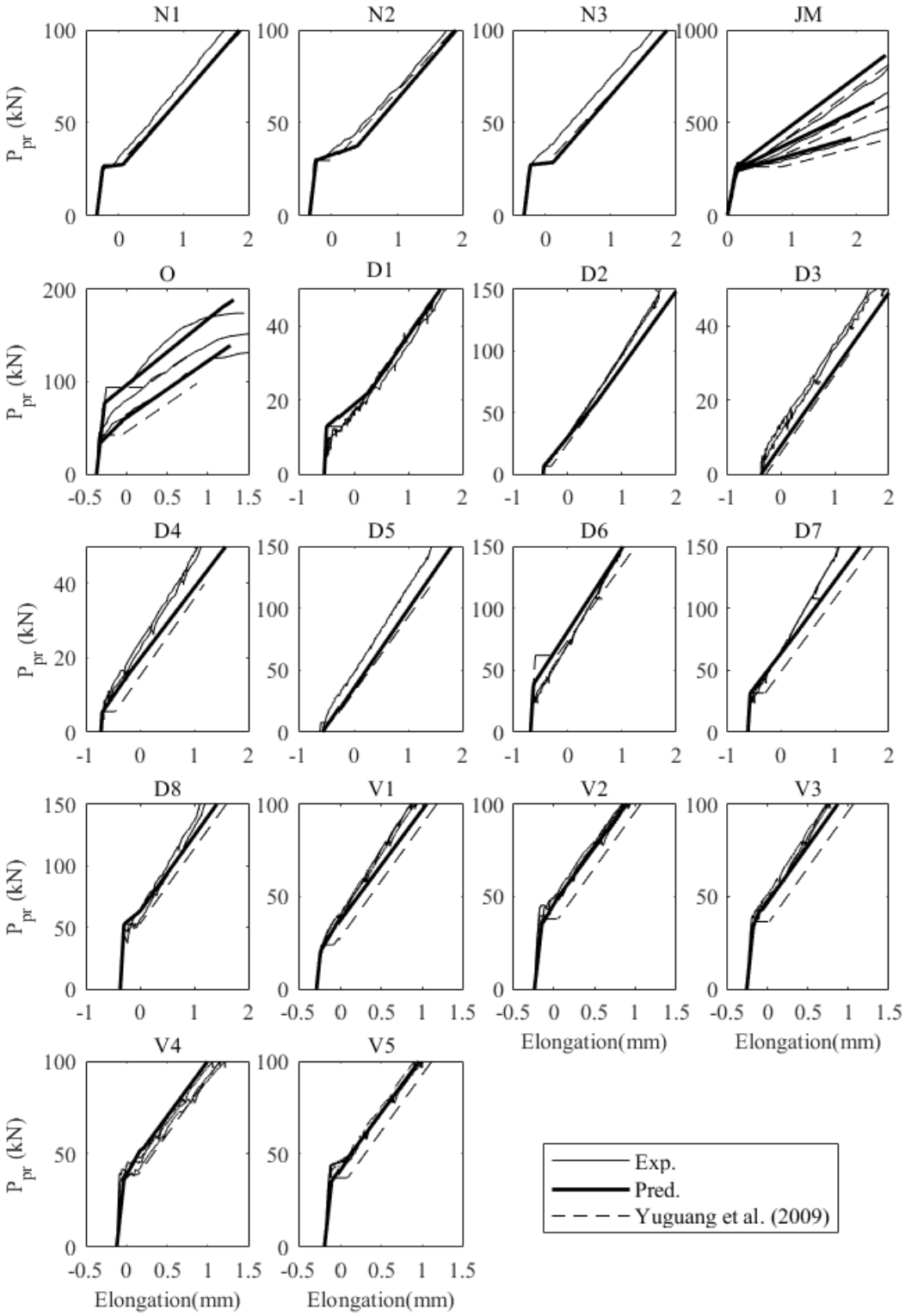

Fig. 7 Comparison of experimental to predicted load elongation curves

For Noghabai (2000) a value of 400 με was assumed based on recommendations by Eurocode 2 (CEN 1992) for high strength concrete. For Jungwirth & Muttoni (2004), the shrinkage was assumed to be zero, because the specimens were submerged in a water bath until testing. The bond properties for specimens with a compressive strength greater than 100 MPa were given by bond model developed for UHPFRC by Sturm & Visintin (2017) whereas for specimens with a lower strength, the model suggested by Harajli et al. (2002) was used instead.

In Fig. 7 note that for JM, three predicted curves are plotted on the same graph corresponding to the three bar diameters that were considered, that is 12, 16 and 20 mm. Oesterlee (2010) performed direct tension tests on both dogbone and sawn panel specimens, therefore the top predicted curve is obtained using the results of the dogbone tests, while the bottom predicted curve is obtained using the results of the sawn specimens.

From Fig. 7, it can be seen that the presented model is in general a good fit to the experimental results, whereas the model of Yuguang et al. (2009) tends to be a lower bound. In particular it should be noted that very close fits were obtained to the test results from Visintin et al. (2018b) and Oesterlee (2010). For Noghabai (2000) the presented solution represents a lower bound, though this may simply be a result of not having accurate shrinkage data for this test. For Jungwirth & Muttoni (2004) close fits are obtained for the smaller bar diameters, while the predicted value is an overestimate for the 20 mm bar diameter case, again this could be a result of the lack of shrinkage data. In the case of Deluce (2011), the fit is generally good but the presented solution represents a lower bound in a number of cases. A contributing factor to this could be the effect of the bond parameters, as Deluce (2011) did not perform any pull out tests whereas the pull out tests performed by Jungwirth & Muttoni (2004) and Oesterlee (2010) were included in the regression of the Sturm & Visintin (2017) bond model for UHPFRC.

In Fig. 8 the experimental crack width distribution is compared to the predicted maximum crack width. The model is shown to accurately predict the maximum crack width, particularly for V2 to V5.

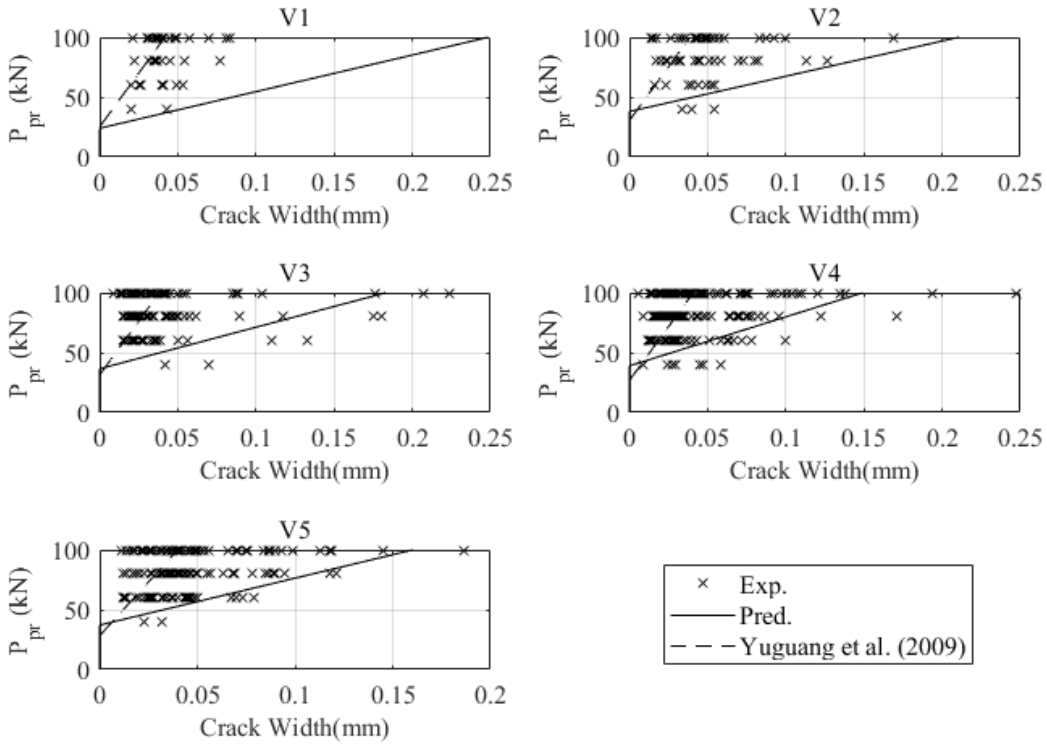

Fig. 8 Comparison of measured crack widths to predicted maximum crack width for Visintin et al. (2018b)

From this validation the applicability of the presented expressions has now been demonstrated over a wide range of different FRCs, ranging from normal strength FRC to very high strength UHPFRC.

CONCLUSION

Tension stiffening is a fundamental concrete behaviour with a major effect on deflections and crack widths under service loads. Fibres, due to the restraint of flexural cracks, give designers a powerful tool to improve the serviceability behaviour of concrete structures. To profit from this improved behaviour, designers require analysis methods that can quantify this improvement.

In this paper a model for tension stiffening was built up from the unreinforced behaviour of FRC, to the uncracked behaviour of reinforced FRC and finally partial interaction mechanics were used to simulate the bond-slip behaviour of the concrete- reinforcing bar interface. This allows the characterisation of the tensile behaviour of cracked reinforced FRC. With the correct governing equation and boundary conditions obtained, closed form solutions were found.

First the CEB-FIP non-linear bond slip relationship was used to quantify the crack spacing. Due to the complexity of the solutions obtained for the load slip relationship, as an alternative a simplified linear ascending bond slip relationship was assumed, to obtain the load slip behaviour. From the derived load slip behaviour, it has been shown that the fibres reduce the stiffness of the reinforcement contribution to the load slip relationship but they also restrain the offset in deformations due to long term effects. The fibres at the crack face greatly increases the force carried in the tension chord.

Using these results an effective modular ratio was defined that takes into account the change in stiffness due to partial interaction, which is particularly useful for inclusion in serviceability analyses. This importantly would remove the need to perform extensive numbers of beam tests to calibrate an effective moment of inertia to determine the deflection behaviour of an FRC beam.

The phenomenon of strain hardening was explored in FRC and it was shown from a parametric study that while the crack spacing and load elongation behaviour is unaffected, crack widths however are reduced.

Finally, experimental results are used to validate the model. Importantly the expressions were validated on the broad range of FRC from normal strength to very high strength UHPFRC. With the validity established these tension stiffening expressions can be incorporated into a serviceability analysis.

ACKNOWLEDGEMENTS

This material is based upon work supported by the Air Force Office of Scientific Research under award number FA2386-16-1-4098.

NOTATION

A_c, A_r = cross-sectional area of concrete and reinforcement, respectively;
c_1, c_2 = constants of integration;
D_r,D_c = axial deformation of concrete and reinforcement, respectively;
d_b = diameter of bar;
E_r, E_c = elastic modulus of concrete and reinforcement, respectively;
E_{SH} = strain hardening modulus of concrete;

f_c = compressive strength of concrete;
f_{ct} = tensile strength of concrete;
f_i = y-intercept of the stress-crack width; the index *i* indicates the piecewise linear component of the stress-crack width being considered;
f_{pc} = post cracking strength of concrete;
f_{SH} = stress to initiate microcracking; stress to induce strain hardening;
K_{PI}, K_{NI} = stiffness of load slip relationship considering partial and no interaction, respectively;
k = stiffness of bond slip relationship;
L_{def} =deformable length;
L_{per} = bonded length of reinforcing bar;
m_i = slope of stress-crack width relationship; the index *i* indicates the piecewise linear component of the stress-crack width being considered;
n_{PI}, n_{FI} = partial interaction modular ratio; full interaction modular ratio
P,P_c, P_r = force; force in the concrete and reinforcement, respectively;
P_{pr} = total force in tension chord
$P_{pr\text{-}cr}$ = force to crack tension chord
S_p = primary crack spacing;
u_c, u_r = axial deformation of concrete and reinforcement, respectively;
V_f = fibre volume;
x = horizontal position along prism;
w = crack width;
α = non-linearity of bond stress- slip relationship
β = axial rigidity parameter;
Δ = half crack width; slip at end of bar;
Δ_0 = offset in the load slip relationship due to shrinkage and fibres
δ = interface slip;
δ_1 = interface slip at peak bond stress
δ' = slip strain; $d\delta/dx$;
ε_c, ε_r = strain in the concrete and reinforcement, respectively; note that ε_c includes the elastic and creep components (as these strains develop stresses in the concrete) and excludes the shrinkage component (as this component does not);
ε_{inel} = inelastic strain associated with microcracking
ε_{sh} = shrinkage strain;
$\varepsilon_{sh\text{-}cr}$ = shrinkage strain to crack tension chord if no load is applied;
λ_1, λ_2 = bond parameter; bond parameter for linear ascending and CEB-FIP bond slip relationships, respectively;
σ_c, σ_r = stress in the concrete and reinforcement, respectively;
σ_f = the quantity of stress carried by the fibres at a given cross-section;
τ = interface shear stress; bond stress;
τ_{max} = maximum bond strength; local property;

REFERENCES

Amin, A., Foster, S. J., and Watts, M. (2015). "Modelling the tension stiffening effect in SFR-RC." *Magazine of Concrete Research*, 68(7), 339-352.

Balazs, G. L. (1993). "Cracking analysis based on slip and bond stresses." *ACI Materials Journal*, 90(4), 340-348.

Barragán, B. E. (2002). “Failure and toughness of steel fiber reinforced concrete under tension and shear.” Ph.D. Thesis, Universitat Politècnica de Catalunya.

Bazant, Z. P. (1972). “Prediction of concrete creep effects using age-adjusted effective modulus method”, *ACI Journal,* 69(4), 212-217.

Bischoff, P. H. (2001). “Effects of shrinkage on tension stiffening and cracking in reinforced concrete”. *Canadian Journal of Civil Engineering,* 28(3), 363-374.

Bischoff, P. H. (2003). “Tension stiffening and cracking of steel fiber-reinforced concrete.” *Journal of Materials in Civil Engineering.,* 15(2), 174-182.

CEB-FIP (Euro-International Committee for Concrete/International Federation for Pre-stressing). (1993). “CEB-FIP Model Code 1990: Design Code.” CEB-FIP, London.

CEN (European Committee for Standardization). (1992). “Design of concrete structures - Part 1-1: General rules and rules for buildings.” *Eurocode 2,* Brussels.

Choi, C. K. and Cheung, S. H. (1996). “Tension stiffening model for planar reinforced concrete members”, *Computers & Structures,* 59(1), 179–190.

Deluce, J. R. (2011). “Cracking behaviour of steel fibre reinforced concrete containing conventional steel reinforcement.” Master’s Thesis, University of Toronto.

Deluce, J. R., Lee, S. C., and Vecchio, F. J. (2014). “Crack model for steel fiber-reinforced concrete members containing conventional reinforcement.” *ACI Structural Journal,* 111(1), 93.

Dilger, W. and Neville, A. M. (1971). “Method of creep analysis of structural members.” *ACI Special Publication,* 27, 349-379.

fib (International Federation for Structural Concrete). (2013). *CEB-FIP Model Code 2010,* Lausanne.

Grünewald, S. (2004). “Performance-based design of self-compacting fibre reinforced concrete.” PhD Thesis, Delft University of Technology.

Gupta, A. K. and Maestrini, S. R. (1990). “Tension stiffening model for reinforced concrete bars”, *Journal of Structural Engineering,* 116(3), 769–790.

Harajli, M., Hamad, B., & Karam, K. (2002). “Bond-slip response of reinforcing bars embedded in plain and fiber concrete.” *Journal of Material in Civil Engineering,* 14(6), 503-511.

Jungwirth, J., and Muttoni, A. (2004). “Structural behavior of tension members in Ultra High Performance Concrete.” *Proc., International Symposium on Ultra High Performance Concrete.* Kassell, 533-544.

Kooiman, A.G. (2000). “Modelling steel fibre reinforced concrete for structural design.” Ph.D. thesis, Delft University of Technology.

Lee, G. G and Foster, S. J. (2007). “Behaviour of Steel Fibre Reinforced Mortar in Shear III: Variable Engagement Model II.” *UNICIV Report No. R-448*, University of New South Wales.

Lee, S. C., Cho, J. Y., and Vecchio, F. J. (2011a). “Diverse embedment model for steel fiber-reinforced concrete in tension: model development”. *ACI Materials Journal*, 108(5), 516-525.

Lee, S. C., Cho, J. Y., and Vecchio, F. J. (2011b). “Diverse embedment model for steel fiber-reinforced concrete in tension: Model verification”. *ACI Materials Journal*, 108(5), 526-535.

Lee, S. C., Cho, J. Y., and Vecchio, F. J. (2013). :Tension-stiffening model for steel fiber-reinforced concrete containing conventional reinforcement”. *ACI Structural Journal*, 110(4), 639.

Leutbecher, T., and Fehling, E. (2012). “Tensile behavior of ultra-high-performance concrete reinforced with reinforcing bars and fibers: minimizing fiber content”. *ACI Structural Journal*, 109(2), 253-263.

Li, V. C., Stang, H., and Krenchel, H. (1993). “Micromechanics of crack bridging in fibre-reinforced concrete.” *Materials and Structures*, 26(8), 486-494.

Löfgren, I., Stang, H., Olesen, J. F. (2004). “Wedge splitting test – A test to determine fracture properties of FRC”, *Proc,. Sixth RILEM Symposium on Fibre-Reinforced Concretes (FRC) - BEFIB 2004*, RILEM, Varenna, 379-388.

Maeder, U., Lallemant-Gamboa, I., Chaignon, J., and Lombard, J.P. (2004). “Ceracem, a new high performance concrete: characterisations and applications.” *Proc., International Symposium on Ultra High Performance Concrete.* Kassell, 59-68.

Meda, A., Plizzari, G. A., Sorelli, L. (2004). “Uni-axial and bending test for the determination of fracture properties of fiber reinforced concrete.” *Proc. Fifth International Conference on Fracture Mechanics of Concrete and Concrete Structures*, Vail, 1163-1170.

Muhamad, R., Mohamed Ali, M. S., Oehlers, D. J., and Griffith, M. C. (2012). “The tension stiffening mechanism in reinforced concrete prisms.” *Advances in Structural Engineering*, 15(12), 2053-2069.

Naaman, A. E. (2007). “Tensile strain-hardening FRC composites: Historical evolution since the 1960.” *Advances in Construction Materials*, 2007, 181-202.

Neville, A.M., Dilger, W.H. and Brooks, J.J. (1983). *Creep of Plain and Structural Concrete*, Construction Press, London.

Noghabai, K. (2000). “Behavior of tie elements of plain and fibrous concrete and varying cross sections.” *ACI Structural Journal*, 97(2), 277-284.

Oesterlee, C. (2010). “Structural response of reinforced UHPFRC and RC composite members.” Ph.D. Thesis, Ecole Polytechnique Federale de Lausanne.

Ouyang, C., Pacios, A., and Shah, S. P. (1994). “Pullout of inclined fibers from cementitious matrix.” *Journal of Engineering Mechanics.*, 120(12), 2641-2659.

Pereira, E.N.B., Barros, J.A.O.; Ribeiro, A.F.; Camões, A. (2004). “Post-cracking behaviour of self-compacting steel fibre reinforced concrete” *Proc. Sixth RILEM Symposium on Fibre Reinforced Concretes (FRC) - BEFIB 2004*, Varenna.

Schumacher, P. (2006) “Rotation Capacity of Self-Compacting Steel Fibre Reinforced Concrete.” Ph.D. Thesis, Delft University of Technology.

Sorelli, L. (2003). “Some studies on the assessment of the fracture toughness of fiber reinforced concrete with an emphasis on hybrid fiber systems.” Ph.D. Thesis, University of Brescia.

Stang, H., and Aare, T. (1992) "Evaluation of crack width in FRC with conventional reinforcement." *Cement and Concrete Composites* 14(2), 143-154.

Sturm A. B., Visintin P. and Oehlers D. J. (2018) “Time-dependent serviceability behavior of reinforced concrete beams: Partial interaction tension stiffening mechanics.” *Structural Concrete,* 19(2), 508-523.

Sturm, A. B. and Visintin, P. (2019) “Local bond slip behaviour of steel reinforcing bars embedded in UHPFRC.” *Structural Concrete,* 20(1), 108-122.

Tjiptobroto, P., and Hansen, W. (1993). “Tensile strain hardening and multiple cracking in high-performance cement-based composites containing discontinuous fibers.” *ACI Materials Journal*, 90(1), 16-25.

Visintin, P., Oehlers, D. J. and Haskett, M. (2013) “Partial-interaction time dependent behaviour of reinforced concrete beams” *Engineering Structures*, 49, 408-420

Visintin, P., Oehlers, D. J. and Sturm, A. B., (2016). “Mechanics Solutions for Deflections and Cracking in Concrete”, *Proceedings of the Institute of Civil Engineers Structures and Buildings*, 169(12), 912-924;

Visintin, P., Oehlers, D. J. (2017) “Fundamental mechanics that govern the flexural behaviour of RC beams with fibre reinforced concrete” *Advances in Structural Engineering*, 21(7), 1088-1102.

Visintin P, Sturm A. B. and Oehlers D. J. (2018a) “Long- and short-term serviceability behavior of reinforced concrete beams: Mechanics models for deflections and crack widths.” *Structural Concrete,* 19(2), 489-507.

Visintin, P., Sturm, A. B., Mohamed Ali, M. S. and Oehlers, D. J. (2018b) "Blending macro and micro fibres to enhance the serviceability behaviour of UHPFRC.” *Australian Journal of Civil Engineering*, 16(2), 106-121.

Wille, K., El-Tawil, S. and Naaman, A. E. (2014). “Properties of strain hardening ultra high performance fiber reinforced concrete (UHP-FRC) under direct tensile loading.” *Cement and Concrete Composites,* 48, 53-66.

Wu, Z., Yoshikawa, H. and Tanabe, T. (1991). “Tension stiffness model for cracked reinforced concrete.” *Journal of Structural Engineering*, 117(3), 715–732.

Yuguang, Y., Walraven, J. C., and Uijl, J. A. (2009). “Combined effect of fibers and steel rebars in high performance concrete.” *Heron*, 54(2–3). 205–224.

Zhang, T., Visintin, P. and Oehlers, D. J., (2017). “Partial-interaction tension-stiffening properties for numerical simulations.” *Advances in Structural Engineering*, 20(5), 812-821.

STATEMENT OF AUTHORSHIP

A rational design approach for the instantaneous and time dependent serviceability deflections and crack widths of FRC and UHPFRC continuous and simply supported beams
Journal of Structural Engineering, 145(11), 04019138.

Sturm, A.B. (Candidate)

Prepared manuscript, performed all analyses, and developed model and theory (80%)

This paper reports on original research I conducted during the period of my Higher Degree by Research candidature and is not subject to any obligations or contractual agreements with a third party that would constrain its inclusion in this thesis. I am the primary author of this paper.

Signed ..... Date 9/07/2020

Visintin, P.

Supervised and contributed to research, and acted as corresponding author (10%)

I certify that the candidate's stated contribution to the publication is accurate (as detailed above); permission is granted for the candidate in include the publication in the thesis; and the sum of all co-author contributions is equal to 100% less the candidate's stated contribution.

Signed ..... Date 07/07/2020

Oehlers, D.J.

Supervised and contributed to research (10%)

I certify that the candidate's stated contribution to the publication is accurate (as detailed above); permission is granted for the candidate in include the publication in the thesis; and the sum of all co-author contributions is equal to 100% less the candidate's stated contribution.

Signed ..... Date 7/7/20

A RATIONAL DESIGN APPROACH FOR THE INSTANTANEOUS AND TIME DEPENDENT SERVICEABILITY DEFLECTIONS AND CRACK WIDTHS OF FRC AND UHPFRC CONTINUOUS AND SIMPLY SUPPORTED BEAMS

Sturm, A.B., Visintin, P. and Oehlers, D.J

ABSTRACT

Novel mechanics based closed form solutions for the long- and short-term serviceability deflections and crack widths of fibre reinforced concrete (FRC) and ultra-high performance fibre reinforced concrete (UHPFRC) beams are presented. These solutions incorporate the bond properties from bond tests directly and as such obviate the need for a constant bond stress simplification and consequently the need for member calibration as is commonly required in code approaches. The closed form solutions are validated on 12 simply supported and 4 continuous UHPFRC beams as well as 10 normal strength FRC beams with good correlation. A design example is also included for a UHPFRC T-beam demonstrating the application of the solutions.

INTRODUCTION

Excessive deflections and crack widths under service loads have a significant negative impact on the long-term functionality, aesthetics and durability of reinforced concrete structures (Gilbert & Ranzi 2010; Standards Australia 2014). The addition of discontinuous fibres to either normal strength concrete to create fibre reinforced concrete (FRC) or to high strength mortars to create ultra-high performance fibre reinforced concrete (UHPFRC) has the potential to reduce the deflections and crack widths by allowing the transfer of stresses across flexural cracks (Stang & Aare 1992; Schumacher 2006).

The design of FRC materials is complicated by the variety of metallic and non-metallic fibres of different shapes and sizes that are now commonly available. Further, these fibres can be used at varying volumes (Brandt 2008) and in concretes of widely varying mix design ranging from normal strength mixes with coarse aggregates (Schumacher 2006) to very high strength mixes without coarse aggregates (Graybeal 2006; Oesterlee 2010; Sobuz et al. 2016). Design is made even more complicated due to the option to blend fibres (Park et al. 2012; Banthia et al. 2014; Fantilli et al. 2018; Visintin et al. 2018a; Sturm et al. 2020). Hence, to be able to efficiently characterise the service deflections and crack widths of members with these materials, generic analysis techniques are required which can be related directly to the results of basic material tests without the need for member calibration.

In this paper, it is shown how a rational design approach for predicting instantaneous and time dependent deflections of FRC and UHPFRC materials can be developed based on fundamental partial interaction mechanics. Significantly, the proposed expressions are not based on experimental calibration, but rather on the direct application of material properties which are easily obtainable from simple, low cost experiments.

In the following, a literature review of current serviceability analysis approaches is first presented. This is followed by a description of the segmental approach (Visintin & Oehlers 2017; Sturm et al. 2020) upon which the design procedure is based. It is then shown how the segmental approach can be used as the basis for developing a simplified design approach for quantifying the instantaneous and time dependent deflections and crack widths of simply supported and continuous FRC and UHPFRC beams. The approach is then validated against 26 existing test results covering a range of material properties. Finally, in the supplementary

material, a realistic worked example is presented to determine the serviceability behaviour of a continuous T-beam.

REVIEW OF EXISTING ANALYSIS AND DESIGN APPROACHES

Existing serviceability analysis and design approaches for UHPFRC and FRC members are largely based on modifications of traditional sectional moment-curvature analyses that are solved either numerically (Barros & Figueiras 1999) or analytically (Taheri et al. 2011; Mobasher et al. 2015). Approaches suggested by national codes of practice such as the fib Model Code 2010 (fib 2013) for normal strength FRC and the AFGC (AFGC 2013) for the design of UHPFRC are also moment-curvature based approaches. Approaches based on computing a flexural rigidity have been suggested by Amin et al. (2017) and AS3600-2018 (Standards Australia 2018). Approaches based on the rotation of a segment rather than the curvature of a cross section have also been suggested by Barros et al. (2015) and Visintin & Oehlers (2018), in their current form they are however more suited for numerical implementation.

As the focus of this paper is on design, the following review focuses on the critical points of analytical models as well as those proposed in the design standards rather than on more complex numerical models.

When considering the contribution of fibres post cracking, a number of existing approaches (Mobasher et al. 2015; Amin et al. 2017; Standards Australia 2018) assume a constant post cracking stress. Although leading to relatively simple analytical solutions, the limitation of this assumption is that it is known that the tensile stress resisted by fibres reduces with continued crack opening (Wille et al. 2014). Hence calibration is required to determine the most appropriate magnitude for the constant post cracking stress based on the expected crack width. To improve the versatility of the solution, in this paper a piecewise linear stress crack width relationship is considered.

In the fib Model Code 2010 (fib 2013) and the AFGC recommendations (AFGC 2013). The tensile stress/crack width relationship is converted into a stress strain relationship by dividing by a characteristic length. In AFGC (2013) this is taken as 2/3 the depth of the section, while in fib (2013) the characteristic length is taken as a function of the crack spacing. The approach taken in the fib Model Code (2010) is followed in this paper as it considers the mechanical relationship between crack widths, crack spacings and deformation in the tensile zone of the beam.

When considering the impact of fibres on tension stiffening behaviour, existing approaches have been found either to not consider the effect of tension stiffening (Taheri et al. (2011), Mobasher et al. (2015), AS3600-2018 (Standards Australia 2018)), or to consider tension stiffening as a constant decrease in curvature (Amin et al. 2017). In Amin et al. (2017) the magnitude of tension stiffening is derived based on the assumption of a constant bond stress between the reinforcement and surrounding concrete. Experimentally it is observed that the bond stress increases with slip (Harajli et al. 1995) and hence this assumption requires calibration based on the expected slip of the reinforcing bar.

In AFGC (2013), tension stiffening is allowed for by multiplying the curvature by the ratio of the reinforcement strain at the crack and the mean reinforcement strain along the tension chord. The mean reinforcement strain is calculated using the expression of the mean difference in

strains between the concrete and the reinforcement in the crack width expression and includes a bond factor which needs to be calibrated for new combinations of materials.

A number of other tension stiffening models are available in the literature which could be used in conjunction with flexural models to predict the tension stiffening effect. For example the widely applied bond factor approach of Bischoff (2003) has been extended to FRC, but as with the model proposed by AFGC (2013) calibration is required for new materials. Models based on the assumption of constant bond stress have also been suggested by Yuguang et al. (2009).

In contrast to these design oriented models, Lee et al. (2012) has suggested a fully non-linear tension stiffening model in which a non-linear bond slip relationship is considered between the reinforcement and the concrete as well as the pull out of each individual fibre. Although this model fully captures the mechanics of tension stiffening, in the context of the work proposed here it is considered too complex for application in a closed form analytical solution.

Hence, in this paper the tension stiffening model proposed by Sturm et al. (2018) will be adopted to compute crack spacing and the response of the tensile reinforcement as it avoids the need for calibration by considering a realistic non-constant tensile stress/crack width response of the tensile concrete and bond stress-slip behaviour of the interface, while still resulting in closed-form solutions. In Sturm et al. (2018), this model has been validated against 18 tension stiffening specimens ranging from normal strength to ultra-high performance FRC. The model demonstrated good fit to both the experimentally observed load-deflection and load-crack width behaviour. This model also allows for the effect of shrinkage to be considered by offsetting the strains between the concrete and reinforcement. The age-adjusted effective modulus method can be used with this model to allow for the creep effects (Gilbert & Ranzi 2010).

Considering the methodologies adopted to determine the neutral axis depth, the majority of approaches suggest either an iterative approach or require the solution of a higher order higher-order polynomial (fib 2013; AFGC 2013; Amin et al. 2017; Standards Australia 2018) which can be done numerically. Alternatively, Taheri et al. (2011) and Mobasher et al. (2015) do not require iteration to solve for the neutral axis depth but the expressions presented are complex. To apply the solution technique of Taheri et al. (2011) the moment and curvature need to be evaluated over a range of tensile strains to obtain a smooth curve, and hence the approach is not suited to design by hand calculation. Mobasher et al. (2015) does provide a simplified bilinear moment curvature relationship defined using the moment and curvature at yield and then at ultimate. However, this is seen to be more suitable for analysis at the ultimate limit state, because assuming that the flexural rigidity at serviceability is given by the secant stiffness through the yield point appears to be overly conservative. Hence in this paper the moment and curvature will be solved for in terms of the bottom fibre strain removing the need to iterate for the neutral axis depth. Also to remove the need to evaluate the moment and curvature for a large number of these points a simplified bilinear moment-curvature relationship is developed.

In terms of crack widths, fib (2013), AFGC (2013) and AS3600-2018 (Standards Australia 2018) all provide relationships in terms of a crack spacing multiplied by a mean difference in strains between the concrete and the reinforcement. However, all the expressions are dependent on the definition of semi-empirical factors. Amin & Gilbert (2018) have also suggested an approach for finding the crack width based on the tension stiffening model in Amin et al. (2017) which is based on the assumption of a constant bond. Other approaches have been suggested by Barros et al. (2018), Fantilli & Chiaia (2018) and Visintin & Oehlers (2018) however these

approaches are not suitable for hand calculations. In this paper a crack width model is proposed that is based on the tension stiffening model in Sturm et al. (2018) which uses realistic non-constant bond-slip and tensile stress/crack width relationships.

Another important factor for the deflection and cracking behaviour is the influence of time effects. In fib (2013) and AFGC (2013) shrinkage is allowed for by evaluating a shrinkage curvature and creep is considered using an age adjusted effective modulus. In AS600-2018 (Standards Australia 2018) time effects are allowed for by multiplying by a factor which is a function of the quantity of compressive reinforcement. In this paper shrinkage is allowed for directly by considering an offset in strains between the reinforcement and the concrete and the effect of creep is allowed for using an age-effected age adjusted modulus (Gilbert & Ranzi 2010).

FRC and UHPFRC COMPONENTS OF RC BEAM

Having reviewed existing approaches and identified the desired features for the new approach, consider the response of the components that comprise the RC beam in Fig. 1(a).

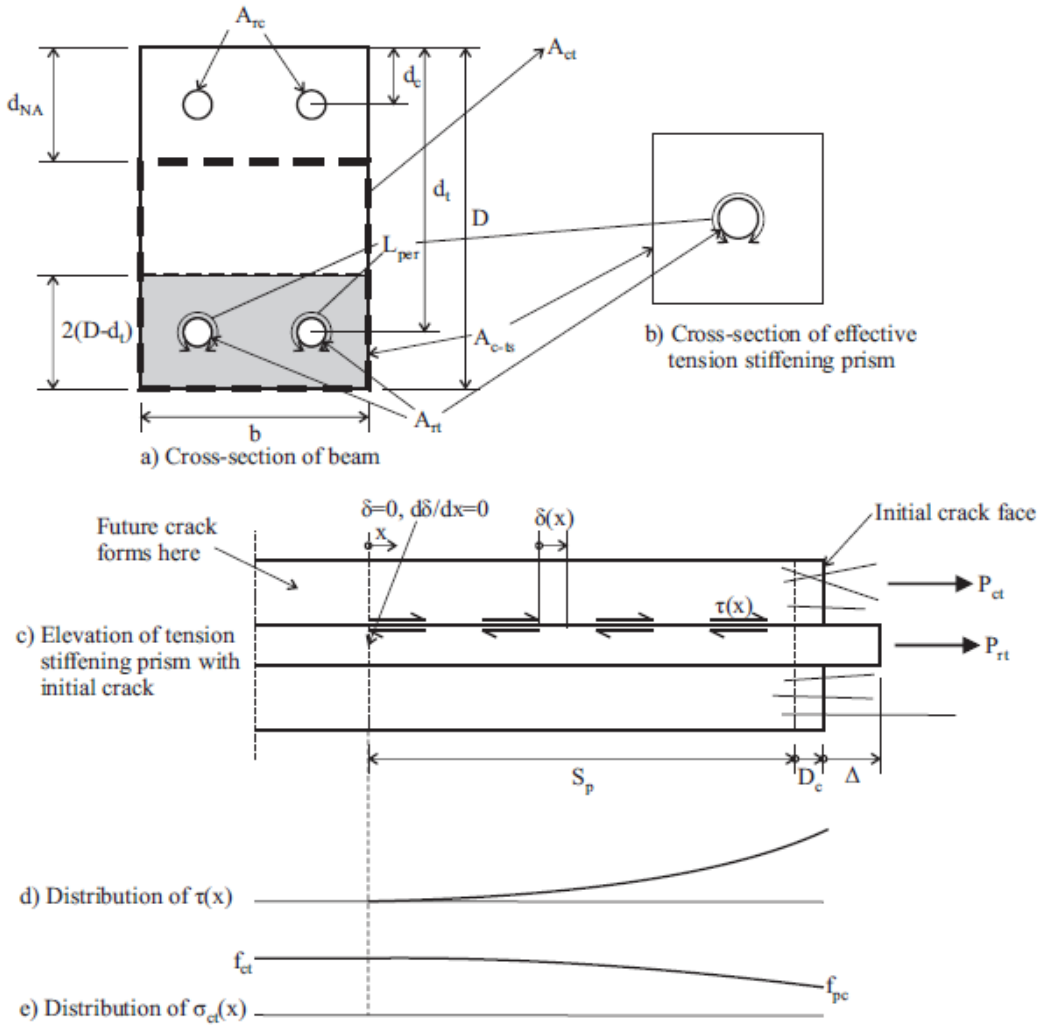

Fig. 1 Tension stiffening prism with an initial crack

Concrete in Tension

Wille et al. (2014) have suggested that the tensile response of UHPFRC can be divided into: (i) a strain based 'linear elastic' portion in the stress/strain relationship in Fig. 2(a); (ii) a strain

based ‘strain hardening’ portion; and (iii) a crack opening based ‘softening’ portion in the stress/crack-width relationship in Fig. 2(b). During the first linear elastic phase in Fig. 2(a), the concrete is uncracked. During the strain hardening phase, microcracks are distributed throughout the volume. Finally, during the softening phase in Fig. 2(b), the deformation localises at a singular macrocrack.

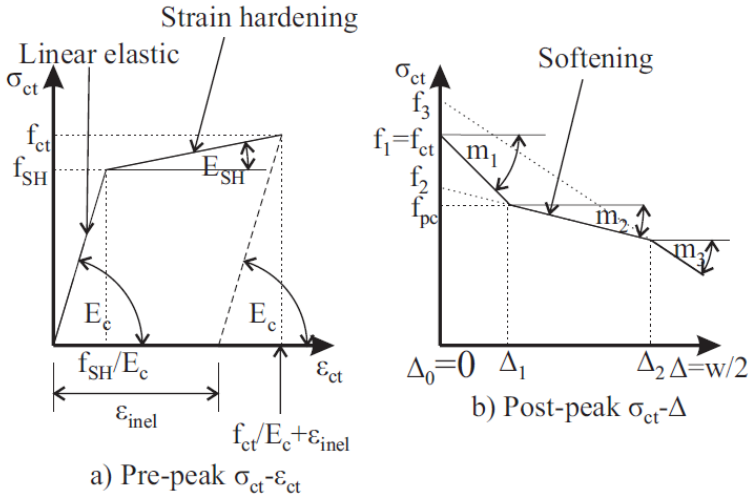

Fig. 2 Tension stress response of FRC

The stress in the concrete σ_{ct} in Fig. 2 can be represented analytically as a piecewise linear function of the strain ε_{ct} and half crack width Δ as:

$$\sigma_{ct} = E_c\varepsilon_{ct}; \varepsilon_{ct} \leq \frac{f_{SH}}{E_c} \tag{1a}$$

$$\sigma_{ct} = f_{SH} + E_{SH}\left(\varepsilon_{ct} - \frac{f_{SH}}{E_c}\right); \frac{f_{SH}}{E_c} < \varepsilon_{ct} < \frac{f_{ct}}{E_c} + \varepsilon_{inel} \tag{1b}$$

$$\sigma_{ct} = f_i - m_i\Delta; \Delta_{i-1} < \Delta < \Delta_i \; for \; i = 1, \dots, n \tag{1c}$$

where in Fig. 2(a), E_c is the elastic modulus of the concrete, f_{SH} is the stress to cause microcracks, E_{SH} is the hardening modulus, f_{ct} is the tensile strength and ε_{inel} is the permanent strain due to microcracking. In Fig. 2(b), the stress f_i, where the subscript i is an integer, is the intercept with the stress axis, m_i is the slope and Δ_i is the right hand limit of the i^{th} component of the stress/half-crack-width relationship. The parameters in Eq. (1) can be obtained by fitted to the tensile response obtained from either a direct tension test or via inverse analysis of a flexural prism test.

It is also worth noting here that the post macrocracking response given by Eq. (1c) is represented as a stress/crack width relationship, and this can be rewritten here in terms of the half crack width by dividing the abscissa by 2. This approach is taken for convenience as it will be shown in the following that analysis can be conducted on a segment of half the crack spacing due to the presence of symmetry.

Having defined the stress-deformation relationship of the tensile concrete in Eq. (1), the axial force in the tensile concrete can be determined by integration as follows

$$P_{ct} = \int_{d_{NA}}^{D-d_{NA}} \sigma_{ct} dA = \sigma_{ct-ave} A_{ct} \tag{2}$$

where, in Fig. 1(a) A_{ct} is the area of concrete in tension and in a rectangular member this is $b(D\text{-}d_{NA})$. Further, the average stress in the tensile concrete $\sigma_{ct\text{-}ave}$ in Eq. (2) can be approximated as a function of the strain at the bottom fibre ε_D in Fig. 3 by simply dividing the area under the stress/strain curve by the strain at the bottom fibre ε_D.as follows:

$$\sigma_{ct-ave} \approx \frac{\int_0^{\varepsilon_D} \sigma_{ct}\, d\varepsilon}{\varepsilon_D} \tag{3}$$

and which is exact if the area of tensile concrete has a constant width *b*.

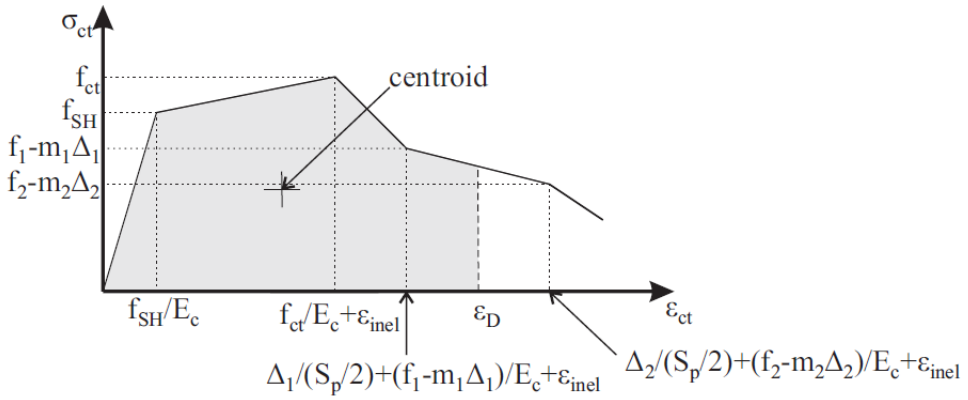

Fig. 3 Effective stress/strain relationship for the tensile concrete

To determine the average tensile stress for a section with macrocracks, the post-peak-stress/crack-width relationship needs to be converted to an equivalent stress/strain relationship. This is determined by considering that the elongation between two points is given by the strain in the material multiplied by the distance between the two points plus the opening of any fractures between the two points (Hillerborg 1978). Hence, the effective strain at a given depth is given by this elongation divided by the gauge length. The effective strain within the cracked region is therefore given by

$$\varepsilon_{ct} = \frac{\Delta}{\left(\frac{S_p}{2}\right)} + \frac{\sigma_{ct}}{E_c} + \varepsilon_{inel} \tag{4}$$

where $\Delta/(S_p/2)$ is the contribution due to crack opening, σ_{ct}/E_c is the component due to the elastic deformation of the concrete between the cracks, and ε_{inel} is the component due to microcracking.

As a simplification to reduce the number of parameters that need to be defined, in this model it is assumed that the loading and unloading stiffnesses for the uncracked concrete are the same, even if the material is strain hardening. At this stage, this assumption is justified on two bases, firstly very little experimental work exists in which the unloading stiffness has been reported and secondly, Wille et al. (2014) has observed experimentally that for strain hardening FRCs the unloading stiffness is softer than the loading stiffness. Hence when determining the stress/crack width relationship by subtracting the elastic deformation from the total measured deformation between two points crossing a crack the assumption of an overly stiff unloading modulus results in a smaller predicted crack width, but as the predicted elastic deformation is greater the overall elongation is conserved.

Applying the above transformation to the stress/crack width relationship in Fig. 2(b) yields the stress/strain relationship in Fig. 3 where the lever arm of the tensile concrete l_{ct}, calculated with respect to the neutral axis is

$$l_{ct} = \frac{\int \sigma_{ct}(y - d_{NA})\, b \cdot dy}{\int_{d_{NA}}^{D-d_{NA}} \sigma_{ct} b \cdot dy} = \eta(D - d_{NA}) \tag{5}$$

In Eq. (5) η is the ratio of the distance of the centroid of the stress distribution from the neutral axis divided by the depth of the concrete in tension and is

$$\eta = \frac{\left(\frac{\int_0^{\varepsilon_D} \sigma_{ct}\ \varepsilon\ d\varepsilon}{\int_0^{\varepsilon_D} \sigma_{ct}\ d\varepsilon}\right)}{\varepsilon_D} = \frac{\int_0^{\varepsilon_D} \sigma_{ct}\ \varepsilon\ d\varepsilon}{\varepsilon_D^2 \sigma_{ct-ave}} \quad (6)$$

which is exact if the area of tension concrete has a constant width. That is, Eq. (6) is the centroid of the area under the stress/strain curve, illustrated in Fig. 3, divided by the strain at the bottom fibre ε_D.

Concrete in Compression

Under serviceability loading, the concrete acting in compression is assumed to be linear elastic as defined by the elastic modulus E_c. Hence for a rectangular compressive section in Fig. 1(a), the axial force in the compressive concrete is

$$P_{cc} = \int_0^{d_{NA}} \sigma_{cc}\, dA = \frac{1}{2} b d_{NA}^2 E_c \chi \quad (7)$$

and the location of the compressive concrete lever arm with respect to the neutral axis is 2/3 d_{NA}.

Reinforcement in Tension

Crack Spacing

The crack spacing, S_p is required to determine both the contribution of the tensile concrete and the width of the cracks. The analysis procedure for determining the crack spacing is based on the partial- interaction bond/slip analysis of an axially loaded prism and this general approach has been widely applied to similar problems in a variety of concretes in the past and with various bond stress slip relationships (Gupta & Maestrini 1990; Wu et al. 1991; Balazs 1993; Choi & Cheung 1996; Muhamad et al. 2012; Zhang et al. 2017; Sturm et al. 2018). Here the approach of Sturm et al. (2018) is taken as it has been explicitly formulated to accommodate both the influence of fibres as well as concrete creep and shrinkage with a non-constant bond stress slip relationship.

For analysis, the shaded region centred on the tensile reinforcement in Fig. 1(a) can be considered as an effective tension stiffening prism, as shown in Fig. 1(b). When an axial force P_{rt} is applied to the end of the reinforcing bar in the tension-stiffening prism in Fig. 1(c), the reinforcing bar slips Δ relative to the position of the crack face. This slip Δ also stresses the fibres spanning the crack width causing an axial force P_{ct} to be developed and the concrete to extent D_c from its original position. The shear stresses $\tau(x)$ in Fig. 1(d) develop along the reinforcing-bar/concrete interface, transferring the axial force into the surrounding concrete. These shear stresses are a function of the slip of the reinforcing bar $\delta(x)$ as given by the interface shear-stress/slip relationship in Fig. 4 and for which several material models for fibre reinforced and UHPFRC concrete are available (Harajli 2009; Yoo et al. 2015; Marchand et al. 2016; Sturm & Visintin 2019). The transfer of stresses along the reinforcing bar/concrete interface results in the distribution of stress in the concrete in Fig. 1(e) which is at a maximum at S_p as shown. From this distribution, it can be seen that there is a minimum distance S_p from the existing crack within which a new crack cannot form as the concrete stresses are below the maximum. The stress in the concrete varies from the post-cracking stress f_{pc} at the existing crack in Fig. 1(e) due to the fibres spanning the crack to the tensile strength f_{ct} at the position of the new crack.

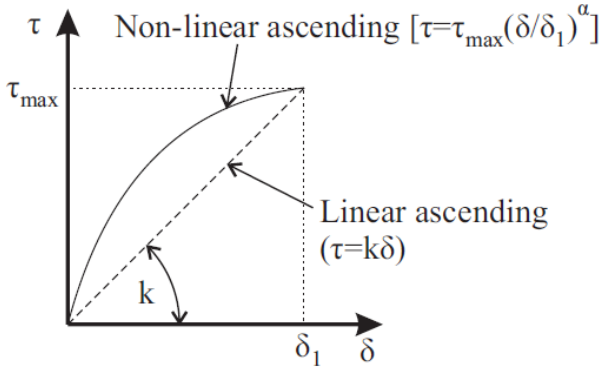

Fig. 4 Bond stress-slip relationship

By considering the definition of the slip $\delta(x)$ and force equilibrium for an infinitesimal segment of the tension stiffening prism, the following classical governing equation for the partial interaction behaviour along a bonded interface between two elastic materials as first developed by Volkersen (1938).

$$\frac{d^2\delta}{dx^2} = \beta\tau \tag{8}$$

where

$$\beta = L_{per}\left(\frac{1}{E_r A_{rt}} + \frac{1}{E_c A_{c-ts}}\right) \tag{9}$$

Considering the boundary condition that full interaction is reached at the new crack where the slip δ and the slip-strain $d\delta/dx$ is zero, and taking the non-linear ascending bond slip relationship in Fig. 4, the following expression for the crack spacing is derived (Sturm et al. 2018)

$$S_p = \left[\frac{2^\alpha(1+\alpha)}{\lambda_2(1-\alpha)^{1+\alpha}}\right]^{\frac{1}{1+\alpha}}\left[\frac{f_{ct}-f_{pc}}{E_c}\left(\frac{E_c A_{c-ts}}{E_r A_{rt}}+1\right)\right]^{\frac{1-\alpha}{1+\alpha}} \tag{10}$$

where

$$\lambda_2 = \frac{\tau_{max} L_{per}}{\delta_1^\alpha}\left(\frac{1}{E_c A_{c-ts}} + \frac{1}{E_r A_{rt}}\right) \tag{11}$$

and τ_{max} is the maximum bond stress, δ_1 is the slip at the maximum bond stress and α is the power of the fitted power law all of which can be determined from the bond-slip relationship in Fig. 4. Eq. (10) is also a function of the post-cracking stress in the tensile concrete, f_{pc} and this is defined as the stress corresponding to the first change of slope in the tensile stress/half crack width relationship and this is shown in Fig. 2(b).

The bond-slip relationship in Fig. 4 is determined from pull out tests performed on reinforcing bars embedded in concrete prisms. Several recommendations exist for performing these simple material tests, for example RILEM has recommendations on how to perform this test for ordinary reinforced concrete (RILEM 1994) and several more recent studies have considered an extension to fibre reinforced concrete such that the suggested material properties are generally available (Harajli et al. 1995; Hota & Naaman 1997; Jungwirth & Muttoni 2004; Campione et al. 2005; Chao et al. 2009; Oesterlee 2010; Yoo et al. 2014, 2015; Marchand et al. 2016; Sturm & Visintin 2019). An inverse analysis can be performed to determine the local bond stress-slip relationship from the results of this test, however, as the bonded length is typically very short (2 bar diameters for UHPFRC, 5 bar diameters for normal strength FRC), it is usually sufficient to assume that the local bond stress-slip relationship is equivalent to the average bond stress versus slip obtained from these tests.

In the approach described above, the concrete tension stiffening prism has been taken to be symmetrical about each layer of the reinforcement as this ensures that a strain gradient is not introduced into the tension stiffening prism which cannot be accommodated for in this analysis. This approach has previously been applied in the numerical analysis of ordinary reinforced concrete (Visintin et al. 2013), fibre reinforced concrete (Visintin & Oehlers 2018) and beams combining prestressed and non-prestressed reinforcement by Knight et al. (2013; 2015). This is also the simplest approach to defining the area of the effective tension stiffening prism which is an advantage when analysing systems where different types and sizes of the reinforcement are considered. Alternatively, the fib Model Code 2010 (fib 2013) provides an expression for calculating the effective area which is not symmetrical, however this requires the use of an effective diameter of reinforcement when reinforcing bars of different sizes are combined or reinforcing bars and tendons are combined. It also requires the neutral axis depth to be known which is an issue for applying this approach as the crack spacing and the effective stiffness of the tensile reinforcement (see next section) are evaluated before the neutral axis depth is determined. The different choices in effective area of concrete results in negligible difference in the load-deflection response as shown in Fig. 5(a) and 5(c) using the properties of beams C1 and M1 from Table 1. The crack widths determined are also similar as shown in Fig. 5(b) and 5(d).

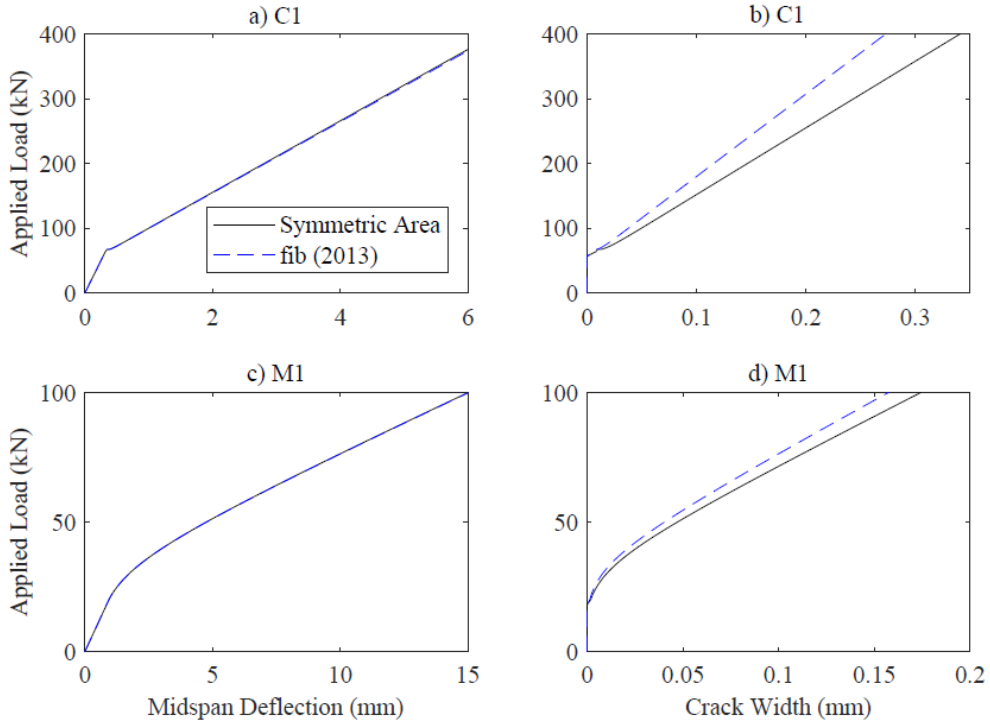

Fig. 5 Effect of the area of the effective tension stiffening prism

Axial force in the reinforcement prior to macrocracking

Before the formation of macrocracks, that is for strains less than $f_{ct}/E_c+\varepsilon_{inel}$, compatibility exists between the reinforcement and the surrounding concrete, therefore the force in the tension reinforcement in the beam in Fig. 1(a) is

$$P_{rt} = n_{FI}A_{rt}E_c\chi(d_t - d_{NA}) + P_{rt0} \quad (12)$$

where the compressive force due to the applied shrinkage strain, ε_{sh} is

$$P_{rt0} = -E_rA_{rt}\varepsilon_{sh} \quad (13)$$

n_{FI} is the modular ratio E_r/E_c and $\chi(d_t-d_{NA})$ is the strain at the level of the tensile reinforcement assuming a linear strain profile defined by a curvature, χ and neutral axis depth, d_{NA}. These are defined in the next section discussing the segmental method.

Axial force in the reinforcement after macrocracking

After the formation of macrocracks, that is for strains greater than $f_{ct}/E_c+\varepsilon_{inel}$, compatibility no longer exists between the concrete and the reinforcement. Hence an effective tension stiffening prism needs to be considered as shown in the cross-sections Figs. 1(a-b) and the elevation between two cracks in Fig. 6.

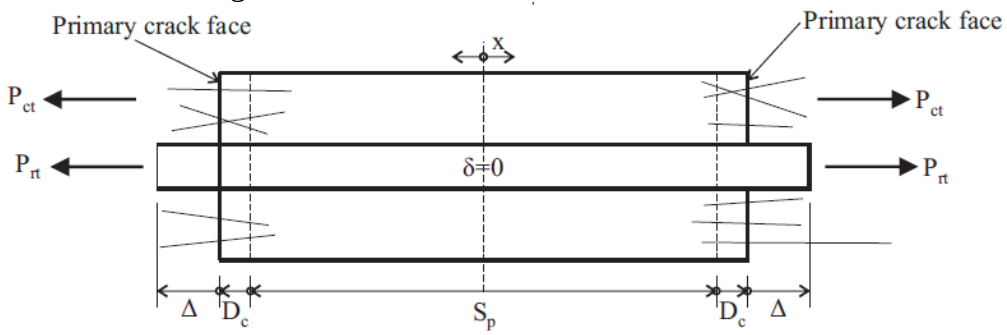

Fig. 6 Tension stiffening prism with two primary cracks

Considering the governing equation (Eq. 8) and the new boundary conditions in Fig. 6, the following expression is obtained for the axial force in the reinforcing bar (Sturm et al; 2018; 2020)

$$P_{rt} = \gamma n_{FI} A_{rt} E_c \chi (d_t - d_{NA}) + P_{rt0} \tag{14}$$

where $\chi(d_t-d_{NA})$ is the strain at the reinforcing bar as defined by a linear strain profile parameterised in terms of a curvature, χ and neutral axis depth, d_{NA}. These are defined in the next section discussing the segmental method. The force due to the applied shrinkage strain and fibres is given by

$$P_{rt0} = -E_r A_{rt} \varepsilon_{sh} - (\gamma - 1) E_r A_{rt} \left(\frac{f_i}{E_c} + \varepsilon_{inel} \right) \approx -E_r A_{rt} \varepsilon_{sh} \tag{15}$$

Further, in Eqns. (14) and (15) γ represents the increased stiffness due to tension stiffening (Sturm et al. 2020) and is defined by

$$\gamma = \frac{\xi - n_f}{1 - n_f + \dfrac{\xi - 1}{\left(\dfrac{E_c A_{c-ts}}{E_r A_{rt}} + 1 \right)}} \tag{16}$$

where the fibre contribution is given by

$$n_f = \frac{m_i}{E_c} \frac{S_p}{2} \tag{17}$$

and the contribution due to the bond is

$$\xi = \frac{\lambda_1 \dfrac{S_p}{2}}{\tanh\left(\lambda_1 \dfrac{S_p}{2} \right)} \tag{18}$$

Where

$$\lambda_1 = \sqrt{k L_{per} \left(\frac{1}{E_r A_{rt}} + \frac{1}{E_c A_{c-ts}} \right)} \tag{19}$$

In Eq. (19) k is defined as the effective linear bond stiffness in Fig. 4 and Eqs. (15) and (16) are functions of f_i and m_i of which there are several possible values. The correct magnitude of

Δ can be determined by checking that the slip at the reinforcing bar, is less than Δ_i and greater than Δ_{i-1} for the given load P_{rt}. In order to check this it is necessary to determine the slip of the reinforcement from the crack face, based on the partial-interaction mechanics above, Sturm et al. (2018) has defined the relationship between P_{rt} and Δ as

$$\Delta = \frac{\frac{P_{rt}}{E_r A_{rt}} + \varepsilon_{sh} - \left(\frac{f_i}{E_c} + \varepsilon_{inel}\right)}{\xi - n_f}\left(\frac{S_p}{2}\right) \tag{20}$$

Significantly, Eq. (14) is in the same form as the expression for the full interaction case in Eq. (12) except that the stiffness of the reinforcement has been increased by the tension stiffening parameter, γ and there is an additional term in P_{rt0} which is a function of the strain in the tensile concrete. This shows that it is possible to directly incorporate the rational basis of tension stiffening and cracking without significantly changing the form of traditional design expressions.

It is also of note that in Eq. (15) a simplification has been suggested based on the observation that the additional stiffness of the reinforcement due to tension stiffening is usually on the order of 10% and hence in the second term of Eq. (15) $(\gamma-1)$ is approximately 0.1. Further, since the shrinkage strain and $(f_i/E_c+\varepsilon_{inel})$ are of similar order of magnitude, the first term of Eq. (15) is an order of magnitude larger than the second, and hence the second can be ignored without significant loss of accuracy.

Reinforcement in compression

The compression reinforcement in Fig. 1(a) is assumed to be linear elastic. Therefore, the axial force in the reinforcement is

$$P_{rc} = n_{FI} A_{rc} E_c \chi (d_c - d_{NA}) + P_{rc0} \tag{21}$$

where the additional force due to the shrinkage strain is given by

$$P_{rc0} = -E_r A_{rc} \varepsilon_{sh} \tag{22}$$

FRC AND UHPFRC SEGMENTAL ANALYSIS

Qualitative description

Having now defined the internal forces in each component of a fibre reinforced concrete member, let us now consider how they can be incorporated into a flexural analysis procedure. To determine the moment-rotation behaviour of a beam, first consider the uncracked segment in Fig. 7(a), where due to symmetry, for analysis the deformation length is L_{def} set equal to the half crack spacing (for an uncracked segment, any segment length is valid as there is no localisation, it is however convenient to set it to the half crack spacing). The initial position of the end of the segment is shown as profile A-A. Over time, a shrinkage strain develops in the segment and if the reinforcement were unbonded, this shrinkage would result in a contraction to profile B-B. However, due to the bond between the concrete and the reinforcement this contraction induces compressive forces in the reinforcement and to maintain equilibrium, tensile forces in the concrete. This results in the deformation profile C-C at a rotation $\theta_{sh.}$ If an external moment is applied, the rotation θ increases, to achieve force and moment equilibrium, resulting in the deformation profile D-D.

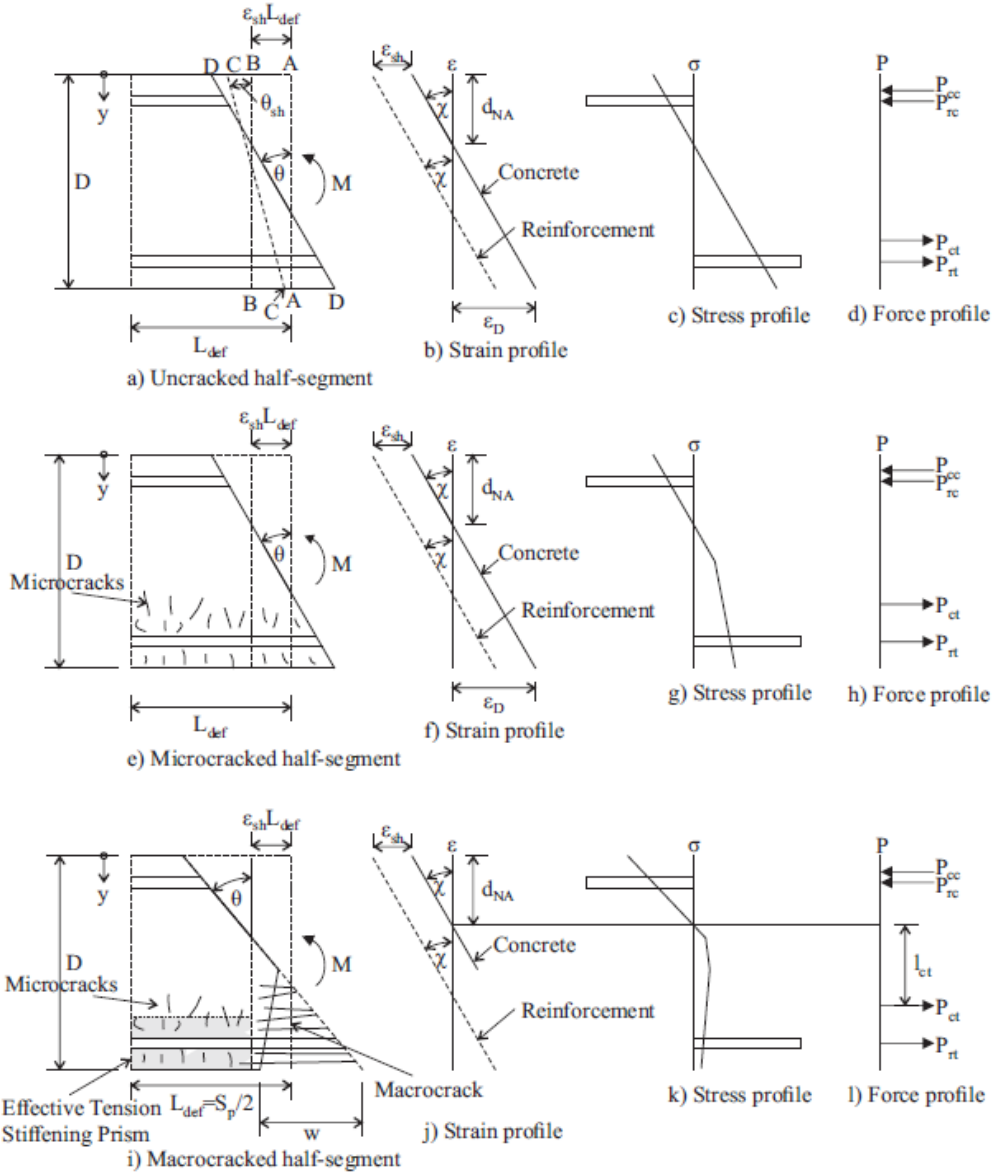

Fig. 7 Deformation, strain, stress and forces within a segment

The profile B-B in Fig. 7(a) represents the point at which the stress in the concrete is zero and profile A-A represents the point at which the stress in the reinforcement is zero. The result of this is that the effect of shrinkage can be modelled as an offset in concrete and reinforcement strains as illustrated Fig. 7(b) (Visintin et al. 2013; Sturm et al. 2020); as such, the concrete strain ε_c is defined as the strains in the concrete that result in stress development. The effects of creep can also be allowed for by adjusting the elastic modulus of the concrete in accordance with the age adjusted effective modulus method (Gilbert & Ranzi 2010).

Dividing the deformation profile in Fig. 7(a) by the half segment length, L_{def}, results in the strain profile shown in Fig. 7(b), which represents the strain after the application of the shrinkage strain and external moment. Importantly a stain profile in Fig. 7(b) is defined for both the concrete and the reinforcement, and these are offset by the shrinkage strain. For further analysis d_{NA} will now be defined as the depth to the position where the strain is zero in the concrete.

Having now quantified the deformation and strain profiles, applying appropriate constitutive laws, the strain profile then results in the stress profile in Fig. 7(c), integration of which results in the force profile in Fig. 7(d). Using force and moment equilibrium, this system can then be solved to yield the relationship between the applied moment M and the rotation of the system θ and consequently from θ/L_{def} the moment and the curvature.

As the moment on the half-segment in Fig. 7(a) is increased, eventually the strain at the bottom fibre ε_D reaches the microcracking strain, f_{SH}/E_c. After this, the segment in Fig. 7(a) is replaced by Fig. 7(e). The presence of microcracks result in the hardening of the stress observed in Fig. 7(g) and when ε_D reaches the macrocracking strain, $f_{ct}/E_c+\varepsilon_{inel}$, macrocracks form as illustrated in Fig. 7(i). In this situation, the width of the macrocrack w is equal to the twice the difference between the deformation profile and the extension of the concrete in the tension stiffening prism given by Eq. 20. This also results in the softening in the tensile response illustrated in Fig. 7(k). At this stage, tension stiffening occurs increasing the effective stiffness of the tensile reinforcement. This is represented by multiplying the axial rigidity of the reinforcement by the tension stiffening parameter given by Eq. (16).

Hence by applying this moment/rotation approach, the moment/curvature and moment/crack-width relationship can be obtained and this allows us to assess the deflections and crack widths within the section.

Quantitative analysis

Having defined qualitatively the manner in which the segmental method can be applied using Fig. 7, and having previously established constitutive relations for both the crack spacing and the axial force/deformation relations for the various components of the beam, a procedure is now established for obtaining the moment/curvature and moment/crack-width relationships. As this approach is derived directly from the segmental analysis without modification, it will be referred to as the exact approach.

First a strain at the bottom fibre of the beam ε_D is imposed. The average stress in the tensile concrete $\sigma_{ct\text{-}ave}$ and the lever arm parameter η can now be evaluated from Eqs. (3) and (6) respectively and from Figs. 7(b), 7(f) and 7(j), the curvature is:

$$\chi = \frac{\varepsilon_D}{D - d_{NA}} \tag{23}$$

The neutral axis depth can be determined by considering force equilibrium and the expression for the curvature in Eq. (23). For a rectangular section and from Eqs. (2), (7), (14) and (21), the following is obtained

$$0 = \gamma n_{FI} A_{rt} E_c \chi (d_t - d_{NA}) + P_{rt0} + n_{FI} A_{rc} E_c \chi (d_c - d_{NA}) + P_{rc0} + \sigma_{ct-ave} b (D - d_{NA}) - \frac{1}{2} b d_{NA}^2 E_c \chi \tag{24}$$

Substituting Eq. (23) into Eq. (24) and rearranging gives the following quadratic equation for the neutral axis depth

$$0 = a_0 + a_1 d_{NA} + a_2 d_{NA}^2 \tag{25}$$

where

$$a_0 = E_c \varepsilon_D (\gamma n_{FI} A_{rt} d_t + n_{FI} A_{rc} d_c) + (P_{rt0} + P_{rc0}) D + \sigma_{ct-ave} b D^2 \tag{26a}$$

$$a_1 = E_c \varepsilon_D (\gamma n_{FI} A_{rt} + n_{FI} A_{rc}) - (P_{rt0} + P_{rc0}) - 2\sigma_{ct-ave} b D \tag{26b}$$

$$a_2 = \sigma_{ct-ave} b - \frac{1}{2} b E_c \varepsilon_D \tag{26c}$$

Having solved for the neutral axis depth in Eq. (26), the curvature can be evaluated using Eq. (23) and the forces in the concrete and reinforcement can then be evaluated using Eqs. (2), (7), (14) and (21). From this, the external moment M on the section can be determined. The crack

width at a given depth can also be evaluated as the crack width w is equal to 2Δ, hence, rearranging Eq. (4) gives

$$w = S_p \left[\chi(y - d_{NA}) - \frac{\sigma_{ct}}{E_c} - \varepsilon_{inel} \right] \geq 0 \quad (27)$$

Using this process, the moment/curvature and moment/crack-width relationships can be evaluated parametrically for a range of bottom strains ε_D. Note that Eq. (27) gives the maximum crack width of the section due to the assumptions made when deriving the crack spacing in Sturm et al. (2018) which result in the definition of the minimum crack spacing. This is deemed sufficient as the maximum crack width is the parameter of interest in design.

This approach is applicable to all three segment types shown in Figs. 7(a), 7(e) and 7(i). For an uncracked segment: $(\varepsilon_D < f_{SH}/E_c)$, γ=1, $\sigma_{ct\text{-}ave} = (1/2)E_c\varepsilon_D$ and η =2/3 and in this case, w=0 for any value of y and a_2 is equal to zero from Eq. (26c). The neutral axis depth d_{NA} can then be evaluated as $-a_0/a_1$.

For a microcracked segment $(f_{SH}/E_c \leq \varepsilon_D < f_{ct}/E_c + \varepsilon_{inel})$, γ=1 while $\sigma_{ct\text{-}ave}$ and η are given by the stress/strain relationship in Fig. 3 and the crack width, w is still taken as zero. The moments to cause micro- and macrocracking can be evaluated by substituting in the appropriate strains at the bottom fibre ε_D. For determining the moment at microcracking, a bottom strain of f_{SH}/E_c is applied while for determining the moment at macrocracking $f_{ct}/E_c + \varepsilon_{inel}$. For a segment with macrocracks $(\varepsilon_D > f_{ct}/E_c + \varepsilon_{inel})$, γ is calculated by Eq. (16) and $\sigma_{ct\text{-}ave}$ and η are given by the stress/strain relationship in Fig. 3.

SIMPLIFIED FRC AND UHPFRC SEGMENTAL ANALYSIS

The above approach is not ideal for hand calculations as it requires the evaluation of the moment, curvature and crack width over a range of bottom strains ε_D to obtain a smooth curve. To simplify this problem, the continuous moment/curvature relationship in Fig. 8(a) is replaced by a bilinear approximation.

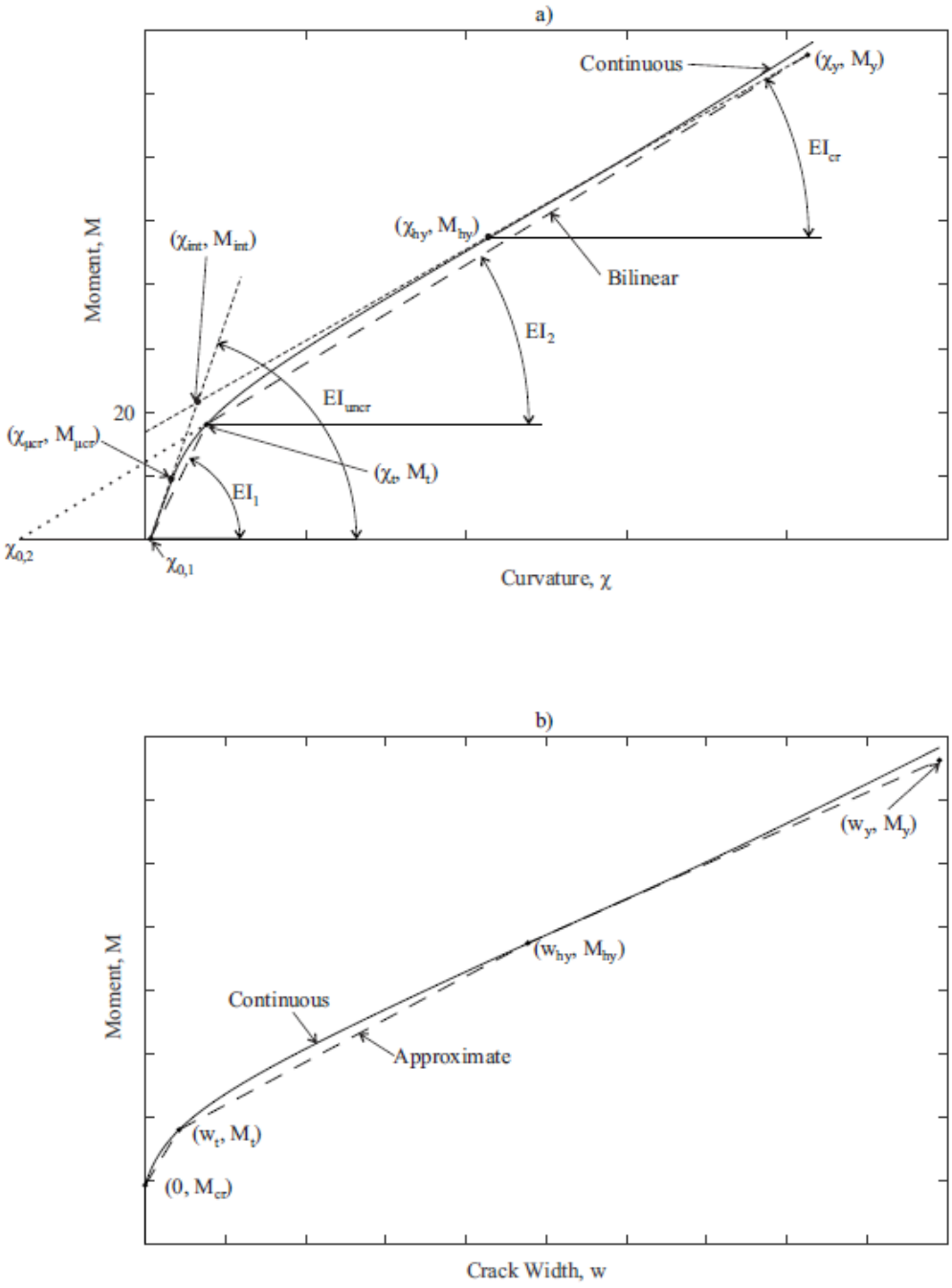

Fig. 8 Simplified moment-curvature and moment-crack width relationships

The functional form of the bilinear curve is

$$\chi = \chi_{0,1} + \frac{M}{EI_1}; M < M_t \tag{28a}$$

$$\chi = \chi_{0,2} + \frac{M}{EI_2}; M_t < M < M_y \tag{28b}$$

where $\chi_{0,1}$ is the curvature at zero moment due to shrinkage. The slope of the first portion of the bilinear curve is

$$EI_1 = \frac{M_t}{\chi_{t-}\chi_{0,1}} \tag{29}$$

The slope of the second portion of the bilinear curve is

$$EI_2 = \frac{M_y - M_t}{\chi_y - \chi_t} \tag{30}$$

and the intersection of the second portion of the bilinear curve with the curvature axis is

$$\chi_{0,2} = \chi_t - \frac{M_t}{EI_2} \tag{31}$$

Curvature at zero moment $\chi_{0,1}$

In this section, the curvature at zero moment is derived for a rectangular section as in Fig. 1(a). When the concrete is uncracked *($\varepsilon_D < f_{SH}/E_c$)*, the axial force is given by integrating the stress σ_c

$$P_c = \int_0^D \sigma_c \, dA = bE_c\chi_{0,1} \int_0^D (y - d_{NA0}) \, dy = bE_c\chi_{0,1} \left[\frac{y^2}{2} - d_{NA0}y\right]_0^D = bDE_c\chi_{0,1}\left(\frac{D}{2} - d_{NA0}\right) \tag{32}$$

In Eq. (32) the stress in the concrete is assumed to be linear elastic because the strain is less than f_{SH}/E_c. The stress is therefore taken to be the elastic modulus, E_c multiplied by the strain, which is itself expressed as a function of the curvature, $\chi_{0,1}$, neutral axis, d_{NA0} and distance from the top of the section, y, as $\chi_{0,1}(y\text{-}d_{NA0})$.

From the reinforcement response Eqs. (12) and (21), force equilibrium gives

$$0 = n_{FI}A_{rt}E_c\chi_{0,1}(d_t - d_{NA0}) - E_rA_{rt}\varepsilon_{sh} + n_{FI}A_{rc}E_c\chi_{0,1}(d_c - d_{NA0}) - E_rA_{rc}\varepsilon_{sh} + bDE_c\chi_{0,1}\left(\frac{D}{2} - d_{NA0}\right) \tag{33}$$

Which upon rearranging in terms of the curvature yields

$$\chi_{0,1} = \frac{E_r\varepsilon_{sh}(A_{rt} + A_{rc})}{E_c(S_0 - A_0d_{NA0})} \tag{34}$$

where the first moment of the transformed area about the top fibre is

$$S_0 = n_{FI}A_{rt}d_t + n_{FI}A_{rc}d_c + \frac{1}{2}bD^2 \tag{35}$$

and the area of the transformed section is

$$A_0 = n_{FI}A_{rt} + n_{FI}A_{rc} + bD \tag{36}$$

The moment about the top fibre due to the concrete forces is

$$M_c = \int_0^D \sigma_c y \, dA = bE_c\chi_{0,1} \int_0^D (y - d_{NA0})y \, dA = bE_c\chi_{0,1}\left[\frac{y^3}{3} - d_{NA0}\frac{y^2}{2}\right]_0^D = bD^2E_c\chi_{0,1}\left(\frac{D}{3} - \frac{d_{NA0}}{2}\right) \tag{37}$$

Hence from moment equilibrium at the top fibre

$$0 = n_{FI}A_{rt}E_c\chi_{0,1}d_t(d_t - d_{NA0}) - E_rA_{rt}d_t\varepsilon_{sh} + n_{FI}A_{rc}E_c\chi_{0.1}d_c(d_c - d_{NA0}) - E_rA_{rc}d_c\varepsilon_{sh} + bD^2E_c\chi_{0,1}\left(\frac{D}{3} - \frac{d_{NA0}}{2}\right) \tag{38}$$

Rearranging (38) in terms of curvature gives

$$\chi_{0,1} = \frac{E_r\varepsilon_{sh}(A_{rt}d_t + A_{rc}d_c)}{E_c(I_0 - S_0d_{NA}0)} \tag{39}$$

where the second moment of the transformed area about the top fibre is

$$I_0 = n_{FI}A_{rt}d_t^2 + n_{FI}A_{rc}d_c^2 + \frac{1}{3}bD^3 \tag{40}$$

Equating Eqs. (34) and (39) gives the neutral axis depth

$$e(S_0 - A_0d_{NA0}) = I_0 - S_0d_{NA0} \tag{41}$$

where

$$e = \frac{A_{rt}d_t + A_{rc}d_c}{A_{rt} + A_{rc}} \tag{42}$$

Such that

$$d_{NA0} = \frac{I_0 - eS_0}{S_0 - eA_0} \tag{43}$$

Having obtained the neutral axis depth using Eq. (43), the curvature at zero moment can be evaluated using Eq. (34) or (39).

Moment M_y and curvature χ_y at yield

The process for determining the moment at yield can be simplified as follows. The bottom strain ε_D in Fig. 3 is unknown at the onset of yield, and is required to determine the average stress in the tensile concrete, $\sigma_{ct\text{-}ave}$ and the lever arm of the tensile concrete, l_{ct}. As a simplification to allow closed form solutions for the yield moment, the portion of the effective tensile stress-strain curve up until microcracking ($\varepsilon_D<f_{SH}/E_c$) is ignored, and a linear relationship is proposed instead (shown in Fig. 9), where the intercept with the stress axis is given as f_1 and the slope is E_f. This simplification is justified as the yield strain, ε_y is typically an order of magnitude larger than the microcracking strain, f_{SH}/E_c, hence the height of the crack has almost reached the neutral axis. Therefore, from Eqs. (3) and (6):

$$\sigma_{ct-ave} = f_1 - \frac{1}{2}E_f\varepsilon_D = f_1 - \frac{1}{2}E_f\chi_y(D - d_{NA,y}) \tag{44}$$

and

$$\eta = \frac{\frac{1}{2}f_1 - \frac{1}{3}E_f\varepsilon_D}{\sigma_{ct-ave}} \tag{45}$$

Setting P_{rt} to the force at yield f_yA_{rt} and rearranging Eq. (14) gives the effective yield strain

$$\varepsilon_y = \frac{1}{\gamma}\left(\frac{f_y}{E_r} + \varepsilon_{sh}\right) \tag{46}$$

Consequently, the curvature at yield is

$$\chi_y = \frac{\varepsilon_y}{d_t - d_{NA-y}} \tag{47}$$

An expression can now be developed for the neutral axis depth. For a rectangular section: the force in the tensile reinforcement is f_yA_{rt} and the force in the compressive reinforcement is given by Eq. (21); the force in the compressive concrete is given by Eq. (7); and the force in the tensile concrete by Eq. (2). Hence, from force equilibrium

$$0 = f_yA_{rt} + n_{FI}A_{rc}E_c\chi_y(d_c - d_{NA-y}) + P_{rc0} + \left[f_1 - \frac{1}{2}E_f(D - d_{NA-y})\right]b(D - d_{NA-y}) - \frac{1}{2}bd_{NA-y}^2E_c\chi_y \tag{48}$$

Substituting Eq. (47) into Eq. (48) gives

$$0 = b_0 + b_1d_{NA-y} + b_2d_{NA-y}^2 \tag{49}$$

where

$$b_0 = \left(f_yA_{rt} + P_{rc0}\right)d_t + bf_iDd_t + \varepsilon_y\left(n_{FI}E_cA_{rc}d_c - \frac{1}{2}E_fbD^2\right) \tag{50a}$$

$$b_1 = -\left(f_yA_{rt} + P_{rc0}\right) - bf_i(D + d_t) - \varepsilon_y\left(n_{FI}E_cA_{rc} - E_fbD\right) \tag{50b}$$

$$b_2 = bf_i - \frac{1}{2}b\varepsilon_y(E_c + E_f) \tag{50c}$$

After the neutral axis depth is evaluated using Eq. (49), the curvature can be evaluated using Eq. (47) and then the moment can be determined after first evaluating the forces and lever arms, then calculating moments.

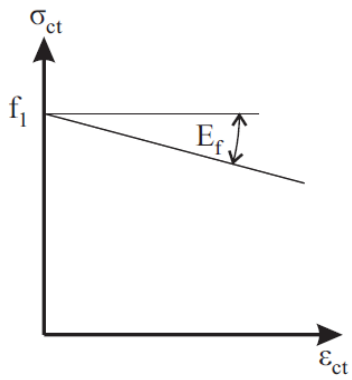

Fig. 9 Simplified tensile stress/strain curve

Moment M_t and Curvature χ_t at transition point

The first step to determine the transition point is to determine the uncracked flexural rigidity EI_{uncr} and the fully cracked flexural rigidity EI_{cr}. The uncracked flexural rigidity can be written as

$$EI_{uncr} = \frac{M_{\mu cr}}{\chi_{\mu cr} - \chi_{0,1}} \tag{51}$$

The moment and curvature at initiation of microcracking, $M_{\mu cr}$ and $\chi_{\mu cr}$ are determined by imposing a bottom strain ε_D of f_{SH}/E_c and following the procedure in the previous section. The fully cracked flexural rigidity is estimated by taking the secant stiffness through the yield point and the point where the bottom fibre strain is equal to 50% of the bottom fibre strain at yield, that is

$$EI_{cr} = \frac{M_y - M_{hy}}{\chi_y - \chi_{hy}} \tag{52}$$

where M_{hy} and χ_{hy} are the moment and the curvature, respectively, determined by setting the bottom strain, ε_D to $0.5\chi_y(D-d_{NA-y})$ and following the solution procedure in the previous section. Having determined the uncracked and fully cracked flexural rigidities, the intersection between the two curves as illustrated in Fig. 8(a) can be found. Equating the curvature at the intersection given by the two curves, gives the curvature at the intersection

$$\chi_{int} = \chi_{0,1} + \frac{M_{int}}{EI_{uncr}} = \chi_y - \frac{M_y - M_{int}}{EI_{cr}} \tag{53}$$

Rearranging Eq. (53) also gives the moment at the intersection

$$M_{int} = \frac{\frac{M_y}{EI_{cr}} + \chi_{0,1} - \chi_y}{\frac{1}{EI_{cr}} - \frac{1}{EI_{\mu cr}}} \tag{54}$$

Hence the moment can be evaluated using Eq. (54) and then the curvature at the intersection from Eq. (53). The transition point is chosen to have the same bottom strain as for this hypothetical intersection point. To determine this, it is assumed that the bottom strain ε_D is proportional to χ. This is justified as ε_D is equal to $\chi(D-d_{NA})$ and the variation in $(D-d_{NA})$ is significantly smaller than χ. The bottom tensile strain at transition is found by linearly interpolating between the strain at microcracking and $0.5\chi_y(d_t-d_{NA})$ as a function of the curvature which gives

$$\varepsilon_{D,t} = \frac{f_{SH}}{E_c} + \left[0.5\chi_y(D - d_{NA}) - \frac{f_{SH}}{E_c}\right]\frac{\chi_{int} - \chi_{\mu cr}}{\chi_{hy} - \chi_{\mu cr}} \tag{55}$$

Having determined the bottom strain, $\varepsilon_{D,t}$, the neutral axis depth can be evaluated with Eq. (25), the curvature with Eq. (23) and the axial forces in the reinforcement and concrete can with Eqs.

(2), (7), (14) and (21). The moment, M_t can then be evaluated by multiplying these forces by their lever arms. The flexural rigidities of each portion of the curve can then be evaluated from Eqs. (29) and (30).

Estimating crack widths
As shown in Fig. 8(b), the crack width can be estimated by linearly interpolating between the crack widths evaluated at macrocracking $(\varepsilon_D = f_{ct}/E_c + \varepsilon_{inel})$, transition $(\varepsilon_{inel} = \varepsilon_{D,t})$, half yield ($\varepsilon_D$ is 50% of the value at yield) and yield.

VALIDATION

Simply Supported Beams
In Fig. 10 the predicted load-deflection curves are compared to experimental results for simply supported UHPFRC beams and in Fig. 11 the predicted load-deflection curves are compared to experimental results for normal strength FRC beams. The details of each test specimen including the geometrical and material properties are summarised in Table 1.

For the UHPFRC beams reinforced with steel bars the bond properties were estimated using the material model detailed in Sturm & Visintin (2019), while for the GFRP reinforced beams tested by Yoo et al. (2016), the bond properties are estimated from the pullout tests contained in Yoo et al. (2015). In all cases, the tensile properties were obtained by fitting the tensile response model in Eq. (1) to the results from associated direct tension tests, however if direct tension test results were not available, inverse analysis of flexural prism tests to yield the stress/strain and stress/crack width behaviour could have been applied.

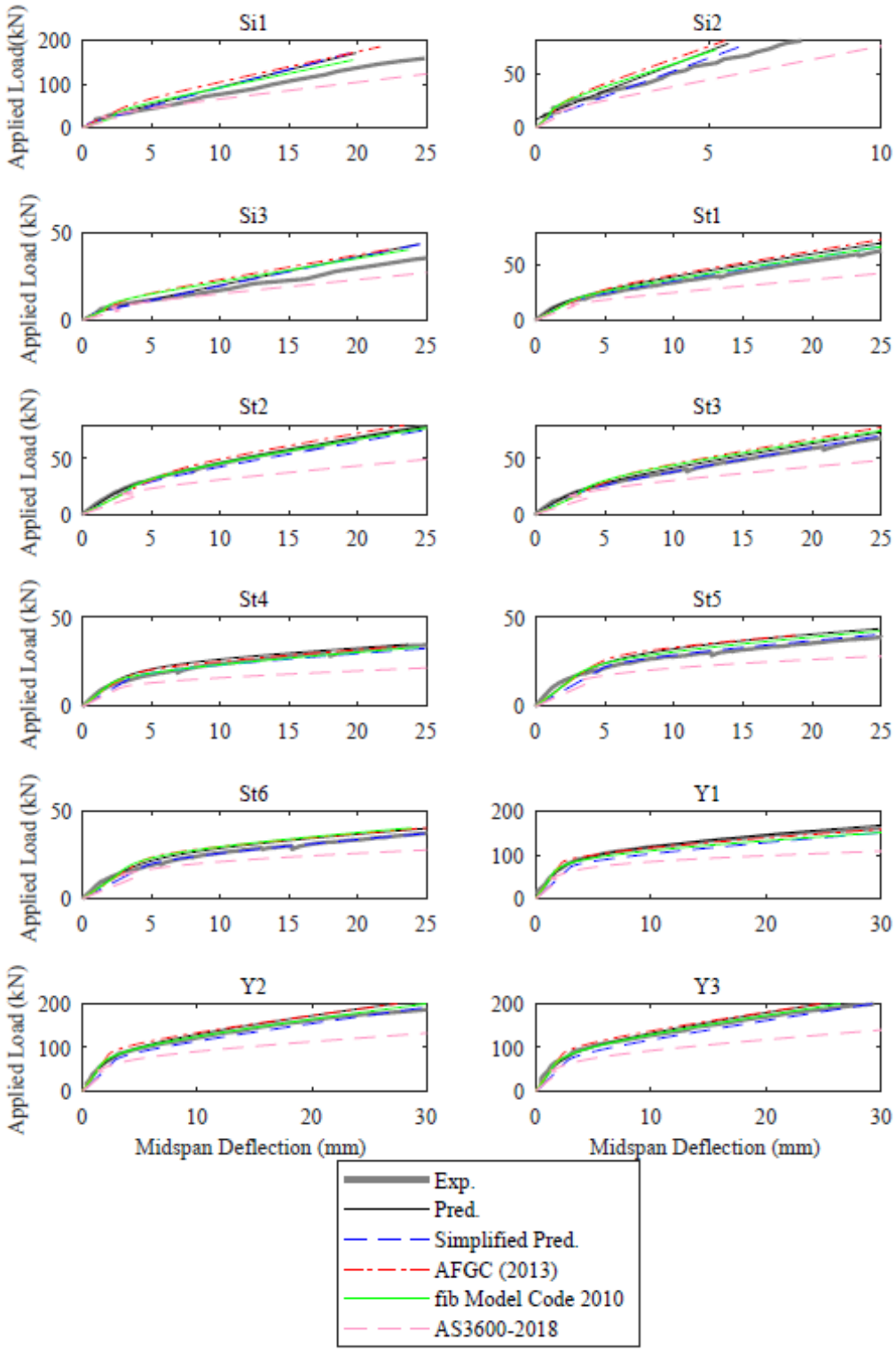

Fig. 10 Comparison of experimental to predicted load deflections for simply supported UHPFRC beams

For the normal strength FRC specimens the bond properties were estimated using the model of Harajli et al. (2009) and the tensile properties were back calculated from prism tests using the design expression in AS3600-2018 (Standards Australia 2018).

The shrinkage strains were determined directly from associated shrinkage tests, or if these were not available the shrinkage strain, ε_{sh} was assumed to be 500 με for UHPFRC beams. The shrinkage strain, ε_{sh} was assumed to be zero for the FRC beams as they were tested shortly after casting.

In the comparisons in Figs. 10 and 11, the mid-span deflection of the beam under four point loading with two different flexural rigidities can be derived using the proposed approach by considering the bending moment diagram under four-point loading. The curvature distribution can then be obtained from Eq. (28). Doubly integrating this curvature distribution while applying the boundary condition that the deflection is zero at the supports the following is obtained

$$\Delta_{mid} = \frac{F(L-a)}{96EI_2}[3L^2 - (L-a)^2] + \frac{1}{8}\chi_{0,2}L^2 - \frac{1}{6}Fx_1^3\left(\frac{1}{EI_2} - \frac{1}{EI_1}\right) - \frac{1}{2}(\chi_{0,2} - \chi_{0,1})x_1^2 \quad (56)$$

where the boundary between the regions with different flexural rigidities is at

$$x_1 = \frac{2M_t}{F} \quad (57)$$

and in which F is the applied load (under four point loading it is the summation of the load applied at both load points), L is the span, and a is the spacing between the load points (this is zero for three point loading).

It can be seen in Figs. 10 and 11 that both the full (labelled Pred.) and approximate (Simplified Pred.) solutions give accurate predictions of the observed load-deflection behaviours (Exp.) for both conventional steel and glass fibre reinforced polymer reinforcement, as well as normal strength FRC and UHPFRC.

In Fig. 10 the results using the models in AFGC (2013), fib (2013) and AS3600-2018 (Standards Australia 2018) approaches are compared to the proposed approach. It is observed that the AFGC (2013) approach tended to underestimate the deflections, while the AS3600-2018 (Standards Australia 2018) approach overestimated the deflection and fib (2013) approach gave similar results to the approach given in this paper.

In Fig. 11 the curves obtained using the approaches suggested by Amin et al. (2017), fib Model Code 2010 (fib 2013) and AS3600-2018 (Standards Australia 2018) are shown for comparison for the FRC test results. For the beams tested by Conforti et al. (2013) and Meda et al. (2012) it was found that all the approaches gave similar results for the load-deflection. For Ning et al. (2012) the approaches in this paper were accurate for N1 and N3 while underestimating the deflection for N2 and N4. Amin et al. (2017) underestimated the deflection for N2. fib Model Code 2010 overestimated the deflection for N1 and N3 while AS3600-2018 overestimated the deflection in every case.

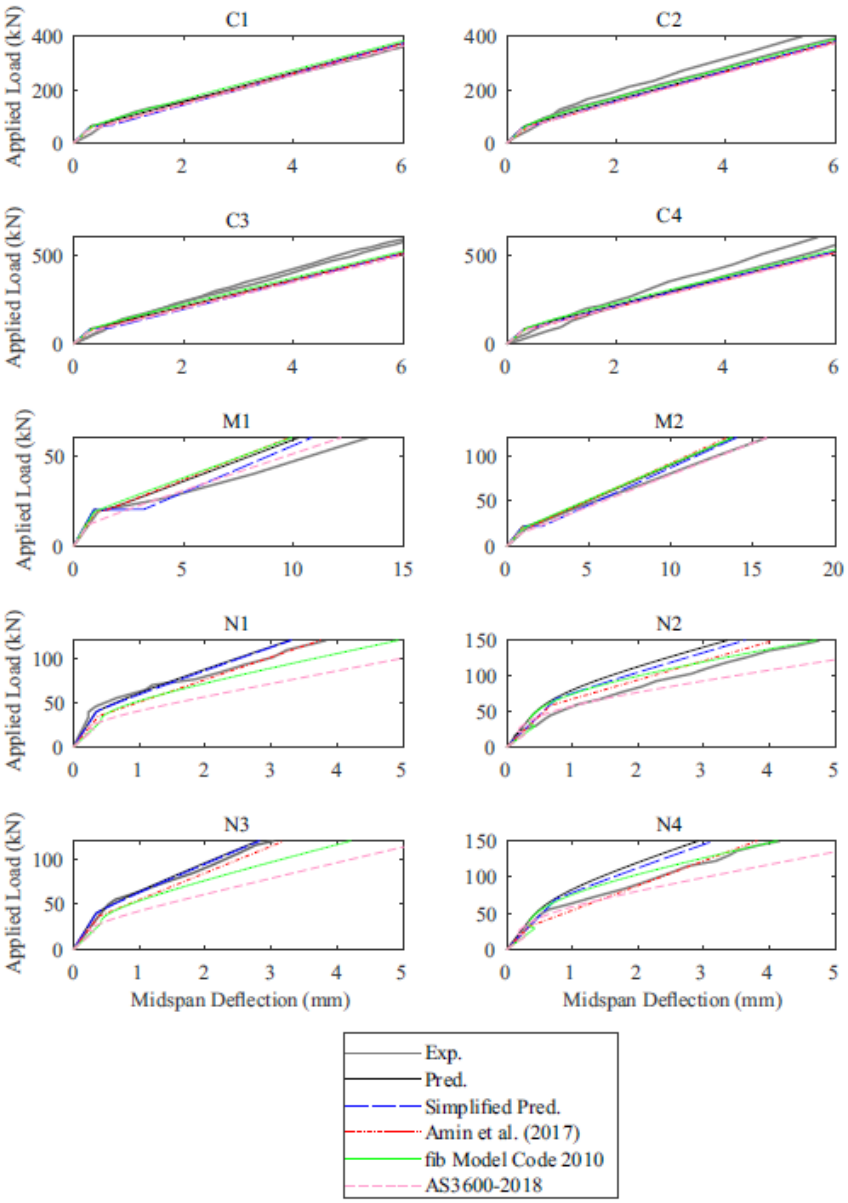

Fig. 11 Comparison of experimental to predicted load deflections for simply supported normal strength FRC beams

The maximum predicted crack widths from the expressions in this paper are compared against the experimental maximum crack widths for the beams tested by Sturm et al. (2020) (St1-St6 in Fig. 12). The crack widths were measured at the depth of the reinforcement. The fit is deemed to be sufficient as the crack widths are characterised by significant random variation particularly in the presence of fibres as discussed in Deluce (2014). The AFGC (2013) expressions underestimates the crack widths in all cases while the fib (2013) and AS3600-2018 (Standards Australia 2018) expressions are close for the St1, St2 and St3 while they overestimate the crack widths for St4, St5 and St6.

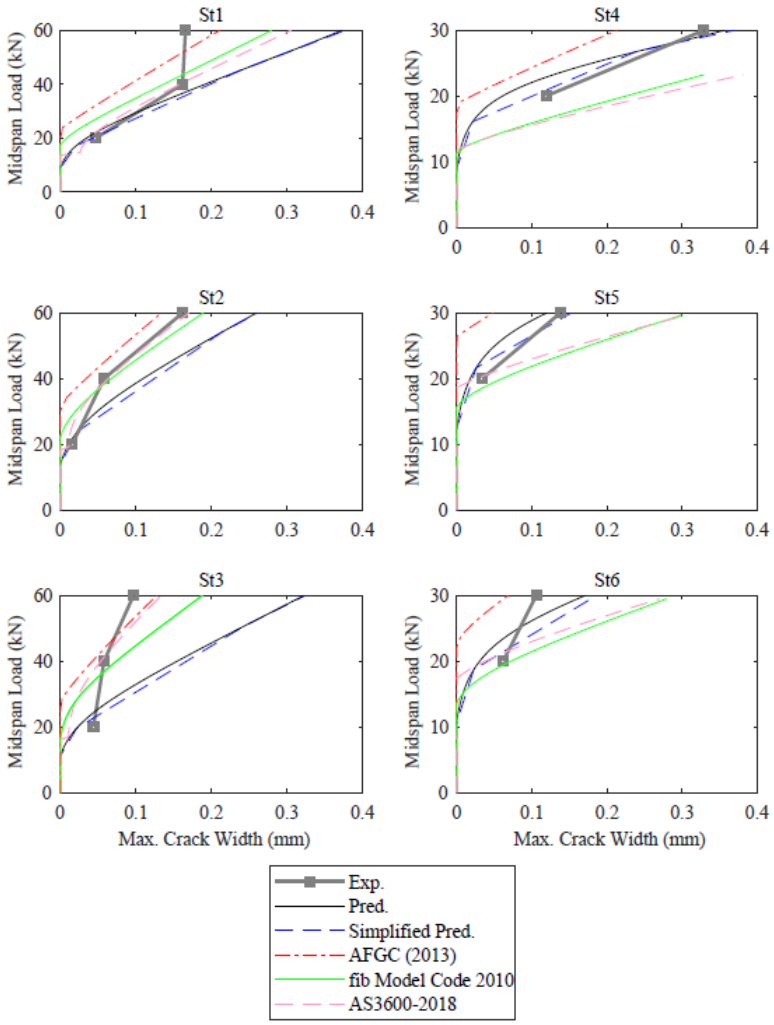

Fig. 12 Comparison of experimental to predicted crack widths for Sturm et al. (2020)

Continuous Beams

The experimental and predicted results of two-span continuous UHPFRC beams tested by Visintin et al. (2018b) are shown in Fig. 13 and the properties of these beams is also summarised in Table 1.

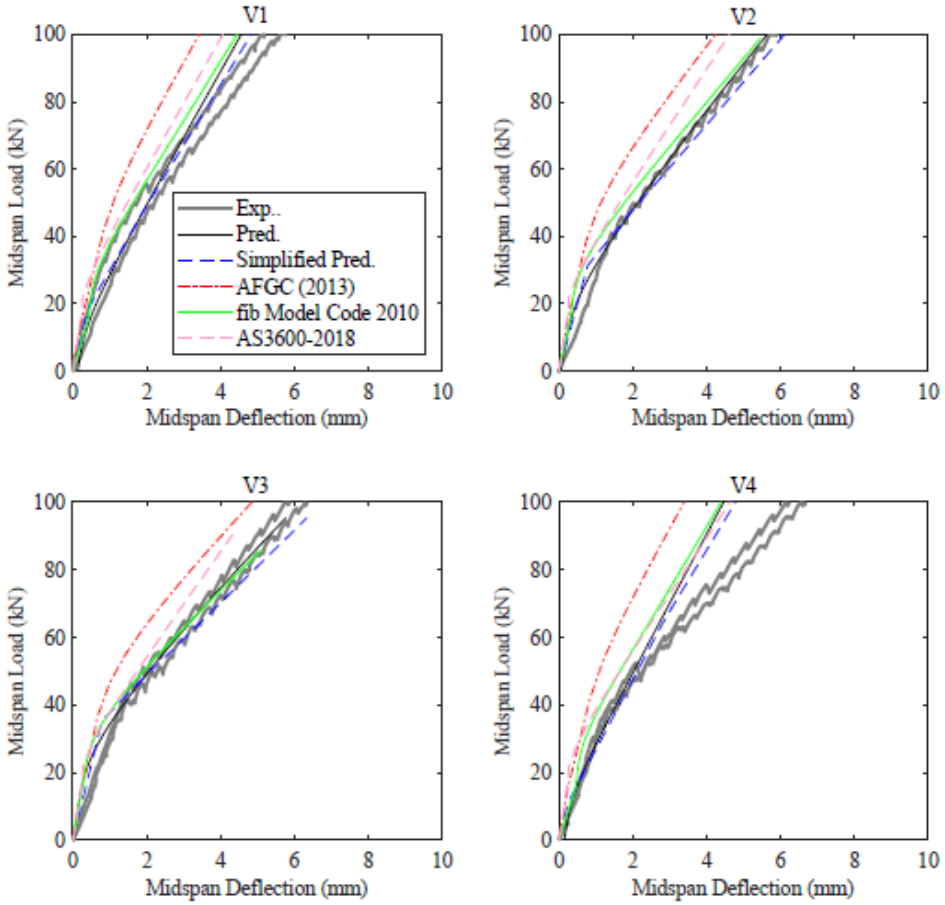

Fig. 13 Comparison of experimental to predicted load deflections for Visintin et al. (2018)

The deflection can be evaluated using any recognised structural mechanics approach using the flexural rigidities and curvature under zero moment presented in this paper. For the comparison with the experimental results, in this paper the deflection of the two span continuous beam loaded at the midpoints with different flexural rigidities in the hogging and sagging regions was obtained by doubly integrating the curvature along the beam to give

$$\Delta_{mid} = \frac{7FL^3}{768EI_{sag}} - \frac{1}{8}\chi_{0,sag}L^2 + \frac{Fx_1}{192}\left(\frac{1}{EI_{hog}} - \frac{1}{EI_{sag}}\right)\left(18L^2 - 51Lx_{hog} + 44x_{hog}^2\right) - \frac{1}{2}\left(\chi_{0,hog} - \chi_{0,sag}\right)x_{hog}\left(L - x_{hog}\right) \quad (58)$$

Where the point of contraflexure is $x_{hog}=(3/11)L$, EI_{sag} is the flexural rigidity and $\chi_{0,sag}$ is the curvature under zero moment due to shrinkage in the sagging region. Similarly, EI_{hog} is the flexural rigidity and $\chi_{0,hog}$ is the curvature under zero moment due to shrinkage in the hogging region.

From Fig. 13, it can be seen that predicted load/deflections were accurate for three of the four beams. The main contributory factors to any inaccuracy is that only two direct tension tests were performed along with the original beam tests and so any scatter in the tensile material properties is difficult to capture. Further, the shrinkage strains were not measured and here are assumed to be 500 με based on later work done on the same concrete cured under the same conditions. The AFGC (2013), AS3600-2018 (Standards Australia 2018) and fib (2013) approaches were also compared where all three were found to underestimate the deflections of the continuous beams however fib (2013) was the closest to the approach suggested in this paper.

CONCLUSION

In this paper, a closed-form approach has been introduced for determining the short- and long-term deflections and crack widths in FRC and UHPFRC beams at serviceability. The advantage of this approach is that the model inputs are directly related to the results of basic material tests such as uniaxial compression, tension (or indirectly if the appropriate inverse analysis is applied), pull-out of embedded reinforcement, shrinkage and creep. Tensile stress/crack width and bond stress/slip relationships can be used in a non-linear form and as such, this approach is not semi-empirical and so does not have to be calibrated with the results of beam tests over a wide variety of beam sizes. The approach should therefore be being useful in the development of new materials, where it can be applied without the need for calibration to beam test results. These closed form solutions were validated with 12 simply supported and 4 continuous UHPFRC beams as well as 10 normal strength FRC beams where a similar level of accuracy was obtained using a range of code approaches. Some of these beams also included glass fibre reinforced polymer reinforcement demonstrating the versatility of the model. A detailed worked example is given in the supplementary material to determine the serviceability deflections and crack widths in a UHPFRC T-beam. This procedure could be used in developing design charts for use in practice for any new type of UHPFRC or FRC.

ACKNOWLEDGEMENTS

This material is based upon work supported by the Air Force Office of Scientific Research under award number FA2386-16-1-4098 and the Australian Research Council Discovery Project 190102650"

NOTATION

A = area;
$A_{c\text{-}ts}$ = area of tension stiffening prism;
A_{ct} = area of tensile concrete;
A_{rc}, A_{rt} = cross-sectional area of the compression and tension reinforcement, respectively;
A_0 = transformed area;
a = distance between load points under four point bending;
a_0, a_1, a_2, b_0, b_1, b_2 = coefficients to quadratic equation;
b, b_f, b_w = width of section; width of flange and width of web, respectively;
D = total depth of the section;
D_c = extension of concrete in tension stiffening prism;
d_c, d_t = depth of the compressive and tensile reinforcement, respectively;
d_f = depth of flange;
d_{NA}, $d_{NA\text{-}y}$, d_{NA0} = neutral axis depth; neutral axis depth at yield and zero moment, respectively;
$d\delta/dx$ = slip strain;
e = centroid of the total reinforcement;
E_c, E_r = elastic moduli of concrete and reinforcement, respectively
$E_{c\text{-}eff}$ = age adjusted effective elastic modulus of the concrete;
E_f = slope of the simplified tensile stress-strain relationship in Fig. 9
E_{SH} = strain hardening modulus;
EI_{cr}, EI_{uncr} = cracked and uncracked flexural rigidity, respectively;
EI_{hog}, EI_{sag} = flexural rigidity in hogging and sagging, respectively;
EI_1, EI_2 = slopes of each part of the bilinear moment-curvature relationship;
$EI_{1,hog}$, $EI_{2,hog}$ = slopes of each part of the bilinear moment-curvature relationship in hogging;

$EI_{1,sag}$, $EI_{2,sag}$ = slopes of each part of the bilinear moment-curvature relationship in sagging;
F = point load;
f_{ct} = tensile strength of concrete;
f_i, f_1, f_2, f_3 = stress intercept of stress-half crack width relationship;
f_{pc} = post-cracking strength of concrete;
f_{SH} = stress to cause microcracking;
f_y = yield stress;
I_0 = second moment of area of transformed section about the top fibre;
k = stiffness of linear ascending bond-slip relationship;
L = span of beam;
L_{def} = deformable length;
L_{per} = bonded perimeter of reinforcing bar in tension chord;
l_{ct} = lever arm of the tensile concrete;
M, M_{hy}, M_{int}, M_t, M_y, $M_{\mu cr}$ = applied moment; moment at half yield, intersection, transition point, at yield, microcracking, respectively;
M_c = moment due to concrete;
m_i, m_1, m_2, m_3 = slope of stress-half crack width relationship;
n_{FI} = modular ratio of reinforcement; E_r/E_c;
n_f = modular ratio of fibres;
P, P_c, P_{cc}, P_{ct}, P_{rc}, P_{rt} = axial force; axial force in the concrete, compressive concrete, tension concrete, compressive reinforcement and tension reinforcement, respectively;
P_{rc0}, P_{rt0} = residual load due to shrinkage and fibres in the compressive and tensile reinforcement;
S_p = primary crack spacing;
S_0 = first moment of area of transformed section about the top fibre;
w, w_{mid}, w_{sup} = crack width; crack width at midspan and support, respectively;
w_{hy}, w_t, w_y = crack width at half yield, transition and yield;
x = position in beam measured from support;
x_{hog} = distance from support to point of contraflexure;
x_1 = location of the transition moment in beam;
y = depth measured from top fibre;
α = non-linearity of non-linear ascending bond-slip relationship;
β = axial rigidity parameter;
γ = increase in stiffness due to tension stiffening;
Δ = half crack width; slip of the reinforcing bar at the crack;
Δ_i, Δ_0, Δ_1, Δ_2 = half crack width at the change in slope of half stress/crack width relationship
Δ_{mid} = midspan deflection;
δ = slip;
δ_1 = slip at maximum bond stress;
ε, ε_D, $\varepsilon_{D,t}$ = strain; strain at the bottom fibre; strain at the bottom fibre at the transition point;
ε_{ct} = effective strain in the tensile concrete;
ε_{inel} = permanent strain due to microcracking;
ε_{sh} = shrinkage strain;
ε_y = yield strain;
η = ratio of the centroid of the stress/strain relationship to the strain at the bottom fibre;
θ, θ_{sh} = rotation; rotation due to shrinkage;
λ_1, λ_2 = bond parameter for a linear ascending and non-linear bond-slip relationships, respectively;
ξ = tension stiffening parameter;

σ, σ_c, σ_{cc}, σ_{ct}, σ_{rt} = stress; stress in concrete, compressive concrete, tensile concrete and tensile reinforcement;
$\sigma_{ct\text{-}ave}$ = average tensile stress;
τ = interface shear stress; bond stress;
τ_{max} = maximum bond stress;
ϕ = creep coefficient;
χ, χ_{hy} χ_{int}, χ_t, χ_y, $\chi_{\mu cr}$, $\chi_{0,1}$ = curvature; curvature at half yield, intersection, transition, yield, microcracking, zero moment, respectively;
$\chi_{0,hog}$, $\chi_{0,sag}$ = intercept with the curvature axis in hogging or sagging, respectively;
$\chi_{0,2}$ = intercept with the curvature axis for the 1st part of the bilinear moment-curvature relationship;
$\chi_{0,1,hog}$, $\chi_{0,1,sag}$ = $\chi_{0,1}$ in hogging and sagging, respectively;
$\chi_{0,2}$ = intercept with the curvature axis for the 2nd part of the bilinear moment-curvature relationship;
$\chi_{02,hog}$, $\chi_{02,sag}$ = $\chi_{0.2}$ in hogging and sagging, respectively;

SUPPLEMENTARY MATERIAL

The supplementary material contains a detailed worked example to demonstrate the application of the approach to determine the serviceability deflections and crack widths in a UHPFRC T-beam.

REFERENCES

AFGC (Association Francaise de Genie Civil). (2013). "Betons fibres a ultra-hautes performances- Recommandations [Ultra high performance fibre reinforced-concretes – Recommendations]." Paris.

Amin, A., Foster, S. J., and Kaufmann, W. (2017). "Instantaneous deflection calculation for steel fibre reinforced concrete one way members." *Engineering Structures*, 131, 438-445.

Amin, A. and Gilbert, R. I. (2018). "Instantaneous Crack Width Calculation for Steel Fiber-Reinforced Concrete Flexural Members." *ACI Structural Journal*, 115(2).

Balazs, G. L. (1993). "Cracking analysis based on slip and bond stresses." *ACI Materials Journal*, 90, 340-340.

Banthia, N., Majdzadeh, F., Wu, J., and Bindiganavile, V. (2014) "Fiber synergy in Hybrid Fiber Reinforced Concrete (HyFRC) in flexure and direct shear." *Cement and Concrete Composites*, 48, 91-97.

Barros, J. A., and Figueiras, J. A. (1999). "Flexural behavior of SFRC: testing and modeling." *Journal of Materials in Civil Engineering*, 11(4), 331-339.

Barros, J. A., Taheri, M., and Salehian, H. (2015). "A model to simulate the moment–rotation and crack width of FRC members reinforced with longitudinal bars." *Engineering Structures*, 100, 43-56.

Barros, J.A., Taheri, M, and Salehian, H. (2018). "A model to predict the crack width of FRC members reinforced with longitudinal reinforcing bars." *ACI Special Publication*, 319, 2.

Bischoff, P. H. (2003). “Tension stiffening and cracking of steel fiber-reinforced concrete.” *Journal of Materials in Civil Engineering*, 15(2), 174-182.

Brandt, A. M. (2008). “Fibre reinforced cement-based (FRC) composites after over 40 years of development in building and civil engineering.” *Composite Structures*, 86(1-3), 3-9.

Campione, G., Cucchiara, C., La Mendola, L., and Papia, M. (2005). “Steel–concrete bond in lightweight fiber reinforced concrete under monotonic and cyclic actions.” *Engineering Structures*, 27(6), 881-890.

Chao, S. H., Naaman, A. E., and Parra-Montesinos, G. J. (2009). “Bond behavior of reinforcing bars in tensile strain-hardening fiber-reinforced cement composites.” *ACI Structural Journal*, 106(6), 897.

Choi, C. K., and Cheung, S. H. (1996). “Tension stiffening model for planar reinforced concrete members.” *Computers & Structures*, 59(1), 179-190.

Conforti, A., Minelli, F., and Plizzari, G. A. (2013). “Wide-shallow beams with and without steel fibres: a peculiar behaviour in shear and flexure.” *Composites Part B: Engineering*, 51, 282-290.

Deluce, J. R., Lee, S. C., and Vecchio, F. J. (2014). “Crack model for steel fiber-reinforced concrete members containing conventional reinforcement.” *ACI Structural Journal*, 111(1), 93.

Fantilli, A.P., Kwon, S., Mihashi, H. and Nishiwaki, T. (2018) “Synergy assessment in hybrid Ultra-High Performance Fiber-Reinforced Concrete (UHP-FRC).” *Cement and Concrete Composites*, 86, 19-29.

Fantilli, A.P. and Chiaia, B. (2018). “Conventional and unconventional approaches for evaluating the crack width in FRC structures.” *ACI Special Publication*, 319, 4.

fib (International Federation for Structural Concrete). (2013). “CEB-FIP Model Code 2010.” Lausanne.

Gilbert, R. I., and Ranzi, G. (2010). *Time-dependent behaviour of concrete structures*. CRC Press, Boca Raton.

Graybeal, B. A. (2006). "Material property characterization of ultra-high performance concrete." *FHWA-HRT-06-103*, Federal Highways Administration, McLean.

Gupta, A. K., and Maestrini, S. R. (1990). “Tension-stiffness model for reinforced concrete bars.” *Journal of Structural Engineering*, 116(3), 769-790.

Harajli, M. H., Hout, M., and Jalkh, W. (1995). “Local bond stress-slip behavior of reinforcing bars embedded in plain and fiber concrete.” *ACI Materials Journal*, 92(4), 343-353.

Harajli, M. H. (2009). “Bond stress–slip model for steel bars in unconfined or steel, FRC, or FRP confined concrete under cyclic loading.” *Journal of Structural Engineering*, 135(5), 509-518.
Hillerborg, A. (1978). “A model for fracture analysis.” *Report No. TVBM-3005*, Lund Institute of Technology.

Hota, S., and Naaman, A. E. (1997). “Bond stress-slip response of reinforcing bars embedded in FRC matrices under monotonic and cyclic loading.” *ACI Structural Journal*, 94(5), 525-537.

Jungwirth, J., and Muttoni, A. (2004). Structural behavior of tension members in Ultra High Performance Concrete. *Proc., International Symposium on Ultra High Performance Concrete.* Kassell, 533-544.

Knight, D., Visintin, P., Oehlers, D. J., and Mohamed Ali, M. S. (2013). “Short-term partial-interaction behavior of RC beams with prestressed FRP and steel.” *Journal of Composites for Construction*, 18(1), 04013029.

Knight, D., Visintin, P., and Oehlers, D. J. (2015). “Displacement-based simulation of time-dependent behaviour of RC beams with prestressed FRP or steel tendons.” *Structural Concrete*, 16(3), 406-417.

Lee, S. C., Cho, J. Y., and Vecchio, F. J. (2013). “Tension-Stiffening Model for Steel Fiber-Reinforced Concrete Containing Conventional Reinforcement.” *ACI Structural Journal*, 110(4).

Marchand, P., Baby, F., Khadour, A., Battesti, T., Rivillon, P., Quiertant, M., Nguyen, H.-H., Genereux, G., Deveaud, J.-P., Simon, A., and Toutlemonde, F. (2016). “Bond behaviour of reinforcing bars in UHPFRC.” *Materials and Structures*, 49(5), 1979-1995.

Meda, A., Minelli, F., and Plizzari, G. A. (2012). “Flexural behaviour of RC beams in fibre reinforced concrete.” *Composites Part B: Engineering*, 43(8), 2930-2937.

Mobasher, B., Yao, Y., and Soranakom, C. (2015). “Analytical solutions for flexural design of hybrid steel fiber reinforced concrete beams.” *Engineering Structures*, 100, 164-177.

Muhamad, R., Mohamed Ali, M. S., Oehlers, D. J., and Griffith, M. (2012). “The tension stiffening mechanism in reinforced concrete prisms.” *Advances in Structural Engineering*, 15(12), 2053-2069.

Ning, X., Ding, Y., Zhang, F., and Zhang, Y. (2015). “Experimental study and prediction model for flexural behavior of reinforced SCC beam containing steel fibers.” *Construction and Building Materials*, 93, 644-653.

Oesterlee, C. (2010). “Structural response of reinforced UHPFRC and RC composite members.” Ph.D. Thesis, Ecole Polytechnique Federale de Lausanne.

Park, S. H., Kim, D. J., Ryu, G. S. and Koh, K. T. (2012). “Tensile behavior of ultra high performance hybrid fiber reinforced concrete.” *Cement and Concrete Composites*, 34(2), 172-184.

RILEM (International Union of Laboratories and Experts in Construction Materials, Systems and Structures) (1994). “RC 6 Bond test for reinforcement steel. 2. Pull-out test, 1983.” *RILEM recommendations for the testing and use of constructions materials*, London, 218-220.

Schumacher, P. (2006) “Rotation capacity of self-compacting steel fibre reinforced concrete.” PhD Thesis, Delft University.

Singh, M., Sheikh, A. H., Mohamed Ali, M. s., Visintin, P., and Griffith, M. C. (2017). “Experimental and numerical study of the flexural behaviour of ultra-high performance fibre reinforced concrete beams.” *Construction and Building Materials*, 138, 12-25.

Sobuz, H. R., Visintin, P., Mohamed Ali, M. S., Singh, M., Griffith, M. C., and Sheikh, A. H. (2016). “Manufacturing ultra-high performance concrete utilising conventional materials and production methods.” *Construction and Building Materials*, 111, 251-261.

Standards Australia (2009) “Concrete Structures”, *AS3600-2009*, Sydney.

Standards Australia (2014). “Concrete structures-Commentary (Supplement to AS3600-2009).” *AS3600 Supplement 1:2014*, Sydney.

Standards Australia (2018) “Concrete Structures”, *AS3600-2018*, Sydney.

Stang H and Aarre T (1992) “Evaluation of crack width in FRC with conventional reinforcement.” *Cement and Concrete Composites*, 14(2), 143–154.

Sturm, A.B., Visintin, P., Oehlers, D.J. and Seracino, R. (2018) “Time dependent tension stiffening mechanics of fibre reinforced and ultra-high performance fibre reinforced concrete.” *Journal of Structural Engineering.*, 144(8), 04018122.

Sturm, A. B. and Visintin, P. (2019) “Local bond slip behaviour of steel reinforcing bars embedded in UHPFRC.” *Structural Concrete*, 20(1), 108-122.

Sturm, A. B., Visintin, P. and Oehlers. D. J. (2020) “Blending fibres to enhance the flexural properties of UHPFRC beams.” *Construction and Building Materials*, 244, 118328.

Taheri, M., Barros, J. A., & Salehian, H. (2011). “A design model for strain-softening and strain-hardening fiber reinforced elements reinforced longitudinally with steel and FRP bars.” *Composites Part B: Engineering*, 42(6), 1630-1640.

Visintin, P., Oehlers, D. J., and Haskett, M. (2013). “Partial-interaction time dependent behaviour of reinforced concrete beams.” *Engineering Structures*, 49, 408-420.

Visintin, P., and Oehlers, D. J. (2017). “Fundamental mechanics that govern the flexural behaviour of reinforced concrete beams with fibre-reinforced concrete.” *Advances in Structural Engineering*, 1369433217739705.

Visintin, P., Sturm, A.B., Mohamed Ali, M.S., and Oehlers, D.J. (2018a). “Blending macro and micro fibres to enhance to the serviceability behaviour of UHPFRC”, *Australian Journal of Civil Engineering*, 16(2), 106-121.

Visintin, P., Ali, M., Xie, T., and Sturm, A. B. (2018b). “Experimental investigation of moment redistribution in ultra-high performance fibre reinforced concrete beams.” *Construction and Building Materials*, 166(1), 433-444.

Volkersen, O. (1938) “Die Nietkrafverteilung in zugbeanspruchten Nietverbindungen mit konstanten Laschenquerschnitten.” *Luftfahrtvorschung*, 15, 41–47.

Wille, K., El-Tawil, S., and Naaman, A. E. (2014). “Properties of strain hardening ultra high performance fiber reinforced concrete (UHP-FRC) under direct tensile loading.” *Cement and Concrete Composites*, 48, 53-66.

Wu, Z., Yoshikawa, H., and Tanabe, T. A. (1991). “Tension stiffness model for cracked reinforced concrete.” *Journal of Structural Engineering*, 117(3), 715-732.

Yoo, D. Y., Shin, H. O., Yang, J. M., and Yoon, Y. S. (2014). “Material and bond properties of ultra high performance fiber reinforced concrete with micro steel fibers.” *Composites Part B: Engineering*, 58, 122-133.

Yoo, D. Y., Kwon, K. Y., Park, J. J., and Yoon, Y. S. (2015). “Local bond-slip response of GFRP rebar in ultra-high-performance fiber-reinforced concrete.” *Composite Structures*, 120, 53-64.

Yoo, D. Y., Banthia, N., and Yoon, Y. S. (2016). “Flexural behavior of ultra-high-performance fiber-reinforced concrete beams reinforced with GFRP and steel rebars.” *Engineering Structures*, 111, 246-262.

Yuguang, Y., Walraven, J. C., and den Uijl, J. A. (2009). “Combined effect of fibers and steel rebars in high performance concrete.” *Heron*, 54(2-3), 205-224.

Zhang, T., Visintin, P., and Oehlers, D. J. (2017). “Partial-interaction tension-stiffening properties for numerical simulations.” *Advances in Structural Engineering*, 20(5), 812-821.

CHAPTER 3

Background

In this chapter the flexural behaviour of UHPFRC is explored at the ultimate limit state experimentally and numerically. Closed-form solutions are also derived for moment redistribution.

The first publication "Blending fibres to enhance the flexural properties of UHPFRC beams" presents an experimental study into the influence of hybridising straight and hooked steel fibres on the flexural response of UHPFRC beams. The results are then analysed using a segmental model that uses partial interaction to simulate the internal reinforcement and shear friction to allow for concrete softening. This model predicts the deflections and crack widths.

The second publication "Flexural performance of pretensioned ultra-high performance fibre reinforced concrete beams with CFRP tendons" presents an experimental study exploring the effect of prestress and fibre reinforced polymer reinforcement on the flexural behaviour of UHPFRC beams. A digital image correlation system is also used to explore the fracture behaviour. A segmental model is again used to predict the deflections and crack widths.

The third publication "Closed form expressions for predicting moment redistribution in reinforced concrete beams with application to conventional concrete and UHPFRC" presents novel closed-form solutions for the moment redistribution behaviour allowing for the variation in stiffness along the span of a member as well as the impact of support conditions.

List of Manuscripts

Sturm, A. B., Visintin, P. and Oehlers. D. J. (2020) "Blending fibres to enhance the flexural properties of UHPFRC beams." *Construction and Building Materials*, 244, 118328.

Sturm, A. B., Visintin, P., Seracino, R., Lucier, G. W. and Oehlers, D. J. (2020) "Flexural performance of pretensioned ultra-high performance fibre reinforced concrete beams with CFRP tendons." *Composite Structures*, 243, 112223.

Sturm, A. B., Visintin, P. and Oehlers. D. J. (2020) "Closed form expressions for predicting moment redistribution in reinforced concrete beams with application to conventional concrete and UHPFRC." *Structural Concrete*, in press.

STATEMENT OF AUTHORSHIP

Blending fibres to enhance the flexural properties of UHPFRC beams
Construction and Building Materials, 244, 118328.

Sturm, A. B. (Candidate)

Prepared manuscript, performed all analyses, and developed model and theory (80%)

This paper reports on original research I conducted during the period of my Higher Degree by Research candidature and is not subject to any obligations or contractual agreements with a third partv that would constrain its inclusion in this thesis. I am the primary author of this paper.

Signed ..... Date 9/07/2020

Visintin, P.

Supervised and contributed to research, and acted as corresponding author (10%)

I certify that the candidate's stated contribution to the publication is accurate (as detailed above); permission is granted for the candidate in include the publication in the thesis; and the sum of all co-author contributions is equal to 100% less the candidate's stated contribution.

Signed ..... Date 07/07/2020

Oehlers, D. J.

Supervised and contributed to research (10%)

I certify that the candidate's stated contribution to the publication is accurate (as detailed above); permission is granted for the candidate in include the publication in the thesis; and the sum of all co-author contributions is equal to 100% less the candidate's stated contribution.

Signed ..... Date 7/7/20

BLENDING FIBRES TO ENHANCE THE FLEXURAL PROPERTIES OF UHPFRC BEAMS

Sturm, A.B., Visintin, P., Oehlers, D.J.

ABSTRACT

In this paper, the flexural behaviour of ultra-high performance fibre reinforced concrete (UHPFRC) beams reinforced with macro-, micro- and a blend of macro- and micro-fibres is investigated at all limit states. The goal of this study is to investigate whether the benefits of fibre blending that are observed at a material scale translate to the structural scale. To this end, six UHPFRC beams with two different cross-sections and three different mix designs were tested. A well-established segmental analysis technique is then applied to predict the measured load-deflection and load-crack width behaviour of the beams and, following validation for beams with blended fibres, it is then used as the basis for a parametric study to further investigate the influence of beam geometry and reinforcing details.

INTRODUCTION

The introduction of steel fibres into a cementitious matrix allows the transfer of stresses across fractures in the material and, therefore, improves material ductility in both compression and tension (Schumacher 2006). At a structural level, this improvement in material performance translates to a reduction in deflections and crack widths at the serviceability limit (di Prisco et al. 2009), and an increase in strength and ductility at the ultimate limit (Oh 1992). The substantial benefits arising from the addition of fibres to concrete and mortars has made it a focus of significant recent research efforts; particularly in the case of ultra-high performance fibre reinforced concrete (UHPFRC) which is generally characterised by strengths of greater than 150 MPa and a high fibre content that allows non-negligible tensile stresses to be developed post-cracking.

A vast array of steel fibres with different shapes and sizes are now available commercially (Katzer & Domski 2012). Extensive research at a material level has explored the potential benefits of blending multiple types of steel fibre within a given normal- or high- strength concrete mix (Sun et al. 2001; Lawler et al. 2003; Sorelli et al. 2005; Markovic 2006; Banthia & Sappakittipakom 2007; Stähli & van Mier 2007; Akcay & Tasdemir 2012) and to a lesser extent in UHPFRC (Kim et al. 2011; Park et al. 2012; Visintin et al. 2018; Fantilli et al. 2018). A summary of the types of fibres blended and the impact on performance is summarised in Table 1 in which is it shown that there is a general consensus that hybridising fibres result in greater ductility in tension, and that substituting micro-fibres for macro-fibres improves the properties of the material.

Table 1: Summary of works on fibre blending at a material level

Reference	f'_c	V_f(%)	Test	Macro-fibre	Micro-fibre	Findings
Sun et al. (2001)	[a]	1.5	Shrinkage, Water Permeation	35/0.43[b]	10/0.2, 5/0.1[b]	Micro-fibres decreased shrinkage and reduced permeation height
Lawler et al. (2003)	[c]	0.5-1	Flexural Tension, Direct Tension	Hooked 30/0.5	Straight 6/0.022	[d]
Sorelli et al. (2005)	29-33	0.38	Flexural Tension, Direct Tension	30/0.6 [b]	12/0.18[b]	Improvement at both large and small crack widths from using hybrid fibres
Markovic (2006)	113-134	1-3	Flexural Tension, Direct Tension	Hooked 40/0.5, Hooked 60/0.7	Straight 13/0.2	[d]
Banthia & Sappakittipakorn (2007)	34-39	0.5-0.75	Flexural Tension	Crimped 30/0.8	Crimped 30/0.45, Crimped 30/0.4	Mixes with thinner fibres had improved performance
Stahli & van Mier (2007)	139	6	Flexure Tension, Flowability	Crimped 30/0.6	Straight 12/0.2, Straight 6/0.15	[e]
Kim et al. (2011)	200	1-2.5	Flexural Tension	Straight 30/0.3, Hooked 30/0.38, Hooked 62/0.78, Twisted 30/0.3	Straight 13/0.2	Hybrid mixes had larger deflections and greater toughness at the peak strength
Akcay & Tasdemir (2012)	115-124	0.75-1.5	Flexure Tension, Splitting Tension	Hooked 30/0.55	Straight 6/0.15	[e]
Park et al. (2012)	200	1-2.5	Direct Tension	Straight 30/0.3, Hooked 30/0.38, Hooked 62/0.78, Twisted 30/0.3	Straight 13/0.2	[d]
Visintin et al. (2018)	150-160	2.85	Direct Tension, Tension Stiffening	Hooked 35/0.55	Straight 13/0.2	Hybrid mixes had greater ductility than the single fibre mixes
Fantilli et al. (2018)	182	0.5-3	Direct Tension	Hooked 30/0.38	Straight 6/0.16	[d]

[a] f_c unknown, w/cm=0.32
[b] geometry unknown
[c] f_c unknown, w/c=0.45
[d] V_f varied between the hybrid and control mixes
[e] Did not include control mixes

Despite the favourable results observed at the material level, investigations on the benefit of fibre blending at the member level are much more limited, with the only study identified being that of Voo and Foster (2006), who tested a single beam failing in shear that contained a blend

of micro- and hooked end macro-fibres. The results of this study were in contrast to those obtained at a material level because it was observed that a reduction in performance occurred as a result of fibre blending. On a smaller scale, Visintin et al. (2018) tested 5 different blends of macro- and micro-fibres to investigate the influence of fibre blending on tension stiffening prisms. It was observed, in this study, that tension stiffening was improved by the blending of fibres and that the overall best performance resulted from a 50:50 blend of macro- and micro-fibres.

The focus of this paper is the further examination of the performance of UHPFRC with blended macro- and micro-fibres by now considering the performance of flexural elements. To this end, six UHPFRC beams with two different cross sections and three different mix designs (100% macro-fibres, 100% micro-fibres and, 50% macro-fibres and 50% micro-fibres) were tested. The experimental load-deflection and load-crack width results are then compared to the predictions obtained using a well-established segmental analysis for which variants of differing complexity have been developed by Bachman (1971), Bigaj (1998), Schumacher (2006), and Visintin & Oehlers (2017). Finally having validated the application of the segmental approach to mixes with blended fibres, a parametric study is conducted to further extend the investigation to beams with different depths and reinforcement ratios.

MATERIALS

The UHPFRC used for the manufacture of all test specimens was developed at the University of Adelaide by Sobuz et al. (2016). The mix design is summarised in Table 2 and is based on the use of a blended binder consisting of a sulphate-resisting cement and silica fume, a washed river sand with a fineness modulus of 2.34, and a third-generation high range water reducing superplasticiser. In all mixes, the total fibre volume has been fixed at 2.8% and the type of fibre has been varied. The macro-fibres are 35 mm long hooked end fibres with an aspect ratio of 65, while the micro-fibres are straight with a length of 13 mm long and an aspect ratio of 65. The macro-fibres have a yield strength of 1100 MPa and the micro-fibres had a yield strength of 2850 MPa. Note that these mixes are a subset of those previously used by the authors to quantify the impact of fibre blending on the tensile (Visintin et al. 2018), bond (Sturm & Visintin 2018) and shear friction (Sturm et al. 2018a) behaviour of UHPFRC.

Table 2: Mix Design

	Unit Weight (kg/m^3)		
Mix	1M:0m[a]	0M:1m	0.5M:0.5m
Cement	950	950	950
Superplasticiser	43	43	43
Water	168	168	168
Silica Fume	253	253	253
Fine Aggregate	943	943	943
Macro-fibres	221	0	111
Micro-fibres	0	221	111

[a]0.5M:0.5m refers to a mixture with 50% macro fibres (M) and 50% micro fibres (m)

The material properties for each mix are summarised in Table 3: the compressive strength is the average of three tests on 100 mm x 200 mm cylinders in accordance with AS1012.9:2014 (Standards Australia 2014); the elastic modulus was obtained from tests on identical cylinders in accordance with AS1012.17-1997 (Standards Australia 1997); and the shrinkage strain was obtained from tests conducted on prismatic sections with a cross section of 75 mm x 75 mm

and a length of 285 mm and which were subjected to the same conditions as the beam specimens and tested in accordance with AS1012.13:2015 (Standards Australia 2015). The full compressive stress strain behaviour is shown in Fig. 1(a) in which compressive stresses and strains are shown as negative. The remaining material properties required for analysis, including the tensile stress-crack width relationship in Fig. 1(b) and the concrete bond stress-slip behaviour in Fig. 1(c), are taken from Visintin et al. (2018) and Sturm & Visintin (2018) where the same mix designs have been used.

Table 3: Material properties for each mix

		1M:0m	0M:1m	0.5M:0.5m
Compressive Strength (MPa)		146	150	128
Elastic Modulus (GPa)		43.9	39.7	36.5
Shrinkage Strain (με)	At testing of beam section	434 (40 days)	439 (34 days)	475 (28 days)
	At testing of slab section	452 (49 days)	475 (41 days)	499 (33 days)

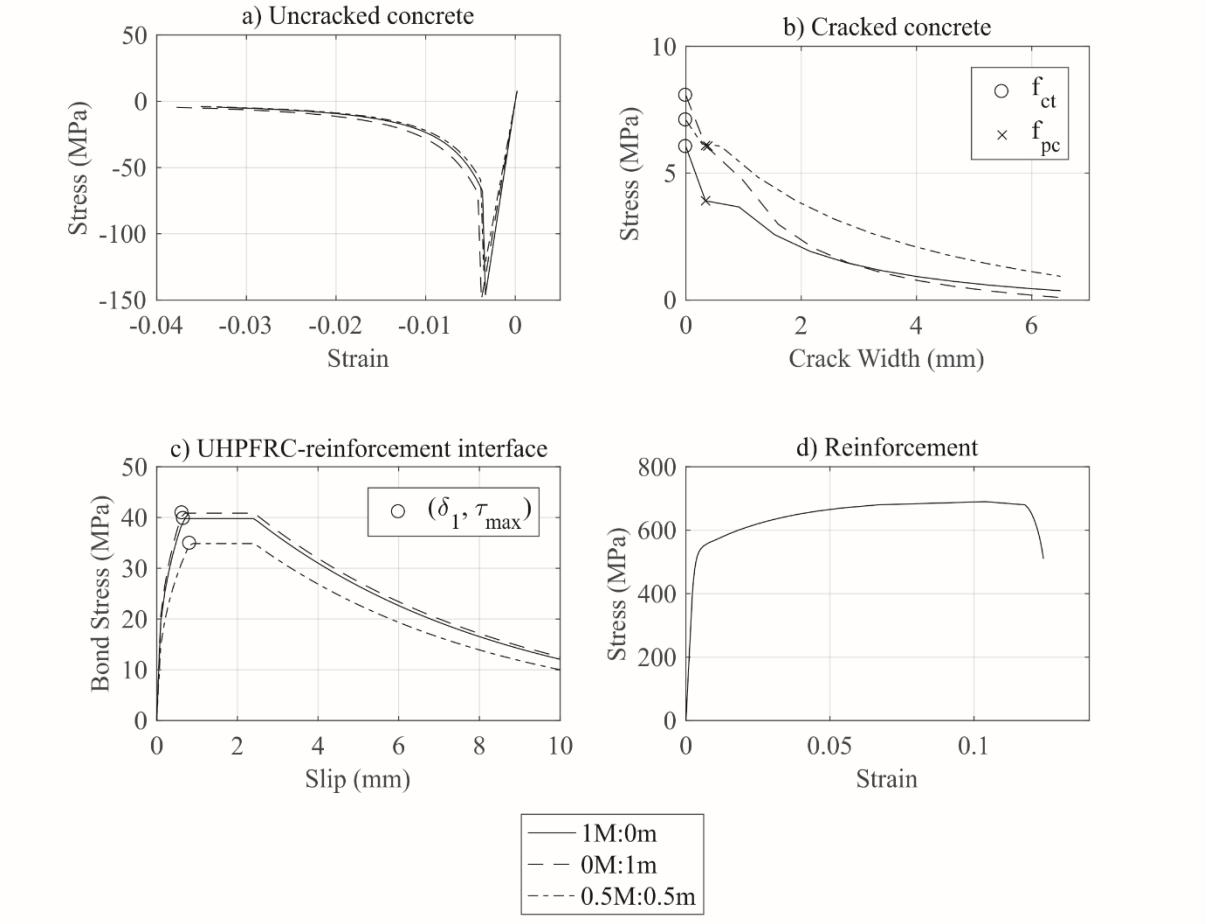

Fig.1 Concrete and reinforcement material properties

All beams were reinforced with deformed steel reinforcing bars complying with AS/NZS 4671:2001 (Standards Australia 2001); the stress-strain relationship of the reinforcement is illustrated in Fig. 1(d) and has a yield strength of 535 MPa, and an ultimate strength of 690 MPa at an average strain of 0.104.

BEAM TEST SPECIMENS

The two cross-sections in Fig. 2 were chosen so that the effect of stirrups and beam size could be studied. The beam has a tensile reinforcement ratio of 1.2% and the slab 0.57%. Significant cover was allowed around all reinforcement to help facilitate uniform fibre distribution.

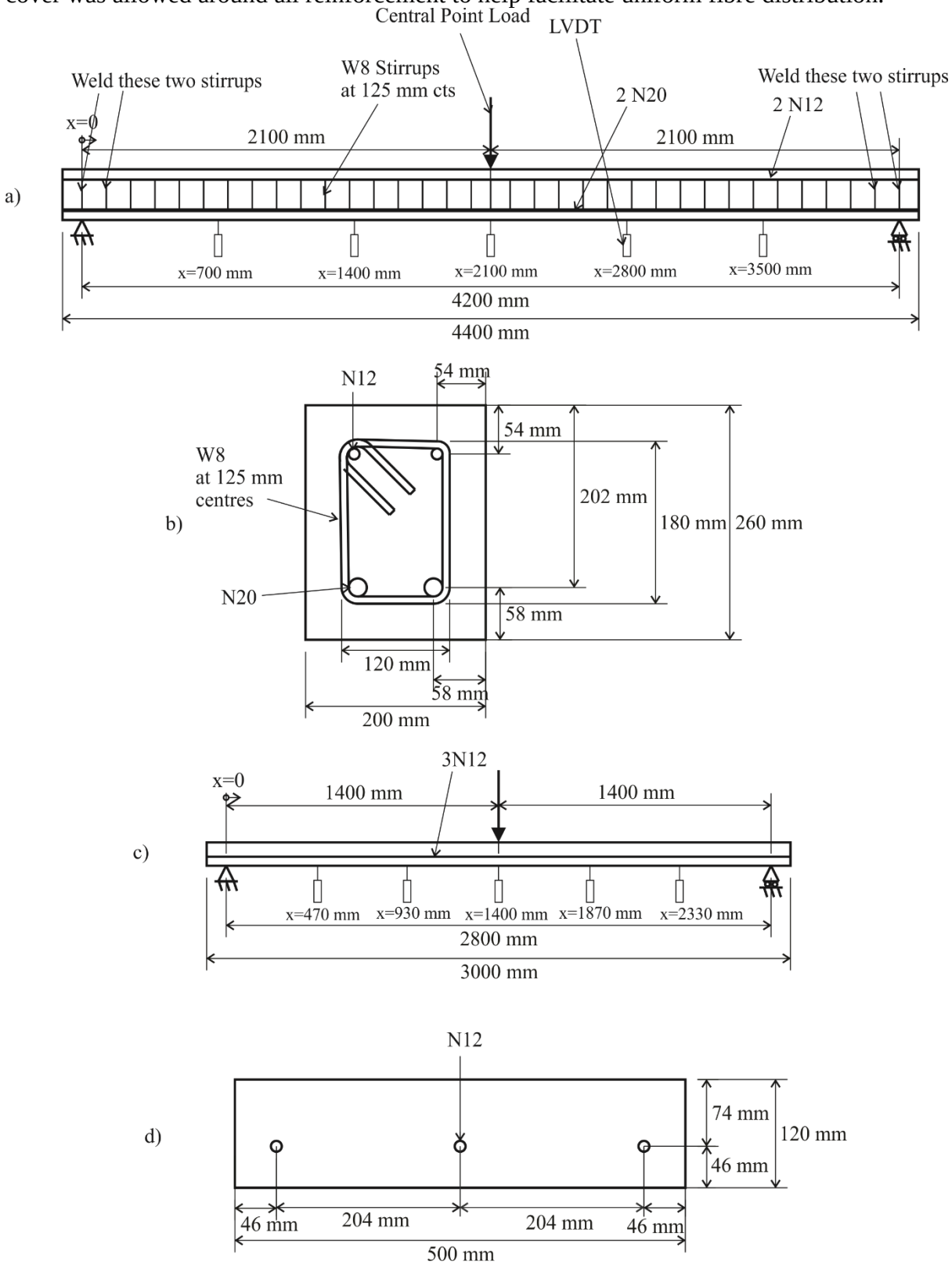

Fig. 2 Test specimens: a) elevation of beam section; b) cross-section of beam section; c) elevation of slab section; d) cross-section of slab section

The UHPFRC was produced in a pan mixer with a capacity of 500 litres by first mixing the sand, cement, silica fume together for 1 minute. The superplasticiser and water were then added and the contents mixed until visibly flowable. Finally, the steel fibres were added and mixed for a further 5 minutes. During casting, a stick vibrator was used sparingly to assist compaction. After casting, the beams and all associated material test specimens were allowed to cure for 28 days by wetting and then covered with plastic to prevent evaporation.

TESTING PROCEDURE

All the members were tested under three point bending at a rate of 2 kN/min for the beams or 1 kN/min for the slabs until the peak load was reached. The test was then continued at a displacement rate of 5 mm/min for both sections until: either the tensile reinforcement ruptured in the beam or a deflection of 100 mm was reached in the slab. This 100 mm limit was put in place to protect the instrumentation. The deflections were measured using a string of 5 LVDTs as shown in Fig. 2(a) and 2(c). The crack widths were measured using a handheld optical microscope with a magnification of 220 times at 20, 40 and 60 kN loads for the beams and at 20 and 30 kN for the slabs,

RESULTS

The mid-span load-deflection responses of all members are given in Fig. 3. Further, a summary of the load and deflections at each load increment at which the crack width was measured as well as at reinforcement yield, commencement of concrete crushing and at reinforcement rupture is given in Table 4.

Table 4. Mid-span Load and Deflection at Key Points

		1M:0m		0M:1m		0.5M:0.5m	
Section		Δ_{mid} (mm)	P (kN)	Δ_{mid} (mm)	P (kN)	Δ_{mid} (mm)	P (kN)
Beam	P=20 kN	3.73	20.0	2.53	20.0	3.12	20.0
	P=40 kN	13.5	40.0	8.24	40.0	10.7	40.0
	P=60 kN	23.1	60.0	16.9	60.0	21.4	60.0
	Yield	33.7	78.0	32.9	91.2	31.1	78.6
	Crushing	61.1	81.3	53.3	86.3	56.3	86.0
	Rupture	139	57.4	131	55.1	127	55.3
Slab	P=20 kN	6.55	20.0	4.53	20.0	5.38	20.0
	P=30 kN	17.5	30.0	13.2	30.0	15.8	30.0
	Yield	30.1	36.1	39.2	43.8	32.4	40.9
	Δ_{mid}=100 mm	100	22.7	100	24.8	100	26.9

Note: Δ_{mid} is the midspan deflection and P is the applied load

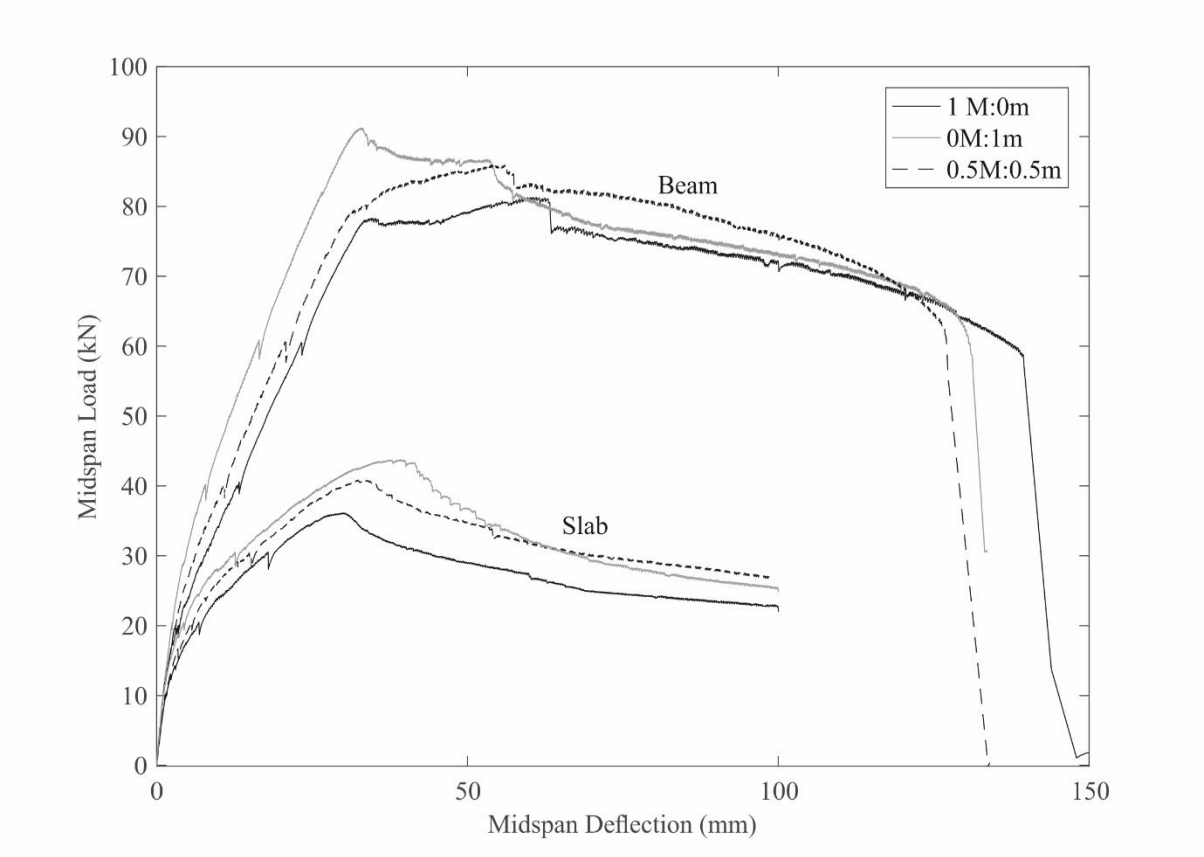

Fig. 3 Mid-span Load-Deflection

From the ascending branches of the load deflection relationships in Fig. 3, it can be seen that replacing micro-fibres with macro-fibres has the following significant effects.

- Reduces the serviceability or ascending branch stiffnesses when the crack widths are small. This is because for a given weight of fibres the macro-fibres have a smaller bonded perimeter than the micro-fibres. Hence their contribution to the axial tensile stiffness will be reduced, at small crack widths, as the stress in a macro-fibre increases more slowly with slip than for micro-fibres (Wille et al. 2012).
- Reduces the moment at yield. This is again because of the reduced bonded perimeter of fibres.
- Increases the deflection at reinforcement fracture that is the ductility. This is because at large crack widths the macro-fibres can span the cracks whilst micro-fibres tend to pull out. Note however that the load carried by the blended mix (0.5M:0.5m) is the greatest after crushing of the concrete. This is due to the micro-fibres contributing at the narrow crack tip while the macro-fibres contribute at the crack mouth.

A summary of the crack widths measured within the central 1 m span of each beam is provided in Table 5. As expected due to the random distribution of fibres and the semi-random nature of cracking the scatter is large (Sturm et al. 2018b). However, it can still be seen that 1M:0m had larger crack widths for every measurement. Furthermore, the maximum crack widths were similar to those of 0.5M:0.5m; this behaviour is to be expected as the inclusion of micro-fibres increases the overall number of fibres crossing a crack and, therefore, it can be expected that the performance during service loading will be improved.

Table 5: Crack Widths

		1M:0m			0M:1m			0.5M:0.5m		
Section	P (kN)	Number of cracks	w_{ave} (mm)	w_{max} (mm)	Number of cracks	w_{ave} (mm)	w_{max} (mm)	Number of cracks	w_{ave} (mm)	w_{max} (mm)
Beam	20	4	0.037	0.047	1	0.016	0.016	2	0.037	0.044
	40	22	0.049	0.162	9	0.027	0.058	23	0.028	0.058
	60	29	0.056	0.166	21	0.047	0.162	31	0.038	0.097
Slab	20	14	0.038	0.119	7	0.026	0.034	10	0.027	0.062
	30	37	0.050	0.329	13	0.060	0.138	20	0.035	0.106

Note: w_{ave} is the average crack width and w_{max} is the maximum crack width

The hinge region at the end of each test is shown in Fig. 4. The beams in Figs. 4(a-c) failed by reinforcement rupture at a large central crack above which minor concrete crushing was observed. In the slabs in Figs. 4(d-f), testing was stopped at a central deflection of 100 mm at which point a large central crack had also occured but there was negligible crushing of the concrete.

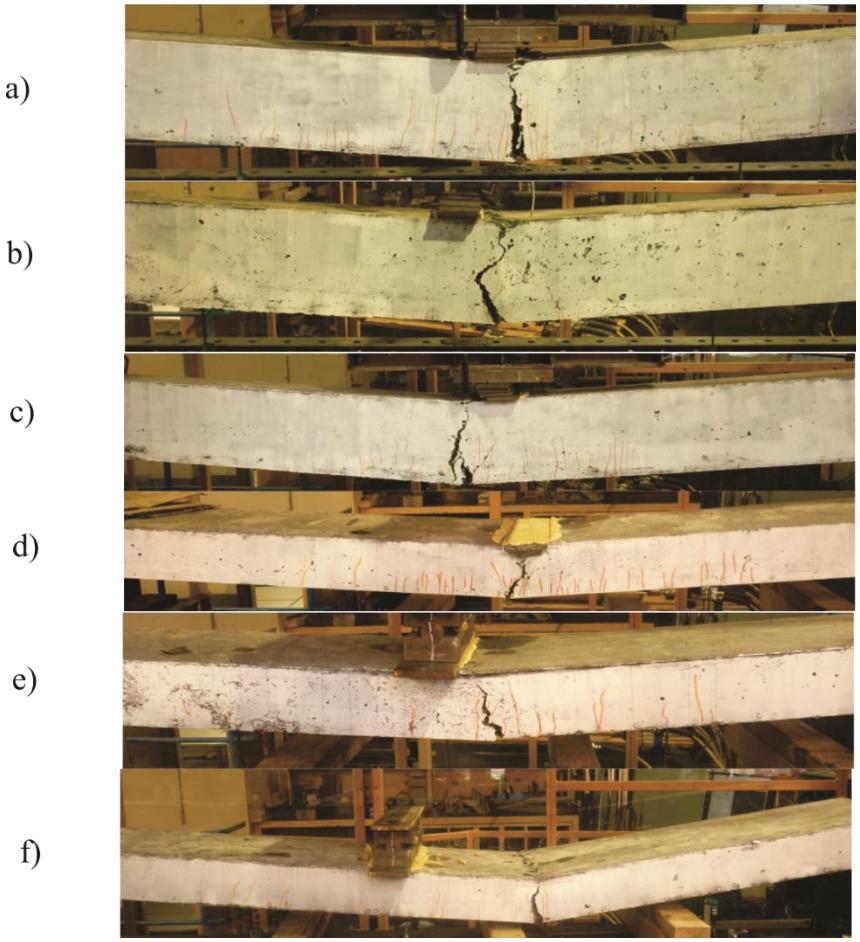

Fig. 4 Hinges at failure: a) 1M:0m (Beam); b) 0M:1m (Beam); c) 0.5M:0.5m (Beam); d) 1M:0m (Slab); e) 0M:1m (Slab); f) 0.5M:0.5m (Slab)

SEGMENTAL ANALYSIS

A displacement based segmental analysis approach for fibre reinforced concrete developed by Visintin & Oehlers (2017) was used in the following analysis as it requires only the input of

basic material properties such as the compressive and tensile stress-strain relationships and the local bond stress-slip relationship. A brief description of the fundamental mechanics of the approach is provided in the following section, but the reader is referred to Visintin & Oehlers (2017) for a full treatment. It should also be noted that a range of other displacement based approaches for the analysis of conventional and fibre reinforced concrete have been developed (Bachman 1971; Bigaj 1998; Schumacher 2006; Visintin & Oehlers 2017), with the main difference being in the level of empirical approximation made in simulating the formation and widening of cracks, tension stiffening and concrete softening.

Consider the segment in the uncracked region of the beam in Fig. 5(a) that is significantly shorter than the span of the beam. In order to determine the sectional properties of the beam, let the segment be subjected to a constant moment such that symmetry around the mid-point of the segment now exists. This allows for the consideration of only the half-segment of length L_{def} as shown in Fig. 5(b). The depth of the neutral axis is d_{NA} and the segment end is rotated about this depth by an angle θ such that the deformation profile along the member depth $D(y)$ is defined.

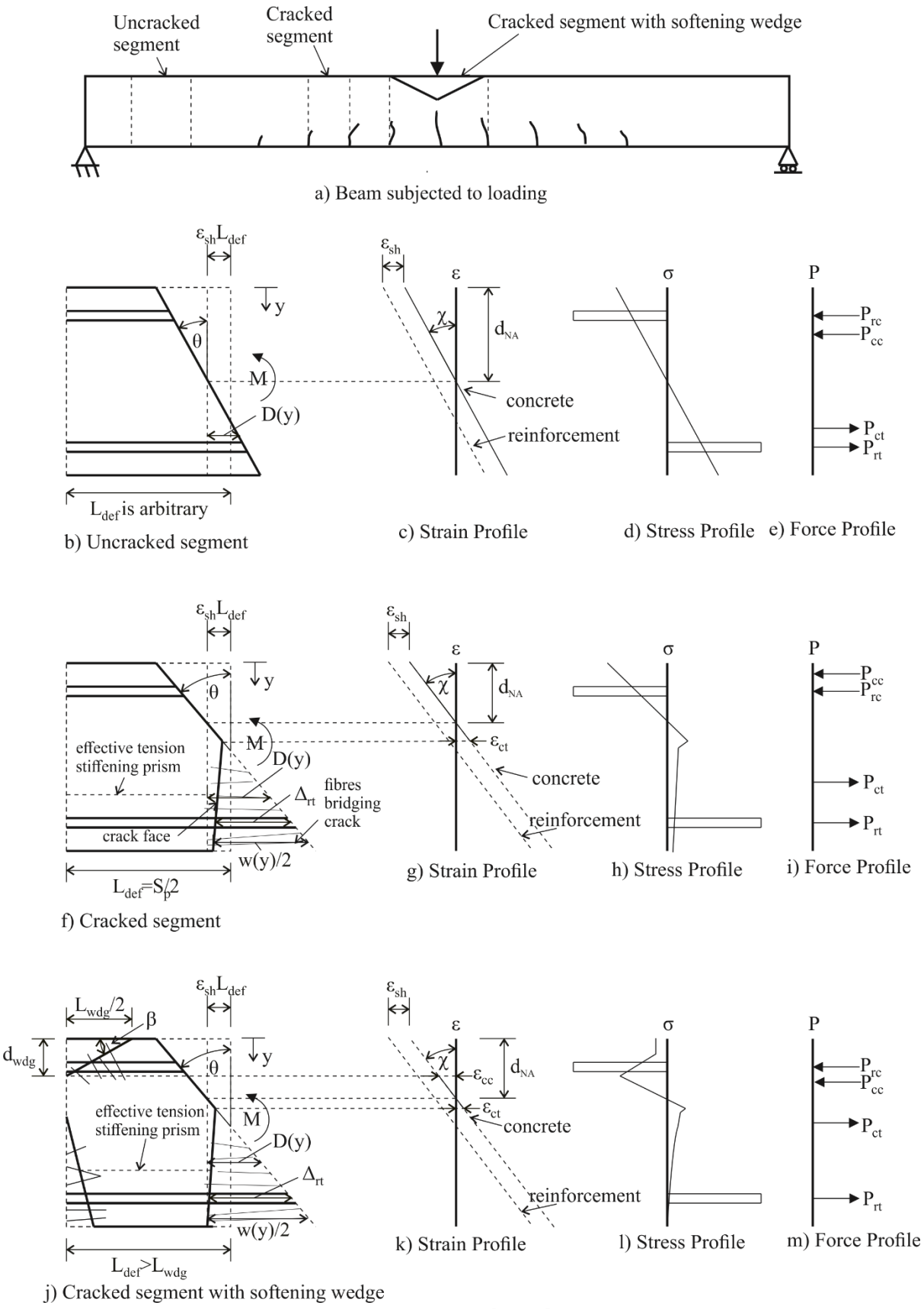

Fig. 5 Segmental Analysis

The strain profile in Fig. 5(c) is simply $D(y)/L_{def}$ and as the segment has been extracted from an uncracked region, the stiffnesses of the reinforcement and concrete in Fig. 1 can now be

used to derive the stress profile in Fig. 5(d). From the stress profile the forces in Fig. 5(e) can be derived, and it is then a matter of adjusting d_{NA} in Fig. 5(b) until longitudinal equilibrium is obtained. This analysis gives the relationship between the segment end rotation θ and the applied moment M. Further, because the curvature χ is θ/L_{def}, the relationship between the curvature and moment, that is, the sectional property, up until a crack forms can also be determined. It is important to note here that because no strain localisations exist, the analysis technique is identical to a standard moment curvature approach and yields identical M/χ relationship regardless of the segment length, hence the segment length at this stage is arbitrary as indicated in Fig. 5(b).

Now consider the cracked segment in Fig. 5(a) of total length equal to the crack spacing S_{cr} such that the deformation length for analysis is $S_{cr}/2$ as in Fig. 5(f). The widening of the crack Δ_{rt} is known to be the result of a build-up of stresses in the tension region through the bond-slip between the reinforcement and the surrounding concrete and will be used directly to determine the force in the tensile reinforcement P_{rt} as described in the following section.

For analysis of the beam segment in Fig. 5(f), a rotation is again applied to the segment end to give the segment deformation $D(y)$. For the compression region and the uncracked tension region, the strain profile in Fig. 5(g) can be determined as for the uncracked region Fig. 5(b) that is material constitutive relationships can be applied to determine the resulting stresses and forces in Figs. 5(h) and (i) respectively. For the cracked concrete in tension in Fig. 5(f), the stress in the concrete can be determined from the deformation profile using the material stress-crack width relationship shown in Fig. 1(b) given a relationship exists between the segment deformation, $D(y)$ and the crack width, $w(y)$. The deformation is given by the addition of the crack opening and the material deformation of the uncracked concrete away from the crack (Hillerborg 1978). That is

$$D(y) = \varepsilon(y)L_{def} = \frac{w(y)}{2}\frac{L_{def}}{\left(\frac{S_{cr}}{2}\right)} + \frac{\sigma_c[w(y)]}{E_c}L_{def} \tag{1}$$

where the first term on the right hand side is the deformation due to crack opening, in which $L_{def}/(S_{cr}/2)$ represents the number of half crack widths in the segment (this allows for concrete crushing where the segment length can extend over multiple crack spacings), and the second term represents the deformation due to the stress in the concrete, $\sigma_c(w)$, which is a function of the crack width and E_c is the elastic modulus of the concrete. In terms of the effective strain Eq. (1) yields

$$\varepsilon(y) = \frac{w(y)}{S_{cr}} + \frac{\sigma_c[w(y)]}{E_c} \tag{2}$$

which can be used to construct a relationship between the effective strain and the crack width by substituting the crack width and corresponding stress for each point in Fig. 1(b) and evaluating the resultant effective strain, $\varepsilon(y)$.

For the reinforcement crossing the crack in Fig. 5(f), the force resisted P_{rt} is a function of the slip of the reinforcement from the crack face Δ_{rt} which can be determined through the application of established partial interaction mechanics (e.g. see Balazs 1993; Haskett et al. 2008; Muhamad et al. 2012; Sturm et al. 2018c) as outlined in the following section. Having now defined all the internal forces in Fig. 5(i), it is again simply a matter of adjusting d_{NA} until force equilibrium is achieved, after which the moment resisted for a given end rotation θ and consequently curvature can be determined. Similarly, the relationship between the moment and the crack width can be determined by evaluating the effective strain at the depth the crack width

is to be evaluated, and then using the relationship defined using by Eq. (2) to find the corresponding crack width.

Partial interaction mechanics to determine crack spacing, S_{cr} and P_{rt}-Δ_{rt} behaviour

To determine the crack spacing S_{cr} and the relationship P_{rt}-Δ_{rt}, consider the tension stiffening prism identified in Fig. 5(f) and with cross-section shown in Fig. 6(a), with the elevation of the tension stiffening prism adjacent to uncracked concrete illustrated in Fig. 6(b) and the elevation of a prism between two adjacent cracks is illustrated in Fig. 6(c). The slip of the reinforcement relative to the concrete in Figs. 6(d) is governed by the slip strain

$$\frac{d\delta}{dx} = \varepsilon_r(x) - \varepsilon_c(x) + \varepsilon_{sh} \tag{3}$$

where $\varepsilon_r(x)$ is the strain in the reinforcement in Figs.6(e),$\varepsilon_c(x)$ is the strain in the concrete in Fig. 6(f) and ε_{sh} is the shrinkage strain. Considering the equilibrium of a single infinitesimal element of length dx extracted from Fig. 6(b-c) and shown in Fig. 6(g), it can be shown that the change in stress across the element is given by

$$\frac{d\sigma_r}{dx} = \frac{\tau(x)L_{per}}{A_{rt}} \tag{4}$$

$$\frac{d\sigma_c}{dx} = -\frac{\tau(x)L_{per}}{A_{ct}} \tag{5}$$

in which L_{per} is the total perimeter length of the reinforcement within the tension stiffening prism, A_{rt} is the total area of reinforcement and A_{ct} is the total area of concrete. In order to ensure that no variation in strain is imposed on the tension stiffening prism, the total height of the prism is taken as twice the cover to the centre of the reinforcement and the width is taken as that of the cross section, as shown in Fig. 6(a).

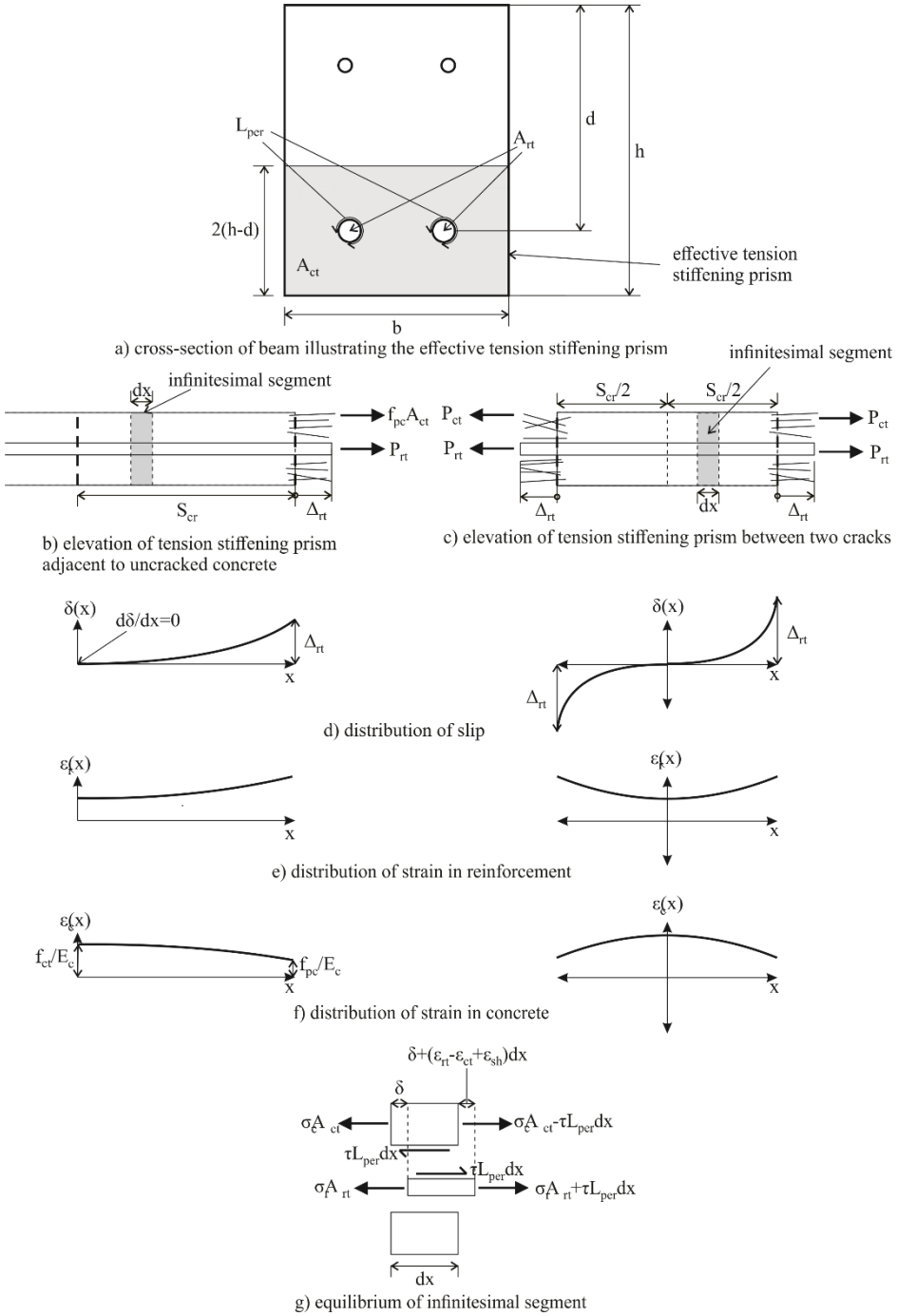

Fig. 6 Analysis of tension chord

For analysis, the three first order differential equations in Eqs. (3-5) can be solved using the initial values for these parameters at the crack face as well as an additional boundary condition depending on the loading scenario. That is to determine the crack spacing S_{cr}, the 'segment adjacent to uncracked region' and extending into the uncracked region in Fig. 6(b) is considered along with the boundary condition that the slip and the slip strain equal zero at the same location and the stress in the concrete is also equal to the tensile strength, f_{ct} at the position of the new crack. Sturm et al. (2018c) solved this problem analytically to yield the following closed form solution for the crack spacing

$$S_{cr} = \left[\frac{2^{\alpha}(1+\alpha)}{\lambda(1-\alpha)^{1+\alpha}}\right]^{\frac{1}{1+\alpha}} \left[\frac{f_{ct}-f_{pc}}{E_c}\left(\frac{E_c A_{ct}}{E_r A_{rt}}+1\right)\right]^{\frac{1-\alpha}{1+\alpha}} \tag{6}$$

where

$$\lambda = \frac{\tau_{max} L_{per}}{\delta_1^{\alpha}} \left(\frac{1}{E_c A_{ct}} + \frac{1}{E_r A_{rt}} \right) \quad (7)$$

and τ_{max} is the maximum bond stress, δ_1 is the slip at the maximum bond stress and α is the non-linearity of the bond stress-slip relationship, f_{pc} is the post-cracking strength, E_c is the elastic modulus of the concrete and E_r is the elastic modulus of the reinforcement. In Fig. 7(a) τ_{max}, δ_1 and α are defined in terms of the diagramatic bond stress-slip relationship and in Fig. 7(b) f_{ct} and f_{pc} are defined in terms of the tensile stress-crack width relationship that is also shown in Fig. 1(b).

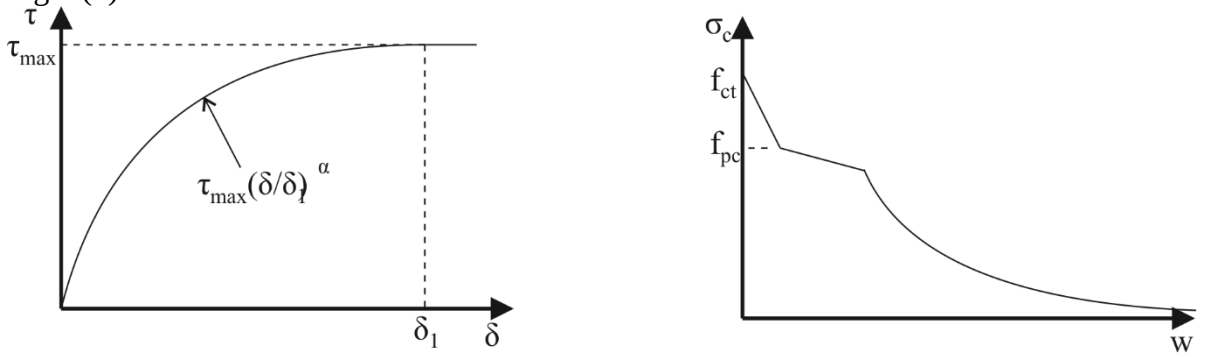

a) Definition of τ_{max}, δ_1 and α from bond stress-slip relationship

b) Definition of f_{ct} and f_{pc} from tensile stress-crack width relationship

Fig. 7 Definition of parameters in crack spacing expression

To determine the P_{rt}-Δ_{rt} relationship, the 'segment between cracks' is considered with the boundary condition that at the mid-point between two cracks the slip is zero, as shown in Fig. 6(c). This procedure to evaluate this relationship is summarised in the flow chart shown in Fig. 8.

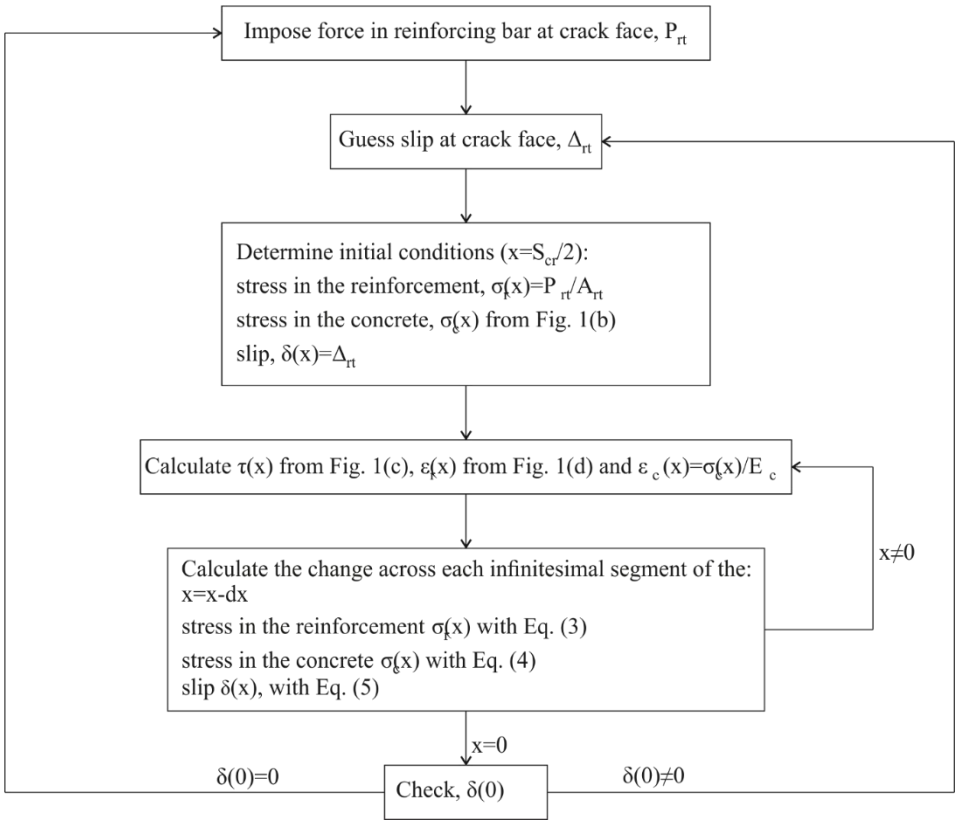

Fig.8: Tension chord analysis procedure

Accommodation of concrete softening

Finally, in order to allow for the formation and sliding of concrete softening wedges in Fig. 5(a), the length of the segment L_{def} is extended to cover sufficient crack spacings such that the wedge length L_{wdg} is encompassed as in Fig. 5(j).

From Fig. 5(j), the depth of the softening wedge is

$$d_{wdg} = d_{NA} + \frac{\varepsilon_{cc}}{\chi} \tag{8}$$

in which ε_{cc} is the strain corresponding to the peak compressive strength f_c.

Based on the depth of the wedge, its length can be determined geometrically as the angle at which it is formed β is known. That is

$$L_{wdg} = \frac{2d_{wdg}}{\tan\beta} \tag{9}$$

in which according to Mohamed Ali et al. (2010)

$$\beta = \arctan\left(-m + \sqrt{m^2 + 1}\right) \tag{10}$$

where m is the slope of the curve relating the shear capacity to the normal stress on the sliding plane. From the shear friction tests conducted by Sturm et al. (2018a) for the same UHPFRC mix design, m is 1.83 hence β is 14°.

Having defined the length of the softening region and consequently L_{def} required for analysis when the concrete is softening, the stress-strain relationship obtained from a standard material prism of height L_{test} can be made size dependent to allow for the change in ductility associated with the length of the softening region L_{def} (Schumacher 2006; Visintin and Oehlers 2018). This size dependent conversion is achieved here using the approach of Chen et al. (2013) as follows

$$\varepsilon_c = \frac{\sigma_c}{E_c} + (\varepsilon_{test} - \sigma_c/E_c)\frac{L_{test}}{L_{def}} \tag{11}$$

in which, ε_{test} is the experimental measured strain and σ_c/E_c is the material strain. The size dependent stress strain relationship is now used in Figs. 5(j-m) to simulate the ductility of the softening region. The procedure is identical to that for the cracked segment in Figs. 5(f-i) described above.

A flow chart outlining the entire analytical procedure described in this section is shown in Fig. 9.

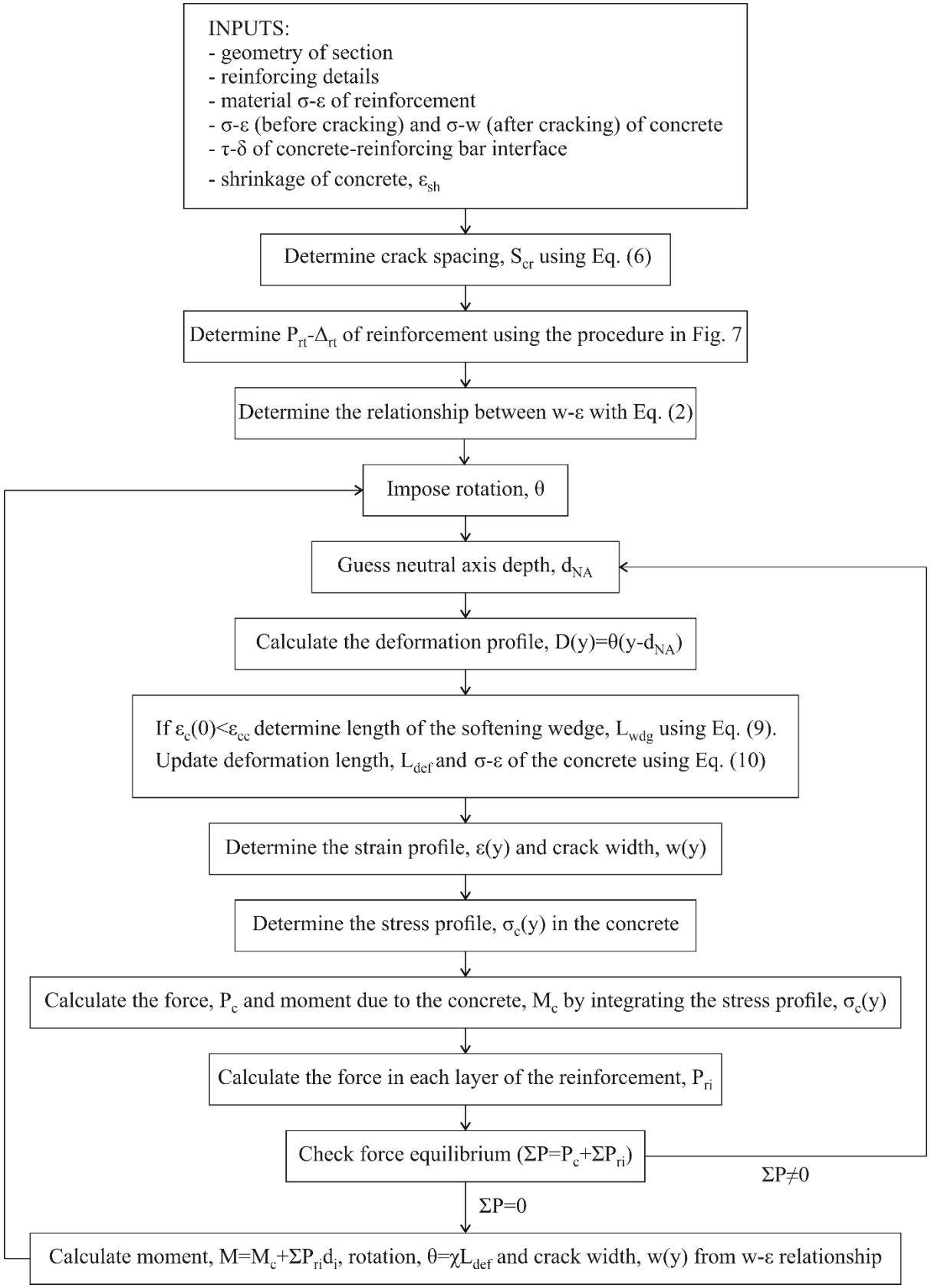

Fig. 9 Procedure for generating moment-rotation, moment-curvature and moment-crack width relationship

VALIDATION

The segmental analysis was used to simulate the tested beams using the material properties in Fig. 1 and Table 1. The load-deflections are compared in Fig. 10 where it can be seen that there is a close correlation. The predicted load-deflections were terminated when the tensile strength of the reinforcement was reached because the length over which necking occurs cannot be predicted. There is a good correlation between the predicted and actual maximum crack widths in Fig. 11 for the slab sections, however for the beam sections, it was found that predictions tended to overestimate the maximum crack width, although, they were closer at lower loads. One cause of this discrepancy is the tendency for secondary cracks to form in between the primary cracks which would decrease crack widths. Scatter of crack widths can also be expected to occur due to the random distribution of fibres within the member.

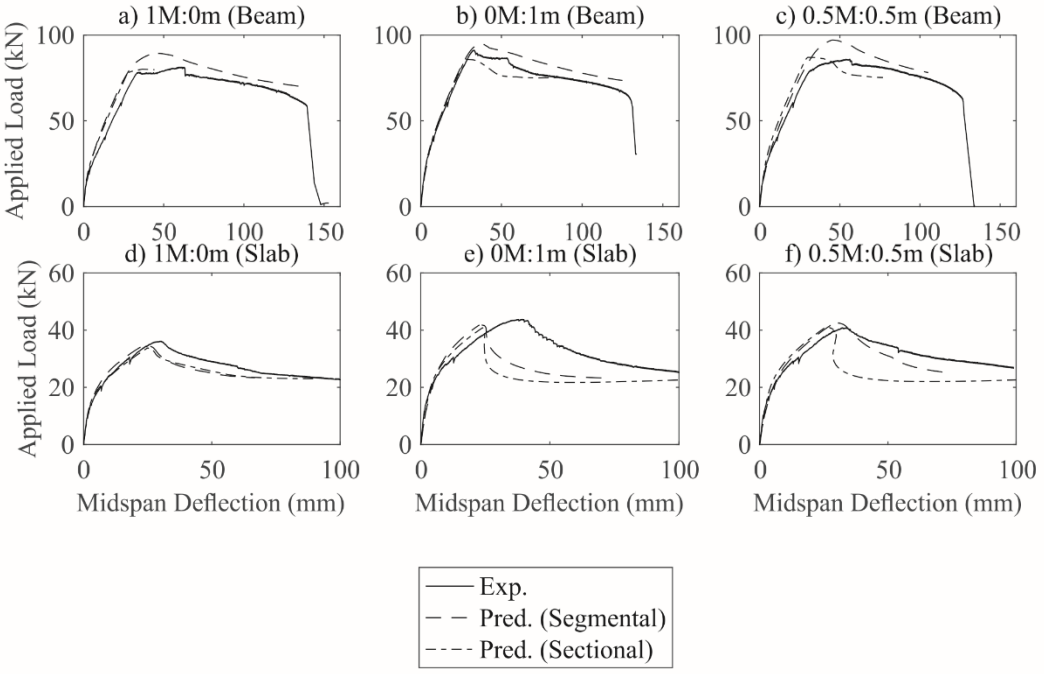

Fig. 10 Predicted to Experimental Load-Deflection

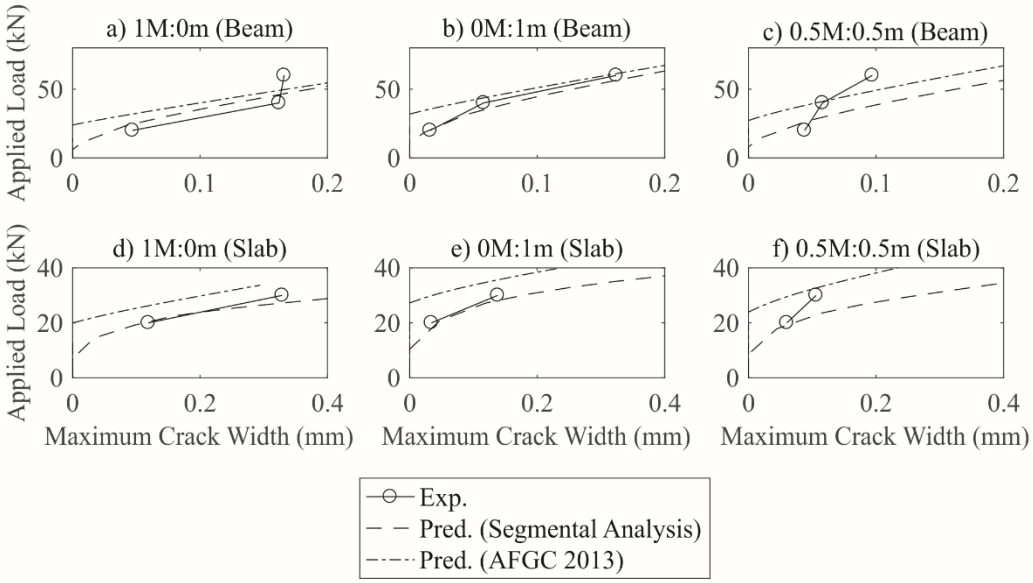

Fig. 11 Predicted to Experimental Load-Crack Width

Of particular importance for the analysis of UHPFRC is the consideration of tension stiffening behaviour post-yield and prior to necking as it was found that bond has a significant impact on the overall strain prior to reinforcement rupture and, therefore, in the prediction of the ductility of the beams. Yielding of the tensile reinforcement results in a reduction of bond stress due to the lateral contraction of the bar. This has been observed experimentally for conventional reinforced concrete structures and many expressions for the reduction of bond after yielding have been suggested (Shima et al. 1987; Sigrist & Marti 1994; Lowes et al. 2004; Ruiz et al. 2007; Wu & Gilbert 2009; fib 2013; Santos & Henriques 2015; Zhou et al. 2017; Malek et al. 2019). No research has however been completed to date on whether this reduction in post-yield behaviour differs for UHPFRC. As no further information was available the expression suggested by Malek et al. (2019) was adopted where the bond stress after yield is given by

$$\tau(\varepsilon_r) = \tau_{max}\left(1 - A\left\{1 - \exp\left[B\left(1 - \frac{\varepsilon_r}{\varepsilon_y}\right)\right]\right\}\right) \quad (12)$$

where A=0.8 and B=0.7 and ε_y is the yield strain. This expression was found to give a close fit for the beam sections, however, for the slab sections the ultimate deflection was underestimated. A better fit was obtained for the slabs when a value of A=1 was used implying that the bond after yielding was lower. The most likely explanation for this discrepancy is the presence of stirrups in the beam section which matches the situation in the tests conducted by Malek et al. (2019). The stirrups allow the transfer of stress between the reinforcement and concrete even when the interface is heavily damaged, hence the bond stress that can be maintained is increased.

Based on the application of the segmental analysis procedure the relative contributions of the fibres and the tensile reinforcement to the tension forces carried by the beams can be determined as shown in Fig. 12. From this it can be seen that the contribution of fibres is greatest before the yielding of the reinforcement and then decreases post yield. This reduction in force carried by the fibres is due to the rapid increase in crack width that occurs at yielding due to the significant rotation that localises at the crack at the centre of the beam (see Fig. 4). It was also found that the contribution of the fibres was greater for the more lightly reinforced slab sections than it was for the more heavily reinforced beam sections. The contribution of the fibres was also greater for mixes containing micro-fibres (0.5M:0.5m and 0M:1m).

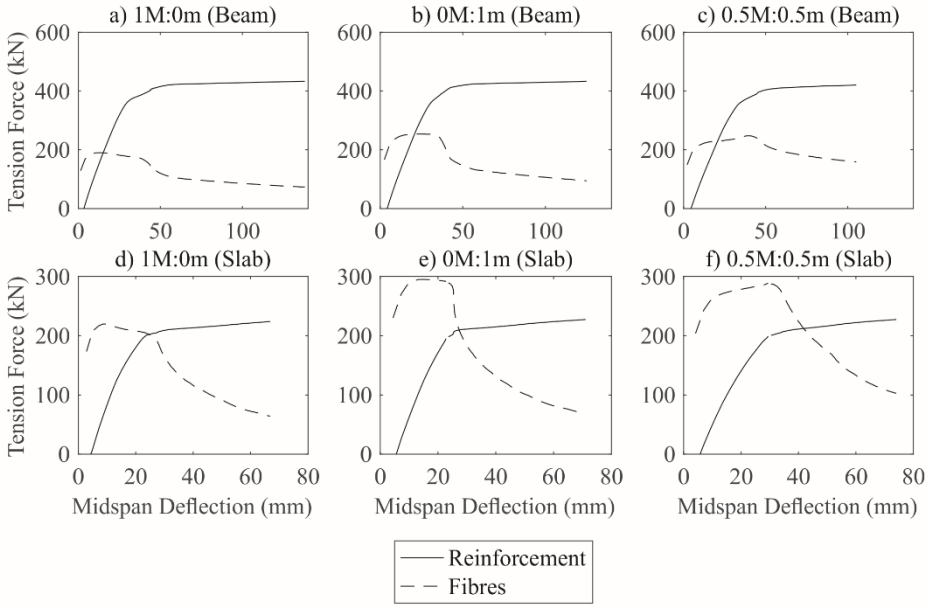

Fig. 12 Relative contribution of reinforcement and fibres

PARAMETRIC STUDY

Having validated the analysis approach in the previous section it is now used to perform a parametric study investigating the effect of varying the depth and reinforcement ratio and whether this modifies the conclusions of the experimental study. In Figs. 13 and 14 the load-deflection and load-crack width relationships are illustrated for the cases where the effective depth, *d* was varied from 202 to 808 mm and the reinforcement ratio, *p* was varied from 1.00% to 3.05%. The span to depth ratio and the ratio of the compressive to tensile reinforcement was kept constant. From this it was found that varying the depth or the reinforcement ratio did not change the conclusions about the effect of fibre type ascertained from the experimental tests.

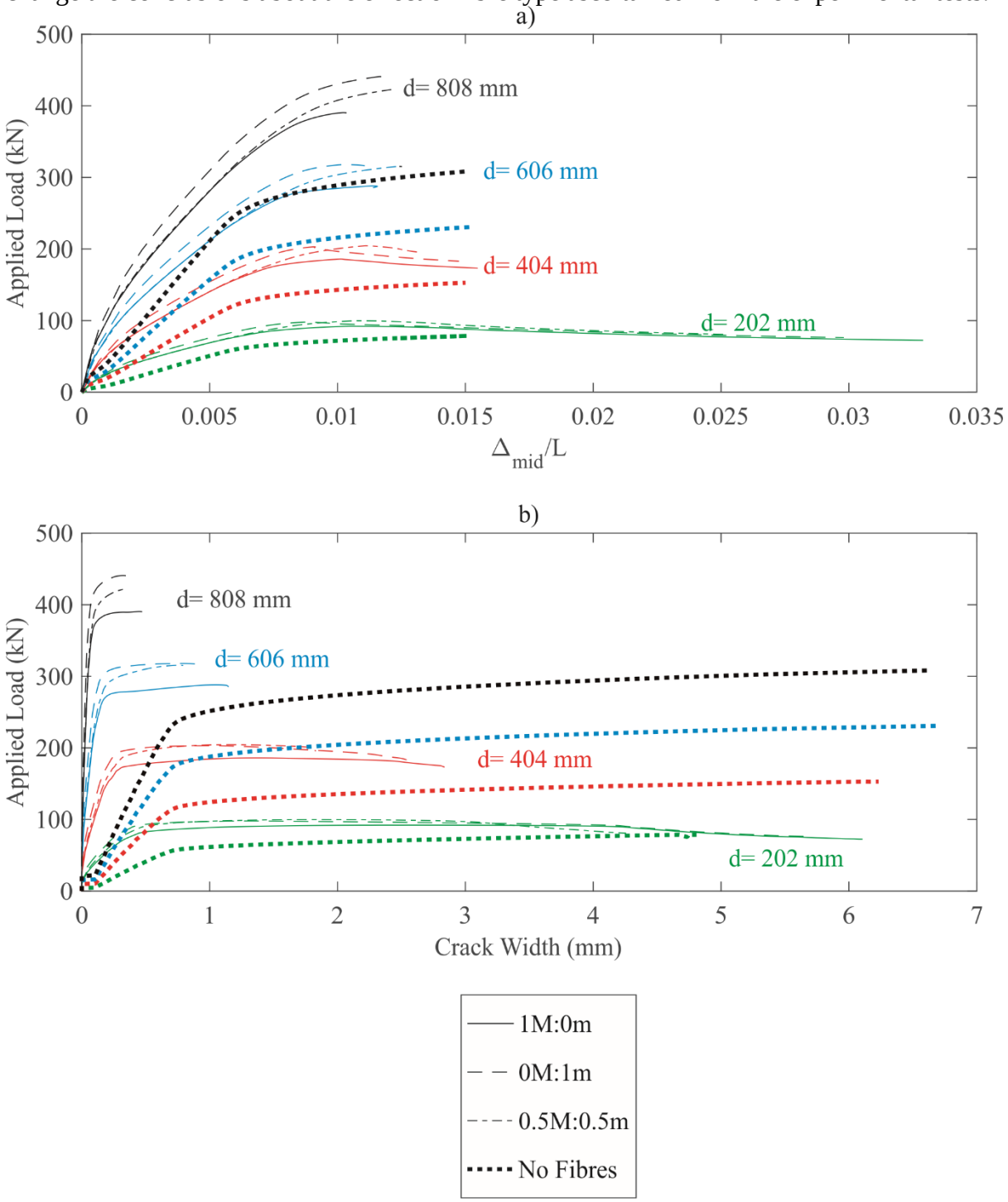

Fig. 13 Effect of depth: (a) load-deflection; (b) load-crack width

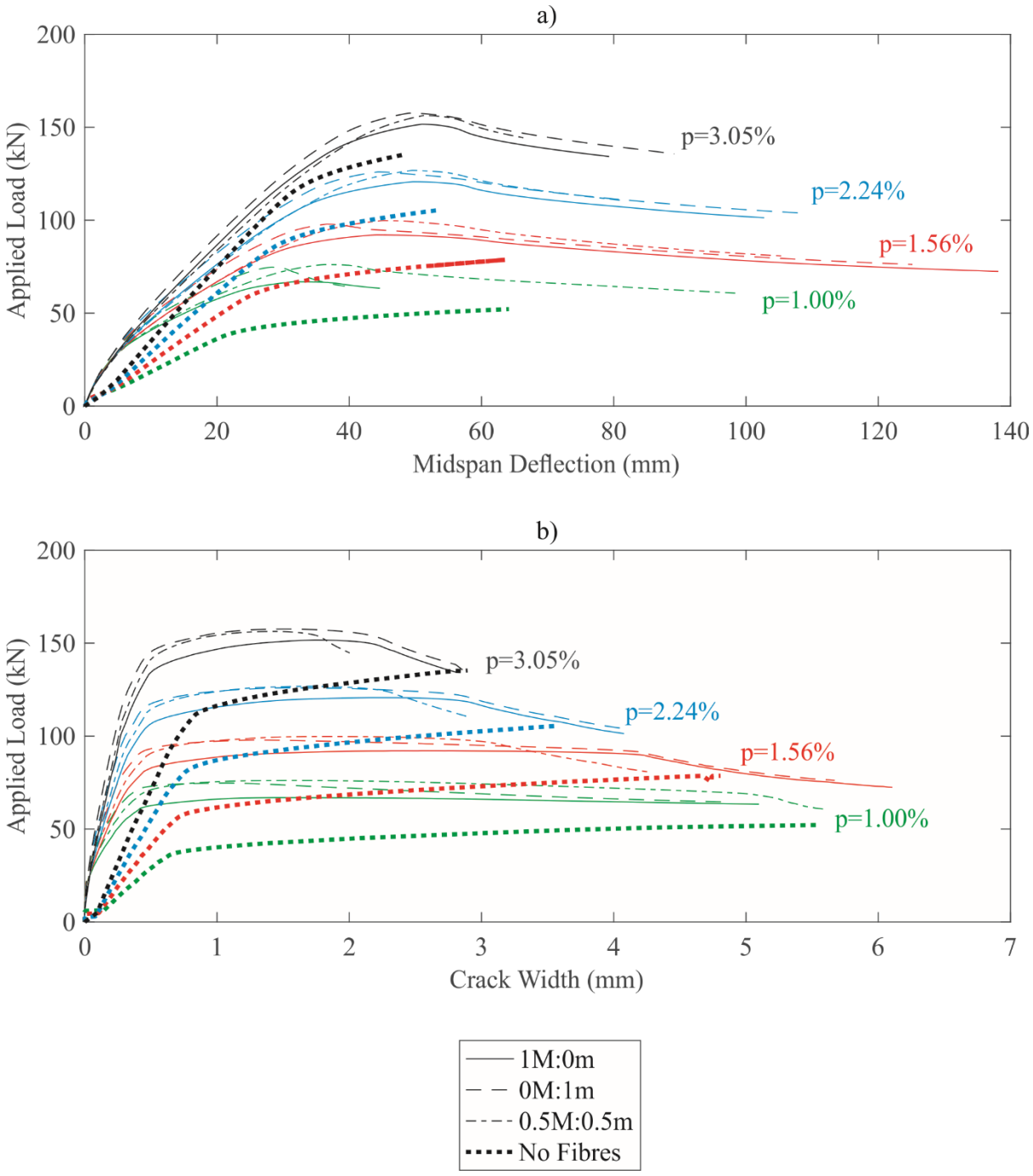

Fig. 14 Effect of reinforcement ratio: (a) load-deflection; (b) load-crack width

As a comparison the segmental approach was also used to simulate a beam without fibres as shown in Figs. 12 and 13. This was performed by assuming that the tensile stress was zero after cracking and the compressive stress was zero after crushing. The concrete strength was assumed to be 160 MPa, the elastic modulus was 48 GPa and the tensile strength was 5.39 MPa as given by Visintin et al. (2018). The efficacy of the fibres in increasing the strength and stiffness of the sections was observed.

From Fig. 13 it was found that increasing the depth of the section reduced the member ductility due to the size-dependence of the compressive stress-strain relationship (Tanigawa et al. 1981; Chen et al. 2013) while the strength and stiffness of the section increased. In Fig. 15 the relative contributions of the reinforcement and fibres are shown, where it is seen that the percentage

contribution of the fibres and reinforcement does not change with depth. The endpoint of the curves in Fig. 15 are achieved when significant crushing has occurred in the compressive concrete and the lack of sensitivity is likely due to the minor impact of fibre blending on the post-softening compressive stress strain behaviour in Fig 1(a).

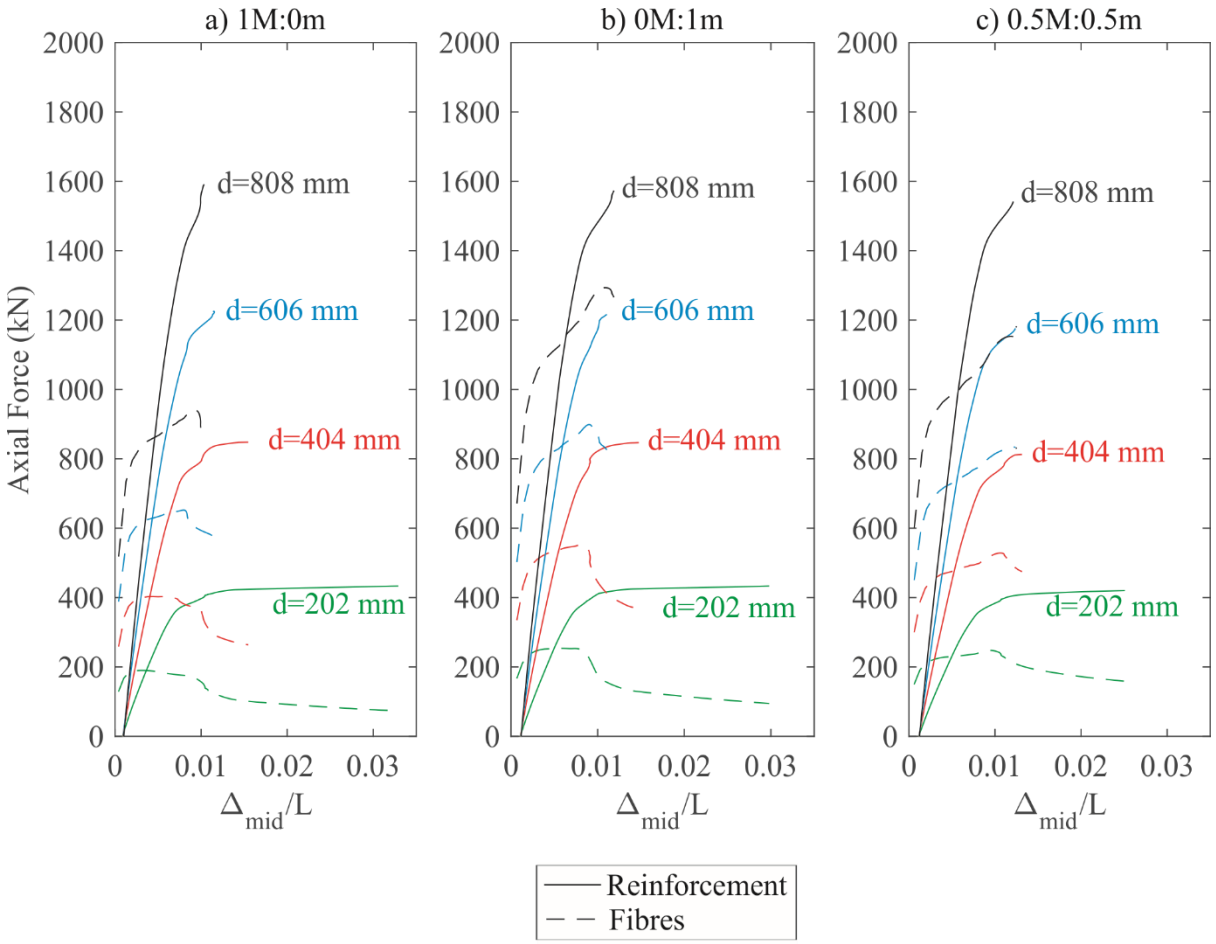

Fig. 15 Relative contribution of reinforcement and fibres when depth is varied

From Fig. 14 it was found that increasing the reinforcement ratio increases the ductility of members that failed by the rupture of the tensile reinforcement, and reduced the ductility decreases of members that failed by compressive concrete crushing. The strength and stiffness increased with increasing quantities of reinforcement.

For sections with low reinforcement ratios, failure is controlled by the rupture of the tensile reinforcement which is a function of the crack width. In this case an increase in reinforcement ratio results in an increase in ductility. This is the case because an increase in reinforcement ratio results in an increase in the neutral axis depth. The result of this is a higher rotation is required in the segment to achieve the same crack width.

However, for sections with higher reinforcement ratios, failure is controlled by concrete crushing which is a function of the strain in the top fibre. As the neutral axis depth increases the curvature required to achieve a given strain at the top fibre decreases, hence a loss in ductility. The different fibre types have limited effect on the neutral axis depth and the crack to cause rupture tensile reinforcement, hence the different types of fibre did not exert significant influence on the ductility in this case.

In Fig. 16 the relative contributions of the fibres and reinforcement are also explored. It is seen that the force carried by the fibres changes negligibly with changes in the reinforcement ratio and a greater proportion of the load is carried by the reinforcement with increasing reinforcement ratio.

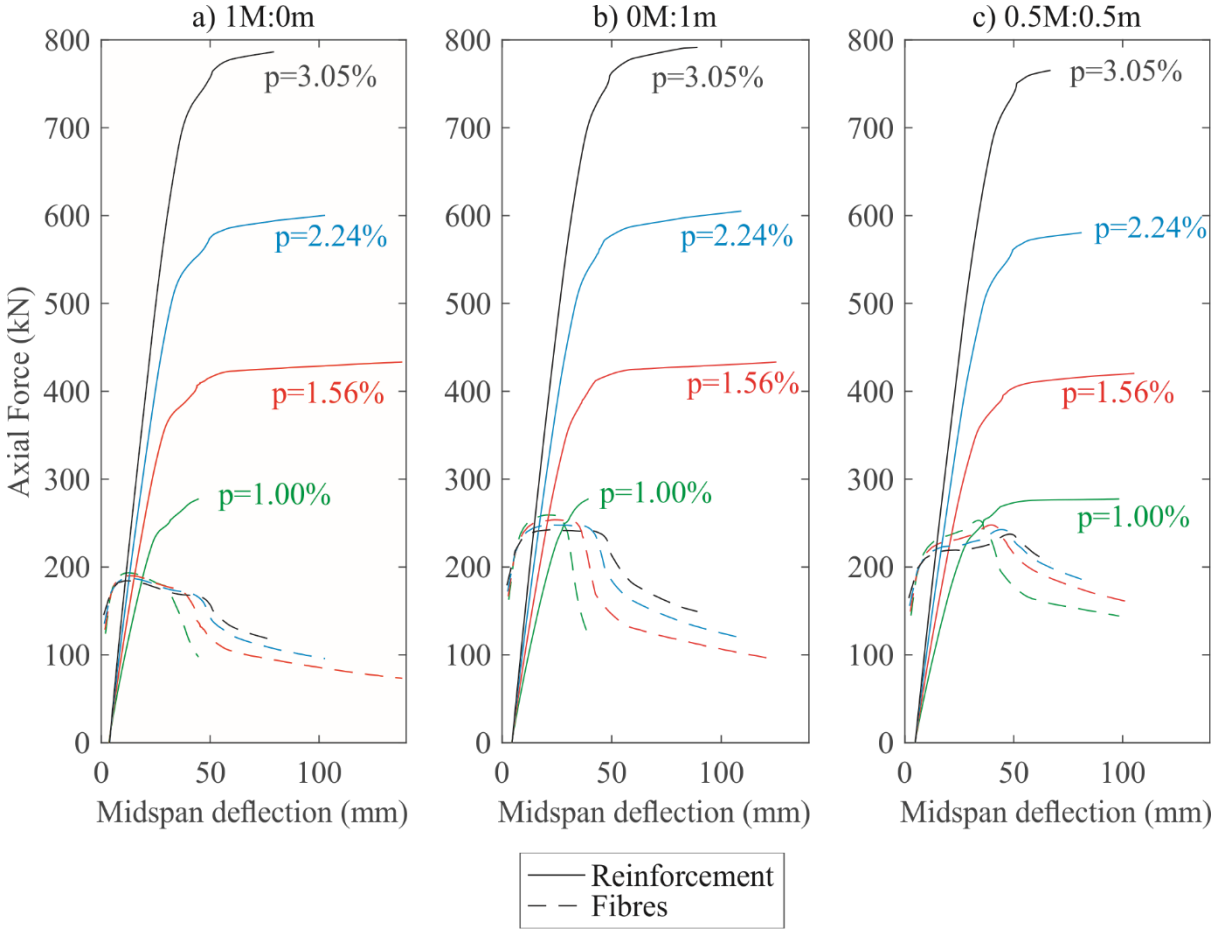

Fig. 16 Relative contribution of reinforcement and fibres where the reinforcement ratio is varied

CONCLUSION

Although the benefits of blending fibres of different sizes has been well established at a material level, to date very little research has considered performance at a structural level. In order to investigate the influence of blending hooked end macro-fibres and straight micro-fibres in UHPFRC a series of six tests were undertaken on slab and beam sections. The results of the experimental work show that members constructed from mixes with only microfibres performed better in terms of increased ultimate strength and reduced deflections and crack widths at serviceability. The substitution of 50% macro-fibres was however found to increase the load that could carried past concrete crushing, although this also reduced the deflection at rupture. In addition to altering mechanical performance, substituting some of the micro-fibres with macro-fibres maybe a valid choice if they improve the economics or reduce the environmental impact of the structure (Stengel & Schieβl 2014).

The results obtained from beam tests were simulated using an established numerical segmental analysis approach capable of predicting both member deflection and crack width. While the segmental approach was shown to be able to simulate behaviour based only on basic material test results (material shrinkage, uniaxial compression, uniaxial tension, bar pullout and direct

tension of the reinforcement) some uncertainty still exists regarding the influence of reinforcement yield on local bond properties. This was found to be particularly important for UHPFRC beams because they are more susceptible to failure by reinforcement rupture rather than concrete crushing. This suggests further research is required to develop a material model for the post-yield bond behaviour of UHPFRC which reflects all the relevant parameters.

Finally a parametric study, was performed to investigate the effect of depth and reinforcement ratio on the behaviour of UHPFRC beams with blended fibres. Varying the depth or the reinforcement ratio did not affect the conclusions regarding the effect of blending fibres. However, a large size effect was predicted on the ductility of UHPFRC beams which should be experimentally verified.

ACKNOWLEDGEMENTS

This material is based upon work supported by the Air Force Office of Scientific Research under award number FA2386-16-1-4098 and Australian Research Council Discovery Project DP190102650. The authors also acknowledge the assistance of Mr Nicholas Burton in measuring the crack widths during the experimental program.

NOTATION

A, B = parameters in post-yield bond stress-reinforcement strain relationship;
A_{ct} = area of tension chord;
A_{rt} = cross-sectional area of reinforcement;
b = width of section;
D = deformation;
d_{NA} = neutral axis depth;
d = effective depth;
d_i = depth of the ith layer of reinforcement;
d_{wdg} = depth of softening wedge;
$d\delta/dx$ = slip strain;
E_c, E_r = elastic modulus of concrete and reinforcement, respectively;
f_c = compressive strength;
f_{ct} = tensile strength;
f_{pc} = post-cracking strength;
h = height of section;
L =span;
L_{def} = deformable length;
L_{per} = bonded perimeter of reinforcement in tension chord;
L_{test} = length of test specimen;
L_{wdg} = length of softening wedge;
M = applied moment;
m = slope of shear strength-normal stress relationship;
M_c = moment in the concrete and the reinforcement, respectively;
P = applied load;
P_c, = axial force in the concrete;
P_{cc} = axial force in the compressive concrete;
P_{ct} = axial force in the tensile concrete;
P_{ri} = azial force in the ith layer of reinforcement;
P_{rc} = axial force in the compressive reinforcement;

P_{rt} = axial force in the tensile reinforcement;
p = reinforcement ratio;
S_{cr} = crack spacing;
V_f = fibre volume
w = crack width;
w_{ave} = average crack width;
w_{max} = maximum crack width;
x= horizontal position
y =depth (with respect to the top fibre);
α = exponent of bond-slip relationship;
β = angle of softening wedge;
Δ_{mid} = midspan deflection;
Δ_{rt} = slip of the reinforcement at crack face;
δ = slip;
δ_1 = slip at maximum bond stress;
ε = effective strain;
ε_c, ε_r =strain in the concrete and the reinforcement, respectively;
ε_{cc} = strain to cause crushing;
ε_{ct} = strain to cause cracking;
ε_{sh} = shrinkage strain;
ε_{test} = strain measured during compression test;
ε_y = yield strain of the reinforcement;
θ = rotation;
λ = bond parameter;
σ_c, σ_r = stress in concrete and reinforcement, respectively;
τ = bond stress;
τ_{max} = maximum bond stress;
χ = curvature;

REFERENCES

Akcay, B., and Tasdemir, M. A. (2012). "Mechanical behaviour and fibre dispersion of hybrid steel fibre reinforced self-compacting concrete." *Construction and Building Materials*, 28(1), 287-293.

Bachmann, H. (1971). "Influence of shear and bond on rotational capacity of reinforced concrete beams." *Bericht Nr. 36,* Eidgenossische Technische Hochschule Zurich.

Balazs, G. L. (1993). "Cracking analysis based on slip and bond stresses". *ACI Materials Journal*, 90, 340-340.

Banthia, N., and Sappakittipakorn, M. (2007). "Toughness enhancement in steel fiber reinforced concrete through fiber hybridization." *Cement and Concrete Research,* 37(9), 1366-1372.

Bigaj. A.J. (1998). "Structural dependence of rotation capacity of plastic hinges in RC beams and slabs", Ph.D. Thesis, Delft University of Technology.

Chen, Y., Visintin, P., Oehlers, D. J., and Alengaram, U. J. (2013). "Size-dependent stress-strain model for unconfined concrete." *Journal of Structural Engineering*, 140(4), 04013088.

Di Prisco, M., Plizzari, G., and Vandewalle, L. (2009). “Fibre reinforced concrete: new design perspectives.” *Materials and Structures*, 42(9), 1261-1281.

Fantilli, A. P., Kwon, S., Mihashi, H., and Nishiwaki, T. (2018). “Synergy assessment in hybrid Ultra-high Performance Fiber-Reinforced Concrete (UHP-FRC).” *Cement and Concrete Composites*, 86, 19-29.

fib (International Federation for Structural Concrete) (2013). “fib Model Code for Concrete Structures 2010.” Lausanne.

Haskett, M, Oehlers, D.J. and Mohamed Ali, M.S. (2008) Local and global bond characteristics of steel reinforcing bars. *Engineering Structures*, 30(2): 376–383.

Hillerborg, A. (1978). “A model for fracture analysis.” *Report No. TVBM-3005*, Lund Institute of Technology.

Katzer, J., and Domski, J. (2012). “Quality and mechanical properties of engineered steel fibres used as reinforcement for concrete.” *Construction and Building Materials*, 34, 243-248.

Kim, D. J., Park, S. H., Ryu, G. S., and Koh, K. T. (2011). “Comparative flexural behavior of hybrid ultra high performance fiber reinforced concrete with different macro fibers.” *Construction and Building Materials*, 25(11), 4144-4155.

Lawler, J. S., Zampini, D., and Shah, S. P. (2002). “Permeability of cracked hybrid fiber-reinforced mortar under load.” *ACI Materials Journal*, 99(4), 379-385.

Lowes, L. N., Moehle, J. P., and Govindjee, S. (2004). “Concrete-Steel Bond Model for Use in Finite Element Modeling of Reinforced Concrete Structures.” *ACI Structural Journal*, 101(4), 501-511.

Malek, A., Scott, A., Pampanin, S., and Hoult, N. A. (2019). “Postyield Bond Deterioration and Damage Assessment of RC Beams Using Distributed Fiber-Optic Strain Sensing System.” *Journal of Structural Engineering*, 145(4), 04019007.

Markovic, I. (2006). “High-performance hybrid-fibre concrete: development and utilisation.” Ph.D. Thesis, Delft University of Technology.

Mohamed Ali, M. S., Oehlers, D. J., and Griffith, M. C. (2010). “The residual strength of confined concrete.” *Advances in Structural Engineering*, 13(4), 603-618.

Muhamad, R., Mohamed Ali, M. S.., Oehlers, D. J., and Griffith, M. C. (2012). “The tension stiffening mechanism in reinforced concrete prisms”. *Advances in Structural Engineering*, 15(12), 2053-2069.

Oh, B. H. (1992). “Flexural analysis of reinforced concrete beams containing steel fibers.” *Journal of Structural Engineering*, 118(10), 2821-2835.

Park, S. H., Kim, D. J., Ryu, G. S., and Koh, K. T. (2012). "Tensile behavior of ultra high performance hybrid fiber reinforced concrete." *Cement and Concrete Composites*, 34(2), 172-184.

Ruiz, M. F., Muttoni, A., and Gambarova, P. G. (2007). "Analytical modeling of the pre-and postyield behavior of bond in reinforced concrete." *Journal of Structural Engineering*, 133(10), 1364-1372.

Santos, J., and Henriques, A. A. (2015). "New finite element to model bond–slip with steel strain effect for the analysis of reinforced concrete structures." *Engineering Structures*, 86, 72-83.

Schumacher, P. (2006). "Rotation capacity of self-compacting steel fiber reinforced concrete." Ph.D. Thesis, Delft University of Technology.

Shima, H., Chou, L. L., & Okamura, H. (1987). "Micro and macro models for bond in reinforced concrete." *Journal of the Faculty of Engineering*, 39(2), 133-194.

Sigrist, V., and Marti. P. (1994). "Ductility of structural concrete: A contribution." *Proc., Workshop: Development of EN 1992 in Relation to New Research Results and to the CEB-FIP Model Code 1990*, Prague, 211–223.

Sobuz, H. R., Visintin, P., Mohamed Ali, M. S., Singh, M., Griffith, M. C., and Sheikh, A. H. (2016). "Manufacturing ultra-high performance concrete utilising conventional materials and production methods." *Construction and Building Materials*, 111, 251-261.

Sorelli, L. G., Meda, A., and Plizzari, G. A. (2005). "Bending and uniaxial tensile tests on concrete reinforced with hybrid steel fibers." *Journal of Materials in Civil Engineering*, 17(5), 519-527.

Stähli, P., and Van Mier, J. G. (2007). "Manufacturing, fibre anisotropy and fracture of hybrid fibre concrete." *Engineering Fracture Mechanics*, 74(1-2), 223-242.

Standards Australia (1997). "Methods of testing concrete-Determination of the static chord modulus of elasticity and Poisson's ratio of concrete specimens." *AS1012.9:2014*, Sydney.

Standards Australia (2001). "Steel reinforcing materials." *AS4671:2001*, Sydney.

Standards Australia (2014). "Methods of testing concrete-compressive strength tests-concrete, mortar and grout specimens." *AS1012.9:2014*, Sydney.

Standards Australia (2015). "Methods of testing concrete-Determination of the drying shrinkage of concrete for samples prepared in the field or in the laboratory." *AS1012.13:2015*, Sydney.

Stengel, T., and Schießl, P. (2014). "Life cycle assessment (LCA) of ultra high performance concrete (UHPC) structures*." Eco-efficient Construction and Building Materials*, 528-564.

Sturm, A. B. and Visintin, P. (2018) "Local bond slip behaviour of steel reinforcing bars embedded in UHPFRC." *Structural Concrete*, 19(2), 508-523.

Sturm, A. B., Visintin, P., Farries, K. and Oehlers, D.J. (2018a) “A new testing approach for extracting the shear friction material properties of ultra-high performance fibre reinforced concrete.” *Journal of Materials in Civil Engineering*, 30(10), 04018235.

Sturm A. B., Visintin P. and Oehlers D. J. (2018b) “Time-dependent serviceability behavior of reinforced concrete beams: Partial interaction tension stiffening mechanics.” *Structural Concrete*, 19(2), 508-523.

Sturm, A. B., Visintin, P., Oehlers, D. J. and Seracino, R. (2018c) “Time dependent tension stiffening mechanics of fibre reinforced and ultra-high performance fibre reinforced concrete.” *Journal of Structural Engineering*, 144(8), 04018122.

Sun, W., Chen, H., Luo, X., and Qian, H. (2001). “The effect of hybrid fibers and expansive agent on the shrinkage and permeability of high-performance concrete.” *Cement and Concrete Research*, 31(4), 595-601.

Tanigawa, Y., Yamada, K. and Hatanaka, S. (1981). “Stress-Strain Behavior of Steel Fiber Reinforced Concrete Subjected to Compressive Load.” *Research Report Faculty of Engineering, Mie University*, 6, 93-106.

Visintin, P., and Oehlers, D. J. (2017). “Fundamental mechanics that govern the flexural behaviour of reinforced concrete beams with fibre-reinforced concrete.” *Advances in Structural Engineering*, 1369433217739705.

Visintin, P., Sturm, A. B., Mohamed Ali, M. S. and Oehlers, D. J. (2018) "Blending macro and micro fibres to enhance the serviceability behaviour of UHPFRC.” *Australian Journal of Civil Engineering*, 16(2), 106-121.

Voo, Y. L., Foster, S. J., and Gilbert, R. I. (2006). “Shear strength of fiber reinforced reactive powder concrete prestressed girders without stirrups.” *Journal of Advanced Concrete Technology*, 4(1), 123-132.

Wille, K., and Naaman, A. E. (2012). “Pullout Behavior of High-Strength Steel Fibers Embedded in Ultra-High-Performance Concrete.” *ACI Materials Journal*, 109(4).

Wu, H. Q., and Gilbert, R. I. (2009). “Modeling short-term tension stiffening in reinforced concrete prisms using a continuum-based finite element model.” *Engineering Structures*, 31(10), 2380-2391.

Zhou, B., Wu, R., and Feng, J. (2017). “Two models for evaluating the bond behavior in pre- and post-yield phases of reinforced concrete.” *Construction and Building Materials*, 147, 847-857.

STATEMENT OF AUTHORSHIP

Flexural performance of pretensioned ultra-high performance fibre reinforced concrete beams with CFRP tendons
Composite Structures, 243, 112223.

Sturm, A. B. (Candidate)

Prepared manuscript, performed all analyses, and developed model and theory (55%)

This paper reports on original research I conducted during the period of my Higher Degree by Research candidature and is not subject to any obligations or contractual agreements with a third party that would constrain its inclusion in this thesis. I am the primary author of this paper.

Signed Date 9/07/2020

Visintin, P.

Supervised and contributed to research, and acted as corresponding author (10%)

I certify that the candidate's stated contribution to the publication is accurate (as detailed above); permission is granted for the candidate in include the publication in the thesis; and the sum of all co-author contributions is equal to 100% less the candidate's stated contribution.

Signed Date 07/07/2020

Seracino, R.

Supervised and contributed to research (10%)

I certify that the candidate's stated contribution to the publication is accurate (as detailed above); permission is granted for the candidate in include the publication in the thesis; and the sum of all co-author contributions is equal to 100% less the candidate's stated contribution.

Signed …….. Date …… July 7, 2020….

Lucier, G. W.

Contributed to research and managed the experimental programme (20%)

I certify that the candidate's stated contribution to the publication is accurate (as detailed above); permission is granted for the candidate in include the publication in the thesis; and the sum of all co-author contributions is equal to 100% less the candidate's stated contribution.

Signed Date ….7/6/2020…..

Oehlers, D. J.

Supervised and contributed to research (5%)

I certify that the candidate's stated contribution to the publication is accurate (as detailed above); permission is granted for the candidate in include the publication in the thesis; and the sum of all co-author contributions is equal to 100% less the candidate's stated contribution.

Signed Date ……7/7/20……

FLEXURAL PERFORMANCE OF PRETENSIONED ULTRA-HIGH PERFORMANCE FIBRE REINFORCED CONCRETE BEAMS WITH CFRP TENDONS

Sturm A. B., Visintin P., Seracino R., Lucier G. W., Oehlers D. J.

ABSTRACT

In this paper, the mechanical performance of pretensioned concrete girders manufactured with ultra-high performance fibre reinforced concrete (UHPFRC) and carbon fibre reinforced polymer (CFRP) tendons is explored both experimentally and analytically. For the experimental investigation, four UHPFRC beams with either steel or CFRP tendons are tested under four point bending to failure. Digital image correlation is used to monitor the development of cracks. These results are then used to validate a rational analysis technique based on the modelling of concrete cracking and crushing through the application of partial interaction mechanics which is then compared to that suggested by codes of practice

INTRODUCTION

High performance materials can be utilized for improved mechanical performance and to extend the service life of concrete bridges. Two materials that are of growing interest in the bridge design community are ultra-high performance fibre reinforced concrete (UHPFRC) and carbon fibre reinforced polymer (CFRP) tendons which can be used to replace conventional concrete and steel tendons in pretensioned concrete girders.

The interest in UHPFRC is largely due to the high compressive strength and durability of the material (AFGC 2013; Thomas et al. 2012). The inclusion of large volumes of fibres may allow for the reduction or removal of shear reinforcement, reduced in service deflections, and reduced crack widths, thereby, simplifying construction and improving performance and durability (Di Prisco et al. 2009; Voo et al. 2006; 2010). As a result of these properties, a number of studies have been presented exploring the flexural (Graybeal 2008; Yang et al. 2011) and shear (Voo et al. 2006; 2010) behaviour of pretensioned UHPFRC beams with steel tendons, including a Type II AASHTO I girder [Graybeal 2008] and a pi girder (Graybeal 2009). Pretensioned UHPFRC girders have also been successfully used to construct a significant number of bridges in Malaysia (Binard 2017).

The main advantage CFRP tendons have with respect to conventional steel tendons is that CFRP tendons are resistant to corrosion [ACI 2004]. This property has resulted in the use of CFRP tendons in the Shinmiya bridge in Japan (Enomoto et al. 2012) and the Baker Street Bridge in Michigan (Grace et al. 2002). The tensile strength of CFRP tendons is also significantly higher than that of steel (Shapack 2015), thereby, allowing for higher compressive stresses to be developed in high strength concretes before failure. Tests have also been performed to investigate the flexural behaviour of pretensioned beams containing CFRP tendons including I-beams (Fam et al. 1997), T-beams (Abdelrahman 15; Grace et al. 2011; Khalafalla 2018), double T beams (Grace et al. 2013), box beams (Grace et al. 2006) and cored slabs (Shapack 2015). In Fam et al. (1997), comparison was made with a beam with steel tendons, and it was found that replacing steel tendons with CFRP tendons increased the ultimate capacity while the ultimate deflection was reduced.

In this paper, the combination of UHPFRC and CFRP is investigated with the motivation of using materials with high compressive and tensile strength to produce a high performance prestressed girder. To date, the only other study known to the authors that explores the

combination of UHPFRC and CFRP is by Stark et al. (2018) who used UHPFRC and CFRP tendons to construct prestressed sandwich panels.

First, an assessment is presented of the mechanical performance of a UHPFRC mix design that meets the minimum 120 MPa requirement for compressive strength set by Canadian and Swiss recommendations (Graybeal et al. 2019). The performance of this material is then characterised in compression, direct tension, indirect tension, bond pullout, and shrinkage tests. Direct tension tests are also used to characterise the steel rebar. Finally, four beams (two with steel tendons and two with CFRP tendons) were tested; where the load-deflection behaviour was recorded, and the formation and widening of cracks were monitored using a digital image correlation (DIC) system.

In the literature, two common approaches are applied to predict the flexural behaviour of prestressed UHPFRC members: a sectional analysis such as in Yang et al. (2011); and a finite element analysis such as in Chen & Graybeal (2011a;b). In this paper, a segmental analysis approach, developed by Knight et al. (2015) for prestressed and post-tensioned normal strength concrete and later extended to conventionally reinforced UHPFRC by Visintin & Oehlers (2017), is further adapted for application to prestressed UHPFRC. Segmental analyses have been widely developed for both conventional and fibre reinforced concretes because, being formulated in terms of displacements rather than strains, the effects of cracking and crushing can be considered directly without the need for experimental calibration. The segmental approach is, therefore, ideal for the rapid application of new materials and, furthermore, can also be solved analytically to develop design approaches (e.g. see Oehlers et al. (2017)). Having described the mechanics and application of the segmental analysis approach, it is then validated based on the experiments performed in this study.

MATERIALS

Mix Design

The UHPFRC mix in Table 1 was designed using materials commercially available for concrete production in North Carolina. Two mix designs are presented: Mix A gives the basic proportions; while Mix B includes the need to add additional mixing water to improve workability halfway through the pour. Importantly, it will be shown that both these mixes achieved a similar compressive strength and hence can be treated as a single mix.

Table 1: Mix Design for UHPFRC

	Unit Weight (kg/m^3)	
	Mix A	Mix B
Cement	973	962
High range water reducing agent	97	96
Water	119	132
Silica Fume	172	170
Fine Aggregate	973	962
Steel Fibres	129	128

The materials used in the UHPFRC mix consist of: a type III cement, as classified by ASTM C150 (ASTM 2019); a densified silica fume meeting the requirements of ASTM C1240 (ASTM 2015); a washed river sand; and a high-range water reducing admixture meeting the requirements for ASTM C494 (ASTM 2017a). The water reducing admixture had a water content of 77.5% and hence the water-to-binder ratio was 0.170 for Mix A and 0.182 for Mix

B. Straight steel fibres with a tensile strength of 2660 MPa, a length of 13 mm and a diameter of 0.2 mm (aspect ratio of 65) were added to the mix at a volume fraction of 1.65%.

Material Properties

Compressive Strength, Elastic Modulus & Poisson's Ratio

The 28 day strengths (ASTM 2017b) were 106 MPa for Mix A and 110 MPa for Mix B. This suggests that the additional water added did not significantly influence the strength. The elastic modulus was 40.6 GPa and the Poisson's ratio was 0.214 based on AS1012.9 (Standards Australia 1997), however, the faster loading rate from ASTM C1856 (ASTM 2017b) was used.

Tensile strength and stress-crack width relationship

The tensile strength and stress/crack-width relationship of concrete was determined by both direct tensile tests and indirect tensile tests on notched prisms. The direct tensile test specimen in Fig. 1(a) is based on that of Visintin et al. (2018), however, the means of transfer of load to the specimen was accomplished through a threaded rod embedded in the end of the specimen rather than by gripping the head of the specimen. Two specimens were tested at a displacement rate of 1.27 mm/min until the stress transferred across the crack approached zero. The stress/crack-width relationship obtained from the tests is shown in Fig. 1b where the mean tensile strength is 6.7 MPa and no strain hardening behaviour was observed.

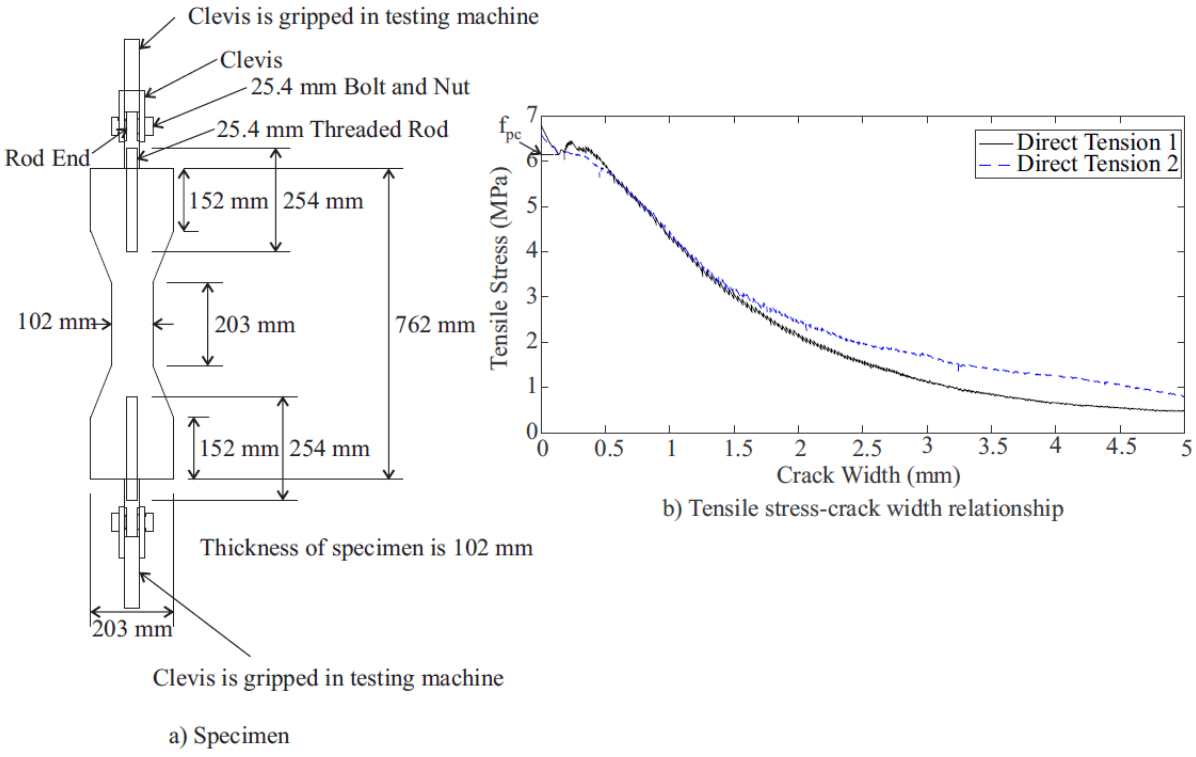

Fig. 1 Direct tension setup

Indirect tension tests were performed on three notched prisms with dimensions of 152x152x508 mm under four point bending where the spacing of the load points was 76 mm. A linear potentiometer was glued across the notch to measure the crack mouth opening displacement. The height of the notch was 13 mm and the width was 3 mm. During testing, load was applied at 110 kN/min until the peak load was reached and then the test continued at an approximate rate of 8 mm/min. The resulting moment versus crack mouth opening displacement is in Fig. 2(a). Inverse analysis according to Annex 3 of the French UHPFRC

recommendations (AFGC 2013) was then applied to obtain the curves in Fig. 2(b). Also in Fig. 2(b), the results of the direct tension tests and inverse analysis tests are compared and it is seen that the indirect test results are an upper bound to the direct tension results.

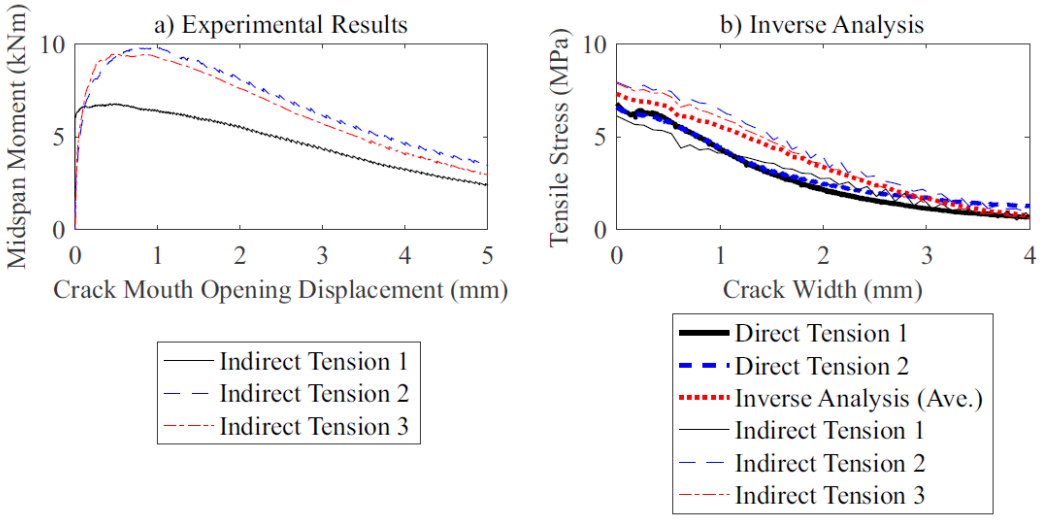

Fig. 2 Indirect tension results

Shrinkage strain

Shrinkage tests were performed according to the requirements of ASTM C157 (ASTM 2017c) on prismatic specimens with dimensions of 50x50x285 mm. The specimens where demoulded and the initial lengths were measured 24 hours after casting. The results of testing are shown in Fig. 3 where it can be observed that, like other UHPFRCs, this material underwent significant early age shrinkage that has implications for prestressing.

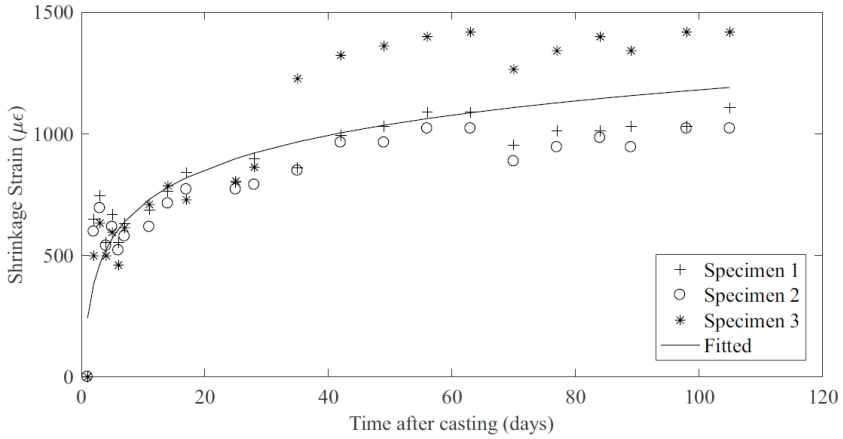

Fig. 3 Evolution of shrinkage

Reinforcement stress strain behaviour

The beams were prestressed with either a 15.2 mm diameter ASTM A416 Grade 270 (ASTM 2018) steel tendon or a 15.2 mm diameter carbon fibre composite cable (CFCC) tendon and were also reinforced with 9.5 mm and 12.7 mm diameter ASTM A706 (ASTM 2016) steel reinforcement. Note that the CFCC tendon was the type of CFRP reinforcement that was used. The steel reinforcement was tested under direct tension at a rate of 7.6 mm/min. During testing, the deformation was measured using an extensometer up until yield, after which the displacement was measured using the inbuilt machine instrumentation. No tests were performed on the CFRP tendons as previous results obtained by Shapack (2015) on the same material were available for use in the subsequent analysis.

The properties of the reinforcement and the tendons are summarised in Table 2 where E is the elastic modulus, f_y the yield strength, f_u the ultimate tensile strength and ε_u is the strain when the ultimate tensile strength is reached. The ultimate properties of the steel tendon were not measured as the tendons tested for material properties failed due to stress concentrations at the grip. As an estimate, the ultimate strain was assumed to be 0.05, the minimum typical value given by PCI Design Handbook (2010), and, extrapolating from the experimental results, the associated ultimate stress was 2030 MPa.

Table 2: Mean Material Properties of the Reinforcement

	E (GPa)	f_y (MPa)	f_u (MPa)	ε_u
15.2 mm Steel Tendon	199	1820	[a]	[a]
15.2 mm CFRP Tendon	152[b]	N/A[c]	3175[b]	0.021[b]
12.7 mm Steel Rebar	187	520	722	0.098

[a] Specimens failed prematurely in chuck.
[b] from Shapack (2015)
[c]CFRP is linear elastic until failure

Bond stress-slip relationship

Pullout tests were performed to assess the bond between the reinforcement and the concrete for both the rebar and the tendons. The pullout test setup for the steel rebar and steel tendon is shown in Fig. 4(a) and that for the CFRP tendon in Fig. 4(b). The prism had dimensions of 152x152x152 mm and the reinforcement had a bonded length of 19 mm (1.5 bar diameters). The bonded length of the tendon was 32 mm (2 bar diameters) and PVC pipe was used as a bond breaker above and below bonded region. Note that due to the low transverse strength of the CFCC, the tendon could not be gripped directly. Instead, a steel pipe was bonded to the tendon with epoxy, which could then be gripped. During testing, a load cell was used to record the applied load and two linear potentiometers were used to monitor the slip of the reinforcement from the free end. A load rate of 15 kN/min was applied until the peak load was reached, and then a displacement rate of 7 mm/min was applied until the end of the test.

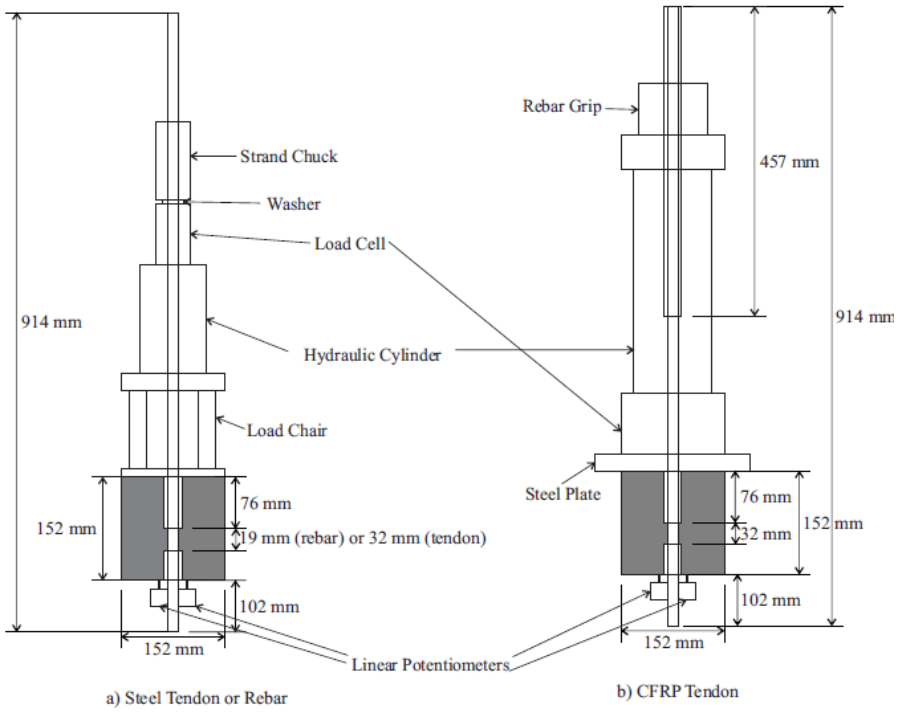

Fig. 4 Pullout test setup

The pull test results are given in Fig. 5 where the bond stress was calculated by assuming that the slip was uniform along the bonded length such that the bond stress is equal to the average bond stress recorded. It can be seen in Fig. 5 that the shape of the bond stress-slip relationship differs significantly between the different types of reinforcement. For the steel reinforcement, the shape is similar to that in the fib Model Code 2010 (fib 2013). For the CFRP tendon, the relationship is approximately linear descending with a peak at a very low slip followed by gradual softening. For the steel tendon, there is an initial peak followed by a sharp decrease, after which the bond stress gradually increases and then gradually decreases. Note that these tests represent a lower bound on the bond stress in the tendons because the confinement generated as the tendons expand upon release of prestress (Hoyer effect) is not considered (Hoyer & Friedrich 1939).

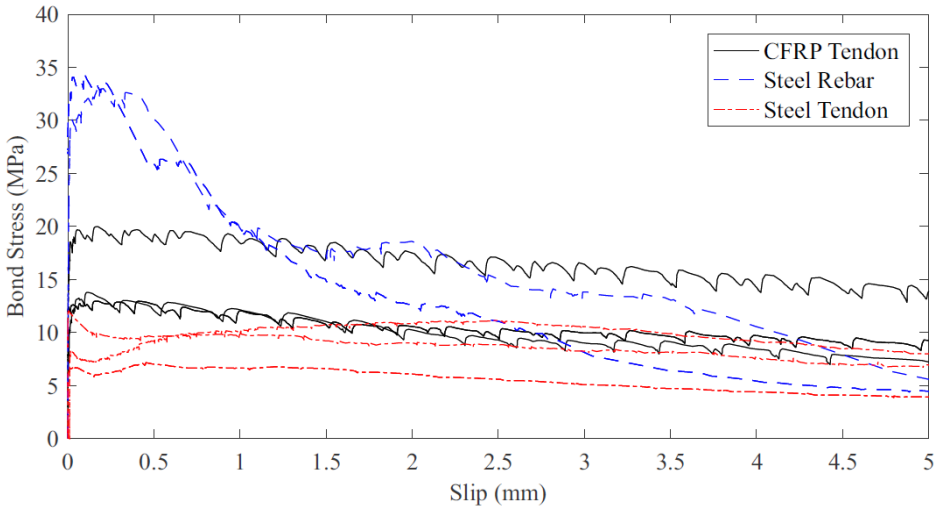

Fig. 5 Bond stress vs. Slip

CONSTRUCTION & TESTING OF THE BEAMS

Four large-scale beams shown in Fig. 6 were cast. The beams had a rectangular cross section to simplify construction and were reinforced with closely spaced stirrups to prevent shear failure. For all beams, the prestressed reinforcement was 0.17% of the cross-section and the non-prestressed tensile reinforcement at the bottom face comprised a further 0.31% of the cross-section. The compressive reinforcement was also 0.31% of the cross-section. Two replicates of each beam were manufactured and tested in order to provide an indication of the scatter in load deflection and load crack width behaviour arising from the local variation in fibre distribution.

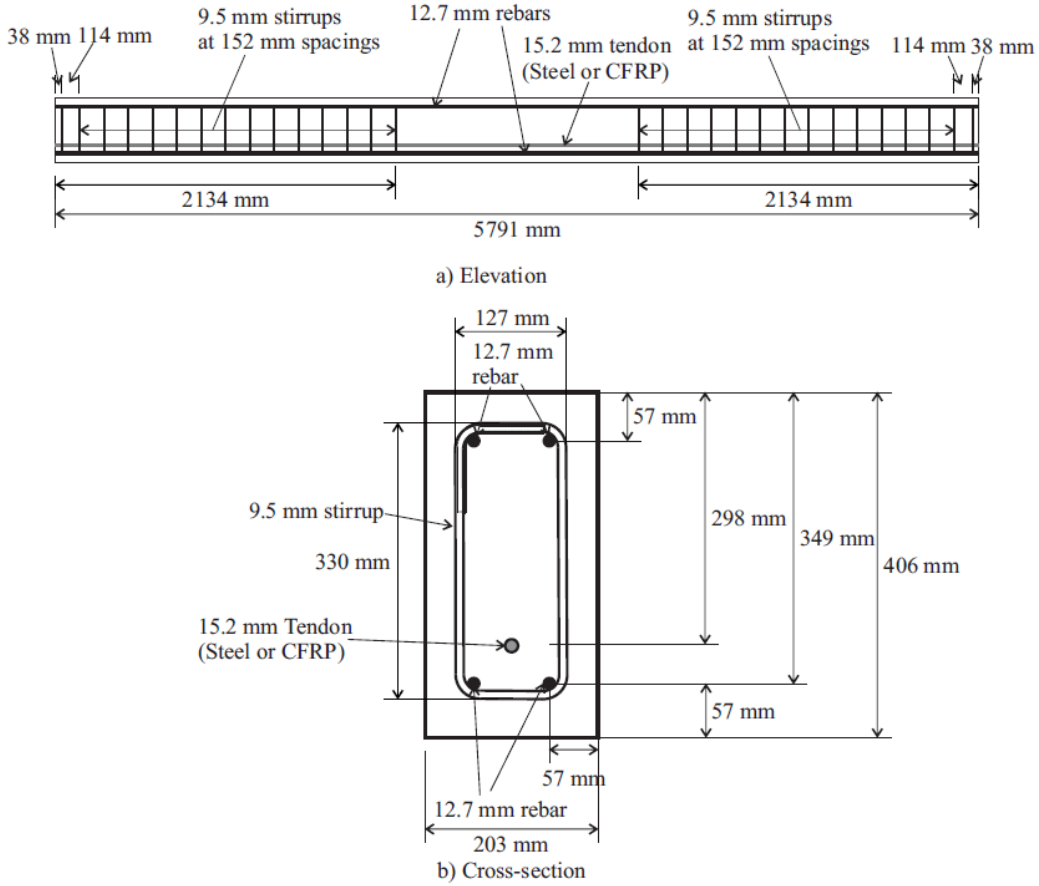

Fig. 6 UHPFRC Beam: a) elevation; b) cross-section

Prior to casting, both the steel and CFRP tendons were stressed with an initial jacking force of 176 kN. At the time of transfer this prestressing force was 156 kN. The initial jacking force was chosen to be 65% of the guaranteed breaking load for the CFRP tendon (270 kN), which corresponds to the maximum jacking force recommended by ACI 440.4R (ACI 2004) for this material.

For casting, 2.6 m^3 of UHPFRC was mixed in a conventional truck-mounted drum mixer. To do so, sand was added to the drum, followed by the superplasticiser and the first 144 litres of water. The cement and silica fume were then added followed by the final 38 litres of water. The concrete was mixed for 15 minutes until a flowable mixture was obtained. Steel fibres were then added to the truck over a period of 20 minutes to avoid balling. Mixing continued for a further 5 minutes to ensure the fibres were well combined. The concrete was poured from the chute of the truck into the forms and mild vibration with a stick vibrator was applied as the

mix compacted under its self-weight. As described in the section on the mix design, due to a loss of workability, an additional 19 litres of water was added to the material remaining in the drum after casting the first two beams.

Following casting, the beams were allowed to cure for three days under wet burlap and plastic upon which a compressive test indicated that a concrete strength of 92 MPa had been achieved. An oxy-acetylene torch was then used to cut the tendons from the abutments, thereby releasing the prestressing. The beams were subsequently demoulded and allowed to cure under wet burlap and plastic for a further five days. All curing occurred inside the conditioned laboratory at ambient temperatures.

Member testing

Figure 7 shows a schematic of the test setup, with each beam having a clear span of 5490 mm. Beams were tested in four-point bending with a constant moment region of 1830 mm. The load was applied by a 1000 kN, 500 mm stroke actuator with an integral load cell and all tests were performed in displacement control at a rate of 2.5 mm/min until the prestressing tendon ruptured. To measure member deflection, three string potentiometers were located within the constant moment region. Additionally, the constant moment region was painted with a speckle pattern so that two cameras (each capturing half the constant moment region) could measure local behaviour using digital image correlation (DIC). Each camera had a resolution of 16 megapixels and the images were recorded at a rate of 1 Hz.

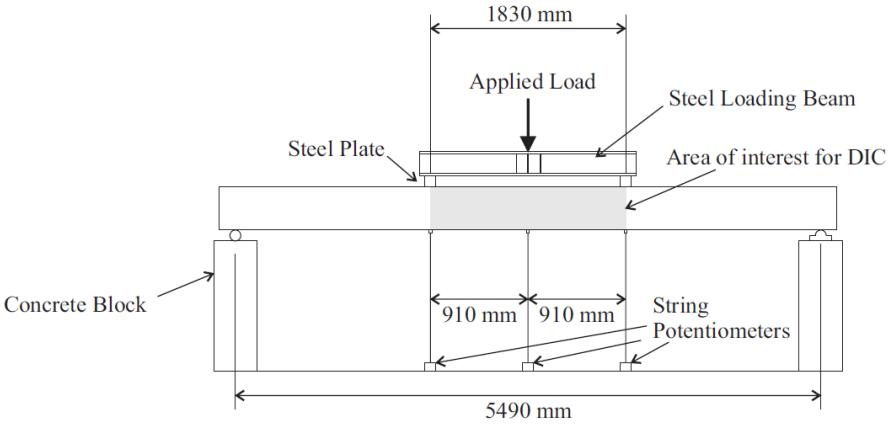

Fig. 7 Test setup

TEST RESULTS

The load-deflection recorded by the mid-span potentiometer is shown in Fig. 8(a). The load and deflection corresponding to the load to cause cracking, the peak load and the load at failure are given in Table 3. The constant moment regions at failure are shown in Figs. 8(e-h).

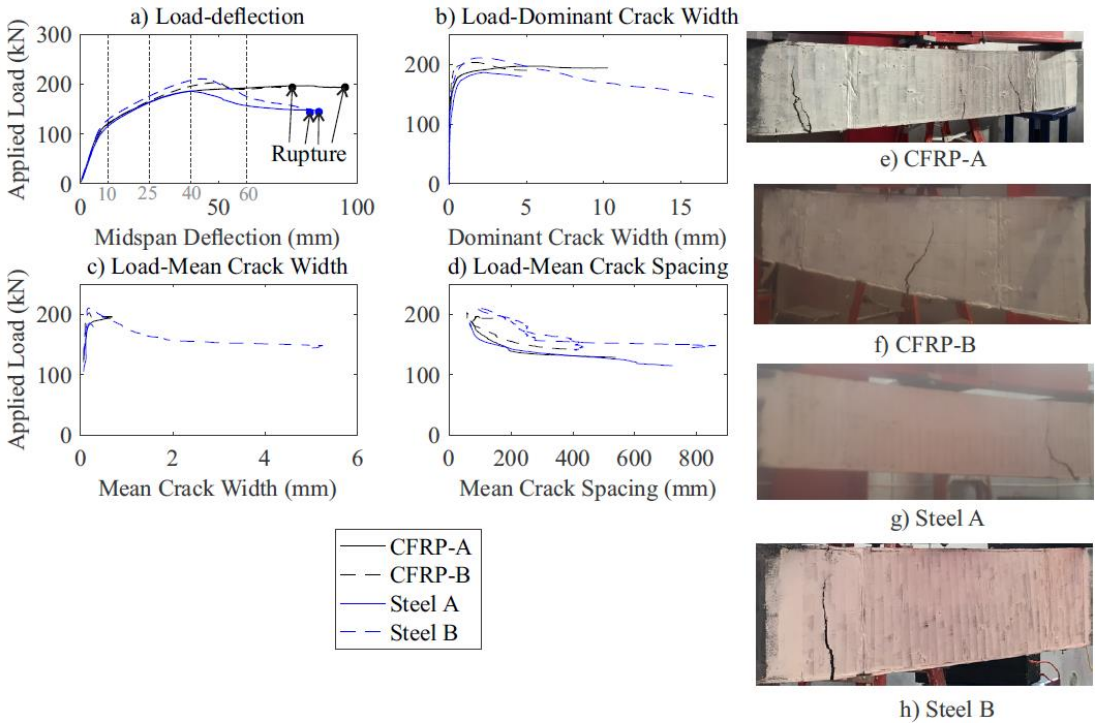

Fig. 8 Results of Beam Test

There are no significant differences prior to the peak loads in Table 3 when comparing members with either CFRP or steel tendons. However after the peak loads are achieved in Fig. 8(a), the beams with steel tendons have a significant reduction in applied load which is not observed for the beams with CFRP tendons. For example from Table 3, the load at failure for the beams with steel tendons is between 68% and 77% of the peak load while that for the beams with CFRP tendons is between 95% and 98%. Consequently, the load carried by the beam reinforced with CFRP tendons is 36% greater than that for a steel reinforced beam just prior to tendon rupture. This difference can be explained by the reduction of stiffness of the steel tendon after yielding, which means the force in the tendon cannot increase at a sufficient rate to compensate for the decrease in the stress carried by the fibres as they pullout. As there is no yield for the CFRP tendon, there is no reduction in stiffness, and hence, the force carried by the tendon increases to compensate for the loss of stress in the fibres.

In Table 3, the cracked stiffness of the ascending branch is also compared between the beams which is computed as the slope of the line on the load-deflection plot between the point of cracking and the position at which the slope of the line changes which is at a midspan deflection of approximately 40 mm. From this, the cracked stiffness of the section reinforced with CFRP tendon is 90% of the steel reinforced section. The ductility factors are also computed using the methodology outlined by Naaman & Jeong (1995). From this result, the average ductility factor for the CFRP reinforced beams was 66% of that for the steel beams. The elastic energy associated with the CFRP reinforced beams is higher with the average total energy increasing by 10% for the beams with CFRP tendons.

Table 3: Key Points

Tendon		CFRP		Steel	
Mix		A	B	A	B
Cracking	Δ_{mid} (mm)	5.1	5.7	4.6	5.3
	F (kN)	85	88	70	90
Peak Load	Δ_{mid} (mm)	82.0	49.0	39.8	43.7
	F (kN)	197	203	186	211
Rupture	Δ_{mid} (mm)	95.6	76.5	82.9	86.1
	F (kN)	194	194	143	144
Cracked Stiffness (kN/mm)		2.89	3.15	3.28	3.40
Total Energy at Failure (kJ)		16.2	12.7	12.2	14.1
Ductility Factor		4.46	3.41	5.15	6.81

The DIC records the longitudinal strains along the surface of the beam, allowing for easy identification of crack formation and continuous measurement of crack width. The longitudinal strain fields are shown in Fig. 9 for the beams with CFRP tendons and in Fig. 10 for those with steel tendons for specific deflections. These deflections are shown in Fig. 8(a) as the dashed vertical lines. Very large strain regions represent cracks and the strains themselves represent the crack width. Videos demonstrating the continuous change in the longitudinal strain field are also available in the supplementary material. Note that recording of the image files terminated after 1405 seconds of testing for CFRP-B and after 1067 seconds for Steel-A, so DIC results are only available to those points.

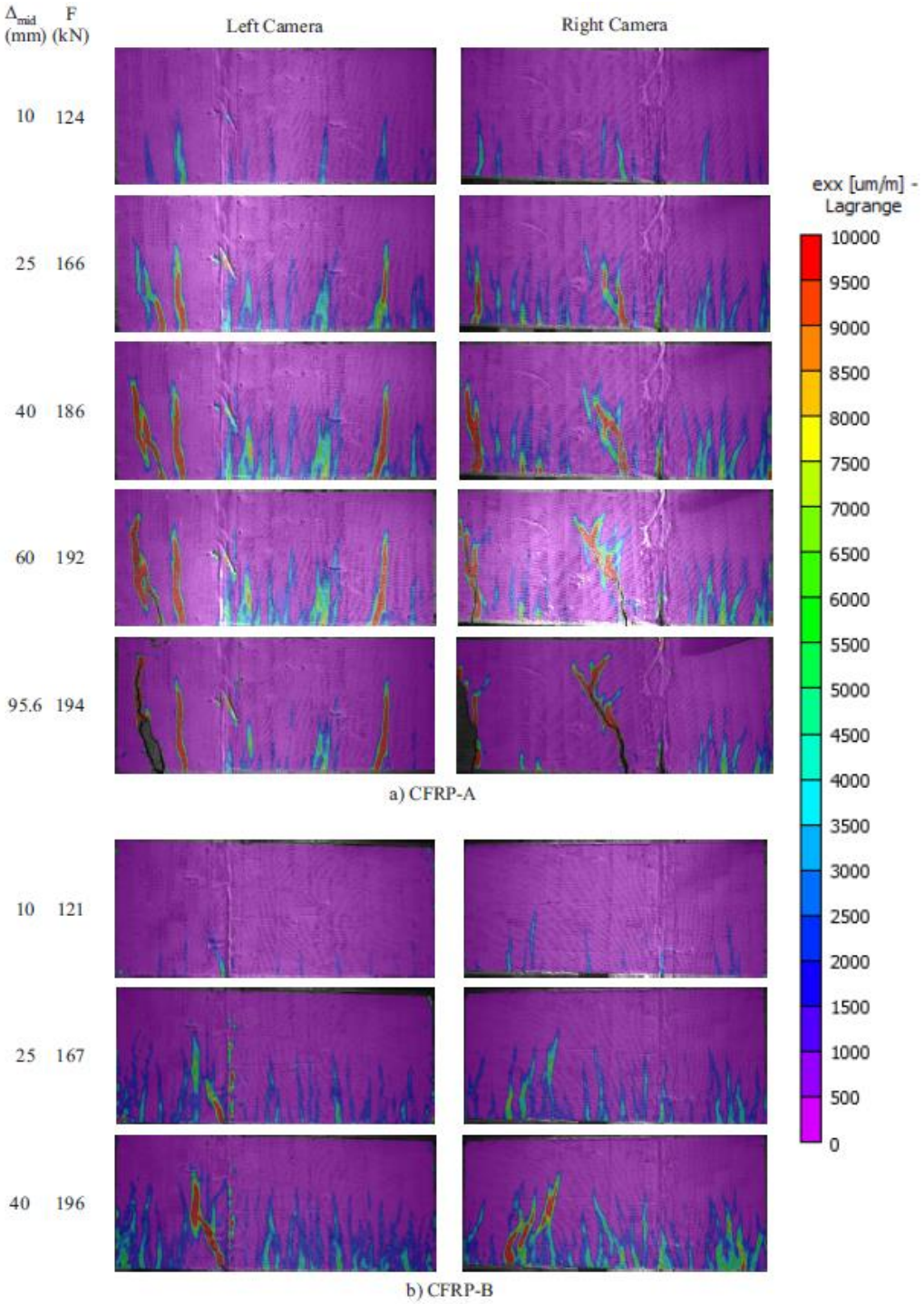

Fig. 9 Longitudinal strain field for beams with CFRP tendons

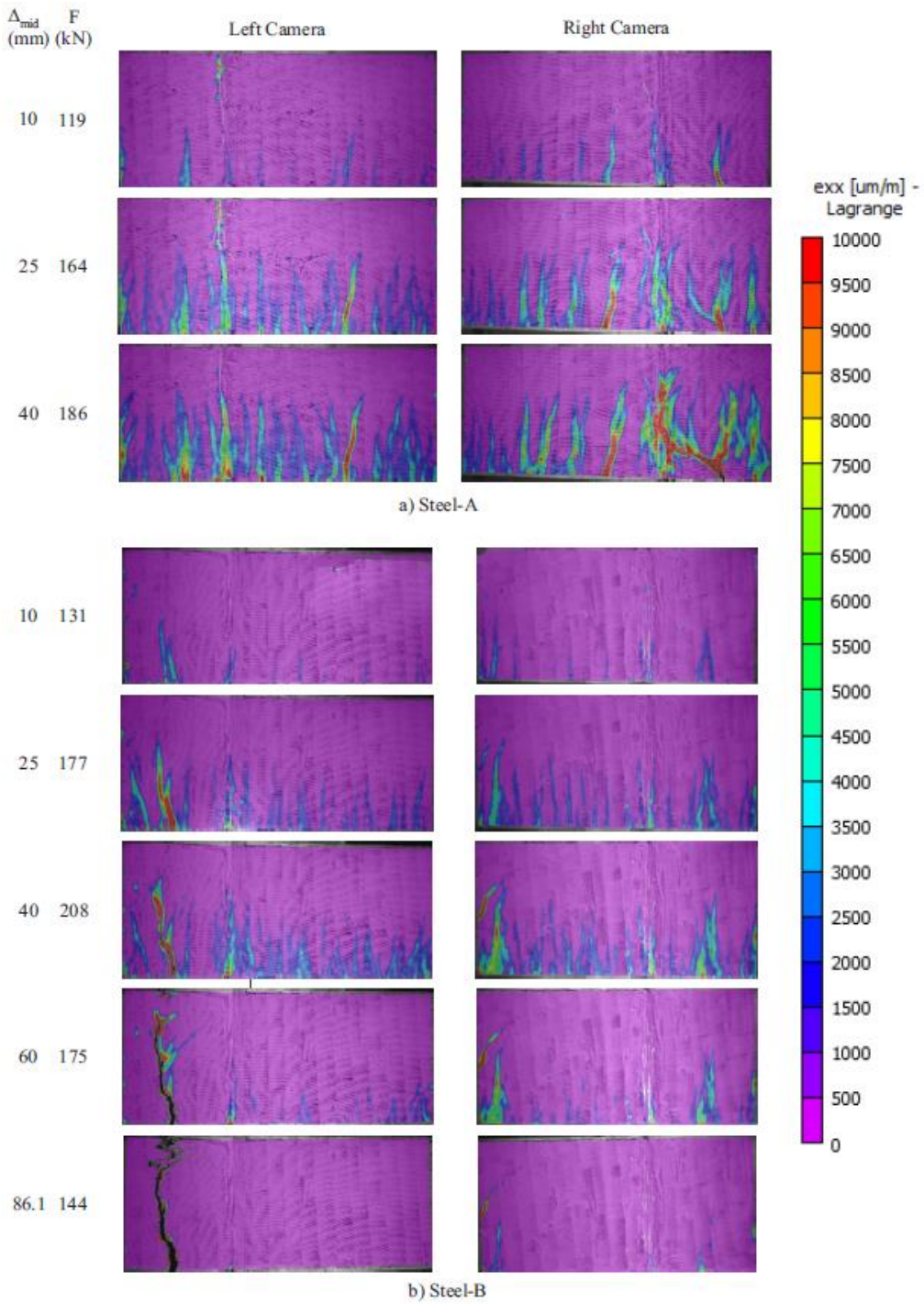

Fig. 10 Longitudinal strain field for beams with Steel tendons

From Figs. 9 and 10, it can be seen that there is considerable variability in the crack pattern with a mixture of wide cracks, visible with the naked eye as seen in Figs. 8(e-h). Bands of narrow cracks are also present which are not visible to the eye, but were detected by their effects on the longitudinal strain fields shown in Figs. 9 and 10. This result differs from that expected for conventional reinforced concrete where the maximum crack widths are typically only twice the minimum values once a stabilised crack pattern has formed (Sturm et al. 2018).

Shortly after cracking has occurred, as shown by the images for a midspan deflection of 10 mm in Figs. 9 and 10, narrow cracks are distributed at a regular spacing along the beam. As cracking

progresses, additional cracks form while existing cracks widen. This process, however, displays considerable variability. Other regions form containing large numbers of narrow cracks and in still others, a single large crack formed. These large cracks are visible to the naked eye, but the regions of narrow cracks are only detectable through their effect on the longitudinal strain field. As loading reaches the peak, as demonstrated by the images for a midspan deflection of 40 mm, the crack pattern has stabilised, however, the cracks are wider. Post-peak behaviour (deflections beyond 60mm) exhibits localized deformation at a single crack for the steel reinforced specimens, and at a reduced number of cracks for the CFRP reinforced beams, while the other cracks close. Rupture of the tendon is achieved, and is indicated by the last of the images - the cracks at which deformation has localised continue to widen while the others continue to close.

The variation of the width of the dominant crack (the crack at which the tendon ruptured) from the DIC readings is plotted in Fig. 8(b). The mean crack width is plotted in Fig. 8(c) and the mean crack spacing is plotted in Fig. 8(d). Note that for determining the crack width and crack spacing, only cracks larger than 0.05 mm were considered, as this was the minimum size that could be positively identified within the uncertainty of the analysis.

It can be seen that the dominant crack widths for specimens with CFRP tendons in Fig. 8(b) is less than that for the steel tendons because of the improved bond to concrete of the CFRP as compared to steel (Fig. 5). For example, the applied load required to achieve a crack width of 0.3 mm was, on average, 12% greater for specimens with CFRP tendons for pairs of beams of the same mix. It can also be seen that the crack width at failure was larger for the steel tendon due to the higher rupture strain of the tendon and the decreased bond strength. Significant differences were not observed for the mean crack width prior to the peak load being reached (Fig. 8(c)). After the peak load was reached, the mean crack width was larger for the specimens with steel tendons due to the increased width of the dominant crack. The mean crack spacing in Fig 8(d) was found to decrease quickly, at least initially, indicating the formation of the primary cracks. This decrease in spacing slowed as secondary cracks formed between the primary cracks and the crack pattern stabilized. The crack patterns were very similar between CFRP-A, CFRP-B, and Steel-A, but the crack spacing was larger for Steel-B. A possible reason for this variation can be seen by comparing Figs. 10(a) and 10(b) at a midspan deflection of 40 mm where Steel-A has more localised cracks while for Steel-B distributed microcracks are present. However, it is unclear beyond natural variation what is causing the distributed microcracks in one case and localised cracks in the other.

SEGMENTAL APPROACH

Segmental Analysis

A segmental analysis technique for designing prestressed fibre reinforced concrete beams is proposed here. This approach is a synthesis of the approaches developed for fibre reinforced concrete by Visintin & Oehlers (2017) and for conventional prestressed concrete by Knight et al. (2015). The segmental approach is considered ideal for the simulation of all types of fibre reinforced concrete members as a displacement based analysis technique can easily allow for the stress contribution of the fibres, which vary with crack width. Additionally, as crack formation, crack opening, and tension stiffening are explicitly modelled based on the local bond stress-slip relationships shown in Fig. 5, it can be applied to either members with steel reinforcement or carbon fibre reinforcement (or both) without the need for modification or empirical correction factors. The inputs required to implement a segmental analysis are available from the following six basic material tests: uniaxial compression; uniaxial tension;

shear friction; shrinkage; tension of the reinforcement; and pullout of the embedded reinforcement.

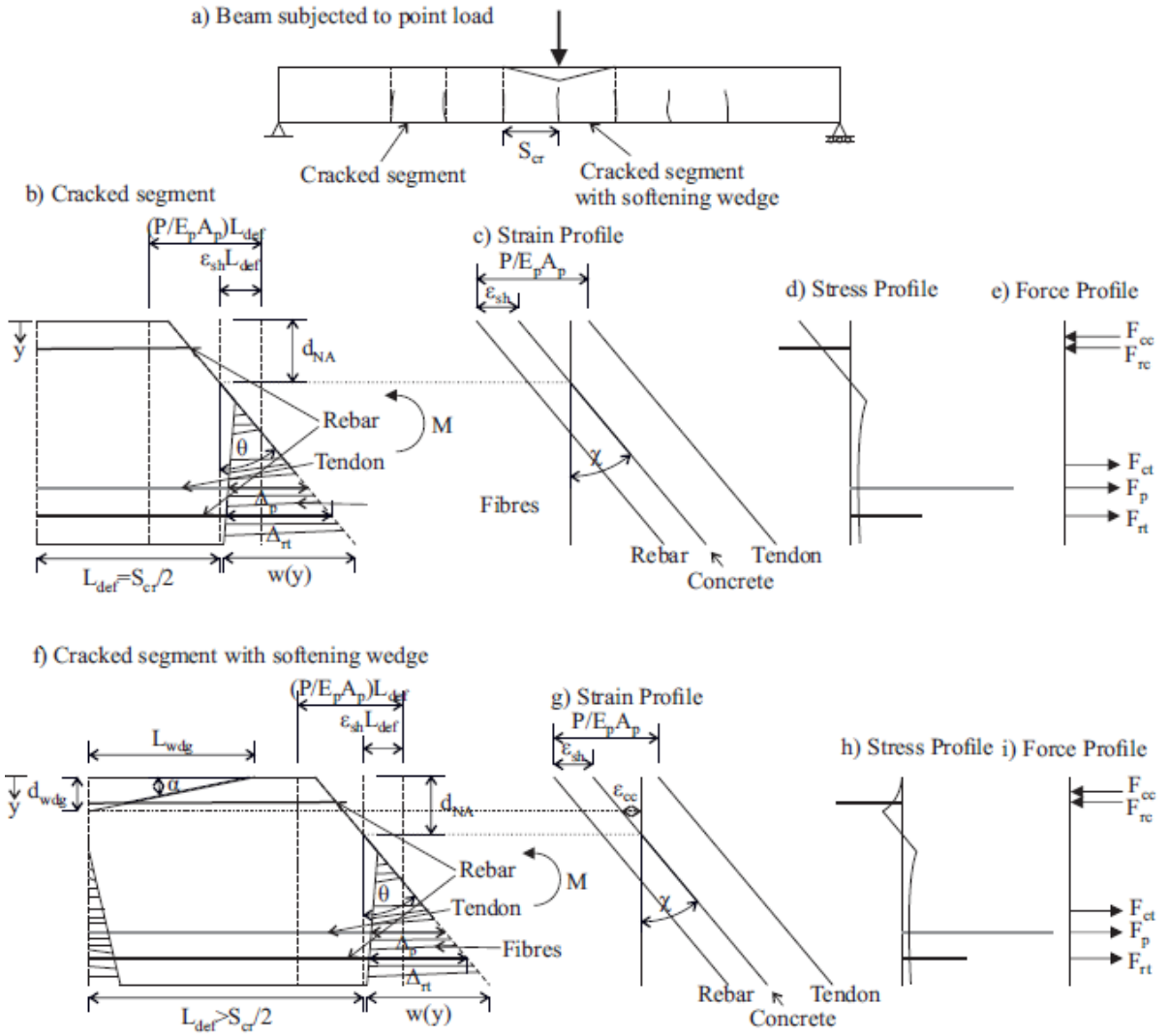

Fig. 11 Segments for analysis

Consider the beam in Fig. 11(a) that is initially uncracked such that compatibility exists between the reinforcement and surrounding concrete. Because there is no localisation of deformation (concrete cracking or softening), traditional analysis procedures are mechanically correct and can fully describe the performance of members with both steel and FRP reinforcement. Using these standard analysis approaches (those based on transformed sections in Appendix A), solutions are presented for the cracking moment and curvature at cracking, including the effect of shrinkage and prestress.

When the applied load in Fig. 11(a) is increased such that a localisation of stress in the form of a crack occurs, then the segmental approach is applied to allow for the loss of compatibility between the reinforcement and concrete. In this approach, a segment of a length that is a function of the crack spacing S_{cr} in Fig. 11(a) is used as in Figs. 11(b-f). The moment applied to each end of the segment is constant to obtain the mean sectional properties, which can then be used in a beam with varying moment as in Fig. 11(a). Once concrete softening occurs to form a hinge as in Fig. 11(f), then as the length of the hinge is small relative to the span of the beam, the moment within the hinge is assumed to be constant such that the results of the

analysis of Fig. 11(f) can be used directly. A rotation θ is then applied to the end of the beam defining a deformation profile *D(y)* and a neutral axis depth with respect to the concrete deformation of d_{NA}. It is then a matter of determining the internal forces induced by the rotation, prestress, and concrete time effects of creep and shrinkage, and adjusting d_{NA} until equilibrium is obtained.

Prior to concrete crushing, the segment of half-length $S_{cr}/2$ in Fig. 11(b) is used to determine the mean sectional properties along the length of the beam in Fig. 11(a). To quantify the internal forces, the deformation profile *D(y)* is first divided by the half segment length L_{def} to obtain the strain profiles in Fig. 11(c). This also allows for the definition of the average curvature $\chi=\theta/L_{def}$ which is required to determine member deflection.

The application of prestress in Fig. 11(b) offsets the strain in the tendon in Fig. 11(c) from the strain profile in the rebars. This offset equals the initial strain induced in the tendon by the prestress strain P_p/E_pA_p (Knight et al. 2013; 2015). Concrete shrinkage further offsets the strain profile in the concrete from the strain profile of the rebars by the shrinkage strain ε_{sh}. From these strain profiles, in the uncracked zone the stresses in Fig. 11(d) can be determined from material stress-strain relationships. However, in the cracked zone: the force in the reinforcement is given by the slip of the reinforcement at the crack face; and the stress in the tensile concrete due to the fibres is given by the crack opening. Hence, a relationship is required to connect the effective strains in the cracked region to the crack width, as will be described in the following section. Having obtained the stress profile in Fig. 11(d), it is then integrated to develop the force profile in Fig. 11(e). These forces are then used to calculate the applied moment *M*. The above approach, illustrated in Figs. 11(b) through (e), gives the moment-rotation, moment-curvature, and moment-crack width relationships for the segment by imposing a rotation, as in Fig. 11(b), and varying the neutral axis depth until the force equilibrium in Fig. 11(e) is reached.

When rotation causes the crushing strain of the concrete to be reached (Fig. 11b), a wedge or hinge forms (Fig. 11f). Now the segment length L_{def} must be large enough to encompass the wedge, but must also remain as small as possible because the moment in the hinge region is assumed to be constant. In this case, concrete softening needs to be incorporated into the analysis by using a size dependent concrete softening material property as will be defined later. Otherwise, the analysis steps illustrated in Figs. 11(f) through (i) are the same as in Figs. 11(b) through (e). Rotation is increased while varying the neutral axis depth to maintain force equilibrium until either the reinforcement ruptures or unloading of the reinforcement occurs.

Allowance for Cracking

Relationship of Crack Width to Effective Strain

A relationship between the deformation of the segment and the crack width is required to determine the forces in both the reinforcement and in the fibres in the cracked zone. From Hillerborg[45], the elongation of a cracked specimen is given by the superposition of the crack opening and the material deformation between the cracks such that

$$D(y) = \varepsilon(y)L_{def} = \frac{w(y)}{2} + \frac{\sigma_c[w(y)]}{E_c}L_{def} \quad (1)$$

where *w(y)* is the crack opening at the depth being considered, L_{def} is the segment length $S_{cr}/2$ in Fig. 11(b) with S_{cr} the crack spacing, $\sigma_c[w(y)]$ is the stress in the concrete given by a tensile-stress/crack-width relationship, and E_c is the elastic modulus. Rearranging allows for the definition of the effective strain:

$$\varepsilon(y) = \frac{w(y)}{S_{cr}} + \frac{\sigma_c[w(y)]}{E_c} \quad (2)$$

Eq. 2 is used to develop a relationship between $\varepsilon(y)$ and $w(y)$ by substituting in values for the crack width and the corresponding concrete stress for that crack width.

Crack Spacing

The crack spacing can be determined by applying a partial interaction tension stiffening model (Gupta & Maestrini 1990; Wu et al. 1991; Balazs 1993; Choi & Cheung 1996; Knight et al. 2013; Sturm et al. 2018a) which requires modification to allow for bond between the reinforcement and the concrete, and also for the presence of fibres and residual strains due to concrete shrinkage and prestress.

First, an expression is developed for the slip of the reinforcement that includes the effect of prestress and shrinkage. Consider the tendon of original length dx in Fig. 12(a). In Fig. 12(b), a prestress P is applied to the tendon, causing the tendon to elongate a distance $(P/E_pA_p)dx$, after which concrete is cast around the tendon as in 12(c). Upon destressing the tendon, a contraction of magnitude $-P/(E_pA_p+E_cA_{ct})dx$ occurs, as in Fig. 12(d). Shrinkage causes an extension of $\varepsilon_{sh}/[1+E_cA_{ct}/(E_pA_p)]dx$, as in Fig. 12(e), because the shrinkage reduces the effective prestress in the section. If a load, F, of a magnitude sufficient to cause cracking is applied to the prism, it will elongate as in Fig. 12(f), such that the tendon slips relative to the surrounding concrete. In this case, the slip of the tendon within this infinitesimal segment is given by:

$$\delta = D_p - D_c - \left(\frac{P}{E_pA_p} - \varepsilon_{sh}\right)dx \quad (3)$$

where D_p is the deformation of the tendon and D_c is the deformation of the concrete.
Differentiating Equation 3 results in the following expression for slip strain

$$\frac{d\delta}{dx} = \varepsilon_p(x) - \varepsilon_c(x) - \frac{P}{E_pA_p} + \varepsilon_{sh} \quad (4)$$

where ε_p is the strain in the tendon and ε_c is the strain in the concrete.
Now, considering the requirements of equilibrium of the element of length dx in Fig. 12(g); For the tendon

$$\frac{d\sigma_p}{dx} = \frac{\tau(x)L_{per}}{A_p} \quad (5)$$

where $\tau(x)$ is the interface shear stress, L_{per} is the bonded perimeter of the tendon, and A_p is the cross-sectional area of the tendon. For the concrete

$$\frac{d\sigma_c}{dx} = -\frac{\tau(x)L_{per}}{A_{ct}} \quad (6)$$

where A_{ct} is the cross-sectional area of concrete in the prism. By solving Eqs. (3-5) for the following boundary conditions, the crack spacing can be determined.

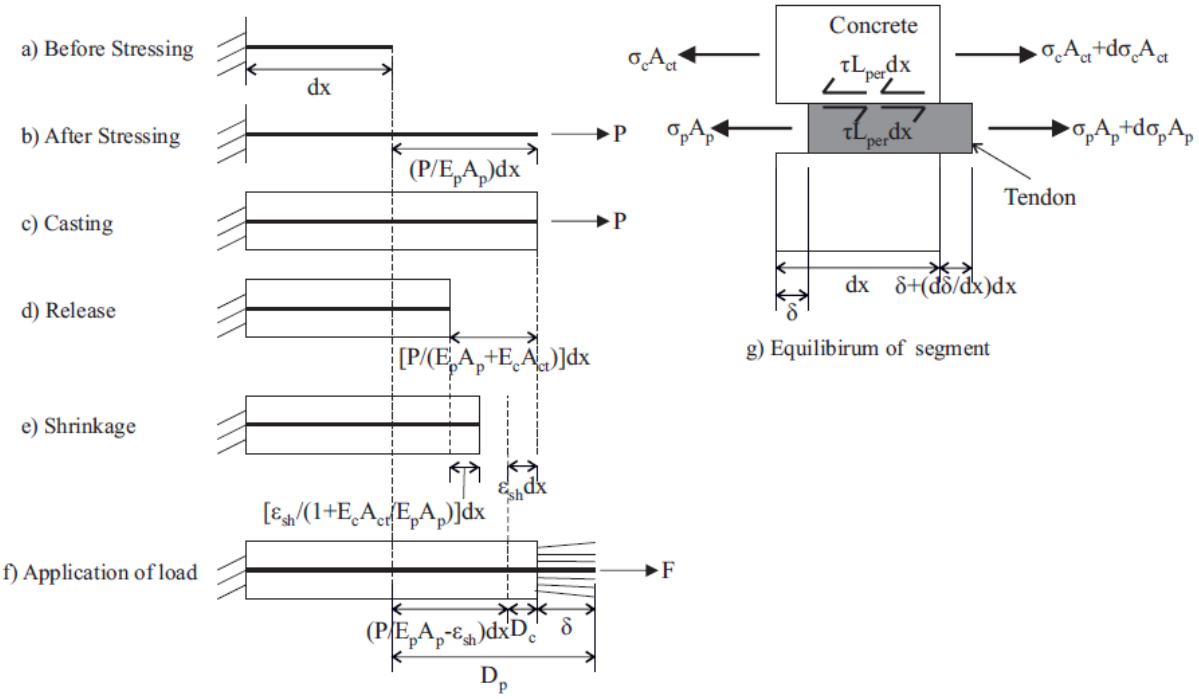

Fig. 12 Definition of slip including prestress and shrinkage with infinitesimal segment

To determine the appropriate boundary conditions, consider the tension stiffening prism with an initial crack in Figs. 13(a) and (e). The variation in slip is illustrated in Fig. 13(b), the stress in the reinforcement in Fig. 13(c), and the concrete stress in Fig. 13(d). At the position of the initial crack, the stress in the reinforcement is $\sigma_p(0)$ and the slip of the reinforcement, $\Delta_p=\delta(0)$, is unknown while the stress in the concrete is given by the post-cracking stress. The post-cracking stress f_{pc} is controlled by the presence of fibre reinforcement and can be determined from the tensile-stress/crack-width relationship as the position at which the slope of the tensile-stress/crack-width relationship changes immediately after cracking. This position corresponds to 6.32 MPa in Fig. 1(b). At the position of the new crack in Fig. 13(a), a distance S_{cr} from the existing crack, the slip δ and slip strain $d\delta/dx$ is equal to zero, while the stress in the tensile concrete is $\sigma_c(S_{cr})=f_{ct}$, the tensile strength of the concrete. Hence, the solution procedure presented in Fig. 13(f) can be applied.

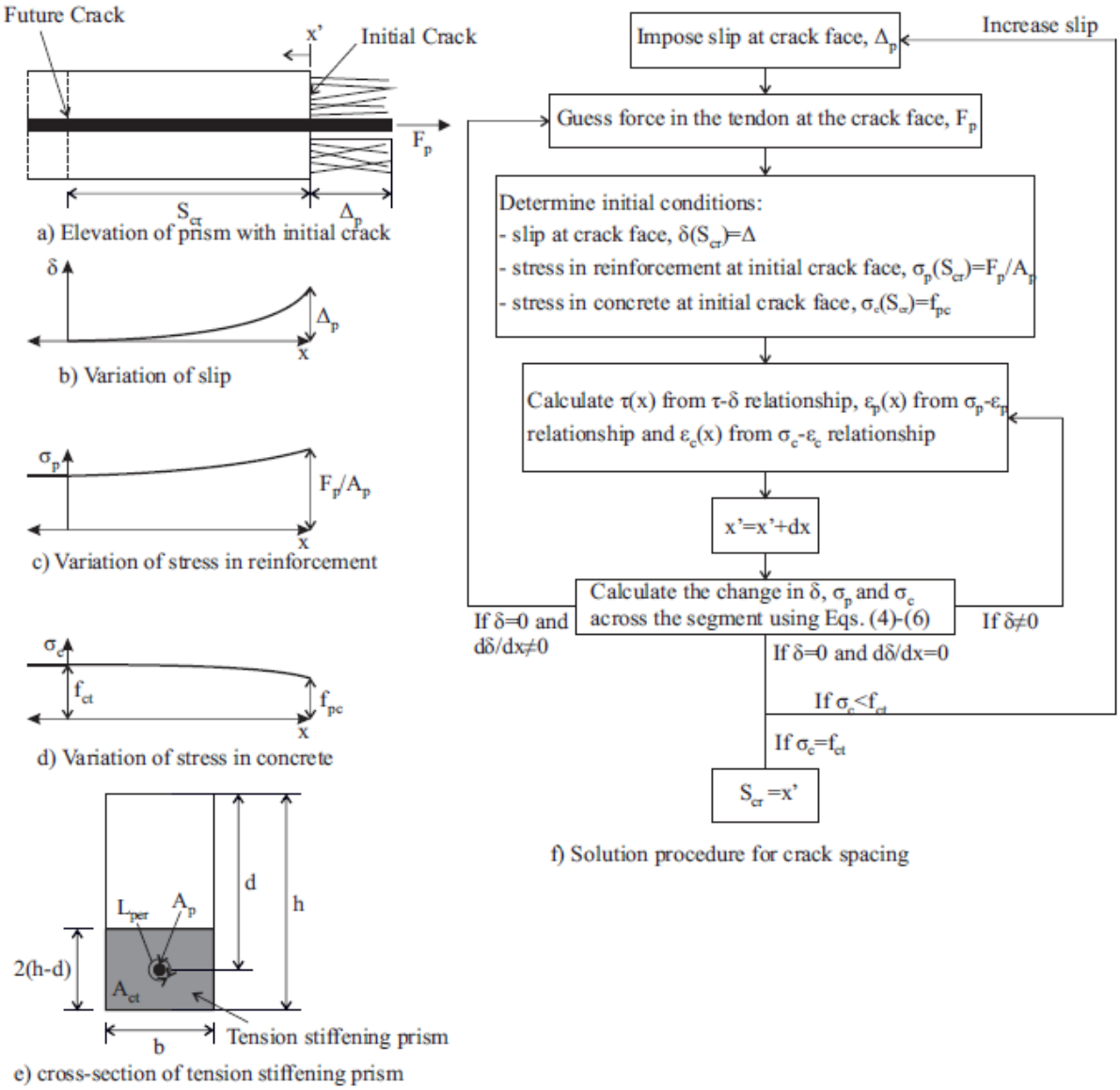

Fig. 13 Tension stiffening prism with initial crack.

The situation becomes more complex when both prestressed and non-prestressed reinforcement are present. In this case, separate tension stiffening prisms are considered for the prestressed and non-prestressed reinforcement, as in Fig. 14, and the results are then combined. In this approach, the transfer length, that is the distance from the initial crack to where the slip is zero, is found for a range of slips at the crack face using the procedure in Fig. 13(f). First, for the prestressed reinforcement, and then the non-prestressed reinforcement, noting the stress in the concrete at the end of the transfer length. Next, for each given value of slip, the stress in the concrete at the end of each transfer length is determined by adding the contributions due to the fibres, the non-prestressed reinforcement, and the prestressed reinforcement. By considering that the total transfer length is given by the maximum transfer length found for the tendon and the non-prestressed reinforcement, a relationship can be found between transfer length and stress in the concrete at the end of the transfer length. The value of transfer length for which the stress in the concrete equals the tensile strength gives the crack spacing.

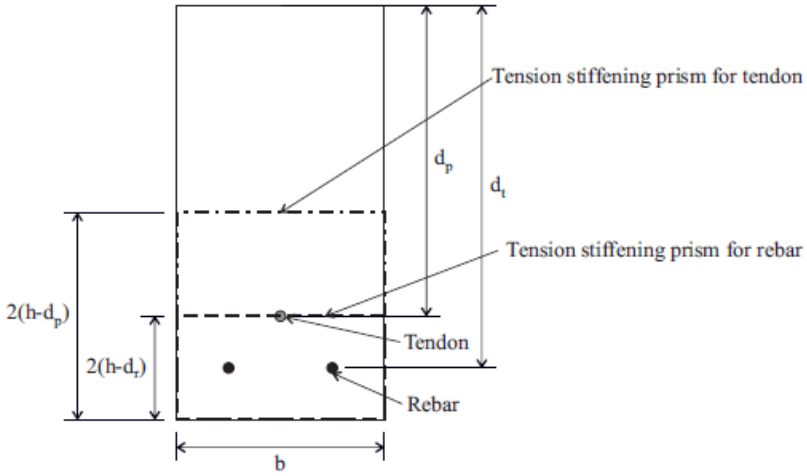

Fig. 14 Tension stiffening prism with prestressed and non-prestressed reinforcement

Load-Slip Relationship for the Reinforcement

Equations (3) and (5) can also be used to determine the load-slip relationship of the prestressed tendon when the appropriate boundary conditions are supplied. A tension stiffening prism with two primary cracks is illustrated in Fig. 15(a). The variation in slip, reinforcement stress, and concrete stress are shown in Figs. 15(b-d), assuming the boundary condition of zero slip at the centre of the prism due to symmetry. Based on this boundary condition, the procedure in Fig 15(e) can be applied.

Sections with both prestressed and non-prestressed reinforcement can be accommodated by calculating the load slip relationship for each type of reinforcement separately using the tension stiffening prisms in Fig. 14.

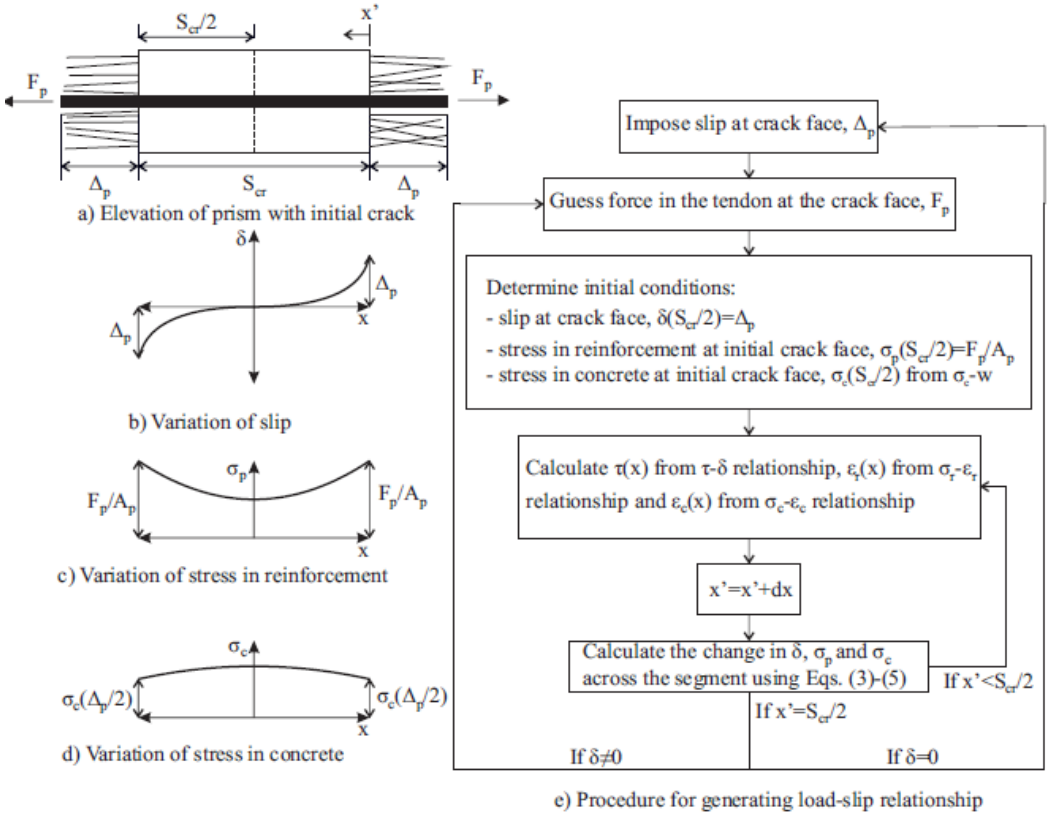

Fig. 15 Tension stiffening prism with primary cracks

Allowance for Crushing

As rotation, θ in Fig. 11(b), increases, eventually the stress reaches the compressive strength of the concrete at the top fibre. At this point, the softening wedge in Fig. 11(f) forms. The segment length in Fig. 11(b) is now increased to accommodate the size of this softening wedge as in Fig. 11(f). The tip of this softening wedge is located at the position where the strain in the concrete is equal to the crushing strain ε_{cc} while the wedge forms at angle of α to the horizontal. This angle is given by the following expression from Mohamed Ali et al. (2010)

$$\alpha = \arctan\left(-m + \sqrt{m^2 + 1}\right) \tag{7}$$

where m is the slope of the shear-capacity/normal-stress relationship determined from shear friction tests. From tests conducted by Sturm et al. (2018b) on UHPFRC, this angle was determined to be 14°.

As a result of the formation of this wedge, the compressive stress-strain relationship becomes size dependent. The following expression, developed by Chen et al. (2013), can be used to allow for this size dependency

$$\varepsilon_c = \varepsilon_{mat} + (\varepsilon_{test} - \varepsilon_{mat})\frac{L_{test}}{L_{def}} \tag{8}$$

where ε_{mat} is the material strain, ε_{test} is the strain as measured in the test, L_{test} is the length of the test specimen and L_{def} is the half segment length. Note that the material strain is calculated as

$$\varepsilon_{mat} = \frac{\sigma_c}{E_c} + \left(\varepsilon_{cc} - \frac{f_c}{E_c}\right) \tag{9}$$

where σ_c is the stress in the concrete and f_c is the compressive strength of the concrete.

Validation

The stress/crack-width relationship in Fig. 1(b) and bond-stress/slip relationship in Fig. 2(b) were obtained directly from tests. The reduction in bond between the concrete and the steel rebar post-yield was captured by using the relationship suggested by Malek et al. (2019). In a previous study, this relationship was found to give accurate results when used to simulate UHPFRC beams reinforced with steel rebars (Sturm et al. 2020). The shrinkage strain measured at the time of testing was 1180 με, of which, 490 με occurred after transfer. Tension tests were also used to determine the stress-strain relationship of the steel rebar and the tendons as shown in Table 2. The concrete strength at the time the beams were tested was 121 MPa while the elastic modulus was 40.6 MPa. However, the full stress-strain relationship was not measured, so the relationship suggested by Sobuz et al. (2016) for UHPFRC was adopted instead, using the measured compressive strength and elastic modulus as inputs. The length of the cylinder was taken as 200 mm for calculating the size-effect in compression since that was the length considered in Sobuz et al. (2016). Shear friction properties used to determine the geometry of the softening wedge were estimated from tests performed by Sturm et al. (2018b). The stress-strain relationship of the CFRP tendon was obtained from tests performed by Shapack (2015). Note that the procedures associated with the segmental method were implemented in MATLAB.

The results obtained from the segmental analysis are compared to the experimental results in Fig. 16 with crack widths for the sectional analysis obtained from the French UHPFRC recommendations (AFGC 2013). For the load-deflection plots shown in Figs. 16(a) and (b), there is good correlation with the experimental results. Note that simulating the descending branch of the load-deflection relationship for the specimens reinforced with steel tendons

required the unloading stiffness for the portions of the beam away from the hinge be assumed equal to the stiffness of the uncracked specimen. In Figs. 16(c-d), the segmental analysis provides an accurate indication of crack widths when these widths remain less than 1 mm, a range of primary interest to designers.

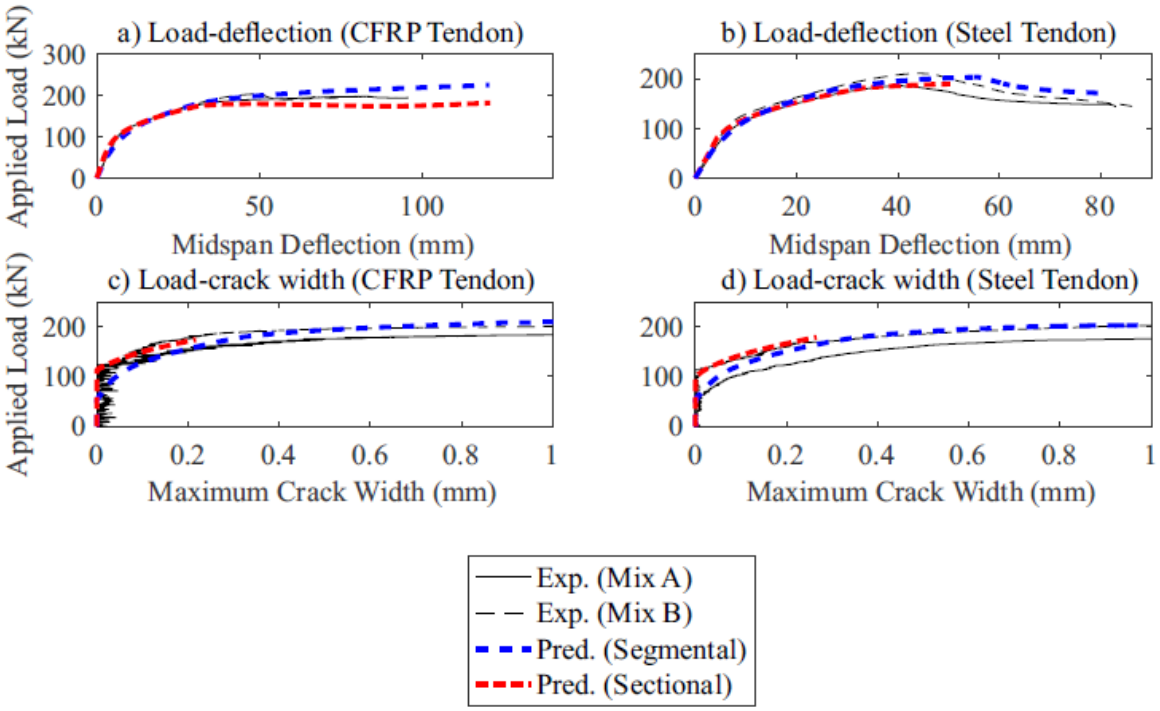

Fig. 16 Validation of segmental analysis

The test results were also compared to the results obtained from a full interaction sectional moment-curvature analysis using the approach suggested by the French UHPFRC recommendations AFGC (2013). In this approach, the effect of bond on the response is neglected, hence, tension stiffening is ignored. To convert the stress-crack width relationship into an equivalent stress-strain relationship, a characteristic length equal to 2/3 the depth of the section was used AFGC (2013). The crack widths corresponding to this approach were predicted by the expressions in the French UHPFRC recommendations AFGC (2013). For the load-deflection response, it was found that the sectional analysis tended to underestimate the peak load when compared to the experimental results and to the segmental analysis. The crack width approach in AFGC (AFGC 2013) tended to underestimate the crack widths when compared to the experimental results and to the segmental analysis.

CONCLUSION

From the experimental study, replacing steel tendons with CFRP tendons in a UHPFRC beam resulted in similar cracking loads, peak loads, and deflections at rupture. However, for beams with steel tendons, the load applied to a given beam reduced by an average of 27.5% from the peak load to the point at which rupture of the tendon occurred. In contrast, for the beams with CFRP tendons, this reduction was only 3.5%. Hence, the load at tendon rupture was 35% higher for beams reinforced with CFRP tendons, meaning a greater load capacity was maintained under large deformations. The dominant crack widths prior to yield were also reduced for the CFRP beams, as compared to steel beams of the same mix design. For example, the force required to achieve a crack width of 0.3 mm was increased by 12% when using CFRP tendons, as compared to steel tendons. The mean crack widths and spacings were of similar magnitude for beams having CFRP and steel tendons. The cracked stiffness of the beams with CFRP

tendons was 90% of that for the beams with steel tendons. The total energy absorbed, as measured by area under the load-deflection curve, increased by 10% for beams with CFRP tendons.

Using the experimental results, a segmental analysis was then validated. This method is a displacement based analysis approach, and is ideal for simulating fibre-reinforced concrete, as it can easily allow for the crack width to depend on fibre stress. This approach was then compared to a conventional sectional analysis, demonstrating the improvements inherent to the segmental analysis approach.

APPENDIX A MOMENT AND CURVATURE ANALYSIS OF AN UNCRACKED SECTION

Consider a transformed section in which the prestress is applied as a tensile force at the tendon and in which concrete shrinkage causes reinforcement compressive forces. The moment at cracking is given by

$$M_{cr} = f_{ct}\frac{I_{T0} - d_{NA}S_{T0}}{h - d_{NA}} - E_r\varepsilon_{sh}S_r + M_{pe0} \tag{A1}$$

where the neutral axis depth is

$$d_{NA} = \frac{f_{ct}S_{T0} - E_r\varepsilon_{sh}A_r h + P_e h}{f_{ct}A_T - E_r\varepsilon_{sh}A_r + P_e} \tag{A2}$$

where f_{ct} is the tensile strength, A_T is the transformed area, S_{T0} is the first moment of the transformed area with respect to the top fibre and I_{T0} is the second moment of the transformed area with respect to the top fibre, h is the total depth of the section, A_r is the total area of reinforcement, S_r is the first moment of area of the reinforcement, ε_{sh} is the shrinkage strain, P_e is the effective prestress (prestress reduced by the losses due to shrinkage) and M_{pe0} is the moment at the top fibre due to the effective prestress.
The curvature at cracking is given by

$$\chi_{cr} = \frac{f_{ct}}{E_c(h - d_{NA})} \tag{A3}$$

where E_c is the elastic modulus of the concrete and h is the depth of the section.
The flexural rigidity of the section before cracking is $E_c(I_{T0}-S_{T0}^2/A_T)$ where

$$A_T = A_c + n_p\sum_i A_{pi} + n_r\sum_j A_{rj} \tag{A4}$$

$$S_{T0} = S_{c0} + n_p\sum_i A_{pi}d_{pi} + n_r\sum_j A_{rj}d_{rj} \tag{A5}$$

$$I_{T0} = I_{c0} + n_p\sum_i A_{pi}d_{pi}^2 + n_r\sum_j A_{rj}d_{rj}^2 \tag{A6}$$

in which A_c is the area, S_{c0} is the first moment of area and I_{c0} is the second moment of area of the concrete section evaluated with respect to the top fibre of the section. The modular ratio of the prestressed reinforcement is n_p, the area of the i^{th} layer of prestressed reinforcement is A_{pi}, the depth of the i^{th} layer is d_{pi}. The modular ratio of the non-prestressed reinforcement is n_{ri}, the area of the j^{th} layer of non-prestressed reinforcement is A_{rj}.

ACKNOWLEDGEMENTS

This work was partially completed under Australian Research Council Discovery Project DP190102650. The authors acknowledge the assistance of the staff and students at the Constructed Facilities Laboratory at North Carolina State University for their assistance with this experimental components of this project (Mr Ye Zhang, Dr. Brad McCoy, Mr Zakariya Bourara, Mr. Jordan Firth, Mr. Johnathan McEntire, Mr. Jerry Atkinson, Mr. Oscar Santoyo, Mr. Luis Aguilar, Mr. Francisco Jativa, Mr. Sheng-Hsuan Lin, Mr. Guillermo Gonzalez, and Mr. Hussam Abu Nimeh). We also acknowledge Mr. Robert Poole and ST Wooten Corporation who provided the concrete truck, as well as Mr. Yoshiaki Yamamoto and Tokyo Rope Corporation who provided the coupling system for the CFCC tendons.

NOTATION

A_c = cross-sectional area of concrete in section;
A_{ct} = cross-sectional area of tension stiffening prism;
A_p = cross-sectional area of prestressed reinforcement;
A_{pi} = area of the i^{th} layer of prestressed reinforcement;
A_r = total area of non-prestressed reinforcement in the section;
A_{rj} = area of the j^{th} layer of non-prestressed reinforcement;
A_T = area of transformed section;
b = width of section;
D, D_c, D_p = deformation; deformation of concrete and tendon, respectively;
d = effective depth of section;
d_{NA} = neutral axis depth;
d_p, d_{pi} = depth of prestressed reinforcement; depth of i^{th} layer of prestressed reinforcement;
d_r, d_{rj} = depth of non-prestressed reinforcement; depth of j^{th} layer of non-prestressed reinforcement;
d_{wdg} = depth of wedge;
dx = infinitesimal length;
E, E_c, E_p, E_r = elastic modulus; elastic modulus of concrete, prestressed reinforcement and non-prestressed reinforcement, respectively;
F= applied force;
F_{cc}, F_{ct}, F_p, F_{rt}, F_{rc} = force in compressive concrete, tensile concrete, prestressed reinforcement, non-prestressed tensile reinforcement and compressive reinforcement, respectively;
f_c = compressive strength of concrete;
f_{ct} = tensile strength of concrete;
f_{pc} = post-cracking strength of concrete;
f_u = ultimate tensile strength of reinforcement;
f_y = yield strength of reinforcement;
h = total depth of section;
I_{c0} = second moment of the concrete area;
I_{T0} = second moment of the transform area;
L_{def} = half segment length;
L_{per} = bonded perimeter;
L_{test} = length of test specimen;
L_{wdg} = length of wedge;
M = applied moment;
M_{cr} = cracking moment;
M_{pe0} = moment at top fibre due to effective prestress;

m = slope of shear capacity-normal stress relationship;
n_p, n_r = modular ratio of prestressed and non-prestressed reinforcement;
P = prestress;
P_e = effective prestress (prestress minus losses due to shrinkage);
S_{c0} = first moment of the concrete area;
S_{cr} = crack spacing;
S_r = first moment of area of the non-prestressed reinforcement in the section;
S_{T0} = first moment of the transformed area;
x = location in tension stiffening prism with respect to partial interaction-full interaction boundary (crack spacing) or with respect to midpoint of prism (load-slip relationship);
x' = location in tension stiffening prism with respect to crack face;
w = crack width;
y = distance from top fibre;
α = angle of the softening wedge with respect to the horizontal;
Δ_{mid} = midspan deflection;
Δ_p, Δ_{rt}= slip of prestressed reinforcement and non-prestressed reinforcement, respectively;
δ = interface shear slip;
ε = effective strain;
ε_c, ε_p = strain in concrete and reinforcement, respectively;
ε_{cc} = strain to cause crushing;
ε_{mat} = material strain;
ε_{sh} = shrinkage strain;
ε_{test} = strain from test;
θ = rotation;
σ_c, σ_p = stress in concrete and prestress, respectively;
$\underline{\tau}$ = interface shear stress;
χ = curvature;
χ_{cr} = curvature at cracking;

REFERENCES

Abdelrahman, A. A., Tadros, G., and Rizkalla, S. H. (1995). "Test Model for First Canadian Smart Highway Bridge." *ACI Structural Journal,* 92(4), 451-458.

ACI (American Concrete Institute) (2004). "Prestressing concrete structures with FRP tendons." *ACI 440.4R-04*, Farmington Hills.

AFGC (Association Francaise de Genie Civil). (2013). "Betons fibres a ultra-hautes performances- Recommandations [Ultra high performance fibre reinforced-concretes – Recommendations]." Paris.

ASTM (American Society of Testing and Materials). (2015). "Standard specification for silica fume used in cementitious mixes." *ASTM C1240-15*, West Conshohocken.

ASTM (American Society of Testing and Materials). (2016). "Standard specification for deformed and plain low-alloy steel reinforcing bars for concrete reinforcement." *ASTM C706-16*, West Conshohocken.

ASTM (American Society of Testing and Materials). (2017a). "Standard specification for chemical admixtures for concrete." *ASTM C494-17*, West Conshohocken.

ASTM (American Society of Testing and Materials). (2017b). “Standard practice for fabricating and testing specimens of ultra-high performance concrete.” *ASTM C1856-17*, West Conshohocken.

ASTM (American Society of Testing and Materials). (2017c). “Standard test method for length change of hardened hydraulic-cement mortar and concrete.” *ASTM C157-17*, West Conshohocken.

ASTM (American Society of Testing and Materials). (2018). “Standard specification for low-relaxation, seven-wire steel strand for prestressed concrete.” *ASTM C416-18*, West Conshohocken.

ASTM (American Society of Testing and Materials). (2019). “Standard specification for portland cement.” *ASTM C150-19*, West Conshohocken.

Balazs, G. L. (1993). “Cracking analysis based on slip and bond stresses.” *ACI Materials Journal*, 90, 340-340.

Binard, J. P. (2017). “UHPC: A game-changing material for PCI bridge producers.” *PCI Journal*, 62(2), 34-46.

Chen, L., and Graybeal, B. A. (2011a). “Modeling structural performance of second-generation ultrahigh-performance concrete pi-girders.” *Journal of Bridge Engineering*, 17(4), 634-643.

Chen, L., and Graybeal, B. A. (2011b). “Modeling structural performance of ultrahigh performance concrete I-girders.” *Journal of Bridge Engineering*, 17(5), 754-764.

Chen, Y., Visintin, P., Oehlers, D. J., and Alengaram, U. J. (2013). “Size-dependent stress-strain model for unconfined concrete.” *Journal of Structural Engineering*, 140(4), 04013088.

Choi, C. K., and Cheung, S. H. (1996). “Tension stiffening model for planar reinforced concrete members.” *Computers & Structures*, 59(1), 179-190.

Di Prisco, M., Plizzari, G., and Vandewalle, L. (2009). “Fibre reinforced concrete: new design perspectives.” *Materials and Structures*, 42(9), 1261-1281.

Enomoto, T., Grace, N. F. and Harada, T. (2012). “Life Extension of Prestressed Concrete Bridges Using CFCC Tendons and Reinforcements.” *Proc., 6th International Conference on FRP Composites in Civil Engineering*, Rome.

Fam, A. Z., Rizkalla, S. H., and Tadros, G. (1997). “Behavior of CFRP for prestressing and shear reinforcements of concrete highway bridges.” *ACI Structural Journal*, 94(1), 77-86.

fib (International Federation for Structural Concrete). (2012). “Model Code 2010.” Lausanne.

Grace, N. F., Navarre, F. C., Nacey, R. B., Bonus, W., and Collavino, L. (2002). “Design-construction of bridge street bridge-first CFRP bridge in the United States.” *PCI Journal*, 47(5).

Grace, N. F., Enomoto, T., Abdel-Sayed, G., Yagi, K., and Collavino, L. (2003). “Experimental study and analysis of a full-scale CFRP/CFCC double-tee bridge beam.” *PCI Journal*, 48(4).

Grace, N. F., Enomoto, T., Sachidanandan, S., and Puravankara, S. (2006). “Use of CFRP/CFCC reinforcement in prestressed concrete box-beam bridges.” *ACI Materials Journal*, 103(1), 123.

Grace, N. F., Enomoto, T., Baah, P., and Bebawy, M. (2011). “Flexural behavior of CFRP precast prestressed decked bulb T-beams.” *Journal of Composites for Construction*, 16(3), 225-234.

Graybeal, B. A. (2008). “Flexural behavior of an ultrahigh-performance concrete I-girder.” *Journal of Bridge Engineering*, 13(6), 602-610.

Graybeal, B. A. (2009). “Structural Behavior of a 2nd Generation UHPC Pi-Girder.” *FHWA-HRT-09-069*, Federal Highway Administration, McLean.

Graybeal, B. A., Crane, C. K., Perry, V., Corvez, D., and Ahlborn, T. M. (2019). “Advancing ultra-high-performance concrete.” *Concrete International*, 41(4), 41-45.

Gupta, A. K., and Maestrini, S. R. (1990). “Tension-stiffness model for reinforced concrete bars.” *Journal of Structural Engineering.*, 116(3), 769-790.

Hillerborg, A. (1978). “A model for fracture analysis.” *Report No. TVBM-3005*, Lund Institute of Technology.

Hoyer. E.. and Friedrich, E. (1939) "Beitrag zur Frage der Haftspannung in Eisenbetonbauteilen.” *Beton und Eisen,* 38(6), 107-110.

Khalafalla, O. M. (2018). “Durability of CFRP prestressing strands for concrete members.” Ph.D. Thesis, North Carolina State University.

Knight, D., Visintin, P., Oehlers, D. J., and Jumaat, M. Z. (2013). “Incorporating residual strains in the flexural rigidity of RC members with varying degrees of prestress and cracking.” *Advances in Structural Engineering*, 16(10), 1701-1718.

Knight, D., Visintin, P., and Oehlers, D. J. (2015). “Displacement-based simulation of time-dependent behaviour of RC beams with prestressed FRP or steel tendons.” *Structural Concrete*, 16(3), 406-417.

Malek, A., Scott, A., Pampanin, S., and Hoult, N. A. (2019). “Postyield Bond Deterioration and Damage Assessment of RC Beams Using Distributed Fiber-Optic Strain Sensing System.” *Journal of Structural Engineering*, 145(4), 04019007.

Mohamed Ali, M. S., Oehlers, D. J., and Griffith, M. C. (2010). “The residual strength of confined concrete.” *Advances in Structural Engineering*, 13(4), 603-618.

Naaman, A. E. and Jeong, S. M. (1995). “Structural Ductility of Concrete Beams Prestressed with FRP Tendons.” *Proc., 2nd International Rilem Symposium (FRPRCS-2)*, Ghent, 379–386.

Oehlers, D. J., Visintin, P., Chen, J. F., Seracino, R., Wu, Y., and Lucas, W. (2017). "Reinforced concrete behavior, research, development, and design through partial-interaction mechanics." *Journal of Structural Engineering*, 143(7), 02517002.

PCI (Precast/Prestressed Concrete Institute). (2010) "PCI Design Handbook, 7th Ed." Chicago.

Shapack, G.L. (2015). "Analysis and design of cored slabs prestressed with carbon fiber strands." Master's Thesis, North Carolina State University.

Sobuz, H. R., Visintin, P., Mohamed Ali, M. S., Singh, M., Griffith, M. C., and Sheikh, A. H. (2016). "Manufacturing ultra-high performance concrete utilising conventional materials and production methods." *Construction and Building Materials*, 111, 251-261.

Standards Australia (1997). "Methods of testing concrete-Determination of the static chord modulus of elasticity and Poisson's ratio of concrete specimens." *AS1012.9:2014*, Sydney.

Stark, A., Classen, M., Knorrek, C., Camps, B., and Hegger, J. (2018). "Sandwich panels with folded plate and doubly curved UHPFRC facings." *Structural Concrete*, 19(6), 1851-1861.

Sturm, A.B., Visintin, P., Oehlers, D.J. and Seracino, R. (2018a) "Time dependent tension stiffening mechanics of fibre reinforced and ultra-high performance fibre reinforced concrete." *Journal of Structural Engineering*, 144(8), 04018122.

Sturm, A. B., Visintin, P., Farries, K. and Oehlers, D. J. (2018b) "A new testing approach for extracting the shear friction material properties of ultra-high performance fibre reinforced concrete." *Journal of Materials in Civil Engineering*, 30(10), 04018235.

Sturm, A. B., Visintin, P. and Oehlers. D. J. (2020) "Blending fibres to enhance the flexural properties of UHPFRC beams." *Construction and Building Materials*, 244, 118328.

Thomas, M., Green, B., O'Neal, E., Perry, V., Hayman, S., and Hossack, A. (2012). "Marine performance of UHPC at Treat Island." *Proc., 3rd International Symposium on UHPC and Nanotechnology for High Performance Construction Materials*, Kassell, 365-370.

Visintin, P., and Oehlers, D. J. (2017). "Fundamental mechanics that govern the flexural behaviour of reinforced concrete beams with fibre-reinforced concrete." *Advances in Structural Engineering*, 21(7), 1088-1102.

Visintin, P., Sturm, A. B., Mohamed Ali, M. S. and Oehlers, D. J. (2018) "Blending macro and micro fibres to enhance the serviceability behaviour of UHPFRC." *Australian Journal of Civil Engineering*, 16(2), 106-121.

Voo, Y. L., Foster, S. J., and Gilbert, R. I. (2006). "Shear strength of fiber reinforced reactive powder concrete prestressed girders without stirrups." *Journal of Advanced Concrete Technology*, 4(1), 123-132.

Voo, Y. L., Poon, W. K., and Foster, S. J. (2010). "Shear strength of steel fiber-reinforced ultrahigh-performance concrete beams without stirrups." *Journal of Structural Engineering*, 136(11), 1393-1400.

Wu, Z., Yoshikawa, H., and Tanabe, T. A. (1991). “Tension stiffness model for cracked reinforced concrete.” *Journal of Structural Eng*ineering, 117(3), 715-732.

Yang, I. H., Joh, C., and Kim, B. S. (2011). “Flexural strength of large-scale ultra high performance concrete prestressed T-beams.” *Canadian Journal of Civil Engineering*, 38(11), 1185-1195.

STATEMENT OF AUTHORSHIP

Closed form expressions for predicting moment redistribution in reinforced concrete beams with application to conventional concrete and UHPFRC
Structural Concrete, in press.

Sturm, A. B. (Candidate)

Prepared manuscript, performed all analyses, and developed model and theory (80%)

This paper reports on original research I conducted during the period of my Higher Degree by Research candidature and is not subject to any obligations or contractual agreements with a third partv that would constrain its inclusion in this thesis. I am the primary author of this paper.

Signed ..... Date 9/07/2020

Visintin, P.

Supervised and contributed to research, and acted as corresponding author (10%)

I certify that the candidate's stated contribution to the publication is accurate (as detailed above); permission is granted for the candidate in include the publication in the thesis; and the sum of all co-author contributions is equal to 100% less the candidate's stated contribution.

Signed ..... Date 07/07/2020

Oehlers, D. J.

Supervised and contributed to research (10%)

I certify that the candidate's stated contribution to the publication is accurate (as detailed above); permission is granted for the candidate in include the publication in the thesis; and the sum of all co-author contributions is equal to 100% less the candidate's stated contribution.

Signed ..... Date 7/7/20

CLOSED FORM EXPRESSIONS FOR PREDICTING MOMENT REDISTRIBUTION IN REINFORCED CONCRETE BEAMS WITH APPLICATION TO CONVENTIONAL CONCRETE AND UHPFRC

Sturm, A. B., Visintin, P. and Oehlers, D. J.

ABSTRACT

The redistribution of moment within a statically indeterminate reinforced concrete beam at the ultimate limit state occurs through variations in the flexural rigidities and through the formation of hinges. The phenomena of moment redistribution is used to increase the efficiency of reinforced concrete design by allowing moments to be transferred away from critical cross-sections thereby resulting in lower design moments. To allow for this effect in design, two main approaches are adopted. The first is to perform an elastic analysis and then to adjust the resulting distribution of moment using a codified moment redistribution factor. The second is to apply a plastic analysis allowing for the formation of hinges, and to calculate the rotational requirements at the hinges from first principles. This paper uses fundamental plastic analyses to derive closed form expressions for the hinge rotational requirements for full moment redistribution (that required to achieve the theoretical maximum applied load within the beam based on the moment capacity of sections within the beam). These closed form solutions are then used to quantify the maximum load on a beam when the rotational capacities at a hinge are less than the rotational requirements for full moment redistribution (partial moment redistribution). Closed form solutions are then used to derive moment redistribution factors which do not require semi-mechanical calibration.

INTRODUCTION

Moment redistribution (MR) allows the transfer of moments away from critical cross-sections towards underutilised cross-sections, thereby allowing for a reduction in member size, a reduction in reinforcement congestion, and an increased efficiently of a given design by allowing for the full capacity of statically indeterminate continuous RC beams to be achieved. Two approaches are available in current design standards to allow for MR while avoiding premature failure due to insufficient rotational capacity of the hinges. The most common approach is to perform an elastic analysis and to then adjust the bending moment diagram according to some MR factor (CEN 2004; ACI 2014; Standards Australia 2018). The second approach is to perform a plastic analysis to determine the rotational demand on the hinges which can then be compared directly to the rotational capacity of the hinges (CEN 2004; fib 2013).

For the first approach, the MR factor is defined as

$$K_{MR} = \frac{M_{el} - M_h}{M_{el}} \tag{1}$$

where M_{el} is the elastic moment and M_h is the actual moment at the position at which the MR factor is being evaluated - typically at the supports. National design standards give different limits for the value of K_{MR} at ultimate which are shown graphically in Fig. 1. For example, AS3600-2018 (Standards Australia 2018) give the maximum MR as a function of the ratio of the neutral axis depth to the effective depth of the section (k_u) and limits MR only to members reinforced with class N reinforcement (rupture strains greater than 0.05). In Eurocode 2 (CEN 2004), the MR factor is a function of $\underline{k_u}$ but is also adjusted for the ductility class of the reinforcement and the concrete strength.

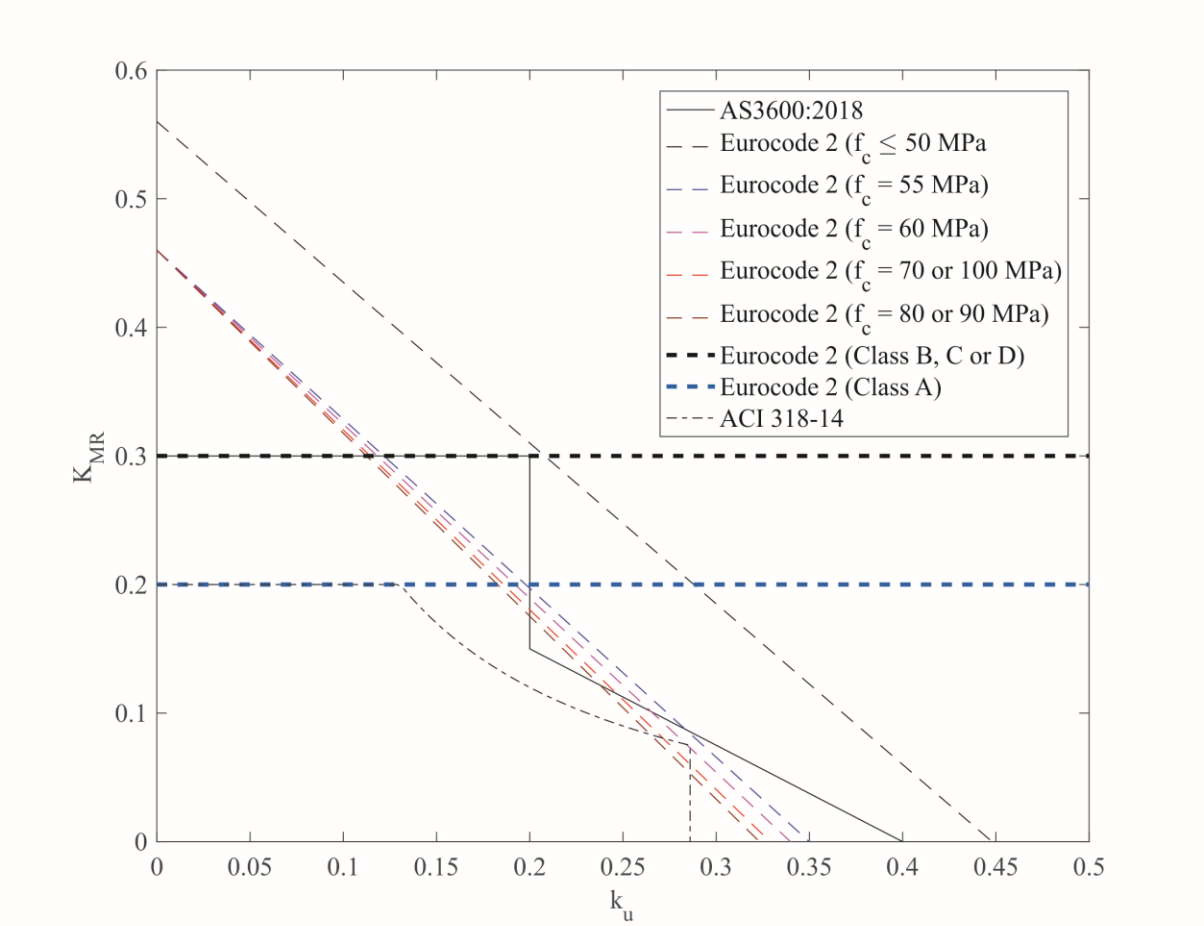

Fig. 1 Code expressions for level of MR

As shown in Fig. 1, K_{MR} is the minimum of the value defined by the concrete strength and the ductility class of the reinforcement. In ACI 318-14 (ACI 2014) the MR factor is given as a function of the strain in the tensile reinforcement, however as the strain at the top fibre is fixed at the ultimate limit, this can also be related to the neutral axis depth.

For AS3600-2018 (Standards Australia 2018), the variation in K_{MR} with k_u was determined by performing a parametric study using a numerical model and then fitting an expression to the results (Gravina & Warner 2003). That is, the relationship is semi-mechanical and calibrated to represent a safe, lower bound prediction. The expressions in the other standards are determined in a similar manner. The observed differences in Fig. 1 are therefore due to the examples considered and the underlying assumptions of the base numerical analysis and the level of conservatism built into each design standard. An identifiable limitation in current practice is, therefore, the inability to extend to applications outside of the original bounds of the parametric study for new materials without repeating the analysis. The expressions in national codes also consider the quantity of MR to be a section property (the neutral axis depth is only a function of the section from which the moment is being redistributed) and neglect the influence of the member properties such as the variation of the flexural rigidity between the hogging and sagging regions, the span of the beam and the type of loading (Oehlers et al. 2010). Where the hogging moment is defined as a moment that creates tension on the top face of the beam and a sagging moment is defined as a moment that creates compression on the bottom face of the beam.

The Eurocode 2 (CEN 2004) facilitates plastic analysis by providing relationships for the rotational capacity as a function of the neutral axis depth, concrete strength and ductility class of the reinforcement. However, the rotation requirement at the hinges needs to be determined from first principles (CEN 2004).

The goal of this paper is therefore to derive mechanics solutions that can quantify the level of MR, this is done with the aim of creating a single generic approach that can be applied to both conventional concretes and emerging materials such as ultra-high performance fibre reinforced concrete (UHPFRC). The solutions are presented in such a way as to provide designers with a choice in terms of implementation approach. They can be implemented by imposing a desired bending moment distribution and solving for the necessary rotational capacities of the hinges to achieve the imposed moment distribution. Alternatively, they can be applied by quantifying the maximum load that a member can resist based on the rotational capacity of the hinges. To allow for the first form of analysis closed form solutions are derived for the rotation at the hinges required to achieve full MR, and to allow for the second form of analysis these solutions are manipulated for application when a beam hinge has insufficient rotational capacity to achieve full MR, that is partial MR. Finally, the expressions derived are compared to experimental results for conventional reinforced concrete beams and current code approaches. To show the generic nature of the approach, the expressions derived are then used to quantify MR in UHPFRC beams.

MECHANICS OF MOMENT REDISTRIBUTION

Moment redistribution at the ultimate limit state

Let us define the mechanics of MR in this paper as the quantification of the maximum load a statically indeterminate beam can withstand as well as the rotation required at any hinges that may have formed to achieve this maximum load. At this maximum load, the beam has not collapsed. However, after this maximum load is attained, any further applied deformations may cause the formation of more hinges which may form at the maximum load or at lower applied loads which then leads to a collapse mechanism.

To allow the derivation of closed form solutions for the MR factors, we will define an elastic analysis of a statically indeterminate beam as an analysis of a beam with a constant flexural rigidity (EI), and in which the material remains elastic and hinges have not formed. Hence any deviation from this elastic distribution of moment is MR and which can now be caused by variations in the flexural rigidities along the beam and the formation of hinges.

Moment-rotation relationship of reinforced concrete

A typical moment-rotation relationship of an RC hinge is shown in Fig. 2 which, for the closed form analyses, is idealised as a linear rising branch of flexural rigidity EI, a plastic plateau at M_h of a rotational capacity θ_h and after which there is a rapidly descending branch. Here the rotational capacity θ_h is defined as the maximum possible rotation less the rotation associated with the rising branch. This definition is imposed as it allows the total rotation be defined as the summation of the rotation due to the flexural rigidity EI, and a point rotation representing the contribution of the plateau (hinge rotation).

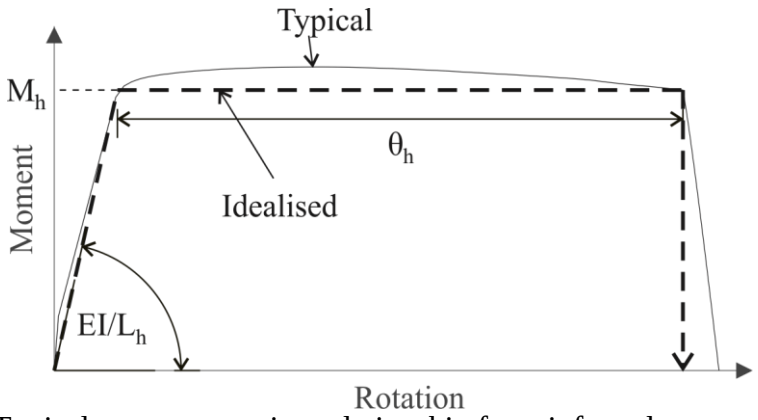

Fig. 2 Typical moment rotation relationship for reinforced concrete hinge

A number of different approaches are available in the literature for predicting the moment-rotation of a hinge in reinforced concrete. These include segmental analysis approaches that give the moment-rotation directly (Bachmann 1971; Bigaj 1999; Gravina 2002; Haskett et al. 2009; Visintin et al. 2012) and which have been extended to fibre reinforced concrete (Schumacher 2006; Visintin & Oehlers 2018), as well as hinge length approaches that allow the moment-rotation to be determined from the moment-curvature relationship (see the review of Panagiotakos & Fardis 2001).

Importantly, softening moment-rotation relationships may occur for FRC and UHPFRC, and these can be accommodated using the idealised representation in Fig. 2. This is achieved by the designer determining how far they are willing to allow the moment to reduce after achieving the peak moment. At this point M_h is the moment reduced by softening and θ_h is equal to the rotation to achieve this reduced moment (less the rotation due to the rising branch).

Moment redistribution mechanism

To discuss MR, consider the continuous beam with a span of L subjected to a uniformly distributed load (UDL) w in Fig. 3(a). The hinge rotation at the support due to w is given by θ_{hog} and the hinge rotation at the point of maximum moment in the midspan is given by θ_{sag}, The moments at each location are M_{hog} and M_{sag}, respectively. The elastic distribution of moment is illustrated in Fig. 3(b) where the moment at the midspan is half that at the supports. This represents the distribution of moment before the moment capacity is reached at any point of the beam (neglecting MR due to variations in EI).

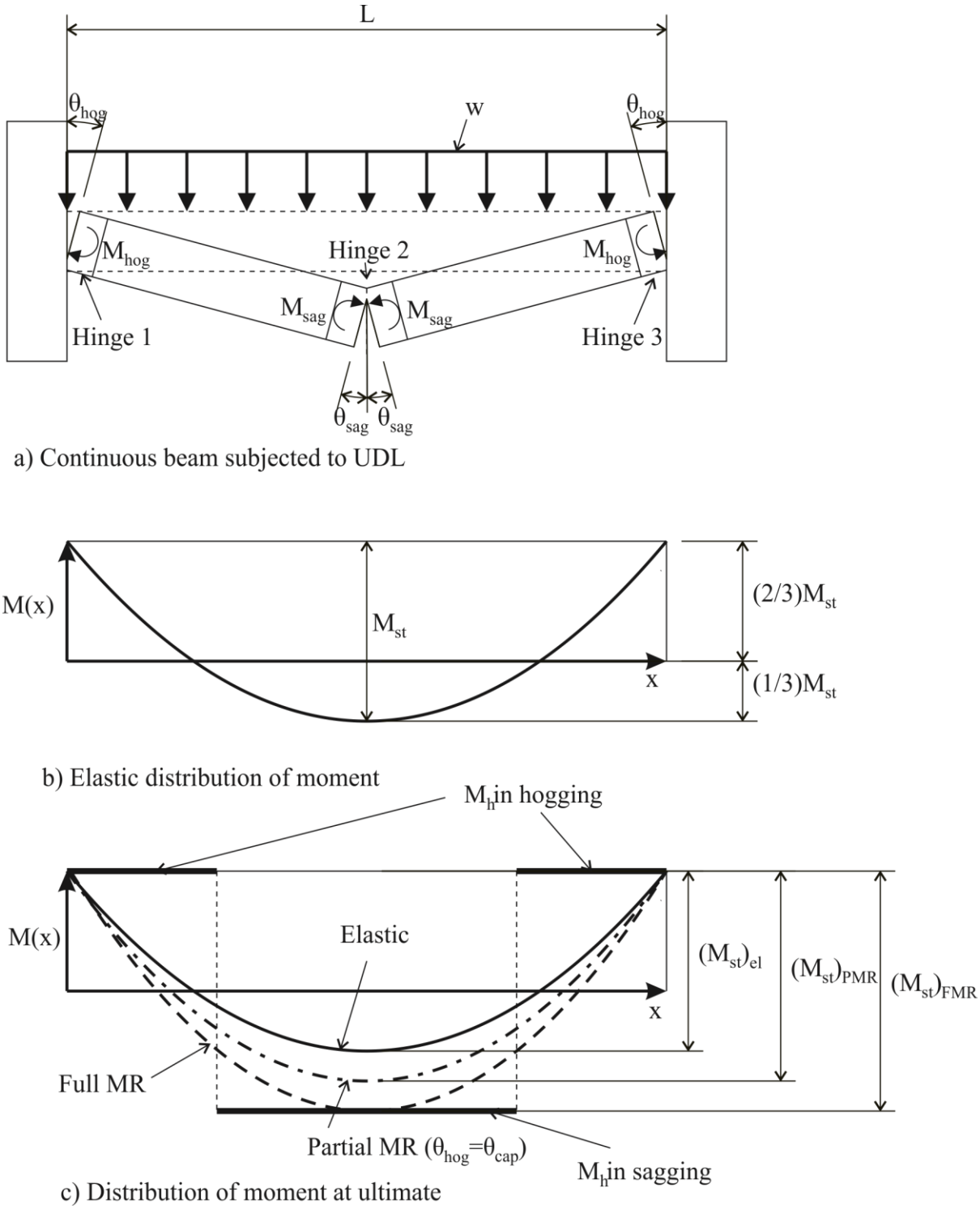

Fig. 3 Reinforced concrete beam at ultimate loading condition

In Fig. 3(c), the hinge moment capacities M_h in the hogging and sagging regions are illustrated. Before a hinge has formed M_{hog} or M_{sag} are less than M_h and after the hinge had formed they are equal to M_h. As the applied load increases, the moment capacity is eventually reached at some point along the beam. If the moment capacity is first reached at the supports, then the bending moment distribution is given by the solid line in Fig. 3(c). For a brittle beam with no rotational capacity this represents the ultimate load.

Hinges in reinforced concrete members have some ductility and therefore rotation can occur to allow the moment to redistribute from a plastic region to another (stiffer) location along the beam where the moment capacity has not yet been reached. When these locations reach their moment capacities full MR has been achieved. For a continuous beam, this occurs when the hinge moment capacity has been reached at three cross-sections: both supports and the point of maximum sagging moment at the midspan. At this point, the ultimate load is reached and the distribution of moment is given by the dashed line in Fig. 3(c). This represents the maximum possible load that could be applied to the beam assuming sufficient rotational capacity exists at the hinges at the supports, as shown by the increase in the static moment $(M_{st})_{FMR}>(M_{st})_{el}$. This situation, where the moment capacities of the sections are achieved and consequently any increase in rotational capacity does not result in an increase in MR, is referred to as full MR.

The distribution of moment associated with full MR can only be achieved if the rotational capacity at the hinges is not exceeded. If the rotational capacity is exceeded at any of the hinges, then the applied load *w* at which this occurs is the maximum capacity of the beam. In this case, the bending moment distribution would be intermediate between those corresponding to the elastic and full MR loads, that is, the dashed-dotted line in Fig. 3(c). This is referred to as partial MR because the level of MR is intermediate and lies between the elastic case and full MR. For partial MR $(M_{st})_{el}<(M_{st})_{PMR}<(M_{st})_{FMR}$, that is the ultimate load *w* is intermediate between that for the elastic and full MR cases.

In the subsequent section, expressions are developed for quantifying the rotational requirements at the hinges as a function of the applied bending moment distribution. Hence a comparison of a section's rotational capacity with the member rotational requirement at that section will determine whether the full MR can be achieved or premature failure occurs due to a lack of ductility that is partial MR.

ROTATIONAL REQUIREMENT FOR FULL MR

Consider the continuous beam with a UDL in Fig. 4(a). This beam is subject to the bending moment distribution in Fig. 4(b) which may cause some rotation at the hinges. To determine these rotations, consider the deflection at the right hand when and the right hand support is removed and the bending moment in Fig. 4(b) is applied. This causes a deflection upwards or downwards as shown in Fig. 4(c). This deflection is referred to as the elastic deflection y_{el} as this is the deflection due to the curvature distributed along the beam. However as the total deflection is required to be zero at the right hand support position, an equal and opposite deflection has to be applied to counteract this elastic deflection y_h. This deflection is generated by the hinges. The total deflection can therefore be written as

$$y = 0 = y_{el} + y_h \tag{2}$$

To determine $\underline{y_h}$ the distribution of hinges needs to be considered. There are three possible hinge locations for a continuous beam: left hand support, right hand support and position of the maximum sagging moment as shown in Fig. 4(a). Next, consider that at the instant before full MR is achieved there are two hinges in the beam. Applying these constraints there are three situations that can occur: (i) hinges at the supports as shown in Fig. 4(d-e); (ii) hinges at the left hand support and the position of maximum sagging moment as shown in Fig. 4(f-g) and (iii) hinge at the position of maximum sagging moment and the right hand support as shown in Fig. 4(h-i).

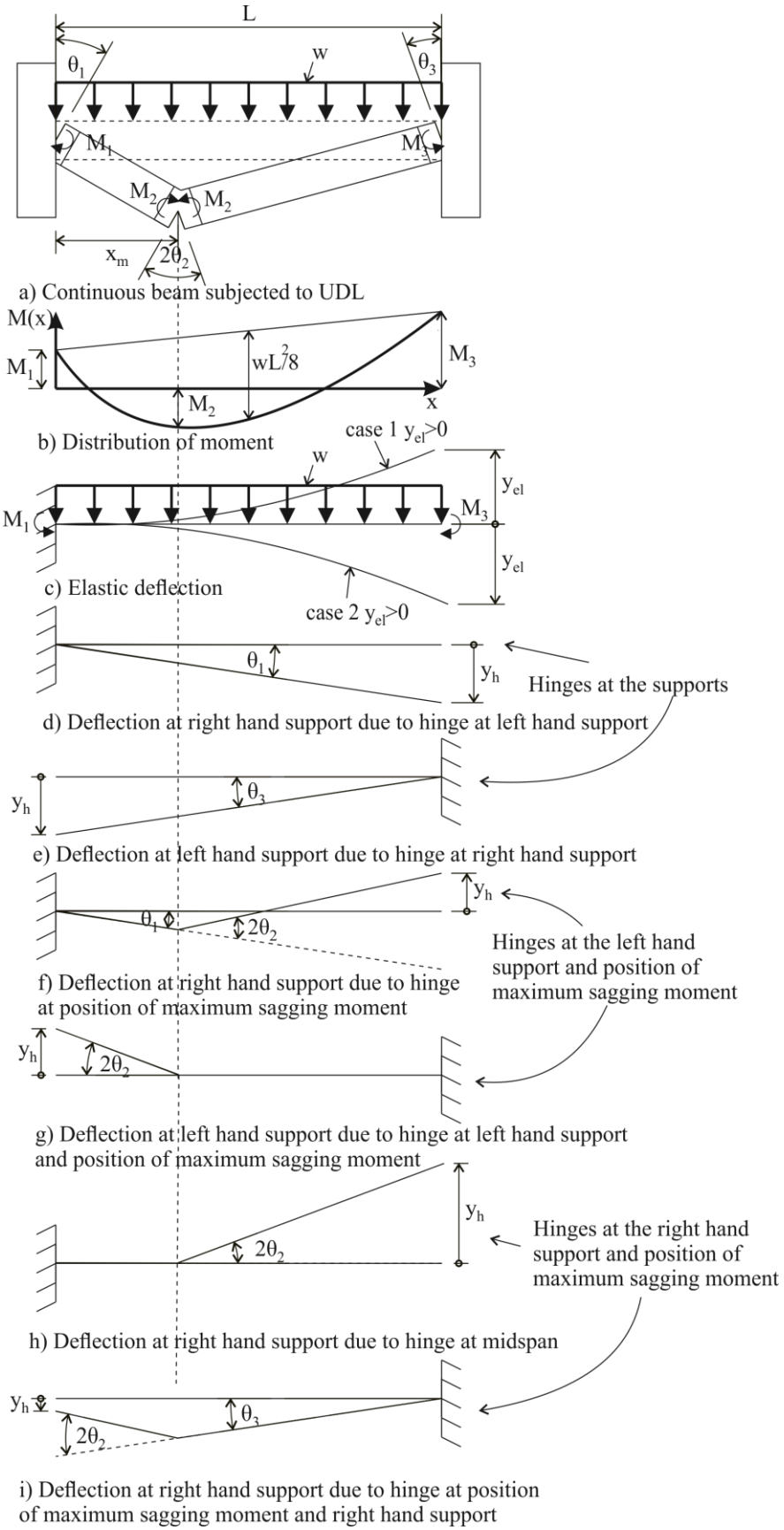

Fig. 4 Elastic and hinge deflections

To decide which situation applies, first release the right hand support in Fig. 4(a) and calculate y_{el} at this position. Next release the left hand support and calculate y_{el} at that position, paying attention to the direction of the deflection. If the elastic deflections y_{el} calculated at the left and right hand supports are both upwards, then the hinges form at the supports to counteract this deflection. The resulting hinge deflections, as shown in Fig. 4(d-e), are given as

$$y_h(0) = \theta_3 L \tag{3}$$

$$y_h(L) = \theta_1 L \tag{4}$$

If the elastic deflection y_{el} at the left hand support is upwards while the elastic deflection y_{el} at the right hand support is downwards, then hinges form at the position of the maximum sagging moment and the right hand support. From Fig. 4(h-i), the resulting deflections are given as

$$y_h(0) = \theta_3 L + 2\theta_2 x_m \tag{5}$$

$$y_h(L) = 2\theta_2 (L - x_m) \tag{6}$$

Conversely if the deflection y_{el} is downwards at the left hand support and upwards at the right hand support, then the hinges form at the left hand support and the position of the maximum sagging moment. That is

$$y_h(0) = 2\theta_2 x_m \tag{7}$$

$$y_h(L) = \theta_1 L + 2\theta_2 (L - x_m) \tag{8}$$

Finally, the last case to consider is when the deflection is downwards at both supports. In this case, first calculate the position of maximum sagging moment rotation required to counteract the hinge deflection at the left hand support and that required to counteract the hinge deflection at the right hand support, ignoring any hinges at the supports. That is

$$(\theta_2)_0 = -\frac{y_{el}(0)}{2x_m} \tag{9}$$

$$(\theta_2)_L = -\frac{y_{el}(L)}{2(L - x_m)} \tag{10}$$

The actual hinge rotation at the position of maximum sagging moment is given by the maximum of Eq. (9) and Eq. (10). For example when $(\theta_2)_0 > (\theta_2)_L$, then the additional hinge forms at left hand support. Conversely when $(\theta_2)_L < (\theta_2)_0$, then the additional hinge forms at the right hand support. In the first case, the hinge deflections are given by Eqs. (7-8) and in the second case the hinge deflections are given by Eqs. (9-10). These different cases are summarised in Table 1 where 1 is the hinge at left hand support, 2 is the hinge at the position of maximum sagging moment and 3 is the hinge at the right hand support.

Table 1: Hinge locations

		$y_{el}(0)>0$	$y_{el}(0)<0$
$y_{el}(L)>0$		1,3 Eq. (3-4)	1,2 Eq. (7-8)
$y_{el}(L)<0$	$(\theta_2)_0>(\theta_2)_L$	2,3 Eq. (5-6)	1,2 Eq. (7-8)
	$(\theta_2)_L<(\theta_2)_0$		2,3 Eq. (5-6)

The next step is to evaluate the elastic deflection y_{el} when the right hand support is released. The variation in curvature is given by the following expression

$$\chi(x) = \frac{M(x)}{EI_i};\ x_{i-1} < x < x_i;\ i \in (1, N) \tag{11}$$

where the beam is divided into N segments where EI_i is the flexural rigidity within the given segment as illustrated in Fig. 5.

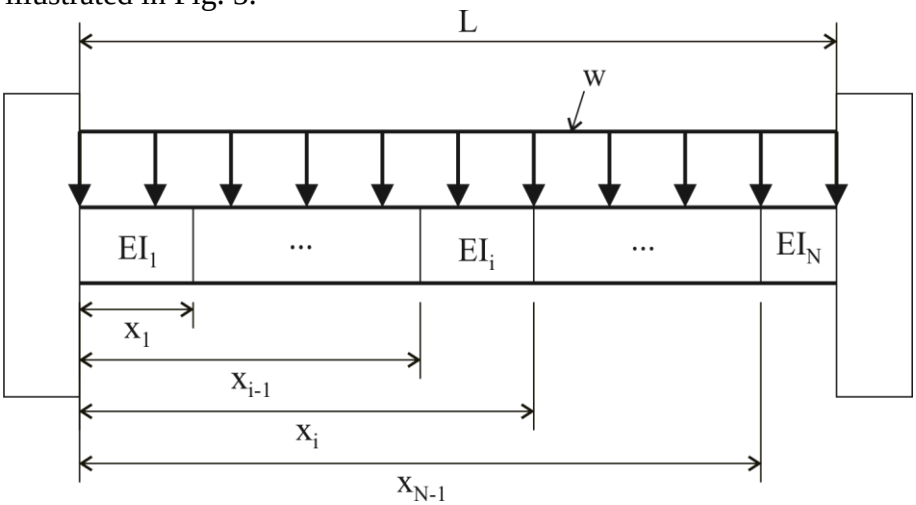

Fig. 5 Flexural rigidity of beam

For a continuous beam subjected to a UDL, the bending moment in Fig. 4(b) is

$$M(x) = w\left(\frac{Lx}{2} - \frac{x^2}{2}\right) + M_1\left(1 - \frac{x}{L}\right) + M_3\left(\frac{x}{L}\right) \tag{12}$$

and the maximum moment occurs at a distance x_m from the left hand support, where the derivative of Eq. (12) is equal to zero, that is

$$\frac{dM}{dx} = 0 = \frac{wL}{2} - wx_m - \frac{M_1}{L} + \frac{M_3}{L} \tag{13}$$

Rearranging Eq. (13) gives the position of the maximum moment as

$$x_m = \frac{L}{2} - \frac{M_1 - M_3}{wL} \tag{14}$$

which also gives the location of the maximum sagging moment, which is a location a hinge may form.

Substituting Eq. (12) into Eq. (11) gives the variation in curvature as a function of position

$$\chi(x) = \frac{w}{EI_i}\left(\frac{Lx}{2} - \frac{x^2}{2}\right) + \frac{M_1}{EI_i}\left(1 - \frac{x}{L}\right) + \frac{M_3}{EI_i}\left(\frac{x}{L}\right);\ x_{i-1} < x < x_i;\ i \in (1, N) \tag{15}$$

Integrating gives the variation in the elastic rotation of the beam, which is the portion of the rotation due to the curvature of the beam between the hinges induced by the applied loading

$$\theta_{el}(x) = \frac{w}{EI_i}\left(\frac{Lx^2}{4} - \frac{x^3}{6}\right) + \frac{M_1}{EI_i}\left(x - \frac{x^2}{2L}\right) + \frac{M_3}{EI_i}\left(\frac{x^2}{2L}\right) + (c_1)_i;\ x_{i-1} < x < x_i;\ i \in (1, N) \tag{16}$$

At the left hand support, the rotation is zero (for the case where the right hand support is released), hence

$$\theta_{el}(0) = 0 = (c_1)_1 \tag{17}$$

The rotation is also continuous across segment boundaries, therefore

$$\theta_{el}(x_{i+1}) = \frac{w}{EI_i}\left(\frac{Lx_{i+1}^2}{4} - \frac{x_{i+1}^3}{6}\right) + \frac{M_1}{EI_i}\left(x_{i+1} - \frac{{x_{i+1}}^2}{2L}\right) + \frac{M_3}{EI_i}\left(\frac{{x_{i+1}}^2}{2L}\right) + (c_1)_i$$
$$= \frac{w}{EI_{i+1}}\left(\frac{Lx_{i+1}^2}{4} - \frac{x_{i+1}^3}{6}\right) + \frac{M_1}{EI_{i+1}}\left(x_{i+1} - \frac{{x_{i+1}}^2}{2L}\right) + \frac{M_3}{EI_{i+1}}\left(\frac{{x_{i+1}}^2}{2L}\right) + (c_1)_{i+1} \quad (18)$$

Rearranging gives

$$(c_1)_{i+1} - (c_1)_i = w\left(\frac{1}{EI_i} - \frac{1}{EI_{i+1}}\right)\left(\frac{Lx_{i+1}^2}{4} - \frac{x_{i+1}^3}{6}\right) + M_1\left(\frac{1}{EI_i} - \frac{1}{EI_{i+1}}\right)\left(x_{i+1} - \frac{{x_{i+1}}^2}{2L}\right)$$
$$+ M_3\left(\frac{1}{EI_i} - \frac{1}{EI_{i+1}}\right)\left(\frac{{x_{i+1}}^2}{2L}\right) \quad (19)$$

Integrating the elastic rotation gives the elastic deflection in Fig. 4(c)

$$y_{el}(x) = \frac{w}{EI_i}\left(\frac{Lx^3}{12} - \frac{x^4}{24}\right) + \frac{M_1}{EI_i}\left(\frac{x^2}{2} - \frac{x^3}{6L}\right) + \frac{M_3}{EI_i}\left(\frac{x^3}{6L}\right) + (c_1)_i x + (c_2)_i;\ x_{i-1} < x < x_i;\ i \in (1, N) \quad (20)$$

At the right hand support the deflection is zero, hence

$$y_{el}(0) = 0 = (c_2)_1 \quad (21)$$

and given the deflection is continuous across segment boundaries

$$y_{el}(x_{i+1}) = \frac{w}{EI_i}\left(\frac{Lx_{i+1}^3}{12} - \frac{x_{i+1}^4}{24}\right) + \frac{M_1}{EI_i}\left(\frac{{x_{i+1}}^2}{2} - \frac{{x_{i+1}}^3}{6L}\right) + \frac{M_3}{EI_i}\left(\frac{{x_{i+1}}^3}{6L}\right) + (c_1)_i x_{i+1} + (c_2)_i$$
$$= \frac{wLx_{i+1}^3}{12EI_{i+1}} - \frac{w{x_{i+1}}^4}{24EI_{i+1}} + \frac{M_1}{EI_{i+1}}\left(\frac{{x_{i+1}}^2}{2} - \frac{{x_{i+1}}^3}{6L}\right) + \frac{M_3}{EI_{i+1}}\left(\frac{{x_{i+1}}^3}{6L}\right) + (c_1)_{i+1} x_{i+1} + (c_2)_{i+1} \quad (22)$$

Rearranging Eq. (22) gives

$$(c_2)_{i+1} - (c_2)_i = w\left(\frac{1}{EI_i} - \frac{1}{EI_{i+1}}\right)\left(\frac{Lx_{i+1}^3}{12} - \frac{x_{i+1}^4}{24}\right) + M_1\left(\frac{1}{EI_i} - \frac{1}{EI_{i+1}}\right)\left(\frac{{x_{i+1}}^2}{2} - \frac{{x_{i+1}}^3}{6L}\right)$$
$$+ M_3\left(\frac{1}{EI_i} - \frac{1}{EI_{i+1}}\right)\left(\frac{{x_{i+1}}^3}{6L}\right) - [(c_1)_{i+1} - (c_1)_i]x_{i+1}$$
$$= -w\left(\frac{1}{EI_i} - \frac{1}{EI_{i+1}}\right)\left(\frac{Lx_{i+1}^3}{6} - \frac{x_{i+1}^4}{8}\right) - M_1\left(\frac{1}{EI_i} - \frac{1}{EI_{i+1}}\right)\left(\frac{{x_{i+1}}^2}{2} - \frac{{x_{i+1}}^3}{3L}\right)$$
$$- M_3\left(\frac{1}{EI_i} - \frac{1}{EI_{i+1}}\right)\left(\frac{{x_{i+1}}^3}{3L}\right) \quad (23)$$

From Eq. (12), the elastic deflection at the right hand support is given by

$$y_{el}(L) = \frac{wL^4}{24EI_N} + \frac{M_1L^2}{3EI_N} + \frac{M_3L^2}{6EI_N} + (c_1)_N L + (c_2)_N = a_1 w + a_2 M_1 + a_3 M_3 \quad (24)$$

where

$$a_1 = \frac{L^4}{24EI_N} + \sum_{i=1}^{N-1}\left(\frac{1}{EI_i} - \frac{1}{EI_{i+1}}\right)\left(\frac{L^2x_{i+1}^2}{4} - \frac{Lx_{i+1}^3}{3} + \frac{x_{i+1}^4}{8}\right) \quad (25a)$$

$$a_2 = \frac{L^2}{3EI_N} + \sum_{i=1}^{N-1}\left(\frac{1}{EI_i} - \frac{1}{EI_{i+1}}\right)\left(Lx_{i+1} - x_{i+1}^2 + \frac{x_{i+1}^3}{3L}\right) \quad (25b)$$

$$a_3 = \frac{L^3}{6EI_N} + \sum_{i=1}^{N-1}\left(\frac{1}{EI_i} - \frac{1}{EI_{i+1}}\right)\left(\frac{x_{i+1}^2}{2} - \frac{x_{i+1}^3}{3L}\right) \quad (25c)$$

Following the same procedure, the elastic deflection at the left hand support when this is released is given by

$$\theta_3 L + 2\theta_2 x_m = -y_{el}(0) = -[a_1{}'w + a_2{}'M_1 + a_3{}'M_3] \quad (26)$$

where

$$a_1' = \frac{L^4}{24EI_1} - \sum_{i=1}^{N-1}\left(\frac{1}{EI_i} - \frac{1}{EI_{i+1}}\right)\left(\frac{L^2 x'^2_{i+1}}{4} - \frac{L x'^3_{i+1}}{3} + \frac{x'^4_{i+1}}{8}\right) \tag{27a}$$

$$a_2' = \frac{L^2}{6EI_1} - \sum_{i=1}^{N-1}\left(\frac{1}{EI_i} - \frac{1}{EI_{i+1}}\right)\left(\frac{x'^2_{i+1}}{2} - \frac{x'^3_{i+1}}{3L}\right) \tag{27b}$$

$$a_3' = \frac{L^2}{3EI_1} - \sum_{i=1}^{N-1}\left(\frac{1}{EI_i} - \frac{1}{EI_{i+1}}\right)\left(Lx'_{i+1} - x'^2_{i+1} + \frac{x'^3_{i+1}}{3L}\right) \tag{27c}$$

where the position with respect to the right hand support is given by

$$x' = L - x \tag{28}$$

From Eqs. (24) and (26), the elastic deflections at the supports can be calculated. Table 1 can then be used to determine the position of the hinges, and therefore the correct expressions for the hinge deflections can be selected from Eqs. (3-8). Hence by substituting the hinge and elastic deflections into Eq. (2) and rearranging, the rotations can be determined. From this and for the case in Fig. 4(d-e)

$$\theta_1 = -\frac{y_{el}(L)}{L} \tag{29}$$

$$\theta_3 = -\frac{y_{el}(0)}{L} \tag{30}$$

For the case in Figs. 4(f-g)

$$\theta_2 = -\frac{y_{el}(0)}{2x_m} \tag{31}$$

$$\theta_1 = -\frac{y_{el}(L)}{L} - 2\theta_2\left(1 - \frac{x_m}{L}\right) \tag{32}$$

For the case in Figs. 4(h-i)

$$\theta_2 = -\frac{y_{el}(L)}{2(L - x_m)} \tag{33}$$

$$\theta_3 = -\frac{y_{el}(0)}{L} - 2\theta_2\frac{x_m}{L} \tag{34}$$

The suggested workflow, for applying this approach to design a beam for moment redistribution, is given in Fig. 6.

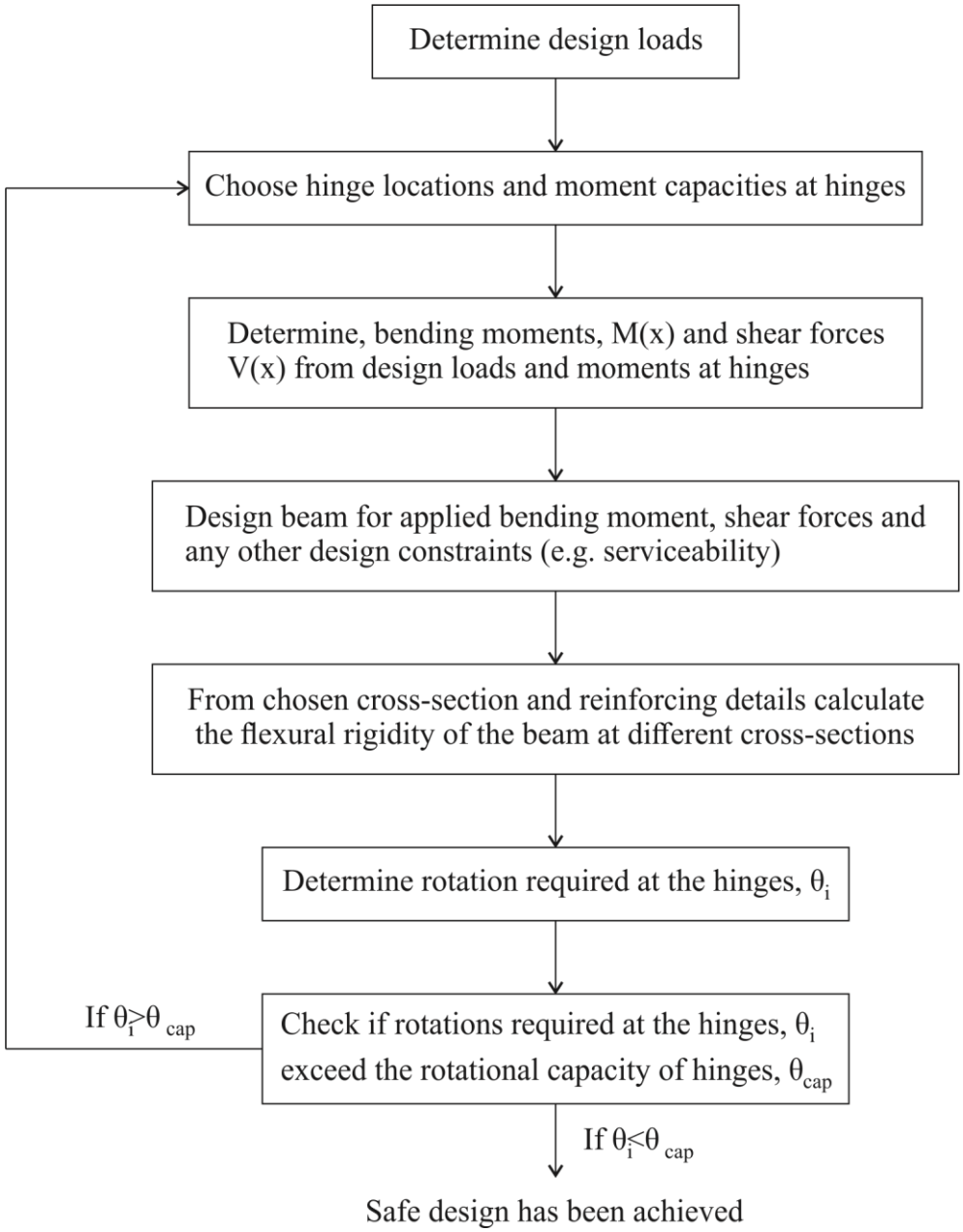

Fig. 6 Design procedure to allow sufficient MR

In this example, a continuous beam with a UDL has been considered, however, other support and loading arrangements can be considered as well. For example a propped cantilever can be considered by setting the moment at the simple support to zero. The required rotation for a continuous beam with a point load is also given in Appendix A.

APPLIED LOAD FOR PARTIAL MR

If insufficient rotational capacity is available at the hinges such that full MR cannot be achieved, the expressions in the previous section can be adapted to calculate the load that can be achieved given the available rotational capacity, that is partial MR. To do this, first a partial mechanism needs to be identified. This can be done by inspecting the elastic distribution of moment to find the location of the first hinge. From this, three partial mechanisms involving a single hinge can be identified: (i) hinge at left hand support; (ii) hinge at right hand support; (iii) hinge at position of maximum sagging moment.

Hinge at left hand support

Substituting Eq. (24) and Eq. (4) into Eq. (2) and rearranging gives the following

$$\theta_1 L = -[a_1 w + a_2 M_1 + a_3 M_3] \tag{35}$$

and as the hinge deflection at the left hand support due to a rotation at this support is zero, the following is obtained by substituting Eq. (26) into Eq. (2)

$$0 = -[a_1' w + a_2' M_1 + a_3' M_3] \tag{36}$$

Solving Eqs. (35) and (36) gives the following applied load and moment at the right hand support

$$M_3 = \frac{M_1(a_2 a_1' - a_1 a_2') + \theta_1 L a_1'}{a_1 a_3' - a_3 a_1'} \tag{37}$$

$$w = -\frac{a_2 M_1 + a_3 M_3 + \theta_1 L}{a_1} \tag{38}$$

Hinge at right hand support

Similarly to the previous case but for a hinge at the right hand support, the moment at the left hand support and the applied load is given by

$$M_3 = \frac{M_3(a_3 a_1' - a_1 a_3') - \theta_3 L a_1}{a_1 a_2' - a_2 a_1'} \tag{39}$$

$$w = -\frac{a_2 M_1 + a_3 M_3}{a_1} \tag{40}$$

Hinge at the position of maximum sagging moment

To solve this, three simultaneous equations are required. Substituting Eq. (24) and Eq. (6) into Eq. (2) gives

$$2\theta_2 (L - x_m) = -[a_1 w + a_2 M_1 + a_3 M_3] \tag{41}$$

From Eq. (26) and Eq. (7)

$$2\theta_2 x_m = -[a_1' w + a_2' M_1 + a_3' M_3] \tag{42}$$

From Eq. (12)

$$M(x_m) = M_2 = w\left(\frac{L x_m}{2} - \frac{x_m^2}{2}\right) + M_1\left(1 - \frac{x_m}{L}\right) + M_3\left(\frac{x_m}{L}\right) \tag{43}$$

x_m is determined from the distribution of moment immediately before the formation of the hinge at the position of maximum sagging moment. Solving gives

$$M_3 = \frac{a_2' M_2 + 2\theta_2\left(x_m - \frac{x_m^2}{L}\right)}{-a_3' + (a_2' + a_3')\frac{x_m}{L}} \tag{44}$$

$$M_1 = \frac{a_3 M_2 + 2\theta_2\left(x_m - \frac{x_m^2}{L}\right)}{a_3 - (a_2 + a_3)\frac{x_m}{L}} \tag{45}$$

$$w = \frac{M_2}{\frac{L x_m}{2} - \frac{x_m^2}{2}} - M_1 \frac{1 - \frac{x_m}{L}}{\frac{L x_m}{2} - \frac{x_m^2}{2}} - M_3 \frac{\frac{x_m}{L}}{\frac{L x_m}{2} - \frac{x_m^2}{2}} \tag{46}$$

After calculating the distribution of moments, the moments at the other possible hinge locations need to be checked. If the hinge moment at any hinge location is exceeded, a partial hinge mechanism with two hinges needs to be considered.

Hinge at left hand support and right hand supports
For this case the uniformly distributed load is given by Eq. (38).

Hinge at the position of maximum sagging moment and left hand support
Substituting Eq. (24) and Eq. (8) into Eq. (1) gives

$$\theta_1 L + 2\theta_2(L - x_m) = -[a_1 w + a_2 M_1 + a_3 M_3] \tag{47}$$

Solving Eq. (47) and Eq. (42)

$$M_3 = \frac{(a_2 a_1' - a_1 a_2')M_1 + \theta_1 L a_1' + 2\theta_2[L a_1' - x_m(a_1 + a_1')]}{a_1 a_3' - a_3 a_1'} \tag{48}$$

And the applied load is given by Eq. (46).

Hinge at maximum sagging moment and right hand support
Similarly for a hinge at the position of maximum sagging moment and right hand support, the moment at the left hand support is given by

$$M_1 = \frac{(a_3 a_1' - a_1 a_3')M_1 - \theta_3 L a_1 + 2\theta_2[L a_1' - x_m(a_1 + a_1')]}{a_1 a_3' - a_3 a_1'} \tag{49}$$

And the applied load is given by Eq. (46).

Hinges at maximum sagging moment, left hand support and right hand support
If after trying a two hinge mechanism, the moment still exceeds the hinge moment at the third hinge location, then a three hinge mechanism needs to be considered. This corresponds to the distribution of moment determined using plastic limit analysis. Rearranging Eq. (30) at this stage gives the applied load as

$$w = \frac{-M_1\left(1 - \frac{x_m}{L}\right) + M_2 - M_3\left(\frac{x_m}{L}\right)}{\frac{L x_m}{2} - \frac{x_m^2}{2}} \tag{50}$$

MOMENT REDISTRIBUTION FACTORS

In this section, a single value of flexural rigidity is attributed to the hogging regions of a beam and a single value is attributed to the sagging region as this is most commonly encountered in design (where the reinforcement ratio is different in each region). Simple expressions are derived for the commonly encountered design cases in Fig. 7. Solutions for other situations are possible. For example they could be derived for all the situations described in the previous section, however, the solutions are complex and have limited applicability and instead the expressions in the previous section could be applied directly.

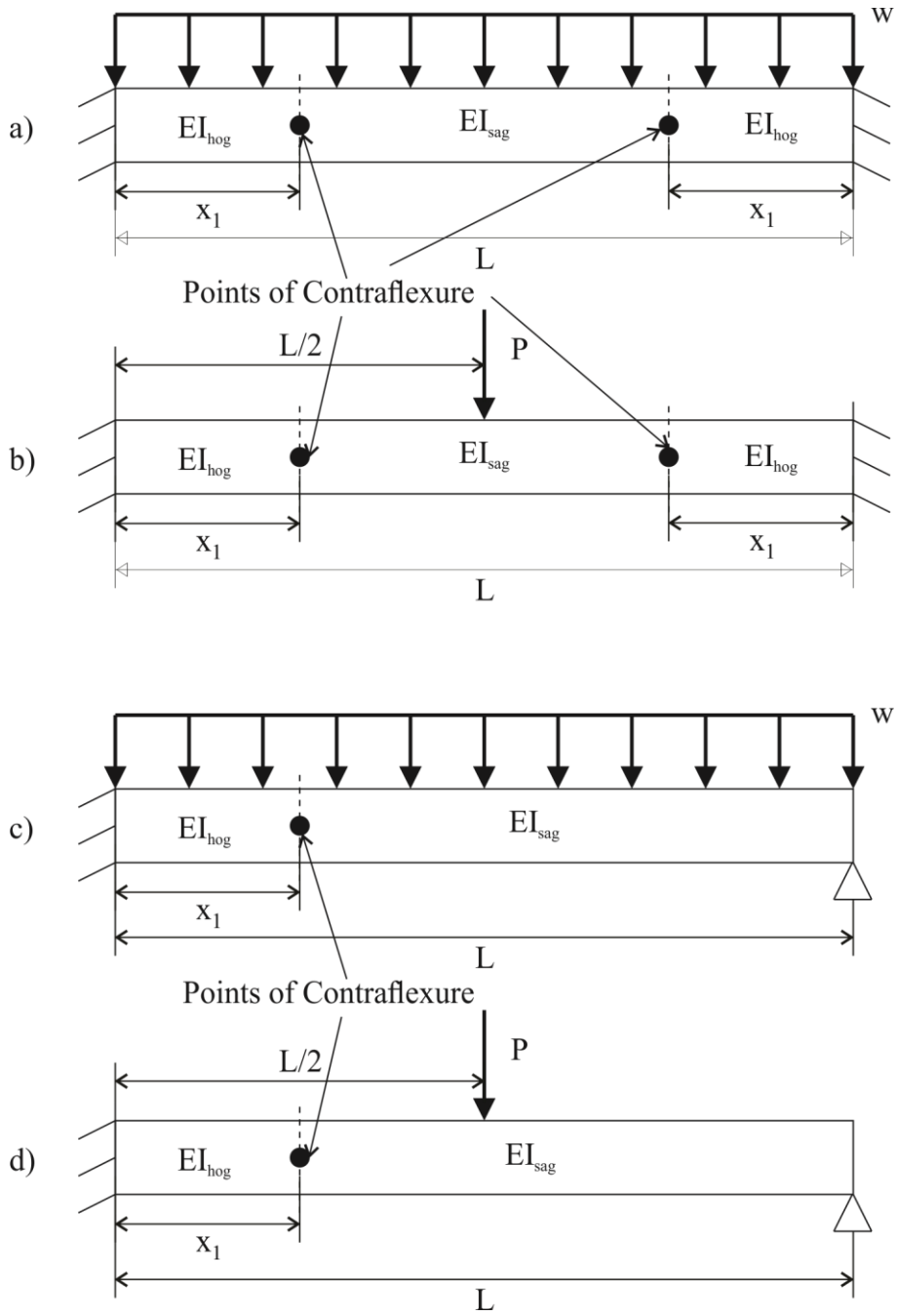

Fig. 7 Cases for simplified expressions; a) continuous beam with identical end moments and UDL; b) continuous beam with identical end moments and central point load; c) propped cantilever with UDL; d) propped cantilever with point load

Hinge at support

Consider the continuous beam in Fig. 7(a) with equal end moments and subject to a UDL. Let $EI_{hog}=EI_1=EI_3$, $EI_{sag}=EI_2$, $M_{hog}=M_1=M_3$ and $\theta_{hog}=\theta_1=\theta_3$. Hence from Eq. (35), the uniformly distributed load is

$$w = -\theta_{hog}\left(\frac{L}{a_1}\right) - M_{hog}\left(\frac{a_2 + a_3}{a_1}\right) \tag{51}$$

The elastic moment at the support is then given by

$$M_{el} = -\frac{wL^2}{12} = \frac{L^2}{12a_1}\left[\theta_{hog}L + M_{hog}(a_2 + a_3)\right] = \frac{\theta_{hog}L + M_{hog}\left[\frac{L^2}{2EI_{sag}} + \left(\frac{1}{EI_{hog}} - \frac{1}{EI_{sag}}\right)Lx_1\right]}{\frac{L^2}{2EI_{sag}} + \left(\frac{1}{EI_{hog}} - \frac{1}{EI_{sag}}\right)\left(3x_1^2 - \frac{2x_1^3}{L}\right)} \quad (52)$$

And from Eq. (1), the MR factor at the support is given as

$$K_{MR,hog} = \frac{1 + \frac{M_{hog}}{\theta_{hog}}\left(\frac{1}{EI_{hog}} - \frac{1}{EI_{sag}}\right)\left(x_1 - \frac{3x_1^2}{L} + \frac{2x_1^3}{L^2}\right)}{1 + \frac{M_{hog}}{\theta_{hog}}\left[\frac{L}{2EI_{sag}} + \left(\frac{1}{EI_{hog}} - \frac{1}{EI_{sag}}\right)x_1\right]} \quad (53)$$

Similar expressions can be derived for other loading conditions, which have the following general form

$$K_{MR,hog} = \frac{1 + \frac{M_{hog}}{\theta_{hog}}L\left(\frac{1}{EI_{hog}} - \frac{1}{EI_{sag}}\right)b_1}{1 + \frac{M_{hog}}{\theta_{hog}}L\left[b_2\frac{1}{EI_{sag}} + \left(\frac{1}{EI_{hog}} - \frac{1}{EI_{sag}}\right)b_3\right]} \quad (54)$$

where b_1, b_2 and b_3 are given in Table 2 and in which $\xi = x_1/L$. This expression gives the moment redistribution at the support when the rotational capacity of the hinge at the support is achieved. This corresponds to partial MR as discussed earlier. However, there is an upper limit on Eq. (54). If the moment at both supports and at the midspan are equal to their hinge moment capacities, then no additional moment redistribution can occur even if the rotation at the hinges is less than the rotational capacity of the hinges. This corresponds to full MR and in a subsequent section an expression for this upper limit is determined using a basic plastic analysis.

Table 2 MR Coefficients for Hinge at Support

	b_1	b_2	b_3
Continuous beam with equal end moments and UDL	$\xi - 3\xi^2 + 2\xi^3$	1/2	ξ
Continuous beam with equal end moments and central point load	$\xi - 2\xi^2$	1/2	ξ
Propped cantilever with UDL	$\xi - 3\xi^2 + 3\xi^3 - \xi^4$	1/3	$\xi - \xi^2 + \frac{1}{3}\xi^3$
Propped cantilever with central point load	$\xi - \frac{7}{3}\xi^2 + \frac{11}{9}\xi^3$	1/3	$\xi - \xi^2 + \frac{1}{3}\xi^3$

As a simplification, b_1 and b_3 can be approximated using the elastic point of contraflexure as shown in Table 3.

Table 3 Approximate MR Coefficients for a Hinge at the Support

	b_1	b_3
Continuous beam with equal end moments and UDL (ξ =0.211)	0.0962	0.211
Continuous beam with equal end moments and central point load (ξ =0.25)	0.125	0.25
Propped cantilever with UDL (ξ =0.25)	0.106	0.193
Propped cantilever with central point load (ξ =3/11)	0.124	0.205

Hinge at the midspan

Similar expressions can also be derived if the hinge is assumed to form in the midspan. From Eq. (41) setting $\theta_2 = \theta_{sag}$ and $x_2 = L/2$ gives the following for the beam in Fig. 7(a)

$$\theta_{sag} = -w\left(\frac{a_1}{L}\right) - M_{hog}\left(\frac{a_2 + a_3}{L}\right) \tag{55}$$

From Eq. (12), the midspan moment is given by

$$M_{sag} = \frac{wL^2}{8} + M_{hog} \tag{56}$$

Rearranging and substituting into Eq. (55) gives the rotation as

$$\theta_{sag} = -w\left[\frac{a_1}{L} - (a_2 + a_3)\frac{L}{8}\right] - M_{sag}\left(\frac{a_2 + a_3}{L}\right) \tag{57}$$

Rearranging gives the UDL as

$$w = -\frac{\theta_{sag}L + M_{sag}(a_2 + a_3)}{a_1 - (a_2 + a_3)\left(\frac{L^2}{8}\right)} \tag{58}$$

The elastic moment is then

$$M_{el} = \frac{wL^2}{24} = -\frac{L^2}{24}\left[\frac{\theta_{sag}L + M_{sag}(a_2 + a_3)}{a_1 - (a_2 + a_3)\left(\frac{L^2}{8}\right)}\right] = \frac{\theta_{sag}L + M_{sag}\left[\frac{L^2}{2EI_{sag}} + \left(\frac{1}{EI_{hog}} - \frac{1}{EI_{sag}}\right)Lx_1\right]}{\frac{L^2}{2EI_{sag}} + \left(\frac{1}{EI_{hog}} - \frac{1}{EI_{sag}}\right)\left(3Lx_1 - 6x_1^2 + \frac{4x_1^3}{L}\right)} \tag{59}$$

From Eq. (1), the MR factor is given by

$$K_{MR,sag} = \frac{1 + \frac{M_{sag}}{\theta_{sag}}\left(\frac{1}{EI_{hog}} - \frac{1}{EI_{sag}}\right)\left(-2x_1 + \frac{6x_1^2}{L} - \frac{4x_1^3}{L^2}\right)}{1 + \frac{M_{sag}}{\theta_{sag}}\left[\frac{L}{2EI_{sag}} + \left(\frac{1}{EI_{hog}} - \frac{1}{EI_{sag}}\right)x_1\right]} \tag{60}$$

Similar expressions can be derived for other loading conditions in the following form

$$K_{MR,sag} = \frac{1 + \frac{M_{sag}}{\theta_{sag}}L\left(\frac{1}{EI_{hog}} - \frac{1}{EI_{sag}}\right)b_4}{1 + \frac{M_{sag}}{\theta_{sag}}L\left[b_5\frac{1}{EI_{sag}} + \left(\frac{1}{EI_{hog}} - \frac{1}{EI_{sag}}\right)b_6\right]} \tag{61}$$

where the coefficients are given in Table 4. ξ can be approximated using the elastic points of contraflexure, resulting in the values in Table 5.

Table 4 MR Coefficients for Hinge at Midspan

	b_4	b_5	b_6
Continuous beam with equal end moments and UDL	$-2\xi + 6\xi^2 - 4\xi^3$	1/2	ξ
Continuous beam with equal end moments and central point load	$-\xi + 2\xi^2$	1/2	ξ
Propped cantilever with UDL	$-\frac{64}{27}\xi + \frac{64}{9}\xi^2 - \frac{64}{9}\xi^3 + \frac{64}{27}\xi^4$	32/27	$\frac{32}{9}\xi - \frac{32}{9}\xi^2 + \frac{32}{27}\xi^3$
Propped cantilever with central point load	$-\frac{6}{5}\xi + \frac{14}{5}\xi^2 - \frac{22}{15}\xi^3$	2/3	$2\xi - 2\xi^2 + \frac{2}{3}\xi^3$

Table 5 Approximate MR Coefficients for a Hinge at the Support

	b_4	b_6
Continuous beam with equal end moments and UDL (ξ =0.211)	-0.192	0.211
Continuous beam with equal end moments and central point load (ξ =0.25)	-0.125	0.25
Propped Cantilever with UDL (ξ =0.25)	-0.25	0.685
Propped Cantilever with Central Point Load (ξ =3/11)	-0.149	0.41

Upper limit on MR

If the hinge moment capacity has been reached at both supports and the midspan, additional moment redistribution cannot occur even if the rotation at these hinges is less than the rotational capacity and hence full MR is achieved. Setting $M_1=M_3=M_{hog}$ and $M_2=M_{sag}$ in Eq. (50), the uniformly distributed load is given as

$$w = \frac{8M_{sag}}{L^2} - \frac{8M_{hog}}{L^2} \tag{62}$$

The elastic moment at the support is then

$$M_{el} = -\frac{wL^2}{12} = -\frac{2}{3}M_{sag} + \frac{2}{3}M_{hog} \tag{63}$$

From Eq. (1), the MR factor at the support is

$$K_{MR,hog} = \frac{-\frac{2}{3}M_{sag} - \frac{1}{3}M_{hog}}{-\frac{2}{3}M_{sag} + \frac{2}{3}M_{hog}} \tag{64}$$

Similar expressions can be derived for other loading conditions in the following form

$$K_{MR,hog} = \frac{b_7 M_{sag} + b_8 M_{hog}}{b_7 M_{sag} + b_9 M_{hog}} \tag{65}$$

where b_7, b_8 and b_9 are given in Table 6.

Table 6 MR Coefficients for upper limit on MR

	b_7	b_8	b_9
Continuous Beam with UDL	-2	-1	2
Continuous Beam with Central Point Load	-1	-1	1
Propped Cantilever with UDL	-16	-9	6
Propped Cantilever with Central Point Load	-6	-5	3

Design Chart

Eq. (54) can be rewritten as

$$K_{MR,hog} = \frac{1 + X(1-\alpha)b_1}{1 + X[\alpha b_2 + (1-\alpha)b_3]} \tag{66}$$

where

$$X = \frac{M_{hog}}{\theta_{hog}} \frac{L}{EI_{hog}} \tag{67}$$

and

$$\alpha = \frac{EI_{hog}}{EI_{sag}} \tag{68}$$

Similarly, Eq. (65) can be rewritten as

$$K_{MR,hog} = \frac{b_7 - b_8\beta}{b_7 - b_9\beta} \tag{69}$$

where

$$\beta = -\frac{M_{hog}}{M_{sag}} \tag{70}$$

From Eqs. (66) and (69) for specific combinations of α and β, K_{MR} can be plotted as a function of X in Fig. 8 that is similar to that by Visintin & Oehlers (2016). Note that α and β have been shown as equal as the stiffness is proportional to the strength for reinforced concrete members (Priestly et al. 2017). The curves are of a similar shape to the code expressions if X is assumed to be proportional to the neutral axis depth to effective depth ratio.

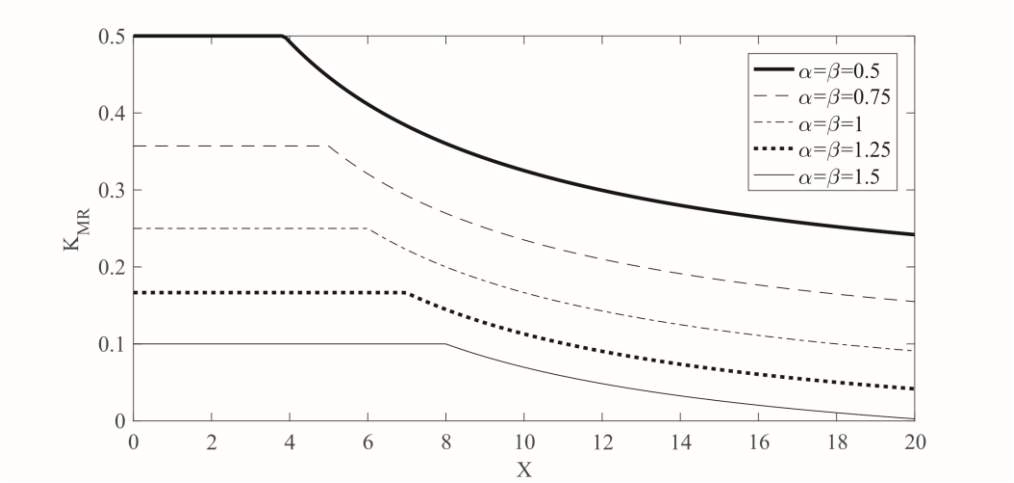

Fig. 8 Design Chart of Continuous Beam subjected to a UDL with constant end moments

COMPARISON TO EXPERIMENTAL RESULTS

The tests by do Carmo & Lopes (2004) and Scott & Whittle (2005) on two-span continuous beams are compared with the theory in Table 7 where: where the column labelled Pred. (Partial MR) refers to the MR estimated considering Partial MR as given by Eq. (66); while Pred. (full MR) refers to the MR obtained assuming full MR as given by Eq. (69).

Table 7 Comparison to Test Results

Reference	Specimen	M_{hog}	M_{sag}	EI_{hog}	EI_{sag}	θ_{hog}	K_{MR}		M_h/M_{el}		
		kNm	kNm	$\times 10^9$ Nmm^2	$\times 10^9$ Nmm^2	radians	Exp.	Pred.		Exp.	Pred.	Exp./ Pred.
								Partial MR	Full MR			
do Carmo & Lopes (2004)	V1-0.8-0.7	20.2	44.3	921	1899	0.0187	0.39	0.53	**0.51**	0.61	0.49	1.24
	V1-0.8-1.4	38.4	44.3	1628	1899	0.0157	0.16	0.35	**0.19**	0.84	0.81	1.04
	V1-0.8-2.1	50.1	60.9	2149	2543	0.0173	0.35	0.38	**0.22**	0.65	0.78	0.83
	V1-0.8-2.9	66.6	89.5	2756	3519	0.0143	0.11	0.35	**0.28**	0.89	0.72	1.24
	V1-0.8-3.8	80.8	89.5	3233	3519	0.0109	0.05	0.25	**0.17**	0.95	0.83	1.14
	V1-0.8-5.0	98.3	89.5	3705	3519	0.0076	-0.02	0.15	**0.05**	1.02	0.95	1.07
Scott & Whittle (2005)	B2T12D	13.5	18	463	643	0.0503	0.27	0.65	**0.27**	0.73	0.73	1.00
	B2T12DX	13.5	18	463	643	0.0503	0.28	0.65	**0.27**	0.72	0.73	0.99
	B2T12DXX	13.5	18	463	643	0.0503	0.34	0.65	**0.27**	0.66	0.73	0.90
	B3T10D	13.6	18	479	643	0.0452	0.26	0.63	**0.27**	0.74	0.73	1.01
	B5T8D	16.1	18	504	643	0.0401	0.22	0.56	**0.18**	0.78	0.82	0.95
	B2T8E	8.2	11.4	232	329	0.0411	0.4	0.57	**0.29**	0.6	0.71	0.85
	B2T8EX	8.2	11.4	232	329	0.0411	0.55	0.57	**0.29**	0.45	0.71	0.63
	B2T20BH	74.3	105	4272	5949	0.0189	0.38	0.55	**0.3**	0.62	0.7	0.89
	B2T20BHX	74.3	105	4272	5949	0.0189	0.33	0.55	**0.3**	0.67	0.7	0.96
	B2T12DH	14.6	22.9	487	682	0.0394	0.4	0.59	**0.35**	0.6	0.65	0.92
	B2T12DHX	14.6	22.9	487	682	0.0394	0.45	0.59	**0.35**	0.55	0.65	0.85
											Mean	0.97
											Std. Dev.	0.15
											C.O.V.	0.16

The actual predicted K_{MR} value, which is in bold in Table 7, is the minimum of the partial and full interaction values. In all cases the beams reached full MR. This demonstrates the difficulty with trying to quantify MR with lab-scale specimens as these specimens tend to be quite ductile which makes partial MR behaviour difficult to explore. This also highlights the importance of the presented theory as this allows us to relate the MR to the rotational capacity which can be measured experimentally in a laboratory setting.

The coefficients used in Eqs. (66) and (69) were given by the values for a propped cantilever with a central point load in Tables 3 and 6 where ξ =3/11 was assumed, which is the elastic point of contraflexure. The moment capacity, rotational capacity and flexural rigidity were evaluated using the numerical segmental model described in Visintin & Oehlers (2018). This approach can simulate concretes without fibres by setting the concrete tensile strength to zero after cracking. The material properties were taken from the published results or were estimated using the relationships in the fib Model Code 2010 (fib 2013).

The errors in Table 7 are presented in terms of M_h/M_{el} which is related to K_{MR} by rearranging Eq. (1) as follows

$$\frac{M_h}{M_{el}} = 1 - K_{MR} \tag{71}$$

M_h/M_{el} is also the parameter by which MR is represented in the fib Model Code 2010 (fib 2013). The reason for this is K_{MR} maybe positive or negative, therefore, the Exp./Pred. values can be difficult to interpret. For example if the predicted K_{MR} is small and positive while the experimental K_{MR} is small and negative this can result in a negative Exp./Pred. As M_h/M_{el} is distributed around 1 ensuring a positive value for Exp./Pred. the interpretation of the errors is more straightforward.

COMPARISON TO CODE APPROACHES

The parametric study in Fig. 9 compares Eq. (53) for full MR to code values that also apply to full MR. The moment capacity, rotational capacity and flexural rigidity of the beam were also calculated using the model in Visintin & Oehlers (2018). The default values in this study are: effective depth of 500 mm; concrete strength of 40 MPa; class N reinforcement; span-to-depth ratio of 20; continuous beam; and the stiffness of the hogging and sagging regions are the same. Each of these parameters are varied while the others are held constant as the influence of each parameter is explored. For all simulations, the hinges are also assumed to form at the supports as this is the usual case considered in the codes. All beams were also singly reinforced and the width was 200 mm, as these parameters were not found to significantly affect MR. For each case considered the reinforcement ratio was varied from 0.25% to 1% to produce the observed variation in neutral axis depth. The neutral axis depth was evaluated for a top strain of 0.003 as required by AS3600-2018 (Standards Australia 2018).

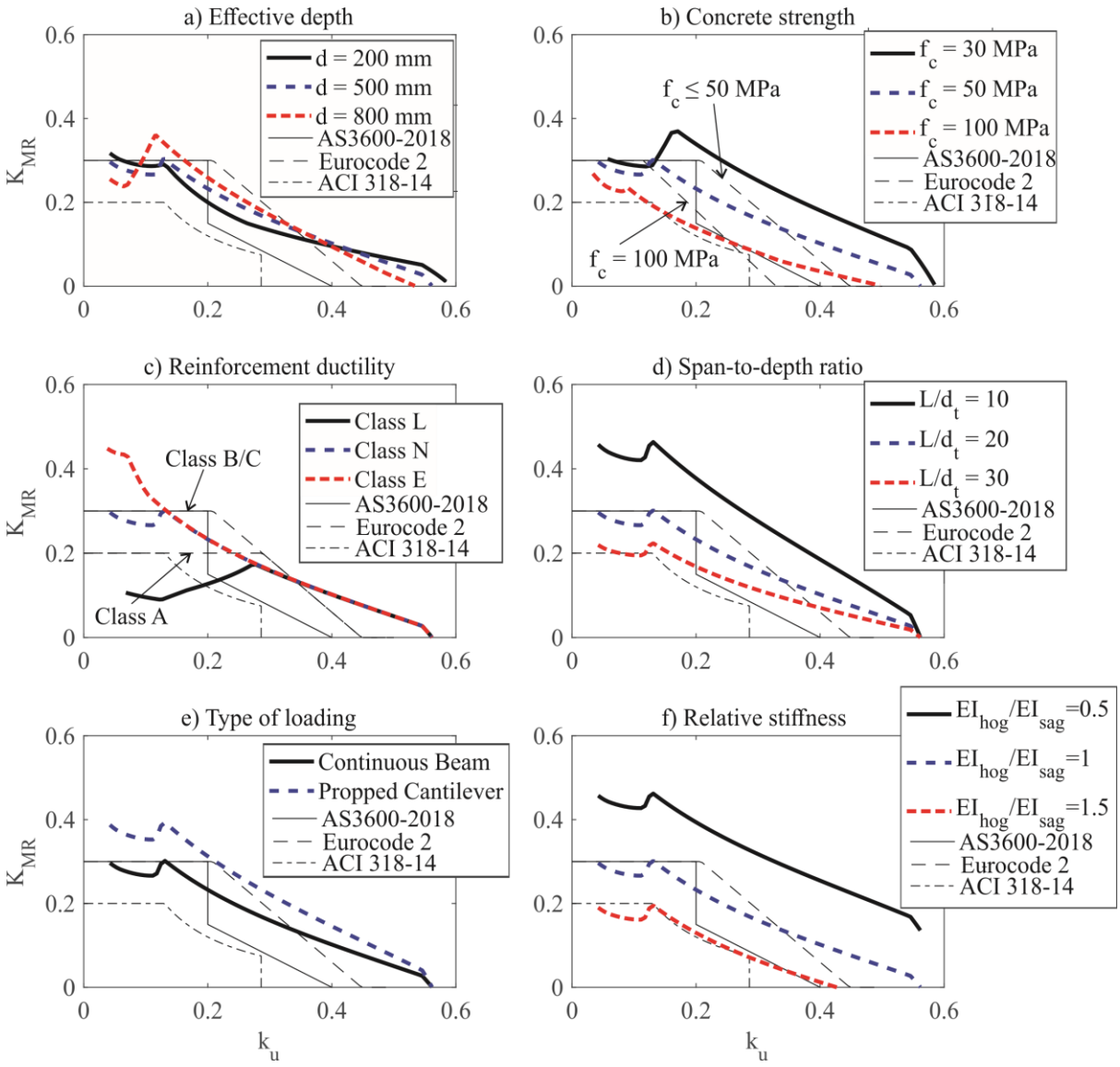

Fig. 9 Comparison to Code Approaches

From Fig. 9(a), it can be seen that the effective depth does not have a strong effect on the level of MR. This is because, even though the curvature is reduced, the size of the hinge increases with beam depth. However, the shape of the curve is different from that in the design codes. The initial branch of the curve is when the rotational capacity is controlled by the tensile failure of the reinforcement and the falling branch is when the rotational capacity is controlled by the crushing of the concrete. The rotational capacity of the section tends to increase with neutral axis depth when this parameter is controlled by the rupture of the reinforcement and the rotational capacity decreases with neutral axis depth when this parameter is controlled by the crushing of the concrete.

In Fig. 9(b), increasing concrete strength results in a decrease in MR. This is consistent with the Eurocode 2 (CEN 2004) which reduces the allowable MR for concretes with a strength greater than 50 MPa.

Fig. 9(c) shows that an increased reinforcement ductility results in an increased level of MR for the cases where the rotational capacity is controlled by the rupture of the tensile reinforcement. However when concrete crushing controls the rotational capacity, the ductility

of the reinforcement has no effect as would be expected. Eurocode 2 (CEN 2004) reduces the maximum level of MR to 0.2 for low ductility reinforcement while AS3600-2018 (Standards Australia 2018) does not allow MR to be considered for low ductility reinforcement. Note that in AS/NZS 4671-2001 (Standards Australia 2001) class E reinforcement has a minimum elongation of 0.1, while class N reinforcement has a minimum elongation of 0.05 and class L reinforcement has a minimum elongation of 0.015. Similarly, in the Eurocode 2 (CEN 2004), class A has a minimum elongation of 0.025, class B has a minimum elongation of 0.05 and class C has a minimum elongation of 0.075.

From Fig. 9(d), the level of MR decreases for beams with greater span to depth ratios. Fig. 9(e) demonstrates that more MR occurs for a propped cantilever than for a continuous beam. Fig. 9(f) found that the stiffer the sagging region is relative to the hogging region, the greater the expected MR is at the support.

From this parametric study, it can be seen that while existing code approaches consider the effect of concrete strength and reinforcement ductility on the MR, the influence of member properties such as span, type of loading and relative stiffness of the midspan and the support are neglected. This suggests that the expressions in this paper could be used as the basis of design expressions which considers the effects of both section and member properties.

APPLICATION TO ULTRA-HIGH PERFORMANCE FIBRE REINFORCED CONCRETE

In Fig. 10, the predicted and experimental MR factors are compared for the UHPFRC beams tested by Visintin et al. (2018). The moment-rotation of these beams were recorded during the tests, hence, these results were used directly rather than from predictive models. It can be seen that the expressions in this paper give a close prediction of the MR. Importantly, to apply the approach to beams constructed from UHPFRC the only change is in the inputs to the model, not in the form of the model. To apply the approach to members where the moment-rotation relationship is unknown, approaches such as those by Schumacher (2006) or Sturm et al. (2020) which allow for tension stiffening and fibre bridging effects for fibre reinforced materials can be applied.

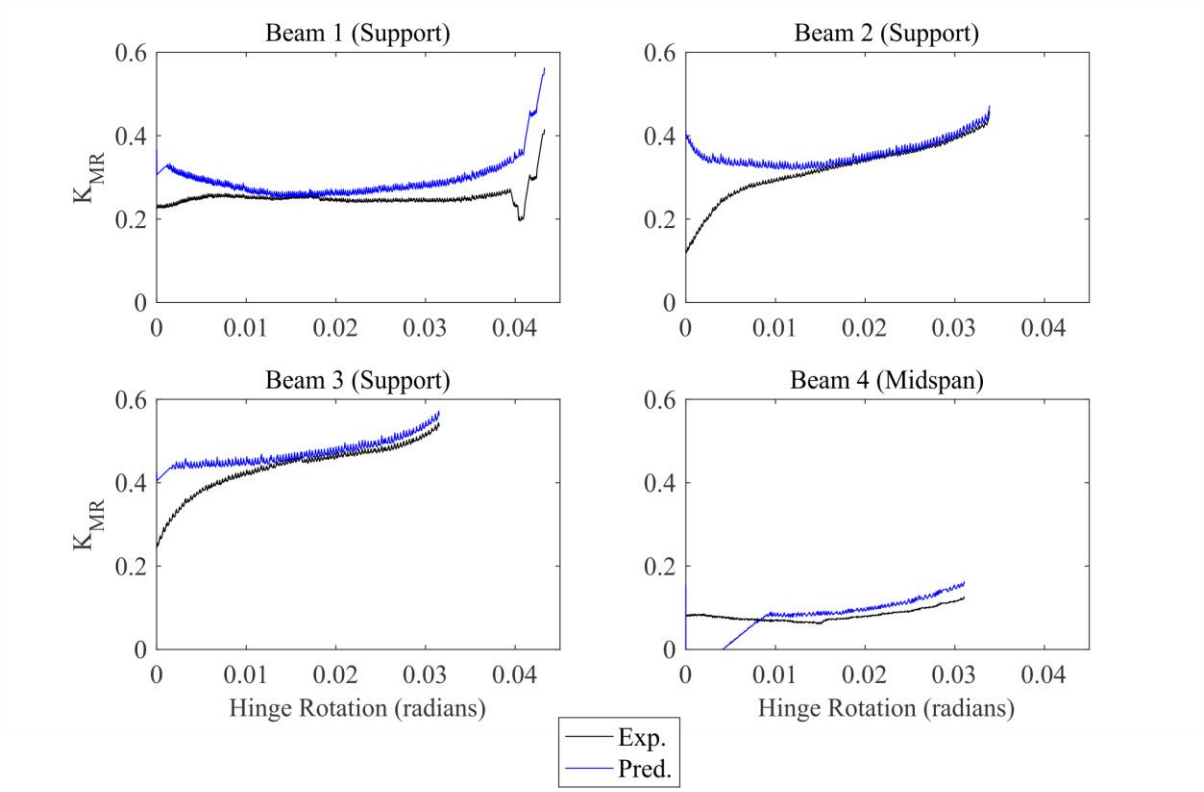

Fig. 10 Comparison of Experimental to Predicted MR for Visintin et al. (2018)

CONCLUSION

Mechanics expressions have been derived for the MR in reinforced concrete beams. These expressions allow the hinge rotation required to achieve full MR to be determined, that is the MR required to achieve the theoretical maximum load based on the sectional moment capacity of the beam. Expressions have also been developed for the maximum load that can applied if the rotational capacity of the hinges is insufficient to reach full MR, that is, partial MR is achieved. Finally, mechanics expressions are derived for the MR factors for a number of common design scenarios. These expressions are functions of the moment capacity of the hinges, rotational capacity of the hinges, flexural rigidity along the member, span of the beam, type of loading as well as the restraint conditions. Hence, these expressions can be applied for beams constructed from any combination of concrete and reinforcement as long as the value of these parameters can be defined.

The expressions are then validated against experimental results for conventional reinforced concrete beams as well as UHPFRC beams with good correlation, demonstrating the versatility of the solutions. Finally, a parametric study was performed comparing the results of using these expressions in national codes of practice to illustrate the importance of the different parameters effecting MR.

APPENDIX A CONTINUOUS BEAM WITH POINT LOAD

Consider the continuous beam in Fig. A1 which is subjected a point load, P, a distance a from the left hand support. It is subjected the distribution of moment as follows

$$M(x) = P\left(1 - \frac{a}{L}\right)x + M_1\left(1 - \frac{x}{L}\right) + M_3\left(\frac{x}{L}\right); 0 < x < a \qquad \text{(A1a)}$$

$$M(x) = P\left(\frac{a}{L}\right)(L-x) + M_1\left(1-\frac{x}{L}\right) + M_3\left(\frac{x}{L}\right); a < x < L \quad \text{(A1b)}$$

The elastic deflection at the right hand support is a superposition of the deflection due to the applied point load and the end moments. From Eq. (3) the curvature due to the point load is

$$\chi(x) = \frac{P}{EI_i}\left(1-\frac{a}{L}\right)x; x_{i-1} < x < x_i; x < a; i \in (1,j) \quad \text{(A2a)}$$

$$\chi(x) = \frac{P}{EI_i}\left(\frac{a}{L}\right)(L-x); x_{i-1} < x < x_i; x > a; i \in (j,N) \quad \text{(A2b)}$$

where j is the segment in which the point load is contained defined as $x_j<a<x_{j+1}$.
Integrating gives the rotation as

$$\theta_{el}(x) = \frac{P}{EI_i}\left(1-\frac{a}{L}\right)\frac{x^2}{2} + (C_1)_i; x_{i-1} < x < x_i; x < a; i \in (1,j) \quad \text{(A3a)}$$

$$\theta_{el}(x) = \frac{P}{EI_i}\left(\frac{a}{L}\right)\left(Lx - \frac{x^2}{2}\right) + (C_2)_i; x_{i-1} < x < x_i; x > a; i \in (j,N) \quad \text{(A3b)}$$

At the left hand support the rotation is zero, therefore

$$\theta(0) = 0 = (C_1)_1 \quad \text{(A4)}$$

The rotation is continuous across segment boundaries, therefore from Eq. (A3a)

$$\theta(x_i) = \frac{P}{EI_i}\left(1-\frac{a}{L}\right)\frac{x_i^2}{2} + (C_1)_i = \frac{P}{EI_{i+1}}\left(1-\frac{a}{L}\right)\frac{x_i^2}{2} + (C_1)_{i+1} \quad \text{(A5)}$$

Rearranging gives

$$(C_1)_{i+1} - (C_1)_i = P\left(\frac{1}{EI_i} - \frac{1}{EI_{i+1}}\right)\left(1-\frac{a}{L}\right)\frac{x_i^2}{2} \quad \text{(A6)}$$

From Eq. (A3b)

$$\theta(x_i) = \frac{P}{EI_i}\left(\frac{a}{L}\right)\left(Lx_i - \frac{x_i^2}{2}\right) + (C_2)_i = \frac{P}{EI_{i+1}}\left(\frac{a}{L}\right)\left(Lx_i - \frac{x_i^2}{2}\right) + (C_2)_{i+1} \quad \text{(A7)}$$

Rearranging gives

$$(C_2)_{i+1} - (C_2)_i = P\left(\frac{1}{EI_i} - \frac{1}{EI_{i+1}}\right)\left(\frac{a}{L}\right)\left(Lx_i - \frac{x_i^2}{2}\right) \quad \text{(A8)}$$

The rotation is also continuous at the point of loading so

$$\theta(a) = \frac{P}{EI_j}\left(1-\frac{a}{L}\right)\frac{a^2}{2} + (C_1)_j = \frac{P}{EI_j}\left(\frac{a}{L}\right)\left(La - \frac{a^2}{2}\right) + (C_2)_j \quad \text{(A9)}$$

From which rearranging gives

$$(C_2)_j - (C_1)_j = -\frac{P}{EI_j}\frac{a^2}{2} \quad \text{(A10)}$$

Integrating Eq. (A3) gives the elastic deflection as

$$y_{el}(x) = \frac{P}{EI_i}\left(1-\frac{a}{L}\right)\frac{x^3}{6} + (C_1)_i x + (C_3)_i; x_{i-1} < x < x_i; x < a; i \in (1,j) \quad \text{(A11a)}$$

$$y_{el}(x) = \frac{P}{EI_i}\left(\frac{a}{L}\right)\left(\frac{Lx^2}{2} - \frac{x^3}{6}\right) + (C_2)_i x + (C_4)_i; x_{i-1} < x < x_i; x > a; i \in (j,N) \quad \text{(A11b)}$$

The deflection is zero at the left hand support, therefore

$$y_{el}(0) = 0 = (C_3)_1 \quad \text{(A12)}$$

The deflection is also continuous across segment boundaries so from Eq. (A11a)

$$y_{el}(x_i) = \frac{P}{EI_i}\left(1-\frac{a}{L}\right)\frac{x_i^3}{6} + (C_1)_i x_i + (C_3)_i = \frac{P}{EI_{i+1}}\left(1-\frac{a}{L}\right)\frac{x_i^3}{6} + (C_1)_{i+1} x_i + (C_3)_{i+1} \quad \text{(A13)}$$

Rearranging gives

$$(C_3)_{i+1} - (C_3)_i = P\left(\frac{1}{EI_i} - \frac{1}{EI_{i+1}}\right)\left(1-\frac{a}{L}\right)\frac{x_i^3}{6} - [(C_1)_{i+1} - (C_1)_i]x_i = -P\left(\frac{1}{EI_i} - \frac{1}{EI_{i+1}}\right)\left(1-\frac{a}{L}\right)\frac{x_i^3}{3} \quad \text{(A14)}$$

From Eq. (A11b)

$$y_{el}(x_i) = \frac{P}{EI_i}\left(\frac{a}{L}\right)\left(\frac{Lx_i^2}{2} - \frac{x_i^3}{6}\right) + (C_2)_i x_i + (C_4)_i = \frac{P}{EI_{i+1}}\left(\frac{a}{L}\right)\left(\frac{Lx_i^2}{2} - \frac{x_i^3}{6}\right) + (C_2)_{i+1} x_i + (C_4)_{i+1} \quad \text{(A15)}$$

Rearranging gives

$$\begin{aligned}(C_4)_{i+1} - (C_4)_i &= P\left(\frac{1}{EI_i} - \frac{1}{EI_{i+1}}\right)\left(\frac{a}{L}\right)\left(\frac{Lx_i^2}{2} - \frac{x_i^3}{6}\right) - [(C_2)_{i+1} - (C_2)_i]x_i \\ &= -P\left(\frac{1}{EI_i} - \frac{1}{EI_{i+1}}\right)\left(\frac{a}{L}\right)\left(\frac{Lx_i^2}{2} - \frac{x_i^3}{3}\right)\end{aligned} \quad \text{(A16)}$$

The deflection is also continuous at the point load, so

$$y_{el}(a) = \frac{P}{EI_j}\left(1-\frac{a}{L}\right)\frac{a^3}{6} + (C_1)_j a + (C_3)_j = \frac{P}{EI_j}\left(\frac{a}{L}\right)\left(\frac{La^2}{2} - \frac{a^3}{6}\right) + (C_2)_j a + (C_4)_j \quad \text{(A17)}$$

Rearranging gives

$$(C_4)_j - (C_3)_j = -\frac{P}{EI_j}\frac{a^3}{3} - \left[(C_2)_j - (C_1)_j\right]a = \frac{P}{EI_j}\frac{a^3}{6} \quad \text{(A18)}$$

The elastic deflection at the right hand support is then given by

$$y_{el}(L) = \frac{P}{EI_N}\frac{aL^2}{3} + (C_2)_N L + (C_4)_N = a_4 P \quad \text{(A19)}$$

where

$$\begin{aligned}a_4 = \frac{1}{EI_N}\frac{L^2 a}{3} &+ \frac{1}{EI_j}\left(-\frac{La^2}{2} + \frac{a^3}{6}\right) + \sum_{i=1}^{j-1}\left(\frac{1}{EI_i} - \frac{1}{EI_{i+1}}\right)\left(1-\frac{a}{L}\right)\left(\frac{Lx_i^2}{2} - \frac{x_i^3}{3}\right) \\ &+ \sum_{i=j}^{N-1}\left(\frac{1}{EI_i} - \frac{1}{EI_{i+1}}\right)\left(\frac{a}{L}\right)\left(L^2 x_i - Lx_i^2 + \frac{x_i^3}{3}\right)\end{aligned} \quad \text{(A20)}$$

Hence the total elastic deflection at the right hand support for a continuous beam with a point load is given by

$$y_{el}(L) = a_4 P + a_2 M_1 + a_3 M_3 \quad \text{(A21)}$$

Similarly the elastic deflection at the left hand support

$$y_{el}(0) = a_4' P + a_2' M_1 + a_3' M_3 \quad \text{(A22)}$$

where

$$\begin{aligned}a_4' = \frac{1}{EI_1}\left(1-\frac{a}{L}\right)\frac{L^3}{3} &+ \frac{1}{EI_j}\left[\frac{(L-a)^3}{6} - \frac{L(L-a)^2}{2}\right] - \sum_{i=1}^{j-1}\left(\frac{1}{EI_i} - \frac{1}{EI_{i+1}}\right)\left(\frac{a}{L}\right)\left(\frac{L(x_i')^2}{2} - \frac{(x_i')^3}{3}\right) \\ &- \sum_{i=j}^{N-1}\left(\frac{1}{EI_i} - \frac{1}{EI_{i+1}}\right)\left(1-\frac{a}{L}\right)\left(L^2 x_i' - L(x_i')^2 + \frac{(x_i')^2}{3}\right)\end{aligned} \quad \text{(A23)}$$

Using the results of Eqs. (A21) and (A22) hinges locations can then be determined using Table 1. The rotation at these hinges can then be determined from Eqs. (29)-(34), choosing the appropriate expressions based on the hinge locations.

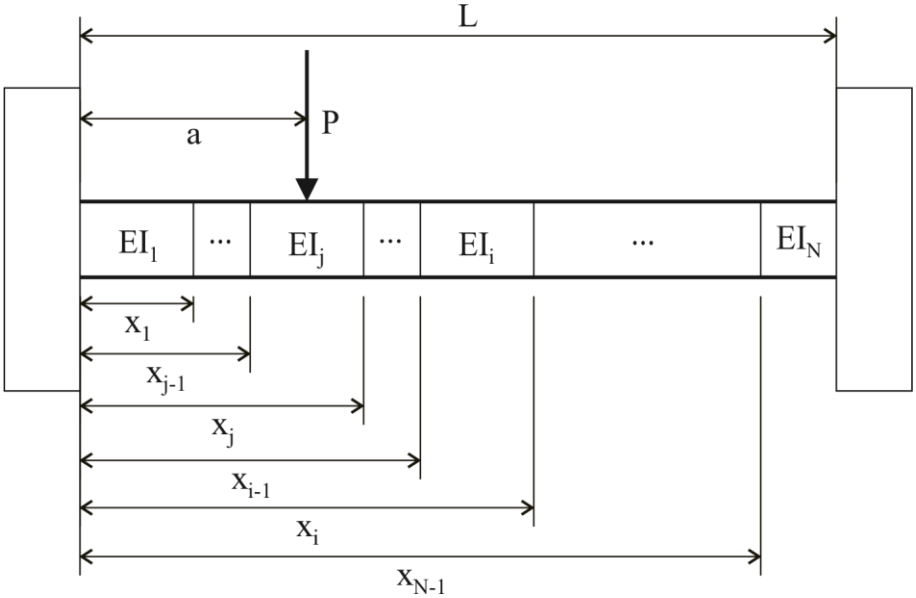

Fig. A1 Continuous Beam with Point Load

NOTATION

a = position of point load with respect to left hand support;
$a_1, a_2, a_3, a_4, a_1', a_2', a_3', a_4'$ = coefficients for the rotational demand;
$b_1, b_2, b_3, b_4, b_5, b_6, b_7, b_8, b_9$ = coefficients for moment redistribution expression;
$(C_1)_i, (C_2)_i, (C_3)_i, (C_4)_i$ = integration coefficients;EI = flexural rigidity;
EI_{hog}, EI_{sag} = flexural rigidity in the hogging and sagging regions, respectively;
EI_i = flexural rigidity of i^{th} segment;
EI_1, EI_2, EI_3 = flexural rigidity of the leftmost hogging region, sagging region and rightmost hogging region;
f_c = concrete strength;
$K_{MR}, K_{MR,hog}, K_{MR,sag}$ = moment redistribution; moment redistribution at support and at the position of maximum sagging moment, respectively;
k_u = ratio between neutral axis and effective depth;
L = span;
L_h = length of hinge;
M, M_{el}, M_h = moment; elastic and hinge moments, respectively;
M_{hog}, M_{sag} = moments at the support in the hogging region and postion of maximum sagging moment, respectively;
$M_{st}, (M_{st})_{el}, (M_{st})_{FMR}, (M_{st})_{PMR}$ = static moment; elastic static moment; static moment at full MR; static moment at partial MR;
M_1, M_2, M_3 = moments at the left hand support, position of maximum sagging moment and right hand support, respectively;
N = number of segments;
P = point load;
w = uniformly distributed load;
X = moment redistribution parameter;
x = position with respect to the left hand support;
x' = position with respect to the right hand support;
x_i = distance from left hand support to the left hand boundary of i^{th-} segment
x_m = distance from left hand support to point of maximum moment;
y, y_{el}, y_h = deflection; elastic and hinge deflections, respectively;

α = ratio of flexural rigidity of the hogging to the sagging region;
β = ratio of moment capacity at the support to the moment capacity at the position of maximum sagging moment;
ε_u = ultimate concrete strain;
θ_{cap} = rotation capacity;
θ_{el}, θ_h = elastic rotation;hinge rotation;
θ_{hog}, θ_{sag} = rotation at support in hogging region and at position of maximum sagging moment, respectively;
θ_1, θ_2, θ_3= hinge rotations at the left hand, position of maximum sagging moment and right hand supports, respectively;
ξ = ratio of distance to the point of contraflexure with respect to the left hand support to the span of the beam;
χ = curvature;

REFERENCES

ACI (American Concrete Institute) (2014) *Building code requirements for structural concrete. ACI 318-14*. Farmington Hills.

Bachmann, H. (1971). "Influence of shear and bond on rotational capacity of reinforced concrete beams." *Bericht Nr. 36*, Eidgenossische Technische Hochschule Zurich.

Bigaj. A. J. (1999). "Structural dependence of rotational capacity of plastic hinges in RC beams and slabs." Ph.D. Thesis, Delft University of Technology.

CEN (European Committee for Standardization). (1992). "Design of concrete structures - Part 1-1: General rules and rules for buildings." *Eurocode 2*, Brussels.

Do Carmo, R. N., and Lopes, S. M. (2005). Ductility and linear analysis with moment redistribution in reinforced high-strength concrete beams. *Canadian Journal of Civil Engineering*, 32(1), 194-203.

Drucker, D. C., Prager, W., and Greenberg, H. J. (1952). Extended limit design theorems for continuous media. *Quarterly of Applied Mathematics*, 9(4), 381-389.

fib (International Federation for Structural Concrete). (2013). *CEB-FIP Model Code 2010*, Lausanne.

Gravina, R.J. (2002) "Non-linear overload behaviour and ductility of reinforced concrete flexural members containing 500MPa grade steel reinforcement." Ph.D. Thesis, University of Adelaide
Gravina, R. J., and Warner, R. F. (2003). "Evaluation of the AS 3600 design clauses for moment redistribution and minimum ductility levels." *Australian Journal of Structural Engineering*, 5(1), 37-45.

Haskett, M., Oehlers, D. J., Mohamed Ali, M. S., and Wu, C. (2009). "Rigid body moment–rotation mechanism for reinforced concrete beam hinges." *Engineering Structures*, 31(5), 1032-1041.

Panagiotakos, T. B., and Fardis, M. N. (2001). “Deformations of reinforced concrete members at yielding and ultimate.” *ACI Structural Journal*, 98(2), 135-148.

Priestly, M. J. N, Calvi, G. M., and Kowalsky, M. J. (2017). *Displacement-based seismic design of structures.* Fondazione Eucentre, Pavia.

Schumacher, P. (2006) “Rotation capacity of self-compacting steel fiber reinforced concrete.” Ph.D. Thesis, Delft University of Technology.

Scott, R. H., and Whittle, R. T. (2005). “Moment redistribution effects in beams.” *Magazine of concrete research*. 57(1), 9-20.

Standards Australia (2001). “Steel reinforcing materials.” *AS/NZS4671:2001*. Sydney.

Standards Australia (2018). “Concrete Structures.” *AS3600:2018*. Sydney.

Sturm, A. B., Visintin, P. and Oehlers. D. J. (2020) “Blending fibres to enhance the flexural properties of UHPFRC beams.” *Construction and Building Materials*, 244, 118328.

Visintin, P., and Oehlers, D. J. (2016). “Mechanics-based closed-form solutions for moment redistribution in RC beams.” *Structural Concrete*, 17(3), 377-389.

Visintin, P., Mohamed Ali, M.S., Xie, T. and Sturm, A.B. (2018) “Experimental investigation of moment redistribution in ultra-high performance fibre reinforced concrete beams.” *Construction & Building Materials*, 166(1), 433-444.

Visintin, P., and Oehlers, D. J. (2018). “Fundamental mechanics that govern the flexural behaviour of reinforced concrete beams with fibre-reinforced concrete.” *Advances in Structural Engineering*, 21(7), 1088-1102.

CHAPTER 4

Background

In this chapter the shear behaviour of UHFPRC is explored. A numerical and analytical model is developed to predict the shear capacity. These solutions are then simplified to produce solutions suitable for routine design.

The first publication "Mechanics of shear failure in fibre reinforced concrete beams." Outlines a mechanical model of shear failure in FRC and UHFPRC beams. Numerical and analytical solutions are then developed for the shear capacity of these beams. These solutions use the segmental method determine the force along a critical shear crack and shear friction theory is used to determine the capacity to resist this force. When this capacity is exceeded shear failure occurs. Partial interaction is also applied to simulate the longitudinal reinforcement and the stirrups. These predictions of these models are then compared to codified approaches as well as approaches from the literature.

The second publication "Design oriented solutions for the shear capacity of reinforced concrete beams with and without fibres" simplifies the solutions from the previous publication such that they can be applied in routine design while retaining superior accuracy to other shear capacity expressions used in practice. In fact the solutions that are developed are simpler to apply then the current Australian standard.

Importantly, the approaches developed are shown through the validation to be suitable for application to conventional concrete, normal strength FRC and UHPFRC without the need for modification of the fundamental mechanics. That is the same approach is applied to conventional concrete by simply setting the fibre contribution to zero.

List of Manuscripts

Sturm, A. B., Visintin, P., and Oehlers, D. J. (2020) "Mechanics of shear failure in fibre reinforced concrete beams." Submitted to *Journal of Structural Engineering*.

Sturm, A. B., Visintin, P., and Oehlers, D. J. (2020) "Design oriented solutions for the shear capacity of reinforced concrete beams with and without fibres." Submitted to *Journal of Structural Engineering*.

STATEMENT OF AUTHORSHIP

Mechanics of shear failure in fibre reinforced concrete beams
Submitted to *Journal of Structural Engineering*

Sturm, A. B. (Candidate)

Prepared manuscript, performed all analyses, and developed model and theory (80%)

This paper reports on original research I conducted during the period of my Higher Degree by Research candidature and is not subject to any obligations or contractual agreements with a third party that would constrain its inclusion in this thesis. I am the primary author of this paper.

Signed Date 9/07/2020

Visintin, P.

Supervised and contributed to research, and acted as corresponding author (10%)

I certify that the candidate's stated contribution to the publication is accurate (as detailed above); permission is granted for the candidate in include the publication in the thesis; and the sum of all co-author contributions is equal to 100% less the candidate's stated contribution.

Signed …… Date 07/07/2020

Oehlers, D. J.

Supervised and contributed to research (10%)

I certify that the candidate's stated contribution to the publication is accurate (as detailed above); permission is granted for the candidate in include the publication in the thesis; and the sum of all co-author contributions is equal to 100% less the candidate's stated contribution.

Signed Date 8/7/20

MECHANICS OF SHEAR FAILURE IN FIBRE REINFORCED CONCRETE BEAMS

Sturm, A.B., Visintin, P., Oehlers, D.J.

ABSTRACT

In this paper, a new model, which can be solved either numerically or analytically, is presented for predicting the shear strength of fibre reinforced concrete beams. This approach is based on predicting the sliding capacity of an inclined crack through the application of fundamental partial-interaction and shear friction theories. A segmental approach is applied to predict this capacity because it has been shown to be able to produce simple analytical solutions while explicitly allowing for the influence of fibre reinforcement and tension stiffening. Once developed, the model is validated against a range of experimental tests and the accuracy is compared to both codified approaches and other approaches in the literature.

INTRODUCTION

Fibre reinforced concrete (FRC) beams have been shown experimentally to have superior shear capacity compared to conventional reinforced concrete beams (Lim et al. 1999; Kwak et al. 2002; Dinh et al. 2011; Aoude et al. 2012; Conforti et al. 2013; Amin & Foster 2016). This improvement has led to the suggestion that steel fibres could either reduce the quantity of transverse reinforcement, or completely replace it, particularly in ultra-high performance fibre reinforced concrete (UHPFRC) members (Casanova & Rossi 1997; Noghabai 2000; Singh & Jain 2014). Given the often catastrophic nature of shear failure, if this is to occur, it is essential that rational and reliable methods for predicting the shear capacity of FRC members are developed.

The observed increase in the shear capacity of FRC compared to RC members can be attributed to both the direct bridging of shear cracks (Choi et al. 2007), and also to an improvement in shear resistance of the uncracked FRC (Valle & Buyukozturk 1993; Sturm et al. 2018a). It is therefore necessary that models which predict the shear capacity of FRC members incorporate these behaviours.

In a recent review of the shear capacity of FRC members, Lansoght (2019) identified that the majority of approaches are empirical and are, therefore, difficult to extend to each new type of FRC developed. In addition to these empirical models, a number of mechanics based models have been developed. These can be categorised into two main types: (i) those that are based on the modified compression field theory (Minelli & Vecchio 2006; Baby et al. 2013; Lee et al. 2016b; Zhang et al. 2016a; Barros & Foster 2018), which was originally developed by Vecchio & Collins (1986) for conventional reinforced concrete, and (ii) those based on stresses that form along a critical diagonal shear crack (Voo et al. 2006; Choi et al. 2007; Lee et al. 2016a).

Approaches based on modified compression field theory can be further subdivided into those that consider the full solution and those that apply the simplified approach. For the full solution, the beam is divided into a series of 2 dimensional elements while for simplified modified compression field theory a single element is considered. In both approaches, the shear capacity of an element is controlled by either the principal stresses on the element or is limited by the stresses that can be transferred across the shear crack due to aggregate interlock. The effect of the fibres is included into the approach either by modifying the constitutive relationships for the concrete (Minelli & Vecchio 2006; Baby et al. 2013; Lee et al. 2016b) or by adding an additional stress due to fibres in the element (Zhang et al. 2016a; Barros & Foster 2018). For

Voo et al. (2006), the shear capacity is controlled by the intersection of the cracking and sliding load determined using an effective plastic compressive and tensile stress where, for FRC, the fibres alter the effective tensile stress.

For approaches that consider the development of stresses along the critical diagonal shear crack, Choi et al. (2007) define the shear capacity as being controlled by both: the uncracked concrete in the flexural compression region of the beam; and the stress carried by the fibres across the shear crack in the tension region. Alternatively in the work of Lee et al. (2016a), the shear capacity is controlled by the aggregate interlock in the flexural tension region and by the uncracked concrete in the flexural compression region. The effect of the fibres is allowed for by increasing the shear capacity of the flexural tension region.

In addition to models developed for research, numerous models are available in national codes of practice. These include the fib Model Code 2010 (fib 2013) which suggests two approaches which are either based on the expression in the Eurocode 2 (CEN 2004) or on a simplified modified compression field theory. The Australian concrete design standard AS3600:2018 (Standards Australia 2018) similarly suggests that the shear capacity of FRC members can be based on the application of a simplified version the modified compression field theory. French recommendations for UHPFRC (AFGC 2013) have a more simplified approach, in which a constant tensile stress due to the fibres is applied along the shear crack. As this crack is inclined, there is a vertical component of this stress that contributes to the shear capacity. The magnitude of this tensile stress is assumed to be equal to the average stress in the fibres at the ultimate limit state.

As highlighted in Lansoght's (2019) review, the existing empirical approaches have limited accuracy with the best performing empirical approach being that suggested by Kwak et al. (2002) which has a coefficient of variation of 28% and a mean of 1.01 when compared to a database of 488 experiments. While the best performing codified approach is that suggested by DAfSt B (2012) with a mean of 1.12 and a coefficient of variation of 27%. The accuracy of the mechanics-based approaches was not compared in Lansoght's (2019) review, however, it was highlighted that none of the approaches accounted for all the mechanisms that contribute to the shear capacity.

This paper will seek to address this limitation via extending the application of the mechanical model of Zhang et al. (2014a,b;2015;2016b) to FRC. This model has previously been applied to reinforced and prestressed concrete with steel or fibre reinforced polymer (FRP) reinforcement, and its accuracy has been demonstrated by comparison to more than 1100 experimental test results. In Zhang's approach, the shear capacity of a beam is based on the shear capacity of the critical diagonal crack, where the shear is primarily resisted by the flexural compression region. In this approach, the width of the shear crack is directly quantified through fundamental partial interaction theory. This is important because the direct application of partial interaction theory has made the approach able to predict the capacity of both steel and FRP reinforced concrete members without modification because the variation in bond and, therefore, tension stiffening between these two types of materials is explicitly considered. For application to FRC, this is also beneficial because it allows for the direct incorporation the fibre contribution through a stress-crack width relationship.

In the remainder of the paper, the extension of Zhang's approach to incorporate FRC is first explained qualitatively. Next, it is shown how the model can be implemented numerically and then analytically. The numerical and analytical models are then validated using a database of

existing and new test results, and finally the accuracy of the approach is compared to other existing models. Importantly, having shown that an accurate analytical solution to predict shear capacity can be developed from fundamental mechanics, it is envisaged that further research can be conducted to further simplify the approach to produce more simplified design rules.

SHEAR FAILURE MODEL FOR FRC

Consider the simply supported beam subjected to a point load in Fig. 1(a). As the beam is loaded, discrete flexural-shear cracks form at the bottom face with a spacing of S_{cr} which is governed by tension stiffening and the tensile strength of the concrete (Balazs 1993; Lee et al. 2013; Sturm et al. 2018b). As the load is increased, these cracks propagate towards the neutral axis and are inclined as shown because they form perpendicular to the direction of the principal tensile stress. In reality these cracks are non-linear (Zarrinpour & Chao 2017). However, to simplify formulation and application of the approach, the non-linear shear crack has been approximated with a straight diagonal crack in Fig. 1(b). A similar assumption has been applied previously in a range of models to predict shear strengths; these include that by Zhang (1997), Hoang & Nielsen (1998) and Zhang et al. (2015,2016b) with which accurate predictions have been achieved. This assumption of a straight diagonal crack is also implicit in simplified modified compression field theory, as the crack forms perpendicular to the inclination angle of the stresses in the element (Bentz et al. 2006).

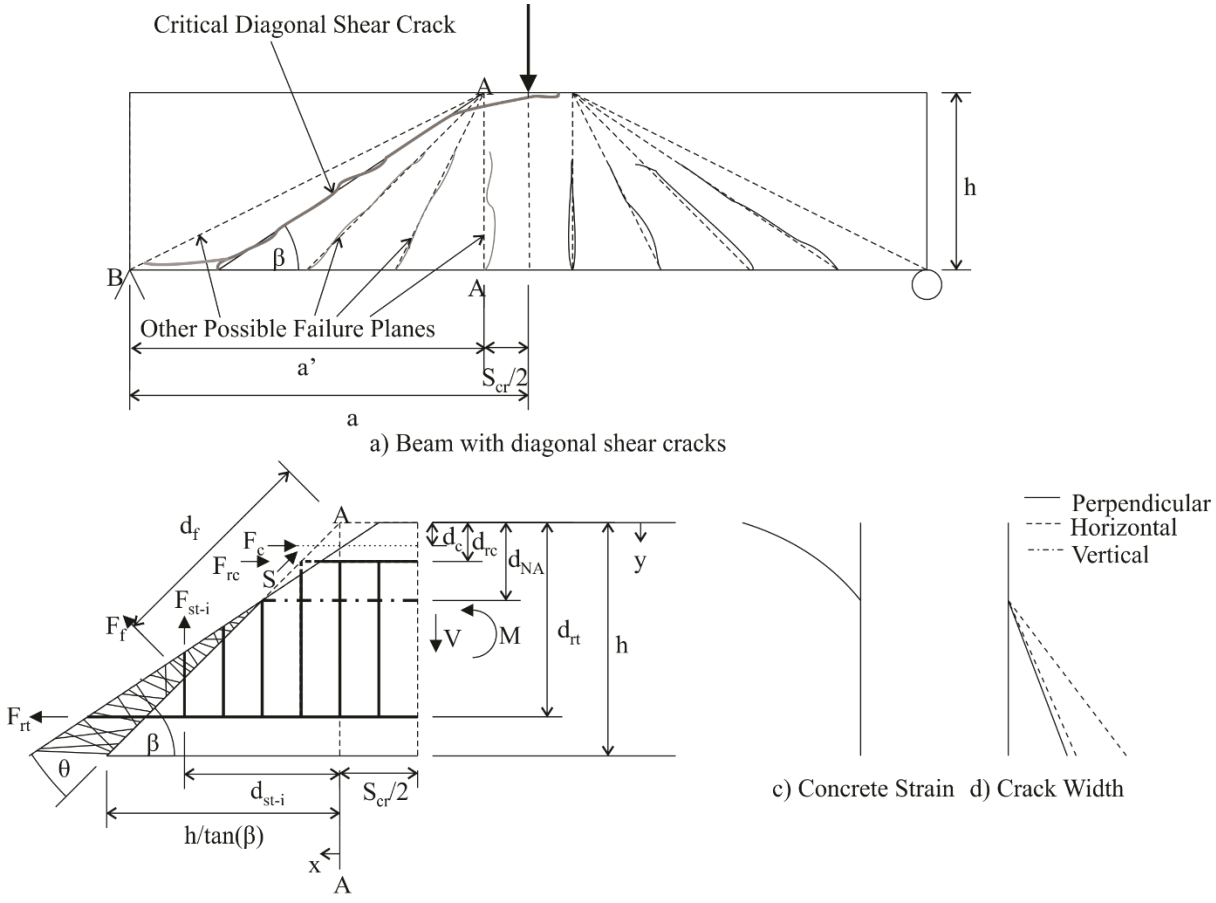

Fig. 1 Mechanics of Shear Failure

Sliding forces develop along the planes defined by each of these shear cracks in Fig. 1(a) to resist the applied shear force (Lucas et al. 2011; Zhang et al. 2015). When and where a sliding force exceeds the capacity of the compressed concrete above the shear crack to resist sliding, a crack penetrates the flexural compression region and the pre-sliding shear capacity is reached; this crack is referred to as the critical diagonal crack and sliding can now occur along the entirety of the shear crack. Once sliding commences, the shear force that can be resisted may or may not increase depending on the rate of increase in normal stress that develops along the sliding plane (σ_N) relative to the rate at which sliding (Δ) occurs. This can be seen in Fig. 2 where typical shear stress versus slip (τ_N/Δ) relationships are presented as a function of the applied normal stress (Chen et al. 2015). In Fig. 2(b), it can be seen that for a constant normal stress the shear resistance reduces as sliding occurs. However, the shear resistance can increase if the normal stress increases, for example if sliding causes the forces in the reinforcement to increase. In this paper, this post-sliding behaviour will be ignored and the shear capacity will be assumed to be equal to the pre-sliding shear capacity. This approach is taken because the pre-sliding capacity is either equal to the shear capacity or is a lower bound to it. Further, Zhang et al. (2015;2016b) showed in a broad validation, to over 1100 experimental test results on reinforced and prestressed concrete beams and columns with either steel or FRP reinforcement, that the pre-sliding capacity provided an accurate prediction of shear capacity. Further, as a result of ignoring post-sliding behaviour, dowel action can be ignored because as shown by Millard & Johnson (1984) in experiments specifically designed to investigate dowel action separately from aggregate interlock, some shear slip is required to generate significant forces due to dowel action.

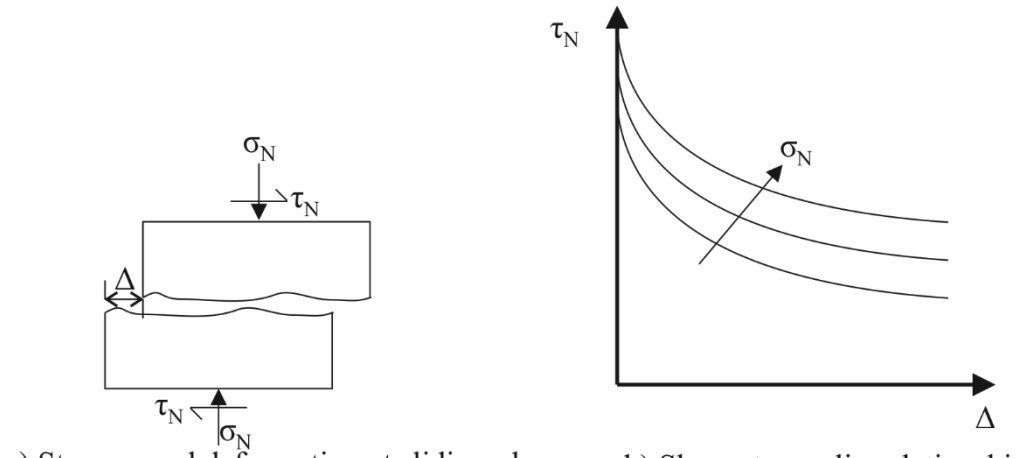

a) Stresses and deformation at sliding plane b) Shear stress-slip relationship

Fig. 2 Shear stress-slip relationship from shear friction tests

Based on the assumption that the pre-sliding capacity is a reasonable approximation to the shear capacity, the shear capacity can be determined by quantifying the sliding force S along the shear crack in Fig. 1(b) as a function of the applied shear force V. Shear failure is then taken to occur when the capacity of the compressed concrete to resist the onset of sliding S_{cap} is reached.

Sliding force along critical diagonal shear crack

To determine the sliding force along the critical diagonal shear crack in Fig. 1(a), consider the free body in Fig. 1(b), where, as a simplification, the real crack geometry has been approximated with a straight line inclined at an angle β. The stress resultants acting on the free body include: the applied shear force V; bending moment M; the force in the longitudinal tension reinforcement F_{rt}; the force in the longitudinal compression reinforcement F_{rc}; the

longitudinal force in the i^{th} stirrup $F_{st\text{-}i}$; the force in the fibres normal to the crack plane F_f; the compressive force in the concrete F_c; and the sliding force S.

From horizontal and vertical force equilibrium:

$$0 = F_{rt} + F_f \sin(\beta) - F_{rc} - F_c - S\cos(\beta) \tag{1}$$

$$V = F_f \cos(\beta) + \sum_i F_{st-i} + S\sin(\beta) \tag{2}$$

and from moment equilibrium:

$$M - V\frac{S_{cr}}{2} = Va' = F_{rt}d_{rt} + F_f d_f + \sum_i F_{st-i}\, d_{st-i} - F_{rc}d_{rc} - F_c d_c \tag{3}$$

where a' is the effective shear span, d_{rt} is the depth of the longitudinal tension reinforcement, d_f is the distance of the force in the fibres to the intersection of profile A-A with the top fibre, $d_{st\text{-}i}$ is the horizontal distance between the i^{th} stirrup and the section A-A, d_{rc} is the depth of the compression reinforcement and d_c is the depth to the compressive force in the concrete.

The forces along the diagonal crack in Fig. 1(b) are a function of the deformations along the shear crack as the forces in the longitudinal tension reinforcement F_{rt}, in the transverse reinforcement $F_{st\text{-}i}$ and in the fibres F_f are functions of the crack width. In contrast, the forces in the compressed concrete F_c and compression reinforcement F_{rc} are functions of the strain.

To determine these deformations, they are assumed to be the result of a linear rotation θ about a neutral axis depth d_{NA}. Consequently, the crack opening at a depth of y measured perpendicular to the crack is given by

$$w_p(y) = \frac{2\theta(y - d_{NA})}{\sin(\beta)} \tag{4}$$

which ignores the tensile strains in the concrete as the elastic deformation of the uncracked concrete away from the shear crack is negligible when compared to the crack opening. Resolving the crack width in Eq. 4, the horizontal component of the crack width is

$$w_x(x) = \frac{w_p(y)}{\sin(\beta)} = \frac{2\theta(y - d_{NA})}{\sin^2(\beta)} \tag{5}$$

and vertical components of is

$$w_y(y) = \frac{w_p(y)}{\cos(\beta)} = \frac{2\theta\left(x - \frac{d_{NA}}{\tan(\beta)}\right)}{\cos^2(\beta)} \tag{6}$$

where x is the horizontal distance measured from profile A-A in Fig. 1(b).

From Fig. 1 (b), the longitudinal strains in the compressed concrete at the location of the sliding plane, as shown in Fig. 1(d), is given by

$$\varepsilon_x(y) = \frac{\theta\left(d_{NA-y}\right)}{\frac{S_{cr}}{2}\sin^2(\beta) + y\sin(\beta)\cos(\beta)} \tag{7}$$

and Eqs. (4-7) can be applied alongside the constitutive relations to solve Eqs. (1-3) for the sliding force S which can be compared with the sliding capacity of the compressed concrete S_{cap}. Hence it can be seen that the beneficial effects of fibres in the concrete can be allowed for directly by including the fibre concrete material properties for shear S_{cap} and for tension F_f.

Significantly, the strain profile in Fig. 1(c) is seen to be non-linear. This is because in the segmental model, the strain in the compression region is taken as the deformation to cause the rotation θ divided by the length over which it is accommodated (the segment length) which varies along the height of the beam due to the inclined sliding plane (Zhang et al. 2014a). Further, in Fig. 1(c) the concrete strain has only been plotted in the compression region because below the neutral axis the concrete is cracked and the concrete strain is taken as zero at the crack face. While the strain in the concrete is taken as zero, the force in the reinforcement is not zero nor is the force in the fibres crossing the crack because these stresses are a function of the crack opening in Fig. 1(d). In the formulation of this approach, the forces in the reinforcement are taken to develop according to partial interaction theory, which describes the force in reinforcement crossing a crack as a function of the bond stresses developed along the segment length and the crack opening in Fig. 1(d).

Capacity to resist sliding S_{cap}

Shear friction theory has typically been applied to predict the stresses that can be transferred across a cracked sliding plane given the crack opening and the slip between the two surfaces (Walraven & Reinhardt 1981). However, it can equally be applied to determine the maximum shear stress that can be transferred for a given applied normal stress for an initially uncracked section (Mattock & Hawkins 1971, Haskett et al. 2011). Hence, shear friction theory can be applied to determine the magnitude of the sliding force that can be resisted along a potential sliding plane as a function of the magnitude of the compressive force normal to the sliding plane (Mohamed Ali et al. 2008; Lucas 2011). This is illustrated in Fig. 3(a), where the inclined shear plane is subjected to the sliding force S and the force in the compressive concrete F_c which is a function of the stresses in the concrete σ_c.

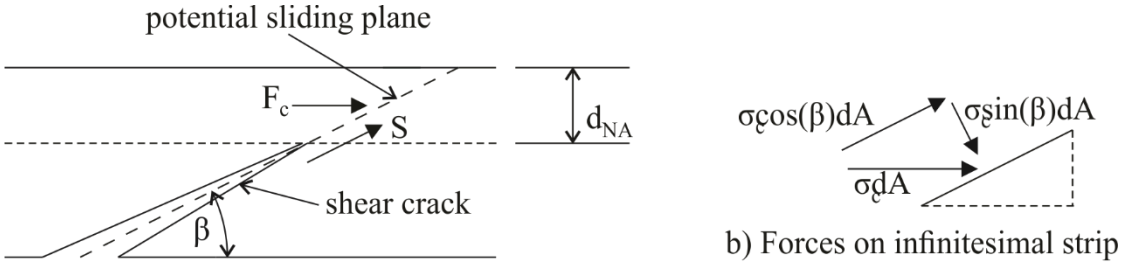

a) Forces applied to shear crack

Fig. 3 Sliding Plane

The magnitude of the normal stress σ_N can be found by considering the infinitesimal strip in Fig. 3(b) which has a cross-sectional area of dA in the vertical plane. The horizontal force applied to this strip is equal to $\sigma_c dA$, such that the component of this force normal to the sliding plane is $\sigma_c sin(\beta) dA$. Since the area of the sliding plane contained inside this infinitesimal strip is $dA/sin(\beta)$, dividing the normal component of the force by this area gives the normal stress σ_N on the sliding plane as equal to $\sigma_c sin^2(\beta)$.

Having determined the applied normal stress from the stress in the compressed concrete, the shear strength of the material $v(\sigma_N)$ can be determined. Integrating this shear strength gives the shear capacity of the initially uncracked plane as

$$Z_{cap} = \int^{A_c} \frac{v(\sigma_N)}{\sin(\beta)} dA \tag{8}$$

where A_c indicates that the integral is performed over the portions of the sliding plane which are in compression. When quantifying the capacity of the sliding plane, it is also important to

consider that there is a component of σ_c parallel to the sliding plane which is equal to $\sigma_c cos(\beta) dA$ and acts to reduce the sliding capacity. Hence

$$S_{cap} = Z_{cap} - F_c \cos(\beta) \tag{9}$$

NUMERICAL IMPLEMENTATION

The above shear failure model can be applied numerically using the procedure in Fig. 4. In this approach, the shear angle β in Fig. 1(b) is varied, starting from the minimum value of β_{min} in Eq. 10, that corresponds to the critical diagonal shear crack that initiates at the support shown as A-B in Fig. 1(a).

$$\beta_{min} = \arctan\left(\frac{h}{a'}\right) \tag{10}$$

For each value of the shear angle β, the rotation θ is incrementally increased to give the relationship between the shear-force and rotation (S/θ), and hence from Eq. (1)

$$S = \frac{F_{rt} - F_{rc} - F_c}{\cos(\beta)} + F_f \tan(\beta) \tag{11}$$

For analysis, the rotation is incrementally increased until either shear failure occurs when $S=S_{cap}$, which then defines the shear capacity of that particular diagonal shear crack $V_{cap\text{-}\beta}$, or until flexural failure occurs. That is, the analysis is terminated when $V_{cap\text{-}\beta}$ exceeds the moment capacity M_{cap} of the beam.

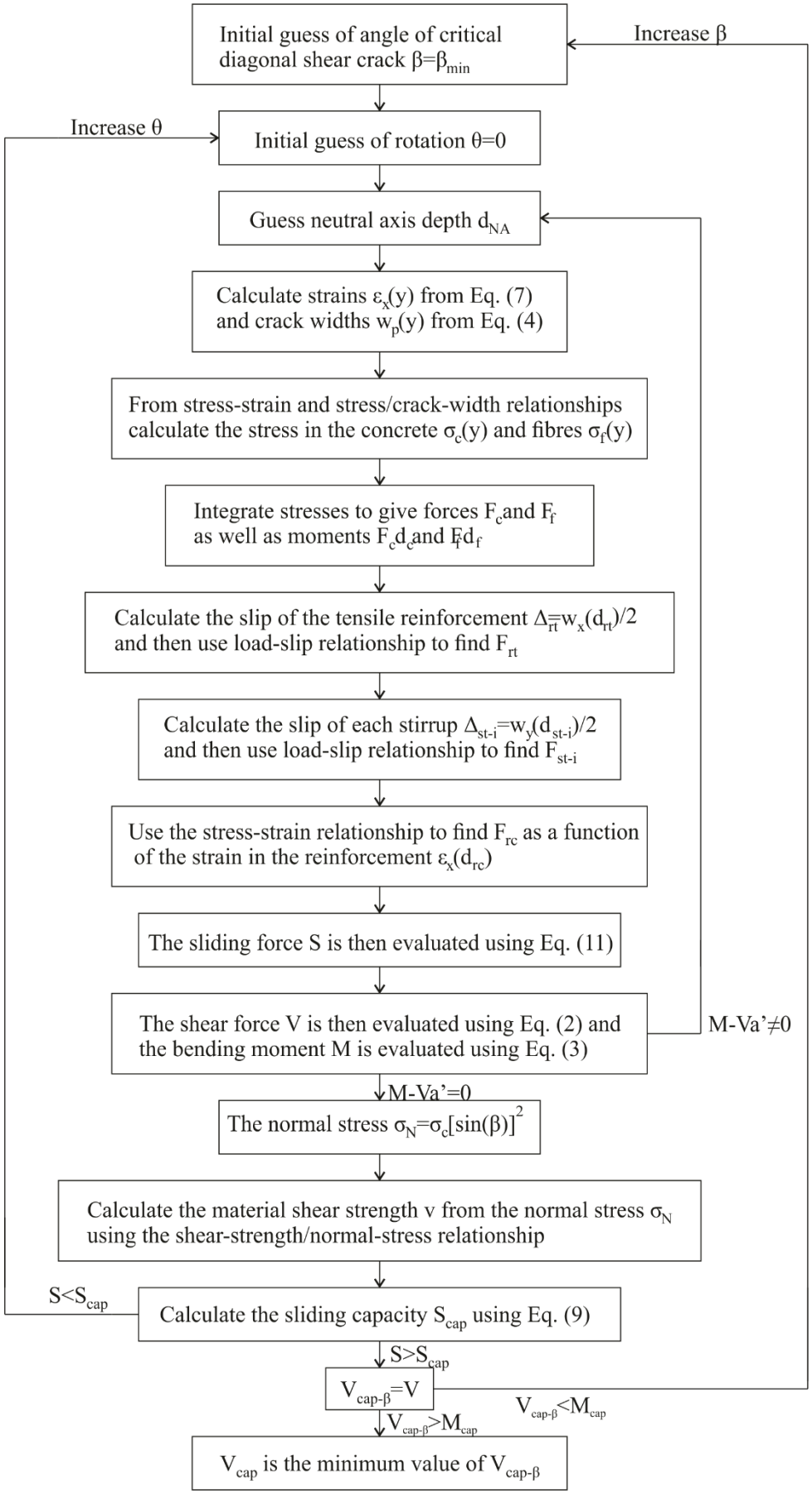

Fig. 4. Numerical Implementation

For low values of β, failure occurs due to sliding, however, as the crack becomes more vertical, flexure will control failure and consequently the analysis is terminated as the flexural capacity is reached. Repeating the analysis for each crack inclination β yields the shear capacity V_{cap} which is given by the minimum value of V_{cap} obtained from all analyses in which β is varied ($V_{cap\text{-}\beta}$).

It may be worth noting that flexural cracks occur at discrete positions as in Fig. 1(a) such that the shear cracks occur at discrete positions and at discrete values of β. Hence this model which considers continuous values of β will give either the actual shear capacity or a lower bound to the shear capacity which explains some of the inherent scatter.

Applying the numerical solution in Fig. 4 requires the compressive stress-strain relationship for the concrete, the tensile-stress/crack-width for the fibres and the shear-strength/normal-stress relationship for the concrete all of which can be determined from simple experiments. It also requires the load-slip relationships for both the longitudinal tension reinforcement and the stirrups as well as the crack spacing which can be determined from established partial interaction theory (Visintin et al. 2013; Zhang et al. 2017b; Sturm et al. 2018b) and which rely on knowledge of the bond stress/slip relationship, which can also be determined from simple material tests.

This numerical implementation is also independent of the shape of the cross-section as the force in the concrete, the force in the fibres and the sliding capacity are integrated over the area of concrete in tension or compression. Hence, I-beams or T-beams can be accommodated without changing the underlying model.

Crack spacing and load-slip relationship of the reinforcement

In this section, the crack spacing and load-slip relationships of the reinforcement used in the validation are outlined. The primary assumption of partial interaction modelling is that after cracking, slip occurs between reinforcement and the surrounding concrete (Balazs 1993; Sturm et al. 2018b). The interface shear stress then becomes a function of this slip (Balazs 1993; Sturm et al. 2018b) which is given by the local bond stress/slip relationship. To analyse this situation a tension chord is extracted from the beam and by considering that the slip strain is equal to the difference in the reinforcement and concrete strains as well as equilibrium of the tension chord a governing equation can be developed relating the slip to the position along the tension chord, as (Balazs 1993; Sturm et al. 2018b)

$$\frac{d^2\delta}{dx^2} = \frac{\tau L_{per}}{\delta_1^{\alpha}}\left(\frac{1}{E_c A_{ct}} + \frac{1}{E_r A_{rt}}\right) \tag{12}$$

where τ is the interface shear stress, L_{per} is the bonded perimeter of the reinforcement, A_{ct} is the area of concrete in the tension chord, A_{rt} is the area of tension reinforcement in the tension chord, E_c is the elastic modulus of the concrete, and E_r is the elastic modulus of the reinforcement. By imposing a local bond stress/slip relationship and boundary conditions, Eq. (12) can be solved for the variation of slip along the tension chord. From this variation of slip, the variation in interface shear stress along the tension chord can be determined. Hence by integrating the interface shear stresses, the stress in the concrete can be determined. The crack spacing is then determined by finding the location where the concrete stress is equal to the tensile strength. Previously this approach has been implemented numerically and a range of analytical solutions have been developed. Here the following approach of Sturm et al. (2018b) is applied because it has been developed for both conventional strength concrete with fibres and ultra-high performance fibre reinforced concrete

$$S_{cr} = \left[\frac{2^{\alpha}(1+\alpha)}{\lambda_2(1-\alpha)^{1+\alpha}}\right]^{\frac{1}{1+\alpha}} \left[\frac{f_{ct} - f_{pc}}{E_c}\left(\frac{E_c A_{ct}}{E_r A_{rt}} + 1\right)\right]^{\frac{1-\alpha}{1+\alpha}} \quad (13)$$

in which

$$\lambda_2 = \frac{\tau_{max} L_{per}}{\delta_1^{\alpha}}\left(\frac{1}{E_c A_{ct}} + \frac{1}{E_r A_{rt}}\right) \quad (14)$$

and where, as shown in Fig. 5, τ_{max} is the maximum bond stress, α is the non-linearity of the bond stress-slip relationship, δ_1 is the slip when the maximum bond stress is achieved, f_{ct} is the tensile strength of the concrete and f_{pc} is the post-cracking strength. The validity of the expression was established in Sturm et al. (2018b) when it was used in conjunction with a load-slip relationship to predict the tension stiffening behaviour of 20 FRC specimens.

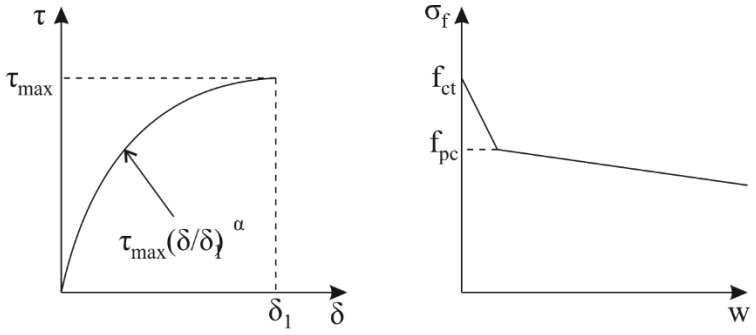

a) Bond-stress/slip relationship b) Tensile-stress/crack-width relationship

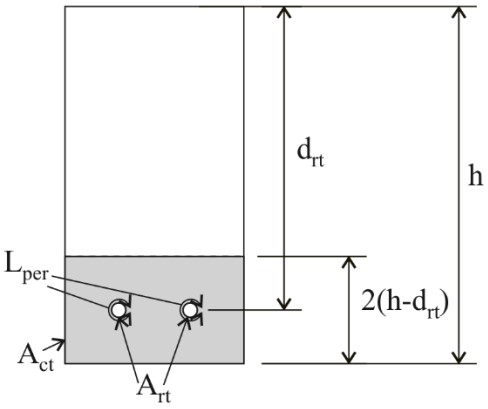

c) Geometry of tension chord

Fig. 5. Parameters for crack spacing expression

The load-slip relationship of the reinforcement can also be determined from the variation of slip along the tension chord yielding the load-slip relationship for the longitudinal tension reinforcement given by the bilinear load-slip relationship in Fig. 6(a) where the crack opening stiffness $\underline{K_{rt}}$ (Sturm et al. 2018b) is given by

$$K_{rt} = E_r A_{rt} \frac{\lambda_1}{\tanh\left(\frac{\lambda_1 S_{cr}}{2}\right)} \quad (15)$$

in which

$$\lambda_1 = \sqrt{k L_{per}\left(\frac{1}{E_r A_{rt}} + \frac{1}{E_c A_{ct}}\right)} \quad (16)$$

and where k is the effective linear bond stiffness taken as τ_{max}/δ_1.

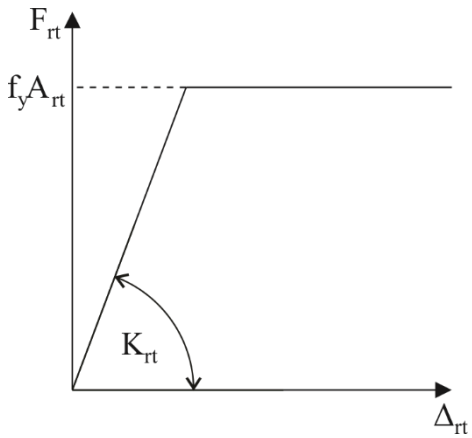

Fig. 6. Load-slip relationship of reinforcement

The load-slip relationship of the stirrups is given by a bilinear relationship of the same form as that used for the longitudinal tension reinforcement such that

$$K_{st-i} = E_r A_{st-i} \frac{2\lambda_{1-st}}{\tanh(\lambda_{1-st} L_{st1}) + \tanh(\lambda_{1-st} L_{st2})} \tag{17}$$

where as derived in Appendix A

$$\lambda_{1-st} = \sqrt{k L_{per-st} \left(\frac{1}{E_r A_{st-i}} + \frac{1}{E_c A_{ct-st}} \right)} \tag{18}$$

and where A_{st-i} is the cross-sectional area of the i^{th} stirrup, L_{st1} is the embedded length above the shear crack, L_{st2} is the embedded below the crack, L_{per-st} is the bonded perimeter of the stirrup and A_{c-st} is the area of the tension chord surrounding the stirrup. These geometric properties are illustrated in Fig. 7.

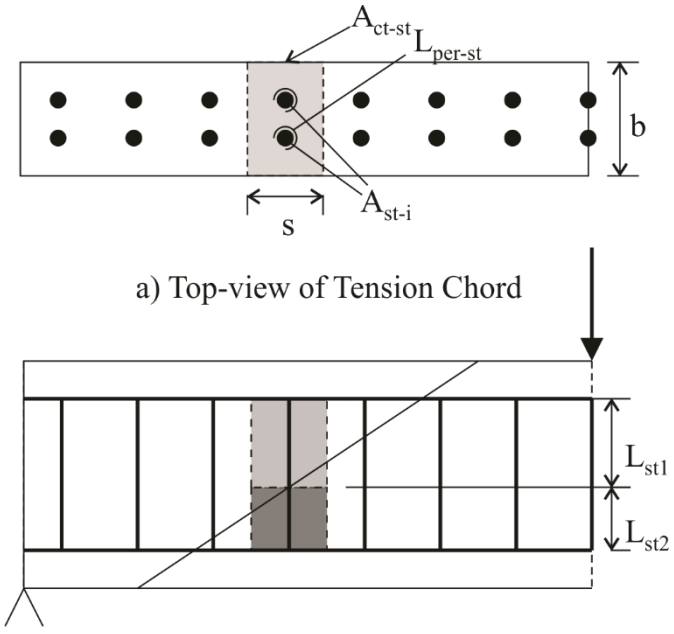

Fig. 7. Definition of tension chord for stirrups

ANALTYICAL IMPLEMENTATION

The shear failure model can also be implemented analytically, which for design may be more convenient to implement in a simple spreadsheet. As noted previously, the purpose of this paper is to develop a fundamental rational approach which captures the underlying mechanism, but it is envisaged that in future work further simplifications could be made. Here as initial approximations, the compression reinforcement will be neglected as too will be the action of the stirrups in the flexural compression region. These approximations are in line with those previously made by Placas & Regan (1971) and Tompos & Frosch (2002) respectively. The following analysis will be conducted assuming that the section is rectangular and the reinforcement is unyielded. However when this is not the case, some of the expressions in the following section can be replaced with the expressions in Appendix B for when the section is either an I-beam or T-beam and with the expressions in Appendix C when the reinforcement has yielded. Note that to determine whether the reinforcement is yielded or unyielded, it is recommended that the section is first analysed as unyielded and then this assumption is checked by determining the force in the reinforcement. Should this force exceed the yield force, then repeat the analysis assuming that that reinforcement has yielded. A worked example is provided in Appendix D.

Idealised material and mechanical behaviours

Reinforcement

For the longitudinal tensile reinforcement, a bilinear load-slip relationship is assumed (Sturm et al. 2018b)

$$F_{rt} = K_{rt}\Delta_{rt} = \frac{K_{rt}\theta(d_{rt} - d_{NA})}{\sin^2(\beta)} \leq f_y A_{rt} \tag{19}$$

where: K_{rt} is the crack opening stiffness and an example of which is given in Appendix A; Δ_{rt} is the slip of the reinforcement which is equal to $w_x(d_{rt})/2$; f_y is the yield stress; and A_{rt} is the cross-sectional area of the reinforcement.

For the transverse or vertical stirrups,

$$F_{st-i} = K_{st-i}\Delta_{st-i} = \frac{K_{st-i}\theta\left(d_{st-i} - \frac{d_{NA}}{\tan(\beta)}\right)}{\cos^2(\beta)} \leq f_{y-st}A_{st-i} \tag{20}$$

where: K_{st-i} is the crack opening stiffness, and an example of how to determine this is given in Appendix A; Δ_{st-i} is the slip of the stirrup which is equal to $w_y(d_{st-i})/2$; f_{y-st} is the yield stress of the stirrup; and A_{st-i} is the cross-sectional area of the stirrup.

Fibres

As a simplification, the stress in the fibres is approximated by a constant stress f_f which is equal to the average tensile stress ranging from a crack width of 0 mm to the crack width at the bottom fibre w_D, as shown in Fig. 8. Since w_D is unknown before the analysis has been performed, it is proposed that f_f is imposed based on the expected crack width. A possible approach for estimating the expected crack width would be to determine this from a flexural analysis with same applied moment M. The crack width could then be estimated directly from a segmental analysis (Sturm et al. 2020) or alternatively from a sectional analysis by multiplying the bottom fibre strain by the crack spacing. This is permissible as the pre-sliding shear capacity is being predicted, hence, significant additional crack opening due to sliding has not yet occurred. This assumption can then be checked by determining the actual width of the shear crack and checking that the average fibre stress corresponding to this crack width is consistent with the value that was assumed. It is consistent if the difference is small and

conservative. As a good rule of thumb, it is suggested that if the difference in stress is less than 10% and underestimated then the error introduced is small and conservative.

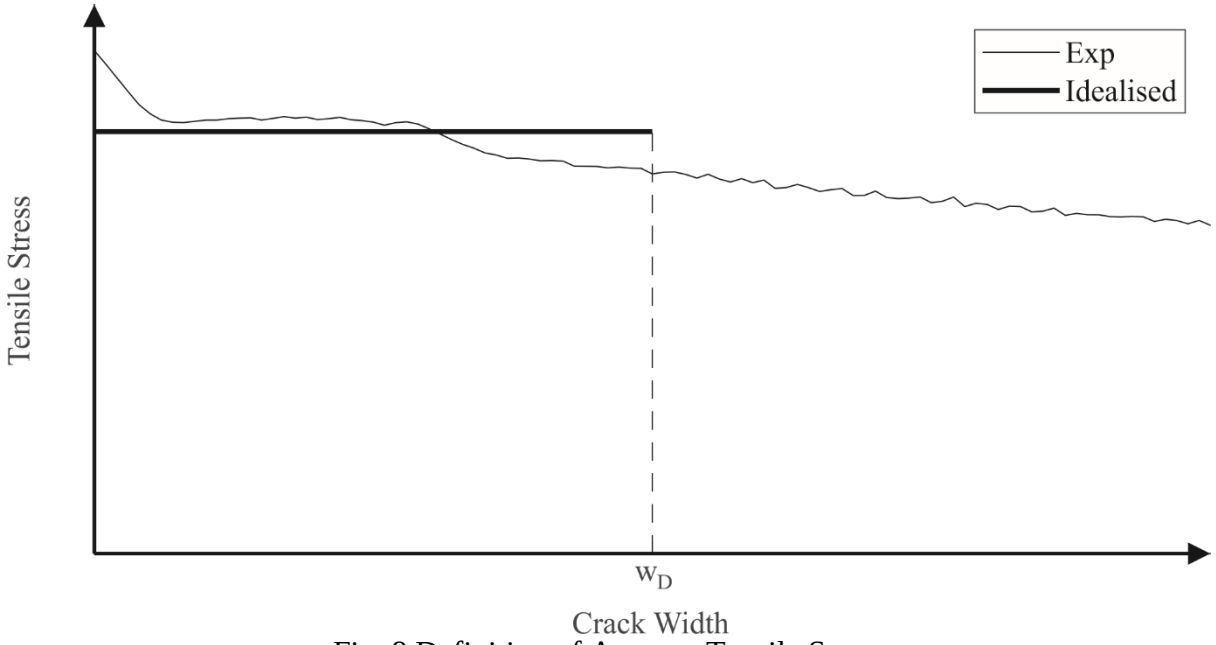

Fig. 8 Definition of Average Tensile Stress

For a rectangular section, the force in the fibres is given by

$$F_f = \frac{f_f b(h - d_{NA})}{\sin(\beta)} \tag{21}$$

and the lever arm between the force in the fibres and the top fibre is given by

$$d_f = \frac{h + d_{NA}}{2\sin(\beta)} \tag{22}$$

For the case of a T-beam or I-beam Eqs. (21) and (22) are replaced by those in Appendix B.

Concrete

Shear failure or sliding is assumed to occur before concrete crushing, hence, the concrete is approximated as linear elastic

$$\sigma_c = E_c \varepsilon_x \tag{23}$$

Above the neutral axis in Fig. 1(c), the strain profile in the concrete is non-linear, because even though the deformation varies linearly as shown, the longitudinal length of concrete over which it acts also varies. As a further simplification, this non-linear strain profile is approximated with the following linear strain profile

$$\varepsilon_x = \frac{\theta(d_{NA} - y)}{\frac{S_{cr}}{2}\sin^2(\beta)} \tag{24}$$

The reason for this simplification is that if the strain profile in Eq. (7) is used, then the integration of the stress to obtain the force in the concrete results in a functional form that prevents an analytical solution from being obtained for the neutral axis depth. Hence as a simplification, the non-linear strain profile is replaced by a linear strain profile where the strain at the neutral axis and at the top fibre are the same as for the actual non-linear strain distribution. This simplification is shown to be acceptable because of the closeness of the numerical and analytical solutions in the validation.

Hence using the simplified stress-strain relationship, the following force in the concrete is obtained by integrating the stress in the concrete over the area of concrete in compression

$$F_c = \frac{1}{2} b d_{NA}^2 E_c \frac{\theta}{\frac{S_{cr}}{2}\sin^2(\beta)} \tag{25}$$

Using the simplified stress-strain relationship, the lever arm between the force in the compressed concrete and the top fibre is

$$d_c = \frac{d_{NA}}{3} \tag{26}$$

For the case of a T-beam or an I-beam, Eqs. (25) and (26) are replaced by the expressions in Appendix B.

The shear strength of the concrete material along the potential sliding plane is assumed to be of the form (Regan & Yu 1973)

$$v = m\sigma_N + c \tag{27}$$

where *m* represents the frictional component of the shear capacity and *c* represents the cohesion.

Shear capacity

Substituting Eq. (27) into Eq. (8) and then substituting Eq. (8) into Eq. (9) gives the shear capacity of the sliding plane as

$$S_{cap} = \int^{A_c} \frac{m\sigma_c \sin^2(\beta) + c}{\sin(\beta)} dA - F_c \cos(\beta) = F_c[m\sin(\beta) - \cos(\beta)] + \frac{cA_c}{\sin(\beta)} \tag{28}$$

where A_c is the area of concrete in compression which is equal to bd_{NA} for a rectangular section. For the case of an I or T beam see Appendix B.

If the sliding force *S* is equated with the sliding capacity S_{cap} in Eq. (28) and then substituted into Eqs. (1) and (2), the following is obtained which, as a reminder, ignores the contribution of the compression reinforcement.

$$0 = F_{rt} + F_f \sin(\beta) - F_c \sin(\beta)\,[m\cos(\beta) + \sin(\beta)] - \frac{cA_c}{\tan(\beta)} \tag{29}$$

$$V_{cap} = \sum_{i=1}^{N} F_{st-i} + F_f \cos(\beta) + F_c \sin(\beta)\,[m\sin(\beta) - \cos(\beta)] + cA_c \tag{30}$$

In Eq. (30), *V* has been replaced by the shear capacity V_{cap} as $S=S_{cap}$ and where *N* refers to the number of stirrups crossing the shear crack below the neutral axis. As the neutral axis is not yet known at this stage of the analysis, as a simplification *N* can be approximated as the number of the stirrups crossing the shear crack at a depth between d_{rt} and *h/2*.

In order to determine the neutral axis depth, now consider the forces developed in the concrete in compression, the fibre reinforcement and the longitudinal tensile reinforcement as a function of the crack rotation θ. Substituting Eqs. (19), (21) and (25) into Eq. (29) and rearranging gives the following expression for the rotation

$$\theta = \frac{A_0 + A_1 d_{NA}}{B_0 + B_1 d_{NA} + B_2 d_{NA}^2} \tag{31}$$

Where

$$A_0 = -f_f bh \tag{32a}$$

$$A_1 = \frac{cb}{\tan(\beta)} + f_f b \tag{32b}$$

$$B_0 = \frac{K_{rt} d_{rt}}{\sin^2(\beta)} \tag{32c}$$

$$B_1 = -\frac{K_{rt}}{\sin^2(\beta)} \tag{32d}$$

$$B_2 = -\frac{b}{2}\frac{E_c}{\frac{S_{cr}}{2}}\left[\frac{m}{\tan(\beta)} + 1\right] \tag{32e}$$

If the section is an I or T beam, Eqs. (32) are replaced by the expressions in Appendix B. If the longitudinal tension reinforcement has yielded, the expressions in Eq. (32) are replaced by those in Appendix C.

Now considering moment equilibrium, substituting Eq. (30) for V_{cap} into Eq. (3) gives

$$0 = F_{rt} d_{rt} + F_f\left[d_f - a' \cos(\beta)\right] + \sum_{i=1}^{N} F_{st-i}\,(d_{st-i} - a') - F_c\{d_c + a' \sin(\beta)\,[m \sin(\beta) - \cos(\beta)]\} - a' c A_c \tag{33}$$

Substituting Eqs. (19), (20), (21), (22), (25) and (26) into Eq. (33) and rearranging gives the following second equation for the rotation which can then be equated to the first to determine the neutral axis depth, d_{NA}

$$\theta = \frac{C_0 + C_1 d_{NA} + C_2 d_{NA}^2}{B_0 + B_1 d_{NA} + B_2 d_{NA}^2 + B_3 d_{NA}^3} \tag{34}$$

where

$$C_0 = -f_f b h\left[\frac{h}{2\sin^2(\beta)} - \frac{a'}{\tan(\beta)}\right] \tag{35a}$$

$$C_1 = a' c b - f_f b \frac{a'}{\tan(\beta)} \tag{35b}$$

$$C_2 = f_f \frac{b}{2\sin^2(\beta)} \tag{35c}$$

$$D_0 = \frac{K_{rt} d_{rt}^2}{\sin^2(\beta)} + \sum_{i=1}^{N} \frac{K_{st-i} d_{st-i}(d_{st-i} - a')}{\cos^2(\beta)} \tag{35d}$$

$$D_1 = -\frac{K_{rt} d_{rt}}{\sin^2(\beta)} - \sum_{i=1}^{N} \frac{K_{st-i}(d_{st-i} - a')}{\sin(\beta)\cos(\beta)} \tag{35e}$$

$$D_2 = -\frac{\frac{E_c}{S_{cr}}}{2} b \frac{a'}{2}\left[m - \frac{1}{\tan(\beta)}\right] \tag{35f}$$

$$D_3 = -\frac{\frac{E_c}{S_{cr}}}{2} \frac{b}{6\sin^2(\beta)} \tag{35g}$$

If the section is an I or T beam, Eqs. (35) are replaced by the expressions in Appendix B. If the longitudinal tension reinforcement or stirrups has yielded, the expressions in Eq. (35) are replaced by those in Appendix C.

Equating Eqs. (24) and (27) and rearranging gives the following polynomial equation

$$0 = P_0 + P_1 d_{NA} + P_2 d_{NA}^2 + P_3 d_{NA}^3 + P_4 d_{NA}^4 \tag{36}$$

where

$$P_0 = A_0 D_0 - B_0 C_0 \tag{37a}$$

$$P_1 = A_0 D_1 + A_1 D_0 - B_0 C_1 - B_1 C_0 \tag{37b}$$

$$P_2 = A_0 D_2 + A_1 D_1 - B_0 C_2 - B_1 C_1 - B_2 C_0 \tag{37c}$$

$$P_3 = A_0 D_3 + A_1 D_2 - B_1 C_2 - B_2 C_1 \tag{37d}$$

$$P_4 = A_1 D_3 - B_2 C_2 \tag{37e}$$

and which can be solved for the neutral axis depth.

The neutral axis depth d_{NA} can now be determined noting that Eq. (37) has four solutions, two of which are complex, and of the real solutions only one will be positive which is the physical solution. This can then be substituted into Eq. (31) to give the rotation θ. The rotation and neutral axis depth can then be substituted into Eqs. (20), (21) and (25) to give the forces in the stirrups $F_{st\text{-}i}$, fibres F_f and compressed concrete F_c. These forces can then be substituted into Eq. (30) to give the shear capacity V_{cap}. The only unknown is the shear angle β.

Theoretically β can be found by minimising V_{cap} with respect to β, however, minimising this analytically does not lead to a simple closed-form solution. It is also impractical for an analytical solution to evaluate V_{cap} for a range of shear angles and then take the minimum value in the same way as is done for the numerical implementation. Instead, as a simplification, it will be assumed that the fibres do not significantly influence the shear angle β which is analogous to the assumption of Zhang et al. (2015) where stirrups were assumed to have no effect on the shear angle. The validity of this assumption is demonstrated by the accuracy of the validation. Hence, the shear capacity without stirrups or fibres from Zhang et al. (2016b) can be minimised to give the shear angle β. The shear capacity without stirrups or fibres is given by (Zhang et al. 2016b)

$$V_{cap-nf} = \frac{b d_{NA} c}{1 - [m \sin(\beta) - \cos(\beta)] \left[\dfrac{a' \sin(\beta) - d_{rt} \cos(\beta)}{d_{rt} - d_c}\right]} \tag{38}$$

Minimising Eq. (38) with respect to β by differentiating and equating with zero yields

$$\frac{dV_{cap-nf}}{d\beta} = 0 = b d_{NA} c \frac{[m\cos(\beta)+\sin(\beta)]\left[\frac{a'}{d_{rt}-d_c}\sin(\beta)-\frac{d_{rt}}{d_{rt}-d_c}\cos(\beta)\right]+[m\sin(\beta)-\cos(\beta)]\left[\frac{a'}{d_{rt}-d_c}\cos(\beta)+\frac{d_{rt}}{d_{rt}-d_c}\sin(\beta)\right]}{1-[m\sin(\beta)-\cos(\beta)]\left[\frac{a'}{d_{rt}-d_c}\sin(\beta)-\frac{d_{rt}}{d_{rt}-d_c}\cos(\beta)\right]^2} \tag{39}$$

Rearranging then gives the following expression for the shear angle

$$0 = \left(m\frac{a'}{d_{rt}} - 1\right) 2\sin(\beta)\cos(\beta) - \left(\frac{a'}{d_{rt}} + m\right)[\cos^2(\beta) - \sin^2(\beta)] \tag{40}$$

Next consider that

$$2\sin(\beta)\cos(\beta) = \frac{2\tan(\beta)}{1+\tan^2(\beta)} \tag{41}$$

and

$$\cos^2(\beta) - \sin^2(\beta) = \frac{1-\tan^2(\beta)}{1+\tan^2(\beta)} \tag{42}$$

Hence substituting Eqs. (41) and (42) into Eq. (40) gives the following quadratic equation in terms of *tan(β)*

$$0 = \left(m\frac{a'}{d_{rt}} - 1\right) 2\tan(\beta) - \left(\frac{a'}{d_{rt}} + m\right)[1 - \tan^2(\beta)] \tag{43}$$

and solving Eq. (43) gives

$$\beta = \arctan\left[\sqrt{1 + \left(\frac{m\dfrac{a'}{d_{rt}} - 1}{m + \dfrac{a'}{d_{rt}}}\right)^2} - \frac{m\dfrac{a'}{d_{rt}} - 1}{m + \dfrac{a'}{d_{rt}}}\right] \geq \beta_{min} \tag{44}$$

From Eq. (44), it is seen that the shear angle is a function of the ratio between the shear span and effective depth and the frictional component of the shear strength. The variation of the shear angle with these parameters is shown in Fig. 9. Note that the inequality comes from the fact that the shear angle cannot be less than β_{min} as defined earlier (Eq. 10) which is limited by the shear crack entering the support. From Fig. 9, it can be seen that as the shear span to depth ratio reduces β increases. An increase in the frictional component of the shear strength results in a decrease in shear angle.

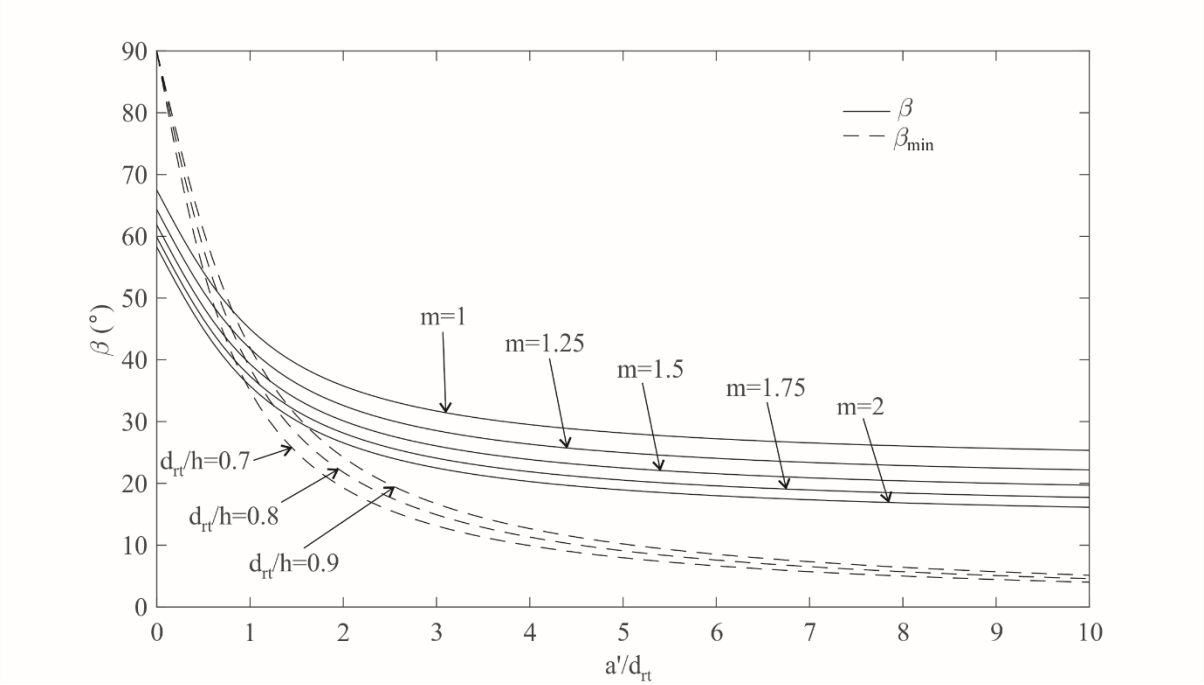

Fig. 9 Variation of shear angle from Eq. (37)

The presented analytical solution has assumed a rectangular cross-section and unyielded reinforcement. However, the model can accommodate other cross-sections, for example, the expressions for I and T beams are given in Appendix B while the expressions for yielded reinforcement are given in Appendix C. To demonstrate the manner in which these different solutions fit together, a flow chart is given in Fig. 10 which outlines the procedure for determining the shear capacity using the analytical solutions. A worked example is also given in Appendix D.

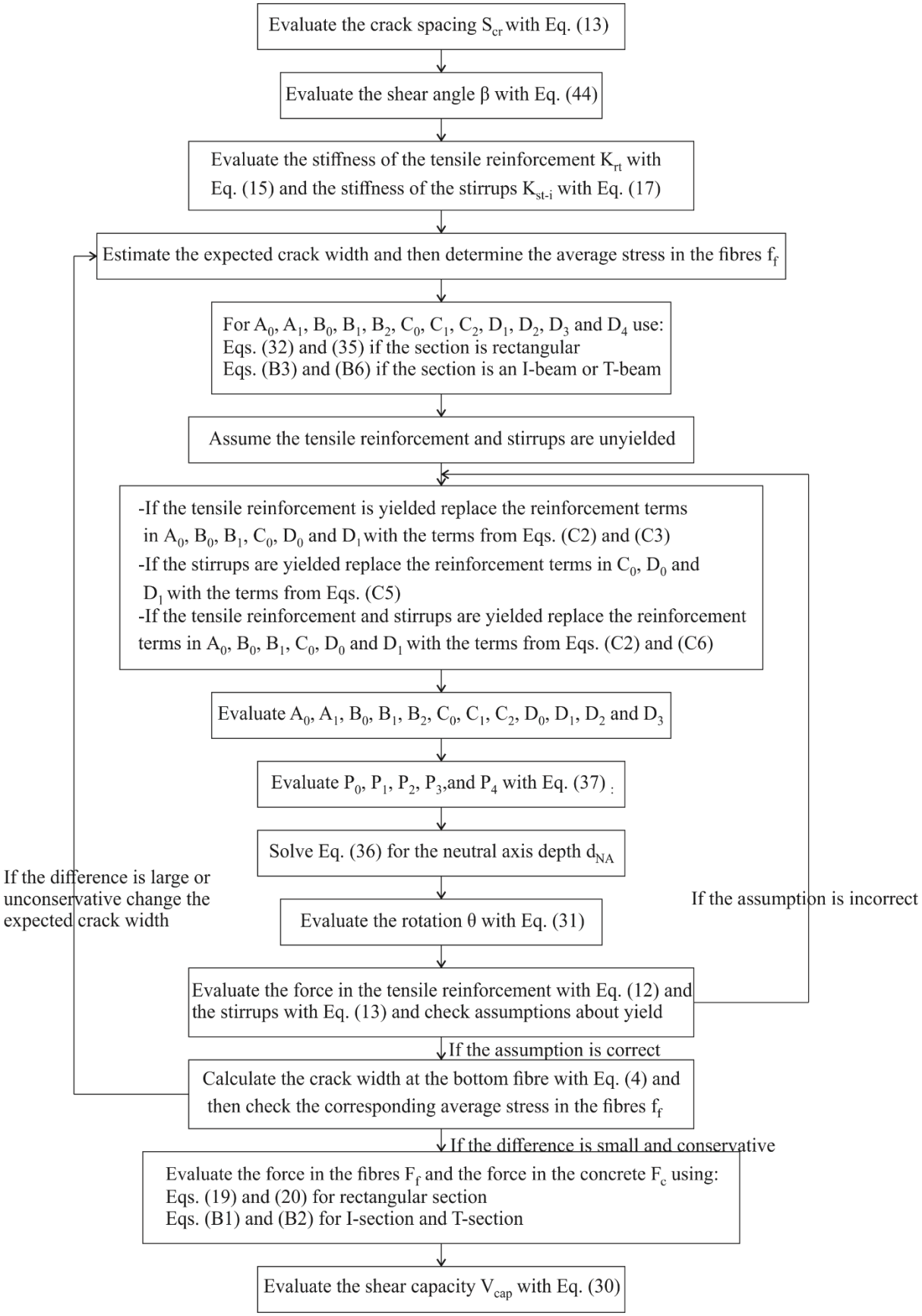

Fig. 10 Analytical Implementation

VALIDATION

The shear capacity models in this paper are compared with 29 experimental tests (Casanova & Rossi (1997), Noghabai (2000) and Amin & Foster (2016) from the literature, as well as an additional 2 tests performed by the authors with details in Appendix E. The tests from the literature were chosen from the data base by Lansoght (2019) where direct tension tests were also available. The examples cover: concrete strengths from 34 to 125 MPa; fibre volumes from 0.29 to 1.28%; beam depths from 250 to 700 mm; and rectangular and I shaped sections.

Comparisons were also made to the codified approaches presented by fib Model Code 2010 (fib 2013), AS3600-2018 (Standards Australia 2018) and AFGC UHPFRC recommendations (AFGC 2013) as well with the approaches of Voo et al. (2006), Choi et al. (2007), Zhang et al. (2016a), Lee et al. (2017) and Foster and Barros (2018). The results are summarised in Fig. 11 which alongside the plot gives the means and coefficients of variation (COV). Note that the *n* in Fig. 11 refers to the number of tests the approach was applied to in the validation. The reason that Voo et al. (2006), Choi et al. (2007) and Zhang et al. (2016a) were compared to less than 31 tests is that they did not include a provision for the allowance of stirrups. In Fig.11(k) that is Foster & Barros, the number of tests for comparison was reduced as the model does not include the case where there is a mix of two different types of fibre. The fib Model Code #1 refers to the approach in the model code which is based on a modified Eurocode approach and fib Model Code #2 refers to an approach based on simplified modified compression field theory.

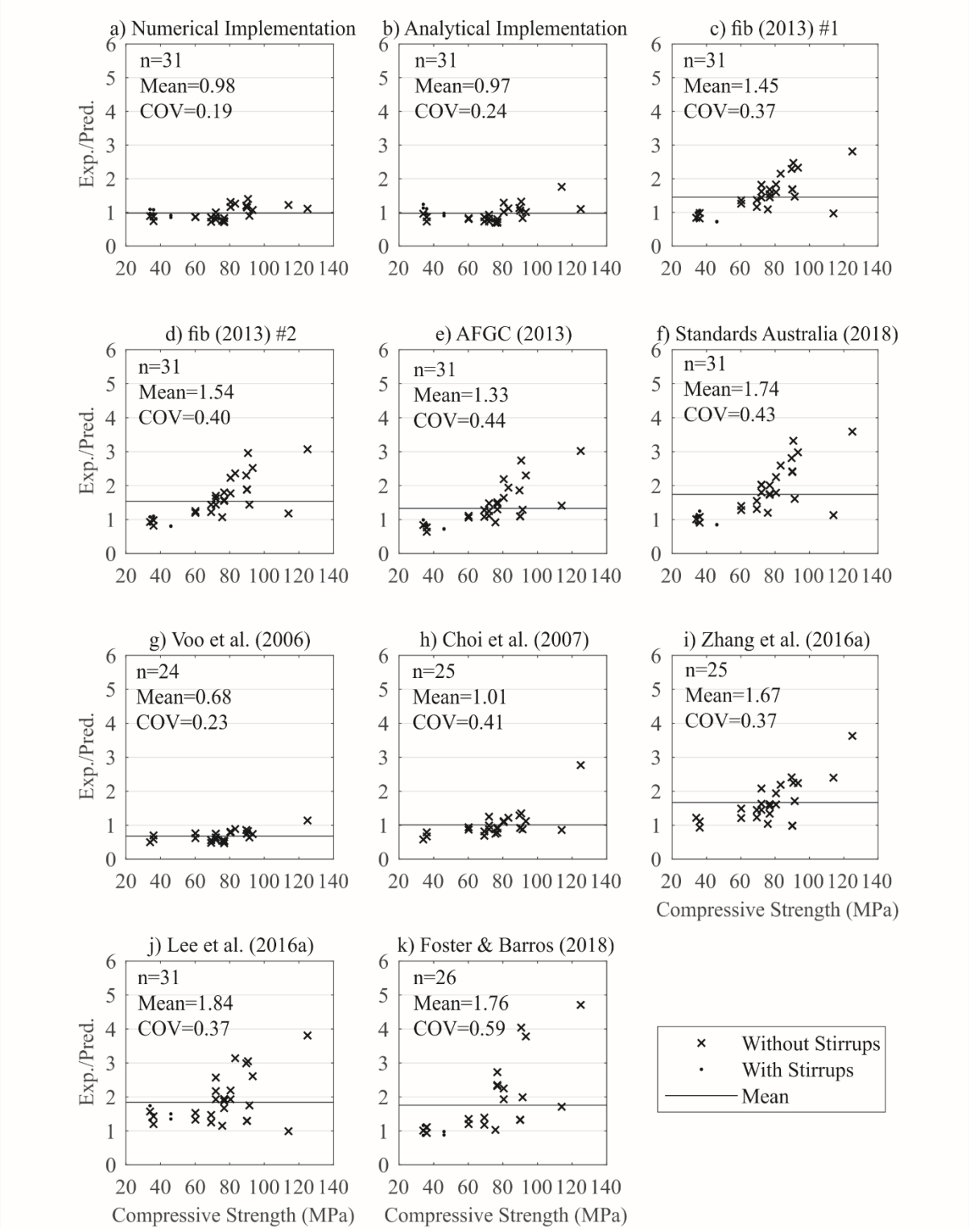

Fig. 11 Comparison of Shear Capacity Models

The results for the numerical approach developed in this paper are shown in Fig. 11(a); these specimens were with and without stirrups and had both normal and high strength FRC. It can be seen that the results are closely distributed about the ordinate 1 with a mean of 0.98 and COV of 0.19 demonstrating the accuracy of the proposed numerical implementation. When using the analytical formulation, the results in Fig. 1(b) have a similar mean to the numerical approach of 0.97, however, the COV has increased slightly to 0.24 due to the simplifications in this approach.

The codified predictions in Figs. 11(c) to (f) are conservative especially for the higher strength FRCs. The COVs are significantly higher than for the approaches developed in this paper of 0.19 and 0.24 with fib(2013)#1 the most accurate with a COV of 0.37 and AFGC (2013) the least with a COV of 0.44. The AFCG (2013) standard is also the least conservative with a mean of 1.33 while Standards Australia (2018) is the most conservative with a mean of 1.74.
Various approaches in the literature are also compared in Figs. 7(g-k). Zhang et al. (2016a), Lee et al. (2016a) and Foster & Barros (2018) approaches show similar patterns to the codified approaches of increasing conservativeness as the concrete strength increases. Voo et al. (2006) shows a different pattern where the approach is accurate for high strength FRC, however, it is unconservative for lower strength FRC. Choi et al. (2007) demonstrates similar accuracy for all concrete strengths. This is also reflected in the means, with Voo et al. (2006) being unconservative with a mean of 0.68 while Choi et al. (2007) is the closest to the experimental values with a mean of 1.01 and the other approaches are conservative with means between 1.67 and 1.84. Inspecting the COVs shows Voo et al. (2006) as being the most accurate with a COV of 0.23 while Foster & Barros (2017) is the least accurate with a COV of 0.59. For the other approaches, the COVs are in the range of the codified approaches. These are all greater than the COVs for the proposed approaches except for Voo et al. (2006) which has a similar COV to the analytical solution, however, Voo et al. (2006) tends to overestimates the shear capacity in most cases.

The following material properties were used in the numerical and analytical implementations for the approaches presented in this paper. The concrete stress-strain relationship in compression was obtained from Ou et al. (2011) for FRC with a strength less than 100 MPa or Sobuz et al. (2016) for FRC with a strength greater than 100 MPa. The tensile-stress/crack-width relationship was obtained from direct tension tests, although the equivalent material property obtained from inverse analysis of flexural tensile tests could also be employed. This was not, however, done here to avoid any increased scatter associated with obtaining the material properties. The material shear strength was obtained from Zhang et al. (2014b). The crack spacing, load-slip relationships and crack opening stiffness were determined in accordance with that presented in Appendix A. Note that these approaches utilise an empirical bond-stress/slip relationship which was obtained from Harajli (2009) for compressive strengths less than 100 MPa and from Sturm & Visintin (2018) for compressive strengths exceeding 100 MPa.

EFFECT OF SIZE, FIBRE STRESS AND CRACK SPACING ON SHEAR CAPACITY

Effect of size on shear capacity

It is a well established phenomenon for both conventional reinforced (Bazant & Kim 1984; Bazant & Sun 1987) and fibre reinforced concrete beams (Shoaib et al. 2014; Minelli et al. 2014; Chao 2020) that the shear capacity does not scale linearly with the size of the beam. Hence, to demonstrate that the model in this paper generates a size effect, a series of analyses were performed using the analytical model. The results are shown in Fig. 12(a) where the shear capacity, that is normalised with respect to the size of the beam, is plotted against the effective depth. It can be seen that the normalised strength reduces with increasing depth, that is, there is a size effect and that this new model does not require an empirically derived factor to allow for the size effect but allows for it automatically through mechanics.

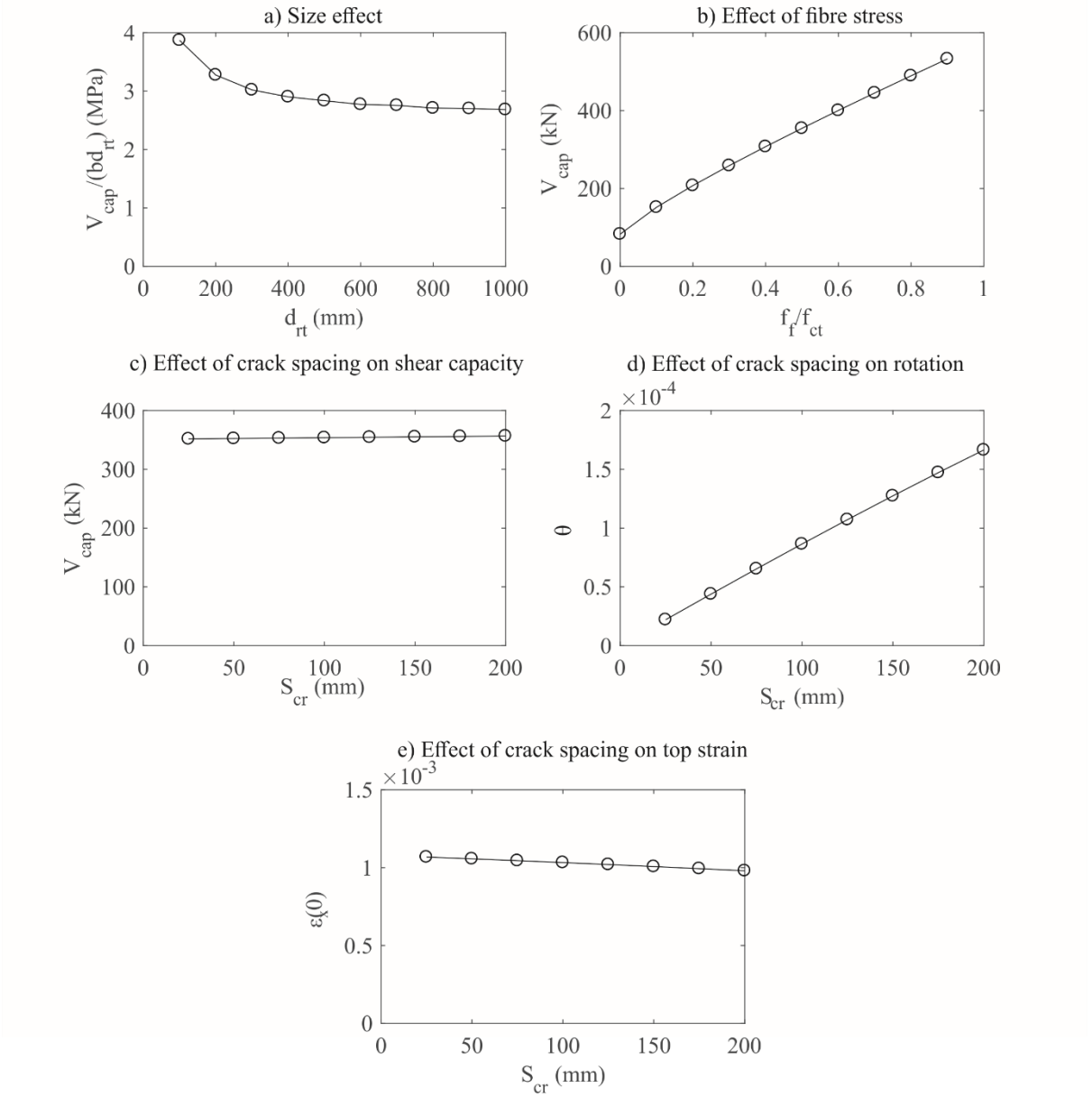

Fig. 12 Effect of size, fibre stress and crack spacing on shear capacity

For the above analyses, the effective depth was varied from 100 mm to 1000 mm, the shear span-to-effective depth ratio was 3, the beam width 250 mm, the cover of the longitudinal reinforcement 50 mm, the reinforcement ratio 0.01 and the concrete strength was 40 MPa. The fibre stress was assumed to be 50% of the tensile strength which was set to 3.5 MPa. The elastic modulus of the concrete was 36 GPa.

Effect of fibre stress on shear capacity

In this section the effect of adding fibres on the shear capacity is explored. Because the exact relationship between the volume of fibres and the stress in the fibres is strongly dependent on mix design, and is usually assessed experimentally, the effect of adding fibres will be simulated considering the simple case of the beam with an effective depth of 500 mm and all other parameters the same as those used to explore the size effect. By varying the fibre stress as a ratio of the fibre stress to the peak tensile strength the result shown in Fig. 12(b) is obtained, where a value of zero is indicative of a plain concrete beam. This demonstrates that the addition

of fibres can result in significant improvements in shear capacity. To place these values in context an addition of 0.3% by volume of fibres resulted in a f_f/f_{ct} of 0.24 and 0.7% by volume of fibres resulted in a f_f/f_{ct} of 0.67 in Amin & Foster (2016) while 1% by volume of fibres resulted in a f_f/f_{ct} of 0.97 for the beams in Appendix E as determined using the analytical solution presented in this paper. It can therefore be seen that the shear capacity increases in proportion to the stress in the fibres.

Sensitivity of the predicted shear capacity to the crack spacing

This model uses the crack spacing as a parameter in determining the shear capacity. As there is a significant random component to predicting crack spacings (Sturm et al. 2018c), the sensitivity analysis in Fig. 12(c) was performed to explore the effect of crack spacing on the predicted shear capacity. The results indicate that the model is insensitive to the assumed crack spacing with only minor variation in the shear capacity even when the crack spacing is varied from 25 mm to 200 mm. The reason for this insensitivity is that as the crack spacing is increased the rotation increases to maintain similar strains on the section. This can be seen by plotting the rotation versus crack spacing as well as top strain versus crack spacing, as shown in Fig. 12(d) and 12(e). In this analysis, the effective depth was taken as 500 mm and the other parameters were the same as those used to investigate the size effect.

CONCLUSION

An approach has been developed for quantifying the shear capacity of FRC beams. The approach is based on the mechanics of shear failure along a sliding plane and uses: the reinforcement partial-interaction bond-slip material property; the concrete partial-interaction shear-friction property; and the partial-interaction fibre properties across a crack or sliding plane. A unique component of this approach is that it quantifies the weakest plane of shear failure and, consequently, automatically allows for the effect of the shear-span/depth and beam size. Being mechanics based, it can cope with a wide variety of member shapes, such as rectangular or I sections, member sizes and FRC material properties and does not require calibration through member testing.

This novel partial-interaction mechanics based approach has been compared with thirty one member tests and shows very good correlation with the measured strengths and a low COV of 19%, which increases to 24% when simplifications are made to produce an analytical solution. The means of the proposed solutions are also 0.98 for the numerical and 0.97 for the analytical implementations. Thus, it has been found to be more accurate than code approaches where the COV was larger with a range of 37 to 44% while the means were conservative with a range of 1.33 to 1.74 and published prediction approaches where the COV ranged from 23% to 59%.Voo et al. (2006) was unconservative with a mean of 0.68 while the mean of Choi et al. (2007) was 1.01. The other published prediction approaches were conservative with means of 1.67 to 1.84.

As this new approach is mechanics-based, it only requires knowledge of the partial-interaction material properties of the FRC concrete for application and as such it does not require calibration by member testing. The procedure can be used to quantify the shear capacity of FRC RC sections and thus has the potential to be used to develop simplified rules for design for any type of FRC member.

APPENDIX A LOAD-SLIP RELATIONSHIP FOR STIRRUPS FROM PARTIAL INTERACTION THEORY

Consider the tension chord in Fig. 7 where the embedded lengths are each side of the crack, that is L_{st-1} and L_{st-2} in Fig. 7(b) are different. Hence the slip from each crack face differs and are given by (Sturm et al. 2018b)

$$\Delta_{st1} = \frac{\frac{F_{st-i}}{E_r A_{st-i}}}{\frac{\lambda_{1-st}}{\tanh(\lambda_{1-st} L_{st1})}} \tag{A1}$$

and

$$\Delta_{st2} = \frac{\frac{F_{st-i}}{E_r A_{st-i}}}{\frac{\lambda_{1-st}}{\tanh(\lambda_{1-st} L_{st2})}} \tag{A2}$$

where F_{st-i} is the force in the stirrup, and λ_{1-st} is given by Eq. (18). Rearranging Eqs. (A1) and (A2) for F_{st-i} and equating gives

$$\frac{\lambda_{1-st} E_r A_{st-i}}{\tanh(\lambda_{1-st} L_{st1})} \Delta_{st1} = \frac{\lambda_{1-st} E_r A_{st-i}}{\tanh(\lambda_{1-st} L_{st2})} \Delta_{st2} \tag{A3}$$

Hence the ratio of the slips from each crack face is given by

$$\frac{\Delta_{st2}}{\Delta_{st1}} = \frac{\tanh(\lambda_{1-st} L_{st2})}{\tanh(\lambda_{1-st} L_{st1})} \tag{A4}$$

The average slip is defined as

$$\Delta_{st-i} = \frac{\Delta_{st1} + \Delta_{st2}}{2} \tag{A5}$$

Hence substituting Eq. (A4) into Eq. (A5) and rearranging gives

$$\Delta_{st1} = \frac{2\Delta_{st-i}}{1 + \frac{\tanh(\lambda_{1-st} L_{st2})}{\tanh(\lambda_{1-st} L_{st1})}} \tag{A6}$$

Substituting into Eq. (A1) and rearranging gives Eq. (17) in the main body of the paper.

APPENDIX B ANALYTICAL SOLUTION FOR I BEAMS AND T BEAMS

Consider a beam with the cross-section in Fig. B1. A T-section can also be considered if (b_{f2}-b_w) is set to zero. If the neutral axis is in the web, the force in the fibres is given by

$$F_f = \frac{f_f}{\sin(\beta)} \left[b_w (h - d_{NA}) + (b_{f2} - b_w) t_{f2} \right] \tag{B1}$$

and the force in the concrete by

$$F_c = \frac{E_c \theta}{\frac{S_{cr}}{2} \sin^2(\beta)} \left[\frac{b_w}{2} d_{NA}^2 + (b_{f1} - b_w) t_{f1} \left(d_{NA} - \frac{t_{f1}}{2} \right) \right] \tag{B2}$$

The area of the concrete in compression is $b_w d_{NA} + (b_{f1} - b_w) t_{f1}$.

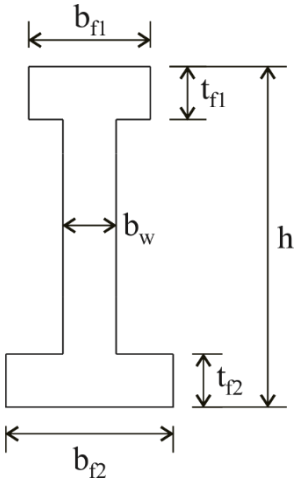

Fig. B1 Geometry of I beam

Substituting Eqs. (B1) and (B2) into Eq. (29) and rearranging for the rotation alters the coefficients in Eq. (31) to the following

$$A_0 = \frac{c\left(b_{f1} - b_w\right)t_{f1}}{\tan(\beta)} - f_f\left[b_w h + \left(b_{f2} - b_w\right)t_{f2}\right] \tag{B3a}$$

$$A_1 = \frac{c b_w}{\tan(\beta)} + f_f b_w \tag{B3b}$$

$$B_0 = \frac{K_{rt} d_{rt}}{\sin^2(\beta)} + \frac{E_c}{\frac{S_{cr}}{2}} \frac{\left(b_{f1} - b_w\right)t_{f1}^2}{2} \left[\frac{m}{\tan(\beta)} + 1\right] \tag{B3c}$$

$$B_1 = -\frac{K_{rt}}{\sin^2(\beta)} - \frac{E_c}{\frac{S_{cr}}{2}} \left(b_{f1} - b_w\right)t_{f1} \left[\frac{m}{\tan(\beta)} + 1\right] \tag{B3d}$$

$$B_2 = -\frac{E_c}{\frac{S_{cr}}{2}} \frac{b_w}{2} \left[\frac{m}{\tan(\beta)} + 1\right] \tag{B3e}$$

The moment about the top fibre due to the fibres is

$$F_f d_f = \frac{f_f}{\sin^2(\beta)}\left[\frac{b_w}{2}\left(h^2 - d_{NA}^2\right) + \left(b_{f2} - b_w\right)t_{f2}\left(h - \frac{t_{f2}}{2}\right)\right] \tag{B4}$$

and the moment about the top fibre due to the uncracked concrete is

$$F_c d_c = \frac{E_c \theta}{S_{cr}}\left[\left(b_{f1} - b_w\right)t_{f1}^2\left(\frac{d_{NA}}{2} - \frac{t_{f1}}{3}\right) + \frac{1}{6} b_w d_{NA}^3\right] \tag{B5}$$

Substituting Eqs. (B1), (B2), (B4) and (B5) into Eq. (33) and rearranging for the rotation alters the coefficients in Eq. (34) to

$$C_0 = a' c\left(b_{f1} - b_w\right)t_{f1} - f_f\left\{b_w\left[\frac{h^2}{2\sin^2(\beta)} - \frac{h a'}{\tan(\beta)}\right] + \left(b_{f2} - b_w\right)\left[\frac{t_{f2}\left(h - \frac{t_{f2}}{2}\right)}{\sin^2(\beta)} - \frac{t_{f2} a'}{\tan(\beta)}\right]\right\} \tag{B6a}$$

$$C_1 = a' c b_w - f_f b_w \frac{a'}{\tan(\beta)} \tag{B6b}$$

$$C_2 = f_f \frac{b_w}{2\sin^2(\beta)} \tag{B6c}$$

$$D_0 = \frac{K_{rt} d_{rt}^2}{\sin^2(\beta)} + \sum_{i=1}^{N} \frac{K_{st-i} d_{st-i}\left(d_{st-i} - a'\right)}{\cos^2(\beta)} + \frac{E_c}{\frac{S_{cr}}{2}}\left(b_{f1} - b_w\right)\left\{\frac{t_{f1}^3}{3\sin^2(\beta)} + \frac{t_{f1}^2 a'}{2}\left[m - \frac{1}{\tan(\beta)}\right]\right\} \tag{B6d}$$

$$D_1 = -\frac{K_{rt} d_{rt}}{\sin^2(\beta)} - \sum_{i=1}^{N} \frac{K_{st-i}(d_{st-i} - a')}{\sin(\beta)\cos(\beta)} - \frac{E_c}{\frac{S_{cr}}{2}}(b_{f1} - b_w)\left\{\frac{t_{f1}^2}{2\sin^2(\beta)} + t_{f1} a' \left[m - \frac{1}{\tan(\beta)}\right]\right\} \quad \text{(B6e)}$$

$$D_2 = -\frac{E_c}{\frac{S_{cr}}{2}} b_w \frac{a'}{2}\left[m - \frac{1}{\tan(\beta)}\right] \quad \text{(B6f)}$$

$$D_3 = \frac{E_c}{\frac{S_{cr}}{2}} \frac{b_w}{6\sin^2(\beta)} \quad \text{(B6g)}$$

Hence these coefficients can now be used to determine the rotation and neutral axis depth at shear failure for I beams using Eqs. (31) and (36).

APPENDIX C ANALYTICAL SOLUTION WHEN REINFORCEMENT HAS YIELDED

When the longitudinal reinforcement has yielded, the force is given by

$$F_{rt} = f_y A_{rt} \quad \text{(C1)}$$

and the coefficients in Eq. (32) become

$$A_0 = -f_y A_{rt} - f_f bh \quad \text{(C2a)}$$

$$B_0 = B_1 = 0 \quad \text{(C2b)}$$

while A_1 and B_2 remain unchanged. In Eq. (35), the coefficients are modified to

$$C_0 = -f_y A_{rt} d_{rt} - f_f bh\left[\frac{h}{2\sin^2(\beta)} - \frac{a'}{\tan(\beta)}\right] \quad \text{(C3a)}$$

$$D_0 = \sum_{i=1}^{N} \frac{K_{st-i} d_{st-i}}{\cos^2(\beta)}(d_{st-i} - a') \quad \text{(C3b)}$$

$$D_1 = -\sum_{i=1}^{N} \frac{K_{st-i}}{\sin(\beta)\cos(\beta)}(d_{st-i} - a') \quad \text{(C3c)}$$

while C_1, C_2, C_3, D_2 and D_3 remain unchanged.

If the stirrups have yielded, the force is given by

$$F_{st-i} = f_{y-st} A_{st-i} \quad \text{(C4)}$$

Hence if N is the total number of stirrups crossing the shear plane in the flexural tension region and n is the number that have yielded then the coefficients in Eq. (32) are modified to

$$C_0 = \sum_{i}^{n} f_{y-st} A_{st-i}\,(d_{st-i} - a') - f_f bh\left[\frac{h}{2\sin^2(\beta)} - \frac{a'}{\tan(\beta)}\right] \quad \text{(C5a)}$$

$$D_0 = \frac{K_{rt} d_{rt}^2}{\sin^2(\beta)} + \sum_{i=n+1}^{N} \frac{K_{st-i} d_{st-i}(d_{st-i} - a')}{\cos^2(\beta)} \quad \text{(C5b)}$$

$$D_1 = -\frac{K_{rt} d_{rt}}{\sin^2(\beta)} - \sum_{i=n+1}^{N} \frac{K_{st-i}(d_{st-i} - a')}{\sin(\beta)\cos(\beta)} \quad \text{(C5c)}$$

If both the longitudinal reinforcement and stirrups have yielded then A_0, B_0 and B_1 are modified as indicated by Eq. (C2) while C_0, D_0 and D_1 are given by

$$C_0 = -f_y A_{rt} d_{rt} - \sum_{i=1}^{n} f_{y-st} A_{st-i}\,(d_{st-i} - a') - f_f b_w h\left[\frac{h}{2\sin^2(\beta)} - \frac{a'}{\tan(\beta)}\right] \quad \text{(C6a)}$$

$$D_0 = \sum_{i=n+1}^{N} \frac{K_{st-i}(d_{st-i})}{\cos^2(\beta)}(d_{st-i} - a') \quad \text{(C6b)}$$

$$D_1 = -\sum_{i=n+1}^{N} \frac{K_{st-i}}{\sin(\beta)\cos(\beta)}(d_{st-i} - a') \quad \text{(C6c)}$$

The best approach for including yielding in this analysis is to first analyse the beam assuming the reinforcement is unyielded and then check the slip of the reinforcement. If the slip exceeds the slip to cause yielding, reanalyse the beam using the expressions in this appendix.

APPENDIX D WORKED EXAMPLE

Consider the beam in Fig. D1. The first step in this solution is to find the crack spacing. Therefore from Eq. (14)

$$\lambda_2 = \frac{(16\ MPa)(226\ mm)}{(1.5\ mm)^{0.3}}\left[\frac{1}{(30000\ MPa)(20000\ mm^2)} + \frac{1}{(200000\ MPa)(1360\ mm^2)}\right] \quad \text{(D1)}$$
$$= 17.1 \times 10^{-6}\ \text{mm}^{-1.3}$$

where L_{per}=226 mm and A_{ct}=20000 mm^2. The crack spacing is then given by Eq. (13)

$$S_{cr} = \left[\frac{2^{0.3}(1.3)}{(17.1 \times 10^{-6}\ \text{mm}^{-1.3})0.7^{1.3}}\right]^{\frac{1}{1.3}}\left\{\frac{2.5\ MPa - 1.5\ MPa}{30000\ MPa}\left[\frac{(30000\ MPa)(20000\ mm^2)}{(200000\ MPa)(1360\ mm^2)} + 1\right]\right\}^{\frac{0.7}{1.3}} \quad \text{(D2)}$$
$$= 69.3\ mm$$

where f_{pc}=1.5 MPa. Hence the effective shear span a'=1170 mm. From Eq. (44),

$$\beta = \arctan\left[\sqrt{1 + \left(\frac{1.27\frac{1170\ mm}{350\ mm} - 1}{\frac{1170\ mm}{350\ mm} + 1.27}\right)^2} - \frac{1.27\frac{1170\ mm}{350\ mm} - 1}{\frac{1130\ mm}{350\ mm} + 1.27}\right] = 0.479\ radians = 27.4° \quad \text{(D3)}$$

From Eq. (10), the minimum shear angle β_{min} is 19.5° hence the actual shear angle is 27.4°
From Eqs. (16) and (15), the stiffness of the longitudinal tension reinforcement is given by

$$\lambda_1 = \sqrt{\left(10.7\frac{MPa}{mm}\right)(226\ mm)\left[\frac{1}{(200000\ MPa)(1360\ mm^2)} + \frac{1}{(30000\ MPa)(20000\ mm^2)}\right]} \quad \text{(D4)}$$
$$= 0.0036\ mm^{-1}$$

$$K_{rt} = (200000\ MPa)(1360\ mm^2)\left\{\frac{0.0036\ mm^{-1}}{\tanh\left[\frac{(0.0036\ mm^{-1})(69.3\ mm)}{2}\right]}\right\} = 7.89 \times 10^6\frac{N}{mm} \quad \text{(D5)}$$

The stirrups that contribute to the shear strength are positioned at d_{st} between $h/[2\tan(\beta)]$=385 mm and $d_{rt}/[\tan(\beta)]$=674 mm. Hence from Fig. D1(b), the stirrups at d_{st}=565 mm contribute to the shear strength. From Eqs. (18) and (17)

$$\lambda_{1-st} = \sqrt{\left(10.7\frac{MPa}{mm}\right)(62.8\ mm)\left[\frac{1}{(200000\ MPa)(157\ mm^2)} + \frac{1}{(30000\ MPa)(40000\ mm^2)}\right]} \quad \text{(D6)}$$
$$= 0.0047\ mm^{-1}$$

$$K_{st} = (200000\ MPa)(157\ mm^2)\frac{2(0.0047\ mm^{-1})}{\tanh[(0.0047\ mm^{-1})(243\ mm)] + \tanh[(0.0047\ mm^{-1})(57\ mm)]} = 274 \times 10^3\frac{N}{mm} \quad \text{(D7)}$$

where L_{per}=62.8 mm, A_{st}=157 mm^2, $A_{ct\text{-}st}$=40000 mm^2, L_{st1}=243 mm and L_{st2}=57 mm.

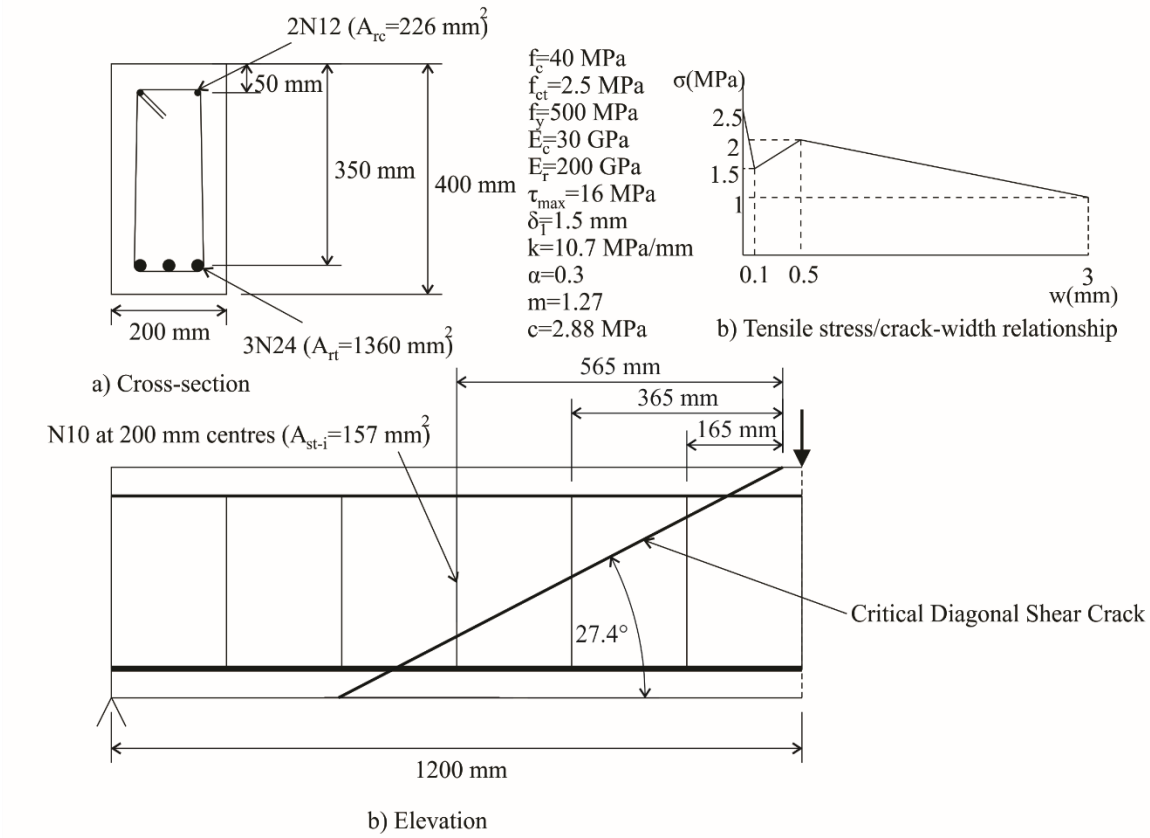

Fig. D1 Worked Example

Assume a crack width at the bottom fibre of 0.1 mm which has a corresponding stress of 1.75 MPa. Hence

$$f_f = 0.5(2.5\ MPa + 1.5\ MPa) = 2\ MPa \tag{D8}$$

Evaluating the coefficients in Eq. (32) and Eq. (35) gives

$$A_0 = -(2\ MPa)(200\ mm)(400\ mm) = -160 \times 10^3\ N \tag{D9a}$$

$$A_1 = \frac{(2.88\ MPa)(200\ mm)}{\tan(0.479)} + (2\ MPa)(200\ mm) = 1.51 \times 10^3\ \frac{N}{mm} \tag{D9b}$$

$$B_0 = \frac{\left(7.89 \times 10^6\ \frac{N}{mm}\right)(350\ mm)}{\sin^2(0.479)} = 13 \times 10^9\ N \tag{D9c}$$

$$B_1 = -\frac{7.89 \times 10^6\ \frac{N}{mm}}{\sin^2(0.479)} = -37.1 \times 10^6\ \frac{N}{mm} \tag{D9d}$$

$$B_2 = -\frac{30000\ MPa}{\frac{69.3\ mm}{2}}\frac{200\ mm}{2}\left[\frac{1.27}{\tan(0.479)} + 1\right] = -296 \times 10^3\ \frac{N}{mm^2} \tag{D9e}$$

$$C_0 = -(2\ MPa)(200\ mm)(400\ mm)\left[\frac{400\ mm}{2\sin^2(0.479)} - \frac{1170\ mm}{\tan(0.479)}\right] = 297 \times 10^6\ Nmm \tag{D9f}$$

$$C_1 = (1170\ mm)(2.88\ MPa)(200\ mm) - (2\ MPa)(200\ mm)\frac{1170\ mm}{\tan(0.479)} = -227 \times 10^3\ N \tag{D9g}$$

$$C_2 = (2\ MPa)\frac{200\ mm}{2\sin^2(0.479)} = 942\ \frac{N}{mm} \tag{D9h}$$

$$D_0 = \frac{\left(7.89 \times 10^6\ \frac{N}{mm}\right)(350\ mm)^2}{\sin^2(0.479)} + \frac{\left(274 \times 10^3\ \frac{N}{mm}\right)(565\ mm)(565 - 1170\ mm)}{\cos^2(0.479\ mm)} = 4.43 \times 10^{12}\ Nmm \tag{D9i}$$

$$D_1 = -\frac{\left(7.89\times10^6\frac{N}{mm}\right)(350\ mm)}{\sin^2(0.479)} - \frac{\left(274\times10^3\frac{N}{mm}\right)(565\ mm - 1170\ mm)}{\sin(0.479)\cos(0.479)} = -12.6\times10^9 N \quad \text{(D9j)}$$

$$D_2 = -\frac{30000\ MPa}{\frac{69.3\ mm}{2}}\frac{(200\ mm)}{2}(1170\ mm)\left[1.27 - \frac{1}{\tan(0.479)}\right] = 66.4\times10^6\frac{N}{mm} \quad \text{(D9k)}$$

$$D_3 = -\frac{30000\ MPa}{\frac{69.3\ mm}{2}}\frac{200\ mm}{6\sin^2(0.479)} = -136\times10^3\frac{N}{mm^2} \quad \text{(D9l)}$$

The coefficients in Eq. (37) are then evaluated as follows

$$P_0 = (-160\times10^3\ N)(4.43\times10^{12}\ Nmm) - (13\times10^9\ N)(297\times10^6\ Nmm) = -4.57\times10^{18}N^2mm \quad \text{(D10a)}$$

$$\begin{aligned} P_1 = {} & (-160\times10^3\ N)(-12.6\times10^9 N) + \left(1.51\times10^3\frac{N}{mm}\right)(4.43\times10^{12}\ Nmm) \\ & - (13\times10^9\ N)(-227\times10^3\ N) - \left(-37.1\times10^6\frac{N}{mm}\right)(297\times10^6\ Nmm) \\ & = 22.7\times10^{15}N^2 \end{aligned} \quad \text{(D10b)}$$

$$\begin{aligned} P_2 = {} & (-160\times10^3\ N)\left(66.4\times10^6\frac{N}{mm}\right) + \left(1.51\times10^3\frac{N}{mm}\right)(-12.6\times10^9 N) \\ & - (13\times10^9\ N)\left(942\frac{N}{mm}\right) - \left(-37.1\times10^6\frac{N}{mm}\right)(-227\times10^3\ N) \\ & - \left(-296\times10^3\frac{N}{mm^2}\right)(297\times10^6\ Nmm) = 37.6\times10^{12}\frac{N^2}{mm} \end{aligned} \quad \text{(D10c)}$$

$$\begin{aligned} P_3 = {} & (-160\times10^3\ N)\left(-136\times10^3\frac{N}{mm^2}\right) + \left(1.51\times10^3\frac{N}{mm}\right)\left(66.4\times10^6\frac{N}{mm}\right) \\ & - \left(-37.1\times10^6\frac{N}{mm}\right)\left(942\frac{N}{mm}\right) - \left(-296\times10^3\frac{N}{mm^2}\right)(-227\times10^3\ N) \\ & = 89.8\times10^9\frac{N^2}{mm^2} \end{aligned} \quad \text{(D10d)}$$

$$P_4 = \left(1.51\times10^3\frac{N}{mm}\right)\left(-136\times10^3\frac{N}{mm^2}\right) - \left(-296\times10^3\frac{N}{mm^2}\right)\left(942\frac{N}{mm}\right) = 73.5\times10^6\frac{N^2}{mm^3} \quad \text{(D10e)}$$

Substituting into Eq. (36) and solving gives the neutral axis depth d_{NA} equal to 149 mm. From Eq. (31) the rotation is equal to

$$\theta = \frac{-160\times10^3\ N + \left(1.51\times10^3\frac{N}{mm}\right)(149\ mm)}{13\times10^9\ N - 37.1\times10^6\frac{N}{mm}(149\ mm) - 296\times10^3\frac{N}{mm^2}(149\ mm)^2} = 72.2\times10^{-6} radians \quad \text{(D11)}$$

This answer can be checked using Eq. (34). Next check that the force in the longitudinal tension reinforcement is less than the yield force using Eqs. (12)

$$F_{rt} = \frac{\left(7.89\times10^6\frac{N}{mm}\right)(72.2\times10^{-6})(350\ mm - 149\ mm)}{\sin^2(0.479)} = 539\ kN \quad \text{(D12)}$$

The yield force is 500 MPa times area of 1360 mm^2 that is 680 kN, hence, the longitudinal force is unyielded. Next check the stirrups using Eq. (19)

$$F_{st} = \frac{\left(274\times10^3\frac{N}{mm}\right)(72.2\times10^{-6})\left[565\ mm - \frac{149\ mm}{\tan(0.479)}\right]}{\cos^2(0.479)} = 7.0\ kN \quad \text{(D13)}$$

The yield force is 500 MPa(157 mm^2)=78.5 kN, hence, the stirrups are unyielded. Next check the actual average stress is in the fibres. From Eq. (6), the crack opening perpendicular to the crack face at the bottom fibre is

$$w_p(h) = \frac{2(72.2\times10^{-6})(400\ mm - 149\ mm)}{\sin(0.479)} = 0.08\ mm \quad \text{(D14)}$$

This corresponds to a stress at the bottom fibre of 1.7 MPa hence the average fibre stress is

$$f_f = 0.5(2.5\ MPa + 1.7\ MPa) = 2.1\ MPa \quad \text{(D15)}$$

As the difference is small and conservative, another iteration is not required. Therefore from Eq. (21), the force in the tensile fibres is

$$F_f = \frac{(2\ MPa)(200\ mm)(400\ mm - 149\ mm)}{\sin(0.479)} = 218\ kN \quad \text{(D16)}$$

From Eq. (25), the compressive force in the concrete is given by

$$F_c = \frac{1}{2}(200\ mm)(149\ mm)^2(30000\ MPa)\frac{72.2 \times 10^{-6}}{\frac{69.3\ mm}{2}\sin^2(0.479)} = 653\ kN \quad \text{(D17)}$$

While the cohesive component of the shear strength is

$$cA_c = 2.88\ MPa(200\ mm)(149\ mm) = 86\ kN \quad \text{(D18)}$$

The shear capacity can now be evaluated using Eq. (30) as

$$V_{cap} = 7.0\ kN + (218\ kN)\cos(0.479) + (653\ kN)\sin(0.479)\,[1.27\sin(0.479) - \cos(0.479)] + 86\ kN = 196\ kN \quad \text{(D19)}$$

APPENDIX E BEAMS TESTED IN SHEAR

Two beams tested by the authors were included in the validation. These specimens were tested to explore the shear capacity of beams constructed using the UHPFRC mix design developed at the University of Adelaide (Sobuz et al. 2016). The first beam did not contain fibres and the second beam contained 1% by volume steel fibres. The dimensions of the specimens were based on those used previously to investigate the shear behaviour of UHPFRC beams (Voo et al. 2006; Baby et al. 2012).

Specimens

The cross-section tested, as shown in Fig. E1(a), was an I-beam. This shape was chosen as it allows a reduced web width increasing the likelihood that shear is the controlling mode of failure. The total depth was 400 mm, the effective depth of 325 mm, the width of the web is 70 mm and the width of the flange is 250 mm. The reinforcement in the tension region included 5 20 mm and one 24 mm diameter bar; the reinforcement ratio was chosen to be sufficient to allow shear failure. The reinforcement was N class reinforcement (Standards Australia 2001) with a yield strength of 500 MPa.

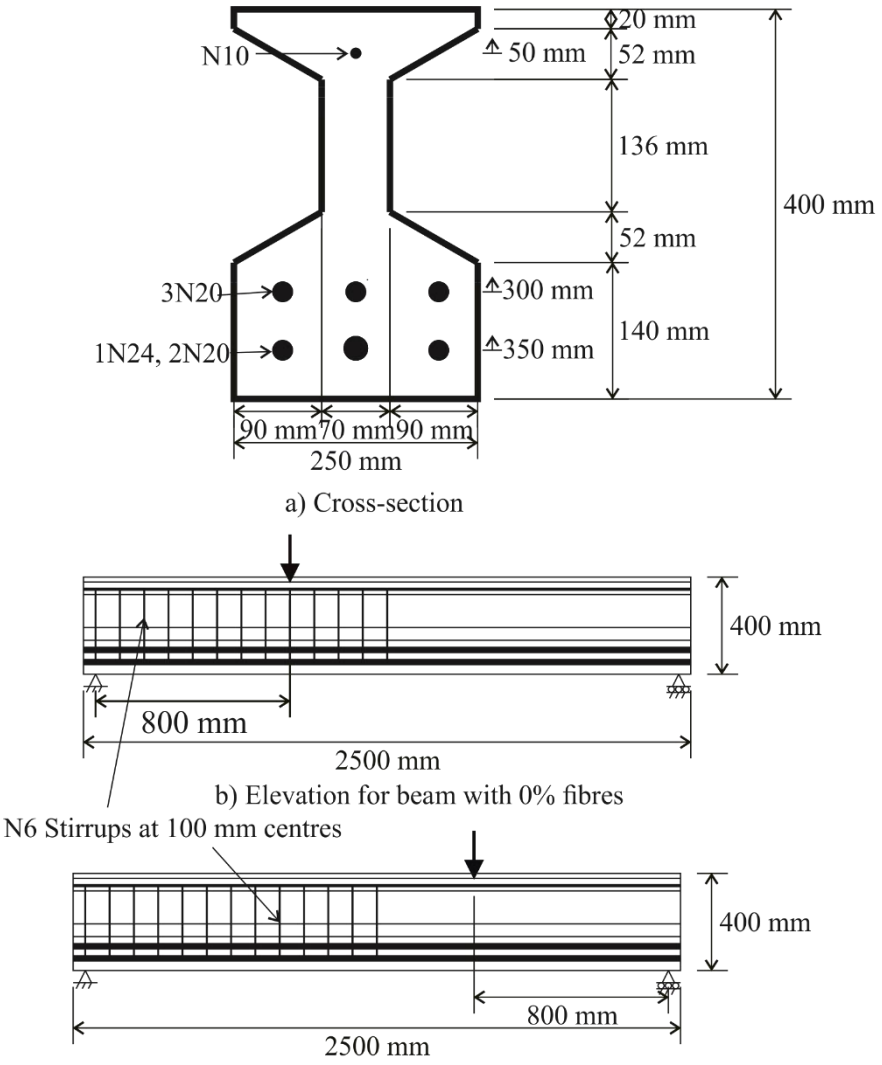

Fig. E1 Cross-section and Elevation of Beam

The elevation of the first beam is shown in Fig. E1(b) and the elevation of the second beam in Fig. E1(c). The span of the beam was 2400 mm. The first beam failed in the long span where the shear span was 1600 mm giving a shear span to effective depth ratio of 4.92. The second beam failed in the short span where the shear span to effective depth ratio was 2.46. 6mm diameter stirrups at 100 mm spacings were provided to ensure shear failure occurred in the expected spans. The shear span-to-effective ratio was chosen as a reduced effective depth-to-shear span ratio is desirable to increase the probability of shear failure, however, previous studies have indicated that a shear span-to-effective depth ratios less than 2.5 tend to result in significant arch action (Kani 1966).

The development of the reinforcement was ensured by the high bond strengths of this material. A previous study by Sturm & Visintin (2018) using the same mix designs as was used in these specimens indicated that bond strengths in excess of 40 MPa could be obtained. Yuan & Graybeal's (2014) indicated that embedment lengths as short as 63.5 mm were sufficient to obtain stresses in the reinforcement in excess of 400 MPa for this type of concrete. Hence, sufficient length was available over the support to fully develop the reinforcement stresses.

Loading setup and instrumentation

For testing, the beam was placed on simple supports with a width of 100 mm. In Fig. 1(c) and (d), it can be seen that one of the supports allowed for both rotation and translation and the support at the other allowing for only rotation. The beams were tested under a single point load applied through a loading plate with a width of 100 mm shown in Fig. E1(d) and allowed for both rotation and translation. Throughout testing the load was applied at a rate of 30 kN/min. The load was recorded using a load cell and the deflection under the load point was also recorded using an LVDT attached to two steel channels underneath the specimen which was attached to the loading frame as shown in Fig. E1(d).

Material behaviour of the UHPFRC

The mix designs that was used is given in Table E1. The fibres that were used where straight steel with a length of 13 mm and a diameter of 0.2 mm. The yield strength of the fibres is 2850 MPa. A sulphate resisting cement was used along with a washed river sand with a fineness modulus of 2.34. The superplasticiser that was used was a third generation high range water reducer.

Table E1 Mix Design

	Unit Weight (kg/m^3)	
	V_f=0%	V_f=1%
Cement	960	949
Silica Fume	255	253
Sand	960	949
Water	182	181
Superplasticiser	43	43
Steel Fibres	0	78

The mechanical properties of the concrete were obtained by testing three 200 mm by 100 mm cylinders in compression as well as three dogbone specimens in direct tension. The dogbone specimens had a square cross-section with a dimension of 120 mm. For more details on the design of the dogbone specimens, the reader is referred to Visintin et al. (2018).

From these tests the compressive strength of the mix without fibres was 114 MPa at the time of testing and the compressive strength of the mix with 1% fibres was 125 MPa. The tensile stress-strain and stress-crack width relationships obtained are shown in Fig. E2(a) and E2(b) respectively. The tensile strength obtained for the 0% fibres mix was 3.75 MPa and the tensile strength for the 1% fibres mix was 4.12 MPa.

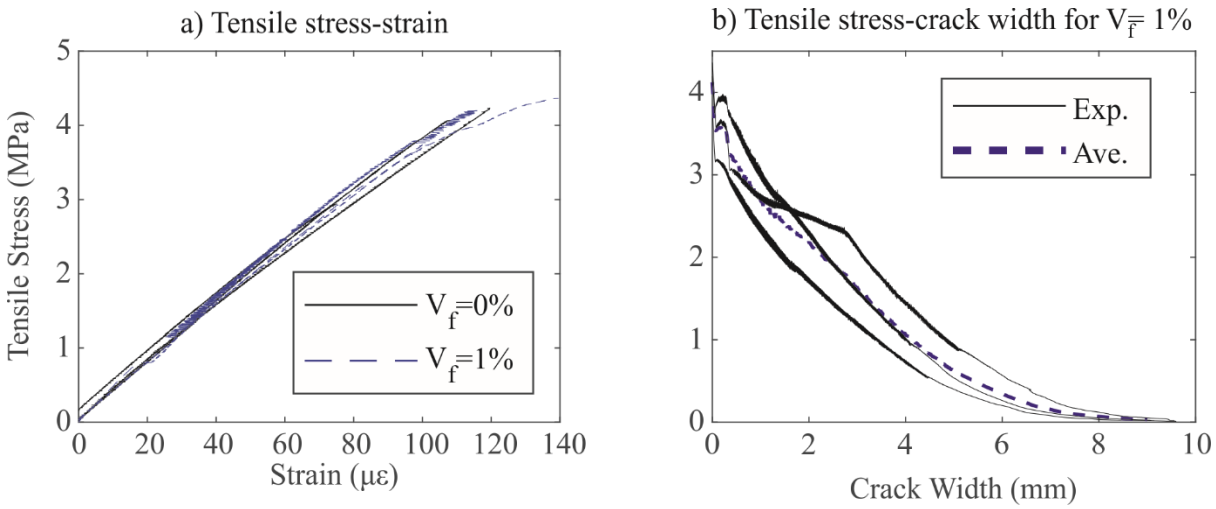

Fig. E2 Direct tension properties

Results

The failure patterns are illustrated in Fig. E3(a) for the beam without fibres and E3(b) for the beams with 1% fibres by volume. In both cases failure was precipitated by a single diagonal crack, while for the beam without fibres there was also a splitting crack that propagated along the longitudinal tension reinforcement. The reason for this is that without fibres there was little to restrain this splitting crack. The shear force versus deflection is also plotted in Fig. E3(c). The shear capacity of the specimen without fibres was 72 kN and the shear capacity of the specimen with fibres was 377 kN.

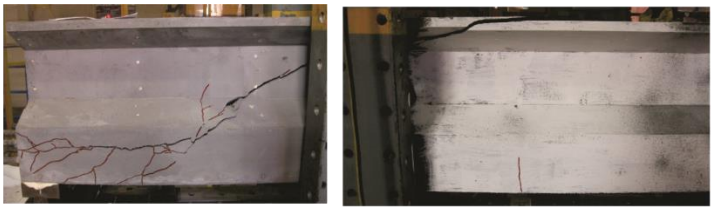

a) Shear crack for beam with 0% fibres

b) Shear crack for beam with 1% fibres

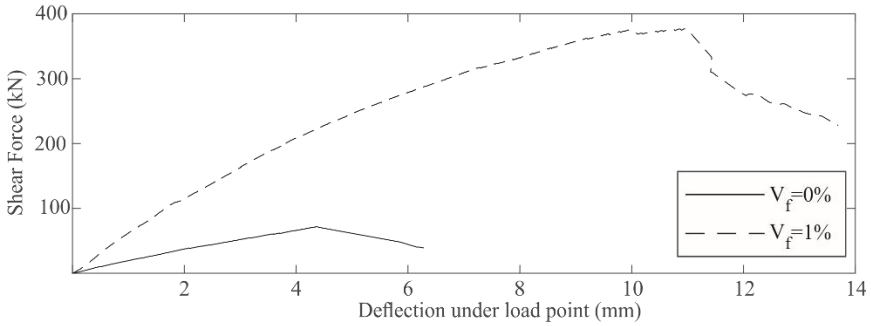

c) Shear force-deflection

Fig. E3 Experimental Results

APPENDIX F SUMMARY OF BEAMS IN VALIDATION

In Table F1, the key parameters for the beams used in the validation are summarised. In Fig. F1, the tensile stress-crack width relationships that were used are plotted. Note that for the tension specimens tested by Amin & Foster (2016), there is a sudden drop in stress after the tensile strength is achieved. This also includes a sudden increase in crack width. Hence, for the missing crack widths, the value is projected back assuming that the tensile stress is constant. Note that for Amin & Foster (2016) the peak tensile strengths obtained for each pour are given as 2.45 MPa, 2.41 MPa and 2.28 MPa for Pour 1, Pour 2 and Pour 3, respectively.

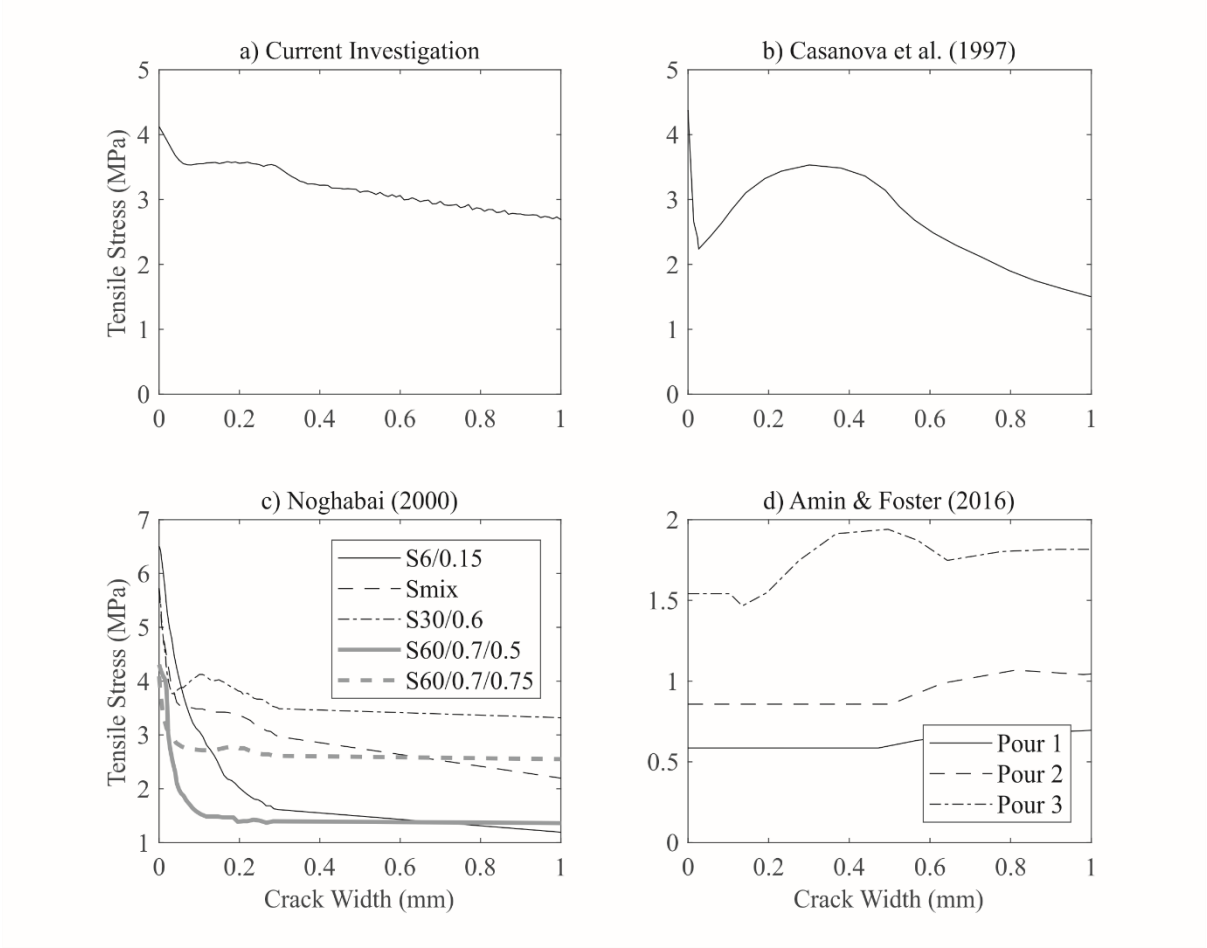

Fig. F1 Tensile stress-crack width relationships used in validation

Table F1 Beams for Validation

Reference	Test	b_w	h	d_{rt}	a/d_{rt}	ρ	f_c	Fibre Type	V_f	A_{st}/s	V_{exp}
		mm	mm	mm			MPa		%		kN
Current Investigation	0%-NST	70	400	325	4.9	0.089	114		0	0	72
	1%-NST	70	400	325	2.5	0.089	125	Straight 13/0.2	1	0	377
Casanova et al. (1997)	HSFRC1	125	250	225	2.9	0.035	90	Hooked 30/0.5	1.3	0	157
	HSFRC2	125	250	225	2.9	0.035	90	Hooked 30/0.5	1.3	0	156
Noghabai (2000)	Type A HSC1-S6/0.15	200	250	180	3.3	0.045	90.6	Straight 6/0.15	1	0	299
	Type A HSC1-Smix	200	250	180	3.3	0.045	83.2	[a]	1	0	295
	Type A HSC1-S60/0.7/0.5	200	250	180	3.3	0.045	80.5	Hooked 60/0.7	0.5	0	252
	Type A HSC1-S60/0.7/0.75	200	250	180	3.3	0.045	80.5	Hooked 60/0.7	0.8	0	262
	Type B HSC2-S30/0.6	200	300	235	2.8	0.043	91.4	Hooked 30/0.6	1	0	310
	Type B HSC2-S6/0.15	200	300	235	2.8	0.043	93.3	Straight 6/0.15	1	0	363
	Type B HSC2- Smix	200	300	235	2.8	0.043	89.6	[a]	1	0	407
	Type C HSC3-S6/0.15 a	200	500	410	2.9	0.031	76.8	Straight 6/0.15	1	0	289
	Type C HSC3-S6/0.15 b	200	500	410	2.9	0.031	76.8	Straight 6/0.15	1	0	336
	Type C HSC3-Smix a	200	500	410	2.9	0.031	72	[a]	1	0	367
	Type C HSC3-Smix b	200	500	410	2.9	0.031	72	[a]	1	0	327
	Type C HSC3-S60/0.7/0.5 a	200	500	410	2.9	0.031	69.3	Hooked 60/0.7	0.5	0	264
	Type C HSC3-S60/0.7/0.5 b	200	500	410	2.9	0.031	69.3	Hooked 60/0.7	0.5	0	312

	Type C HSC3-S60/0.7/0.75 a	200	500	410	2.9	0.031	60.2	Hooked 60/0.7	0.8	0	339
	Type C HSC4-S60/0.7/0.75 b	200	500	410	2.9	0.031	75.7	Hooked 60/0.7	0.8	0	292
	Type D HSC3-S6/0.15	200	700	570	3.0	0.043	76.8	Straight 6/0.15	1	0	445
	Type D HSC4-Smix	200	700	570	3.0	0.043	72	[a]	1	0	596
	Type D HSC3-S60/0.7/0.75	200	700	570	3.0	0.043	60.2	Hooked 60/0.7	0.8	0	509
Amin & Foster (2016)	B25-0-0-0	300	700	622	2.8	0.020	34	Hooked 60/0.9	0.3	0	274
	B50-0-0-0	300	700	622	2.8	0.020	36	Hooked 60/0.9	0.7	0	344
	B50-0-0-0R	300	700	622	2.8	0.020	36	Hooked 60/0.9	0.7	0	409
	B25-550-6-450	300	700	622	2.8	0.020	34	Hooked 60/0.9	0.3	0.13	363
	B25-450-10-450	300	700	622	2.8	0.020	34	Hooked 60/0.9	0.3	0.35	334
	B25-400-6-300	300	700	622	2.8	0.020	46	Hooked 60/0.9	0.3	0.19	322
	B25-300-10-300	300	700	622	2.8	0.020	46	Hooked 60/0.9	0.3	0.52	357
	B50-550-6-450	300	700	622	2.8	0.020	36	Hooked 60/0.9	0.7	0.13	462
	B50-450-10-450	300	700	622	2.8	0.020	36	Hooked 60/0.9	0.7	0.35	535

[a] 0.5% Hooked 30/0.6 and 0.5% Straight 6/0.15

ACKNOWLEDGEMENTS

This material is based upon work supported by the Australian Research Council Discovery Project 190102650"

NOTATION

A_0, A_1, B_0, B_1, B_2 = coefficients for Eq. (31);
A_c = area of concrete in compression;
A_{ct} = area of concrete in tension chord;
$A_{ct\text{-}st}$ = area of concrete in tension chord around the stirrup;
A_{rt} = area of the longitudinal tension reinforcement;
$A_{st\text{-}i}$ = area of i^{th} stirrup;
a = shear span;
a' = effective shear span;
b = width of section;
b_{f1} = width of top flange;
b_{f2} = width of bottom flange;
b_w = width of web;
C_0, C_1, C_2, D_0, D_1, D_2, D_3 = coefficients for Eq. (34);
c = cohesive component of shear capacity;
d_c = depth to compressive force in the concrete;
d_f = distance from the force in the fibres to the top fibre;
d_{NA} = depth to neutral axis;
d_{rc} = depth to the compression reinforcement;
d_{rt} = depth to the longitudinal tension reinforcement;
$d_{st\text{-}i}$ = horizontal distance between stirrup and profile A-A in Fig. 1(a);
E_c = elastic modulus of concrete;
E_r = elastic modulus of reinforcement;
F_c = compressive force in the concrete;
F_f = force in fibres bridging shear crack;
F_{rc} = force in the compression reinforcement;
F_{rt} = force in longitudinal tension reinforcement;
$F_{st\text{-}i}$ = force in the i^{th} stirrup;
f_{ct} = tensile strength;
f_f = average tensile stress in the fibres for a given crack opening displacement;
f_{pc} = post-cracking strength;
f_y = yield strength of longitudinal reinforcement;
$f_{y\text{-}st}$ = yield strength of stirrups;
h = depth of section;
K_{rt} = stiffness of longitudinal tension reinforcement;
$K_{st\text{-}i}$ = stiffness of the stirrups;
k = effective linear bond stiffness;
L_{per} = bonded perimeter;
$L_{per\text{-}st}$ = bonded perimeter of the stirrup;
L_{st1}, L_{st2} = distance from crack face to intersection of stirrup and longitudinal reinforcement;
M = bending moment;
M_{cap} = moment capacity;
m = frictional component of material shear capacity;
N = number of stirrups crossing the shear crack below the neutral axis;

n = number of stirrups that have yielded crossing the shear crack below the neutral axis;
P_0, P_1, P_2, P_3, P_4 = coefficients for Eq. (30);
S = sliding force along shear crack;
S_{cap} = maximum sliding force;
S_{cr} = crack spacing;
s = stirrup spacing;
t_{f1} = thickness of top flange;
t_{f2} = thickness of bottom flange;
V = shear force;
V_{cap} = shear capacity;
$V_{cap-\beta}$ = shear capacity corresponding to shear angle β;
V_{cap-nf} = shear capacity without fibres;
V_{exp} = experimental shear capacity;
V_f = fibre volume;
v = material shear strength;
w_D = crack width at bottom fibre (measured perpendicular to the crack face);
w_p = crack opening perpendicular to the crack face;
w_x = horizontal crack opening;
w_y = vertical crack opening;
x= distance from profile A-A in Fig. 1(a);
y = depth with respect to the top fibre;
Z_{cap} = shear capacity of uncracked sliding plane;
α = non-linearity of bond-stress/slip relationship;
β = angle of critical diagonal shear crack to the horizontal;
β_{min} = minimum shear angle;
Δ_{rt} = slip of the longitudinal tension reinforcement;
Δ_{st-i} = average slip of i^{th} stirrup;
Δ_{st1}, Δ_{st2} = slip of the stirrup from each crack face;
δ_1 = slip at maximum bond stress;
ε_x = longitudinal strain;
θ = rotation at critical diagonal shear crack;
λ_1 = bond parameter for load-slip relationship of the longitudinal reinforcement;
λ_{1-st} = bond parameter for load-slip relationship of the stirrups;
λ_2 = bond parameter for crack spacing;
ρ = reinforcement ratio;
σ_c = stress in concrete;
σ_f = stress in fibres;
σ_N = normal stress;
τ_{max} = maximum bond stress;
τ_N = shear stress at sliding plane;

REFERENCES

AFGC (Association Francaise de Genie Civil) (2013) *Ultra High Performance Fibre-Reinforced Concretes: Recommendations.* Paris.

Amin, A., and Foster, S. J. (2016). "Shear strength of steel fibre reinforced concrete beams with stirrups." *Engineering Structures*, 111, 323-332.

Aoude, H., Belghiti, M., Cook, W. D., and Mitchell, D. (2012). "Response of Steel Fiber-Reinforced Concrete Beams with and without Stirrups." *ACI Structural Journal*, 109(3).

Baby, F., Marchand, P., Atrach, M., and Toutlemonde, F. (2013). "Analysis of flexure-shear behavior of UHPFRC beams based on stress field approach." *Engineering Structures*, 56, 194-206.

Balazs, G. L. (1993). "Cracking analysis based on slip and bond stresses." *ACI Materials Journal*, 90, 340-340.

Barros, J. A., and Foster, S. J. (2018). "An integrated approach for predicting the shear capacity of fibre reinforced concrete beams." *Engineering Structures*, 174, 346-357.

Bazant, Z. P., and Kim, J. K. (1984). "Size Effect in Shear Failure of Longitudinally Reinforced Beams." *ACI Journal Proceedings*, 81(5), 456-468.

Bazant, Z. P., and Sun, H. H. (1987). "Size effect in diagonal shear failure: influence of aggregate size and stirrups." *ACI Materials Journal*, 84(4), 259-272.

Bentz, E. C., Vecchio, F. J., and Collins, M. P. (2006). "Simplified modified compression field theory for calculating shear strength of reinforced concrete elements." *ACI Materials Journal*, 103(4), 614.

Casanova, P., and Rossi, P. (1997). "Can steel fibers replace transverse reinforcements in reinforced concrete beams?" *ACI Materials Journal*, 94(5), 341-354.

CEN (European Committee for Standardisation) (2004). *Eurocode 2: Design of concrete structures - Part 1-1: General rules and rules for building.* EN 1992-1-1:2004, Brussels, Belgium.

Chao, S. H. (2020). "Size Effect on Ultimate Shear Strength of Steel Fiber-Reinforced Concrete Slender Beams." *ACI Structural Journal*, 117(1).

Chen, Y., Visintin, P., and Oehlers, D. J. (2015). "Concrete shear-friction material properties: Derivation from actively confined compression cylinder tests." *Advances in Structural Engineering*, 18(8), 1173-1185.

Choi, K.K., Park, H.G. and Wight, J.K. (2007). "Shear strength of steel fiber-reinforced concrete beams without web reinforcement." *ACI Structural Journal*, 104(1), 12-21.

Conforti, A., Minelli, F., and Plizzari, G. A. (2013). "Wide-shallow beams with and without steel fibres: a peculiar behaviour in shear and flexure." *Composites Part B: Engineering*, 51, 282-290.

DAfStB (Deutscher Ausschuss fur Stahlbeton) (2012). *DAfStB-Richtlinie Stahlfaserbeton*, Berlin, Germany.

Dinh, H. H., Parra-Montesinos, G. J., and Wight, J. K. (2010). "Shear strength model for steel fiber reinforced concrete beams without stirrup reinforcement." *Journal of Structural Engineering*, 137(10), 1039-1051.

fib (International Federation for Structural Concrete) (2013). *fib Model Code for Concrete Structures 2010*. Ernst & Sohn, Berlin, Germany.

Harajli, M. H. (2009). "Bond stress–slip model for steel bars in unconfined or steel, FRC, or FRP confined concrete under cyclic loading." *Journal of Structural Engineering*, 135(5), 509-518.

Haskett, M., Oehlers, D. J., Mohamed Ali, M. S., and Sharma, S. K. (2011). "Evaluating the shear-friction resistance across sliding planes in concrete." *Engineering Structures*, 33(4), 1357-1364.

Hoang, L. C., and Nielsen, M. P. (1998). "Plasticity approach to shear design." *Cement and Concrete Composites*, 20(6), 437-453.

Kani, G. N. J. (1966). "Basic facts concerning shear failure." *ACI Journal Proceedings*, 63(6), 675-692.

Kwak, Y. K., Eberhard, M. O., Kim, W. S., and Kim, J. (2002). "Shear strength of steel fiber-reinforced concrete beams without stirrups." *ACI Structural Journal*, 99(4), 530-538.

Lantsoght, E. O. (2019). "Database of Shear Experiments on Steel Fiber Reinforced Concrete Beams without Stirrups." *Materials*, 12(6), 917.

Lee, S. C., Cho, J. Y., and Vecchio, F. J. (2013). "Tension-Stiffening Model for Steel Fiber-Reinforced Concrete Containing Conventional Reinforcement." *ACI Structural Journal*, 110(4).

Lee, D.H., Han, S.J., Kim, K.S. and LaFave, J.M. (2016a). "Shear capacity of steel fiber-reinforced concrete beams." *Structural Concrete*, 18, 278-291.

Lee, S. C., Cho, J. Y., and Vecchio, F. J. (2016b). "Analysis of steel fiber-reinforced concrete elements subjected to shear." *ACI Structural Journal*, 113(2), 275.

Lim, D. H., and Oh, B. H. (1999). "Experimental and theoretical investigation on the shear of steel fibre reinforced concrete beams." *Engineering Structures*, 21(10), 937-944.

Lucas W, Oehlers D.J., and Mohamed Ali M.S. (2011) "Formulation of a shear resistance mechanism for inclined cracks in RC beams." *Journal of Structural Engineering*, 137(12): 1480-1488.

Mattock, A. H., and Hawkins, N. M. (1972). "Shear transfer in reinforced concrete—Recent research." *PCI Journal*, 17(2), 55-75.

Millard, S. G., and Johnson, R. P. (1984). "Shear transfer across cracks in reinforced concrete due to aggregate interlock and to dowel action." *Mag. Concr. Res*. 36 (126): 9–21.

Minelli, F., and Vecchio, F. J. (2006). "Compression field modeling of fiber-reinforced concrete members under shear loading." *ACI Materials Journal*, 103(2), 244-252.

Minelli, F., Conforti, A., Cuenca, E., and Plizzari, G. (2014). “Are steel fibres able to mitigate or eliminate size effect in shear?” *Materials and structures*, 47(3), 459-473.

Mohamed Ali, M. S., Oehlers, D. J., and Griffith, M. C. (2008). “Shear transfer across cracks in FRP strengthened RC members.” *Journal of Composites for Construction*, 12(4), 416-424.

Noghabai, K. (2000). “Beams of fibrous concrete in shear and bending: experiment and model.” *Journal of Structural Engineering*, 126(2), 243-251.

Ou, Y. C., Tsai, M. S., Liu, K. Y., and Chang, K. C. (2011). “Compressive behavior of steel-fiber-reinforced concrete with a high reinforcing index.” *Journal of Materials in Civil Engineering*, 24(2), 207-215.

Placas A and Regan PE (1971) “Shear failure of reinforced concrete beams.” *ACI Journal Proceedings*, 68(10): 763-773.

Regan, P. E., and Yu, C. W. (1973). *Limit state design of structural concrete*. Chatto & Windus, London.

Shoaib, A., Lubell, A. S., and Bindiganavile, V. S. (2014). “Size effect in shear for steel fiber-reinforced concrete members without stirrups.” *ACI Structural Journal*, 111(5), 1081.

Singh, B., and Jain, K. (2014). “Appraisal of Steel Fibers as Minimum Shear Reinforcement in Concrete Beams.” *ACI Structural Journal*, 111(5).

Sobuz, H. R., Visintin, P., Ali, M. M., Singh, M., Griffith, M. C., and Sheikh, A. H. (2016). “Manufacturing ultra-high performance concrete utilising conventional materials and production methods.” *Construction and Building Materials*, 111, 251-261.

Standards Australia (2001). “Steel reinforcing materials.” *AS/NZS4671:2001*. Sydney.

Standards Australia (2018). *Concrete Structures*. AS3600:2018. Sydney, Australia.

Sturm, A.B. and Visintin, P. (2018) “Local bond slip behaviour of steel reinforcing bars embedded in UHPFRC.” *Structural Concrete*, 20(1), 108-122.

Sturm, A. B., Visintin, P., Farries, K., and Oehlers, D. J. (2018a). “New Testing Approach for Extracting the Shear Friction Material Properties of Ultra-High-Performance Fiber-Reinforced Concrete.” *Journal of Materials in Civil Engineering*, 30(10), 04018235.

Sturm, A.B., Visintin, P., Oehlers, D.J. and Seracino, R. (2018b) “Time dependent tension stiffening mechanics of fibre reinforced and ultra-high performance fibre reinforced concrete.” *Journal of Structural Engineering*, 144(8), 04018122.

Sturm, A. B., Visintin, P., and Oehlers, D. J. (2018c). “Time-dependent serviceability behavior of reinforced concrete beams: Partial interaction tension stiffening mechanics.” *Structural Concrete*, 19(2), 508-523.

Sturm, A.B., Visintin, P. and Oehlers. D.J. (2020) “Blending fibres to enhance the flexural properties of UHPFRC beams.” *Construction and Building Materials*, 244, 118328.

Tompos, E. J., and Frosch, R. J. (2002). “Influence of beam size, longitudinal reinforcement, and stirrup effectiveness on concrete shear strength.” *ACI Structural Journal*, 99(5), 559-567.

Valle, M., and Buyukozturk, O. (1993). “Behavior of fiber reinforced high-strength concrete under direct shear.” *ACI Materials Journal*, 90(2), 122-133.

Vecchio, F. J., and Collins, M. P. (1986). “The Modified Compression-Field Theory for Reinforced Concrete Elements Subjected to Shear.” *ACI Journal Proceedings*, 83(2), 219-231.

Visintin, P., Oehlers, D. J., and Haskett, M. (2013). “Partial-interaction time dependent behaviour of reinforced concrete beams.” *Engineering Structures*, 49, 408-420.

Visintin, P., Sturm, A. B., Mohamed Ali, M. S., and Oehlers, D. J. (2018). “Blending macro- and micro-fibres to enhance the serviceability behaviour of UHPFRC.” *Australian Journal of Civil Engineering*, 16(2), 106-121.

Voo, Y. L., Foster, S. J., and Gilbert, R. I. (2006). “Shear strength of fiber reinforced reactive powder concrete prestressed girders without stirrups.” *Journal of Advanced Concrete Technology*, 4(1), 123-132.

Walraven, J. C., and Reinhardt, H. W. (1981). “Theory and Experiments on the Mechanical Behaviour of Cracks in Plain and Reinforced Concrete Subjected to Shear Loading.” *Heron*, 26 (1A), 1981.

Yuan, J., & Graybeal, B. A. (2014). Bond behavior of reinforcing steel in ultra-high performance concrete (No. FHWA-HRT-14-090). United States. Federal Highway Administration. Office of Infrastructure Research and Development.

Zarrinpour, M. R., and Chao, S. H. (2017). “Shear Strength Enhancement Mechanisms of Steel Fiber-Reinforced Concrete Slender Beams.” *ACI Structural Journal*, 114(3).

Zhang, F., Ding, Y., Xu, J., Zhang, Y., Zhu, W., and Shi, Y. (2016a). “Shear strength prediction for steel fiber reinforced concrete beams without stirrups.” *Engineering Structures*, 127, 101-116.

Zhang, T., Visintin, P., Oehlers, D. J., and Griffith, M. C. (2014a). “Presliding shear failure in prestressed RC beams. I: Partial-Interaction mechanism.” *Journal of Structural Engineering*, 140(10), 04014069.

Zhang, T., Oehlers, D. J., and Visintin, P. (2014b). “Shear strength of FRP RC beams and one-way slabs without stirrups.” *Journal of Composites for Construction*, 18(5), 04014007.

Zhang, T., Visintin, P., and Oehlers, D. J. (2015). “Shear strength of RC beams with steel stirrups.” *Journal of Structural Engineering*, 142(2), 04015135.

Zhang, T., Visintin, P., and Oehlers, D. J. (2016b). “Shear strength of RC beams without web reinforcement.” *Australian Journal of Structural Engineering*, 17(1), 87-96.

Zhang, T., Visintin, P., and Oehlers, D. J. (2017b). “Partial-interaction tension-stiffening properties for numerical simulations.” *Advances in Structural Engineering*, 20(5), 812-821.

STATEMENT OF AUTHORSHIP

Design-oriented solutions for the shear capacity of reinforced concrete beams with and without fibres
Submitted to *Journal of Structural Engineering*

Sturm, A. B. (Candidate)

Prepared manuscript, performed all analyses, and developed model and theory (80%)

This paper reports on original research I conducted during the period of my Higher Degree by Research candidature and is not subject to any obligations or contractual agreements with a third party that would constrain its inclusion in this thesis. I am the primary author of this paper.

Signed ..... Date 9/07/2020

Visintin, P.

Supervised and contributed to research, and acted as corresponding author (10%)

I certify that the candidate's stated contribution to the publication is accurate (as detailed above); permission is granted for the candidate in include the publication in the thesis; and the sum of all co-author contributions is equal to 100% less the candidate's stated contribution.

Signed ..... Date 07/07/2020

Oehlers, D. J.

Supervised and contributed to research (10%)

I certify that the candidate's stated contribution to the publication is accurate (as detailed above); permission is granted for the candidate in include the publication in the thesis; and the sum of all co-author contributions is equal to 100% less the candidate's stated contribution.

Signed ..... Date 8/7/20

DESIGN ORIENTED SOLUTIONS FOR REINFORCED CONCRETE BEAMS WITH AND WITHOUT FIBRES

Sturm, A.B., Visintin, P., Oehlers, D.J.

ABSTRACT

The inclusion of fibres substantially improves the shear resistance of reinforced concrete beams. Fibres can, therefore, be used as a partial or full substitute for traditional transverse reinforcement. Hence, reliable expressions which incorporate the effect of fibres are required. In a previous study, a mechanics approach based to quantify the pre-sliding shear capacity of fibre reinforced concrete beams was developed and broadly validated against experimental data and compared to existing design approaches. While accurate, the numerical solution is too complicated for routine design and hence, in this paper, simplified solutions are developed. To validate the simplified solitons, they are used to predict the capacity of tests on 626 reinforced concrete beams without stirrups, 176 reinforced concrete beams with stirrups and 23 fibre reinforced concrete beams. Importantly these simplified solutions largely retain the accuracy of the numerical approach and show an improved fit compared to currently available solutions.

INTRODUCTION

The design of reinforced concrete members is based on the assumption that ductile flexural failure always precedes brittle shear failure. As such, reliable approaches for predicting the shear capacity of a member and specifying the concrete and transverse reinforcement contributions to shear capacity are essential to the design process. With recent developments in concrete technology, the use of fibre reinforced concrete (FRC) has progressed significantly. Member level testing has identified a significant improvement in shear capacity can be achieved by the addition of fibres and it has been suggested that fibre reinforcement may reduce or entirely replace traditional transverse reinforcement (Casanova et al. 1997, Amin & Foster 2016).

To quantify the increase in shear capacity arising from fibre addition and, therefore, allow for the increased capacity to be considered in design practice, Australian standard AS3600:2018 (Standards Australia 2018) includes expressions for quantifying the shear capacity of FRC members. In this approach a simplified modified compression field theory is applied to predict the concrete contribution to the shear capacity; a traditional truss model is used to determine the steel contribution; and a constant stress in the fibres is used to simulate the fibre contribution. Additional empirical factors are included to account for fibre orientation and size effect on the tensile stress in the fibres. The fib Model Code 2010 (fib 2012) has also included an expression to determine the shear capacity which considers the concrete and fibre contribution together based on the expression for shear capacity in the Eurocode 2 (CEN 2004). The fib Model Code 2010 (fib 2012) also outlines an alternative approach in the commentary based on modified compression field theory similar to the approach in AS3600:2018. The Association Francaise de Genie Civil (AFGC 2013) has developed shear capacity expressions for ultra-high performance fibre reinforced concrete beams. In this approach, the shear capacity is increased by the vertical component of the force in the fibres; the stress in the fibres is taken as the average stress when the flexural strength is achieved and the force in the fibres is assumed to be perpendicular to the principal compressive stress.

Other empirical approaches are also available in the literature as demonstrated by Lantsoght's (2019) comparison of 15 different approaches which identified the model of Kwak et al. (2002) to be the best performing. While several of the approaches reviewed showed satisfactory

performance, the disadvantage of these empirical formulations is the difficulty in extending the results beyond the bounds of the existing testing regime.

In more recent work, Sturm et al. (2020) developed a new approach for predicting the shear capacity of FRC beams based on the pre-sliding mechanical model of Zhang et al. (2016a, b) which was originally developed for conventional concrete beams with steel or fibre reinforced polymer (FRP) reinforcement. This approach was compared to five other existing mechanical models and the four codified approaches identified above. In this comparison, the first model was the plasticity based model suggested by Voo et al. (2006). The second model was that suggested by Choi et al. (2007), who calculated the concrete contribution to the shear capacity as a function of the shear force required to crack the flexural compression region and the fibre contribution as a function of a constant stress imposed on an inclined crack. The third approach is that of Lee et al. (2016) who suggested an alternative approach in which the shear demand and capacity attributed to the compression zone and tension zone is determined and shear failure occurs when either of these values are exceeded. The fourth approach was that of Zhang et al. (2016c) who suggested an approach based on simplified modified compression field theory, in which the stress in the fibre is determined as a function of the bond strength of a single fibre. Finally to the model of Foster & Barros (2018) who also developed a model for the shear capacity of FRC beams where the contribution of the fibres is determined by considering the pullout of a single fibre at various inclinations to the crack.

From the above comparisons in Sturm et al. (2020), the proposed approach based on the model of Zhang et al. (2016a;b) was found to be the best performing approach in terms of precision and accuracy. The approach also has the advantage over previous work of not requiring the results of single fibre pullout tests, which are not always readily available, thereby, making the approach more practical. The major disadvantage of Sturm et al.'s (2020) approach is that the numerical formulation may be too complicated for routine design. In an attempt to address this, a non-iterative solution was also developed in the same paper, however it too could be considered too complex for routine design because of the need to solve a quartic equation. Hence, in this paper the approach of Sturm et al. (2020) is simplified into a form suitable for routine design and it is found that the resulting solutions are simpler in functional form to the refined analysis proposed in AS3600:2018 (Standards Australia 2018) as iteration is not required to evaluate a longitudinal strain.

The simplified design expressions are validated and compared to existing approaches using tests on 626 reinforced concrete beams without stirrups, 176 reinforced concrete beams with stirrups and 23 FRC beams. From this, the reliability of the proposed expressions was explored. This is important since these expressions give the mean shear strength, however in design, the characteristic shear strength is required. Hence, factors were derived that could be used in conjunction with these expressions to give the characteristic shear strength.

SHEAR CAPACITY OF FIBRE REINFORCED CONCRETE BEAMS

First consider the fundamental mechanics of Sturm et al.'s (2020) model as illustrated in Fig. 1(a) where the forces on the free body on the right hand side A-B-C-D are shown. As the shear force V_u increases, flexural cracks form in the flexural tension region at the bottom face and propagate towards the load point. While tests have shown these cracks to follow a non-linear path, a simplification is applied here in which the non-linear crack is replaced with an equivalent diagonal crack A-B with an angle of β to the horizontal as shown. This approximation, which allows for significant simplification has also been implemented in the

approaches of Zhang (1997), Huang & Nielsen (1998), Zhang et al. (2016a;b) and Sturm et al. (2020)

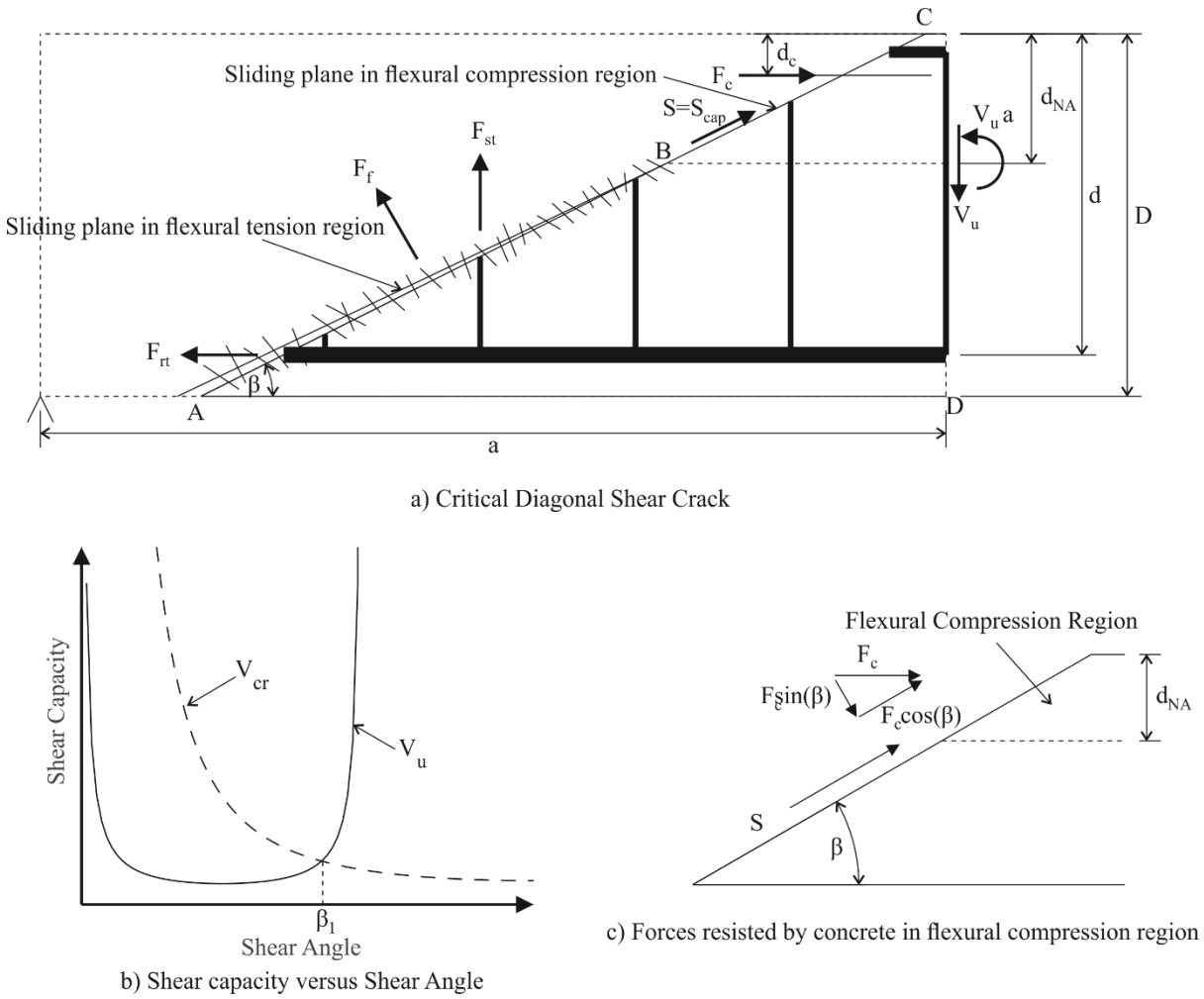

Fig. 1 Mechanics of Shear Failure

As rotation occurs about this critical shear crack A-B in Fig. 1(a), forces develop in the: tensile reinforcement F_{rt}; compressive concrete F_c; fibres F_f; and in the stirrups F_{st}. In line with the simplifying assumption of Placas & Regan (1971), the compression reinforcement is ignored. In order to maintain equilibrium with the imposed shear force and moment, a force S also occurs along the inclined plane as shown. This sliding force S is resisted along B-C by the concrete in compression and shear failure is considered to occur at the point in which the sliding force S exceeds the shear capacity S_{cap} of the potential sliding plane B-C, at which point a fracture plane extends through the flexural compression region along B-C.

The shear stress at the initiation of sliding that is the material shear capacity v can be derived from shear friction theory (Regan & Yu 1973) such that

$$v = m\sigma_N + c \quad (1)$$

where: σ_N is the normal stress which is a function of F_c in Fig. 1(a); m is the frictional component of the shear strength; and c is the cohesion.

The shear strength of the potential sliding plane S_{cap} can be determined by integrating v over this plane in the flexural compression region. Importantly in this approach, the shear capacity is taken as the capacity just prior to the sliding plane extending into the flexural compression

region, that is just prior to sliding in the flexural compression region. This is done as once sliding occurs, the material shear capacity reduces (Chen et al. 2015) when σ_N remains the same. Hence, this paper takes the shear capacity as equal to the pre-sliding capacity because this is equal to or a lower bound to the actual shear capacity. This same approach has been adopted by Zhang et al. (2016a;b) and Sturm et al. (2020) where accurate predictions were obtained in comparison to more than 1100 test observations.

From a numerical analysis (Zhang et al. 2016a; Sturm et al. 2020), it can be shown that the shear capacity V_u, through failure along A-B-C in Fig. 1(a), varies with the inclination of the sliding plane β as shown in Fig. 1(b) (Sturm et al. 2020). However, this failure mode can only occur after the sliding plane A-B in Fig. 1(a) has formed. The shear load to form the sliding plane A-B in Fig. 1(a) has been defined by Zhang (1997) as

$$V_{cr} = \frac{f_{ct}^* b D^2}{a \sin^2(\beta)} \tag{2}$$

in which: f_{ct}^* is the effective tensile strength which is equal to $0.6f_{ct}$ where f_{ct} is the concrete tensile strength (Zhang 1997); b is the width of the section; D is the total depth; and a is the shear span.

Consider the variations V_{cr} and V_u in Fig. 1(b). To the right of β_1, V_u exceeds V_{cr} such that the sliding plane forms at V_{cr} before failure at an increased load V_u. To the left of β_1, V_{cr} exceeds V_u such that the sliding plane fails at V_{cr} as the strength then reduces to V_u. Hence the intercept at β_1 governs the ultimate strength.

Having now defined the general mechanics of the approach, now let us consider the mathematical formulation. From vertical equilibrium of the forces illustrated in Fig. 1(a)

$$V_u = S_{cap} \sin(\beta) + F_{st} + F_f \cos(\beta) \tag{3}$$

where F_{st} is the force in the stirrups and F_f is the force in the fibres. For convenience in design, Eq. (3) can be rewritten in the same form as AS3600:2018 (Standards Australia 2018) that is

$$V_u = V_{uc} + V_{us} + V_{uf} \tag{4}$$

in which the contribution of the concrete to the shear capacity is

$$V_{uc} = S_{cap} \sin(\beta) \tag{5}$$

the contribution of the stirrups to the shear capacity is

$$V_{us} = F_{st} \tag{6}$$

and the contribution of the fibres to the shear capacity is

$$V_{uf} = F_f \cos(\beta) \tag{7}$$

Concrete contribution to the shear capacity

The concrete contribution to the shear capacity uses the closed form expression derived by Zhang et al. (2016a) for the shear capacity of reinforced concrete beams without stirrups. From horizontal, vertical and rotational equilibrium

$$0 = F_{rt} - F_c - S_{cap} \cos(\beta) \tag{8}$$

$$V_{uc} = S_{cap} \sin(\beta) \tag{9}$$

$$V_{uc} a = F_{rt} d - F_c d_c \tag{10}$$

where the sliding capacity S_{cap} is obtained by integrating the material shear strength in Eq. (1) over the area of the sliding plane in compression. This sliding capacity is a function of the normal stress due to F_c given by

$$\sigma_N = \frac{F_c \sin(\beta)}{\left[\frac{b d_{NA}}{\sin(\beta)}\right]} = \frac{F_c \sin^2(\beta)}{b d_{NA}} \tag{11}$$

where $F_c \sin(\beta)$ is the component of F_c normal to the sliding plane, whereas, $bd_{NA}/\sin(\beta)$ is the area of the sliding plane in the flexural compression region as illustrated in Fig. 1(c).

The component of F_c parallel to the sliding plane $F_c \cos(\beta)$ in Fig. 1(c) has the corresponding shear stress

$$\tau_N = \frac{F_c \cos(\beta)}{\left[\frac{bd_{NA}}{\sin(\beta)}\right]} = \frac{F_c \sin(\beta)\cos(\beta)}{bd_{NA}} \tag{12}$$

Consequently, the sliding capacity is given by

$$S_{cap} = \int^{\frac{bd_{NA}}{\sin(\beta)}} (v - \tau_N) dA = \frac{C_1 F_c + cbd_{NA}}{\sin(\beta)} \tag{13}$$

which is the material shear strength less the shear component of F_c.

Substituting Eq. (13) into Eq. (8) and rearranging gives the force in the longitudinal tension reinforcement

$$F_{rt} = F_c \left[1 + \frac{C_1}{\tan(\beta)}\right] + \frac{cbd_{NA}}{\tan(\beta)} \tag{14}$$

where substituting Eq. (13) into Eq. (9) then rearranging gives the force in the concrete

$$F_c = \frac{V_{uc} - cbd_{NA}}{C_1} \tag{15}$$

Further substituting Eqs. (14) and (15) into Eq. (10) then rearranging gives the shear capacity

$$V_{uc} = \frac{cbd_{NA}}{C_2} \tag{16}$$

where

$$C_2 = 1 - C_1 \frac{a - \frac{d}{\tan(\beta)}}{d - d_c} \tag{17}$$

in which

$$C_1 = \sin(\beta)\left[m\sin(\beta) - \cos(\beta)\right] \tag{18}$$

where d is the effective depth, d_{NA} is the neutral axis depth and d_c is the lever arm of the concrete.

The primary differences between the above solution and that in Sturm et al. (2020) are the unknown variables when solving Eqs. (8-10). In the numerical model, the unknown variables were the shear capacity V_{uc}, the rotation θ and the neutral axis depth d_{NA}. However, in the solution presented here, d_{NA} is approximated as that from a flexural analysis allowing for θ and d_{NA} to be presented as a function of F_{rt} and F_c. This approximation significantly simplifies the solution because as shown in Sturm et al. (2020) without it d_{NA} must be quantified by solving a quartic equation. In this simplified case, there are no terms that are products of F_{rt} and F_c and hence Eqs. (8-10) form a system of linear simultaneous equations which are straightforward to solve. This change in unknowns also means that the stress-strain relationship of the concrete or the load-slip relationship of the reinforcement is not directly required in the solution further reducing complexity.

Neutral axis depth

To solve Eq. 18, the neutral axis depth can be approximated using the flexural cracked neutral axis (Zhang et al. 2016a). For an FRC beam this is complicated by the fact the cracked neutral axis depth varies with the applied moment and is not a constant (Sturm et al. 2019). Hence, as

a lower bound on the neutral axis depth the value at the yield of the longitudinal reinforcement can be used. At yield the force in the reinforcement is given by

$$F_{rt} = E_r A_{rt} \chi (d - d_{NA}) = f_y A_{rt} \tag{19}$$

where E_r is the elastic modulus of the reinforcement, A_{rt} is the cross-sectional area of the tensile reinforcement, χ is the curvature, d is the effective depth, d_{NA} is the neutral axis depth and f_y is the yield strength of the reinforcement. Hence rearranging Eq. (19) gives the curvature

$$\chi = \frac{f_y}{E_r (d - d_{NA})} \tag{20}$$

The force in the fibres is then given by

$$F_f = f_f b (D - d_{NA}) \tag{21}$$

where f_f is the stress in the fibres, b is the width of the section and D is the total depth. The force in the concrete is

$$F_c = \frac{1}{2} b d_{NA}^2 E_c \chi \tag{22}$$

where E_c is the elastic modulus of the concrete.

Hence from horizontal equilibrium

$$0 = F_{rt} + F_f - F_c = f_y A_{rt} (d - d_{NA}) + f_f b (h - d_{NA})(d - d_{NA}) - \frac{1}{2} b d_{NA}^2 E_c \frac{f_y}{E_r} \tag{23}$$

which can be solved to yield the neutral axis depth

$$d_{NA} = d \left(\frac{a_2 - \sqrt{a_2^2 - 4 a_1 a_3}}{2 a_1} \right) \tag{24}$$

in which

$$a_1 = -\frac{1}{2n} + \frac{f_f}{f_y} \tag{25}$$

$$a_2 = \rho + \frac{f_f}{f_y} \left(1 + \frac{D}{d} \right) \tag{26}$$

$$a_3 = \rho + \frac{f_f}{f_y} \frac{D}{d} \tag{27}$$

and ρ is the reinforcement ratio, n is the modular ratio, f_f is the fibre stress, f_y is the yield stress and D is the total depth. Note that if f_f is set to zero the neutral axis depth for a section without fibres is obtained. As the concrete is taken to be in its elastic state in Eq. (23), the lever arm of the concrete force is taken as $d_{NA}/3$ from the compression face.

Shear Angle

The development of a fully closed form solution for the shear angle is the primary change from that presented in Zhang et al. (2016a) which used a semi-mechanical expression based on a numerical model. A further benefit of this closed form solution is that it can incorporate new materials, whereas, the semi-mechanical expressions need to be recalibrated. From Fig. 1(b) the shear angle is given when the sliding capacity given by Eq. (16) is equal to the shear force to cause diagonal cracking given by Eq. (2). Rearranging this gives the following equation for β_1

$$0 = 1 - \sin^2(\beta_1) \left(\frac{ma}{d - d_c} + C_3 \right) + \sin(\beta_1) \cos(\beta_1) \frac{md + a}{d - d_c} - \cos^2(\beta_1) \frac{d}{d - d_c} \tag{28}$$

where

$$C_3 = \frac{c a d_{NA}}{f_{ct}^* D^2} \tag{29}$$

Applying trigonometric identities (Olver et al. 2010)

$$\sin(\beta)\cos(\beta) = \frac{\tan(\beta)}{1+\tan^2(\beta)} \tag{30}$$

$$\sin^2(\beta) = \frac{1}{2} - \frac{1}{2}\left[\frac{1-\tan^2(\beta)}{1+\tan^2(\beta)}\right] \tag{31}$$

$$\cos^2(\beta) = \frac{1}{2} + \frac{1}{2}\left[\frac{1-\tan^2(\beta)}{1+\tan^2(\beta)}\right] \tag{32}$$

and rearranging gives

$$0 = b_1\tan^2(\beta_1) + b_2\tan(\beta_1) + b_3 \tag{33}$$

where

$$b_1 = 1 - \frac{ma}{d-d_c} - C_3 \tag{34}$$

$$b_2 = \frac{md+a}{d-d_c} \tag{35}$$

$$b_3 = 1 - \frac{d}{d-d_c} \tag{36}$$

Hence the shear angle is given by

$$\beta_1 = \arctan\left(\frac{-b_2 - \sqrt{b_2^2 - 4b_1b_3}}{2b_1}\right) \tag{37}$$

Stirrup contribution to the shear capacity

In Zhang et al. (2016b) and Sturm et al. (2020), the contribution of the stirrups to the shear capacity was determined by evaluating the force in each individual stirrup as a function of the vertical opening of the shear crack. This crack opening is a function of the neutral axis depth d_{NA} and rotation. This approach is not applicable to our simplified solution as the rotation is not quantified. For the closed-form solution in Zhang et al. (2016b), this issue was mitigated by geometrically relating the force in the stirrups to the force in the reinforcement. The solution, however, is still not ideal for design as there is uncertainty about whether the stirrups have or have not yielded. To resolve this problem, Zhang's solution required the shear capacity to be determined assuming the stirrups are elastic then checking whether the stirrups should have yielded. If some of the stirrups should have yielded, the shear capacity would be assessed using the correct assumption. Another problem is that the exact position of the stirrups with respect to the shear crack is not known.

To overcome the above uncertainties and to simplify the problem, the conventional solution of smeared and yielded stirrups was adopted. Applying these assumptions the force in the stirrups in Fig. 1(a) is

$$V_{us} = f_y\frac{A_{rv}}{s}\frac{d-d_{NA}}{\tan(\beta)} \tag{38}$$

where A_{rv} is the area of transverse reinforcement and s is the spacing. This assumption can appear to be unconservative because, as shown by the numerical analyses conducted by Zhang et al. (2016b) and the experimental work of Wu & Hu (2017), rarely are all the stirrups yielded in practice at the onset of shear failure. This is mitigated by the fact that while Eq. (38) overstates the direct contribution of the stirrups to the shear capacity, the increase in the force in the concrete F_c due to the stirrups (Zhang et al. 2016b) was not included in the derivation of V_{uc}. To determine whether this is a reasonable approximation a subset of beams with stirrups taken from the ensuing validation were analysed using both the above smeared approach and the discrete crack model presented in Zhang et al. (2016b). The results of this analysis are

shown in Fig. 2 in which the results above the diagonal line show the smeared approach to underestimate the strength and vice versa. Hence it can be seen that the smeared approach is generally safe.

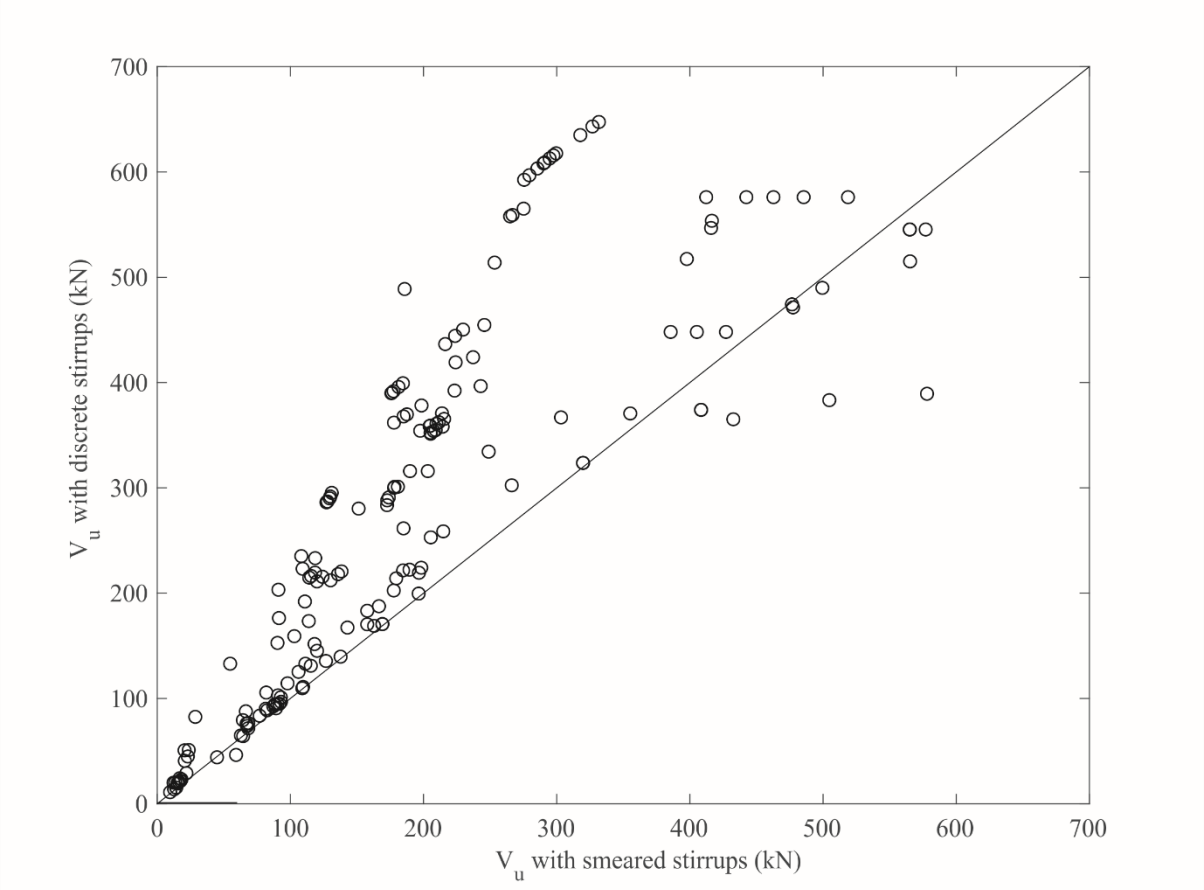

Fig. 2 Comparison of smeared and discrete stirrup models

Fibre contribution to the shear capacity

The force in the fibres F_f in Fig. 1(a) is given by integrating the stress in the fibres over the area of the sliding plane that is in tension

$$F_f = \int^{\frac{b(h-d_{NA})}{\sin(\beta)}} \sigma_f(w) dA = f_f \frac{b(D-d_{NA})}{\sin(\beta)} \tag{39}$$

where $\sigma_f(w)$ is the stress in the fibres as a function of the crack width w and f_f is the average fibres stress that is constant over the depth. The resulting fibre contribution to the shear capacity is given by

$$V_{uf} = f_f \frac{b(D-d_{NA})}{\tan(\beta)} \tag{40}$$

The fibre stress f_f depends on both the magnitude and variation of the crack width along the tensile region of the sliding plane. In general, the fibre stress reduces with crack width being a maximum near the top of the crack and a minimum near the longitudinal tension reinforcement. Hence to achieve a simple and conservative solution, the fibre stress is chosen to correspond to the crack width at the depth of the tensile reinforcement. Furthermore, to provide an upper bound to the crack width and, therefore, a lower bound to f_f, the reinforcement strain is set to the yield strain ε_y so that the crack width can be approximated as

$$w_d = \varepsilon_y S_{cr} \tag{41}$$

where S_{cr} is the crack spacing which can be determined using the following expression from Sturm et al. (2018)

$$S_{cr} = \left[\frac{2^{\alpha}(1+\alpha)}{\lambda_2(1-\alpha)^{1+\alpha}}\right]^{\frac{1}{1+\alpha}} \left[\frac{f_{ct} - f_{pc}}{E_c}\left(\frac{E_c A_{ct}}{E_r A_{rt}} + 1\right)\right]^{\frac{1-\alpha}{1+\alpha}} \quad (42)$$

in which

$$\lambda_2 = \frac{\tau_{max} L_{per}}{\delta_1^{\alpha}}\left(\frac{1}{E_c A_{ct}} + \frac{1}{E_r A_{rt}}\right) \quad (43)$$

where τ_{max} is the maximum bond stress, δ_1 is the slip at the maximum bond stress, α is the non-linearity, L_{per} is the bonded perimeter, A_{rt} is the cross-sectional area of tensile reinforcement, A_{ct} is the cross-sectional area of the tension chord, E_c is the elastic modulus of the concrete and f_{pc} is the post-cracking stress which can be estimated as the first local minimum after the peak. The bond parameters τ_{max}, δ_1 and α can be identified from the bond stress-slip relationship determined from pullout tests on embedded reinforcement as shown in Fig. 3(a). Where experimental data is unavailable, the expressions suggested by Harajli (2009) for FRCs with strengths less than 100 MPa and Sturm & Visintin (2018) for FRCs with strengths exceeding 100 MPa can be used. The geometry of the tension chord is illustrated in Fig. 3(b) as this defines L_{per} and $A_{ct.}$

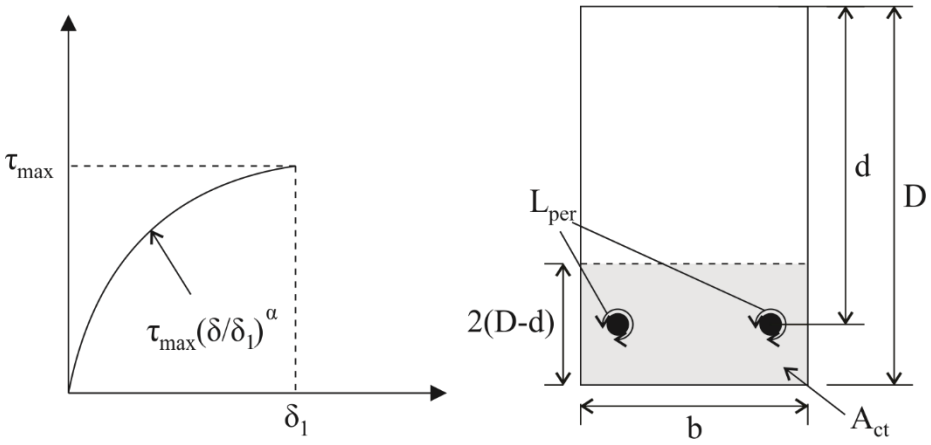

Fig. 3 Bond stress-slip relationship and geometry of tension chord

To use the crack width from Eq. (41), the tensile stress-crack width relationship is required. As there are as of yet no general material models that cover the full range of FRC mixes, this needs to be determined experimentally. There has been little uniformity in terms of the testing approaches applied to FRC to characterise the tensile response. In the opinion of the authors, the best approach is to measure this directly is through the use of specimens sufficiently large such that the 3D orientation of the fibres in not disturbed such as those suggested by AS3600:2018 (Standards Australia 2018) or Visintin et al. (2018). Specimens that are not sufficiently large may disturb the distribution of the fibres such that they become aligned with the applied force, hence, overestimating the tensile strength for members where this is not the case.

VALIDATION

Reinforced concrete members without stirrups

The shear capacity expressions proposed in this paper for reinforced concrete members without stirrups are first validated against a database of 626 tests from 26 references (Moody et al. 1954; Morrow & Viest 1957; Chang & Kesler 1958; Watstein & Mathey 1958; Sozen et al. 1959; Diaz de Cossio & Siess 1960; Diaz de Cossio 1962; Leonhardt & Walther 1962; Bresler

& Scordelis 1963; Mathey & Watstein 1963; Kani 1966; Krefeld & Thurston 1966; Kani 1967; Bhal 1968; Mattock 1969; Placas & Regan 1971; Taylor 1972; Walraven 1978; Chana 1981; Mphonde & Frantz 1984; Kotsovos 1987; Papadakis 1996; Collins & Kuchma 1999; Kim & White 1999; Yost et al. 2001; Tang et al. 2009) compiled by Zhang et al (2016). The details of the tests used for the validation are summarised in a spreadsheet in the supplementary material. The tests are compared in Fig. 4 to the procedure in this paper as well as the codified approaches in AS3600:2018 (Standards Australia 2018), ACI 318-19 (ACI 2019) and in Eurocode 2 (CEN 2004). For the validation, the elastic modulus of the reinforcement was assumed to be 200 GPa while the elastic modulus of the concrete and the tensile strength where estimated using the expressions in the fib Model Code 2010 (fib 2013). The shear friction material properties suggested by Zhang et al. (2014) were used in this validation, that is,

$$m = \frac{0.389 f_c - c}{0.250\ f_c} \tag{44}$$

$$c = 1.15 f_{ct} \tag{45}$$

in which f_c is the concrete compressive strength and f_{ct} the tensile strength.

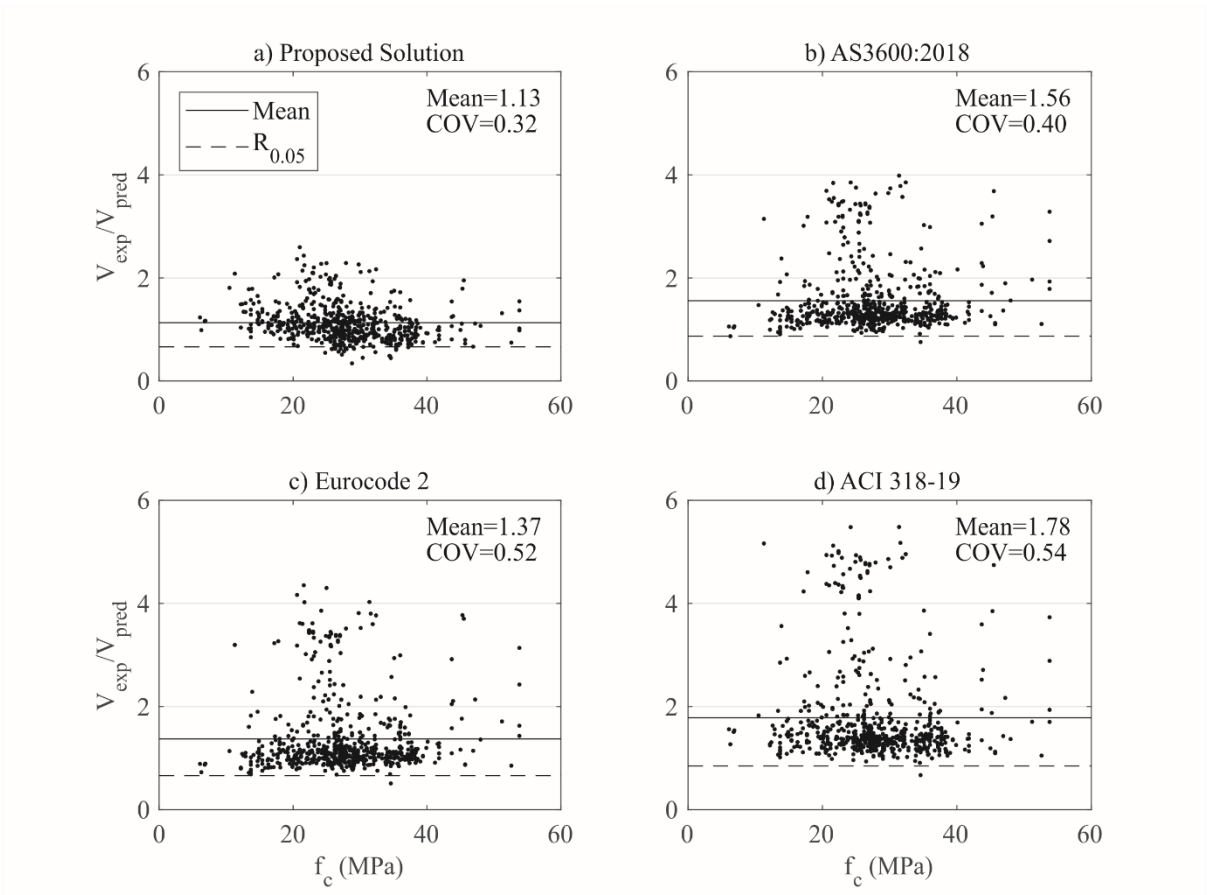

Fig. 4 Validation for reinforced concrete beams without stirrups

It can be seen in Fig. 4 that the proposed approach has a coefficient of variation (COV) of 0.32 which is a significant improvement over the codified approaches where the COV ranges from 0.40 to 0.54. For design, the characteristic shear capacity is

$$V_d = 0.66 V_{uc} \tag{46}$$

which was estimated by fitting a lognormal distribution according to

$$R_{0.05} = \exp(\lambda - 1.645\varepsilon) \tag{47}$$

in which λ is the mean of *log(x)*, ε is the standard deviation of *log(x)* and *x* is the ratio of the experimental to predicted values. The reader is directed to Appendix A for a complete derivation of Eq. 47.

Reinforced concrete members with stirrups

The shear capacity expressions for reinforced concrete members with stirrups are validated against a database of 176 tests from 16 references (Clark 1951; Bresler & Scordelis 1963; Krefeld & Thurston 1966; Placas & Regan 1971; Swamy & Andriopoulos 1974; Mattock & Wang 1984; Mphonde & Frantz 1985; Elzanaty et al. 1986; Anderson & Ramirez 1989; Sarsam & Al-Musawi 1992; Xie et al. 1994; Yoon et al. 1996; Frosch 2000; Tompos & Frosch 2002; Lee & Hwang 2010; Lee et al. 2011) compiled by Zhang et al. (2016b). The results are compared in Fig. 5 to the procedure in this paper as well as the codified approaches from AS3600:2018 (Standards Australia 2018), ACI 318-19 (ACI 2019) and Eurocode 2 (CEN 2004). The proposed approach has the best COV of 0.22 which is a minor improvement over the codified approaches that range between a COV of 0.23 and 0.36. However, the better fit to beams without stirrups and to FRC beams generally validates this approach. Hence the design shear capacity in this case is given by

$$V_d = 0.95(V_{uc} + V_{us}) \tag{48}$$

For the validation, the elastic modulus of the reinforcement was again assumed to be 200 GPa while the elastic modulus and tensile strength of the concrete were estimated with the expressions in the fib Model Code 2010 (fib 2013) and Eqs. (44) and (45) to determine the shear friction material properties.

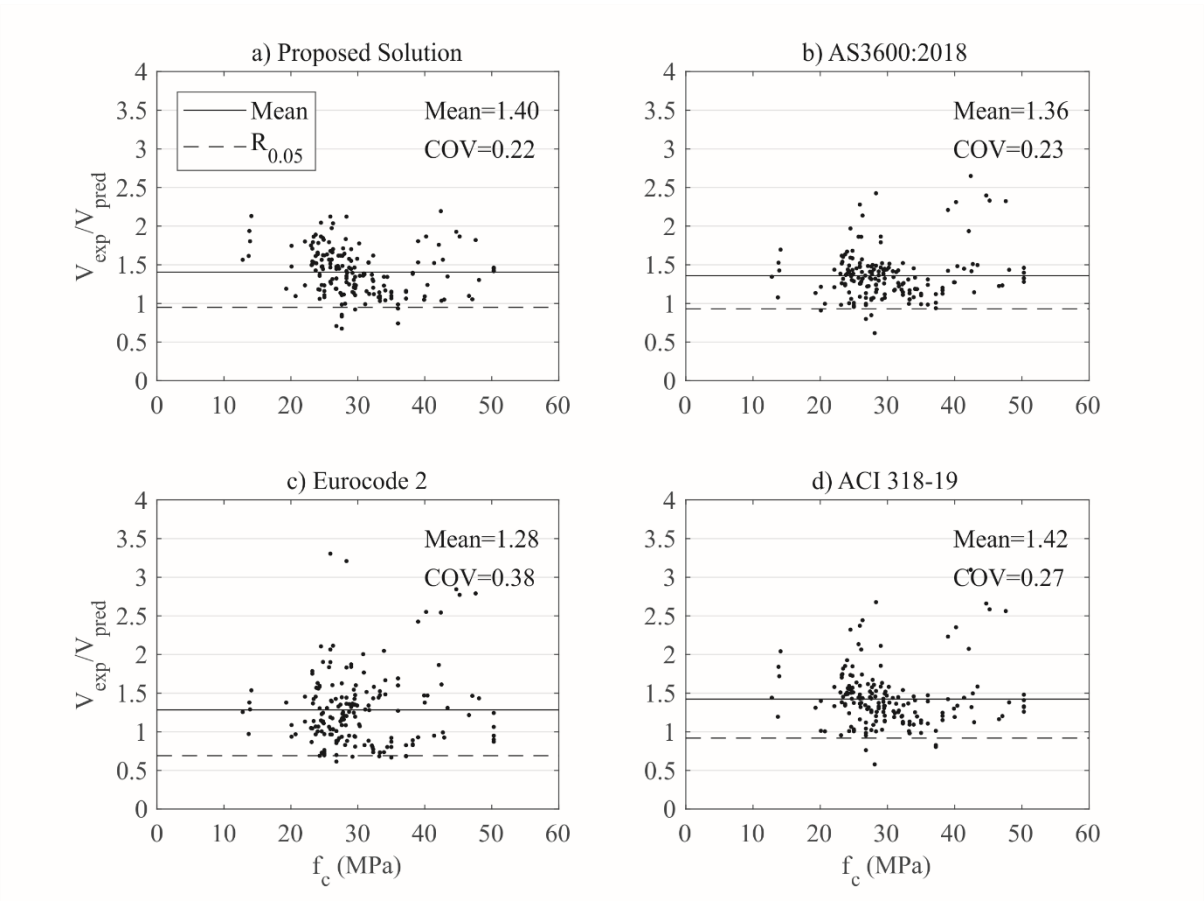

Fig. 5 Validation for reinforced concrete beams with stirrups

FRC members without stirrups

The shear capacity of FRC members is validated against a database of 23 tests from 3 references (Casanova et al. 1997; Noghabai 2000; Amin & Foster 2016). Although there has been a large number of shear tests performed on FRC beams as evidenced by Lantsoght's (2019) review, in the majority of these experimental campaigns the tensile response of the FRC was poorly characterised making it difficult to differentiate between the errors arising from the shear model and the errors arising from characterisation of the tensile properties. Hence, in this comparison only tests where the tensile response was characterised over a range of crack widths using direct tension tests are considered. This is not to say that the approach cannot be used unless direct tension test results are available, but rather that for the purpose of validate only tests in which no further interpretation of test data is required have been chosen.

The tests are compared in Fig. 6 to the proposed approach as well as the solutions in Sturm et al. (2020a)[a], Sturm et al. (2020)[b], AS3600:2018 (Standards Australia 2018), AFGC (2013) and fib Model Code 2010 (fib 2012), Choi et al. (2007), Zhang et al, (2016c) and Lee et al. (2016); where "Sturm et al. (2020)[a]" refers to a numerical solution and "Sturm et al. (2020)[b]" refers to the non-iterative solution. Additionally, "fib Model Code 2010[a]" refers to the solution based on the Eurocode 2 shear capacity expression while "fib Model Code 2010[b]" refers to the shear capacity expression based on simplified modified compression field theory. In this comparison the shear friction material properties were again estimated using Eqs. (44) and (45).

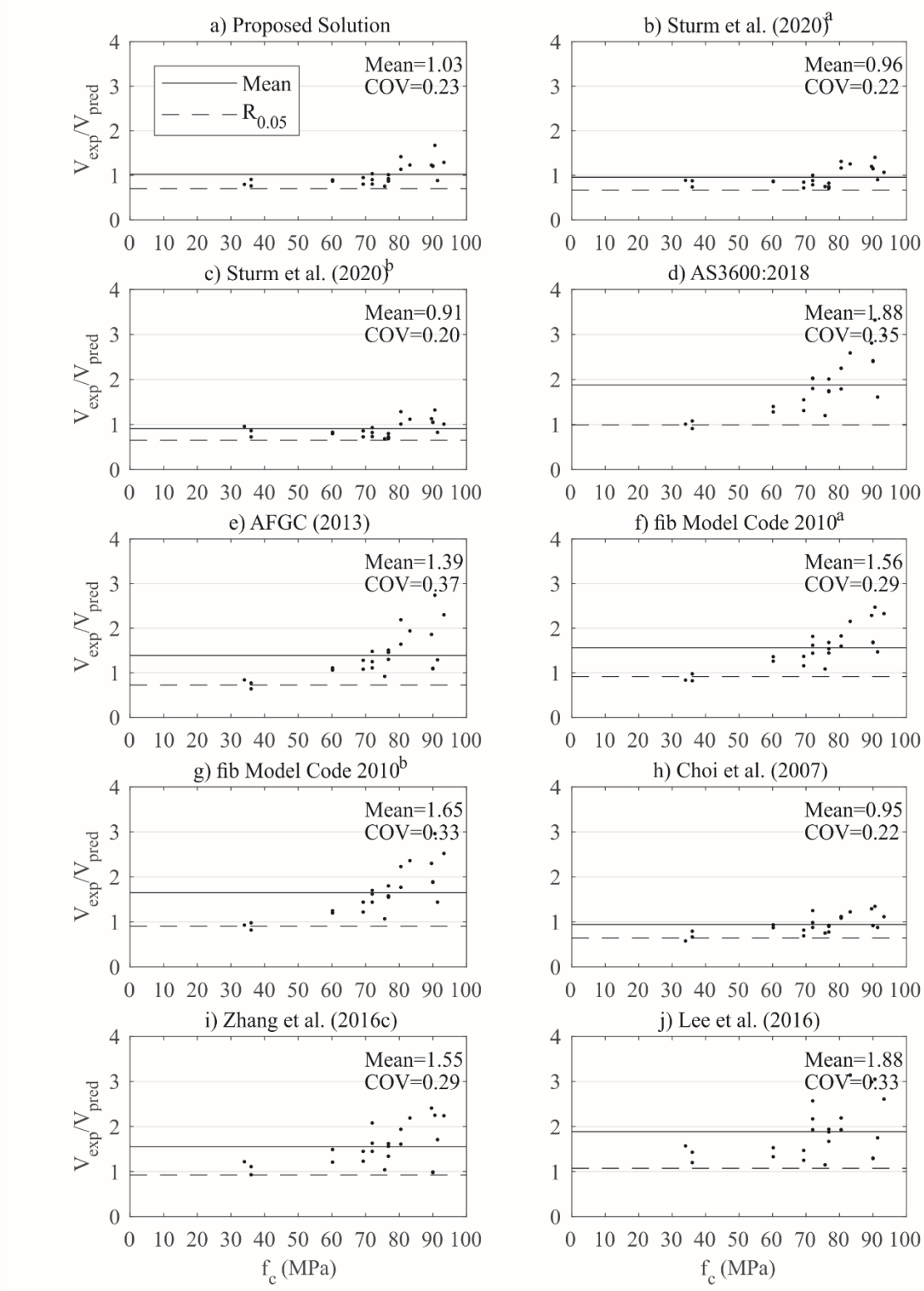

Fig. 6 Validation for FRC beams

From the comparisons in Fig. 6, the proposed solution was found to have a COV of 0.23 which can be compared to a COV of 0.20-0.22 for the approaches proposed in Sturm et al. (2020). Hence, the significant simplifications in this paper have only produced a minimal loss in accuracy. The COV of 0.23 is also a significant improvement on the codified approaches which had COVs between 0.29 and 0.37. The codified approaches are also conservative with means between 1.39 and 1.88 as compared to the 1.03 for the proposed solution. Zhang et al. (2016c)

and Lee et al. (2016) had means and COVs in the same range as the codified approaches, while the mean and COV for Choi et al. (2007) is in the same range as the proposed solution. This is interesting as they propose a similar shear failure mechanism to Sturm et al. (2020) where the shear failure is controlled by the shear crack penetrating the flexural compression region. The proposed solution however is simpler as it does not require iteration to determine the maximum compressive strain at the loading point. The design shear capacity in this case is given by

$$V_d = 0.70\left(V_{uc} + V_{uf}\right) \tag{49}$$

FRC members with stirrups

Further avenues for research include FRC beams with stirrups as it would be useful to determine the reliability of these expressions when applied in this case. This was not done in this study as the only study available in the literature where the tensile response was well characterised was performed by Amin & Foster (2016), hence, sufficient data to determine the reliability of these expressions is not available.

ANALYSIS WORKED EXAMPLE

To assist in the application of the approach the solution to a worked example where the member geometry and transverse reinforcement is known and is now provided, this scenario would be followed to assess the shear capacity of an existing beam.

Consider the FRC beam in Fig. 7. The first step is to estimate the crack spacing, so starting with the bond parameter from Eq. (43)

$$\lambda_2 = \frac{(15.4\ MPa)(528\ mm^2)}{(1.5\ mm)^{0.3}}\left[\frac{1}{(43000\ MPa)(46800\ mm^2)} + \frac{1}{(200000\ MPa)(3690\ mm^2)}\right] = 13.3 \times 10^{-6}\ mm^{-0.3} \tag{50}$$

where τ_{max} is 15.4 MPa, δ_1 is 1.5 mm, α is 0.3 using the expressions in Harajli (2009). Furthermore, A_{ct} is 46800 mm^2 and L_{per} is 528 mm^2. Hence the crack spacing is given by Eq. (42) as

$$S_{cr} = \left[\frac{2^{0.3}(1.3)}{(13.3 \times 10^{-6}\ mm^{-0.3})(0.7)^{1.3}}\right]^{\frac{1}{1.3}}\left[\frac{2.28\ MPa - 1.47\ MPa}{43000\ MPa}\left(\frac{(43000\ MPa)(46800\ mm^2)}{(200000\ MPa)(3690\ mm^2)} + 1\right)\right]^{\frac{0.7}{1.3}} = 67.0\ mm \tag{51}$$

The crack width at the depth of the tensile reinforcement is given by Eq. (45) using the yield strain 0.0025

$$w_d = 0.0025(42.0\ mm) = 0.168\ mm \tag{52}$$

Hence, the fibre stress f_f is 1.51 MPa. The next step is to evaluate the neutral axis depth. From Eqs. (25-27)

$$a_1 = -\frac{1}{2(4.65)} + \frac{1.51\ MPa}{500\ MPa} = -0.105 \tag{53}$$

$$a_2 = 0.0198 + \frac{1.51\ MPa}{500\ MPa}\left(1 + \frac{700\ mm}{622\ mm}\right) = 0.0262 \tag{54}$$

$$a_3 = 0.0198 + \frac{1.51\ MPa}{500\ MPa}\frac{700\ mm}{622\ mm} = 0.0232 \tag{55}$$

where the modular ratio n is 4.65 and the reinforcement ratio is ρ is 0.0198. Substituting in Eqs. (25-27) into Eq. (24)

$$\frac{d_{NA}}{d} = \frac{0.0262 - \sqrt{(0.0262)^2 + 4(0.105)(0.0232)}}{-2(0.105)} = 0.362 \tag{56}$$

Hence, the neutral axis depth d_{NA} is 225 mm such that the lever arm of the concrete d_c is 75 mm. The shear friction material properties can be estimated using Eqs. (44-45) to give m of 1.26 and c of 2.62 MPa. The next step is to evaluate the shear angle. Thus from Eq. (29)

$$C_3 = \frac{(2.62MPa)(1750\ mm)(225\ mm)}{(1.37\ MPa)(700\ mm)^2} = 1.54 \quad (57)$$

where the effective tensile strength f_{ct}* is 1.37 MPa. From Eq. (34-36)

$$b_1 = 1 - \frac{(1.26)(1750\ mm)}{622\ mm - 75\ mm} - 1.54 = -4.57 \quad (58)$$

$$b_2 = \frac{(1.26)(622\ mm) + 1750mm}{622\ mm - 75\ mm} = 4.63 \quad (59)$$

$$b_3 = 1 - \frac{622\ mm}{622\ mm - 75\ mm} = -0.137 \quad (60)$$

Hence the shear angle given by Eq. (37) is

$$\tan(\beta_1) = \frac{-4.63 - \sqrt{(4.63)^2 - 4(4.57)(0.137)}}{-2(4.57)} = 0.983 \quad (61)$$

which corresponds to 0.777 radians or 44.5°. The shear contribution due to the concrete can now be evaluated using Eqs. (16-18) as follows:

$$C_1 = \sin(0.777)\,[1.26\ \sin(0.777) - \cos(0.777)] = 0.120 \quad (62)$$

$$C_2 = 1 - 0.120\frac{1750\ mm - \frac{622\ mm}{0.983}}{622\ mm - 75\ mm} = 0.755 \quad (63)$$

$$V_{uc} = \frac{(2.62\ MPa)(300\ mm)(225\ mm)}{0.755} = 234kN \quad (64)$$

The contribution of the stirrups is given by Eq. (38) as

$$V_{us} = (500\ MPa)\left(0.349\frac{mm^2}{mm}\right)\frac{622\ mm - 225\ mm}{0.983} = 70.5\ kN \quad (65)$$

And the contribution of the fibres is given by Eq. (40) as

$$V_{uf} = (1.51\ MPa)\frac{(300\ mm)(700\ mm - 225\ mm)}{0.983} = 219\ kN \quad (66)$$

Hence the shear capacity is

$$V_u = 234\ kN + 70.5\ kN + 219\ kN = 524\ kN \quad (67)$$

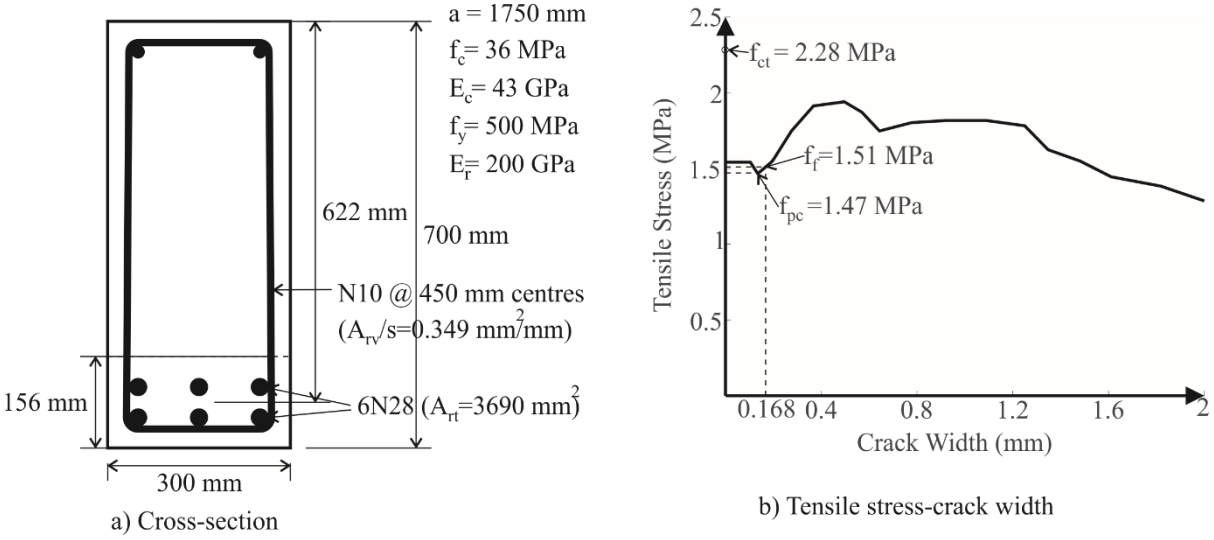

Fig. 7 Analysis worked example

DESIGN WORKED EXAMPLE

Now let us consider a design example, that is where the member geometry and flexural reinforcement ratio has been set and the transverse reinforcement ratio needs to be determined.

Here we will also include the fibre content as a design variable, but this may have been fixed in earlier flexural design.

Consider the beam in Fig. 8 which is subjected to as shear force V^* of 100 kN. First let us determine the shear capacity of the section without fibres or stirrups. From Eqs. (44-45) the shear friction material properties are m equal to 1.29 and c equal to 2.62 MPa. Next we must evaluate the neutral axis depth using Eqs. (25-27)

$$a_1 = -\frac{1}{2(6.1)} = -0.082 \tag{68}$$

$$a_2 = a_3 = \rho = 0.0225 \tag{69}$$

in which the modular ratio n is 6.1 and the reinforcement ratio ρ is 0.0225. From Eq. (24) the neutral axis depth as a function of member effective depth is

$$\frac{d_{NA}}{d} = \frac{0.0225 - \sqrt{(0.0225)^2 + 4(0.082)(0.0225)}}{-2(0.082)} = 0.404 \tag{70}$$

such that the neutral axis depth d_{NA} is 108 mm and the concrete lever arm d_c is 36 mm.
Next evaluate the shear angle; using Eq. (29)

$$C_3 = \frac{(2.62\ MPa)(1250\ mm)(108\ mm)}{(1.37\ MPa)(300\ mm)^2} = 2.87 \tag{71}$$

and evaluating constants b_1 to b_3 Eqs. (34-36)

$$b_1 = 1 - \frac{(1.29)(1250\ mm)}{268\ mm - 36\ mm} - 2.87 = -8.82 \tag{72}$$

$$b_2 = \frac{(1.29)(268\ mm) + 1250mm}{268\ mm - 36\ mm} = 6.88 \tag{73}$$

$$b_3 = 1 - \frac{268\ mm}{268\ mm - 36\ mm} = -0.155 \tag{74}$$

Hence the shear angle is given by Eq. (37) as

$$\tan(\beta_1) = \frac{-6.88 - \sqrt{6.88^2 - 4(8.82)(0.155)}}{-2(8.82)} = 0.757 \tag{75}$$

Which corresponds to 0.648 radians or 37.1°. The shear contribution of the concrete is now given by Eqs. (16-18)

$$C_1 = \sin(0.648)\,[1.29\sin(0.648) - \cos(0.648)] = -0.0113 \tag{76}$$

$$C_2 = 1 + 0.0113\frac{1250\ mm - \frac{268\ mm}{0.757}}{268\ mm - 36\ mm} = 1.04 \tag{77}$$

$$V_{uc} = \frac{(2.62\ MPa)(150\ mm)(108\ mm)}{1.04} = 40.8\ kN \tag{78}$$

Hence, if the total required shear capacity is 100 kN then an additional 59.2 kN is required from the fibres and/or the transverse reinforcement. First let us consider if the additional shear capacity can be derived from the fibres alone. Rearranging Eq. (40) gives the required stress in the fibres as

$$f_f = \frac{V_{uf}}{b(D - d_{NA})}\tan(\beta) = \frac{59200\ N}{(150\ mm)(300\ mm - 108\ mm)}0.757 = 1.56\ MPa \tag{79}$$

Next we must determine the crack width at shear failure which generates this required stress. From Eqs. (50-51) the crack spacing is given by

$$\lambda_2 = \frac{(16.3\ MPa)(151\ mm^2)}{(1.5\ mm)^{0,3}}\left[\frac{1}{(32800\ MPa)(9600\ mm^2)} + \frac{1}{(200000\ MPa)(905\ mm^2)}\right] \tag{80}$$
$$= 19 \times 10^{-6} mm^{-0.3}$$

$$S_{cr} = \left[\frac{2^{0.3}(1.3)}{(19\times10^{-6}\ mm^{-0.3})\ (0.7)^{1.3}}\right]^{\frac{1}{1.3}}\left\{\frac{2.28\ MPa - 1.56\ MPa}{32800\ MPa}\left[\frac{(32800\ MPa)(9600\ mm^2)}{(200000\ MPa)(905\ mm^2)}+1\right]\right\}^{\frac{0.7}{1.3}} \quad (81)$$
$$= 46.9mm$$

in which τ_{max} is 16.3 MPa, δ_1 is 1.5 mm and α is 0.3 using the expressions in Harajli (2009). From the geometry of the tension chord in Fig. B1 L_{per} is 151 mm and A_{ct} is 9600 mm^2. Hence, from Eq. (45) the crack width is given by

$$w_d = 0.0025(46.9\ mm) = 0.117\ mm \quad (82)$$

Therefore, if FRC with a minimum tensile stress of 1.25 MPa at a crack width of 0.142 mm is specified then the required shear strength can be obtained without the need for transverse reinforcement.

If the required shear strength is now increased to 150 kN then this 50 kN shortfall could be accommodated by including transverse reinforcement. To quantify the required area of reinforcement rearranging Eq. (38) gives

$$\frac{A_{rv}}{s} = \frac{V_{us}}{f_y(d-d_{NA})}\tan(\beta) = \frac{50000\ N}{500\ MPa(268\ mm - 108\ mm)}(0.874) = 0.546\ mm^2/mm \quad (83)$$

where the yield strength of the transverse reinforcement is 500 MPa. Hence, this requirement can be met by providing 8 mm diameter stirrups at 150 mm spacings.

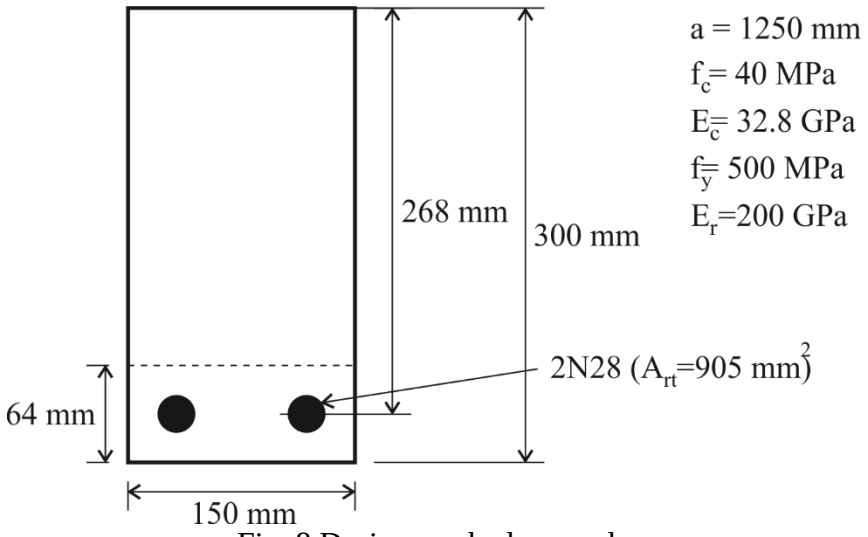

Fig. 8 Design worked example

CONCLUSION

Based on free body mechanics, simple design rules have been developed for the shear capacity of reinforced concrete beams. These rules separate the contributions of the concrete, stirrups and fibres to the shear capacity and as such can be used by engineers as a convenient tool to design members with any combination of concrete, stirrups and fibres and with new types of materials. To illustrate the convenience of this approach, a worked example of a design is given.

The design approach developed has been validated and compared to codified solutions where it was found that for reinforced concrete beams without stirrups the COV was 0.32 compared to 0.40 for the best codified solution. For reinforced concrete beams with stirrups, the COV was 0.22 compared to 0.23 for the best codified solution. For FRC beams, the COV was 0.23 compared to 0.35 for the current Australian standard. The solution also retains much of the accuracy of the numerical solutions presented in Sturm et al. (2020) with the COV increasing to only 0.23 from a COV of 0.20. The presented solutions are also simpler than the current

Australian standard as no iteration is required to determine the longitudinal strain. Additionally, a log-normal distribution was fitted to the experimental to predicted results to allow the characteristic shear strength to be determined from the mean values. The primary improvement over previous codified expressions for shear is that the concrete and fibre contributions are related to the neutral axis depth. The solution also includes a simple method to estimate the fibre stress which does not require either the use of an excessively conservative value or iteration to determine the fibre stress.

APPENDIX A CHARACTERISTIC RESISTANCE FOR LOG-NORMAL DISTRIBUTION

The characteristic value is defined as the value for which only 5% of observations are less than the given value. The cumulative distribution function for a log-normal distribution (Melchers & Beck 2018) is

$$F(x) = \Phi\left[\frac{\ln(x) - \lambda}{\varepsilon}\right] \tag{A1}$$

where x is the random variable, $\Phi(x)$ is the cumulative distribution function for a normal distribution, λ is the mean of $log(x)$ and ε is the standard deviation of $log(x)$. Hence setting $F(x)$ to 0.05 gives

$$\frac{\ln(R_{0.05}) - \lambda}{\varepsilon} = \Phi^{-1}(0.05) = -1.645 \tag{A2}$$

where $R_{0.05}$ is the characteristic value and $\Phi^{-1}(x)$ is the inverse cumulative distribution function for a normal distribution. Rearranging gives the characteristic value as

$$R_{0.05} = \exp(\lambda - 1.645\varepsilon) \tag{A3}$$

ACKNOWLEDGEMENTS

This material is based upon work supported by the Australian Research Council Discovery Project 190102650"

NOTATION

A_{ct} = cross-sectional area of tension chord;
A_{rt} = cross-sectional area of tensile reinforcement;
A_{rv} = cross-sectional area of stirrups;
a = shear span;
a_1, a_2, a_3 = parameters for Eq. (24)
b = width;
b_1, b_2, b_3 = parameters for Eq. (33);
C_1, C_2 = parameters for Eq. (16);
C_3 = parameter for Eq. (34);
c = cohesive component of the shear strength;
D = total depth;
d = effective depth;
d_c = lever arm of the compressive concrete;
d_{NA} = neutral axis depth;
E_c = elastic modulus of the concrete;
E_r = elastic modulus of the reinforcement;
$F(x)$ = cumulative distribution function for log-normal distribution;
F_c = force in the compressive concrete;

F_f = force in the fibres;
F_{rt} = force in tensile reinforcement;
F_{st} = force in the stirrups;
f_c = concrete strength;
f_{ct} = tensile strength;
f_{ct}^* = effective tensile strength;
f_f = stress in the fibres;
f_{pc} = post cracking stress;
f_y = yield strength;
L_{per} = bonded perimeter;
m = frictional component of the shear strength;
n = modular ratio ($=E_r/E_c$);
$R_{0.05}$ = characteristic value;
S_{cap} = sliding capacity;
S_{cr} = crack spacing;
s = stirrup spacing;
V_{cr} = shear force to cause cracking;
V_d = design shear capacity;
V_u = mean shear capacity;
V_{uc} = contribution of the concrete to the shear capacity;
V_{uf} = contribution of the fibres to the shear capacity;
V_{us} = contribution of the stirrups to the shear capacity;
v = material shear strength;
w_d = crack width at the effective depth;
x = random variable;
α = non-linearity;
β = shear angle;
β_1 = angle of critical diagonal shear crack;
δ_1 = slip at the maximum bond stress;
ε = standard deviation of log(x);
ε_d = strain at the effective depth;
θ = rotation;
λ = mean of log(x);
λ_2 = bond parameter;
ρ = reinforcement ratio ($=A_{rt}/bd$);
σ_N = normal stress;
τ_{max} = maximum bond stress;
$\Phi(x)$ = cumulative distribution function for normal distribution;
χ = curvature;

REFERENCES

ACI (American Concrete Institute) (2019). "Building Code Requirements for Structural Concrete." *ACI 318-19*, Farmington Hills.

AFGC (Association Francaise de Genie Civil) (2013) "Ultra High Performance Fibre-Reinforced Concretes: Recommendations." Paris.

Amin, A., and Foster, S. J. (2016). "Shear strength of steel fibre reinforced concrete beams with stirrups." *Engineering Structures*, 111, 323-332.

Anderson, N. S., and Ramirez, J. A. (1989). “Detailing of stirrup reinforcement.” *ACI Structural Journal*, 86(5), 507-515.

Bhal, N. S. (1968) “Uber den Einfluss der Balkenhöhe auf Schubtragfähigkeit von einfeldrigen Stahlbetonbalken mit und ohne Schubbewehrung.” PhD thesis, University of Stuttgart.

Bresler, B. and Scordelis, A. C. (1963) “Shear strength of reinforced concrete beams.” *ACI Journal Proceedings*, 60(1), 51-74.

Casanova, P., Rossi, P. and Schaller, I. (1997). “Can steel fibers replace transverse reinforcements in reinforced concrete beams?” *ACI Materials Journal*, 94(5), 341-354.

CEN (European Committee for Standardisation) (2004). “Eurocode 2: Design of concrete structures - Part 1-1: General rules and rules for building.” *EN 1992-1-1:2004*, Brussels,.

Chang, T. S. and Kesler, C. E. (1958) “Static and fatigue strength in shear of beams with tensile reinforcement.” *Journal of the American Concrete Institute*, 54(6), 1033-1057.

Chen, Y., Visintin, P., and Oehlers, D. J. (2015). “Concrete shear-friction material properties: Derivation from actively confined compression cylinder tests.” *Advances in Structural Engineering*, 18(8), 1173-1185.

Chana, P. S. (1981). “Some aspects of modelling the behaviour of reinforced concrete under shear loading.” *Tech. Rep. No. 543*, Cement and Concrete Association.

Choi, K. K., Hong-Gun, P., and Wight, J. K. (2007). “Shear strength of steel fiber-reinforced concrete beams without web reinforcement.” *ACI Structural Journal*, 104(1), 12.

Clark, A. P. (1951). “Diagonal tension in reinforced concrete beams.” ACI Journal Proceedings, 48(10), 145-156.

Collins, M. P. and Kuchma, D. (1999) “How safe are our Large, lightly reinforced concrete beams, slabs, and footings?” *ACI Structural Journal*, 96(4), 482-490.

Diaz de Cossio, R. and Seiss, C. P. (1960) “Behavior and strength in shear of beams and frames without web reinforcement.” *Journal of the American Concrete Institute*, 56(2), 695-736.

Diaz de Cossio R (1962). “Discussion to 326 report.” *ACI Journal Proceedings*, 59(11), 1323-1349.

Elzanaty, A. H., Nilson, A. H., and Slate, F. O. (1986). “Shear capacity of reinforced concrete beams using high-strength concrete.” *ACI Journal Proceedings*, 83(2), 290-296.

fib (International Federation for Structural Concrete). (2013). “fib model code for concrete structures 2010.” Lausanne.

Frosch, R. J. (2000). “Behavior of large-scale reinforced concrete beams with minimum shear reinforcement.” *ACI Structural Journal*, 97(6), 814-820.

Harajli, M. H. (2009). “Bond stress–slip model for steel bars in unconfined or steel, FRC, or FRP confined concrete under cyclic loading.” *Journal of Structural Engineering*, 135(5), 509-518.

Kani, G. N. J. (1966) “Basic facts concerning shear failure.” *Journal of the American Concrete Institute*, 63(6), 675-692.

Kani, G. N. J. (1967) “How safe are our large reinforced concrete beams?” *Journal of the American Concrete Institute*, 64(3), 128-141.

Kim, W. and White, R. N. (1999) “Shear-critical cracking in slender reinforced concrete beams.” *ACI Structural Journal*, 96(5), 757-766.

Kotsovos, M. D. (1987) “Shear failure of reinforced-concrete beams.” *Engineering Structures*, 9(1), 32-38.

Krefeld, W. J. and Thurston, C. W. (1966) “Studies of the shear and diagonal tension strength of simply supported reinforced concrete beams.” *ACI Journal Proceedings*, 63(4), 451-476.

Kwak, Y. K., Eberhard, M. O., Kim, W. S., and Kim, J. (2002). “Shear strength of steel fiber-reinforced concrete beams without stirrups.” *ACI Structural Journal*, 99(4), 530-538.

Lantsoght, E. O. (2019). “Database of Shear Experiments on Steel Fiber Reinforced Concrete Beams without Stirrups.” *Materials*, 12(6), 917.

Lee, J.-Y., and Hwang, H.-B. (2010). “Maximum shear reinforcement of reinforced concrete beams.” *ACI Structural Journal*, 107(5), 580-588.

Lee, J.-Y., Choi, I.-J., and Kim, S.-W. (2011). “Shear behavior of reinforced concrete beams with high-strength stirrups.” *ACI Structural Journal*, 108(5), 620-629.

Lee, D.H., Han, S.J., Kim, K.S. and LaFave, J.M. (2016). “Shear capacity of steel fiber-reinforced concrete beams.” *Structural Concrete*, 18, 278-291.

Leonhardt, F. and Walther, R. (1962). “Schubversuche an einfeldrigen Stahlbetonbalken mit und ohne Schubbewehrung zur Ermittlung der Schubtragfähigkeit und der oberen Schubspannungsgrenze.” DAfStb.

Mathey, R. G. and Watstein, D. (1963) “Shear strength of beams without web reinforcement containing deformed bars of different yield strengths.” *Journal of the American Concrete Institute*, 60(2), 183-208.

Mattock, A. H. (1969). “Diagonal tension cracking in concrete beams with axial forces.” *Journal of the Structural Division*, 95(9), 1887–1900.

Mattock, A. H., and Wang, Z. (1984). “Shear strength of reinforced concrete members subject to high axial compressive stress.” *ACI Journal Proceedings*, 81(3), 287-298.

Melchers, R. E., and Beck, A. T. (2018). *Structural reliability analysis and prediction*. John Wiley & Sons.

Moody, K. G., Viest, I. M., Elstner, R. C. and Hognestad, E. (1954) “Shear strength of reinforced concrete beams part 1 -tests of simple beams.” *Journal of the American Concrete Institute,* 51(12), 317-332.

Morrow, J. and Viest I. M. (1957) “Shear strength of reinforced concrete frame members without web reinforcement.” *Journal of the American Concrete Institute*, 53(3), 833-869.

Mphonde, A. G. and Frantz, G. C. (1984) “Shear tests of high-strength and low-strength concrete beams without stirrups.” *Journal of the American Concrete Institute*, 81(4), 350-357.

Mphonde, A. G., and Frantz, G. C. (1985). “Shear tests of high- and low-strength concrete beams with stirrups.” *ACI Special Publication*, 87, 179-186.

Noghabai, K. (2000). “Beams of fibrous concrete in shear and bending: experiment and model.” *Journal of Structural Engineering*, 126(2), 243-251.

Olver, F. W., Lozier, D. W., Boisvert, R. F., and Clark, C.W. (2010) *NIST handbook of mathematical functions*. Cambridge University Press.

Papadakis, G. (1996) “Shear failure of reinforced concrete beams without stirrups.” PhD Thesis, Aristotle University of Thessaloniki.

Placas, A. and Regan, P. E. (1971) Shear failure of reinforced concrete beams. *ACI Journal Proceedings*, 68(10): 763-773.

Regan, P. E., and Yu, C. W. (1973). *Limit state design of structural concrete*. Chatto & Windus, London.

Sarsam, K. F., and Al-Musawi, J. M. S. (1992). “Shear design of high- and normal strength concrete beams with web reinforcement.” *ACI Structural Journal*, 89(6), 658-664.

Sozen, M. A., Zwoyer, E. M. and Siess, C. P. (1959) “Investigation of prestressed reinforced concrete for highway bridges. Part 1: strength in shear of beams without web reinforcement.” *Engineering Experimental Station Bulletin No. 452*, University of Illinois.

Standards Australia (2018). “Concrete Structures.” *AS3600:2018*. Sydney.

Sturm, A. B., Visintin, P., Oehlers, D. J. and Seracino, R. (2018) “Time dependent tension stiffening mechanics of fibre reinforced and ultra-high performance fibre reinforced concrete.” *Journal of Structural Engineering*, 144(8), 04018122.

Sturm, A. B. and Visintin, P. (2018) “Local bond slip behaviour of steel reinforcing bars embedded in UHPFRC.” *Structural Concrete*, 20(1), 108-122.

Sturm, A. B., Visintin, P., and Oehlers, D. J. (2019). “Rational design approach for the instantaneous and time-dependent serviceability deflections and crack widths of FRC and UHPFRC continuous and simply supported beams.” *Journal of Structural Engineering*, 145(11), 04019138.

Sturm, A. B., Visintin, P., and Oehlers, D. J. (2020) "Mechanics of shear failure in fibre reinforced concrete beams." Submitted to *Journal of Structural Engineering*.

Swamy, R. N., and Andriopoulos, A. D. (1974). "Contribution of aggregate interlock and dowel forces to the shear resistance of reinforced beams with web reinforcement." *ACI Special Publication,* 42, 129-166.

Tang, C. W., Yen, T. and Chen, H. J. (2009) "Shear behavior of reinforced concrete beams made with sedimentary lightweight aggregate without shear reinforcement." *Journal of Materials in Civil Engineering*, 21(12): 730-739.

Taylor, H. P. J. (1972) "Shear strength of large beams." *Journal of the Structural Division*, 98(11), 2473–2490.

Tompos, E. J., and Frosch, R. J. (2002). "Influence of beam size, longitudinal reinforcement, and stirrup effectiveness on concrete shear strength." *ACI Structural Journal*, 99(5), 559-567.

Visintin, P., Sturm, A. B., Mohamed Ali, M. S., and Oehlers, D. J. (2018). "Blending macro- and micro-fibres to enhance the serviceability behaviour of UHPFRC." *Australian Journal of Civil Engineering*, 16(2), 106-121.

Walraven, J. C. (1978) "The influence of depth on the shear strength of lightweight concrete beams without shear reinforcement." *Rep. No. 5-78-4*, Delft University of Technology.

Watstein, D. and Mathey, R. C. (1958) "Strains in beams having diagonal crack." *Journal of the American Concrete Institute*, 55(12), 717-728.

Wu, Y. F., and Hu, B. (2017). Shear strength components in reinforced concrete members. *Journal of Structural Engineering*, 143(9), 04017092.

Xie, Y., Ahmad, S. H., Yu, T., Hino, S., and Chung, W. (1994). "Shear ductility of reinforced concrete beams of normal and high-strength concrete." *ACI Structural Journal*, 91(2), 140-149.

Yoon, Y.-S., Cook, W. D., and Mitchell, D. (1996). "Minimum shear reinforcement in normal, medium, and high-strength concrete beams." *ACI Structural Journal*, 93(5), 576-584.

Yost, J. R., Gross, S. P. and Dinehart, D. W. (2001) "Shear strength of normal strength concrete beams reinforced with deformed GFRP bars." *Journal of Composites for Construction*, 5(4), 268-275.

Zhang, J. P. (1997). "Diagonal cracking and shear strength of reinforced concrete beams." *Magazine of Concrete Research*, 49(178), 55-65.

Zhang, T., Oehlers, D. J., and Visintin, P. (2014). "Shear strength of FRP RC beams and one-way slabs without stirrups." *Journal of Composites for Construction*, 18(5), 04014007.

Zhang, T., Visintin, P., and Oehlers, D. J. (2016a). "Shear strength of RC beams without web reinforcement." *Australian Journal of Structural Engineering*, 17(1), 87-96.

Zhang, T., Visintin, P., and Oehlers, D. J. (2016b). “Shear strength of RC beams with steel stirrups.” *Journal of Structural Engineering*, 142(2), 04015135.

Zhang, F., Ding, Y., Xu, J., Zhang, Y., Zhu, W., and Shi, Y. (2016c). “Shear strength prediction for steel fiber reinforced concrete beams without stirrups.” *Engineering Structures*, 127, 101-116.

CHAPTER 5

Background

In this chapter the behaviour of FRP plates bonded to brittle substrates is explored. This is an extension of the tension stiffening model explored in Chapter 2 demonstrating the versatility and fruitfulness of that approach.

The first publication "Modelling FRP-to- substrate joints using the bilinear τ-δ rule with allowance for friction—Full-range analytical solutions for long and short bonded lengths" wherein closed-form solutions are derived for the push-pull behaviour of FRP to brittle substrates. These solutions are then used to optimise the local bond-slip properties based on the global behaviour.

The second publication "Analytical approach for global load-slip behaviour of FRP plates externally bonded to brittle substrates with anchors" presents closed form solutions for the push-pull behaviour of FRP plates bonded to brittle substrates with anchors. The solutions utilise an innovative transfer matrix approach to avoid having to define a large number of different solution cases.

List of Manuscripts

Vaculik, J., Sturm, A. B., Visintin, P. and Griffith, M. C. (2018) "Modelling FRP-to- substrate joints using the bilinear τ-δ rule with allowance for friction—Full-range analytical solutions for long and short bonded lengths." *International Journal of Solids & Structures*, 135, 245-260.

Sturm, A. B., Visintin, P., Vaculik, J., Oehlers, D. J., Seracino, R., and Smith, S. T. (2019) "Analytical approach for global load-slip behaviour of FRP plates externally bonded to brittle substrates with anchors." *Composites Part B: Engineering*, 160(2019), 177-194.

STATEMENT OF AUTHORSHIP

Modelling FRP-to- substrate joints using the bilinear τ-δ rule with allowance for friction—Full-range analytical solutions for long and short bonded lengths
International Journal of Solids & Structures, 135, 245-260

Vaculik, J.

Prepared manuscript, developed optimisation procedure for determining local properties and acted as corresponding author (42.5%)

I certify that the candidate's stated contribution to the publication is accurate (as detailed above); permission is granted for the candidate in include the publication in the thesis; and the sum of all co-author contributions is equal to 100% less the candidate's stated contribution.

Signed Date 7/07/2020

Sturm, A. B. (Candidate)

Developed closed form solutions (42.5%)

This paper reports on original research I conducted during the period of my Higher Degree by Research candidature and is not subject to any obligations or contractual agreements with a third partv that would constrain its inclusion in this thesis. I am the primary author of this paper.

Signed Date 9/07/2020

Visintin, P.

Supervised and contributed to research (10%)

I certify that the candidate's stated contribution to the publication is accurate (as detailed above); permission is granted for the candidate in include the publication in the thesis; and the sum of all co-author contributions is equal to 100% less the candidate's stated contribution.

Signed Date 07/07/2020

Griffith, M. C.

Contributed to research (5%)

I certify that the candidate's stated contribution to the publication is accurate (as detailed above); permission is granted for the candidate in include the publication in the thesis; and the sum of all co-author contributions is equal to 100% less the candidate's stated contribution.

Signed Date …7 July 2020…….

MODELLING FRP-TO-SUBSTRATE JOINTS USING THE BILINEAR BOND-SLIP RULE WITH ALLOWANCE FOR FRICTION-FULL-RANGE ANALYTICAL SOLUTIONS FOR LONG AND SHORT BONDED LENGTHS

Vaculik, J., Sturm, A. B., Visintin, P., Griffith, M. C.

ABSTRACT

Methods for simulating the mechanics of debonding and predicting global load-slip (P-Δ) response from local bond stress versus slip (τ-δ) relationships can vary significantly in their complexity. It is generally accepted that an adequate representation of intermediate crack debonding can be achieved by considering only mode-II (shear) fracture along the interfacial bond, a problem that can be solved by accounting for one-dimensional fields of elastic stress and strain in the substrate and plate, and nonlinear interfacial slip and shear stress along the bond. In this paper, full-slip-range analytical solutions are presented for the bilinear τ-δ rule with allowance for residual friction. The procedure is capable of modelling the entire debonding process over both long and short bonded lengths. This is an extension of previous works which are either inapplicable to all bonded lengths or do not allow for residual strength. Applicability of the formulation can range from externally-bonded or near-surface-mounted FRP plates, to embedded bars or bolts in brittle substrates such as concrete, rock or masonry. The versatility and low computational effort required to apply the developed formulation makes it ideal for both directly predicting the P-Δ relationship from known τ-δ parameters, or conversely for extracting a τ-δ relationship from a reference P-Δ curve using inverse calibration. While it is not the purpose of this paper to propose a bond model for any specific type of system, a framework is proposed for doing so. Significantly this framework addresses the difficulty in identifying a unique solution of local properties from experimental data, and highlights that the bonded length has an important influence on the reliability of extracted results.

INTRODUCTION

The design of fibre-reinforced polymer (FRP) retrofits of brittle substrates such as concrete and masonry is dependent on an understanding of the tensile load versus end slip (P-Δ) behaviour of the plate relative to the substrate. This behaviour controls the peak load which may be developed as well as the detailing requirements (anchorage length). Experimental and analytical research into bond-slip behaviour between reinforcement and brittle substrates has become well established in the fields of both concrete and masonry, and it has become commonly accepted that shear interfacial bond can be modelled on a local level using various constitutive relationships between the shear stress (τ) and shear slip (δ).

Predictive techniques for modelling the mechanics of debonding and simulating global P-Δ response from local τ-δ can vary significantly in their complexity. They can range from finite-element modelling approaches capable of handling realistic, nonlinear material properties as well as the mechanical interaction between mode-II (shear) and mode-I fracture along the bond (e.g. Camata et al. 2007; Grande et al. 2008). When simulating the mechanism of debonding in concrete beams or small-scale test specimens, such techniques have been demonstrated to produce good agreement with experimental results (Lu et al. 2005; Chen et al. 2011). However, the numerical nature of these solutions limits their direct application in design due to the computational effort involved.

Research has also shown that good prediction of intermediate crack debonding between plates and brittle substrates can be achieved by considering only mode-II fracture (Oehlers et al.

2008). This has led to the development of one-dimensional partial-interaction (PI) models which can be solved either numerically or analytically. The one-dimensional PI concept is shown in Fig. 1 for the case of a finite bonded length under push-pull boundary conditions. At its core, the PI model simulates the stress and strain fields in the plate and substrate that are linked via the slip of the plate relative to the substrate. This model is driven by the local constitutive τ-δ model, the form of which has been the topic of intense research effort. The ease with which subsequent solutions can be obtained is highly dependent on the shape and complexity of the τ-δ model.

Numerical finite-difference schemes in which the plated region of the beam is discretised and solved for specific boundary conditions are particularly suited to complex, multi-regional τ-δ relationships, or non-homogeneous substrates (Haskett et al. 2008; Kashyap et al. 2011). Closed-form analytical solutions have also been developed for a range of τ-δ models of various levels of complexity under both the push-pull (Yuan et al. 2004; Ren et al. 2010; Cornetti & Carpinteri, 2011; Caggiano & Martinelli, 2012; Caggiano et al. 2012) and tension-stiffening (Teng et al. 2006; Chen et al. 2007) loading scenarios. The advantage of closed-form solutions is that they are less demanding on computational effort and they also have wider potential to be incorporated into practical design procedures.

In the interpretation of experimental bond research, the three-parameter bilinear rule, containing an initial elastic branch followed by a softening branch has been widely accepted to provide a reasonable compromise between accuracy and simplicity (Yuan et al. 2004; Lu et al. 2005). This model is primarily applicable to externally-bonded FRP retrofits possessing zero residual shear stress capacity. For circumstances where a residual stress occurs, such as near-surface-mounted strips, the bilinear rule can be adapted to contain a residual frictional component through the inclusion of τ_r in the bilinear rule as shown in Fig. 2.

Numerous researchers have successfully developed closed-form analytical solutions for the bilinear rule under push-pull loading, as summarised in Table 1, albeit with various limitations. Yuan et al. (2014) developed full-Δ-range solutions for the three-parameter bilinear rule, and also provided a qualitative description of the debonding process and its link to the various stages of the P-Δ response. This work was later extended by Ren at al. (2012) who with the incorporation of a frictional component furthered the applicability of the model toward embedded reinforcement. The limitations of both these approaches however, is that they do not consider a full-softening-zone slip distribution state which limits their applicability toward long bonded lengths only. Additionally, both approaches implement algebraic simplifications which mean that while the methods are mechanically correct, they are not mathematically exact (though this effect is very minor as will be shown later). Caggiano et al. (2012) later revisited the three-parameter bilinear rule without friction and showed that by expressing the solution in terms of the location of the transitions between the various stages in the local τ-δ rule (zones I, II and III as shown in Fig. 2), the solutions could be made mathematically exact over any range. The incorporation of a softening zone solution meant that the formulation of Caggiano et al. also became applicable to any bonded length. In similar work, Caggiano & Martinelli (2012) also devised analytical solutions for a bilinear τ-δ rule incorporating a truncated descending branch and demonstrated its applicability toward the analysis of short, randomly-distributed fibres in fibre-reinforced concrete.

The objective of the present paper is to address the remaining limitations of the work by Yuan, Ren, and Caggiano by developing full-range analytical solutions for both short and long bonded length with the bilinear rule whilst allowing for residual friction. The next section of this paper

will present the derivation of the proposed mathematical formulation and describe the various stages in the evolution of debonding. Section 3 will compare the results obtained to existing analytical techniques. Finally, Section 4 demonstrates the application of the proposed method to research, with a particular focus on the use of the technique toward inverse calibration of local τ-δ properties from experimental data. It should be noted that it is not the intention of this paper to propose a bond model but rather to provide a framework for doing so. Significantly this framework will highlight the mechanics behind the dependency of parameters and therefore the sensitivity of results obtained from the inverse calibration approach. It is intended that this discussion may lead to an improved and more consistent approach for developing bond models in the future.

It should be noted that although the narrative of this paper focuses on FRP retrofits, the generic nature of the analytical solutions and inverse analysis techniques mean they can be applied to any other scenario in which a reinforcement is bonded to a brittle substrate for example embedded steel or FRP reinforcement in concrete, rock or masonry. Some of these applications are further explored in the comparison to test results in Section 5.

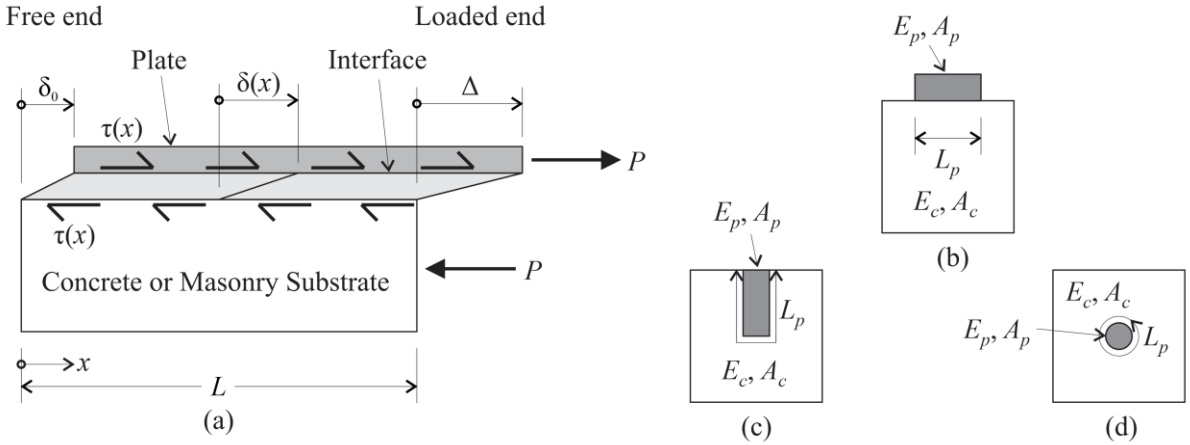

Fig. 1 Plate-to-substrate composite system subjected to the push-pull loading condition; (a) generic longitudinal section, and cross sections for (b) EB plate, (c) NSM plate, and (d) embedded bar.

Table 1: Examples of analytical solutions to piecewise-linear τ-δ models and their constraints.

Reference	Shape	Bonded length applicability
Yuan et al. (2004)	3-parameter bilinear ($\tau_r = 0$)	Long L only
Ren et al. (2010)	4-parameter bilinear with friction	Long L only
Caggiano et al. (2012)	3-parameter bilinear ($\tau_r = 0$)	Long and short L
Proposed	4-parameter bilinear with friction	Long and short L

ANALYTICAL FORMULATION

Governing Equations

Consider an externally-bonded (EB) or near-surface-mounted (NSM) FRP plate or rod (hereafter referred to as 'plate' for brevity) adhesively bonded to either concrete or masonry (hereafter referred to as 'substrate').

Fig. 1 shows the scenario of subjecting a system to push-pull loading over bonded length L. In a generic state the plate is subjected to a tensile load P, shear slip distribution $\delta(x)$, and interfacial shear stress distribution $\tau(x)$. The slip applied at the loaded end ($x = L$) is denoted as Δ, and slip at the free end ($x = 0$) as δ_0.

By considering equilibrium and compatibility requirements and assuming that the plate and substrate remain linear-elastic, the slip δ can be related to the shear stress τ by the second-order ordinary differential equation:

$$\frac{d^2\delta}{dx^2} = \tau\beta \tag{1}$$

together with

$$\beta = L_p\left(\frac{1}{E_pA_p} + \frac{1}{E_cA_c}\right) \tag{2}$$

where L_p is the bonded perimeter of the plate, E_p and E_c are the elastic moduli of the plate and substrate, respectively; and A_p and A_c are their cross-sectional areas as indicated in Fig. 1(b)-(d).

Eq. (1) is the governing equation of the partial-interaction mechanism as originally conceived by Volkersen (1938), whose rearrangements and variants have since been used extensively to describe the behaviour of the bonded interface around internal reinforcement including the mechanisms associated with the formation and widening of cracks, tension-stiffening and load development (Balazs 1993; Cosenza et al. 2002; Lee et al. 2012; Muhamad et al. 2012; Sturm et al. 2018a; Sturm et al. 2018b). This approach has also been used as the basis for bond studies on the behaviour of FRP-plated sections (Yuan et al. 2004; Teng et al. 2006; Chen et al. 2007; Ren et al. 2010; Cornetti & Carpinteri, 2011; Caggiano et al. 2012). Each of these different situations can be modelled by solving Eq. (1) in accordance with their respective boundary conditions and specific form of the interface shear stress-slip function, $\tau(\delta)$.

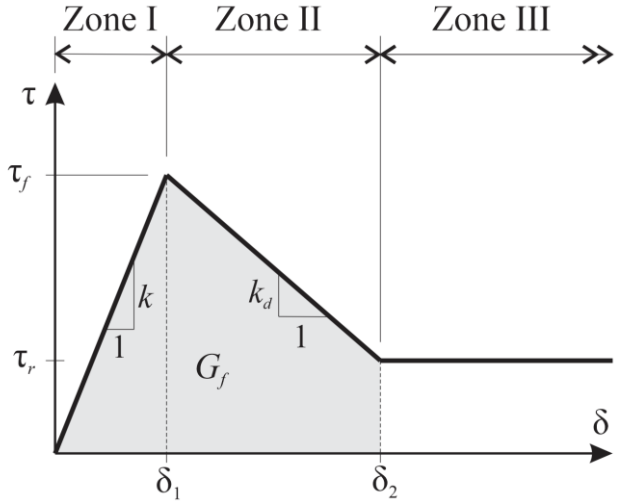

Fig. 2 Local τ-δ rule to represent the bond behaviour along the bond interface.

In the remainder of this section, Eq. (1) will be solved to establish load versus end-slip (P-Δ) relationships for plate-to-substrate joints subjected to the push-pull scenario depicted in Fig. 1(a). The local τ-δ behaviour at the interface will be represented using the bilinear-frictional rule, which consists of three zones: elastic (I), softening (II), and residual (III), as shown in Fig. 2. This can be expressed as

(3a)
(3b)

$$\tau(\delta) = \begin{cases} k\delta & \text{for } \delta \le \delta_1, \quad \text{(zone I)} \\ \tau_f - k_d(\delta - \delta_1) & \text{for } \delta_1 < \delta \le \delta_2, \quad \text{(zone II)} \\ \tau_r & \text{for } \delta > \delta_2 \quad \text{(zone III)} \end{cases} \tag{3c}$$

where $k = \tau_f / \delta_1$ and $k_d = (\tau_f - \tau_r)/(\delta_2 - \delta_1)$. The interfacial fracture energy, G_f, is classically defined as the area under the τ-δ curve. However, if $\tau_r > 0$ then this integral becomes unbounded, and thus, throughout the qualitative discussions in this paper, G_f is treated as the integral up to the slip at debonding, δ_2.

For push-pull loading, illustrated in Fig. 1(a), an equal and opposite load is applied to the plate and substrate. Thus, the difference between plate and substrate strain, referred to as the slip strain, at the loaded end of the prism is given by

$$\left.\frac{d\delta}{dx}\right|_{x=L} = \varepsilon_p - \varepsilon_c = P\left(\frac{1}{E_p A_p} + \frac{1}{E_c A_c}\right) \tag{4}$$

This defines the first boundary condition. The second boundary condition is obtained from the free end, where the strain in both the substrate and plate must be zero, and therefore

$$\left.\frac{d\delta}{dx}\right|_{x=0} = 0 \tag{5}$$

Range of Possible Solutions

Having defined the local τ-δ relationship and boundary conditions, the governing equation [Eq. (1)] can now be solved. First though it has to be considered that due to the piecewise nature of the assumed τ-δ relationship, a series of six possible solutions can arise depending on the portions of the τ-δ relationship present across the domain x. These solutions will be referred using the convention I, I-II, I-III, II, II-III, and III, where I denotes the elastic zone, II denotes the softening zone, and III denotes the debonded zone, as per Fig. 2. Each of the six different solutions as well as the possible pathways for the evolution of debonding along the prism are demonstrated by Fig. 3.

The pathway of debonding (Fig. 3) is fundamentally controlled by the length of the prism, as illustrated by the shear stress distributions in Fig. 4. This in turns defines the global P-Δ behaviour in Fig. 5. When a slip is first applied, a prism of any length initiates in the zone-I response range [Fig. 4(b),(h)], throughout which the P-Δ response remains linear-elastic. Reaching $\Delta = \delta_1$ at transition point A marks the onset of the I-II response range [Fig. 4(c),(i)], which is accompanied by a continual reduction in the P-Δ tangent stiffness.

The next stage depends on whether the prism is long or short. A short prism whose L is less than the limiting length L_{II} [to be defined later, by Eq. (48)], enters into the full softening range II [Fig. 4(d)] at the transition point B defined by $\delta_0 = \delta_1$. The global load resistance continually reduces until Δ reaches δ_2 at point C, following which response enters into the II-III range [Fig. 4(e)]. Transition point D is reached when $\delta_0 = \delta_2$, at which point the entire prism has reached the zone-III range and thus become fully debonded. With an ongoing increase to Δ, the residual load resistance remains constant.

Alternatively, a long prism ($L > L_{II}$) exits zone I-II response when Δ reaches δ_2 at point B' and enters into the I-III response range [Fig. 4(j)]. This is accompanied by a continual reduction in tangent stiffness of the P-Δ curve. The prism enters into the II-III range [Fig. 4(k)] when δ_0 reaches δ_1 at point C'. If the length is sufficiently large [$L >$ approx. L_c, as defined later by Eq. (59)], the P-Δ response will exhibit snapback as shown in Fig. 5. Once δ_0 reaches δ_2, full zone-III response ensues and the residual load remains constant [Fig. 4(l)]. Note that under

displacement-control, the snapback portion of the curve is bypassed through the sudden drop indicated by the dashed line in Fig. 5.

Mathematical solutions for each of these cases will now be developed, beginning with the solutions where only a single zone is present (I, II and III) as these form the basis for the more complex solutions (I-II, I-III and II-III).

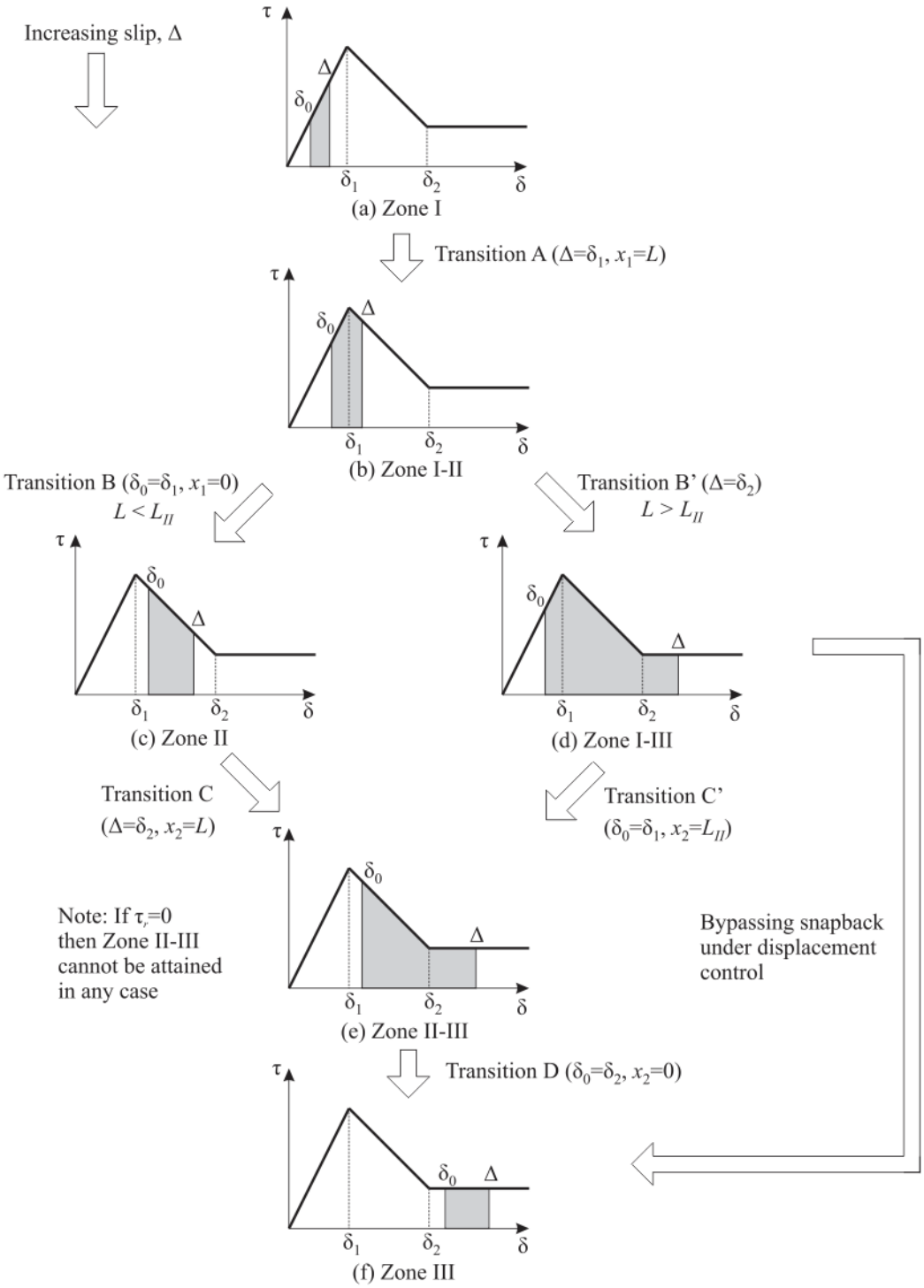

Fig. 3 Various possible stages of debonding.

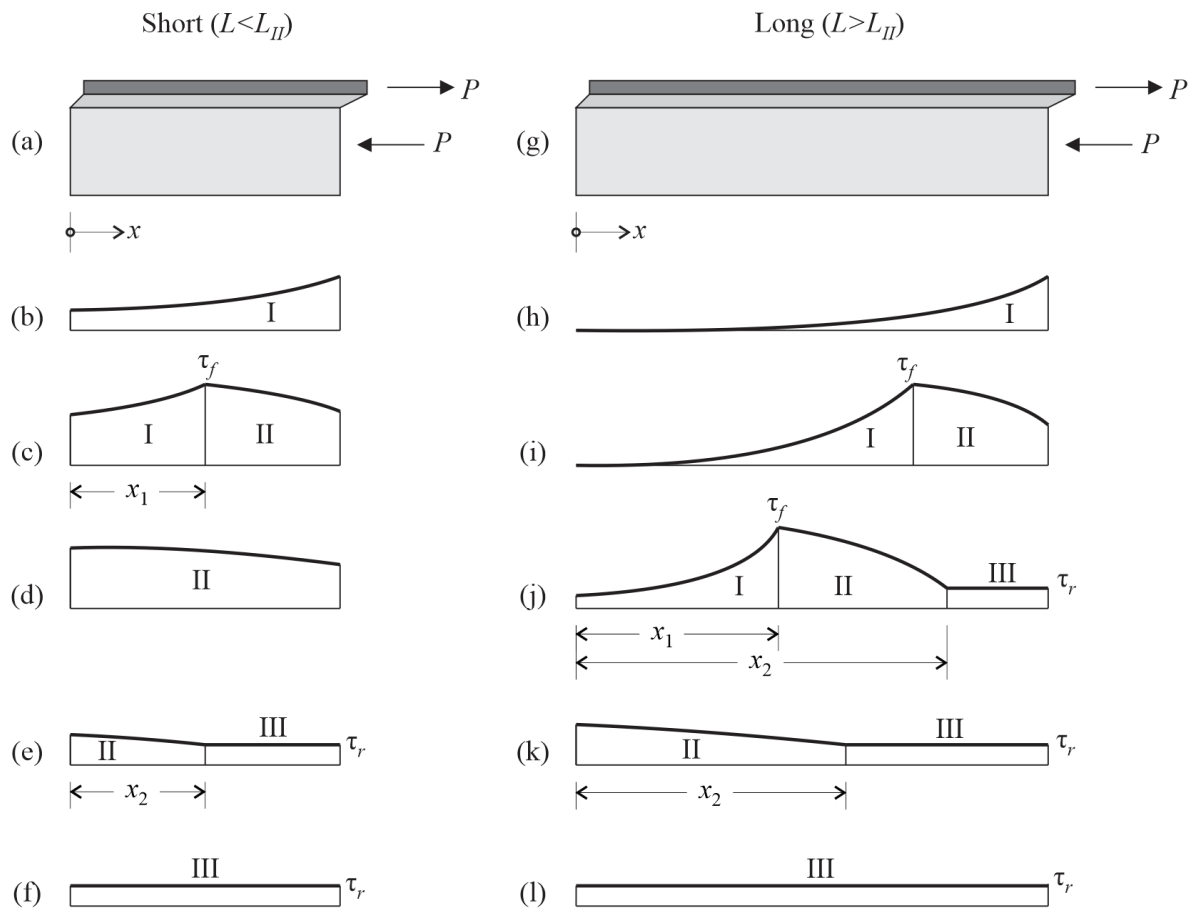

Fig. 4 Progression of the debonding process and associated shear stress (τ) distributions over short lengths ($L < L_{II}$) and long lengths ($L > L_{II}$).

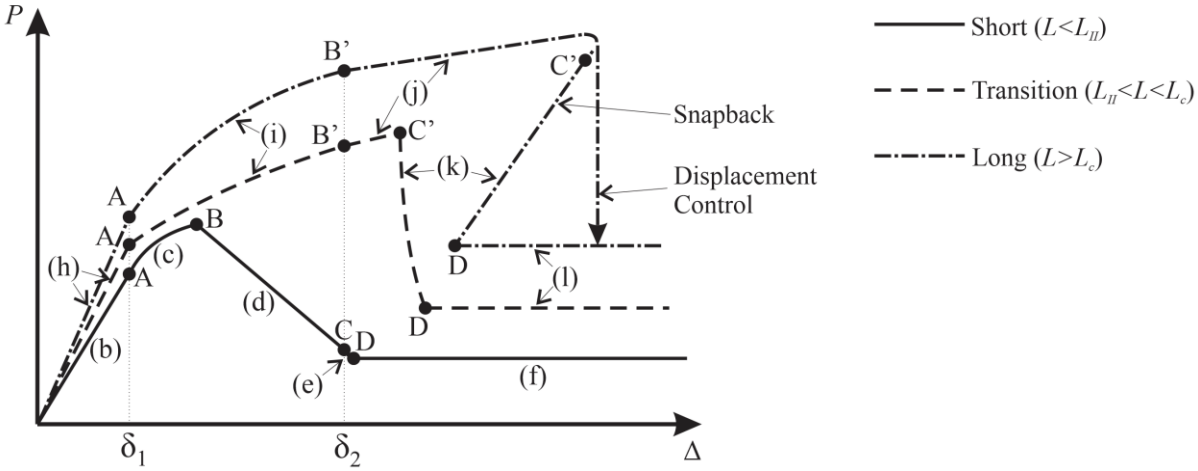

Fig. 5 Generalised load-slip behaviour for the different possible types of debonding evolution sequences. Upper case letters A, B, B', C, C', and D denote the transition states defined in Fig. 3. Lower case letters (b-f, h-l) denote the shear stress distribution states shown in Fig. 4.

Zone I Solution

This range of solution defines the linear-elastic range of the *P-Δ* response shown by Fig. 3(a). Substituting Eq. (3a) into Eq. (1) gives the following second-order differential equation, valid for $\delta(x) \leq \delta_1$:

$$\frac{d^2\delta}{dx^2} = k\beta\delta \tag{6}$$

Solving this yields the following variation in slip

$$\delta = c_1 \sinh(\lambda_1 x) + c_2 \cosh(\lambda_1 x) \tag{7}$$

and slip strain

$$\frac{d\delta}{dx} = \lambda_1 c_1 \cosh(\lambda_1 x) + \lambda_1 c_2 \sinh(\lambda_1 x) \tag{8}$$

where

$$\lambda_1 = \sqrt{k\beta} \tag{9}$$

Applying the boundary condition in Eq. (5) to Eq. (8) gives

$$\left.\frac{d\delta}{dx}\right|_{x=0} = 0 = \lambda_1 c_1 \tag{10}$$

which leads to $c_1 = 0$. From Eq. (7), the slip at the loaded end of the prism is given by

$$\Delta = \delta(x = L) = c_2 \cosh(\lambda_1 L) \tag{11}$$

implying that

$$c_2 = \frac{\Delta}{\cosh(\lambda_1 L)} \tag{12}$$

Load-slip relationship

Applying the boundary condition in Eq. (4) to Eq. (8) gives

$$\left.\frac{d\delta}{dx}\right|_{x=L} = P\left(\frac{1}{E_p A_p} + \frac{1}{E_c A_c}\right) = \lambda_1 \Delta \tanh(\lambda_1 L) \tag{13}$$

which yields the following expression for P as a function of Δ:

$$P = \left[\frac{\lambda_1 \tanh(\lambda_1 L)}{\frac{1}{E_p A_p} + \frac{1}{E_c A_c}}\right]\Delta \tag{14}$$

Importantly, this demonstrates the load-slip response in this range to be linear-ascending. The corresponding slip at the free end is given by

$$\delta_0 = c_2 = \frac{\Delta}{\cosh \lambda_1 L} \tag{15}$$

Limits of solution

The left-side limit of the zone-I solution is $\Delta = 0$, and the right-side limit occurs at transition point A, defined by $\Delta = \delta_1$.

Zone II Solution

This range of solution is shown in Fig. 3(c). Substituting Eq. (3b) into Eq. (1) gives the following differential equation, valid for $\delta_1 \leq \delta(x) \leq \delta_2$:

$$\frac{d^2\delta}{dx^2} = \tau_f \beta - k_d \beta(\delta - \delta_1) \tag{16}$$

To solve this equation, we first find the solution to the following homogenous equation

$$\frac{d^2\delta_h}{dx^2} + k_d \beta \delta_h = 0 \tag{17}$$

which has the solution

$$\delta_h = c_3 \sin(\lambda_2 x) + c_4 \cos(\lambda_2 x) \tag{18}$$

where

$$\lambda_2 = \sqrt{k_d \beta} \tag{19}$$

Next, the particular solution is found by assuming that δ_p is a constant; hence from Eq. (16):

$$\delta_p = \delta_1 + \frac{\tau_f}{k_d} \tag{20}$$

Therefore, the variation in slip is

$$\delta = \delta_h + \delta_p = c_3 \sin(\lambda_2 x) + c_4 \cos(\lambda_2 x) + \delta_p \tag{21}$$

and the variation in slip strain is

$$\frac{d\delta}{dx} = \lambda_2 c_3 \cos(\lambda_2 x) - \lambda_2 c_4 \sin(\lambda_2 x) \tag{22}$$

Applying the boundary condition in Eq. (5) to Eq. (22) gives

$$\left.\frac{d\delta}{dx}\right|_{x=0} = 0 = \lambda_1 c_3 \tag{23}$$

This implies that $c_3 = 0$. From Eq. (21) the slip at the loaded end is given by

$$\Delta = c_4 \cos(\lambda_2 L) + \delta_p \tag{24}$$

and rearranging gives c_4 as

$$c_4 = \frac{\Delta - \delta_p}{\cos(\lambda_2 L)} \tag{25}$$

Load-slip relationship

Applying the boundary condition in Eq. (4) to Eq. (22) gives

$$\left.\frac{d\delta}{dx}\right|_{x=L} = P\left(\frac{1}{E_p A_p} + \frac{1}{E_c A_c}\right) = -\lambda_2(\Delta - \delta_p)\tan(\lambda_2 L) \tag{26}$$

which gives the following expression for P as a function of Δ:

$$P = \left[\frac{\lambda_2 \tan(\lambda_2 L)}{\frac{1}{E_p A_p} + \frac{1}{E_c A_c}}\right](\delta_p - \Delta) \tag{27}$$

This implies that load-slip relationship in this range is linear-descending. The corresponding slip at the free end is given by

$$\delta_0 = \frac{\Delta - \delta_p}{\cos(\lambda_2 L)} + \delta_p = \frac{\Delta}{\cos(\lambda_2 L)} + \delta_p\left[1 - \frac{1}{\cos(\lambda_2 L)}\right] \tag{28}$$

Limits of solution

The left limit to this solution occurs when the free-end slip δ_0 reaches δ_1. This happens when the loaded-end slip [from Eq. (28)] becomes equal to Δ_B as per the following, using the definition of δ_p in Eq. (20):

$$\Delta_B = \delta_1 \cos(\lambda_2 L) + \delta_p[1 - \cos(\lambda_2 L)] = \delta_1 + \frac{\tau_f}{k_d}[1 - \cos(\lambda_2 L)] \tag{29}$$

The load at this point is obtained by substituting Eq. (29) into Eq. (27). The right limit of the solution occurs when the loaded-end slip reaches δ_2.

Zone III Solution

This range of solution is shown in Fig. 3(f). Substituting Eq. (3c) into Eq. (1) gives the following differential equation, valid for $\delta(x) \geq \delta_2$:

$$\frac{d^2\delta}{dx^2} = \tau_r \beta \tag{30}$$

Integrating this gives the slip strain as

$$\frac{d\delta}{dx} = \tau_r \beta x + c_5 \tag{31}$$

Integrating gives the variation in slip as

$$\delta = \frac{1}{2}\tau_r \beta x^2 + c_5 x + c_6 \tag{32}$$

Applying the boundary condition in Eq. (5) to Eq. (31) gives

$$\left.\frac{d\delta}{dx}\right|_{x=0} = 0 = c_5 \tag{33}$$

Load-slip relationship

Applying the boundary condition in Eq. (4) to Eq. (31) gives

$$\left.\frac{d\delta}{dx}\right|_{x=L} = P\left(\frac{1}{E_pA_p}+\frac{1}{E_cA_c}\right) = \tau_r\beta L \tag{34}$$

This gives the load as

$$P = \tau_r L_p L \equiv P_{\text{res}} \tag{35}$$

In other words, the load remains constant at the residual load P_{res} independent of the slip. From Eq. (32) the slip at the free end, δ_0, is equal to c_6. Thus, the lag between the free-end and loaded-end slip is given by

$$\Delta - \delta_0 = \frac{1}{2}\tau_r\beta L^2 \tag{36}$$

From Eqs. (35) and (36) it follows that if the residual stress τ_r is zero, the residual strength must also be zero, and the free- and loaded-end slips become equalised.

Limits of solution

The left-side limit to this solution is obtained by setting δ_0 to δ_2, which occurs at the slip

$$\Delta_{\text{D}} = \delta_2 + \frac{1}{2}\tau_r\beta L^2 \tag{37}$$

This slip becomes equal to δ_2 if the frictional component is set to zero.

Zone I-II Solution

This range of solution, depicted by Fig. 3(b), involves a transition from zone I to II at the point $x = x_1$ [shown in Fig. 4(c)]. Accounting for the presence of two zones requires the continuity of slip and slip strain across the transition. To simplify the solution process, it is convenient to formulate expressions for P and Δ as a function of the transition coordinate x_1. To solve for this case, we first consider the distributions of slip and slip strain for zones I and II as given by Eqs. (7), (9) (21), and (22).

Applying the boundary condition in Eq. (4) gives $c_1 = 0$ [see Eq. (10)]. From the continuity of slips at $x = x_1$ we get

$$\delta_1 = c_2\cosh(\lambda_1 x_1) = c_3\sin(\lambda_2 x_1) + c_4\cos(\lambda_2 x_1) + \delta_p \tag{38}$$

and hence

$$c_2 = \frac{\delta_1}{\cosh(\lambda_1 x_1)} \tag{39}$$

From this, and the continuity of slip strain at $x = x_1$, it follows that

$$\lambda_1\delta_1\tanh(\lambda_1 x_1) = \lambda_2 c_3\cos(\lambda_2 x_1) - \lambda_2 c_4\sin(\lambda_2 x_1) \tag{40}$$

From Eqs. (38) and (40), we get

$$c_3 = -\frac{\frac{\tau_f}{k_d}}{\sin(\lambda_2 x_1)} - \frac{c_4}{\tan(\lambda_2 x_1)} = \frac{\lambda_1}{\lambda_2}\delta_1\frac{\tanh(\lambda_1 x_1)}{\cos(\lambda_2 x_1)} + c_4\tan(\lambda_2 x_1) \tag{41}$$

Rearranging for c_4 gives

$$c_4 = -\frac{\tau_f}{k_d}\cos(\lambda_2 x_1) - \frac{\lambda_1}{\lambda_2}\delta_1\tanh(\lambda_1 x_1)\sin(\lambda_2 x_1) \tag{42}$$

Substituting back into Eq. (41) then gives

$$c_3 = -\frac{\tau_f}{k_d}\sin(\lambda_2 x_1) + \frac{\lambda_1}{\lambda_2}\delta_1\tanh(\lambda_1 x_1)\cos(\lambda_2 x_1) \tag{43}$$

Load-slip relationship

Applying the boundary condition in Eq. (4) to the slip strain variation in Eq. (23) gives

$$\left.\frac{d\delta}{dx}\right|_{x=L} = P\left(\frac{1}{E_pA_p}+\frac{1}{E_cA_c}\right) = \lambda_2 c_3\cos(\lambda_2 L) - \lambda_2 c_4\sin(\lambda_2 L) \tag{44}$$

Substituting Eqs. (42) and (43) into Eq. (44) yields the following expression for P as a function of x_1:

$$P = \frac{\lambda_2\frac{\tau_f}{k_d}\sin[\lambda_2(L-x_1)] + \lambda_1\delta_1\tanh(\lambda_1 x_1)\cos[\lambda_2(L-x_1)]}{\frac{1}{E_pA_p}+\frac{1}{E_cA_c}} \tag{45}$$

From Eq. (21), the corresponding slip at the loaded end is given by

$$\Delta = \delta_p - \frac{\tau_f}{k_d}\cos[\lambda_2(L-x_1)] + \frac{\lambda_1}{\lambda_2}\delta_1\tanh(\lambda_1 x_1)\sin[\lambda_2(L-x_1)] \tag{46}$$

The slip at the free end is obtained from Eq. (7), which gives

$$\delta_0 = \frac{\delta_1}{\cosh(\lambda_1 x_1)} \tag{47}$$

Limits of solution

The left-side limit to this solution occurs when $\Delta = \delta_1$, and $x_1 = L$ at transition point A (Fig. 3). The right-side limit is in turn controlled by the length of the prism, and is achieved either when δ_0 reaches δ_1 (transition B) or when Δ reaches δ_2 (transition B'), whichever occurs first. The first of these cases is then followed by the zone II solution, and the second by the I-III solution as shown in Fig. 3. To determine which case applies, consider that if the zone II solution is to be attained ($\delta_0 = \delta_1$) then the loaded-end slip Δ_B as given by Eq. (29) must be less than δ_2 at the point of transition. Thus, the limiting case between a zone II and a zone I-III solution is obtained when $\Delta_B = \delta_2$. This criterion can be used to define the following limiting length

$$L_{II} = \frac{\arccos\left(\frac{\tau_r}{\tau_f}\right)}{\lambda_2} \tag{48}$$

which controls the pathway taken; i.e. if $L < L_{II}$ then the I-II solution is followed by the zone II solution, and if $L > L_{II}$ then it is followed by the zone I-III solution. If the frictional component is zero, Eq. (48) simplifies to $L_{II} = (\pi/2)/\lambda_2$.

Zone I-III Solution

In this solution range, all three zones are present as depicted by Fig. 3(d). Therefore, we first consider the distributions of slip and slip strain for each zone as given by Eqs. (7), (9), (21), (22), (31), and (32). As with the zone I-II solution, let us obtain expressions for P and Δ in terms of the transition coordinate x_1.

As the boundary conditions at the free end and at transition point x_1 both remain the same as for the I-II solution, Eqs. (38)-(43) continue to apply. Furthermore, applying continuity of slip and slip strain at $x = x_2$ gives

$$\delta_2 = c_3\sin(\lambda_2 x_2) + c_4\cos(\lambda_2 x_2) + \delta_p = \frac{1}{2}\tau_r\beta x_2^2 + c_5 x_2 + c_6 \tag{49}$$

$$\lambda_2 c_3\cos(\lambda_2 x_2) - \lambda_2 c_4\sin(\lambda_2 x_2) = \tau_r\beta x_2 + c_5 \tag{50}$$

From Eq. (50),

$$c_5 = \lambda_2\frac{\tau_f}{k_d}\sin[\lambda_2(x_2-x_1)] + \lambda_1\delta_1\tanh(\lambda_1 x_1)\cos[\lambda_2(x_2-x_1)] - \tau_r\beta x_2 \tag{51}$$

and hence from Eq. (49),

$$c_6 = \delta_2 + \frac{1}{2}\tau_r\beta x_2^2 - \lambda_2\frac{\tau_f}{k_d}x_2\sin[\lambda_2(x_2-x_1)] - \lambda_1\delta_1 x_2\tanh(\lambda_1 x_1)\cos[\lambda_2(x_2-x_1)] \tag{52}$$

To find a relationship between x_1 and x_2, consider Eq. (49), which gives

$$\delta_2 - \delta_p = -\frac{\tau_f}{k_d}\cos[\lambda_2(x_2 - x_1)] + \frac{\lambda_1}{\lambda_2}\delta_1 \tanh(\lambda_1 x_1)\sin[\lambda_2(x_2 - x_1)] \tag{53}$$

Solving this equation using the half-angle tangent substitution results in the following expression for x_2 in terms of x_1:

$$x_2 = x_1 + \frac{2}{\lambda_1}\left(\arctan\left\{\frac{\frac{\lambda_1}{\lambda_2}\delta_1 \tanh\lambda_1 x_1 - \sqrt{\left[\frac{\lambda_1}{\lambda_2}\delta_1 \tanh(\lambda_1 x_1)\right]^2 - (\delta_2 - \delta_1)\left(\delta_2 - \delta_1 - 2\frac{\tau_f}{k_d}\right)}}{\delta_2 - \delta_1 - 2\frac{\tau_f}{k_{des}}}\right\}\right) \tag{54}$$

Load-slip relationship

From Eq. (31) and the boundary condition in Eq. (4),

$$\left.\frac{d\delta}{dx}\right|_{x=L} = P\left(\frac{1}{E_p A_p} + \frac{1}{E_c A_c}\right) = \tau_r \beta L + c_5 \tag{55}$$

Therefore the load P as a function of x_1 and x_2 is

$$P = \frac{\tau_r \beta(L - x_2) + \lambda_2 \frac{\tau_f}{k_d}\sin[\lambda_2(x_2 - x_1)] + \lambda_1 \delta_1 \tanh(\lambda_1 x_1)\cos[\lambda_2(x_2 - x_1)]}{\frac{1}{E_p A_p} + \frac{1}{E_c A_c}} \tag{56}$$

The loaded-end slip is obtained from Eq. (32) as

$$\Delta = \delta_2 + \frac{1}{2}\tau_r \beta(L - x_2)^2 + \lambda_2 \frac{\tau_f}{k_d}(L - x_2)\sin[\lambda_2(x_2 - x_1)] + \lambda_1 \delta_1 (L - x_2)\tanh(\lambda_1 x_1)\cos[\lambda_2(x_2 - x_1)] \tag{57}$$

The free-end slip is given by Eq. (47).

Limits of solution

Importantly, the left-side starting value of x_1 is taken from the last value of x_1 before the transition from Zone I-II. This occurs for $L > L_{II}$ when Δ reaches δ_2, defining transition point B' [Fig. 3(d)].

The right-side limit of this solution (transition point C') is reached when $\delta_0 = \delta_1$, at which $x_1 = 0$. It is worth noting that the onset of snapback can begin before reaching this point. From Eq. (54) it follows that at this boundary, $x_2 = L_{II}$. From Eq. (57), the corresponding loaded-end slip is

$$\Delta_{C'} = \delta_2 + \frac{1}{2}\tau_r \beta(L - L_{II})^2 + \lambda_2 \frac{\tau_f}{k_{des}}(L - L_{II})\sin(\lambda_2 L_{II}) \tag{58}$$

From this, we can define critical length L_c by setting $\Delta_{C'} = \Delta_D$ using Eqs. (37) and (58). This gives

$$L_c = \frac{\lambda_2 \frac{\tau_f}{k_d} L_{II}\sin(\lambda_2 L_{II}) - \frac{1}{2}\tau_r \beta L_{II}^2}{\lambda_2 \frac{\tau_f}{k_d}\sin(\lambda_2 L_{II}) - \tau_r \beta L_{II}} \tag{59}$$

The significance of L_c is that it is the shortest length that can accommodate progressive debonding under displacement control. In other words, it allows for a progressive shift of the bonded profile along the prism and enables the joint to maintain a load above P_{res} for slip exceeding Δ_D as given by Eq. (37). Note that in the case without friction, lengths L_c and L_{II} become equivalent, and signify the shortest length where a load can be maintained beyond $\Delta > \delta_2$.

Zone II-III Solution

This phase of response involves zones II and III, as shown in Fig. 3(e). Therefore, we utilise the slip and slip strain distributions as given by Eqs. (21), (22), (31), and (32). It is convenient

to formulate both P and Δ in terms of the transition coordinate x_2, as shown in Fig. 4(e) and (k).

From the boundary condition in Eq. (5), it follows that $c_3 = 0$ in Eq. (23). Furthermore, from continuity of slip and slip strain at $x = x_2$ gives

$$\delta_2 = c_4 \cos(\lambda_2 x_2) + \delta_p = \frac{1}{2}\tau_r \beta x_2^2 + c_5 x_2 + c_6 \tag{60}$$

$$-\lambda_2 c_4 \sin(\lambda_2 x_2) = \tau_r \beta x_2 + c_5 \tag{61}$$

From Eq. (60),

$$c_4 = \frac{\delta_2 - \delta_p}{\cos(\lambda_2 x_2)} \tag{62}$$

and from Eq. (61),

$$c_5 = -\tau_r \beta x_2 - \lambda_2 \big(\delta_2 - \delta_p\big) \tan(\lambda_2 x_2) \tag{63}$$

Rearranging Eq. (60) gives c_6 as

$$c_6 = \delta_2 + \frac{1}{2}\tau_r \beta x_2^2 + \lambda_2 \big(\delta_2 - \delta_p\big) x_2 \tan(\lambda_2 x_2) \tag{64}$$

Load-slip relationship

Substituting Eq. (63) into Eq. (55) gives the load P as a function of x_2 as follows:

$$P = \frac{\tau_r \beta (L - x_2) - \lambda_2 \big(\delta_2 - \delta_p\big) \tan(\lambda_2 x_2)}{\frac{1}{E_p A_p} + \frac{1}{E_c A_c}} \tag{65}$$

The loaded-end slip is obtained from Eq. (32) as

$$\Delta = \delta_2 + \frac{1}{2}\tau_r \beta (L - x_2)^2 - \lambda_2 \big(\delta_2 - \delta_p\big)(L - x_2) \tan(\lambda_2 x_2) \tag{66}$$

The free-end slip is obtained from Eq. (21) as

$$\delta_0 = c_4 + \delta_p = \frac{\delta_2}{\cos(\lambda_2 x_2)} + \delta_p \left[1 - \frac{1}{\cos(\lambda_2 x_2)}\right] \tag{67}$$

Limits of solution

The left-side limit of this solution range depends on the preceding phase of solution. For short bonded lengths ($L < L_{II}$) this occurs at $x_2 = L$, and for long lengths ($L > L_{II}$) at $x_2 = L_{II}$. The right-side limit occurs when $x_2 = 0$, regardless of L.

It is worth noting that this stage of response exhibits snapback over long bonded lengths, as shown in Fig. 5. Consequently, if $L > L_c$, then this stage of solution cannot be entered under displacement control. Note further that this stage becomes effectively bypassed for any bonded length if friction is zero, since Eq. (37) gives $\Delta_D = \delta_2$.

Solving for the full-range response

As the preceding derivation did not follow the order of response, the sequence for constructing a full-range P-Δ curve will now be described. The initial step in this process is to determine L_{II} from Eq. (48) as this controls the pathway through the solutions.

Zone I: The first solution range is within zone I as illustrated in Fig. 3(a). Since the response during this phase is linear, only two points are required to define this segment—the left side being the origin and the right side being the transition point A, occurring at $\Delta = \delta_1$, where the corresponding P is obtained from Eq. (14).

Zone I-II: Solution range I-II then follows [Fig. 3(b)] regardless of L. In this range, both P and Δ are parametric in terms of x_1, and are obtained using Eqs. (45) and (46) respectively. This

phase initiates at $x_1 = L$ after which x_1 is incrementally reduced based on a user-specified discretisation. In short bonded lengths ($L < L_{II}$), this phase ends at transition point B when $x_1 = 0$. In long bonded lengths ($L > L_{II}$), the phase ends at transition point B' when Δ, calculated using Eq. (46), reaches δ_2.

Zone II: Over short bonded lengths ($L < L_{II}$), the next phase is the zone II solution [Fig. 3(c)]. In this phase, the response is linear, so P and Δ need to be determined only at the transition points B and C. Point B has already been defined at the end of the previous phase. Point C occurs at $\Delta = \delta_2$, with the corresponding P obtained using Eq. (27).

Zone I-III: Over long bonded lengths ($L > L_{II}$), the zone I-II solution is followed by the zone I-III solution [Fig. 3(d)], which initiates at transition point B' at the last obtained value of x_1. The solutions for P and Δ in this range are parametric in terms of x_1 and x_2, and are obtained using Eqs. (56) and (57). Note that x_2 is obtained from x_1 using Eq. (54). The value of x_1 continues to be incrementally decreased until $x_1 = 0$, which defines transition point C'. Note that at this point $x_2 = L_{II}$.

Zone II-III: This zone [Fig. 3(e)] begins either at point C or C', obtained from the preceding phase. Solutions for P and Δ are parametric in terms of x_2, obtained using Eqs. (65) and (66). If $L < L_{II}$ then x_2 initiates at L, and if $L > L_{II}$, x_2 initiates at L_{II}. Throughout this phase, the value of x_2 continues to be incrementally reduced until $x_2 = 0$, defining transition point D.

Zone III: In this phase, the load remains constant at the value given by Eq. (35).

COMPARISON WITH EXISTING APPROACHES

To highlight its range of applicability, the developed formulation will now be compared to the closed-form analytical solutions by Ren at al. (2010) and Caggiano et al. (2012), both of which consider the bilinear τ-δ rule. It is worth noting that in the context of these comparisons the approaches are treatable as generic, although they have been applied by their respective authors to modelling the behaviour of grouted rock bolts and FRP-to-concrete joints, respectively.

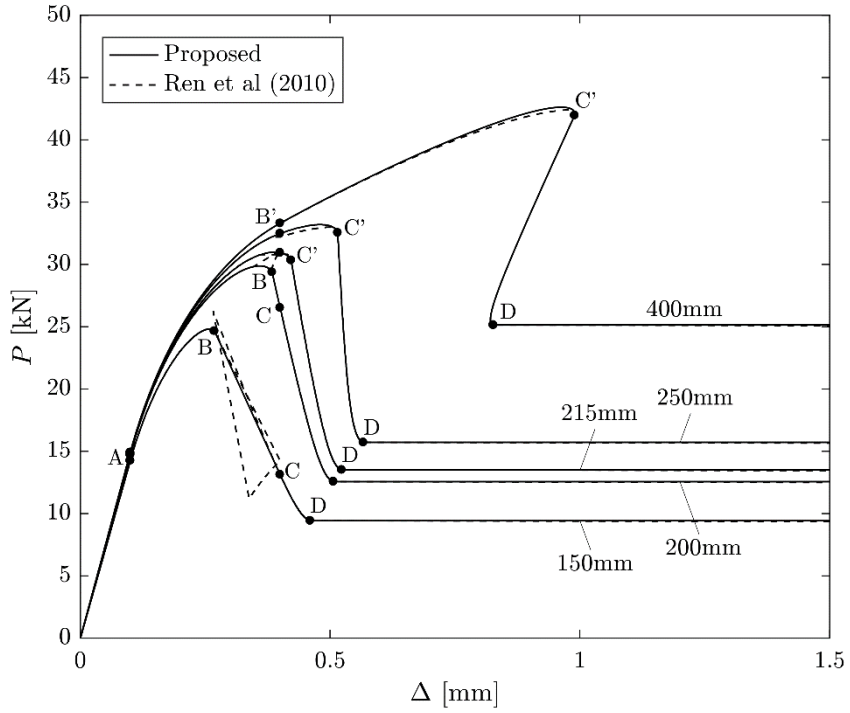

Fig. 6 Comparison of the proposed formulation (solid line) to existing solutions by Ren et al. (2010) (dashed line) for lengths around the transition range between long and short L. Considers 10 mm diameter round bar with A_p = 78.5 mm^2 and L_p = 31.4 mm. Bond properties taken as: τ_f = 6 MPa, δ_2 = 0.4 mm, k = 60 MPa/mm, and τ_r = 1 MPa. Limiting lengths for this set of properties are L_{II} = 211 mm and L_c = 243 mm.

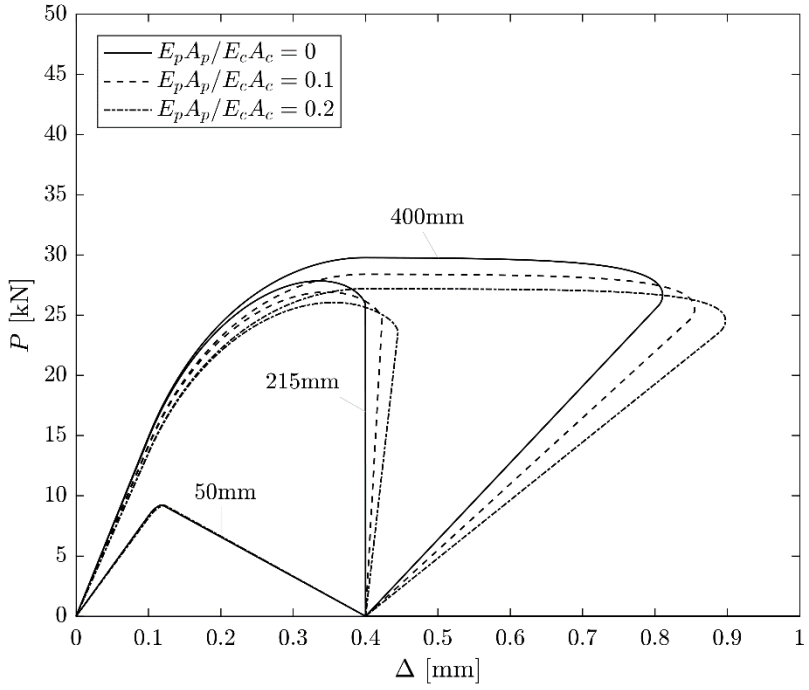

Fig. 7 Effect of finite substrate stiffness in the proposed approach. Example considers the same reinforcement and bond properties as Fig. 6 but with τ_r = 0 MPa. The proposed method becomes equivalent to the method of Caggiano et al. (2012) for E_pA_p / E_cA_c = 0.

Comparison to approach by Ren et al. (2010)

The approach by Ren et al. (2010) uses the four-parameter bilinear-frictional rule (Fig. 2), and is formulated to specifically handle circular reinforcement. However, unlike the proposed approach which is applicable to long and short bonded length, a limitation of the approach by Ren is that its applicability is restricted to long bonded lengths only. Additionally, the present approach has the capability to allow for any reinforcement shape controlled by separate input of A_p and L_p, and also for compressibility of the substrate through E_c and A_c.

Importantly, the fact that Ren's solution does not apply to short L values ($< L_{II}$) is not a critique of their method, but rather a feature of its intended application toward the problem of grouted rock bolts, where practical lengths tend to exceed L_c.

A comparison of predictions is demonstrated in Fig. 6. As the formulation by Ren assumes circular reinforcement, the example shown considers a 10 mm diameter FRP bar with E_p = 150,000 MPa, τ_f = 6 MPa, δ_1 = 0.1 mm, δ_2 = 0.4 mm, τ_r = 1 MPa. The limiting lengths for this set of parameters are L_{II} = 211 mm and L_c = 243 mm, as calculated using Eqs. (48) and (59). Fig. 6 plots solutions for several L values close to the transition range between long and short lengths.

It is seen that for long lengths $L \gg 243$ mm, both formulations provide very similar results, although Ren's solution slightly underestimates P within the latter phase of the I-III solution close to the peak load (between points B' and C'). As L is reduced below L_{II}, Ren's solution begins to yield unstable between points B and C. This arises from the fact that Ren's solution does not consider the zone II solution range which occurs in short lengths. In other words, it only considers the RHS of Fig. 3.

Comparison to approach by Caggiano et al. (2012)

Using a derivation approach similar to the present paper, Caggiano et al. (2012) developed analytical solutions for the P-Δ response for the three parameter bilinear τ-δ rule in terms of τ_f, δ_2 and δ_1 but ignoring the possibility of residual friction (i.e. τ_r = 0) and the potential compressibility of the substrate. Importantly, within its range of intended use, the approach by Caggiano et al. is identical to that proposed here, that is, both sets of solutions are equivalent and mathematically exact for both long and short L. The proposed approach is further applicable to cases where the substrate is compressible or where a residual stress capacity is present. The first generalisation of the proposed approach may be significant for soft substrates such as clay brick masonry. The second generalisation is relevant to applications involving non-externally bonded reinforcement such as NSM retrofits. It may also be applied to embedded bars as long as a bilinear rule can capture the local τ-δ behaviour, which has been shown to be the case for rock bolts (Chen & Ren 2008) and corroded reinforcement in concrete (Feng et al. 2015).

Fig. 7 demonstrates the influence of compressibility of the substrate on the P-Δ behaviour. It can be seen that an increase in the flexibility of the substrate causes a reduction in the resisted load but an increase to the overall deformability. The consideration of friction is discussed in detail in Section 4 where it will be shown analytically that the effect of friction on the P-Δ behaviour is to produce a secondary ascending branch following the initial elastic phase of response. In Section 5 this will be confirmed through comparison to test results.

APPLICATION TO RESEARCH

Prediction of global *P-Δ* curves from known local *τ-δ* properties

The direct application of the developed formulation is to calculate global *P-Δ* response from known values of local bond parameters τ_f, δ_1, δ_2, and τ_r. This process can be used in both research and design of structural retrofits to quantify properties such as peak load capacity, deformation capacity, and required anchorage lengths.

Typical examples of computed *P-Δ* response are shown in Fig. 8, demonstrating the influence of the bonded length L and residual stress τ_r. The values chosen are intended to simulate a 2.8 × 15 mm NSM carbon FRP plate with A_p = 42 mm^2, L_p = 32.8 mm, E_p = 150,000 MPa, with interfacial bond properties τ_f = 6 MPa, δ_2 = 0.4 mm, δ_1 = 0.1 mm. The residual friction (τ_r) along the interface is varied between 0, 1, and 3 MPa. Each plot demonstrates the effect of varying the bonded length for L = 50, 100, 200, and 350 mm, as well as the critical length L_c and infinite length.

The key points along a generic *P-Δ* are defined in Fig. 9, including the peak load $P_{\max}$, slip at debonding Δ_{db}, and the yield slip Δ_y.

The following generalities can be observed from Fig. 8:

- At very short bonded length, the shape of the global *P-Δ* curve approaches that of the local *τ-δ* curve. This arises from the fact that as L is reduced toward 0, the slip distribution becomes uniform, and thus load response follows Eq. (35).
- In absence of friction, a continual increase to the bonded length causes the peak load $P_{\max}$ to asymptote toward the full debonding capacity given by the well-established expression

$$P_{ic} = \sqrt{2G_f}\sqrt{E_p A_p L_p} \tag{68}$$

- If friction is added, then the debonded zone (i.e. zone III) provides residual resistance. Thus, for long bonded lengths ($L > L_c$) the *P-Δ* curve continues to rise at increasing slip. Notably, with increasing L the curve asymptotes toward a straight line with a constant positive tangent stiffness as seen from the $L = \infty$ cases in Fig. 8 (b) and (c).
- Over any bonded length, the residual capacity τ_r enhances both the peak load ($P_{\max}$) and also the slip at full debonding (Δ_{db}). This influence becomes most pronounced over long lengths.
- Consider the absence of friction [Fig. 8(a)]. For short bonded lengths ($L \leq L_c$) the slip at full debonding (Δ_{db}) remains constant and coincides with δ_2. However for long lengths ($L > L_c$) the debonding slip increases with L. Notably under displacement-control, debonding over long L coincides with reaching the snap-back portion of response, which causes the load to drop suddenly as indicated by a dashed line.
- In the case of friction ($\tau_r > 0$), the above statement can be generalised, in that for short bonded lengths, the debonding slip remains constant at $\Delta_{db} = \Delta_D$ as given by Eq. (37). Similarly to the zero-friction case, over long bonded length any increase to L above L_c causes the debonding slip to also increase.

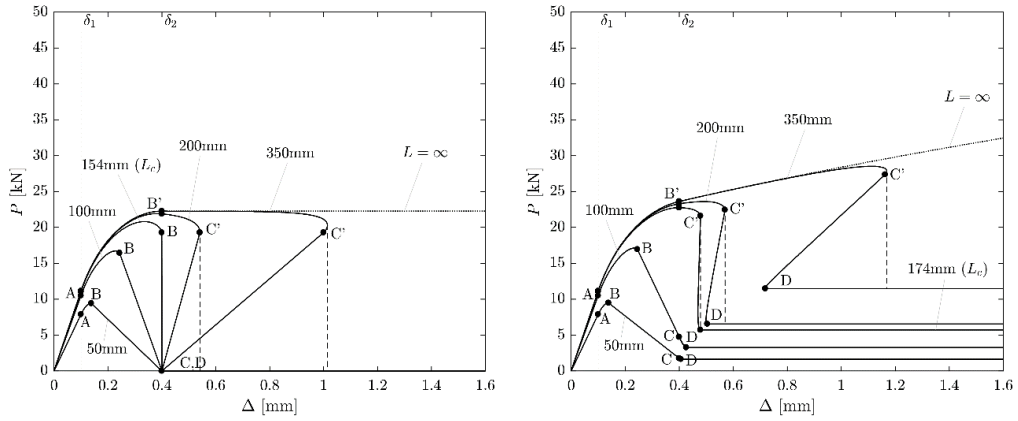

(a) no friction, τ_r = 0 MPa (b) τ_r = 1 MPa

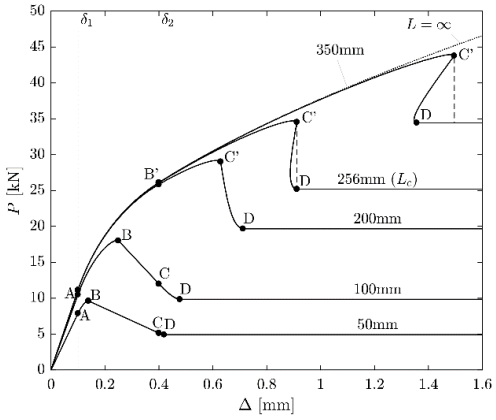

(c) τ_r = 3 MPa

Fig. 8 *P-Δ* behaviour for a NSM retrofit system with E_p = 150,000 MPa, A_p = 42 mm^2, L_p = 32.8 mm, with the substrate treated as incompressible. Bond properties taken as: τ_f = 6 MPa, δ_2 = 0.4 mm, k = 60 MPa/mm, at three levels of friction: τ_r = 0, 1, and 3 MPa. Bonded length is varied between L = 50, 100, 200, and 350 mm, critical length (L_c) at each value of friction, and infinite length. At long lengths ($L > L_c$), a vertical dashed line bypassing the snap-back region is used to indicate the sudden drop-off in P that would occur under monotonic Δ control. Each plot indicates the transition points (A, B, …) as defined in Figs. 3 and 4.

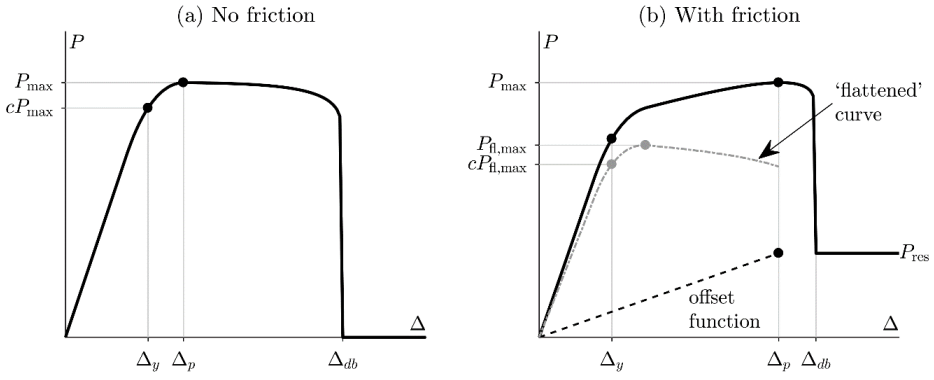

Fig. 9 Identification of key points on the *P-Δ* curve, including P_{max}, Δ_{db} and Δ_y. Cases are shown (a) without friction, and (b) with friction. In the latter, an offset function is used to construct a 'flattened' curve as $P_{fl} = P - P_{offset}$, which is then used to identify Δ_y as the slip at c times the peak load. In the parametric studies undertaken, c is taken as 0.9 (refer to Figs. 10 and 12).

Calibration of local τ-δ parameters from global P-Δ curves

A recent review of existing experimental research on bond between FRP and masonry substrates has identified two main techniques used for calibrating local τ-δ parameters from test results (Vaculik et al. 2017). The first is by using strain gauge readings, and the second is through inverse calibration, with the developed formulation being applicable toward the latter. The concept of inverse calibration is to firstly postulate the functional form for the τ-δ rule, and then undertake a series of analyses where the input properties are optimised until good agreement is obtained with experimental P-Δ behaviour. The main appeal of this approach is that it reduces the demand on test instrumentation by not requiring strain readings.

However, whilst this technique has been used extensively in the fields of both masonry and concrete, there is, to the knowledge of the authors, very limited guidance available on its implementation. Consequently, there appears to be considerable inconsistency in how the approach is applied, which is likely to partially explain the large scatter in bond properties derived from past testing (Vaculik et al, 2017). It is therefore the authors' view that in order for the results of this process to be reliable, it is important to understand the interdependency of the local τ-δ parameters and global P-Δ behaviour. Significantly, the limitations of the technique with regard to the confidence in the extracted parameters need to be recognised, and in particular, the implications arising from short versus long bonded lengths. Explaining these trends through examples using the developed formulation is the objective of the remainder of this section.

Examples using analytical reference curves

The reliability of the inverse calibration process will now be demonstrated using a parametric study. This study uses analytically generated reference P-Δ curves (as opposed to real experimental data) to allow us to focus only on the fundamental trends.

The goodness-of-fit between a reference P-Δ curve and a hypothesised curve is quantified using two types of error norms. The first is a root-mean-squared (RMS) error, computed as

$$\mathrm{err(rms)} = \frac{\sqrt{\int \left(P_{\mathrm{ref}} - P_{\mathrm{hyp}}\right)^2 \mathrm{d}x}}{\sqrt{\int {P_{\mathrm{ref}}}^2 \mathrm{d}x}} \tag{69}$$

where P_{ref} and P_{hyp} are the load ordinates in the reference curve and hypothesised curve. This gives a measure of the overall fit between the two curves without specifically focusing on any particular key point.

The second is by calculating the error in the values of specific key properties, according to the expression

$$\mathrm{err}(X) = \left|X_{\mathrm{ref}} - X_{\mathrm{hyp}}\right| / X_{\mathrm{ref}} \tag{70}$$

where X can be either $P_{\max}$, Δ_{db}, or Δ_y, and X_{ref} and X_{hyp} are the respective values in the reference curve and hypothesised curve.

Because the reference curves used in the upcoming example are analytically generated, both k ($\equiv \tau_f / \delta_1$) and τ_r can be deterministically identified from the onset of the analysis from the initial slope and residual strength (P_{res}) observed in the reference curve. Note that in application toward real experimental data the user may relax these parameters and optimise them as part of the overall calibration process.

Let us demonstrate the sensitivity of the two remaining parameters τ_f and δ_2 on the goodness-of-fit by adopting the example cases in Fig. 8(b), where τ_f = 6 MPa, δ_2 = 0.4 mm, k = 60 MPa/mm, and τ_r = 1 MPa as the references curves. Consider the bonded lengths of 350, 200, 100, and 50 mm, noting that the transition from long to short bond length at the reference parameters occurs at L_c = 174 mm.

Fig. 10 shows the effect of varying τ_f and δ_2, in terms of contour plots of $P_{\max}$, Δ_{db} and Δ_y, as well as maps of the various errors. Black regions within the error maps indicate that the error is minimised, and thus it is possible to determine unique values of τ_f and δ_2 only where the minimisation occurs within a localised patch. In each plot, the critical bond length (L_c) is indicated by a dashed line that separates zones of long L above and short L below.

The following generalities can be observed with regard to calibrating τ_f and δ_2:

- Standalone consideration of only the RMS error is sufficient to yield unique parameter solutions for short L but not for long L [Fig. 10(a)]. For long bonded lengths, the error becomes minimised along a region where $\tau_f \delta_2 \propto 1$, indicating that the fit is sensitive to the fracture energy G_f. A visual comparison of curves that each give a low RMS error are shown in Fig. 11(a) demonstrating the similar global behaviour that can arise from vastly different combinations of τ_f and δ_2.
- Peak strength $P_{\max}$ and its error are G_f-sensitive for long L, and τ_f-sensitive for short L [Fig. 10(b) and (c)]. This behaviour follows from Eqs. (35) and (68) respectively.
- Debonding slip Δ_{db} and its error are G_f-sensitive for long L, and δ_2-sensitive for short L [Fig. 10(d) and (e)].

The properties considered so far ($P_{\max}$ and Δ_{db}) are insufficient to be able to identify τ_f and δ_2 in the long L range, since both properties are sensitive to G_f. A visual comparison of curves each with the same $P_{\max}$ but generated using very different combinations of τ_f and δ_2 is provided in Fig. 11(b). It is seen that the main distinguishing feature of these curves is the rate at which they reach their peak load. Therefore, as a quantitative indicator of this behaviour, we introduce the 'yield' slip Δ_y. This slip was quantified as shown in Fig. 9 for cases with and without friction; however, other commonly accepted methods for quantifying Δ_y such as the bilinear approximation could also be used.

- As shown by Fig. 10 (f) and (g), yield slip Δ_y and its error are δ_2-sensitive for long L, and τ_f-sensitive for short L (the latter arising from the fact that k is being held constant).

Importantly, it has been demonstrated that due to the transition in behaviour from short to long bonded length, no individual property $P_{\max}$, Δ_{db} or Δ_y, nor the RMS error is sufficient to calibrate parameters τ_f and δ_2. The properties are however complimentary, in that considering them simultaneously can identify combinations of τ_f and δ_2 where their errors become minimised. This is demonstrated using the combined error measure

$$\mathrm{err}\left(P_{\max}, \Delta_{db}, \Delta_y\right) = \sqrt{\frac{1}{3}\left[\mathrm{err}(P_{\max})^2 + \mathrm{err}(\Delta_{db})^2 + \mathrm{err}\left(\Delta_y\right)^2\right]} \tag{71}$$

which becomes minimised only within the proximity of the reference parameter values as seen in Fig. 10(h).

The trends observed in Fig. 10, which are based on an example with low friction (τ_r / τ_f = 0.17), are consistent with those which develop with no friction as demonstrated in Vaculik et al. (2017). Now consider the same parametric study, but with higher friction by taking τ_r = 3 MPa (τ_r / τ_f = 0.5). The results of the study are shown in Fig. 12. While the general trends discussed

previously still hold, the fact that the minimisation of error occurs over a wider parameter range indicates that for high values of friction the calibration becomes slightly less reliable in terms of quantifying τ_f and δ_2. The greater degree of uncertainty becomes particularly evident in the use of the RMS error, and error in $P_{\max}$ and Δ_{db} over long bonded lengths. However, over short bonded length the reliability appears unchanged compared to the low friction case.

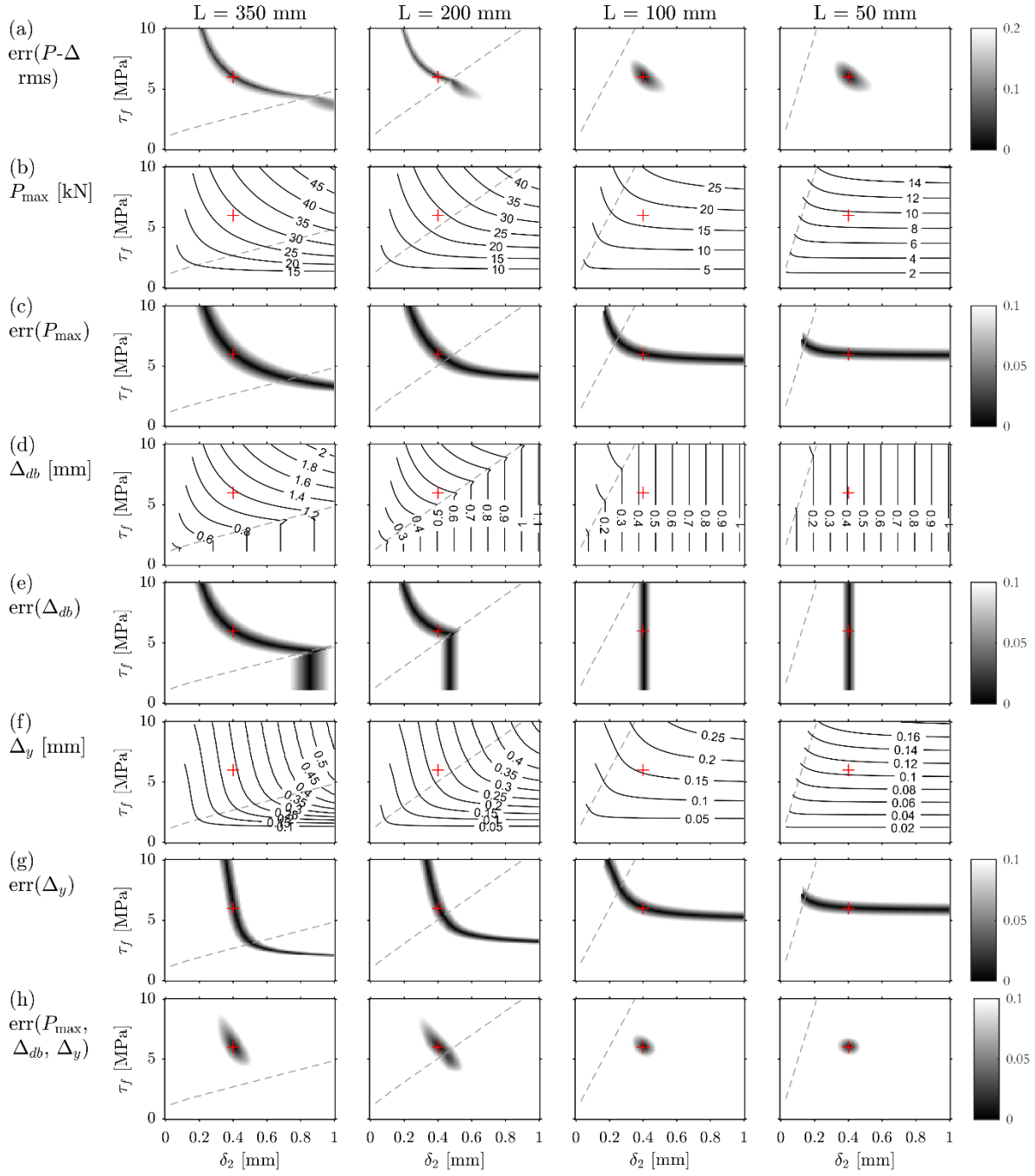

Fig. 10 Inverse calibration of τ_f and δ_2 for case of low friction (τ_r = 1 MPa). Example uses identical values of constants E_p, A_p and L_p to Fig. 8. Error norms are computed with respect to the reference parameters τ_f = 6 MPa, δ_2 = 0.4 mm, and k = 60 MPa/mm. Dashed line indicates the boundary between long and short L above and below, respectively.

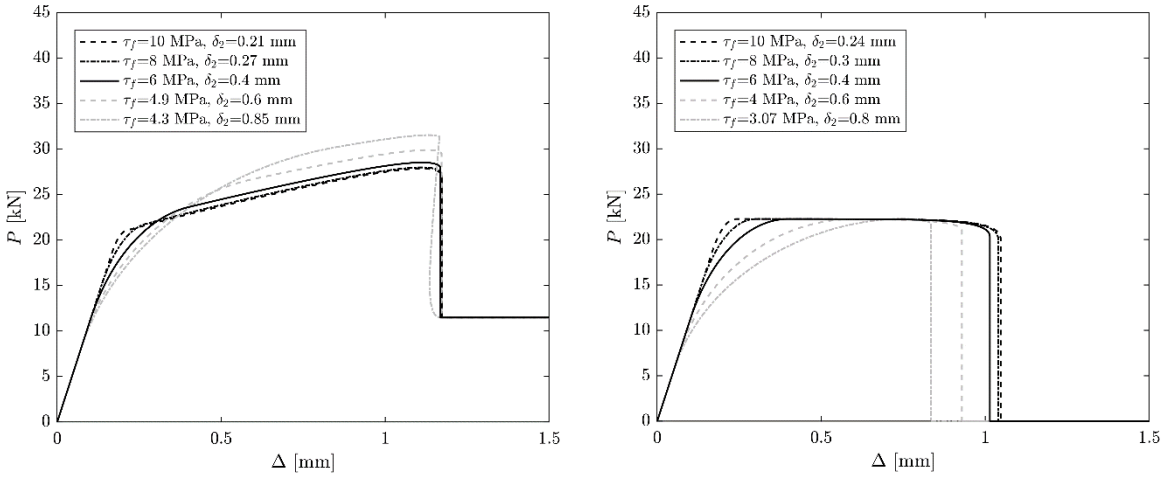

(a) (b)

Fig. 11 Examples where considerably different combinations of τ_f and δ_2 produce similar global behaviour over a long bonded length. Computed for L= 350 mm using the same values of other properties as in Fig. 8. Part (a) shows curves along the minima in the P-Δ curve RMS error measure with τ_r = 1 MPa [refer Fig. 10(a)]. Part (b) shows curves that have identical peak load (P_{max}) for zero residual capacity (τ_r = 0).

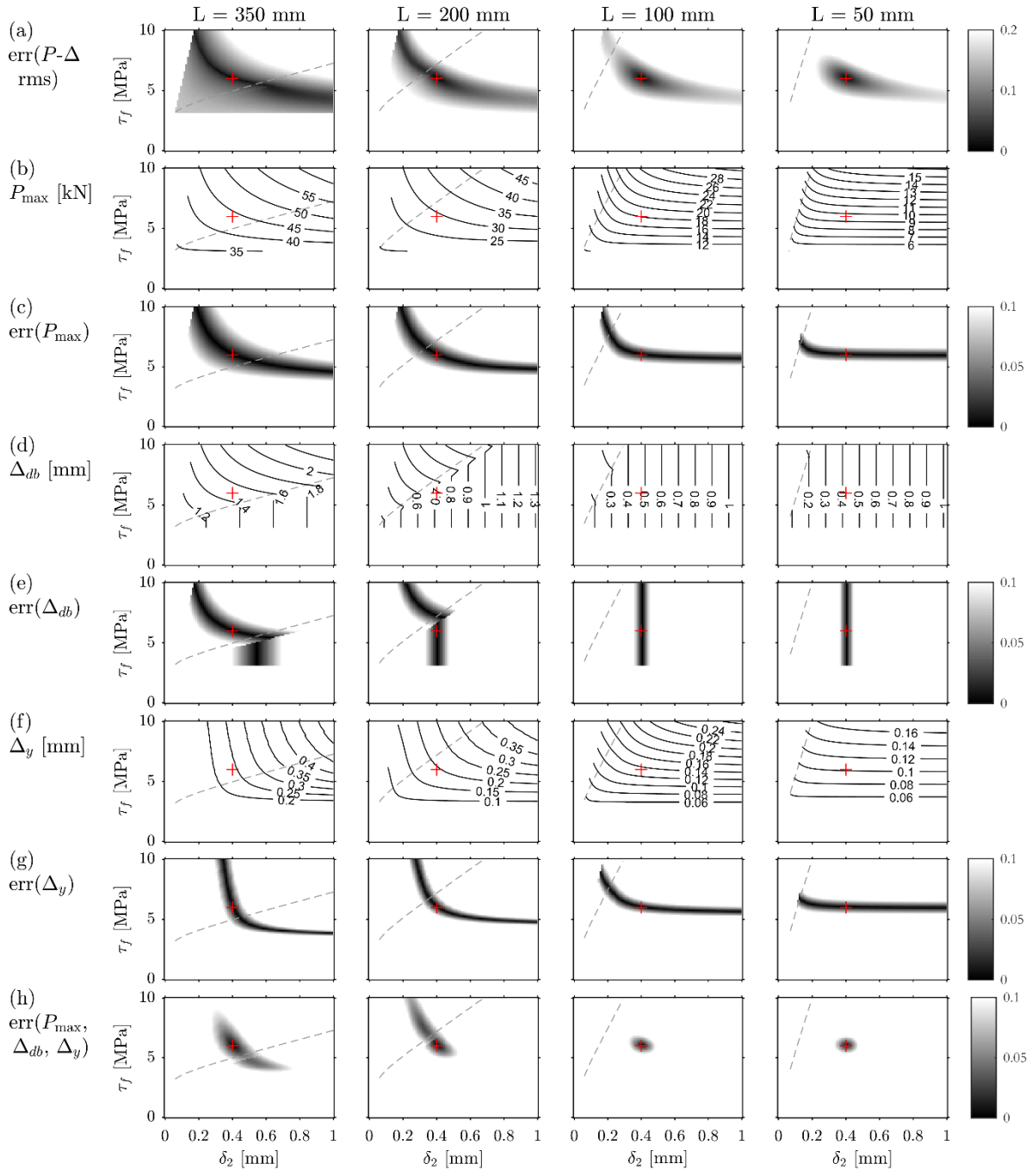

Fig. 12 Inverse calibration of τ_f and δ_2 for case of high friction (τ_r = 3 MPa). Values of all other input properties are identical to those used for Fig. 10,

Limitations of application to real experimental data

In the preceding examples, the inverse calibration process was applied toward an idealised scenario where the reference curve was generated using the same τ-δ functional form as the hypothesised curves. This ensured the existence of a particular combination of input parameters (τ_f and δ_2) guaranteed to produce perfect fit between the hypothesised and reference curves, and thus to simultaneously minimise error for each individual property (P_{max}, Δ_{db}, Δ_y). However, application of the approach toward real experimental data requires consideration of several limitations, which will now be briefly discussed.

In P-Δ data with a high level of noise it may sometimes be difficult to reliably identify key points Δ_{db} and Δ_y. This problem can generally be addressed through data smoothing (e.g. moving average filter). However, as previously demonstrated, the capability to obtain reliable estimates of τ_f and δ_2 over long bonded lengths requires the consideration of Δ_y, otherwise it is only possible to estimate the energy term G_f.

The experimental reference curve must be considered over its full range of response up to the point of full debonding Δ_{db} (refer Fig. 9). Often however, the experimental P-Δ curves presented in published works tend to be truncated before a stable residual load P_{res} can be observed. The ambiguity about how to interpret such results can introduce significant error into the calibration process. For example, an incomplete curve stopped at some load $P > 0$ could mean that: (a) the test was stopped early, (b) the load suddenly dropped to 0, or (c) the load remained stable at the final value. Each of these alternative interpretations will lead to vastly different values of calibrated parameters. Complete reporting of experimental P-Δ data is therefore essential for the application of this method.

Importantly, it might not be possible—and in general will not be—to minimise all of the individual errors simultaneously. This is partially due to the fact that the bilinear-frictional τ-δ rule is merely an approximation of the complex and highly nonlinear bond fracture process. However, there are also insufficient degrees-of-freedom in the partial-interaction model to ensure that all properties can be fitted simultaneously. For example, over long bonded lengths, situations can easily develop where P_{max} and Δ_{db} cannot both provide good fit, because both become G_f-sensitive and thus approximately proportional to each other (refer Figs. 10 and 12). A potential means of introducing additional degrees-of-freedom is through the inputs E_pA_p and L_p, in that researchers have not yet reached full consensus regarding the appropriate way to adopt effective values of these properties for analysis. In general, however, application of the inverse calibration process to real experimental data must consider a suitable compromise between the fit of the various key points.

Finally, it is recommended that inverse calibration should consider and ideally also report values of derived material properties such as τ_f, δ_2, and G_f together with their likely range by considering the sensitivity of the results. This can be accomplished by plotting error maps such as those shown in Figs. 10 and 12, in order to visualise the range of uncertainty.

APPLICATION TO EXPERIMENTAL DATA

To demonstrate the applicability of the developed formulation on a range of substrate and reinforcement materials, let us consider examples of four different types of system that involve a residual shear stress due to friction, including (a) NSM carbon-FRP strip retrofit of clay brick masonry (Kashyap et al. 2012); (b) NSM glass-FRP bar retrofit of concrete (De Lorenzis et al. 2004); and stranded steel wire cable embedded in (c) concrete (Benmokrane et al. 1995) and; (d) rock (Chen & Ren 2008; as reported in Ren et al. 2010). These examples have been chosen to cover a wide range of bonded lengths, with the ratio of bonded length to critical bond length ranging from 0.16 to 21 as shown in Table 2. Also listed in Table 2 are the geometric and material properties of each system as well as the bond-slip model parameters used to produce the theoretical load-slip curve.

The comparison of the predicted to experimental results for each system is shown in Fig. 13. In each plot, the solid line indicates the predicted behaviour by allowing for a residual friction component whilst the dashed line indicates behaviour predicted by setting ignoring friction.

From the two cases of long bonded length [parts (a) and (d)], it can be seen that inclusion of friction is necessary in order to capture the rising slope of the post-elastic branch response. Moreover, each of the long bonded length cases shows good agreement between the predicted and experimental debonding slip (Δ_{db}), even though the residual friction branch has not been reported in either of the original experimental works. In contrast, in the short bonded length cases [parts (b) and (c)], the presence of the frictional component is immediately apparent from the experimental *P*-Δ curve, and ignoring friction would result in a considerable underestimate in the residual load capacity.

It should be noted that for the tests by Benmokrane et al. (1995), De Lorenzis et al. (2004) and Chen & Ren (2008) the bond-slip parameters were derived via the inverse calibration approach outlined in Section 4.2. For the test by Kashyap et al. (2012) the bond-slip properties used were extracted from strain gauge readings as reported therein. The choice to use strain gauge readings for Kashyap's tests was made to further demonstrate the predictive capability of the approach; that is, by using bond-slip properties that have been derived independently from the load-slip behaviour being predicted.

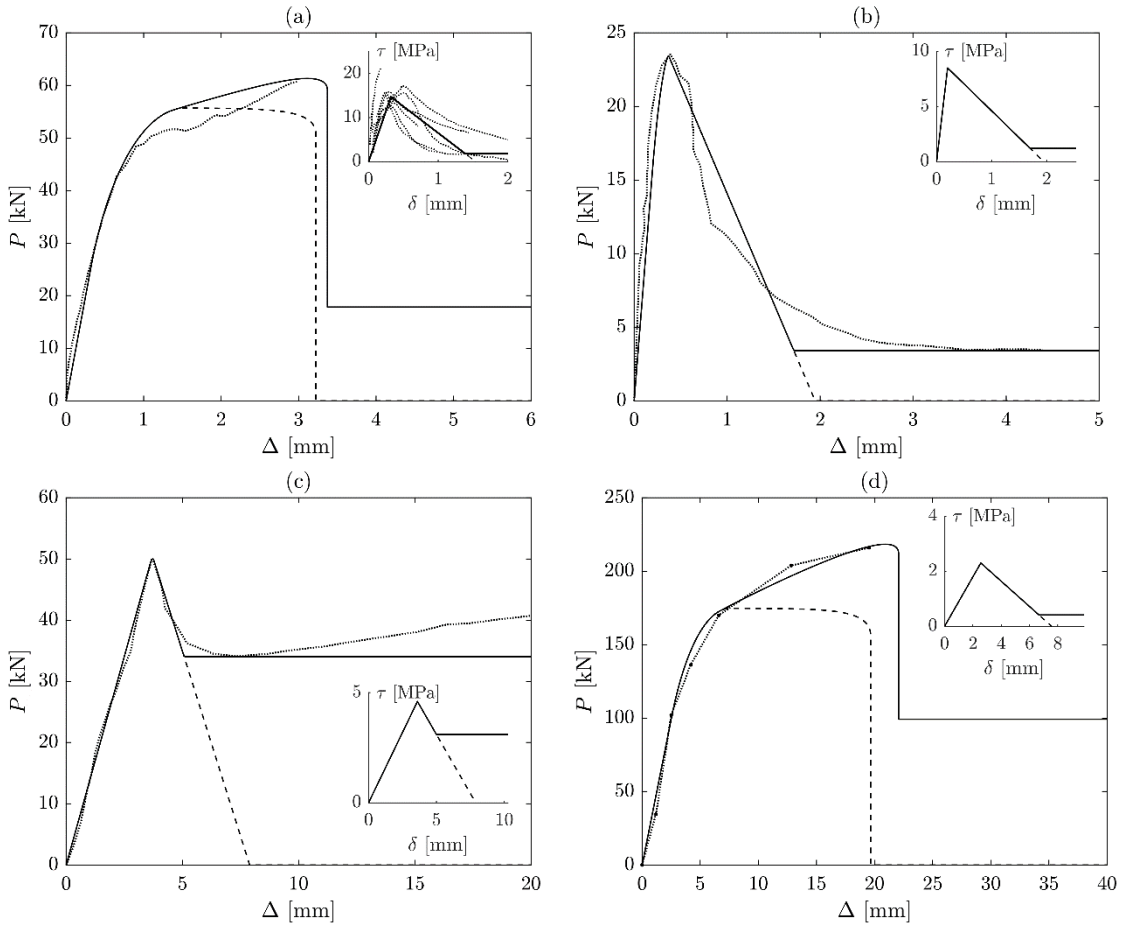

Fig. 13 Comparison of load-slip response obtained using the proposed formulation to test data from: (a) Kashyap et al. (2012), (b) De Lorenzis et al. (2004), (c) Benmokrane et al. (1995), and (d) Chen & Ren (2008). Shown inset in each graph is the local τ-δ model used in generating the global *P*-Δ curves. For each data set, the solid line indicates theoretical response by including friction, dashed line indicates theoretical response by ignoring friction, and the dotted line indicates experimental data.

Table 2: Test studies used for comparison to the developed approach.

Reference	Specimen ID	Substrate	Reinforcement	E_c (GPa)	A_c (mm^2)	E_p (GPa)	A_p (mm^2)	L (mm)	L_p (mm)	τ_f (MPa)	τ_r (MPa)	δ_1 (mm)	δ_2 (mm)	L/L_c
Benmokrane et al. (1995)	AL=20φ (Stranded Cable)	Concrete	Stranded steel wire cable	30	7,850	200	196	221	49.6	4.6	3.1	3.6	5	0.93
De Lorenzis et al. (2004)	GR3/k2.27.104-c	Concrete	GFRP Bar (NSM)	22.5[a]	45,000	37.2	70.9	38	75	8.5	1.2	0.2	1.7	0.16
Chen & Ren (2008)	-	Rock	Stranded steel wire cable	-	-	200	183	5000	44	2.3	0.4	2.56	6.67	21
Kashyap et al. (2012)	M-SG-3.6-10-3	Clay Brick	CFRP Strip (NSM)	10.7	25,300	165	36	420	23.6	14.7	1.8	0.32	1.39	1.8

[a] Estimated from AS 3600-2009 (Standards Australia 2009)

CONCLUSION

In this paper a closed-form analytical solution for the full range load-slip behaviour of plate or bar bonded to a brittle substrate is developed for the push-pull loading scenario. This solution is based on the bilinear τ-δ relationship incorporating the possibility of residual stress, and significantly can be applied to any bonded length.

As these solutions allow for the influence of friction, any bonded length, and the compressibility of the substrate, they can be applied to various generic scenarios in which the load-slip behaviour of reinforcement and substrate must be considered. Typical examples include the design of FRP retrofits (externally-bonded or near-surface-mounted), and the simulation of the load-slip behaviour of embedded reinforcing bars or bolts in brittle substrates such as concrete, rock or masonry.

Another major implementation of the analytical solutions is to the extraction of local τ-δ properties from experimental data using inverse calibration. To this end it has been shown that depending on the bonded length, inverse calibration techniques can fail to yield unique τ-δ properties such as the peak stress capacity and displacement capacity. To address this is limitation and to improve reliability, it is shown that various key points must be considered along the *P*-Δ curve including: the peak load, debonding slip, and yield slip. Whilst this demonstration has been made using the bilinear-frictional rule, the general trends and concepts can be treated as generic and applicable toward other types of fundamental τ-δ models.

It is intended that together the mathematical formulation and the trends demonstrated can act as a framework for extracting local bond properties for the development of improved material models.

ACKNOWLEDGEMENTS

The authors gratefully acknowledge the financial support from the ARC through its Discovery Grant Program (DP140102695) and the Bushfire and Natural Hazards CRC. The findings and views expressed are those of the authors and not necessarily those of the sponsors.

REFERENCES

Balazs, G. L. (1993). "Cracking analysis based on slip and bond stresses." *ACI Materials Journal*, 90(4), 340-348.

Benmokrane, B., Chennouf, A., and Mitri, H. S. (1995). "Laboratory evaluation of cement-based grouts and grouted rock anchors." *Journal of Rock Mechanics and Mining Sciences & Geomechanics Abstracts*, 32(7), 633-642.

Caggiano, A., and Martinelli, E. (2012). "A unified formulation for simulating the bond behaviour of fibres in cementitious materials." *Materials and Design*, 42, 204-213.

Caggiano, A., Martinelli, E., and Faella, C. (2012). "A fully-analytical approach for modelling the response of FRP plates bonded to a brittle substrate." *International Journal of Solids and Structures*, 49(17), 2291-2300.

Camata, G., Spacone, E., and Zarnic, R. (2007). "Experimental and nonlinear finite element studies of RC beams strengthened with FRP plates." *Composites Part B: Engineering*, 38(2), 277-288.

Chen, W. W., and Ren, F. F. (2008). "Mechanical behavior of the bamboo-steel composite rockbolt." *Report 2006BAK30B02*, Center of Lanzhou University.

Chen, J. F., Yuan, H., and Teng, J. G. (2007). "Debonding failure along a softening FRP-to-concrete interface between two adjacent cracks in concrete members." *Engineering Structures*, 29(2), 259-270.

Chen, G. M., Teng, J. G., and Chen, J. F. (2011). "Finite-element modeling of intermediate crack debonding in FRP-plated RC beams." *Journal of Composites for Construction*, 15(3), 339-353.

Cosenza, E., Manfredi, G., and Realfonzo, R. (2002). "Development length of FRP straight rebars." *Composites Part B: Engineering*, 33(7), 493-504.

Cornetti, P., and Carpinteri, A. (2011). "Modelling the FRP-concrete delamination by means of an exponential softening law." *Engineering Structures*, 33(6), 1988-2001.

De Lorenzis, L., Lundgren, K., and Rizzo, A. (2004). "Anchorage Length of Near-Surface Mounted Fiber-Reinforced Polymer Bars for Concrete Strengthening - Experimental Investigation and Numerical Modeling." *ACI Structural Journal*, 101(2), 269-278.

Feng, Q., Visintin, P., and Oehlers, D. J. (2015). "Deterioration of bond–slip due to corrosion of steel reinforcement in reinforced concrete." *Magazine of Concrete Research*, 68(15), 768-781.

Grande, E., Milani, G., and Sacco, E. (2008). "Modelling and analysis of FRP-strengthened masonry panels." *Engineering Structures*, 30(7), 1842-1860.

Haskett, M., Oehlers, D. J., and Mohamed Ali, M. S. (2008). "Local and global bond characteristics of steel reinforcing bars." *Engineering Structures*, 30(2), 376-383.

Kashyap, J., Griffith, M. C., Mohamed Ali, M. S., and Oehlers, D. J. (2011). "Prediction of load-slip behavior of FRP retrofitted masonry." *Journal of Composites for Construction*, 15(6), 943-951.

Kashyap, J., Willis, C. R., Griffith, M. C., Ingham, J. M., and Masia, M. J. (2012). "Debonding resistance of FRP-to-clay brick masonry joints." *Engineering Structures*, 41, 186-198.

Lee, S.-C., Cho, J.-Y., and Vecchio, F. J. (2013). "Tension-Stiffening Model for Steel Fiber-Reinforced Concrete Containing Conventional Reinforcement." *ACI Structural Journal*, 110(4), 639-648.

Lu, X. Z., Teng, J. G., Ye, L. P., and Jiang, J. J. (2005). "Bond-slip models for FRP sheets/plates bonded to concrete." *Engineering Structures*, 27(6), 920-937.

Lu, X. Z., Ye, L. P., Teng, J. G., and Jiang, J. J. (2005). "Meso-scale finite element model for FRP sheets/plates bonded to concrete." *Engineering Structures*, 27(4), 564-575.

Muhamad, R., Mohamed Ali, M. S., Oehlers, D. J., and Griffith, M. C. (2012). "The Tension Stiffening Mechanism in Reinforced Concrete Prisms." *Advances in Structural Engineering*, 15(12), 2053-2069.

Oehlers, D. J., Seracino, R., and Smith, S. T. (2008). "Design handbook for RC structures retrofitted with FRP and metal plates: beams and slabs HB 305-2008." Standards Australia, Sydney.

Ren, F. F., Yang, Z. J., Chen, J. F., and Chen, W. W. (2010). "An analytical analysis of the full-range behaviour of grouted rockbolts based on a tri-linear bond-slip model." *Construction and Building Materials*, 24(3), 361-370.

Standards Australia (2009). "Concrete Structures." *AS 3600-2009*, Standards Australia, Sydney.

Sturm A. B., Visintin P. and Oehlers D. J. (2018a) "Time-dependent serviceability behavior of reinforced concrete beams: Partial interaction tension stiffening mechanics." *Structural Concrete*, 19(2), 508-523.

Sturm, A. B., Visintin, P., Oehlers, D. J. and Seracino, R. (2018b) "Time dependent tension stiffening mechanics of fibre reinforced and ultra-high performance fibre reinforced concrete." *Journal of Structural Engineering*, 144(8), 04018122.

Teng, J. G., Yuan, H., and Chen, J. F. (2006). "FRP-to-concrete interfaces between two adjacent cracks: Theoretical model for debonding failure." *International Journal of Solids and Structures*, 43(18-19), 5750-5778.

Yuan, H., Teng, J. G., Seracino, R., Wu, Z. S., and Yao, J. (2004). "Full-range behavior of FRP-to-concrete bonded joints." *Engineering Structures*, 26(5), 553-565.

Vaculik, J., Visintin, P., Burton, N. G., Griffith, M. C., and Seracino, R. (2018). "State-of-the-art review and future research directions for FRP-to-masonry bond research: Test methods and techniques for extraction of bond-slip behaviour." *Construction and Building Materials*, 183, 325-345.

Volkersen, O. (1938). "Die Nietkrafverteilung in zugbeanspruchten Nietverbindungen mit konstanten Laschenquerschnitten." *Luftfahrtvorschung*, 15, 41-47.

STATEMENT OF AUTHORSHIP

Analytical approach for global load-slip behaviour of FRP plates externally bonded to brittle substrates with anchors
Composites Part B: Engineering, 160(2019), 177-194

Sturm, A. B. (Candidate)

Prepared manuscript, performed all analyses, and developed model and theory (65%)

This paper reports on original research I conducted during the period of my Higher Degree by Research candidature and is not subject to any obligations or contractual agreements with a third party that would constrain its inclusion in this thesis. I am the primary author of this paper.

Signed … Date 9/07/2020

Visintin, P.

Supervised, contributed to research and acted as corresponding author (10%)

I certify that the candidate's stated contribution to the publication is accurate (as detailed above); permission is granted for the candidate in include the publication in the thesis; and the sum of all co-author contributions is equal to 100% less the candidate's stated contribution.

Signed …… Date 07/07/2020

Vaculik, J.

Contributed to research (10%)

I certify that the candidate's stated contribution to the publication is accurate (as detailed above); permission is granted for the candidate in include the publication in the thesis; and the sum of all co-author contributions is equal to 100% less the candidate's stated contribution.

Signed Date 7/07/2020

Oehlers, D.J.

Supervised and contributed to research (5%)

I certify that the candidate's stated contribution to the publication is accurate (as detailed above); permission is granted for the candidate in include the publication in the thesis; and the sum of all co-author contributions is equal to 100% less the candidate's stated contribution.

Signed Date 7/7/20

Seracino, R.

Contributed to research (5%)

I certify that the candidate's stated contribution to the publication is accurate (as detailed above); permission is granted for the candidate in include the publication in the thesis; and the sum of all co-author contributions is equal to 100% less the candidate's stated contribution.

Signed …….. Date … July 7, 2020…….

Smith, S. T.

Contributed to research (5%)

I certify that the candidate's stated contribution to the publication is accurate (as detailed above); permission is granted for the candidate in include the publication in the thesis; and the sum of all co-author contributions is equal to 100% less the candidate's stated contribution.

Signed Date 7 July 2020

ANALYTICAL APPROACH FOR GLOBAL LOAD-SLIP BEHAVIOUR OF FRP PLATES EXTERNALLY BONDED TO BRITTLE SUBSTRATES WITH ANCHORS

Sturm, A. B., Visintin, P., Vaculik. J., Oehlers, D. J., Seracino, R., Smith, S. T.

ABSTRACT

A partial interaction procedure is developed for obtaining analytical solutions for the global load-slip behaviour of fibre-reinforced polymer plates adhesively bonded and mechanically anchored to brittle substrates. This is performed by adopting a matrix approach where the slip and slip strain at any point is given by the product of a solution matrix which is a function of: the position; the zone of solution - whether it is elastic, softening or debonding; and a coefficient vector. It is shown that the procedure can be used as a convenient research tool for extracting the material bond properties from standard experimental pull-push tests, or for use in advanced numerical simulations to develop anchorage systems for structures retrofitted with fibre-reinforced polymer (FRP) composites.

INTRODUCTION

The practice of retrofitting structures with fibre-reinforced polymers (FRPs) is becoming increasingly common due to the significant financial and environmental benefits over replacement. These retrofits commonly consist of an FRP plate externally bonded to the tensile face of reinforced concrete beams (Bank & Arora 2007; Wu et al. 2008; Wu et al. 2009; Smith et al. 2011; Koutas & Triantafillou 2012) or unreinforced masonry walls (Tan & Patoary 2004; Fagone & Ranocchiai 2018; Reboul et al. 2018) for flexural strengthening. Due to very low tensile strength of the substrate compared to the FRP, the failure of retrofitted sections typically occurs by the mechanism of interfacial debonding which involves fracture of the substrate adjacent to the bonded interface at a strain significantly lower than FRP rupture strain.

It has been demonstrated that supplementing bonded plates with mechanical anchors can be an effective means for increasing the interaction between the FRP and brittle substrate and therefore utilising the strain capacity of the FRP plate. Significant empirical research has led to the development of a wide range of anchor types which have been extensively detailed and reviewed in (Kalfat et al. 2011; Grelle & Sneed 2013), where it was found the most commonly investigated anchors are the FRP anchor spike and the plate anchor. An anchor spike consists of a bundle of fibres that is rolled by hand and embedded within an epoxy-filled hole in the substrate at one end, whilst at the other end the fibres are fanned and embedded within the composite matrix during the wet-lay-up process (Smith et al. 2011). Alternatively, plate anchors consist of transverse FRP or steel plates that are bonded to the main longitudinal FRP plate and then embedded into the substrate using conventional screw fixings (Wu et al. 2008; Wu et al. 2009).

The most basic form of testing used to assess the efficiency systems with or without anchorage is the single- or double-lap push-pull test (Vaculik et al. 2018a), and this form of testing has been widely applied to both spike and plate anchors systems for concrete and masonry substrates (Niemitz et al. 2010; Realfonzo et al. 2013; Zhang et al. 2012; Fagone et al. 2014; Kalfat & Al-Mahaidi 2016; Ceroni 2017). The results of push-pull testing has shown that the addition of mechanical anchors to adhesively bonded joints leads to a substantial increase in both the debonding resistance and slip at which debonding occurs. Although widely observed, the large range of variables required to be covered by testing, and the generally limited number of test results, particularly for masonry, means to date no wide ranging material model to predict the debonding resistance and slip capacity of an adhesively bonded and mechanically

anchored system is available. Instead general guidance has been obtained from larger scale member level testing, which is further complicated by the additional testing variables associated with the geometry of the retrofitted member. That is, at the member level, flexural testing of retrofitted reinforced concrete beams (Bank & Arora 2007; Wu et al. 2008; Wu et al. 2009; Smith et al. 2011; Koutas & Triantafillou 2012) and masonry walls (Tan & Patoary 2004; Fagone & Ranocchiai 2018; Reboul et al. 2018) have shown that the addition of anchors leads to a significant improvement in the load and displacement capacity. Several investigations, such as those by (Smith et al. 2011; Koutas & Triantafillou 2012) have sought to empirically identify the influence of anchor number, spacing and location and in some instances preliminary design guidance has been provided on the basis of test results (Bank & Arora 2007; Orton et al. 2008). To provide additional design guidance, numerical and analytical modelling, including those based on finite element analysis (Wu et al. 2009; Grande et al, 2013) and the application of segmental analysis techniques (Oehlers et al. 2016) have also been conducted. A significant limitation of these analysis approaches, is however, the numerically intensive nature of the modelling and the requirement for material models that adequately describe the load-slip behaviour of the mechanical anchors. Hence, despite extensive proof-of-concept testing, a substantiative and easy to apply design methodology has yet to be developed, such that design practitioners can specify – with confidence and without the need for experimentation – the type, the number and location of mechanical anchors required to achieve a given design strength (Kalfat et al. 2011; Grelle & Sneed 2013; ACI 2017).

To help address this limitation, in the paper a procedure is developed for obtaining analytical solutions for the global load-slip behaviour of FRP plates adhesively bonded and anchored to brittle substrates. This is performed by adopting a matrix approach where the slip and slip strain at any point is given by the product of a solution matrix, which is a function of the position and the zone of solution (elastic, softening or debonding), and a coefficient vector. Importantly, this solution can allow for any number of anchors with any given load-slip relationship. The primary advantage of this solution over conventional finite difference based methods is that no iterative root finding is required, thus improving the computational efficiency of the implementation. It will be shown that the procedure can be used as a convenient research tool for extracting the material bond properties from standard experimental pull-push tests for use in advanced numerical simulations to develop effective FRP anchorage systems.

In the following, analytical solutions for the global load-slip behaviour of FRP plates adhesively bonded and anchored to brittle substrates are first derived. This is followed by a validation of the approach to an accepted finite difference model and a parametric study to investigate the influence of anchor location and number. It is then shown how the approach can be used as a research tool for extracting the bond stress-slip behaviour of the adhesive FRP to concrete interface as well as the load-slip behaviour of the anchor. Finally, a worked example is presented in Appendix A to demonstrate the application of the approach.

MATRIX FORMULATION FOR PULL-PUSH BEHAVIOUR OF EXTERNALLY BONDED FRP PLATE BONDED TO A BRITTLE SUBSTRATE

In this section, a matrix-based formulation will be developed for the analysis of an externally bonded (EB) FRP plate bonded to a brittle substrate with or without anchors. First, the case without anchors will be considered. Variables in bold and upper case are 2x2 matrices while variables in bold and lower case represent 2x1 column vectors.

Formulation without an anchor

Consider an externally bonded FRP plate as illustrated in Fig. 1 where the bonded length of the plate is L, the cross-sectional area of the plate is A_p, the cross-sectional area of the substrate is A_c, the bonded perimeter is L_p, the elastic modulus of the plate is E_p, and the elastic modulus of the substrate is E_c.

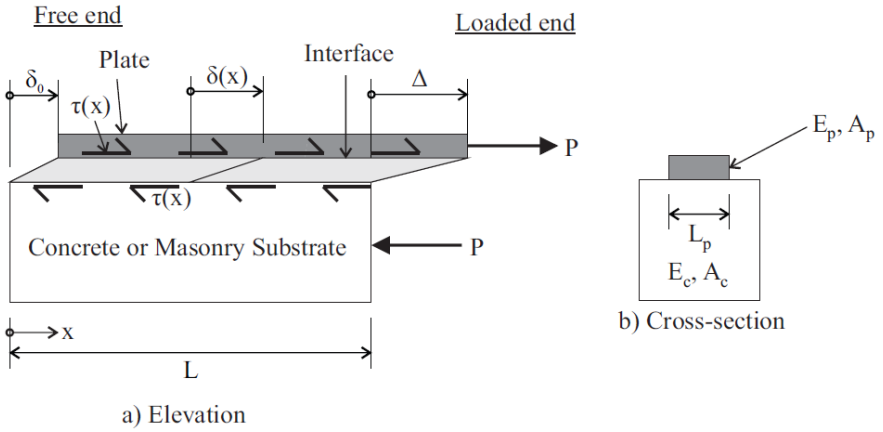

Fig. 1 EB FRP plate bonded to brittle substrate

If a load P is applied to the end of the plate as illustrated in Fig. 1, a slip occurs along the length of the plate $\delta(x)$, where the slip at the loaded end is Δ and the slip at the free end is δ_0. The load P is transferred from the plate into the substrate by the interface shear stresses $\tau(x)$ that develop due to bond between the plate and the substrate. The variation in slip along the length of the prism can be relate to the interface shear stress by the following 2nd Order Differential Equation

$$\frac{d^2\delta}{dx^2} = \tau\beta \tag{1}$$

where the shear stress τ is a function of the slip δ as is given by the assumed bond stress-slip (τ-δ) relationship and in which

$$\beta = \frac{L_p}{EA_{eff}} \tag{2}$$

and the effective axial rigidity of the plate-substrate system EA_{eff} is given as

$$EA_{eff} = \frac{1}{\left(\frac{1}{E_pA_p} + \frac{1}{E_cA_c}\right)} \tag{3}$$

Eq. (1) is the fundamental expression for the shear-slip behaviour of a bonded interface for linear elastic plate and substrate material properties. This expression was first developed by (Volkersen 1938) and its rearrangements and variants have since been used extensively to describe the behaviour of the bonded interface around internal reinforcement including the cracking behaviour, tension stiffening and load development (Balazs 1993; Cosenza et al. 2002; Lee et al. 2013; Muhamad et al. 2012; Sturm et al. 2018). This approach has also been used to study externally bonded and near-surface mounted FRP plated sections as well as rock bolts (Yuan et al. 2004; Teng et al. 2006; Chen et al. 2007; Ren et al. 2010; Cornetti & Carpinteri 2011; Caggiano et al. 2012; Vaculik et al. 2018b).

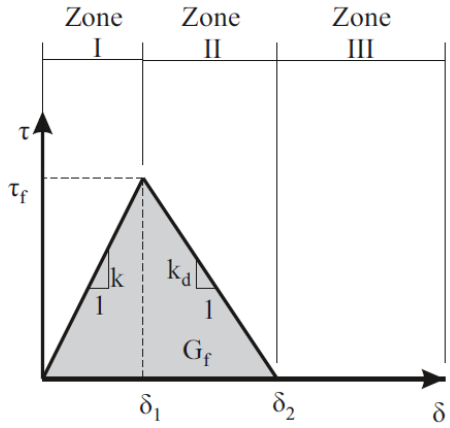

Fig. 2 Bilinear τ-δ relationship defining interface bond behaviour

It should be noted that Eq. (3) and the solutions that follow are limited to plates and substrates that behave elastically. In some instances FRPs can be made to behave in a ductile inelastic manner, such as through the use of ductile polymers, or by via the modification of epoxy resins (Torabi et al. 2017; Rahimi et al, 2018; Torabi eat al. 2018). Moreover, some polymers such as poly methyl methacrylate (PMMA) may behave in a brittle, quasi-brittle, or ductile way (Cicero et al. 2018). For these materials the following derivation can only be applied up to the elastic limit.

In this paper, the τ-δ relationship of the interface of an externally bonded plate is assumed to be bilinear without friction, as has been done by (Yuan et al. 2004; Caggiano et al. 2012) and as is illustrated in Fig. 2. This can be expressed as

$$\tau = k\delta; \delta < \delta_1 \quad (4a)$$

$$\tau = \tau_f - k_d(\delta - \delta_1); \delta_1 < \delta < \delta_2 \quad (4b)$$

$$\tau = 0; \delta > \delta_2 \quad (4c)$$

where $k=\tau_f/\delta_1$ and $k_d=\tau_f/(\delta_2-\delta_1)$. Note that Eq. (4) defines the zones of solution shown in Fig. 2. In the next section, it will be shown how the governing equation [Eq (1)] can be solved for each zone in Figure 2.

Solution for Zone I ($\delta<\delta_1$)

Substituting Eq. (4a) into Eq. (1) gives the following governing equation for Zone I

$$\frac{d^2\delta}{dx^2} = \lambda_1^2\delta \quad (5)$$

where

$$\lambda_1 = \sqrt{k\beta} \quad (6)$$

Solving Eq. (5) gives the variation in slip

$$\delta = c_1 \sinh(\lambda_1 x) + c_2 \cosh(\lambda_1 x) \quad (7)$$

and differentiating Eq. (7) gives the variation in slip strain

$$\frac{d\delta}{dx} = \lambda_1 c_1 \cosh(\lambda_1 x) + \lambda_1 c_2 \sinh(\lambda_1 x) \quad (8)$$

in which c_1 and c_2 are constants.

The above can be expressed more compactly in matrix form

$$\begin{bmatrix} \delta \\ \frac{d\delta}{dx} \end{bmatrix} = \begin{bmatrix} \sinh(\lambda_1 x) & \cosh(\lambda_1 x) \\ \lambda_1 \cosh(\lambda_1 x) & \lambda_1 \sinh(\lambda_1 x) \end{bmatrix} \begin{bmatrix} c_1 \\ c_2 \end{bmatrix} = \boldsymbol{S_1\, c} \quad (9)$$

where $\boldsymbol{S_1}$ is the solution matrix and $\boldsymbol{c}$ is the coefficient vector. Note that $\boldsymbol{S_1}$ is a function of x. Hence if this matrix is to be evaluated for a specific value of x this would be indicated as $\boldsymbol{S_1}|_{x=L}$ if for instance the slip and slip strain at $x=L$ are to be determined.

Solution for Zone II

Substituting Eq. (4b) into Eq. (1) gives the following governing equation for Zone II

$$\frac{d^2\delta}{dx^2} = \tau_f\beta - k_d\beta(\delta - \delta_1) \tag{10}$$

which can be solved by considering the homogenous and particular solution of this problem. The homogenous equation is

$$\frac{d^2\delta_h}{dx^2} + k_d\beta(\delta_h - \delta_1) = 0 \tag{11}$$

with a solution of

$$\delta_h = c_1 \sin(\lambda_2 x) + c_2 \cos(\lambda_2 x) \tag{12}$$

and in which

$$\lambda_2 = \sqrt{k_d\beta} \tag{13}$$

The particular solution is found by assuming that δ_p is a constant, hence from Eq. (10)

$$\delta_p = \delta_1 + \frac{\tau_f}{k_d} = \delta_2 \tag{14}$$

Combining the homogenous and particular solutions yields the full solution as

$$\delta = \delta_h + \delta_p = c_1 \sin(\lambda_2 x) + c_2 \cos(\lambda_2 x) + \delta_2 \tag{15}$$

Differentiating gives the slip strain as

$$\frac{d\delta}{dx} = \lambda_2 c_1 \cos(\lambda_2 x) - \lambda_2 c_2 \sin(\lambda_2 x) \tag{16}$$

Hence in matrix form, the slip and slip strain can be represented as

$$\begin{bmatrix} \delta \\ \frac{d\delta}{dx} \end{bmatrix} = \begin{bmatrix} \sin(\lambda_2 x) & \cos(\lambda_2 x) \\ \lambda_2 \cos(\lambda_2 x) & -\lambda_2 \sin(\lambda_2 x) \end{bmatrix} \begin{bmatrix} c_1 \\ c_2 \end{bmatrix} + \delta_p \begin{bmatrix} 1 \\ 0 \end{bmatrix} = \boldsymbol{S_2}\,\boldsymbol{c} + \delta_2\,\boldsymbol{e_1} \tag{17}$$

where $\boldsymbol{e_1}$ is a standard basis vector of a 2D space, that is $[1\ 0]^T$.

Solution for Zone III

Substituting Eq. (4c) into Eq. (1) gives the following governing equation for Zone III

$$\frac{d^2\delta}{dx^2} = 0 \tag{18}$$

Integrating Eq. (18) gives the slip strain

$$\frac{d\delta}{dx} = c_1 \tag{19}$$

Integrating Eq. (19) gives the slip

$$\delta = c_1 x + c_2 \tag{20}$$

In matrix representation, Eqs. (19) and (20) give

$$\begin{bmatrix} \delta \\ \frac{d\delta}{dx} \end{bmatrix} = \begin{bmatrix} x & 1 \\ 1 & 0 \end{bmatrix} \begin{bmatrix} c_1 \\ c_2 \end{bmatrix} = \boldsymbol{S_3}\,\boldsymbol{c} \tag{21}$$

Boundary Conditions

In the previous section, it was shown how the slip and slip strain can be represented by a matrix that is a function of position multiplied by a vector of constants. In this section, it will be shown how the initial value of the coefficient vector at the free end can be determined using the boundary condition at this point. It will then be shown with the second boundary condition how the coefficient vector at the loaded end can be related to the slip and load at this point.

Note that the load is zero at the end of the plate and the substrate, hence the strains are also zero. As the slip strain is equal to the difference in strain between the plate ε_p and the substrate ε_c, this implies that

$$\left.\frac{d\delta}{dx}\right|_{x=0} = \varepsilon_p\big|_{x=0} - \varepsilon_c|_{x=0} = 0 \tag{22}$$

Hence the slip and slip strain at the free end can be represented as

$$\left.\begin{bmatrix}\delta \\ \dfrac{d\delta}{dx}\end{bmatrix}\right|_{x=0} = \delta_0 \begin{bmatrix}1 \\ 0\end{bmatrix} = \delta_0 \boldsymbol{e_1} \tag{23}$$

Eq. (23) can be used to define the initial coefficient vector at the free end. Hence from Eqs. (9) and (21), the coefficient vector is given by the following for Zones I and III

$$\boldsymbol{c_1} = \delta_0 \boldsymbol{e_2};\ \delta_0 < \delta_1\ and\ \delta_0 > \delta_2 \tag{24}$$

From Eq. (17), the initial value of the coefficient vector in Zone II is given as follows

$$\boldsymbol{c_1} = (\delta_0 - \delta_2)\boldsymbol{e_2};\ \delta_1 < \delta_0 < \delta_2 \tag{25}$$

where $\boldsymbol{e_2}$ is a standard basis vector of a 2D space, that is $[0\ 1]^T$.

Note that at the loaded end, since the loads in the plate and the concrete are equal and opposite and equal to the applied load P, the slip strain is known at this position and given by

$$\left.\frac{d\delta}{dx}\right|_{x=L} = \varepsilon_p\big|_{x=L} - \varepsilon_c|_{x=L} = \frac{P}{E_p A_p} + \frac{P}{E_c A_c} = \frac{P}{EA_{eff}} \tag{26}$$

The slip and slip strain at the loaded end can then be represented as

$$\left.\begin{bmatrix}\delta \\ \dfrac{d\delta}{dx}\end{bmatrix}\right|_{x=L} = \begin{bmatrix}\Delta \\ \dfrac{P}{EA_{eff}}\end{bmatrix} \tag{27}$$

If multiple zones of solution are present along the bonded length, additional boundary conditions are obtained as the slip and slip strain are continuous across these boundaries. Hence in the next section, it will be shown how to determine the location of these transitions as well as the change in the coefficient vector **c** at these points.

Zone I-II Transition

The first transition that is considered is the transition from Zone I (linear elastic) to Zone II (softening). This occurs at the point where the slip $\delta(x) = \delta_1$. To find the location of this transition, consider that the slip at this point can be written as follows using Eq. (9)

$$\delta_1 = [\sinh(\lambda_1 x_1) \quad \cosh(\lambda_1 x_1)]\boldsymbol{c} = c_1 \sinh(\lambda_1 x_1) + c_2 \cosh(\lambda_1 x_1) \tag{28}$$

in which $\boldsymbol{c}=[c_1\ c_2]^T$. For the section with the elevation shown in Fig. 3(a), x_1 can be defined as the position at which the slip is equal to δ_1 as shown in Fig. 3(b).

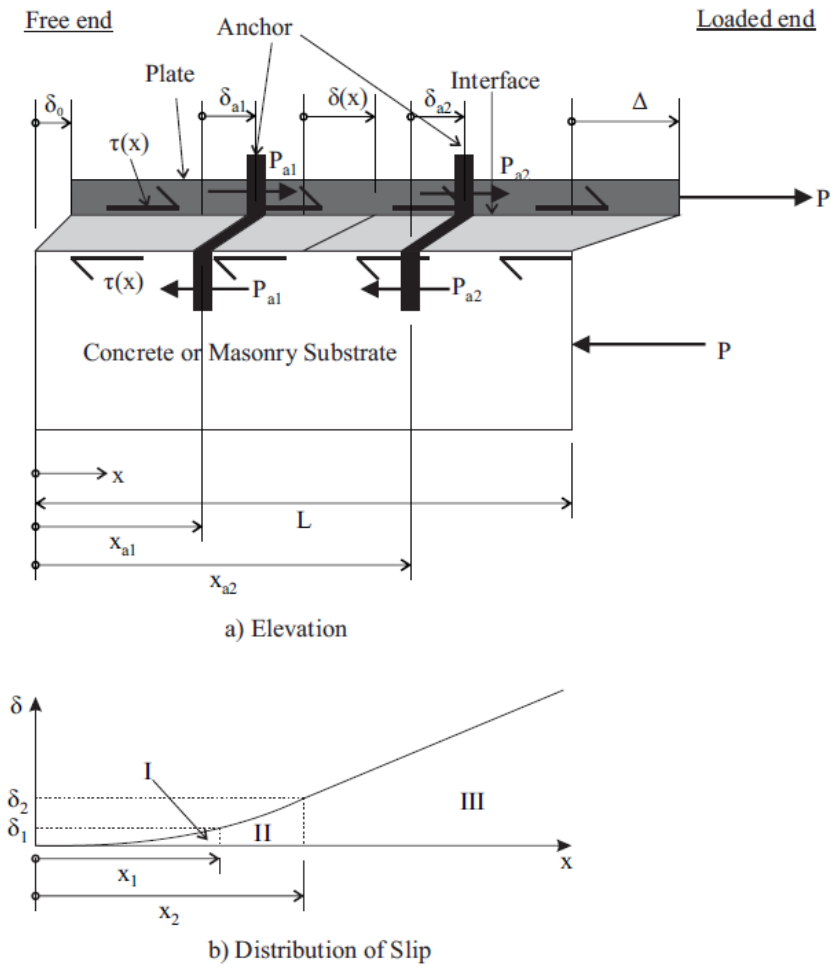

Fig. 3 EB FRP plate bonded to brittle substrate with anchors

Using the definition of the hyperbolic function in terms of exponential functions, Eq. (28) can be rewritten as

$$\delta_1 = \left(\frac{c_1 + c_2}{2}\right) e^{\lambda_1 x_1} + \left(\frac{c_2 - c_1}{2}\right) e^{-\lambda_1 x_1} \tag{29}$$

Multiplying through by $exp(\lambda_1 x_1)$, gives

$$0 = \left(\frac{c_1 + c_2}{2}\right) \left(e^{\lambda_1 x_1}\right)^2 - \delta_1 e^{\lambda_1 x_1} + \left(\frac{c_2 - c_1}{2}\right) \tag{30}$$

Equation (30) is quadratic in terms of $exp(\lambda_1 x_1)$, so applying the quadratic formula gives

$$e^{\lambda_1 x_1} = \frac{\delta_1 \pm \sqrt{\delta_1^2 + c_1^2 - c_2^2}}{c_1 + c_2} \tag{31}$$

Hence the transition point x_1 is

$$x_1 = \frac{1}{\lambda_1} \ln\left(\frac{\delta_1 + \sqrt{\delta_1^2 + c_1^2 - c_2^2}}{c_1 + c_2}\right) \tag{32}$$

At the boundary, the slip and slip strains from each zone are equal. Hence from Eqs. (9) and (17)

$$\boldsymbol{S_1}|_{x=x_1} \boldsymbol{c_i} = \boldsymbol{S_2}|_{x=x_1} \boldsymbol{c_{i+1}} + \delta_2 \boldsymbol{e_1} \tag{33}$$

Rearranging gives

$$\boldsymbol{c_{i+1}} = (\boldsymbol{S_2})^{-1}|_{x=x_1} \boldsymbol{S_1}|_{x=x_1} \boldsymbol{c_i} - \delta_2 (\boldsymbol{S_2})^{-1}|_{x=x_1} \boldsymbol{e_1} = \boldsymbol{T_{12}} \boldsymbol{c_i} - \delta_2 \begin{bmatrix} \sin(\lambda_2 x_1) \\ \cos(\lambda_2 x_1) \end{bmatrix} \tag{34}$$

Zone II-III Transition

The second transition that is considered is the transition from Zone II (softening) to Zone III (debonding) and this occurs when $\delta(x)=\delta_2$. From Eq. (17), the slip at this position is given by

$$\delta_2 = [\sin(\lambda_2 x_2) \quad \cos(\lambda_2 x_2)]\boldsymbol{c} + \delta_2 \tag{35}$$

which rearranges to

$$0 = c_1 \sin(\lambda_2 x_2) + c_2 \cos(\lambda_2 x_2) \tag{36}$$

Note that x_2 is the position at which the slip is equal to δ_2 as shown in Fig. 3(b).

Using the half-angle tangent substitution, this can be rewritten as

$$-c_2\left[\tan\left(\frac{\lambda_2 x_2}{2}\right)\right]^2 + 2c_1\left[\tan\left(\frac{\lambda_2 x_2}{2}\right)\right] + c_2 = 0 \tag{37}$$

Using the quadratic formula, this is solved to yield

$$\tan\left(\frac{\lambda_2 x_2}{2}\right) = \frac{-2c_1 \pm \sqrt{4c_1^2 + 4c_2^2}}{-2c_2} = \frac{c_1}{c_2} \pm \sqrt{1 + \left(\frac{c_1}{c_2}\right)^2} \tag{38}$$

Rearranging this for x_2 yields

$$x_2 = \frac{2}{\lambda_2}\left\{\arctan\left[\frac{c_1}{c_2} - \sqrt{1 + \left(\frac{c_1}{c_2}\right)^2}\right]\right\} \tag{39}$$

Equating Eqs. (17) and (21), the change in the coefficient vector $\boldsymbol{c}$ can be determined at this point and it is given by

$$\boldsymbol{S_2}|_{x=x_2}\, \boldsymbol{c_i} + \delta_p\, \boldsymbol{e_1} = \boldsymbol{S_3}|_{x=x_2}\, \boldsymbol{c_{i+1}} \tag{40}$$

which can be rearranged to give

$$\boldsymbol{c_{i+1}} = (\boldsymbol{S_3})^{-1}\big|_{x=x_2} \boldsymbol{S_2}|_{x=x_2} \boldsymbol{c_1} + \delta_p (\boldsymbol{S_3})^{-1}\big|_{x=x_2} \boldsymbol{e_1} = \boldsymbol{T_{23}} \boldsymbol{c_i} + \delta_2 \boldsymbol{e_2} \tag{41}$$

Inclusion of the anchor

The arrangement in Fig. 1 has now been modified to include a series of anchors as illustrated in Fig. 3(a). The anchor serves to transfer load from the plate into the substrate at a discrete point. The load P_a that is transferred is a function of the assumed load-slip (P_a-δ_a) relationship of the anchor. An example load-slip relationship is illustrated in Fig. 4 which is of the functional form considered by Zhang et al. (2017).

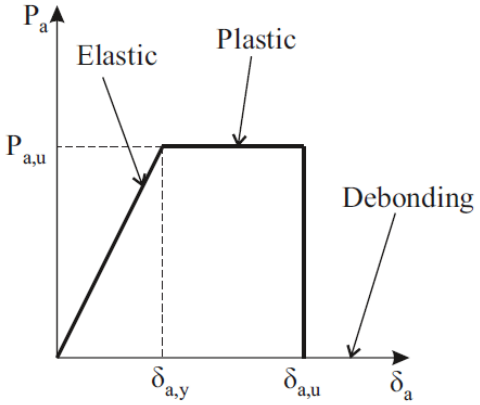

Fig. 4 Elastic-plastic-debonding relationship defining the P_a-δ_a behaviour of an anchor

It is considered that the slip is continuous over the anchor, however due to the discrete transfer of load between the plate and the substrate, there is a discontinuity in slip strain. To determine the value of this discontinuity, consider that the load in the plate to the right of the anchor is given as

$$P_{p,R} = P_{p,L} + P_a \tag{42}$$

Similarly, the load in the substrate to the right of the anchor is given as

$$P_{c,R} = P_{c,L} - P_a \tag{43}$$

From this, the change in slip strain is given as

$$\left.\frac{d\delta}{dx}\right|_{x_a,R} - \left.\frac{d\delta}{dx}\right|_{x_a,L} = \left(\frac{P_{p,L} + P_a}{E_p A_p} - \frac{P_{c,L} - P_a}{E_c A_c}\right) - \left(\frac{P_{p,L}}{E_p A_p} - \frac{P_{c,L}}{E_c A_c}\right) = \frac{P_a}{EA_{eff}} \tag{44}$$

Eq. (44) is then used in the next section to show how the coefficient vector changes across each anchor as a function of the zone of solution.

Effect of an anchor in Zone I ($\delta_a<\delta_1$)

From Eqs. (9) and (44), the change in slip and slip strain at the anchor is given as

$$\begin{bmatrix} 0 \\ \dfrac{P_a}{EA_{eff}} \end{bmatrix} = \boldsymbol{S_1}|_{x=x_a}(\boldsymbol{c_{i+1}} - \boldsymbol{c_i}) \tag{45}$$

where the slip is continuous over the anchor. Rearranging gives the change in the coefficient vector

$$\boldsymbol{c_{i+1}} - \boldsymbol{c_i} = (\boldsymbol{S_1})^{-1}|_{x=x_a} \begin{bmatrix} 0 \\ \dfrac{P_a}{EA_{eff}} \end{bmatrix} = \frac{P_a}{\lambda_1 EA_{eff}} \begin{bmatrix} \cosh(\lambda_1 x_a) \\ -\sinh(\lambda_1 x_a) \end{bmatrix} \tag{46}$$

Effect of an anchor in Zone II ($\delta_1<\delta_a<\delta_2$)

From Eqs. (17) and (44), the change in slip and slip strain at the anchor is

$$\begin{bmatrix} 0 \\ \dfrac{P_a}{EA_{eff}} \end{bmatrix} = \boldsymbol{S_2}|_{x=x_a}(\boldsymbol{c_{i+1}} - \boldsymbol{c_i}) \tag{47}$$

and rearranging gives the change in the coefficient vector

$$\boldsymbol{c_{i+1}} - \boldsymbol{c_i} = (\boldsymbol{S_2})^{-1}|_{x=x_a} \begin{bmatrix} 0 \\ \dfrac{P_a}{EA_{eff}} \end{bmatrix} = \frac{P_a}{\lambda_2 EA_{eff}} \begin{bmatrix} \cos(\lambda_2 x_a) \\ -\sin(\lambda_2 x_a) \end{bmatrix} \tag{48}$$

Effect of an anchor in Zone III ($\delta_a>\delta_3$)

From Eqs. (21) and (44), the change in slip and slip strain at the anchor is

$$\begin{bmatrix} 0 \\ \dfrac{P_a}{EA_{eff}} \end{bmatrix} = \boldsymbol{S_3}|_{x=x_a}(\boldsymbol{c_{i+1}} - \boldsymbol{c_i}) \tag{49}$$

and rearranging gives the change in the coefficient vector

$$\boldsymbol{c_{i+1}} - \boldsymbol{c_i} = (\boldsymbol{S_3})^{-1}|_{x=x_a} \begin{bmatrix} 0 \\ \dfrac{P_a}{EA_{eff}} \end{bmatrix} = \frac{P_a}{EA_{eff}} \begin{bmatrix} 1 \\ -x_a \end{bmatrix} \tag{50}$$

LOAD-SLIP BEHAVIOUR OF AN FRP PLATE WITH ANCHORS

The expressions derived in the previous section can be used to parametrically define the global load-slip (P-Δ) relationship in terms of the free end slip δ_0. This procedure is performed by considering that the slip and slip strain at any point is given by the solution matrix $\boldsymbol{S}$ multiplied by the coefficient vector $\boldsymbol{c}$ as shown by Eqs. (9), (17) and (21). The solution matrix $\boldsymbol{S}$ is a function of the position x as well as the zone of the bond-slip relationship, while the coefficient vector $\boldsymbol{c}$ is constant between zone boundaries and anchors. Hence this system can be solved by

finding the initial value of the coefficient vector $\boldsymbol{c}$ at the free end using the boundary condition in Eq. (23). The value of the coefficient vector $\boldsymbol{c}$ can then be determined as it crosses zone boundaries and anchors as it is propagated from the free end towards the loaded end. Once the value at the loaded-end is determined, the slip Δ and load P can be evaluated. This procedure is outlined in the flow chart in Fig. 5. Note that when imposing δ_0 values, a constant increment is not appropriate as δ_0 does not vary linearly with the loaded end slip as illustrated in Fig. 6, especially for long bonded lengths. Instead, it is seen that the free end slip remains very small until the plate is almost debonded. The free end slip then proceeds to increase rapidly as debonding occurs. Good results were, however, obtained using logarithmically spaced values of δ_0. Snapback, indicated by the reduction in free end slip Δ, could also be seen for the long bonded length in Fig. 6.

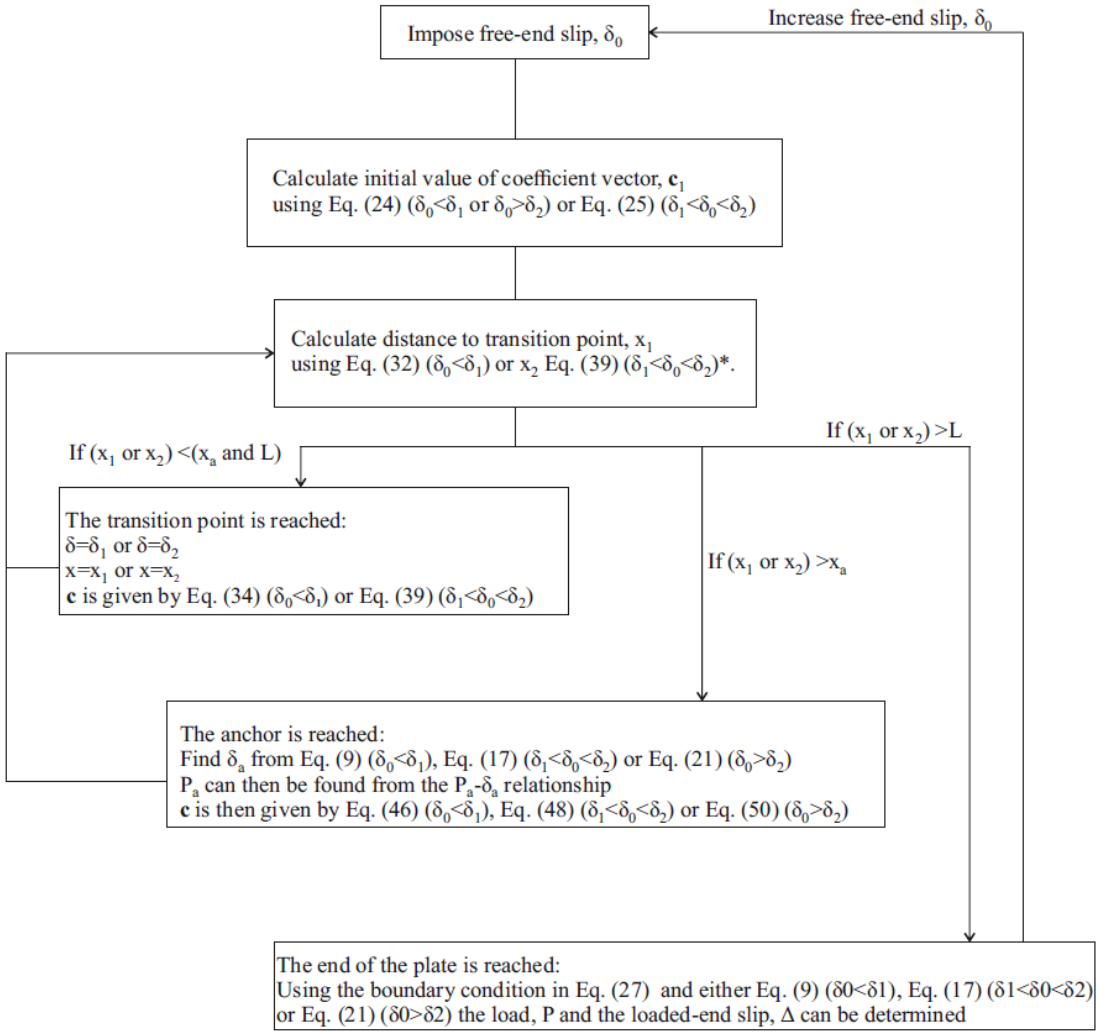

* Note that if δ0>δ2 then transition distance can be assumed to be infinite

Fig. 5 Flow chart for analytical solution

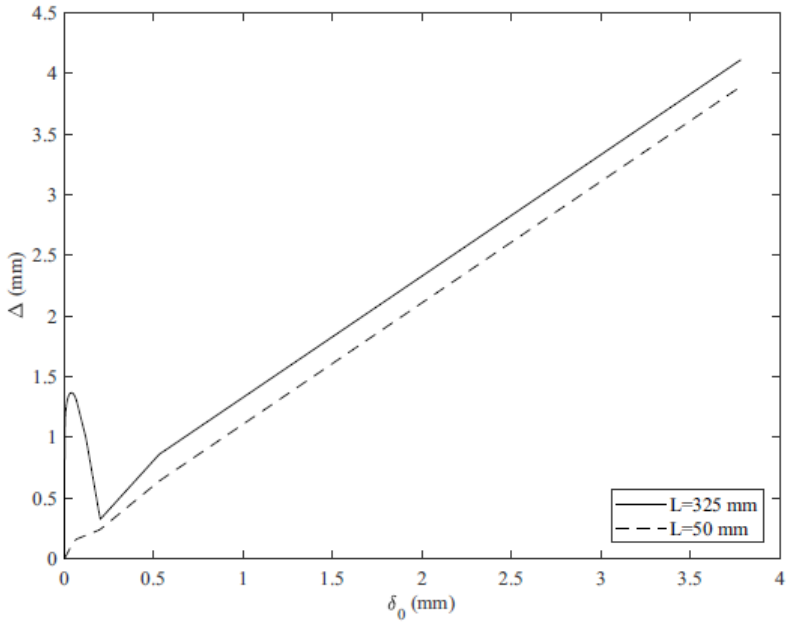

Fig. 6 Typical variation of δ_0 with Δ.

Note that if the approach were to be applied to a linear descending bond stress-slip relationship instead of a bilinear relationship a slight modification is required. That is the case as full interaction ($\delta=0$, $d\delta/dx=0$) can be obtained at some point for a finite length prism which is not the case for bilinear relationships with a finite initial stiffness. Hence in this case initially the position of full interaction is incremented moving from the loaded to the free end. When the free end is reached then free end slips are incremented as usual.

VALIDATION

To validate the proposed mathematical formulation, its predictions are compared to the numerical solution produced by (Zhang et al. 2017) and the experimental results produced by (Zhang 2013) for the global load-slip behaviour of carbon fibre-reinforced polymer (CFRP) plates anchored with FRP anchors. The geometry of the specimens used for the validation is illustrated in Fig. 7. The elastic modulus of the CFRP plate was 227 GPa and the assumed elastic modulus of the concrete substrate was 31.5 GPa which was determined using the AS3600-2009 (Standards Australia 2009) code approach. A bond-slip relationship of the concrete-CFRP interface of the form shown in Fig. 2 was assumed, where the peak bond stress, τ_f is 5.99 MPa, δ_1 is 0.07 mm and δ_2 is 0.2 mm. An elastic-plastic-debonding load slip relationship was assumed for the anchor with a peak load of $P_{a,u}$ of 19.6 kN and this load is reached when the slip at the anchor, $\delta_{a,y}$ is 0.53 mm. The debonding slip, $\delta_{a,u}$ of the anchor is 3.82 mm. The bond-slip relationship of the interface and the load-slip relationship of the anchor are parameterised with the same values as those used by (Zhang et al. 2017) for their analysis.

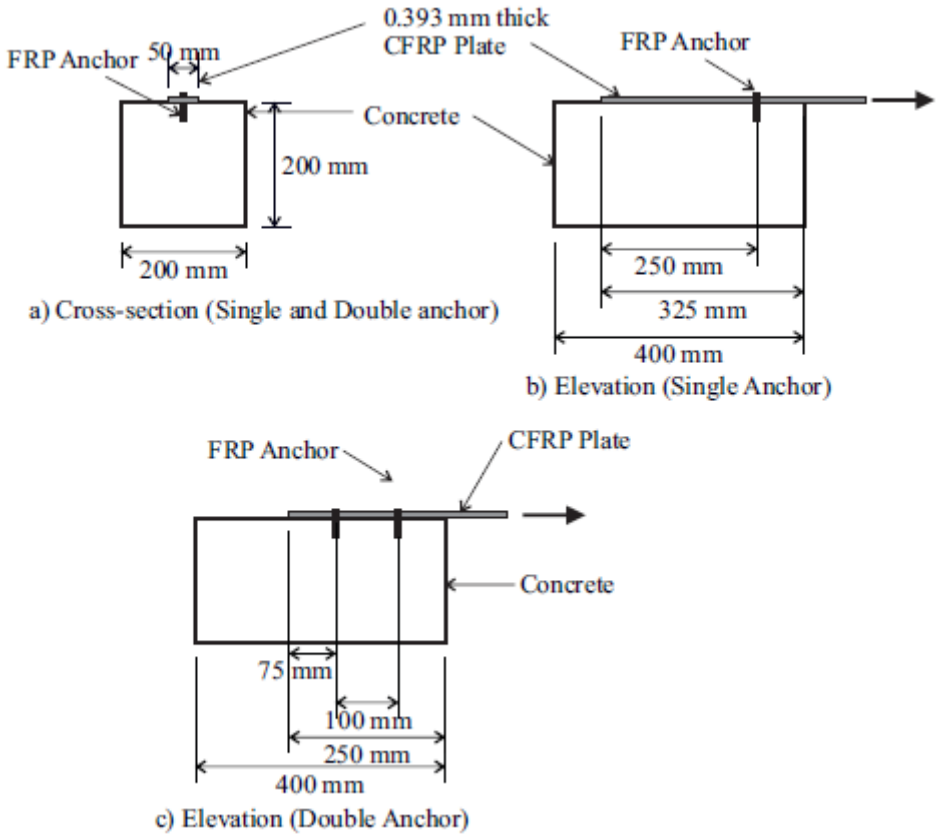

Fig. 7 Geometry of tests used for validation

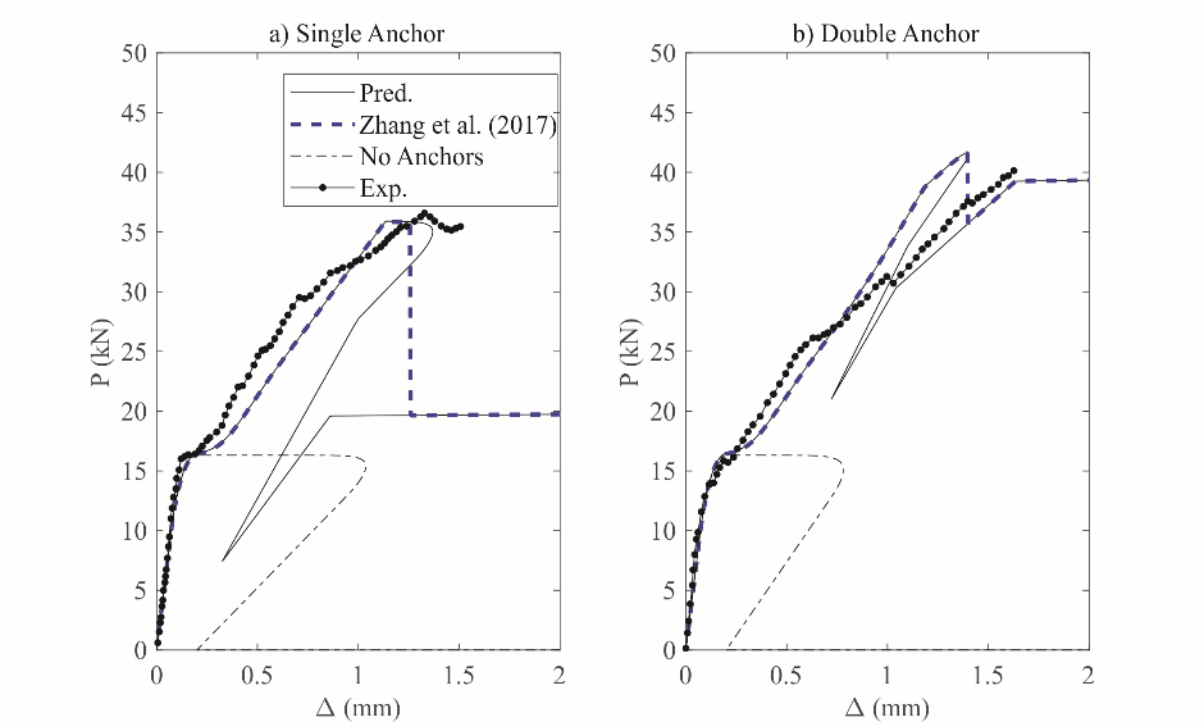

Fig. 8 Comparison of global load-slip response

In Figs. 8(a) and 8(b), the generated global load-slip relationship (labelled 'Pred.') is compared to the numerical analysis proposed by Zhang et al. (2017) [labelled Zhang et al (2017)] and the experimental results in Zhang (2013) (labelled 'Exp.'). The approach in this paper and the approach by Zhang et al. (2017) give identical results except that the approach in this paper

captures the snapback phenomenon. This is to be expected as both the model in this paper and the model presented by Zhang et al. (2017) are based on the same fundamental mechanics. Zhang et al. (2017) expresses the solution in terms of a finite difference scheme, whereas, this paper uses the concept of a coefficient vector that becomes transformed at anchor locations and zone boundaries. The advantage of the proposed method is that it removes the need for numerical root finding which increases the computational efficiency.

A notable feature of the proposed method is that it has the capability to capture snapback; that is, a reversal in Δ with continued increase to δ_0, which is an inherent feature of the response over long bonded lengths (as seen in Fig. 6). While snapback is not a physical phenomenon in the sense of being experimentally observable, it does tell us about the mechanical stability of the debonding process. That is, the presence of snapback is indicative of a progressive shift of the load transfer zone along the member which is eventually met by sudden debonding failure under increasing loaded-end slip (Vaculik et al. 2018b). Note that the snapback branch is bypassed in Zhang et al. (2017) as the model operates under loaded-end slip (Δ) control.

PARAMETRIC STUDY

As the solution methodology has been validated, parametric studies are performed to investigate the load-slip behaviour of FRP plated sections with anchors. In Fig. 9, the geometry for each parametric study is shown. The bond stress-slip of the interface, the load-slip of the anchor and the other material properties are the same as that assumed in the 'Validation' section. Hence, the case investigated here represents the case where $\delta_2/\delta_{a,y} \approx 0.4$ and if this was significantly different it is expected that the observations would change. This was the ratio observed in (Zhang 2013) experimental investigation.

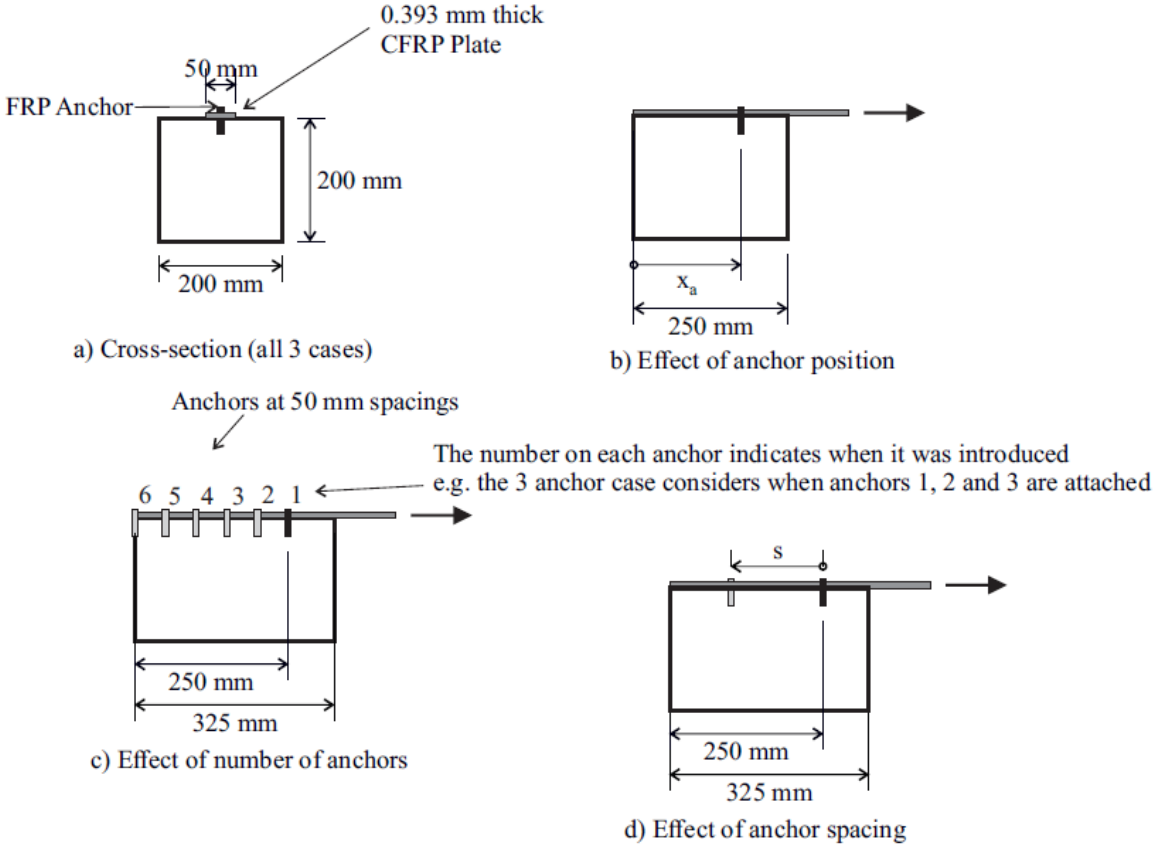

Fig. 9 Geometry of sections for parametric study

Effect of the anchor position for a single anchor

Fig. 10 demonstrates the influence of the position of a single anchor, x_a, on the load-slip relationship, maximum load, and slip at debonding. From part (a) and part (b) it can be seen that moving the anchor from the free end toward the loaded end causes a progressive increase to the peak system load, P_{max}. For x_a within 0 and 30 mm the maximum load before debonding (solid line) remains approximately constant and equal to the capacity of the bond, P_{ic}. Note however that this load is surpassed once the plate debonds and the anchor reaches its full capacity (dashed line). This corresponds to the case where significant loads are developed in the anchor only after the plate has already completely debonded. As the anchor is moved toward the loaded end (x_a between 30 and 185 mm), the amount of force it can develop whilst P_{ic} is still active progressively increases. Beyond anchor location x_a = 185 mm the load approximately plateaus as both the anchor and interfacial bond are now able to reach their full capacities concurrently.

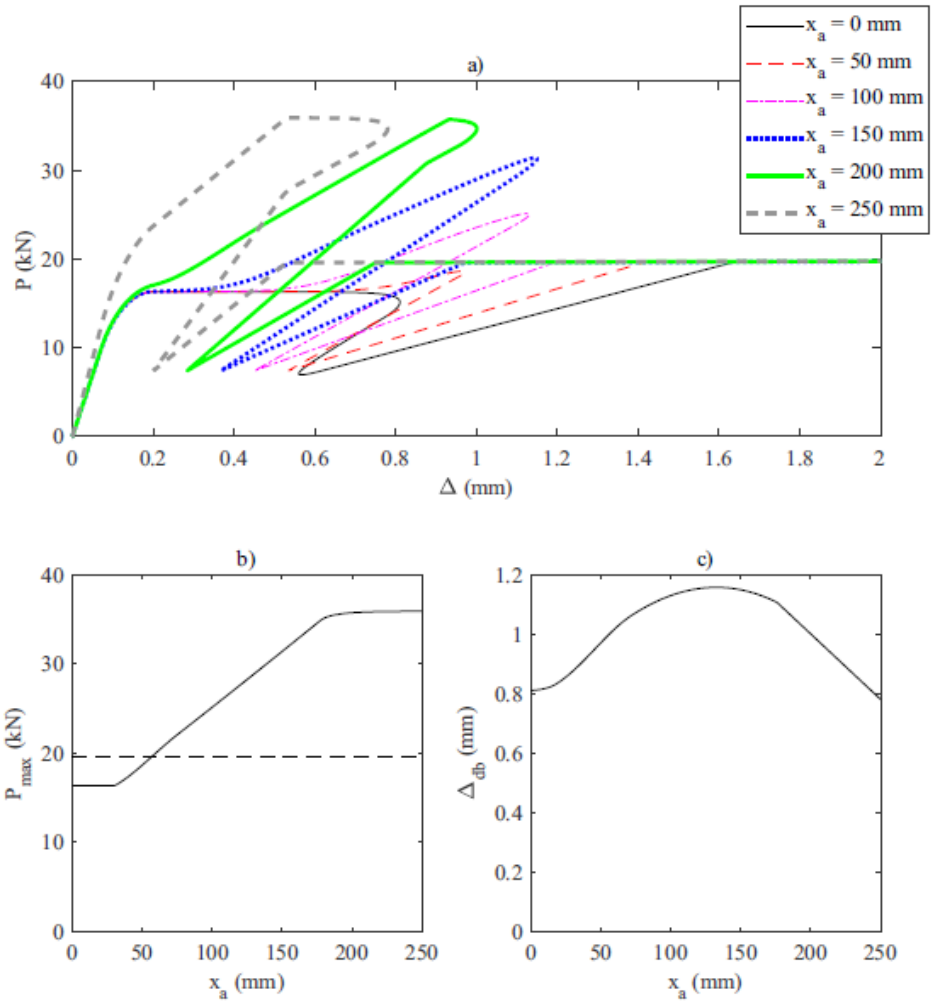

Fig. 10 Effect of anchor position on maximum load and slip at debonding

The slip at debonding is also investigated in Fig. 10(c) and it can be seen that if the anchor is moved towards the loaded end then the slip at debonding increases until the anchor is 130 mm away from the loaded end. After this, the slip reduces as the anchor is moved. The slip initially increases as the anchor is moved towards the loaded end. This is the case, because as the slip at the anchor increases the load increases, resulting in a greater slip strain and therefore a greater loaded end slip. The reduction which occurs at anchor locations greater than x_a = 145 mm arises because this increased slip strain is being imposed over a shorter length which results

in a reduced end slip. From this, it can be seen that the load that can be resisted is maximum when the anchor is at the loaded end; however, the slip before debonding is reduced, and to maximise this slip at debonding the anchor needs to be placed near the centre of the plate.

Effect of adding additional anchors

The effect of adding an additional anchor is investigated using the configuration shown in Fig. 9(c). Note that in the load-slip relationship in Fig. 11(a) snapback has been removed to improve clarity. The influence of the number of anchors is shown in Fig. 11(b) and the slips at debonding in Fig. 11(c). It can be seen that adding extra anchors significantly increases the load that can be carried both before and after debonding. The increase however reduces with each additional anchor. Additional anchors also increase the load to cause debonding of the plate. Note that if enough anchors are added the peak load occurs after the plate has debonded. The slip at debonding also increases as anchors are added.

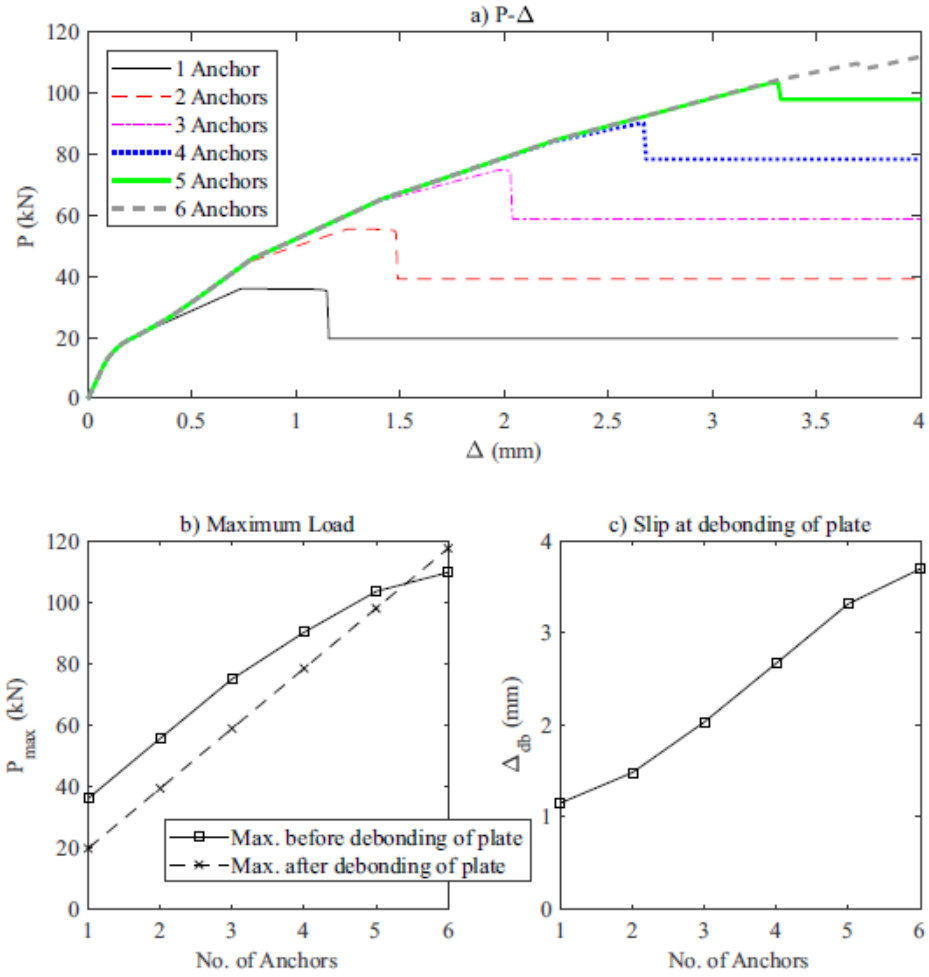

Fig. 11 Effect of additional anchors

Effect of anchor spacing with 2 anchors

In Fig. 12 the effect of anchor spacing as shown in Fig. 9(d) is investigated. Note that in Fig. 12(a) the snapback portion of the curve has again been removed for clarity. It is seen in Fig. 12(b) that the maximum load possible first decreases as the spacing between the anchors s increases. Initially this rate of decrease is small. This is followed by a rapid increase at 78 mm upon which it plateaus again at a spacing of 220 mm. The slip at debonding increases in Fig. 12(c) until at a spacing of 78 mm after it increases. This is a similar trend that was observed to moving a single anchor where the maximum load is increased by placing anchors near the loaded end while the debonding slip will increase to a maximum value and decrease as the

anchors are moved towards the loaded end. This indicates that the most efficient spacing is that which produces the highest slip and therefore load in each of the anchors. This occurs in this case when the spacing is reduced.

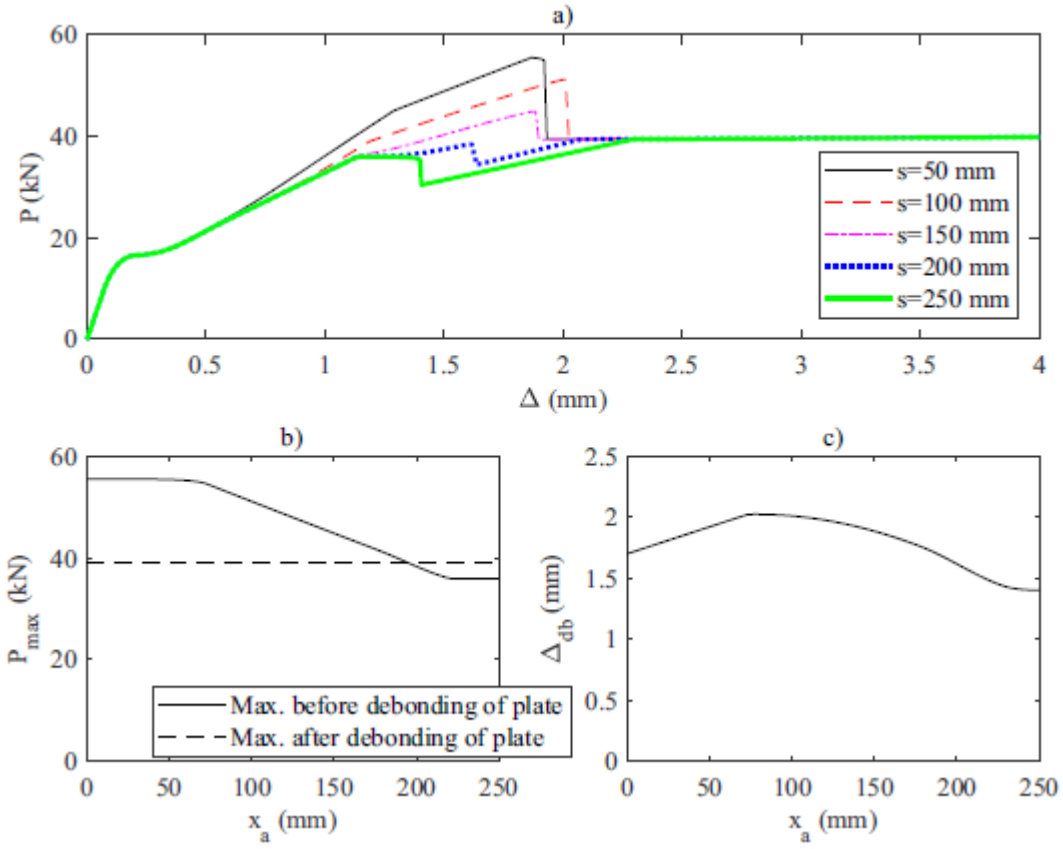

Fig. 12 Effect of anchor spacing

BEHAVIOUR OF SYSTEM

The model developed in this paper can also be used to determine the variation in shear stress τ and slip δ along the plate. This is illustrated in Fig. 13 for the single anchor case and in Fig. 14 for the double anchor case from the validation. Note that the following analysis is specific to the case considered in the validation and is based on the specimen geometry and material properties of (Zhang et al. 2017). For situations where the material properties vary significantly from these the observations reported here will change, particularly if the assumption that $\delta_{a,y}$ is significantly larger than δ_2 does not hold.

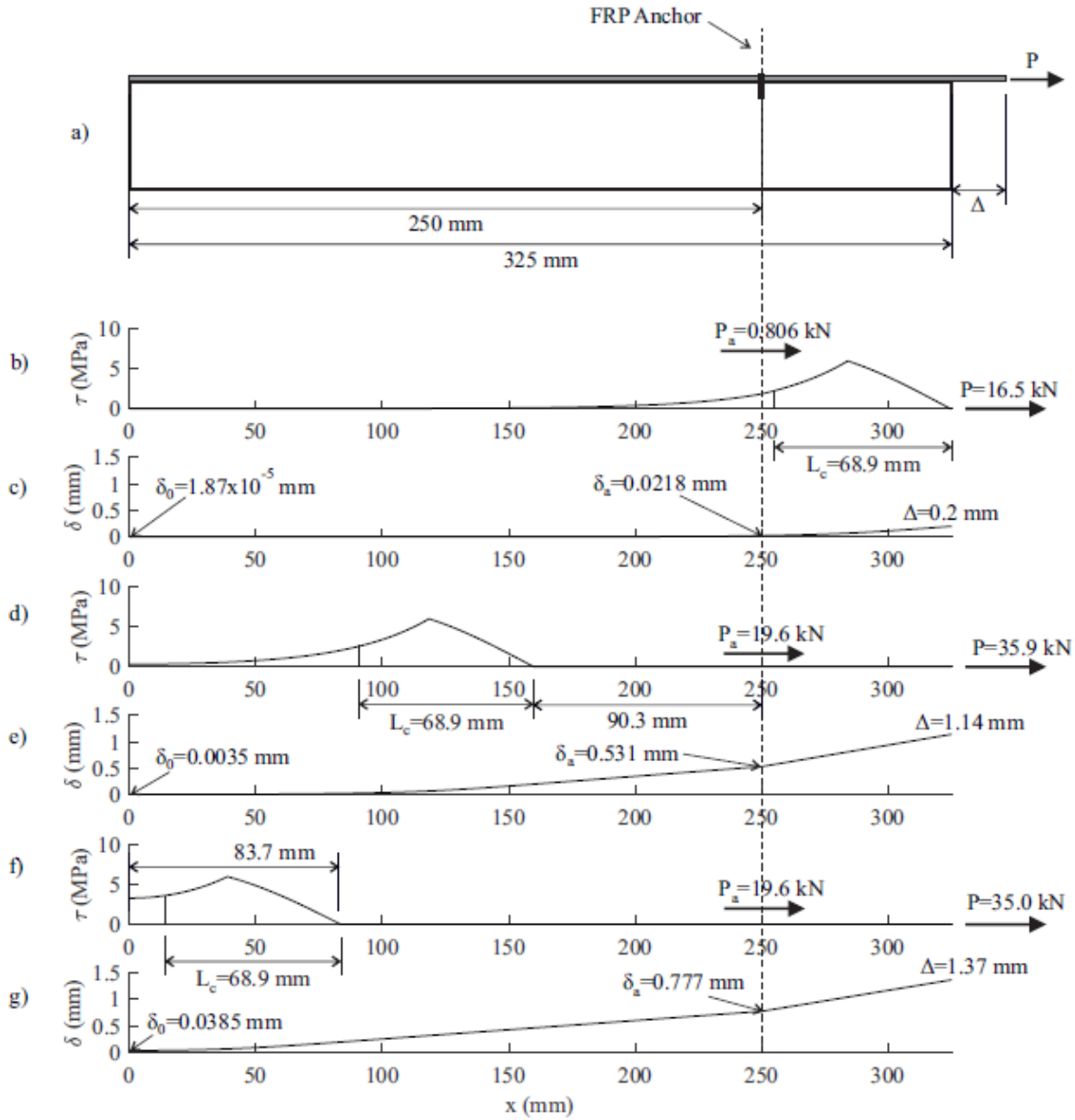

Fig. 13 Variation of δ and τ for a single anchor; (a) elevation of setup; (b,c) τ and δ when $\Delta=\delta_2$; (d,e) τ and δ at maximum P; (f,g) τ and δ at complete debonding of plate

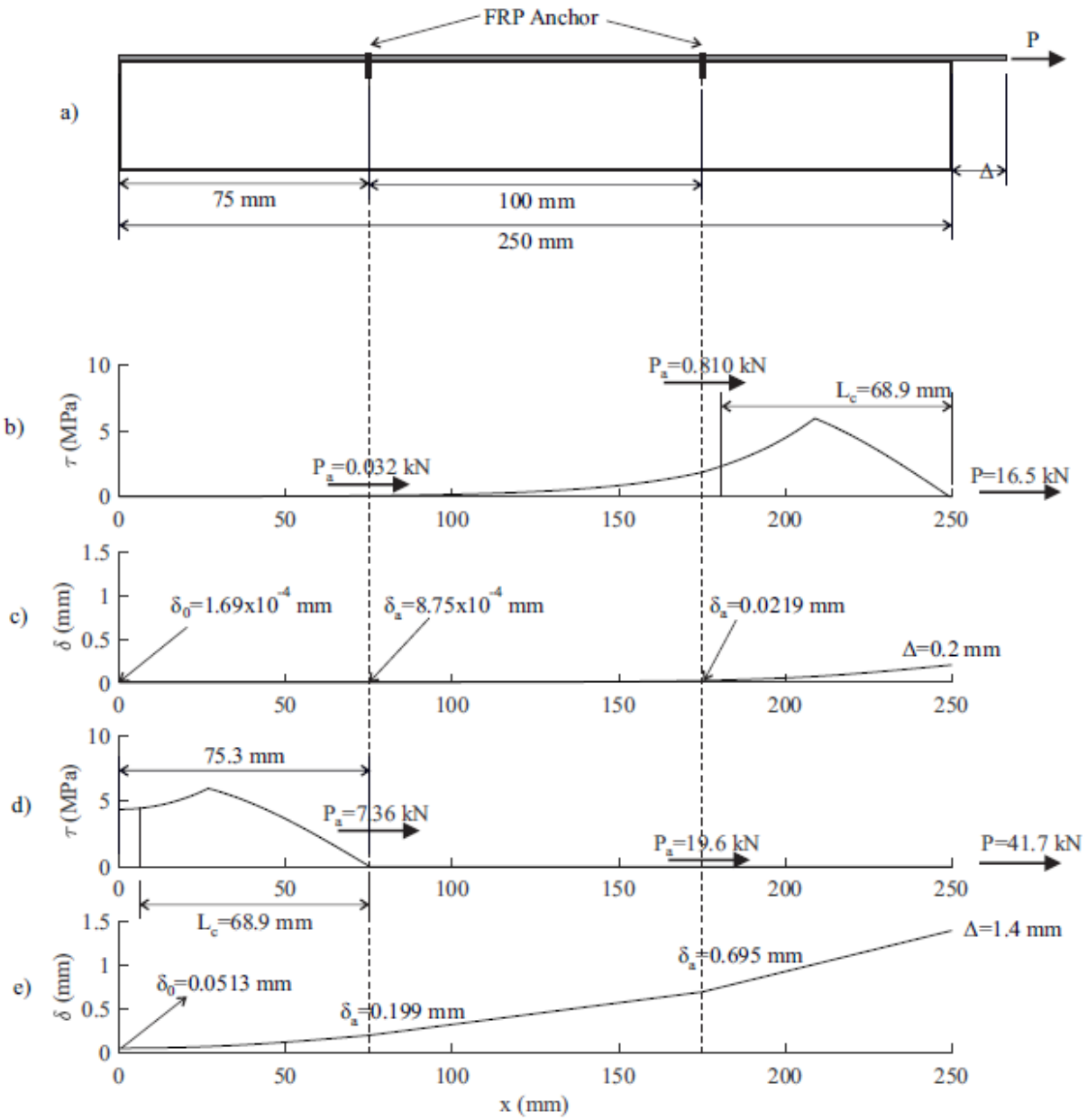

Fig. 14: Variation of δ and τ for two anchors; (a) elevation of setup; (b,c) τ and δ when $\Delta=\delta_2$; (d,e) τ and δ at maximum P and complete debonding of plate

To analyse the systems in Figs. 13 and 14, a number of key parameters are evaluated. The first is the IC debonding load P_{IC} which is taken to be

$$P_{IC} = \sqrt{2G_f L_P E_p A_p} \tag{51}$$

and which represents the peak load for a linear descending bond stress-slip relationship or the asymptotic peak load for specimens with a bilinear bond stress-slip relationship without friction.

It is also assumed that the effective axial stiffness of the system EA_{eff} is the same as that of the plate E_pA_p. This assumption has been taken on the basis that a typical axial stiffness of the plate is 4.44×10^6 N while the axial stiffness of the system is 4.46×10^6 N [see appendix A for full detail of the worked example which is based on the test specimens considered by Zhang (2013)]. As the axial rigidity of the substrate is small relative to that of the plate it has little

effect on the overall stiffness of the system and hence can be ignored without a significant loss of accuracy. The fracture energy G_f is calculated as the area under the bond stress-slip relationship which in the case of a bilinear relationship is $0.5\tau_f\delta_2$. For the specific material properties being considered, this equates to 0.599 N/mm. Together these properties give an IC debonding resistance of

$$P_{IC} = \sqrt{2G_f L_P E_p A_p} P_{IC} = \sqrt{2\left(0.599\frac{N}{mm}\right)(50\ mm)(4.46\times 10^6 N)} = 16.3\ kN \quad (52)$$

and a critical length for a bilinear bond-slip

$$L_c = \frac{\pi}{2\lambda_2} = \frac{\pi}{2(0.0228\ mm^{-1})} = 68.9\ mm \quad (53)$$

Single Anchor Case

First consider the single anchor case from the validation. The cross-section is shown in Fig. 7(a), the elevation is shown in Fig. 7(b) and the material properties are defined in the validation. The slip and shear stress distributions for key points are illustrated in Figure 13.

In Figs. 13(b-c), the first point that is considered is when the plate initiates debonding at the loaded end. At this stage the load in the anchor is small, as the slip in the anchor (0.0218 mm) in Fig. 10b is much smaller than the yield slip of the anchor of 0.53 mm and also much smaller than the debonding slip of the plate of 0.2 mm. At this point, a load of 15.7 kN is developed due to the interfacial bond of the plate which is near the IC debonding load.

After IC debonding, the shear stress and slip distributions are illustrated for the maximum load in the plate, as shown in Figs. 13(d-e). This is obtained when the anchor yields. In this situation 16.3 kN of the total load is developed by the plate (which is equal to the IC debonding load). At this stage, a 165.2 mm length of plate has debonded (that is 90.3 mm plus 75 mm). Note that the minimum distance beyond the point at which the plate debonds required to yield the anchor is given by

$$x_y = \frac{\delta_y - \delta_2}{\left(\frac{P_{IC}}{E_p A_p}\right)} = \frac{0.53\ mm - 0.2\ mm}{\left(\frac{16300\ N}{4.46\times 10^6 N}\right)} = 90.3\ mm \quad (54)$$

This is the same value as the 50.3 mm observed between the point of debonding and the anchor shown in Fig. 13(d).

The next situation that is considered in Figs. 13(f-g) is when the plate completely debonds. In this case, 15.4 kN can be attributed to the interfacial bond of the plate and 19.6 kN to the anchor so that both the adhesive bond and the anchorage are contributing significantly to the overall strength. Note that the actual distance from the free end to the point of debonding is somewhat greater than the actual critical length.

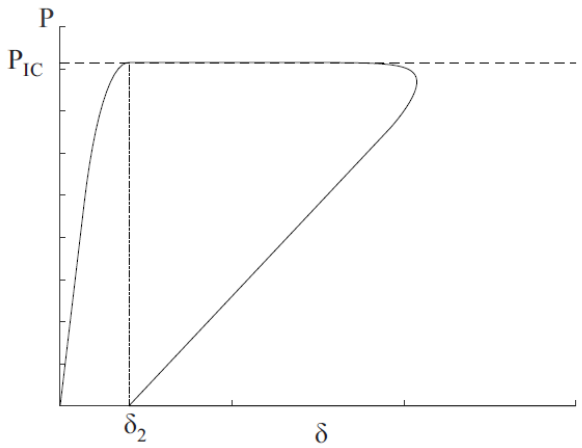

Fig. 15: Load-slip relationship of an unanchored bonded joint.

Two-Anchor Case

Next consider the double anchor case from the validation. The cross-section is shown in Fig. 7(a), the elevation is in Fig. 7(c) and the material properties are defined in the validation. The slip and shear stress distributions for key points are illustrated in Figure 14.

In Figs. 14(b-c) the shear stress and slip distributions are illustrated for the double anchor case when the plate initiates debonding. The load due to the adhesive bond transfer is again 15.7 kN and the load is again small in each anchor. This is almost identical to the single anchor case in Fig. 13(b-c); that is, the addition of the second anchor has virtually no effect on the initiation of debonding.

In Figs. 14(d-e), the shear stress and slip distributions are illustrated for the maximum load in the plate. The load due to the interfacial bond of the plate is given by 14.7 kN and the bonded length is less than the critical length. The second anchor has yielded at this stage, however the first anchor is still in the elastic range. This suggests that a larger maximum load could be achieved if the first anchor was placed such that 90.3 mm separated the anchor and the point where debonding initiates. This can be ensured by placing the anchor a minimum of 159.2 mm from the loaded end (68.9 mm + 90.3 mm).

It can be seen from the above analyses that the strengths obtained from pull tests are unlikely to give the bond properties directly but depend to a large extent on the geometry of the plate and anchors. However they do indicate that the bond properties can be extracted from the test data with the use of the model developed in this paper as will be illustrated in the next section.

CALIBRATION OF PARAMETERS FROM TESTS

Determination of the model-defining parameters in the interface bond-slip model and the anchor load-slip model using experimental pull-push tests can be of considerable research value, as the established local behaviour may be subsequently used to predict the general behaviour of retrofits. By adopting the three-parameter bilinear model for the bond-slip behaviour at the interface (Fig. 2) together with the three-parameter elastic-plastic-debonding model for the anchor (Fig. 4), the behaviour of the overall system becomes defined by a total of six parameters. However, it imposes a significant computational and data-interpretation effort to simultaneously fit this number of parameters to data from a single pull-push test that involves both a bonded FRP interface and an anchor (Vaculik et al. 2018a). This difficulty can

be overcome for a subset of pull-push tests through a proposed calibration strategy involving two tests. The first test involves a specimen with bonded plate only (no anchor), which is used to calibrate the three parameters defining the τ-δ model at the interface. The second test is performed on a system comprising a bonded plate in addition to an anchor, which (by assuming the previously determined τ-δ model) is used to calibrate the remaining three parameters in the P_a-δ model controlling the anchor. This procedure will now be outlined in more detail.

Calibration of the interface bond-slip model

For the following approach to be applicable, the bonded length must exceed L_c such that a long bonded length is achieved. This can be checked by observing whether a plateau is present in the experimental load-slip relationship for the unanchored bonded joint.

For an unanchored bonded joint, the maximum load is P_{IC}, and hence Eq. (51) can be rearranged to yield the fracture energy G_f. The plateau in the load-slip relationship begins when the slip at the loaded end Δ is equal to δ_2, hence this parameter is identified from this point. The maximum bond stress τ_f can then be found from G_f. The value of δ_1 can then be calibrated based on comparing the experimental and predicted load-slip relationships while varying δ_1 to minimise the mean square error between the curves. Hence, by using this additional information, the complexity of the problem has been reduced as only one, rather than three parameters, require calibration.

Calibration of the anchor load-slip model

In order to apply the following approach for an anchored bonded joint the anchor must be located a distance greater than $L_c + x_y$ from the free end of the plate and with $\delta_{a,y} > \delta_2$, The arising global load-slip relationship is shown in Fig. 16. These two conditions can be checked by observing whether there is a plateau in the experimental load-slip relationship and the second condition can be checked by observing whether the initial response of the anchored and unanchored pull-push tests is the same. Assuming that $\delta_2 < \delta_{a,y}$, the plate and anchor can be considered separately. Hence at the maximum load, the load due to the interfacial bond of the plate is P_{IC} while the load in the anchor is $P_{a,u}$. The slip $\delta_{a,y}$ can then be obtained by comparing the predicted and experimental load-slip relationships and also varying $\delta_{a,y}$ to minimise the mean square error.

Note that the debonding slip δ_{db} can be determined by considering that once the plate has completely debonded, the slip at the loaded end is given by

$$\Delta = \delta_a + \frac{P_{max}}{E_p A_p}(L - x_a) \tag{55}$$

Eq. (55) can be rearranged give the slip at the anchor when the plate debonds.

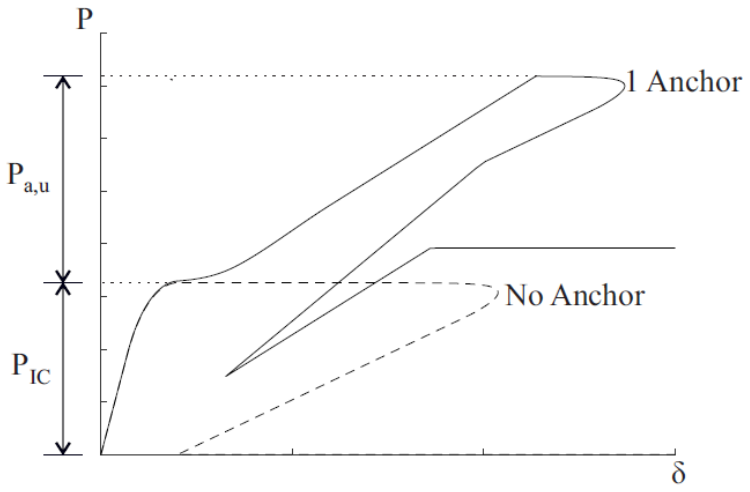

Fig. 16: Load-slip relationship of anchored bonded joint

Example

As an example of this process the bond-slip relationship of the interface and the load-slip relationship of the anchor will be calibrated for the test results produced by (Zhang 2013). The unanchored tests are taken from series CN 1~3 and the anchored test is taken from PL-325-3 in Zhang (2013). The anchored specimen is the same as the single anchor specimen in the validation. The unanchored specimens had a bonded length of 250 mm and otherwise exactly the same as the anchored specimen. Key properties extracted from the unanchored tests are summarised in Table 1. P_{IC} was estimated from the maximum load and δ_2 was determined by considering the slip at which the maximum load was reached.

From Table 1 the average value of P_{IC} is 17.1 kN hence rearranging Eq. (51) gives the fracture energy as 0.659 N/mm. The average value of δ_2 is 0.31 mm and therefore τ_f is 4.21 MPa to maintain the average fracture energy. Using these values for τ_f and δ_2, δ_1 was calibrated for each test with 0.1 mm obtained for the first test, 0.13 mm for the second test and 0.27 mm for the third test. Hence the average of these three values for δ_1 is 0.17 mm. The global load-slip relationship obtained with these properties is compared to the experimental curves in Fig. 17. It is noted that there is considerable variability in these tests which suggests that in practice more tests may be required.

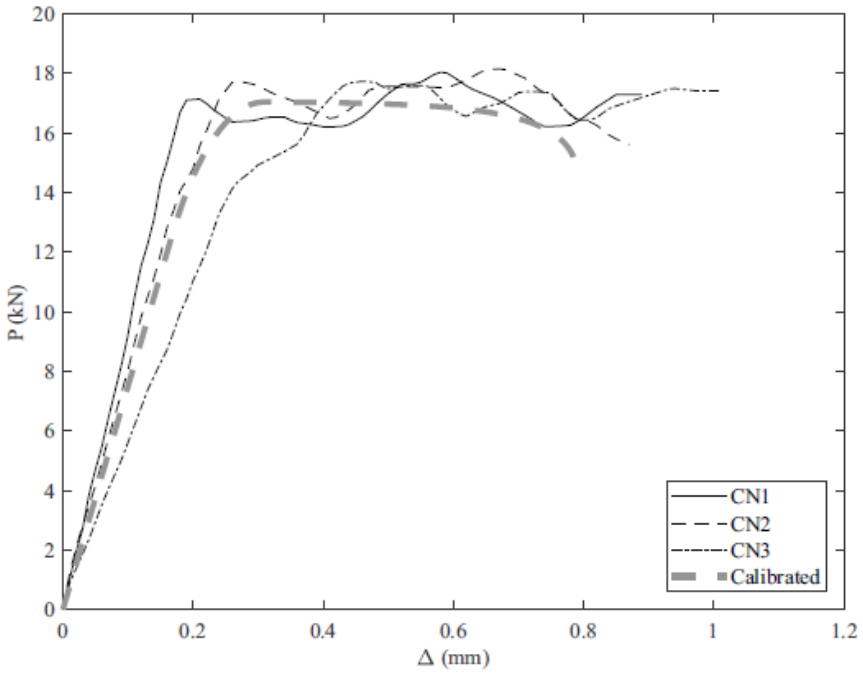

Fig. 17: Global bond properties

The single anchor specimen test will now be used to determine the load-slip properties of the anchor. Note that because there is a short plateau at the maximum load the simplified analysis can be applied. The maximum load in the anchored plate in Fig. 14(a) is 36.6 kN and from the bond-slip properties defined earlier P_{IC} in this case is given by 17.1 kN. Hence the maximum load in the anchor, $P_{a,u}$ is given by 19.5 kN. From this a slip to yield the anchor of 0.45 mm was calibrated. In Fig. 8, it can be seen visually that the calibrated properties give a reasonable fit in terms of the peak load and the debonding slip. Quantitively the root mean square error is 0.0857 kN for the single anchor case and 0.123 kN for the two anchor case. The definition of the root mean square error is given by (Vaculik et al. 2018b). This demonstrates that this simplified method can be used to reduce the computational effort required to determine these properties and provide reasonable results even when only a limited number of tests are used for the calibration (3 tests were used to determine the bond-slip properties of the interface and 1 test was used to determine the response of the anchor). The fit is expected to improve if a more significant number of tests were performed.

CONCLUSION

A relatively straightforward matrix-based formulation has been developed that simulates the partial interaction behaviour of FRP plates that are adhesively bonded and anchored to brittle substrates. Though as the primary focus has been on concrete more research maybe required for the specific application to masonry. In the matrix formulation, the slip and slip strain at any point is given by the product of a solution matrix, which is itself a function of the position and the zone of solution (elastic, softening or debonding) and a coefficient vector.

The procedure has been used to simulate push-pull tests to explain their behaviour. From these analyses, it has been shown that the behaviour of push-pull tests is complex because of the influence and interaction of the bond properties of the adhesive interface and the mechanical anchorage. Because of this, it is extremely difficult to extract the bond properties of the adhesive bond and the anchor directly through tests alone. However, it has been shown with examples that the use of this partial interaction procedure in conjunction with tests allows these

bond properties to be extracted directly and accurately. This should assist in the development of mechanical anchors and provide accurate bond properties for the simulation of FRP retrofitted beams for use in design.

ACKNOWLEDGEMENTS

The authors acknowledge the financial support of the Australian Government Research Training Program Scholarship awarded first author.

APPENDIX A WORKED EXAMPLE

To demonstrate the application of the developed solution method, a worked example is now provided. The geometry of the assumed arrangement is illustrated in Fig. A1 where the bond-slip relationship of the interface and the load-slip relationship of the anchor is the same as for the validation. Let us arbitrarily impose a free-end slip (δ_0) of 0.04 mm and calculate the corresponding P and Δ.

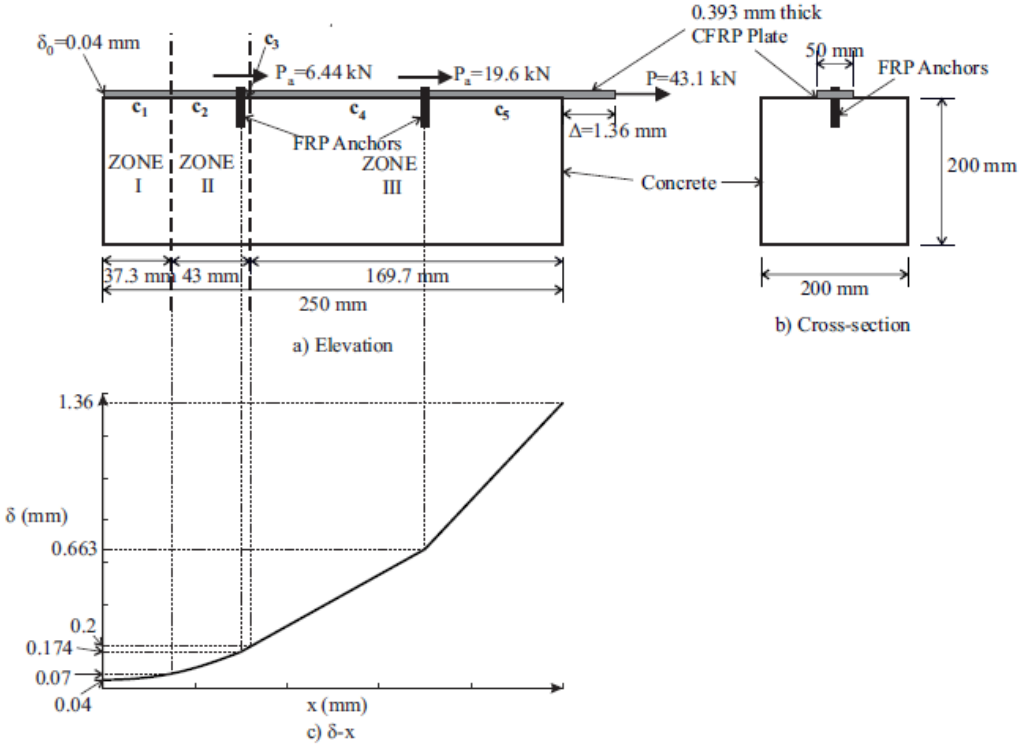

Fig. A1: Geometry for worked solution

First calculate the effective axial rigidity of the system. So from Eq. (3),

$$EA_{eff} = \frac{1}{\frac{1}{227000\ MPa\ (50\ mm)\ (0.393\ mm)} + \frac{1}{31500\ MPa\ (200\ mm)^2}} = 4.44 \times 10^6\ N \quad \text{(A1)}$$

which is marginally less than the axial rigidity of the plate (E_pA_p = 4.46x10^6 N). Hence the flexibility of the concrete block tends to be of little consequence in this case.

From Eq. (2), the β factor is given as

$$\beta = \frac{50\ mm}{4.44 \times 10^6\ N} = 11.2 \times 10^{-6}\frac{mm}{N} \quad \text{(A2)}$$

The slope of the ascending portion of the bond-slip relationship is given as

$$k = \frac{\tau_f}{\delta_1} = \frac{5.99\ MPa}{0.07\ mm} = 85.6\frac{MPa}{mm} \quad \text{(A3)}$$

Therefore from Eq. (6)

$$\lambda_1 = \sqrt{85.6\frac{MPa}{mm}\left(11.2\times10^{-6}\frac{mm}{N}\right)} = 0.0310\frac{1}{mm} \tag{A4}$$

The slope of the linear descending portion is given by

$$k_d = \frac{\tau_f}{\delta_2 - \delta_1} = \frac{5.99\ MPa}{0.2\ mm - 0.07\ mm} = 46.1\frac{MPa}{mm} \tag{A5}$$

Therefore from Eq. (13)

$$\lambda_2 = \sqrt{46.1\frac{MPa}{mm}\left(11.2\times10^{-6}\frac{mm}{N}\right)} = 0.0228\frac{1}{mm} \tag{A6}$$

Now impose a free end slip δ_0 of 0.04 mm; hence from Eq. (24)

$$\boldsymbol{c_1} = \begin{bmatrix} 0 \\ 0.04\ mm \end{bmatrix} \tag{A7}$$

The next step is to calculate the distance x_1 to the next transition point, so from Eq. (32)

$$x_1 = \frac{1}{0.0310\frac{1}{mm}}\ln\left(\frac{0.07\ mm + \sqrt{(0.07\ mm)^2 - (0.04\ mm)^2}}{0.04\ mm}\right) = 37.3\ mm \tag{A8}$$

Since the projected location of x_1 is 37.3 mm and the closest anchor is at x=75 mm, a zone transition occurs at x = 37.3 mm. To use Eq. (34) to determine the new value of the coefficient vector, $\mathbf{(S_2)^{-1}}|_{x=x1}$ and $\mathbf{S_1}|_{x=x1}$ are next evaluated, where these matrices are defined in Eq. (9) and (17)

$$\begin{aligned}(\boldsymbol{S_2})^{-1}|_{x=x_1} &= -\frac{1}{0.0228\frac{1}{mm}}\begin{bmatrix} -\left(0.0228\frac{1}{mm}\right)\sin\left[\left(0.0228\frac{1}{mm}\right)37.3\ mm\right] & -\cos\left[\left(0.0228\frac{1}{mm}\right)37.3\ mm\right] \\ -\left(0.0228\frac{1}{mm}\right)\cos\left[\left(0.0228\frac{1}{mm}\right)37.3\ mm\right] & \sin\left[\left(0.0228\frac{1}{mm}\right)37.3\ mm\right] \end{bmatrix} \\ &= \begin{bmatrix} 0.752 & 29.0 \\ 0.660 & -33.0 \end{bmatrix}\end{aligned} \tag{A9}$$

and

$$\begin{aligned}\boldsymbol{S_1}|_{x=x_1} &= \begin{bmatrix} \sinh\left[\left(0.0310\frac{1}{mm}\right)37.3\ mm\right] & \cosh\left[\left(0.0310\frac{1}{mm}\right)37.3\ mm\right] \\ \left(0.0310\frac{1}{mm}\right)\cosh\left[\left(0.0310\frac{1}{mm}\right)37.3\ mm\right] & \left(0.0310\frac{1}{mm}\right)\sinh\left[\left(0.0310\frac{1}{mm}\right)37.3\ mm\right] \end{bmatrix} \\ &= \begin{bmatrix} 1.44 & 1.75 \\ 0.0543 & 0.0446 \end{bmatrix}\end{aligned} \tag{A10}$$

Hence from Eq. (34), the coefficient vector is given by

$$\boldsymbol{c_2} = \begin{bmatrix} 0.752 & 29.0 \\ 0.660 & -33.0 \end{bmatrix}\begin{bmatrix} 1.44 & 1.75 \\ 0.0543 & 0.0446 \end{bmatrix}\begin{bmatrix} 0 \\ 0.04\ mm \end{bmatrix} - 0.2\ mm\begin{bmatrix} \sin\left[\left(0.0228\frac{1}{mm}\right)37.3\ mm\right] \\ \cos\left[\left(0.0228\frac{1}{mm}\right)37.3\ mm\right] \end{bmatrix} = \begin{bmatrix} -0.0460 \\ -0.145 \end{bmatrix} \tag{A11}$$

So now calculate the distance to the next transition point. From Eq. (39)

$$\begin{aligned} x_2 &= \frac{2}{0.0228\frac{1}{mm}}\left\{\arctan\left[\frac{-0.0460}{-0.145} \pm \sqrt{1 + \left(\frac{-0.0460}{-0.145}\right)^2}\right] + n\pi\right\} \\ &= (-55.5\ mm\ or\ 82.5\ mm) + n\ (276\ mm) \end{aligned} \tag{A12}$$

The projected location of x_2 is 82.5 mm. However, the next anchor is located closer at 75 mm, and thus x = 75 mm defines the next transition point. From Eq. (17), the slip at the anchor is given by

$$\delta_a = \left[\sin\left[\left(0.0228\frac{1}{mm}\right)75\ mm\right] \quad \cos\left[\left(0.0228\frac{1}{mm}\right)75\ mm\right]\right]\begin{bmatrix} -0.0460 \\ -0.145 \end{bmatrix} + 0.2\ \text{mm} = 0.174\ \text{mm} \tag{A13}$$

As the slip is less than 0.53 mm (δ_y), the anchor remains linear elastic. Thus,

$$P_a = \frac{19600\ N}{0.53\ mm}0.174\ mm = 6440\ N \tag{A14}$$

The change in the coefficient vector is given by Eq. (48) as

$$\boldsymbol{c_3} = \boldsymbol{c_2} + \frac{6440\ N}{\left(0.0228\frac{1}{mm}\right)(4.44\times10^6\ N)}\begin{bmatrix}\cos\left[\left(0.0228\frac{1}{mm}\right)75\ mm\right]\\ -\sin\left[\left(0.0228\frac{1}{mm}\right)75\ mm\right]\end{bmatrix} = \begin{bmatrix}-0.0547\\ -0.208\end{bmatrix} \quad \text{(A15)}$$

The distance to the next transition can again be calculated using Eq. (39).

$$x_2 = \frac{2}{0.0228\frac{1}{mm}}\left\{\arctan\left[\frac{-0.0547}{-0.208} - \sqrt{1+\left(\frac{-0.0547}{-0.208}\right)^2}\right]\right\} = 80.3\ mm \quad \text{(A16)}$$

From this, x_2 is equal to 80.3 mm, therefore, the Zone II to III transition occurs here. To use Eq. (41) to compute the change in the coefficient vector at this location $\boldsymbol{(S_3)^{-1}}|_{x=x2}$ and $\boldsymbol{S_2}|_{x=x2}$ need to be evaluated, where these matrices are defined in Eqs. (9) and (17). Therefore

$$(\boldsymbol{S_3})^{-\mathbf{1}}\big|_{x=x_2} = -\begin{bmatrix}0 & -1\\ -1 & 80.3\ mm\end{bmatrix} \quad \text{(A17)}$$

$$\boldsymbol{S_2}|_{x=x_1} = \begin{bmatrix}\sin\left[\left(0.0228\frac{1}{mm}\right)80.3\ mm\right] & \cosh\left[\left(0.0228\frac{1}{mm}\right)80.3\ mm\right]\\ \left(0.0228\frac{1}{mm}\right)\cos\left[\left(0.0228\frac{1}{mm}\right)80.3\ mm\right] & \left(0.0228\frac{1}{mm}\right)\sin\left[\left(0.0228\frac{1}{mm}\right)80.3\ mm\right]\end{bmatrix} = \begin{bmatrix}0.967 & -0.255\\ -0.0058 & 0.0220\end{bmatrix} \quad \text{(A18)}$$

So from Eq. (41), the new coefficient vector can be computed as

$$\boldsymbol{c_4} = \begin{bmatrix}0 & 1\\ 1 & -80.3\ mm\end{bmatrix}\begin{bmatrix}0.967 & -0.255\\ -0.0058 & 0.0220\end{bmatrix}\begin{bmatrix}-0.0547\\ -0.208\end{bmatrix} + \begin{bmatrix}0\\ 0.2\ mm\end{bmatrix} = \begin{bmatrix}0.0049\\ -0.193\end{bmatrix} \quad \text{(A19)}$$

As Zone III is now achieved, the next change in the coefficient vector is achieved at the second anchor. So the slip at the next anchor is given by Eq. (21) as

$$\delta_a = [175\ mm \quad 1]\begin{bmatrix}0.0049\\ -0.193\end{bmatrix} = 0.663\ mm \quad \text{(A20)}$$

This slip is between 0.53 mm (δ_y) and 3.82 mm (δ_{db}) and so the second anchor is within the plastic region; thus providing the load 19600 N. The change in the coefficient vector is then given by Eq. (50) as

$$\boldsymbol{c_5} = \boldsymbol{c_4} + \frac{19600\ N}{4.44\times10^6\ N}\begin{bmatrix}1\\ -175\ mm\end{bmatrix} = \begin{bmatrix}0.0093\\ -0.964\end{bmatrix} \quad \text{(A21)}$$

After this anchor, the end of the plate is then reached. At this point the load and slip are given by the boundary condition in Eq. (27) and Eq. (21), the slip and slip strain at the end of the plate are given by

$$\begin{bmatrix}\Delta\\ P\\ \overline{EA_{eff}}\end{bmatrix} = \begin{bmatrix}250\ mm & 1\\ 1 & 0\end{bmatrix}\begin{bmatrix}0.0093\\ -0.964\end{bmatrix} = \begin{bmatrix}1.36\\ 0.0093\end{bmatrix} \quad \text{(A22)}$$

Therefore, at the imposed δ_0 value of 0.04 mm, the loaded-end slip is Δ = 1.36 mm, and the load is P = 41.3 kN.

NOTATION

A_p, A_c = cross-sectional area of plate and substrate, respectively;
$\boldsymbol{c}$, $\boldsymbol{c_i}$ = 2x1 coefficient vector; note the subscript i is a label that is used to distinguish between the coefficient vector along different portions of the bonded length;
c_1, c_2 = elements of coefficient vector; $\boldsymbol{c} = [c_1\ c_2]^T$;
$d\delta/dx$ = slip strain;
E_p, E_c = elastic modulus of plate and substrate, respectively;
$\boldsymbol{e_1}, \boldsymbol{e_2}$ = standard basis vectors of 2D space;
EA_{eff} = effective axial rigidity of system;

G_f = fracture energy;
k, k_d = magnitude of the slope of the bond-slip relationship for the ascending and descending portions, respectively;
L = bonded length;
L_c = critical length: length required to obtain P_{IC};
L_p = bonded perimeter of interface between plate and substrate;
P = load applied to end of plate;
P_a, $P_{a,u}$ = load in anchor; ultimate load in anchor;
$P_{c,L}$, $P_{c,R}$ = load in substrate at left and right side of the anchor, respectively;
$P_{c,L}$, $P_{p,R}$ = load in plate at left and right side of the anchor, respectively;
P_{IC} = Load at IC debonding;
P_{max} = maximum load;
P_{pl} = plastic load in anchor;
s = spacing between anchors;
$\boldsymbol{S_1}$, $\boldsymbol{S_2}$, $\boldsymbol{S_3}$ = 2x2 solution matrix; the subscript indicates the zone;
$\boldsymbol{T_{12}}$, $\boldsymbol{T_{23}}$ = 2x2 transition matrix;
x = position along plate;
x_a = position of anchor;
x_{db} = distance from free end to debond anchor;
x_y = distance from the free end to yield the anchor;
x_1, x_2 = location of transition between zone I and II, and zones II and III, respectively;
β = ratio of the effective axial rigidity to the bonded perimeter;
Δ = loaded end slip;
δ = slip;
δ_a, $\delta_{a,u}$, $\delta_{a,y}$ = slip at anchor; ultimate slip of anchor; yielding slip of anchor;
δ_h = homogeneous solution;
δ_p = particular solution;
δ_0 = free end slip;
δ_1 = slip at peak bond stress;
δ_2 = slip at debonding;
ε_p, ε_c = axial strain in plate and substrate, respectively;
λ_1, λ_2 = bond parameter for Zones I and II;
τ = interface shear stress; bond stress;
τ_f = peak bond stress;

REFERENCES

ACI (American Concrete Institute) (2017) “440.2R-17 Guide for the Design and Construction of Externally Bonded FRP Systems for Strengthening Concrete Structures.” *ACI 440.2R-17*, Farmington Hills.

Balazs, G. L. (1993) "Cracking analysis based on slip and bond stresses." *ACI Materials Journal*, 90(4), 340-348.

Bank, L. C. and Arora, D. (2007) “Analysis of RC beams strengthened with mechanically fastened FRP (MF-FRP) strips.” *Composite Structures*. 79(2), 180-191.

Caggiano, A., Martinelli, E. and Faella, C. (2012) “A fully-analytical approach for modelling the response of FRP plates bonded to a brittle substrate.” *International Journal of Solids and Structures*. 49(17), 2291-2300.

Ceroni, F. (2017) “Bond tests to evaluate the effectiveness of anchoring devices for CFRP sheets epoxy bonded over masonry elements.” *Composites Part B: Engineering*. 113, 317-330.

Chen, J. F., Yuan, H. and Teng, J. G. (2007) “Debonding failure along a softening FRP-to-concrete interface between two adjacent cracks in concrete members.” *Engineering Structures*. 29(2), 259-270.

Cicero, S., Torabi, A. R., Madrazo, V. and Azizi, P. (2018) “Prediction of fracture loads in PMMA U-notched specimens using the equivalent material concept and the theory of critical distances combined criterion.” *Fatigue & Fracture of Engineering Materials & Structures*. 41(3), 688-699.

Cornetti, P. and Carpinteri, A. (2011) “Modelling the FRP-concrete delamination by means of an exponential softening law.” *Engineering Structures*. 33(6), 1988-2001.

Cosenza, E., Manfredi, G. and Realfonzo, R. (2002) “Development length of FRP straight rebars.” *Composites Part B: Engineering*. 33(7), 493-504.

Fagone, M., Ranocchiai, G., Caggegi, C., Bati, S. B. and Cuomo, M. (2014) “The efficiency of mechanical anchors in CFRP strengthening of masonry: an experimental analysis.” *Composites Part B: Engineering*. 64, 1-15.

Fagone, M. and Ranocchiai, G. (2018) “Experimental investigation on out-of-plane behavior of masonry panels strengthened with CFRP sheets.” *Composites Part B: Engineering*. 150, 14-26.

Grande, E., Imbimbo, M. and Sacco, E. (2013) “Finite element analysis of masonry panels strengthened with FRPs.” *Composites Part B: Engineering*. 45(1), 1296-1309.

Grelle, S. V. and Sneed, L. H. (2013) “Review of anchorage systems for externally bonded FRP laminates.” *International Journal of Concrete Structures and Materials*. 7(1):17-33.

Kalfat, R., Al-Mahaidi, R. and Smith, S.T. (2011) “Anchorage devices used to improve the performance of reinforced concrete beams retrofitted with FRP composites: State-of-the-art review.” *Journal of Composites for Construction*. 17(1),14-33.

Kalfat, R. and Al-Mahaidi, R. (2016) “Mitigation of premature failure of FRP bonded to concrete using mechanical substrate strengthening and FRP spike anchors.” *Composites Part B: Engineering*. 94, 209-217.

Koutas, L. and Triantafillou, T. C. (2012) “Use of anchors in shear strengthening of reinforced concrete T-beams with FRP.” *Journal of Composites for Construction*. 17(1), 101-107.

Lee, S. C., Cho, J. Y. and Vecchio, F. J. (2013) “Tension-Stiffening Model for Steel Fiber-Reinforced Concrete Containing Conventional Reinforcement.” *ACI Structural Journal*. 110(4), 639-648.

Muhamad, R., Mohamed Ali, M. S., Oehlers, D. J. and Griffith, M. C. (2012) "The tension stiffening mechanism in reinforced concrete prisms." *Advances in Structural Engineering*. 15(12), 2053-2069.

Niemitz, C. W., James, R. and Breña, S. F. (2010) "Experimental behavior of carbon fiber-reinforced polymer (CFRP) sheets attached to concrete surfaces using CFRP anchors." *Journal of Composites for Construction*. 14(2), 185-194.

Oehlers, D. J., Visintin, P. and Lucas, W. (2016) "Fundamental mechanics governing FRP-retrofitted RC beams with anchored and prestressed FRP plates." *Journal of Composites for Construction*. 20(6), 04016047.

Orton, S. L., Jirsa, J. O. and Bayrak, O. (2008) "Design considerations of carbon fiber anchors." *Journal of Composites for Construction*. 12(6), 608-616.

Rahimi, A. S., Ayatollahi, M. R. and Torabi, A. R. (2018) "Fracture study in notched ductile polymeric plates subjected to mixed mode I/II loading: Application of equivalent material concept." *European Journal of Mechanics-A/Solids*. 70, 37-43.

Realfonzo, R., Martinelli, E., Napoli, A. and Nunziata, B. (2013) "Experimental investigation of the mechanical connection between FRP laminates and concrete." *Composites Part B: Engineering*. 45(1), 341-355.

Reboul, N., Larbi, A.S. and Ferrier, E. (2018) "Two-way bending behaviour of hollow concrete block masonry walls reinforced by composite materials." *Composites Part B: Engineering*. 137, 163-177.

Ren, F. F., Yang, Z. J., Chen, J. F. and Chen, W. W. (2010) "An analytical analysis of the full-range behaviour of grouted rockbolts based on a tri-linear bond-slip model." *Construction and Building Materials*. 24(3), 361-370.

Smith, S. T., Hu, S., Kim, S. J. and Seracino, R. (2011) "FRP-strengthened RC slabs anchored with FRP anchors." *Engineering Structures*. 33(4), 1075-1087.

Standards Australia (2009). "Concrete Structures", *AS3600-2009*, Sydney.

Sturm, A. B., Visintin, P. and Oehlers, D. J. (2018) "Time-dependent serviceability behavior of reinforced concrete beams: Partial interaction tension stiffening mechanics." *Structural Concrete*. 19(2), 508-523.

Tan, K. H. and Patoary, M. K. (2004) "Strengthening of masonry walls against out-of-plane loads using fiber-reinforced polymer reinforcement." *Journal of Composites for Construction*. 8(1), 79-87.

Teng, J. G., Yuan, H. and Chen, J. F. (2006) "FRP-to-concrete interfaces between two adjacent cracks: Theoretical model for debonding failure." *International Journal of Solids and Structures*. 43(18-19), 5750-5778.

Torabi, A. R., Rahimi, A. S. and Ayatollahi, M. R. (2017) "Tensile fracture analysis of a ductile polymeric material weakened by U-notches." *Polymer Testing*. 64, 117-126.

Torabi, A. R., Rahimi, A. S. and Ayatollahi, M. R. (2018) “Fracture study of a ductile polymer-based nanocomposite weakened by blunt V-notches under mode I loading: Application of the Equivalent Material Concept.” *Theoretical and Applied Fracture Mechanics*. 94, 26-33.

Vaculik, J., Visintin, P., Burton, N. G., Griffith, M. C. and Seracino, R. (2018a) “State-of-the-art review and future research directions for FRP-to-masonry bond research: Test methods and techniques for extraction of bond-slip behaviour.” *Construction and Building Materials*. 183, 325-345.

Vaculik, J., Sturm, A. B., Visintin, P. and Griffith, M. C. (2018b) “Modelling FRP-to- substrate joints using the bilinear τ-δ rule with allowance for friction—Full-range analytical solutions for long and short bonded lengths.” *International Journal of Solids & Structures*, 135, 245-260.

Volkersen, O. (1938) "Die Nietkrafverteilung in zugbeanspruchten Nietverbindungen mit konstanten Laschenquerschnitten." *Luftfahrtvorschung*, 15, 41-47.

Wu, Y. F. and Huang Y. (2008) “Hybrid bonding of FRP to reinforced concrete structures.” *Journal of Composites for Construction*. 12(3), 266-273.

Wu, Y. F., Wang, Z., Liu, K., He, W. and Wang, Z. (2009) “Numerical Analyses of Hybrid-Bonded FRP Strengthened Concrete Beams.” *Computer-Aided Civil and Infrastructure Engineering*. 24(5), 371-384.

Yuan, H., Teng, J. G., Seracino, R., Wu, Z. S., Yao, J. (2004) “Full-range behavior of FRP-to-concrete bonded joints.” *Engineering Structures*. 26(5), 553-565.

Zhang, H. W., Smith, S. T. and Kim, S. J. (2012) “Optimisation of carbon and glass FRP anchor design.” *Construction and Building Materials*. 32, 1-12.

Zhang, H., (2013) “Influence of FRP anchors on FRP-to-concrete bonder interfaces.” Ph.D. Thesis, The University of Hong Kong.

Zhang, H., Smith, S. T., Gravina, R. J. and Wang, Z. (2017) “Modelling of FRP-concrete bonded interfaces containing FRP anchors.” *Construction and Building Materials*. 139, 394-402.

CHAPTER 6

Concluding Remarks

In this thesis solutions for the flexural and shear behaviour of ultra-high performance fibre reinforced concrete (UHPFRC) beams have been developed by applying the principles of partial interaction, segmental method and shear friction. Further, the inputs for these solutions are all available from basic material tests such as compression, tension, pullout, shear, shrinkage and creep. Being based only on the inputs of these basic material tests is significant as it removes the need to calibrate empirical factors with member level tests thereby significantly reducing the cost and speeding up the development of new materials.

First the material properties used later in the thesis were obtained and a new testing apparatus was designed to obtain the shear friction properties. The effect of fibre type was also investigated where the effect was found to be significant for tension and tension stiffening. This was not the case however for bond and shear friction.

Closed-form solutions were then derived by applying partial interaction theory and segmental analysis and validated for the crack spacing, load-slip relationship of tensile reinforcement, serviceability deflections and crack widths.

The effect of fibre type was then investigated for the flexural behaviour of a UHPFRC beam where the effect of fibre type was again found to be significant. The effect of prestress and fibre reinforced polymer (FRP) reinforcement was also investigated where it was found that using carbon fibre reinforced polymer tendons significantly increased the force that could be applied to the section at the rupture of the tendon as compared to conventional steel tendons. A segmental analysis was also validated for predicting the deflections and crack widths of UHPFRC beams with and without prestress where partial interaction was used to simulate the reinforcement and shear friction was used to simulate concrete softening. Closed-form solutions were also developed for the moment redistribution of all types of reinforced concrete and UHPFRC beams.

Numerical and analytical solutions are derived for the shear capacity of UHPFRC beams which were than validated and compared to existing solutions demonstrating their accuracy. These solutions utilised segmental analysis to determine the sliding force applied to a critical shear crack and then shear friction was applied to determine the resistance to this force. These solutions were then simplified to produce solutions for the shear capacity of fibre reinforced concrete beams that are more accurate and simpler to apply than the current Australian standard.

Finally, the versatility of the approach developed in this paper is demonstrated with closed form solutions for FRP plates bonded to brittle substrates with and without anchors using the same underlying mechanics.

Possible extensions of this work include developing a material model for the post-yield bond of steel reinforcement embedded in UHPFRC. This is important as the failure of UHPFRC beams are typically controlled by the rupture of the reinforcement for practical reinforcement ratios due to the high concrete strength. This would then allow the development of closed form solutions for the ultimate rotation of UHPFRC members as well as solutions for the development length of reinforcement embedded in UHPFRC. Another possible extension of this work is the applications of these methods to the behaviour of UHPFRC columns subject

to seismic loads. This is important as accurate predictions of deflections under a combination of axial and cyclic loads are required for the application of displacement based seismic design. The approaches presented here are ideal for extension as most current approaches for predicting deflections that are used with displacement-based design utilise an empirical hinge length. However, the combination of shear friction theory and segmental analysis allows the hinge length to be determined from mechanics. This will facilitate the extension of displacement based seismic design to new materials without having to rederive an empirical expression for the hinge length.